

Determination of the strong coupling α_s from transverse energy-energy correlations in multi-jet events at $\sqrt{s} = 13 \text{ TeV}$ with the ATLAS detector

Memoria de Tesis Doctoral realizada por
Manuel Álvarez Estévez
para optar al Título de Doctor en Física Teórica

Tesis Doctoral dirigida por
Fernando Barreiro Alonso
y **Javier Llorente Merino**

Facultad de Ciencias
Departamento de Física Teórica
UNIVERSIDAD AUTÓNOMA DE MADRID
Madrid, Noviembre de 2022

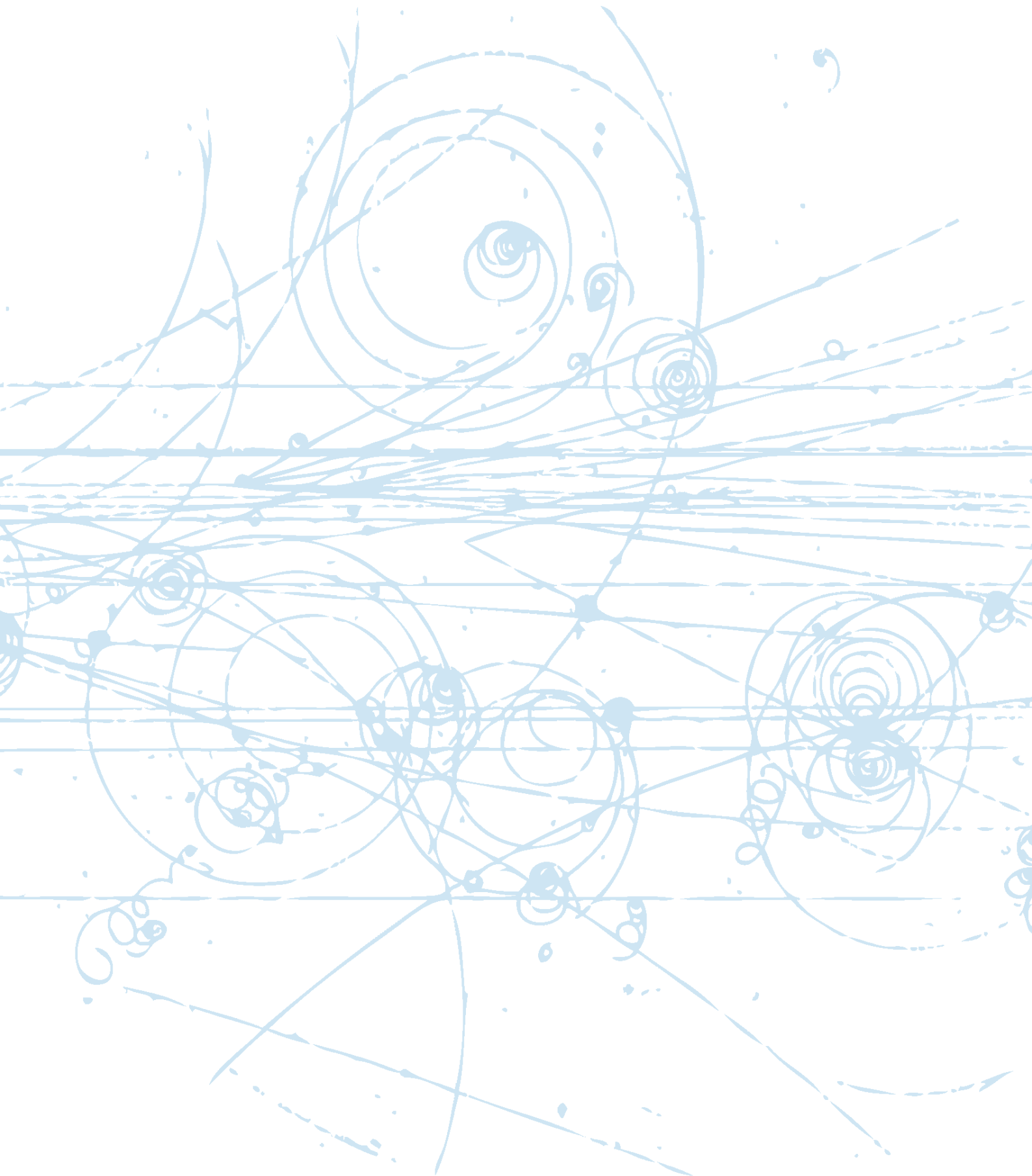
Copyright © 2022 by M. Álvarez Estévez
All rights reserved.

A mi familia y amigos

Few people who are not actually practitioners of a mature science realize how much mop-up work of this sort a paradigm leaves to be done or quite how fascinating such work can prove in the execution. And these points need to be understood. Mop-ping-up operations are what engage most scientists throughout their careers. They constitute what I am here calling normal science. Closely examined, whether historically or in the contemporary laboratory, that enterprise seems an attempt to force nature into the preformed and relatively inflexible box that the paradigm supplies.¹

Thomas S. Kuhn, *The Structure of Scientific Revolutions* III (1962).

¹Pocas personas que no sean realmente practicantes de una ciencia madura llegan a comprender cuánto trabajo de limpieza de esta especie deja un paradigma para hacer, o cuán atrayente puede resultar la ejecución de dicho trabajo. Y es preciso comprender estos puntos. Las operaciones de limpieza son las que ocupan a la mayoría de los científicos durante todas sus carreras. Constituyen lo que llamo aquí ciencia normal. Examinada de cerca, tanto históricamente como en el laboratorio contemporáneo, esa empresa parece ser un intento de obligar a la naturaleza a que encaje dentro de los límites pre establecidos y relativamente inflexibles que proporciona el paradigma.



Contents

Preface	vii
1 Historical context	1
2 Theoretical framework	4
2.1 Quantum Chromodynamics	5
2.1.1 Gauge theory	6
2.1.2 Renormalization	9
2.1.3 Factorization	12
2.1.4 Hadron structure	15
2.2 Collider techniques	18
2.2.1 Coordinate system	19
2.2.2 Higher-order emissions	20
2.2.3 Fragmentation schemes	22
2.2.4 Event-shape variables	23
2.2.5 Jet algorithms	26
2.2.6 Underlying event	28
2.2.7 Monte Carlo methods	29
3 Experimental setup	31
3.1 The LHC accelerator	31
3.2 The ATLAS detector	34
3.2.1 Inner Detector	35
3.2.2 Calorimeter System	37
3.2.3 Muon Spectrometer	39
3.2.4 Trigger and Data-Acquisition System	41
4 Computing projects	43
4.1 Monte Carlo Event Generators	44
4.1.1 Fixed-order generators	45
4.1.2 General-purpose generators	46
4.2 The Worldwide LHC Computing Grid	47
4.3 ATLAS Computing and Software	47
4.3.1 Data preparation	48
4.3.2 Monte Carlo production	48

5 Object reconstruction and calibration	51
5.1 Tracks and vertices	51
5.2 Jet reconstruction	52
5.2.1 Topological clusters	53
5.2.2 Particle-flow reconstruction technique	54
5.3 Jet energy scale calibration	56
5.3.1 Simulation-based calibration	57
5.3.2 <i>In situ</i> calibration	59
5.3.3 Systematic uncertainties	60
5.4 Jet energy resolution	62
5.4.1 Resolution measurement	62
5.4.2 Noise measurement	63
5.4.3 Total <i>in situ</i> combination	63
5.4.4 Systematic uncertainties	63
5.5 Jet quality criteria	64
6 Asymptotic freedom beyond the TeV scale	66
6.1 Data and Monte Carlo samples	68
6.1.1 Control plots for MC predictions	69
6.2 Detector-level results	72
6.3 Iterative Bayesian unfolding	80
6.4 Statistical uncertainty	86
6.5 Systematic uncertainties	95
6.5.1 Unfolding Closure Test	124
6.6 Experimental results	131
6.7 Theoretical predictions	158
6.7.1 Theoretical systematic uncertainties	169
6.8 Comparison of theory and experiment	174
6.9 Determination of the strong coupling	188
6.9.1 Scale evolution of the coupling	190
6.9.2 Correlations between fits	191
6.9.3 Fits to the TEEC function	193
6.9.4 Fits to the ATEEC function	210
6.9.5 Comparison with previous extractions	227
7 Summary and conclusions	228
A Appendix	232
A.1 Complementary and additional studies	232
A.1.1 Dead tile modules	232
A.1.2 Bin-by-bin migrations	232
A.1.3 Jets' collections	233
A.1.4 Parton showers and hadronization schemes	233
A.2 Fits using the binning in data	244

Preface

The production of multi-jet events in particle colliders is widely used to determine fundamental parameters such as the strong coupling constant. The objective of this PhD thesis is to determine this parameter at high energy scales with great precision through measurements in multi-jet events of observables such as transverse energy-energy correlations. To date, the Large Hadron Collider (LHC) has produced a large number of these events at a center-of-mass energy of $\sqrt{s} = 13$ TeV, collected with multi-purpose detectors like ATLAS.

Although the ATLAS collaboration has published measurements of these observables [1, 2], this analysis extends previous results to higher energy scales, achieving great precision and covering a wider range. The first experimental results were made public for the 40th International Conference on High Energy Physics (ICHEP) [3]. Subsequently, they have been improved and used for the determination of the strong coupling constant. It should be noted that this study contains the first determination of this parameter at next-to-next-to-leading-order (NNLO) accuracy in multi-jet events.

This PhD thesis is structured in seven chapters. Chapters 1 and 2 introduce both the historical context and the theoretical framework required to understanding the thesis. For instance, an explanation of the theory that describes strong interactions, Quantum Chromodynamics. This theory was experimentally verified in particle colliders, whose experiments along with the most relevant techniques and observables are briefly discussed at the end of these chapters. Chapter 3 focuses specifically on the operation of the LHC accelerator and the ATLAS detector at CERN. The detector components are presented separately to capture the complexity of the entire system. For completeness, Chapter 4 explains in a nutshell the huge computational infrastructure that has been required, mentioning the main projects and simulations. Chapter 5 discusses the detector performance in terms of reconstruction and calibration of objects used in the analysis, which can be found in Chapter 6. Finally, Chapter 7 contains a summary of the thesis and its conclusions. The last chapter is written in English and Spanish. The other contents can only be found in English with the exception of the acknowledgments that are written in Spanish. In addition, this preface is translated into Spanish hereunder.

Presentación

La producción de sucesos multi-jet en colisionadores de partículas es ampliamente utilizada para la determinación de parámetros fundamentales como la constante de acople fuerte. El objetivo de esta tesis doctoral es determinar este parámetro a altas escalas de energía y con gran precisión a través de mediciones en sucesos multi-jet de observables como las correlaciones de energía-energía transversa. A día de hoy, el gran colisionador de hadrones (LHC) ha proporcionado una enorme cantidad de estos sucesos a una energía de centro-de-masas de $\sqrt{s} = 13$ TeV y registrados por detectores multi-propósito como ATLAS.

Aunque la colaboración ATLAS ha publicado análisis de estos observables [1, 2], el presente análisis extiende estos resultados a escalas de energía más altas, destacando por la precisión de sus medidas y el amplio rango que cubren. Los primeros resultados experimentales se hicieron públicos para la cuadragésima Conferencia Internacional de Física de Altas Energías (ICHEP) [3]. Posteriormente, se han mejorado y utilizado para la determinación de la constante de acople fuerte. Tenemos que acentuar que este estudio contiene la primera determinación de dicho parámetro con precisión *next-to-next-to-leading-order* (NNLO) en sucesos multi-jet.

La presente tesis doctoral está estructurada en siete capítulos. Los capítulos 1 y 2 introducen tanto el contexto histórico como el marco teórico necesario para comprender la tesis. En ellos encontramos una explicación de la teoría que describe la interacción fuerte, cromodinámica cuántica. Esta teoría fue corroborada experimentalmente en los colisionadores de partículas, cuyos experimentos junto con las técnicas y los observables más relevantes se discuten brevemente al final de estos capítulos. El capítulo 3 se centra específicamente en el acelerador LHC y el detector ATLAS que operan en el CERN. Las componentes del detector se exponen separadamente con el objetivo de captar la complejidad de todo el sistema. Por completitud, el capítulo 4 explica superficialmente la enorme infraestructura computacional que ha sido requerida, mencionando los proyectos y las simulaciones principales. El capítulo 5 discute la actividad del detector en términos de reconstrucción y calibración de los objetos empleados en el análisis, el cual se encuentra en el capítulo 6. Finalmente, el capítulo 7 contiene un resumen de la tesis y sus conclusiones. Este último capítulo ha sido redactado en inglés y en español. El resto de la tesis doctoral se encuentra únicamente en inglés con la excepción de los agradecimientos que se han escrito en español.

Agradecimientos

Esta tesis doctoral es el resultado del trabajo llevado a cabo tanto por mí como por todas las personas que me han ayudado a lo largo de estos años. Destacando a Fernando Barreiro y Javier Llorente, no sólo por la supervisión de mi trabajo, sino también por su inmenso apoyo y dedicación. Me siento afortunado de haber

trabajado con personas tan valiosas a nivel humano y profesional. Mi estima hacia ellos es alta y estoy seguro que siempre lo será.

Agradezco a la UAM todo lo que ha hecho por mí durante tanto tiempo. En particular, a todo su equipo de ATLAS formado por Juan Terrón, Claudia Glasman y José del Peso. Todos ellos junto con Almudena Montiel han sido un enorme apoyo a nivel científico, administrativo e informático, aspectos cruciales para el desarrollo óptimo de esta tesis doctoral. No me olvido de Ana Cueto, Sergio Calvete y Daniel Camarero, antiguos estudiantes de doctorado y ahora doctores, así como inmejorables compañeros a los que les deseo lo mejor en sus carreras.

También quiero reconocer el papel del CERN por el excelente funcionamiento del LHC y la WLCG, así como a todos los miembros de la colaboración ATLAS responsables de la adecuada actividad del detector. Me gustaría mencionar a los convocantes del grupo *Standard Model* y el subgrupo *Jet & Photon* que han ayudado a conformar el resultado final del análisis presentado en esta tesis: Josu Cantero, Jennifer Kathryn Roloff, Matt LeBlanc, Andrew Denis Pilkington, Evelin Meoni, Oldrich Kepka, Monica Dunford y Philip Sommer. La presidenta del Editorial Board, Amanda Cooper-Sarkar, merece toda mi gratitud, así como Rodney Walker por su labor gestionando los recursos de la WLCG. Igualmente, quiero recordar al equipo de LAr ATLAS y a Pavol Strizenec quien supervisó mis tareas de cualificación como autor.

Añado un agradecimiento especial para Rene Poncelet, Alexander Mitov y otros miembros del laboratorio Cavendish de Cambridge por la fructífera colaboración que hemos mantenido los últimos años. Permitiendo que nuestros esfuerzos por llevar la física a otro nivel se vean reflejados en los resultados de esta tesis doctoral.

Además de todos estos agradecimientos, quiero recordar al resto de personas que he conocido a lo largo de estos años. Entre ellas, mis amigos de Ginebra: Sérgio, Joan y Eda, así como mis compañeros del CERN: Mercedes, Carlos, Pili, Guillermo y Juan Carlos. Las experiencias que hemos vivido juntos han hecho mis estancias en el extranjero más que agradables. Por último, quiero agradecer a mi familia y amigos en Madrid su apoyo incondicional y todo lo que han hecho por mí durante tanto tiempo. Especialmente a mi padres Antonio y Mayte, mi hermana Bibiana, mi abuela Tere y mi sobrina Ágata. A todos vosotros os dedico esta tesis doctoral.

Manuel Álvarez Estévez

Madrid,

15 de noviembre de 2022

CHAPTER 1

Historical context

The progress of science is closely related to the study of nature. In ancient times, it was restricted to qualitative knowledge of things. However, the notion of phenomenon as a quantitative abstraction and the role it plays from the 17th century as a scientific object allowed the development of classical physics.

The 19th century was a triumphal period for classical physics. Nevertheless, despite brilliant successes, physics suffered from certain hidden malaises. For instance, the presence of discontinuities in nature. Although most physicists used continuous representations to describe physical phenomena, experimental results started to emerge in favour of a discontinuous nature for matter and electricity. The discovery of cathode rays indicated that electricity was always carried by extremely light corpuscles, which were called electrons. This was shown by Joseph J. Thomson in 1897.

Thereafter, the assertion that corpuscular discontinuities play an essential role was increasingly corroborated. The appearance of these quanta was vital to explain the black-body radiation. The spectral radiation density for this object was described by Max Planck in 1900 using an heuristically derived formula, which resolved the problem of the ultraviolet catastrophe predicted by classical physics. This idea was specified by Albert Einstein in 1905 thanks to the photoelectric effect. He proposed that a beam of light is a swarm of discrete energy quanta, which were called photons.

These ideas were considered to design new atomic models. For instance, the one of Ernest Rutherford in 1911, which theorized a small atomic nucleus. Although this model was incompatible with classical theories of radiation, the problem was solved with the ideas introduced by Niels Bohr in 1913 which explained the emission spectrum of atomic hydrogen. In 1917, Ernest Rutherford also proved that the hydrogen nucleus is present in other nuclei, a result generally described as the discovery of protons. However, a satisfactory theory should be able to deduce these phenomenological laws from more fundamental principles. These foundations were established by two equivalent formalisms developed between 1924 and 1928. On the one hand, the wave formulation initiated by Louis de Broglie with the discovery of the wave nature of electrons, and concluded by Erwin Schrödinger. On the other hand, the matrix formulation initiated by Werner Heisenberg using operators to represent observable quantities, and later developed independently by Paul Dirac and

Max Born. Many other physicists contributed to the new quantum theory, among them Wolfgang Pauli, who enunciated an exclusion principle for assigning quantum numbers to electrons in the hydrogen atom. That would lead to classifying quantum particles based on their spin, following either a Bose-Einstein statistics or a Fermi-Dirac one. Paul Dirac also theorized an antiparticle for the electron, the positron, which was discovered by Carl Anderson in 1932.

In addition, James Chadwick also discovered a new particle called neutron, laying a solid foundation for future nuclear models. The similarity between protons and neutrons led Werner Heisenber to introduce a global symmetry called isospin. However, their strong interactions inside the nuclei had not been well understood yet. So as to describe their attraction, Hideki Yukawa theorized in 1935 a new particle called meson, acting as carrier particles for the strong nuclear force. The next year Carl Anderson discovered a new particle called muon while working with cosmic rays. Although this particle was initially thought to be the predicted meson, one has to wait until 1947 to find the first true mesons, which were the charged pions found in a collaboration lead by Cecil F. Powell. Hideki Yukawa was awarded with the Nobel Prize in Physics 1949 “for his prediction of the existence of mesons on the basis of theoretical work on nuclear forces”, whereas Cecil F. Powell with the one in Physics 1950 “for his development of the photographic method of studying nuclear processes and his discoveries regarding mesons made with this method”. Afterwards, more bound states began to be found in experiments. Therefore, physicists required schemes to classify them, theories to understand their behavior and laboratories to perform their experiments.

In 1954, CERN «*Conseil européen pour la recherche nucléaire*» was established by twelve European governments in Geneva. The aim was to build a laboratory devoted to the study of nuclear and particle physics, similar to the Brookhaven National Laboratory. The next years, other organizations emerged with the same purpose like DESY in Hambrug, SLAC in Stanford and Fermilab in Chicago. These organizations operated sophisticated particle accelerators like cyclotrons, synchrotrons and linear accelerators, which were originally used in fixed-target experiments, and later, implemented in particle colliders. Figure 1.1 shows the main colliders operated by the previous mentioned organizations. In particular, CERN’s particle colliders have been vital to attain the Nobel Prize in Physics 1984 awarded to Carlo Rubbia and Simon van der Meer “for their decisive contributions to the large project, which led to the discovery of the field particles W and Z, communicators of weak interaction”, and the one in Physics 2013 awarded to Peter Higgs and François Englert “for the theoretical discovery of a mechanism that contributes to our understanding of the origin of mass of subatomic particles, and which recently was confirmed through the discovery of the predicted fundamental particle, by the ATLAS and CMS experiments at CERN’s Large Hadron Collider”.

Nowadays, laboratories designed for particle experiments are vital for the development of science and technology. New ground-breaking collider-based experiments are planned and the future of particle physics is widely open to outstanding discoveries.

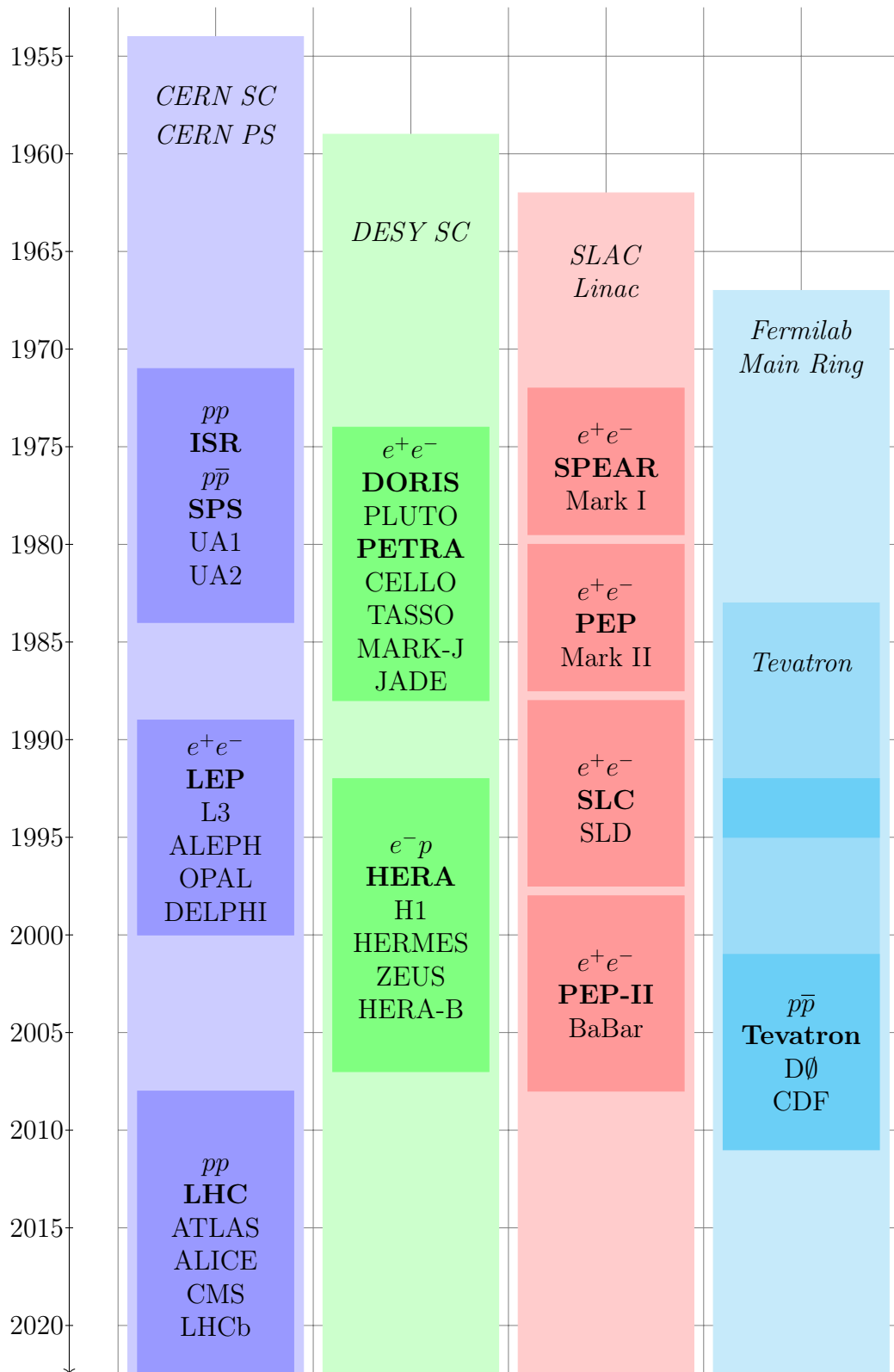


Figure 1.1: Timeline of main particle colliders operating at CERN, DESY, SLAC, and Fermilab. They are written in boldface along with the particles collided above and their main experiments below. For completeness, the first accelerators of these organizations are shown in italics.

CHAPTER 2

Theoretical framework

Fundamental interactions arise from the constraints imposed by gauge symmetries, in which case the transformations are continuous and local varying from point to point in space and time. The procedure of postulating a specific gauge symmetry leads to a unique quantum field theory described by a Lagrangian which is invariant under these transformations. Moreover, the Lagrangian must be also Hermitian and Lorentz covariant, and CPT symmetry must hold for all physical phenomena.

In general, a set of transformations can be associated to an algebraic structure called group and consisting of a set of elements equipped with a binary operation in such a way that the axioms of closure, associativity, identity, and invertibility are satisfied. Additionally, the group is Abelian if it obeys the axiom of commutativity. A group representation describes these abstract groups in terms of linear transformations of vector spaces where the elements are represented as matrices equipped with the matrix multiplication. There is a kind of groups widely used in physics called Lie groups. A Lie group is a continuous group that is also a differentiable manifold and any Lie group gives rise to a Lie algebra, which is the tangent space at the identity. The most considered ones are the unitary groups $U(N)$ whose elements are $N \times N$ unitary matrices over \mathbb{C} equipped with matrix multiplication.

The first developed gauge theory was Quantum Electrodynamics (QED). This theory emerges from the gauge symmetry group $U(1)_{\text{EM}}$ and describes the electromagnetic interactions of photons and charged particles, i.e. the radiation and matter electromagnetic interaction. The theory was systematized in 1949 by Freeman Dyson after demonstrating the equivalence of the two current formulations at that time [4]. The established one used by Shin'ichiro Tomonaga and Julian Schwinger to independently discover a renormalization method for ultraviolet divergences [5], and the alternative one introduced by Richard Feynman as a pictorial representation of the behaviour and interaction of particles [6]. They were awarded with the Nobel Prize in Physics 1965 “for their fundamental work in quantum electrodynamics, with deep-ploughing consequences for the physics of elementary particles”.

The concept of gauge theory was extended to non-Abelian groups in 1954 by Chen-Ning Yang and Robert Mills at the Brookhaven National Laboratory [7]. Nowadays, this paradigm remains as the core for understanding strong and weak interactions.

2.1 Quantum Chromodynamics

Quantum Chromodynamics (QCD) is a Yang-Mills theory with gauge symmetry group $SU(3)_C$ that describes strong interactions of gluons and coloured quarks. There are 3 different colours for each quark flavour and also 8 different colour combinations for the gluon, which is the gauge vector boson mediating strong interactions. The theory was independently formulated in 1973 by David Gross and Franck Wilczek at Princeton University and by Hugh David Politzer at Harvard University, explaining the weakness of strong interactions at short distances due to asymptotic freedom [8, 9]. They were awarded with the Nobel Prize in Physics 2004 “for the discovery of asymptotic freedom in the theory of the strong interaction”.

Any Yang-Mills theory corresponds to a continuous and local $SU(N)$ symmetry of the Lagrangian. The special unitary group $SU(N)$ is a subgroup of the unitary group consisting of elements with determinant unity. The elements of the group can be mapped around the identity as $U = \exp(-ig\phi)$ where g is the coupling and ϕ is a function varying from point to point in space and time that can be expanded in terms of the generators in the Lie algebra $\mathfrak{su}(N)$. These generators are Hermitian and traceless operators that satisfy the commutation relation $[T^a, T^b] = if^{abc}T^c$ where the structure constants are real and completely antisymmetric. For this group the number of generators is $(N^2 - 1)$ and the rank is $(N - 1)$.

The main irreducible representations of the group are the fundamental one F and the anti-fundamental one \bar{F} both with dimension N . Thanks to the Young tableaux technique one can relate them as $\bar{F} \otimes F = 1 \oplus A$ where the adjoint representation A has dimension $(N^2 - 1)$. The generators of each representation are square matrices of the corresponding dimension. Using matrix notation, the generators for the adjoint representation can be derived from the structure constants as $(T_A^a)^{bc} = -if^{abc}$.

The following normalization conditions are satisfied by the generators of the group:

$$\text{tr}(T^a T^b) = T_F \delta^{ab}; \quad T^a T^a = C_F \mathbb{I}; \quad f^{acd} f^{bcd} = C_A \delta^{ab}.$$

The normalization coefficients take values $T_F = 1/2$ and $C_F = (N^2 - 1)/2N$ for the fundamental representation, along with $C_A = N$ for the adjoint one.

In the symmetry group $SU(3)$ postulated by QCD, the generators for the fundamental representation are given by the Gell-Mann matrices divided by a factor 2 due to normalization. These matrices were derived by Murray Gell-Mann as analogous to the Pauli matrices from $SU(2)$ and they take the form:

$$\lambda_1 = \begin{pmatrix} 0 & 1 & 0 \\ 1 & 0 & 0 \\ 0 & 0 & 0 \end{pmatrix} \quad \lambda_2 = \begin{pmatrix} 0 & -i & 0 \\ i & 0 & 0 \\ 0 & 0 & 0 \end{pmatrix} \quad \lambda_3 = \begin{pmatrix} 1 & 0 & 0 \\ 0 & -1 & 0 \\ 0 & 0 & 0 \end{pmatrix}$$

$$\lambda_4 = \begin{pmatrix} 0 & 0 & 1 \\ 0 & 0 & 0 \\ 0 & 0 & 0 \end{pmatrix} \quad \lambda_5 = \begin{pmatrix} 0 & 0 & -i \\ 0 & 0 & 0 \\ 0 & 0 & 0 \end{pmatrix}$$

$$\lambda_6 = \begin{pmatrix} 0 & 0 & 0 \\ 0 & 0 & 1 \\ 0 & 1 & 0 \end{pmatrix} \quad \lambda_7 = \begin{pmatrix} 0 & 0 & 0 \\ 0 & 0 & -i \\ 0 & i & 0 \end{pmatrix} \quad \lambda_8 = \frac{1}{\sqrt{3}} \begin{pmatrix} 1 & 0 & 0 \\ 0 & 1 & 0 \\ 0 & 0 & -2 \end{pmatrix}$$

The structure constants of the symmetry group SU(3) are found below and all other constants not related to these by permuting indices are zero:

$$f^{123} = 1; \quad f^{147} = f^{246} = f^{257} = f^{345} = 1/2; \\ f^{156} = f^{367} = -1/2; \quad f^{458} = f^{678} = \sqrt{3}/2.$$

2.1.1 Gauge theory

The action in a Yang-Mills theory is a functional of a gauge potential A , a spinor field Ψ and its conjugate spinor field $\bar{\Psi} = \Psi^\dagger \gamma^0$. The action of the physical system is then computed as the integral of the Lagrangian over a whole four-dimensional Lorentzian manifold \mathcal{M} . This manifold describes a set of points in space and time where any point x in the manifold is specified through a given chart using coordinates $\{x^\mu\}$. Locally, a Lorentzian manifold is reduced to a Minkowskian space equipped with a metric tensor $\eta = \eta_{\mu\nu} dx^\mu \otimes dx^\nu$ taking the same form at all points. The signature is positive in time direction and the inverse metric comes from $\eta_{\mu\nu} \eta^{\nu\rho} = \delta_\mu^\rho$.

The gauge potential is a 1-form in the manifold, while the spinor fields are simply 0-forms and the gamma matrices expressed in the Weyl basis are written as a 1-form. The exterior covariant derivative is introduced as $D = d + igA$ and the gauge field strength tensor is a 2-form in the manifold obtained from $D \wedge D = igF$.

The action of a Yang-Mills theory like QCD is simply given by

$$S[A, \Psi, \bar{\Psi}] = \int_{\mathcal{M}} \left\{ -\text{tr}(F \wedge *F) + i\bar{\Psi}\Gamma \wedge *\overset{\leftrightarrow}{D}\Psi - \bar{\Psi}M \wedge *\Psi \right\}$$

where the derivative operator is defined as $\overset{\leftrightarrow}{D} = (1/2)(D - D^\dagger)$ to preserve the Hermitian requirement of the Lagrangian and M is the mass coupling for spinors. Note that under a gauge symmetry of element U the spinor field transforms as $\Psi \rightarrow \Psi' = U\Psi$ and the conjugate spinor field transforms as $\bar{\Psi} \rightarrow \bar{\Psi}' = \bar{\Psi}U^\dagger$. In order to preserve gauge invariance in the Lagrangian, the gauge potential must then transform as $igA \rightarrow igA' = \overset{\leftrightarrow}{D}U^\dagger = UigAU^\dagger - (dU)U^\dagger$.

It is convenient to show explicitly all the interactions between fields in the Lagrangian. The first step is to expand the gauge potential in the fundamental representation $A = A_\mu^a T^a dx^\mu$ as different combinations of the gauge boson. Using this notation the gauge field strength tensor takes the form $F = (1/2)F_{\mu\nu}^a T^a dx^\mu \wedge dx^\nu$. Thus, given the definition $F = dA + igA \wedge A$, its components are

$$F_{\mu\nu}^a = \partial_\mu A_\nu^a - \partial_\nu A_\mu^a - g f^{abc} A_\mu^b A_\nu^c.$$

The spinor field is an array of the different charged spinor fields ψ with a mass m for

each flavour. The number of active flavours in the theory is given by n_f . Moreover, each of these fields presents N different colour states than may be explicitly indicated as ψ_i when using the matrix notation for the generators of the group in the fundamental representation T_{ij}^a . As the spinor fields transform in the fundamental representation, then the covariant derivative acts like $D_{ij\mu} = \delta_{ij}\partial_\mu + igT_{ij}^a A_\mu^a$. It can also be defined a covariant derivative acting in the adjoint representation, where the derivative behaves like $D_{A\mu}^{ac} = \delta^{ac}\partial_\mu - gf^{abc}A_\mu^b$.

Perturbative theory

The gauge coupling g is the fundamental parameter in any gauge theory as it copies the strength of the interaction. The QCD parameter may be rewritten as $\alpha_s = g^2/4\pi$ or even as $a = (g/4\pi)^2$ depending on the normalization. This gauge coupling is a small parameter, so one can perform a perturbative expansion in powers of the coupling when computing physical observables or applying infinitesimal transformations.

Under an infinitesimal gauge transformation $U = \mathbb{I} - ig\phi^a T^a + \mathcal{O}(g^2)$, the gauge potential transforms as $A_\mu^a \rightarrow A'_\mu^a = A_\mu^a + D_{A\mu}^{ac}\phi^c$. Thus, the function varying from point to point in space and time behaves as a massless scalar field transforming in the adjoint representation. This is going to be vital when implementing the Lorenz gauge condition $\partial^\mu A_\mu^a = 0$ in the perturbative calculation.

Additional terms need to be included in the Lagrangian to perform a perturbative calculation, namely, the gauge fixing term with the Feynman-'t Hooft parameter $\xi = 1$ and the Faddeev-Popov ghost field c that transforms in the adjoint representation. The Faddeev-Popov anti-ghost and ghost fields are anticommuting scalar fields. They do not satisfy the spin-statistics theorem and they are their own antiparticles, $\bar{c} = \bar{c}^\dagger$ and $c = c^\dagger$. The Lagrangian when including these terms takes the form

$$L_{p\text{YM}} = -\frac{1}{4}F^{a\mu\nu}F_{\mu\nu}^a - \frac{1}{2\xi}(\partial^\mu A_\mu^a)^2 + (\partial^\mu \bar{c}^a)D_{A\mu}^{ac}c^c + \sum_{k=1}^{n_f} \bar{\psi}_i^{(k)} \left(i\gamma^\mu \overset{\leftrightarrow}{D}_{ij\mu} - m^{(k)}\delta_{ij} \right) \psi_j^{(k)}.$$

Thus, the Lagrangian in a perturbative Yang-Mills theory like perturbative QCD (pQCD) where all propagators and interactions are shown explicitly is given by

$$\begin{aligned} L_{p\text{YM}} = & +\frac{1}{2}A_\mu^a\delta^{ac}\left[\eta^{\mu\nu}\square - \left(1 - \frac{1}{\xi}\right)\partial^\mu\partial^\nu\right]\left(A_\nu^c - g\eta^{\mu\nu}f^{abc}(\partial^\rho A_\mu^a)A_\nu^b A_\rho^c\right. \\ & - \frac{1}{4}g^2\eta^{\mu\rho}\eta^{\nu\sigma}f^{abc}f^{ade}A_\mu^b A_\nu^c A_\rho^d A_\sigma^e - \bar{c}^a\delta^{ac}\square c^c - g(\partial^\mu \bar{c}^a)f^{abc}c^c A_\mu^b \\ & \left. + \sum_{k=1}^{n_f} \left[\bar{\psi}_i^{(k)}\delta_{ij} \left(i\gamma^\mu \overset{\leftrightarrow}{\partial}_\mu - m^{(k)} \right) \psi_j^{(k)} - g\bar{\psi}_i^{(k)}\gamma^\mu T_{ij}^a\psi_j^{(k)} A_\mu^a \right] \right) \end{aligned}$$

Physical predictions for observables are obtained computing Feynman diagrams. For such interaction vertices and propagators are required, which are directly obtained from the perturbative Lagrangian. Afterwards, the computation is performed in momentum space keeping in mind that momenta always flow by convention towards

the interaction point. Functions in position and momentum spaces are related by a Fourier transform. For example, the gauge potential transforms as

$$A_\mu^a(x) = \iint \frac{d^4 p}{(2\pi)^4} A_\mu^a(p) e^{-ip \cdot x}.$$

Note that the dependence of functions with the position is only explicitly shown here to distinguish them from their Fourier transforms in momentum space.

The Feynman rules for the propagators correspond with two-point functions. They can be derived from the free perturbative Lagrangian of a particular field. For instance, in the case of the gauge boson propagator:

$$\langle 0 | \mathcal{T}\{A_\mu^a(x)A_\nu^b(y)\} | 0 \rangle = G_{F\mu\nu}^{ab}(x-y) = \iint \frac{d^4 p}{(2\pi)^4} G_{F\mu\nu}^{ab}(p) e^{-ip \cdot (x-y)}; \\ \left[\frac{\partial G_{F\mu\nu}^{ab}(p)/i}{\delta A_\nu^b(p)} \right] \frac{(2\pi)^4 \delta}{\delta A_\nu^b(p)} \frac{(2\pi)^4 \delta}{\delta A_\rho^c(q)} \int d^4 x L_{\text{prop.}}(x) = (2\pi)^4 \delta^4(p+q) \delta_\mu^\rho \delta^{ac}.$$

The Feynman rule for an interaction vertex can be derived too from its respective term in the perturbative Lagrangian. As an example, the triple interaction between gauge bosons and spinors simply comes from the relation:

$$\frac{(2\pi)^4 \delta}{\delta A_\mu^a(p)} \frac{(2\pi)^4 \delta}{\delta \psi_j(q)} \frac{(2\pi)^4 \delta}{\delta \bar{\psi}_i(k)} \int d^4 x L_{\text{inter.}}(x) = (2\pi)^4 \delta^4(p+q+k) \left[V_{Fij}^{a\mu}(p, q, k)/i \right]$$

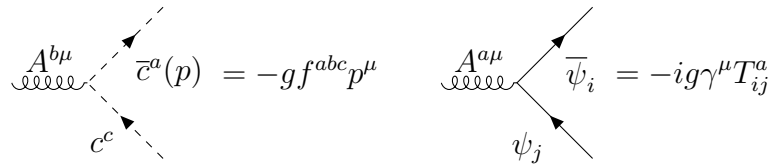
That way all Feynman rules for any quantum field theory can be easily derived. For pQCD they can be found below when computed in momentum space. Nevertheless, to compute physical observables one also need to implement the asymptotic states and symmetry factors in the perturbative calculation.

Feynman rules for pQCD:

Propagators:

$$A_{\mu\lambda}^{b\nu} A_{\lambda\lambda}^{a\mu} = \frac{-i\delta^{ab}}{p^2 + i\epsilon} \left[\eta^{\mu\nu} - (1-\xi) \frac{p^\mu p^\nu}{p^2} \right] \\ \begin{array}{ccc} c^b \rightarrow \bar{c}^a & = \frac{i\delta^{ab}}{p^2 + i\epsilon} & \psi_j \rightarrow \bar{\psi}_i & = \frac{i\delta_{ij}}{p^2 - m^2 + i\epsilon} (\gamma^\mu p_\mu + m) \end{array}$$

Triple interactions:



$$\begin{array}{c}
 \text{Feynman diagram:} \\
 \text{A vertex labeled } A^{b\nu}(p) \text{ has two external lines.} \\
 \text{A vertex labeled } A^{a\mu}(k) \text{ has three external lines.} \\
 \text{A vertex labeled } A^{c\rho}(q) \text{ has two external lines.}
 \end{array}
 = -g f^{abc} [\eta^{\mu\nu}(k-p)^\rho + \eta^{\nu\rho}(p-q)^\mu + \eta^{\rho\mu}(q-k)^\nu]$$

Quartic interactions:

$$\begin{array}{c}
 \text{Feynman diagram:} \\
 \text{Four vertices labeled } A^{a\mu}, A^{b\nu}, A^{c\rho}, A^{d\sigma} \text{ are connected by four internal lines.}
 \end{array}
 = -ig^2 [f^{abe} f^{cde} (\eta^{\mu\rho}\eta^{\nu\sigma} - \eta^{\mu\sigma}\eta^{\nu\rho}) + f^{ace} f^{bde} (\eta^{\mu\nu}\eta^{\rho\sigma} - \eta^{\mu\sigma}\eta^{\nu\rho}) \\
 + f^{ade} f^{bce} (\eta^{\mu\nu}\eta^{\rho\sigma} - \eta^{\mu\rho}\eta^{\nu\sigma})]$$

2.1.2 Renormalization

In any perturbative quantum field theory logarithmically divergent integrals arise when computing loop Feynman diagrams due to contributions of objects with unbounded energy, or, equivalently, because of physical phenomena at infinitesimal distances. The ultraviolet divergences encountered in these loop integrals are removed through renormalization.

These divergent integrals are first regularized by computing them in $4 - 2\epsilon$ dimensions. Afterwards, renormalization relies on dimensional regularization and treats divergences by altering coupling values to compensate for effects of their self-interactions. Therefore, in order to absorb ultraviolet divergences, any bare coupling in the Lagrangian is rewritten as a renormalized coupling. The latter has a dependence with an arbitrary mass scale μ_R at which ultraviolet divergences are subtracted. The QCD bare gauge coupling a_0 is therefore rewritten as

$$a_0 = \mu_R^{2\epsilon} Z_a a$$

where a is the renormalized gauge coupling, Z_a is the renormalization constant of the coupling a and the arbitrary mass scale μ_R is the unphysical renormalization scale. The renormalization constant Z_a compensates the divergences encountered in loop integrals and the dependence of the renormalized coupling a with the mass scale μ_R is encoded in the β function.

Ultraviolet divergences are separated in $1/\epsilon$ poles and absorbed into redefinitions of the coupling. The Laurent series of the β and $Z_a a$ functions are rewritten as

$$\beta = \frac{da}{d \ln \mu_R^2} = \sum_{k=-\infty}^{+\infty} b_k \left(\frac{1}{\epsilon}\right)^k \quad \text{and} \quad Z_a a = \sum_{k=-\infty}^{+\infty} z_k \left(\frac{1}{\epsilon}\right)^k.$$

In addition, the bare coupling a_0 must be independent of the arbitrary mass scale at which ultraviolet divergences are subtracted. Therefore, the bare coupling satisfies

$$\frac{da_0}{d \ln \mu_R^2} = 0.$$

This condition implies that the coefficients in the Laurent series must satisfy the following relation derived from the Cauchy product:

$$z_{k+1} + \sum_{j=-\infty}^k b_j \frac{dz_{k-j}}{da} = 0.$$

Any physical observable R must also be independent of the renormalization scale. In pQCD a physical observable R is described using a perturbative expansion in powers of the physical coupling $a(\mu_R^2)$. Then, any observable is expressed as

$$R(\ln(Q^2/\mu_R^2), a(\mu_R^2), \chi) = \sum_{n=0}^{\infty} [\mu(\mu_R^2)]^{n+k} r_n(\ln(Q^2/\mu_R^2), \chi)$$

where χ is a given kinematic variable, Q is the scale of momentum transferred and k is the power of the coupling at leading-order. So as to obtain fixed-order finite predictions, the physical observable R must satisfy ultraviolet safety. Consequently, the renormalization group equation (RGE) happens to be fulfilled at any order in the perturbation expansion for any physical observable:

$$\frac{dR}{d \ln \mu_R^2} = \left[\frac{\partial}{\partial \ln \mu_R^2} + \frac{da}{d \ln \mu_R^2} \frac{\partial}{\partial a} \right] R = 0.$$

Modified Minimal Subtraction

In order to absorb ultraviolet divergences into redefinitions of the coupling, the subtraction procedure is here performed in the $\overline{\text{MS}}$ renormalization scheme using pQCD in the massless limit. The first non-trivial coefficient of the $Z_a a$ expansion is $z_0 = a$ and the next coefficient z_1 is given by a perturbative expansion:

$$z_1 = - \sum_{n=0}^{\infty} \mu^{n+2} \frac{\beta_n}{n+1}.$$

The analytical expressions up to the 3-loop solution for these β_n coefficients as a function of the number of active quark flavours n_f are given by

$$\begin{aligned} \beta_0 &= \frac{11}{3} C_A - \frac{4}{3} T_F n_f; \\ \beta_1 &= \frac{34}{3} C_A^2 - 4 C_F T_F n_f - \frac{20}{3} C_A T_F n_f; \\ \beta_2 &= \frac{2857}{54} C_A^3 + 2 C_F^2 T_F n_f - \frac{205}{9} C_F C_A T_F n_f - \frac{1415}{27} C_A^2 T_F n_f + \frac{44}{9} C_F T_F^2 n_f^2 \\ &\quad + \frac{158}{27} C_A T_F^2 n_f^2. \end{aligned}$$

These coefficients were calculated in Ref. [10] and can be also found in the PDG [11]. However, the β_0 coefficient is going to be derived now from the QCD counter-terms.

So as to do that the bare parameters and fields in the Lagrangian have to be renormalized by introducing their respective normalization constants:

$$g_0 = \mu_R^\epsilon \sqrt{Z_a} g; \quad \psi_{0i} = \sqrt{Z_2} \psi_i; \quad A_{0\mu}^a = \sqrt{Z_3} A_\mu^a; \quad \xi_0 = Z_3 \xi; \quad Z_2 m_0 = Z_m m.$$

For the QCD vertex one introduces the additional constant $Z_1 = Z_2 \sqrt{Z_3 Z_a}$. These renormalization constants are real and can be expanded as $Z_n = 1 + \delta_n$ due to its perturbative nature. The counter-terms required can be found below.

$$\begin{aligned} \text{Diagram: } & \text{A loop with two external gluon lines } A_{\mu\nu}^{ab} \text{ and two fermion lines } \psi_j \text{ and } \bar{\psi}_i. \\ & \text{Equation: } -i\delta_3 (\not{p}^\mu \eta^{\mu\nu} - p^\mu p^\nu) \not{q}^{ab}; \quad \delta_3 = a \left(\frac{5}{3} C_A - \frac{4}{3} T_F n_f \right) \left(\frac{1}{\epsilon} \right) \left(\frac{1}{\epsilon} \right) \\ \text{Diagram: } & \text{A loop with one external gluon line } A_{\mu\nu}^{ab} \text{ and two fermion lines } \psi_j \text{ and } \bar{\psi}_i. \\ & \text{Equation: } i(\delta_2 \gamma^\mu p_\mu - \delta_m m) \delta_{ij}; \quad \delta_2 = -a C_F \left(\frac{1}{\epsilon} \right) \left(\frac{1}{\epsilon} \right) \quad \delta_m = -a 4 C_F \left(\frac{1}{\epsilon} \right) \left(\frac{1}{\epsilon} \right) \end{aligned}$$

Combining previous counter-terms one can obtain the first non-trivial terms of the Larent expansion for the $Z_a a$ function. The term z_1 is computed now only at leading-order. Thus, the analytical expression for the β_0 coefficient is determined from

$$Z_a a = a - a^2 \left(\frac{1}{3} C_A - \frac{4}{3} T_F n_f \right) \left(\frac{1}{\epsilon} \right) \left(\frac{1}{\epsilon} \right) + \mathcal{O}(1/\epsilon^2).$$

Asymptotic freedom and confinement

The evolution of $a(\mu_R^2)$ is simply given by the solution of the RGE for a encoded in the β function which at any order in the perturbative expansion takes the form

$$\beta = \frac{da}{d \ln \mu_R^2} = -a\epsilon + a \frac{dz_1}{da} - z_1 + \mathcal{O}(1/\epsilon) = -a\epsilon - \sum_{n=0}^{\infty} a^{n+2} \beta_n + \mathcal{O}(1/\epsilon).$$

Integrating this differential equation, one obtains the analytical expression for the 3-loop solution to the RGE for a evaluated at a mass scale μ_R in the $\overline{\text{MS}}$ scheme

$$a_{\overline{\text{MS}}}(\mu_R^2) = \frac{1}{\beta_0 t} \left[1 - \frac{\beta_1}{\beta_0^2} \frac{\ln t}{t} + \frac{\beta_1^2}{\beta_0^4 t^2} \left(\ln^2 t - \ln t - 1 + \frac{\beta_2 \beta_0}{\beta_1^2} \right) \right] \quad (2.1)$$

where $t = \ln(\mu_R^2 / \Lambda_{\text{QCD}}^2)$ and Λ_{QCD} is the scale at which the coupling diverges. The evolution of the coupling given in Eq. (2.1) is represented in Figure 2.1 where one observes the behaviour of the coupling with the interaction scale.

The coupling behaves then as a running coupling with the scale to compensate the effects of self-interactions. Moreover, if the unphysical mass scale μ_R is evaluated close to the scale of momentum transferred Q in a given process, the coupling $a(Q^2)$ becomes an indicative of the effective strength of the interaction.

Thus, the strong interactions of colour charged particles present two main properties with the interaction scale:

Asymptotic freedom which becomes dominant at high-energy scales where partons interact weakly creating a quark-gluon plasma as the effective strength of the interaction decreases. In this case, strong interactions can be described using a perturbative expansion in powers of the coupling.

Confinement which becomes dominant at low-energy scales where particle detection occurs in collider experiments. In this case, partons cannot be isolated singularly, and therefore, cannot be directly observed because the effective strength does not diminish as they are separated due to the emission of massless colour charged particles. They are forever bound into colourless bound states called hadrons. The hadron structure has then a non-perturbative nature.

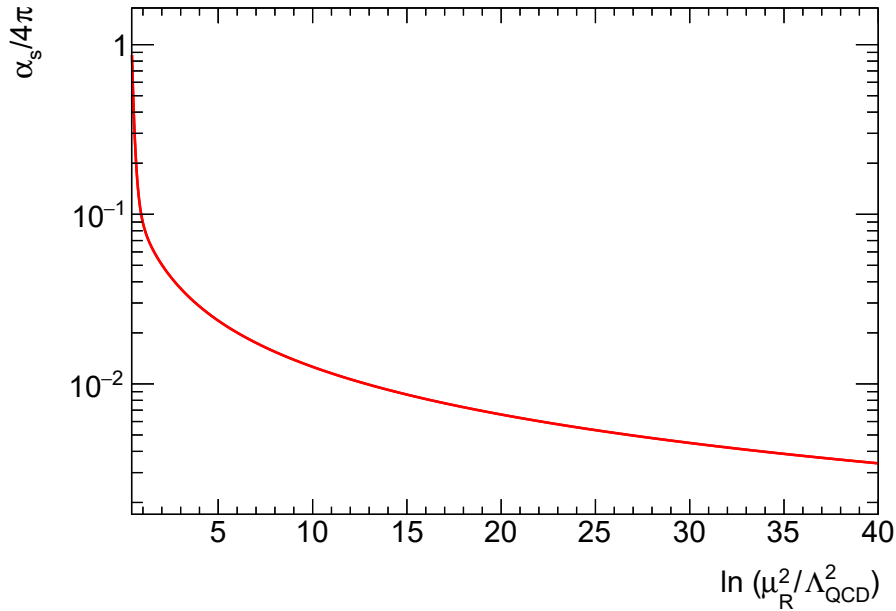


Figure 2.1: Running of the strong coupling constant $a(\mu_R^2)$ for a number of active flavours $n_f = 6$ based on the 3-loop solution to the RGE performed in the $\overline{\text{MS}}$ scheme using pQCD in the massless limit. The gauge symmetry group is $\text{SU}(3)_C$.

2.1.3 Factorization

In a perturbative quantum field theory divergent integrals also arise due to the emission of massless charged particles with arbitrarily small momentum, or equivalently, because of physical phenomena at long distances. Consequently, the infrared divergences encountered in these integrals imply large non-perturbative effects. These

problems start to show up when $2 \rightarrow 3$ kinematics becomes $2 \rightarrow 2$ kinematics, which happens at the edges of phase space when one partons becomes soft or two partons become collinear.

The Kinoshita-Lee-Nauenberg (KLN) theorem states that any physical observable must be infrared safe in the massless limit, i.e. zero-momentum charged particles do not contribute and collinear splitting does not change the observable. Therefore, an observable R with n partons in the asymptotic states must satisfy the limits:

$$\lim_{p_{n+1} \rightarrow 0} R^{(n+1)}(p_1, \dots, p_n, p_{n+1}) = R^{(n)}(p_1, \dots, p_n);$$

$$\lim_{p_n \parallel p_{n+1}} R^{(n+1)}(p_1, \dots, p_n, p_{n+1}) = R^{(n)}(p_1, \dots, p_n + p_{n+1})$$

where p_i is the momenta of the either incoming or outgoing particle i . Then, infrared divergences cancel exactly at any order in perturbative theory after integration of real and virtual contributions in dimensional regularization, allowing fixed-order finite predictions [12]. To achieve this, observables must be totally inclusive quatities over all charged particles in both asymptotic states, the initial and the final one.

In e^+e^- collisions all observables are totally inclusive in the initial state. Therefore, any observable which is totally inclusive over the final state is an infrared safe quantity, insensitive to long-distance phenomena like hadron structure. The main one for this process is the cross section $\sigma(e^+e^- \rightarrow X)$ whose result is calculable at parton level and it is still valid at particle level.

In hadron collisions observables are not inclusive in the initial state. As a result, infrared divergences owing to collinear emissions from incoming partons are not cancelled by virtual contributions, and therefore, they are not infrared safe by themselves. To account for this effect, divergences are factorized out from the perturbative computation at a certain mass scale μ_F . Any observable should be independent of the unphysical scales at which divergences are subtracted. Not currently close to this ideal situation, the practice consists in defining a theoretical scale uncertainty as the range of results within $\mu_{R,F}/2 < \mu_{R,F} < 2\mu_{R,F}$. See more details in Ref. [13].

For a process with an incoming hadron A carrying momenta p_A , consider a physical observable R which is totally inclusive in the final state. The factorization procedure separates the observable into a perturbatively calculable quantity associated to short-distance effects and the universal non-perturbative functions associated to long-distance effects. Hence, the observable is given by the formula:

$$R_A = \sum_i^{\text{part.}} \int_0^1 dx f_{i/A}(x, \mu_F^2) \hat{R}_i(p_i, \ln(Q^2/\mu_F^2), \ln(Q^2/\mu_R^2), a(\mu_R^2), \chi) \left(\right)$$

where χ is a given kinematic variable and Q is the scale of momentum transferred. The parton distribution function $f_{i/A}(x)$ represents the probability density for finding a parton i inside the hadron A carrying a certain momentum fraction x . On the other hand, the perturbatively calculable quantity \hat{R}_i corresponds with a certain subprocess with incoming parton i carrying a momentum $p_i = xp_A$.

Parton Distribution Functions

The universal long-distance functions include the parton distribution functions (PDF) to factorize hadron-parton transitions in the initial state and the fragmentation functions (FF) to factorize parton-hadron transitions in the final state. They are measured with global fit to experiments and their evolution with the unphysical scale follows the Dokshitzer-Gribov-Lipatov-Altarelli-Parisi (DGLAP) equation:

$$\frac{\partial f_{i/A}(x)}{\partial \ln \mu_F^2} = 2a(\mu_F^2) \sum_j^{\text{part.}} \int_x^1 \frac{dz}{z} P_{i \leftarrow j}(z) f_{j/A}\left(\frac{x}{z}, \mu_F^2\right)$$

where $P_{i \leftarrow j}$ are the splitting kernels of a given parton into another one. The partons involved in QCD are the gluon g and the quark q . The latter presented in different flavours. The gluon can split independently into a pair of quarks and a pair of gluons but a quark can only radiate a gluon, which implies $P_{q \leftarrow q}(1-x) = P_{g \leftarrow q}(x)$.

The splitting kernel $P_{g \leftarrow q}$ diverges for $x \rightarrow 0$, whereas $P_{q \leftarrow q}$ diverges for $x \rightarrow 1$. Therefore, the presence of a soft divergence makes crucial to include virtual contributions in order to cancel exactly the singularity. The analytical expressions for the leading-order kernels in the + notation that avoids a soft cutoff are given by

$$\begin{aligned} P_{q \leftarrow q}(x) &= C_F \frac{1+x^2}{(1-x)_+} + \frac{3}{2} C_F \delta(1-x) \\ P_{g \leftarrow q}(x) &= C_F \frac{1+(1-x)^2}{x} \\ P_{q \leftarrow g}(x) &= T_F [x^2 + (1-x)^2] \\ P_{g \leftarrow g}(x) &= 2C_A \left[\frac{1-x}{x} + x(1-x) + \frac{x}{(1-x)_+} \right] + \frac{\beta_0}{2} \delta(1-x) \end{aligned}$$

where $1/(1-x)_+$ is defined by its action on a function $f(x)$ regular at $x = 1$ as

$$\frac{1}{(1-x)_+} f(x) = \frac{f(x) - f(1)}{1-x}.$$

These expressions are derived in numerous references like Ref. [14]. The evolution of the parton distribution functions was published in 1977 by Guido Altarelli and Giorgio Parisini [15], even though an equivalent formula had been proposed independently by Vladimir Gribov and Lev Lipatov in 1972. Initially, fixed-target experiments were the main source on parton distributions inside hadrons at high x in the kinematic plane (x, Q). Afterwards, the measured regions were extended at low x in collider experiments like HERA. The major groups back then providing results from global fits to these experiments were CTEQ5 [16] and MRST [17]. Nowadays, there is a wide range of groups regularly updating the parton distributions.

At very low x in the kinematic plane, the DGLAP evolution is no longer applicable and a BFKL description must be considered. In this scenario, the partonic content increases as x decreases. Then, partons start to recombine and eventually saturate.

Leading-Logarithm Approximation

The perturbative expansion in powers of the coupling used to describe the splitting kernels is not valid anymore at low x due to large logarithms $\ln(1/x)$ contained in the higher-order corrections. Nevertheless, these large logarithms can be controlled by rearranging terms in the perturbative expansion. This procedure called resummation was accomplished by the Balitsky–Fadin–Kuraev–Lipatov (BFKL) equation.

Logarithm enhancement may also occur for any observable containing terms proportional to powers of $a \ln^k(Q^2/\mu_{R,F}^2)$. These terms appear in renormalization and factorization procedures but also as Sudakov logarithms for $k = 2$. The latter arises when particles get both very soft and collinear. In resummation, one uses a factorized expression of an observable, and from that derives an expression that absorbs the large logarithms into an exponent. Hence, this procedure allows going from a perturbative expansion in terms of the coupling a to one in terms of $a \ln(Q^2/\mu_{R,F}^2)$, so that the perturbative expansion is not threatened anymore.

2.1.4 Hadron structure

Fixed-target experiments used to probe the inside of hadrons revealed that the point-like scattering distributions were damped by form factors showing that hadrons are not point-like and indeed are bound states of partons. The low-resolution picture of the hadron structure corresponds then with a combination of valence quarks that only accounts for its quantum numbers. However, a high-resolution picture of the hadron structure consider that the valence quarks are dressed with a sea of gluons and quark pairs due to the action of the splitting kernels.

These experiments where operating since 1967 at the Stanford Linear Accelerator Cente (SLAC), where electron beams were scattered on proton targets at energies of about 20 GeV to reveal the internal structure of the proton. Richard Feynman interpreted the results in terms of a model in which protons were composed of generic point-like constituents called partons [18]. Thereafter, the study of the produced deep-inelastic scattering (DIS) data led to the development of the quark-parton model of the proton [19]. Jerome Friedman, Henry Kendall, and Richard Taylor were awarded with the Nobel Prize in Physics 1990 “for their pioneering investigations concerning deep inelastic scattering of electrons on protons and bound neutrons”.

The DIS cross section $\sigma(e^- p \rightarrow e^- X)$ in the proton rest frame where X is anything the proton can break up into, is expressed in terms of the scattering angle θ as

$$\frac{d\sigma}{d\Omega dE'} = \frac{\alpha^2}{4E^2 \sin^4(\theta/2)} \left[W_2(\nu, Q^2) \cos^2 \frac{\theta}{2} + 2W_1(\nu, Q^2) \sin^2 \frac{\theta}{2} \right] \left(\dots \right)$$

where $\nu = E - E'$ with E and E' the energies of the incoming and outgoing electron, respectively, Q is the scale of momentum transferred, and α is the fine-structure constant. It is usual to define $x = Q^2/2m_p\nu$ which can be interpreted as the momentum fraction involved in the parton-level scattering. The form factors W_1 and W_2 can

be determined by measuring the energy and angular dependence of the outgoing electron. If the struck partons are point-like spin-1/2 particles, as expected in the quark model, the following two relations are derived

$$\nu W_2(\nu, Q^2) \rightarrow F_2(x) = \sum_i^{\text{part.}} e_i^2 x f_{i/p}(x)$$

$$m_p W_1(\nu, Q^2) \rightarrow F_1(x) = \frac{1}{2x} F_2(x)$$

where e_i is the electric charge of the struck parton i within the proton. The fact that at fixed Q^2 the cross section depends only on the variable x is known as Bjorken scaling. The relation $F_2(x) = 2xF_1(x)$ is known as the Callan-Gross relation.

Quark model

The quark model is a non-dynamical classification scheme for hadrons in terms of their valence quarks. For energy scales above Λ_{QCD} the quarks flavours up, down and strange are relativistic. Thus, the strong interactions have a SU(3) flavour symmetry associated. The quark model underlies this global symmetry and it is referred to as the Eightfold Way. The idea was proposed in 1961 by Murray Gell-Mann and Yuval Ne'eman to explain the hadron quantum numbers [20, 21].

Hadrons are characterized by their quantum numbers $I^G(J^{PC})$. One set comes from the Lorentz symmetry where $J = L \oplus S$ is the total angular momentum, P is parity and C is charge conjugation. The others are isospin I that corresponds to the third component of the SU(2) flavour symmetry and G-parity.

The SU(3) flavour symmetry has eight generators whose correspond to the Gell-Mann matrices divided by a factor two. These matrices are used to determine the isospin $I = \lambda_3/2$ and strong hypercharge $Y = \lambda_8/\sqrt{3}$ operators. The hypercharge is the sum of the baryon number which adds 1/3 for each valence quark and of the strangeness which adds -1 for each strange valence quark. In this model, the electric charge of the hadron may be calculated as $Q = I + Y/2$.

Hadrons must be invariant under the gauge symmetry $SU(3)_C$ due to confinement. Singlets of colour are produced by either quark-antiquark or three quarks combinations. Hadrons made of quarks $q\bar{q}$ are called mesons, while hadrons made of quarks qqq are called baryons. It is usual to write their wave function as

$$|\text{hadron}\rangle = |\text{colour}\rangle \times |\text{space}\rangle \times |\text{spin}\rangle \times |\text{flavour}\rangle .$$

For mesons $|q\bar{q}\rangle$, parity is given by $P = -(-1)^L$ and their bound states are the flavour octet and singlet with $J^P = 0^-$ or $J^P = 1^-$ in the ground state $L = 0$. They are represented in Figure 2.2. For neutral mesons, charge conjugation is given by $C = (-1)^{L+S}$. The tensor products decompose into irreducible representations as

$$| \text{SU}(2) \text{ spin } \mathbf{2} \otimes \mathbf{2} = \mathbf{1} \oplus \mathbf{3} | \text{ SU}(3) \text{ flavour } \mathbf{3} \otimes \overline{\mathbf{3}} = \mathbf{1} \oplus \mathbf{8} |$$

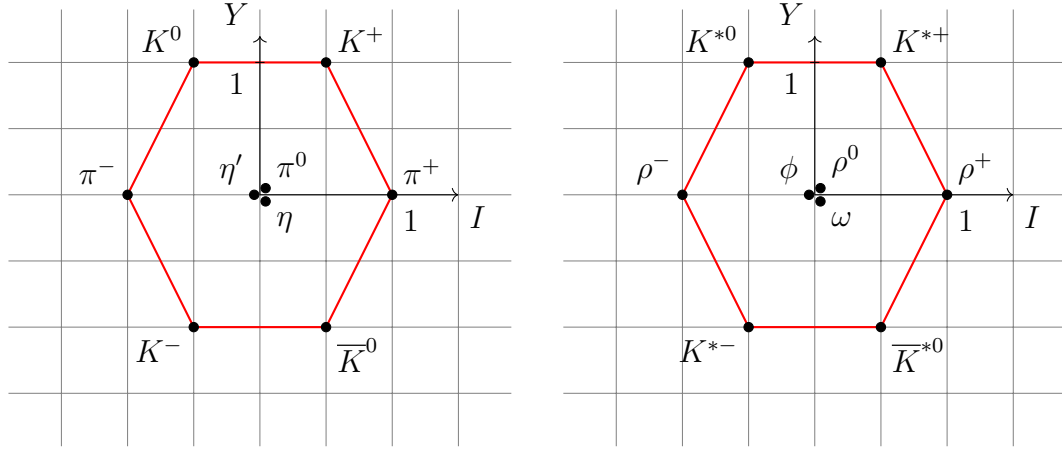


Figure 2.2: Mesons in the ground state from the flavour octet and singlet with $J^P = 0^-$ (left) and with $J^P = 1^-$ (right). They are mixed into a flavour nonet.

For baryons $|qqq\rangle$, the possible combinations in the ground state are the flavour decuplet with $J^P = 3/2^+$ and the flavour octet with $J^P = 1/2^+$. They are represented in Figure 2.3. The corresponding tensor products decompose into irreducible representations as

$$\begin{array}{c|cc} \text{SU(2) spin} & \mathbf{2} \otimes \mathbf{2} \otimes \mathbf{2} = \mathbf{2}_M \oplus \mathbf{2}_M \oplus \mathbf{4}_S \\ \text{SU(3) flavour} & \mathbf{3} \otimes \mathbf{3} \otimes \mathbf{3} = \mathbf{1}_A \oplus \mathbf{8}_M \oplus \mathbf{8}_M \oplus \mathbf{10}_S \end{array}$$

The subscripts indicate their behaviour under the interchange of any two identical quarks: A purely antisymmetric, M mixed, and S purely symmetric. In this case, $|\text{space}\rangle \propto (-1)^L$ is symmetric and $|\text{colour}\rangle$ is completely antisymmetric. Hence, the combination $|\text{spin}\rangle \times |\text{flavour}\rangle$ must be always symmetric.

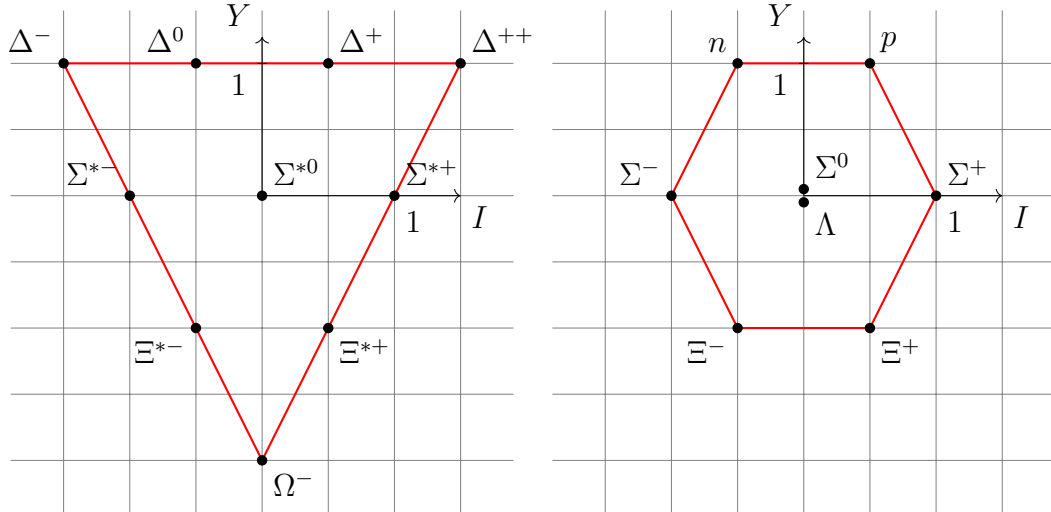


Figure 2.3: Baryons in the ground state from the flavour decuplet with $J^P = 3/2^+$ (left) and the flavour octet with $J^P = 1/2^+$ (right).

2.2 Collider techniques

Particle collider experiments emerged after fixed-target experiments by bringing together two opposite particle beams. The main advantage for colliders is that larger energy scales can be achieved in deep-inelastic interactions.

Initially, these experiments crossed an electron beam with a positron beam to produce e^+e^- annihilation. This interaction was recorded for the first time in 1964 by the Istituto Nazionale di Fisica Nucleare (INFN). Afterwards, larger experiments like the LEP collider at CERN were designed. This collider started to operate in 1989 and accelerated positrons and electrons to a total energy of 45 GeV. Other experiments like the HERA accelerator at DESY were fed with electrons and protons to produce e^-p collisions and test the proton structure. This experiment started to operate in 1992 with an energy of around 320 GeV at the interaction point.

Hadron colliders allowed increasing the energy scale at the interaction point even more. The main ones consist in a circular ring and have been built at either CERN or Fermilab. For pp collisions the first one was the Intersecting Storage Rings (ISR) and for $p\bar{p}$ collisions the Super Proton Synchrotron (SPS), both located at CERN. Afterwards, the Tevatron synchrotron at Fermilab started to accelerate protons and antiprotons in 1992 to energies of up to 1 TeV. Nowadays, the largest collider is the LHC at CERN that mainly brings together two proton beams moving in opposite directions with an energy of 13 TeV.

In order to better understand these collisions, consider first an experiment throwing a particle beam against a fixed target. A bunch of particles in the beam has velocity \vec{v} and moves perpendicular to a certain surface of area A . The number of particles passing through the section in a given period of time can be calculated from $\Delta \text{particles} = nA|\vec{v}|\Delta t$ where n is the number density of particles. The incident flux density for this system is simply given by the quantity

$$\Phi = \frac{1}{A} \frac{\Delta \text{particles}}{\Delta t} = n|\vec{v}|.$$

Then, one of those particles with mass m_a and located in the beam collides with a fixed target with mass m_b . In this collision, the number density of particles is given by $n = 1/V$ where V is the volume where the interaction occurs and the velocity of the centre of mass is calculated as $\vec{v}_{\text{com}} = m_a\vec{v}/(m_a + m_b)$.

Placed in the centre of mass frame, this is simply a collision between a particle that moves with velocity $\vec{v}_a = \vec{v} - \vec{v}_{\text{com}}$ and another one with velocity $\vec{v}_b = -\vec{v}_{\text{com}}$ instead of a fixed target. That way the relation $|\vec{v}| = |\vec{v}_a - \vec{v}_b|$ is recovered. Therefore, the centre of mass frame may correspond with the laboratory frame in a collider experiment bringing together two particle beams moving in opposite directions. The incident flux density for this new system is given by $\Phi = (1/V) |\vec{v}_a - \vec{v}_b|$.

The product of the incident flux density and the cross section corresponds to the probability per unit time of interaction, $dP/dt = \sigma\Phi$. The cross section is the main observable in particle collider experiments because the probability of interaction can

be calculated from the theory but also measured by counting the number of events recorded over time for a certain integrated luminosity.

Hence, the differential cross section for an experiment that has been carried out for a certain period of time T can be derived from the relation:

$$d\sigma = \frac{1}{T\Phi} dP.$$

To calculate the differential probability of interaction from theory, consider a scattering process with asymptotic states $p_a + p_b \rightarrow p_1 + \dots + p_n$, which comes from

$$dP^{(n)} = \frac{|\langle f; +\infty | i; -\infty \rangle|^2}{\langle f; +\infty | f; +\infty \rangle \langle i; -\infty | i; -\infty \rangle} \prod_{i=1}^n \left(\frac{d^3 p_i}{(2\pi)^3 2E_i} \right).$$

The scattering matrix, also called S -matrix, arises once the differential probability of interaction is computed in the interaction picture $\langle f; +\infty | i; -\infty \rangle = \langle f | S | i \rangle$. It can be expanded as $S = \mathbb{I} + i\mathcal{M}(2\pi)^4\delta^4(\Sigma p)$. Then, for a deep inelastic scattering:

$$dP^{(n)} = \frac{(2\pi)^4\delta^4(\Sigma p)TV|\mathcal{M}|^2}{(2E_aV)(2E_bV)} \prod_{i=1}^n \frac{d^3 p_i}{(2\pi)^3 2E_i}$$

where the matrix element $|\mathcal{M}|^2 = |\langle f | i\mathcal{M} | i \rangle|^2$ is calculated using the Feynman diagrams of a certain perturbative quantum field theory. The differential cross section for this deep inelastic scattering process is then derived from the formula:

$$d\sigma^{(n)} = \frac{1}{(2E_a)(2E_b)|\vec{v}_a - \vec{v}_b|} |\mathcal{M}|^2 d\Pi_{\text{LIPS}}^{(n)}$$

where the Lorentz invariant phase space (LIPS) represents all possible outgoing states of the process and its differential quantity is given by

$$d\Pi_{\text{LIPS}}^{(n)} = (2\pi)^4\delta^4 \left\{ p_a + p_b - \sum_{i=1}^n p_i \right\} \prod_{i=1}^n \left(\frac{d^3 p_i}{(2\pi)^3 2E_i} \right).$$

2.2.1 Coordinate system

Incoming particles move along the direction of the beam pipe and collide at the interaction point (IP) with an energy \sqrt{s} . The outgoing products of the collision are registered by particle physics detectors. From now on, consider a detector with a forward-backward symmetric cylindrical geometry and a solid angle coverage of almost 4π . The detector uses a right-handed coordinate system with its origin at the nominal IP in the centre of the detector and the z -axis along the beam pipe. The x -axis points from the IP to the centre of the hadron collider ring, and the y -axis points upward. Thus, the longitudinal direction corresponds to the z -axis and the transverse plane with the x - y plane.

In experiments with incoming hadrons, the hard interaction is the subprocess between their partons, carrying a fraction of the hadron momentum. The energy carried by partons is not well defined and the laboratory frame is neither the c.o.m. frame. Therefore, observables have to require longitudinally invariant expressions along the beam pipe direction. For instance, momenta are decomposed into their transverse and longitudinal components $\vec{p} = \vec{p}_\perp + \vec{p}_\parallel$ with respect to the beam pipe.

Particle physics detectors use a system of coordinates determined by the energy E , the momentum component in the transverse plane $p_T = |\vec{p}_\perp|$, the azimuthal angle around the beam pipe φ and the pseudo-rapidity η which is based on the polar angle. The definition of the pseudo-rapidity and its hyperbolic functions are given by

$$\eta = -\ln \left(\tan \frac{\theta}{2} \right) = \frac{1}{2} \ln \left(\frac{|\vec{p}| + |\vec{p}_\parallel|}{|\vec{p}| - |\vec{p}_\parallel|} \right) \left(\sinh \eta = \frac{1}{\tan \theta} = \frac{|\vec{p}_\parallel|}{\sqrt{|\vec{p}|^2 - |\vec{p}_\parallel|^2}}; \quad \cosh \eta = \frac{1}{\sin \theta} = \frac{|\vec{p}|}{\sqrt{|\vec{p}|^2 - |\vec{p}_\parallel|^2}}. \right)$$

The same way that the transverse momentum was defined, one can introduce a transverse energy $E_T = \sqrt{E^2 - p_L^2}$ which is also longitudinally invariant along the beam pipe. Another variable called rapidity y may be also introduced which is associated with the velocity in longitudinal direction, $\tanh y = |\vec{v}_\parallel| = p_L/E$. The definition of the rapidity and its hyperbolic functions are given by

$$y = \frac{1}{2} \ln \left(\frac{E + |\vec{p}_\parallel|}{E - |\vec{p}_\parallel|} \right) \left(\sinh y = \frac{p_T}{E_T} \sinh \eta; \quad \cosh y = \frac{E}{E_T}. \right)$$

Note that even if the rapidity is not longitudinally invariant by itself, the difference of rapidities is always going to be invariant. The invariant mass is another important variable which comes from the relation $m^2 = E^2 - |\vec{p}|^2 = E_T^2 - p_T^2$.

Furthermore, the inner product of two four-momenta and the four-momentum's components can be rewritten in the notation using detector coordinates as:

$$p_i \cdot p_j = E_{Ti} E_{Tj} \cosh \Delta y_{ij} - p_{Ti} p_{Tj} \cos \Delta \varphi_{ij}; \\ E = E_T \cosh y; \quad p_z = E_T \sinh y; \quad p_x = p_T \cos \varphi; \quad p_y = p_T \sin \varphi.$$

2.2.2 Higher-order emissions

The matrix elements required to get the cross sections are calculated using a perturbative expansion in the coupling $a(\mu_R^2)$. The first non-trivial contribution is called leading-order (LO). Higher-order terms in the perturbative expansion are simply corrections to the LO prediction. The first ones come from the next-to-leading-order (NLO) corrections and so on. These corrections can be real emissions, increasing the number of particles in the asymptotic states, or virtual loops, increasing the complexity within the hard interaction.

However, to avoid loop calculations, higher-order real-emission corrections may be considered through parton showers, where parton splitting kernels are used to simulate gluon emissions during the QCD cascade. This radiation corresponds to the QCD bremsstrahlung where emissions are soft and collinear, involving Sudakov logarithms that may spoil the perturbative expansion. In that case, the first logarithms must be absorbed in the leading-logarithm (LL) resummation. Thereafter, higher-order factors require a next-to-leading-logarithm (NLL) treatment and so on.

Parton showers

Hard interactions involve large momentum transfers, and therefore, partons are violently accelerated. This accelerated colour-charged partons emit QCD radiation in the form of gluons which emit even further radiation, leading to a cascade that parton showers can simulate. During the parton showering the interaction scale falls and the coupling rises into the hadronization regime, where partons are bound into hadrons owing to confinement. Many of them are unstable and later decay.

In principle, parton showers represent higher-order emissions to the hard process which are calculated in an approximation scheme, where only the dominant contributions are included at each order. These dominant contributions correspond to soft gluon emission and collinear parton splitting. The probability of not splitting during evolution of the cascade is given by the Sudakov form factors.

The simplest variable to understand the evolution is the virtual mass-squared of the partons q^2 . The reason is that the dominant contributions come from configurations in which the virtualities are strongly ordered, with the parton nearest to the hard process farthest from its mass shell and the virtualities falling sharply as the shower evolves away from it. However, many evolution variables can be considered, like the opening angle of emissions θ or the transverse momentum of partons p_T .

The Sudakov form factor representing the probability of not collinear splitting for parton i when evolving from the initial scale q_0^2 to the final one q_1^2 is given by

$$\Delta_i(q_0^2, q_1^2) = \exp \left\{ \left(\int_{q_0^2}^{q_1^2} \frac{dq^2}{q^2} 2a(q^2) \sum_j^{\text{part.}} \int_0^1 dz P_{j \leftarrow i}(z) \right) \right\}$$

where $P_{j \leftarrow i}$ is the associated splitting kernel and z is the momentum fraction of parton i carried by j . This probability is used by Monte Carlo event generators to determine the splitting and create a cascade, which is developed by sequential application of these splittings until the hadronization regime is reached. This Monte Carlo event generators are virtuality-ordered, angular-ordered or p_T -ordered depending on the choice of the evolution variable.

An alternative treatment of parton showers is dipole showering, where gluon emission is generated according to the dipole radiation pattern of a pair of partons instead of parton splitting. In this treatment, each pair of colour partners forms a dipole which splits into two dipoles when it emits a gluon. Thus, the dipole splitting is a $2 \rightarrow 3$

process, whereas the parton splitting was a $1 \rightarrow 2$ one. These dipoles generate a cascade by splitting again and again until the hadronization regime is reached.

2.2.3 Fragmentation schemes

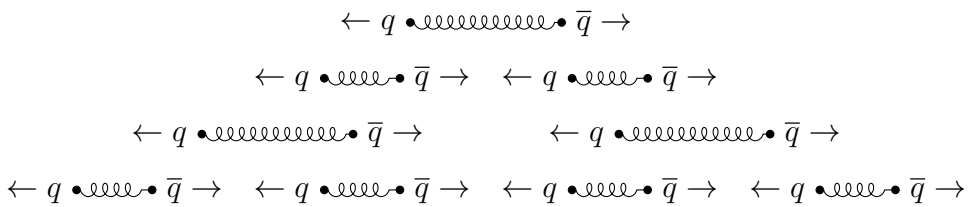
The radiation stops when the evolution variable reaches the hadronization regime. Then, perturbation theory becomes invalid and partons are bound into final-state hadrons due to confinement. Hadron structure has a non-perturbative nature, and therefore, hadronization models must rely on general features of QCD to simulate their formation. These models can also include the sequential decay of unstable hadrons produced and the radiation of soft photons until recorded by detectors in collider experiments. The main hadronization models are the cluster hadronization model and the Lund string fragmentation model, both based on different features of the theory which are explained below.

Cluster hadronization model

The cluster hadronization model is used by Monte Carlo event generators to form colourless groups in the final-state. Primary clusters are formed by combining the colour connected partners into a cluster as the scale in the cascade evolves. The invariant mass distribution of the clusters is independent of the nature and scale of the hard interaction. This idea is supported by the preconfinement property of QCD discovered by Daniele Amati and Gabriele Veneziano in 1979 [22]. Eventually, these clusters decay into the observed final-state hadrons at the hadronization scale.

Lund string fragmentation model

The Lund string fragmentation model is another model used by Monte Carlo event generators. This model was presented in 1983 by Bo Andersson and Gösta Gustafson [23]. It treats all gluons as field lines attracting to each other due to their self-interactions and forming a colour flux tube, usually called string. In the hadronization regime, the effective strength between a single quark-antiquark pair connected by one of these colour flux tubes increases as they are separated. Then, at a certain range it is more energetically favorable to create a new quark-antiquark pair rather than continue to elongate the same colour flux tube. This procedure occurs until these pairs form the observed final-state hadrons and is schematically depicted in the figure below.



The hadronization of a system more complicated than a single quark-antiquark pair depends on its colour structure. Each parton in the system has a unique colour partner, connected to it by a string segment which stretches and breaks as described before to eventually form the observed hadrons.

2.2.4 Event-shape variables

In 1979 events with three collimated bunches of hadrons in the final state were recorded by PETRA experiments at DESY for the first time. The gauge vector boson mediating the strong interactions called gluon was discovered. Thereafter, several observables were designed and measured to test the nature and behaviour of QCD in e^+e^- collisions. These observables were the event-shape variables. They are defined as functions of the final-state particle four-momenta and characterize the hadronic energy flow in a certain collision.

The classical event-shape variable is the Thrust [24, 25]. The idea is to select the axis that maximizes the projections of the momentum components. The formal definition of this variable and its complementary one, Thrust minor, are

$$T = \max_{\vec{n}_T} \frac{\sum_i |\vec{p}_i \cdot \vec{n}_T|}{\sum_i |\vec{p}_i|}; \quad T_m = \frac{\sum_i |\vec{p}_i \times \vec{n}_T|}{\sum_i |\vec{p}_i|}.$$

where \vec{n}_T is the unit vector of the thrust axis which is the one that maximize the quantity and the sum runs over all particles in the final state. Note that this variable is infrared and collinear safe, and therefore, not affected by long-distance effects like hadronization.

The Thrust variable takes values between 1 and 1/2 depending on the final-state configuration. For back-to-back configurations, also called pencil-like, it takes value 1 and for planar configurations 2/3. The spherically symmetric configurations correspond with 1/2. The analytical expression for the cross section distribution with the Thrust calculated using pQCD at LO in the massless limit is given by Eq. (2.2) which is represented in Figure 2.4.

$$\frac{1}{\sigma_0} \frac{d\sigma}{dT} = a(\mu_R^2) 2C_F \left[\frac{2(3T^2 - 3T + 2)}{T(1-T)} \ln \left(\frac{2T-1}{1-T} \right) \right] \left(\frac{3(3T-2)(2-T)}{(1-T)} \right) \quad (2.2)$$

Additionally, there is a family of event-shape variables derived from the eigenvalues of the regularized sphericity tensor [26]. Its formal definition is given by

$$M^{\mu\nu} = \frac{\sum_i \vec{p}_i^\mu \vec{p}_i^\nu |\vec{p}_i|^{r-2}}{\sum_i |\vec{p}_i|^r}; \quad \mu, \nu = 1, 2, 3$$

where the sum runs over all particles in the final state and the parameter usually takes values $r = 0, 1$. This tensor is collinear unsafe but it is still a good quantity to extract information of the isotropy of the final-state energy distribution. Its eigenvalues satisfy the closure $\lambda_1 + \lambda_2 + \lambda_3 = 1$ and are ordered so that $\lambda_1 \geq \lambda_2 \geq \lambda_3$.

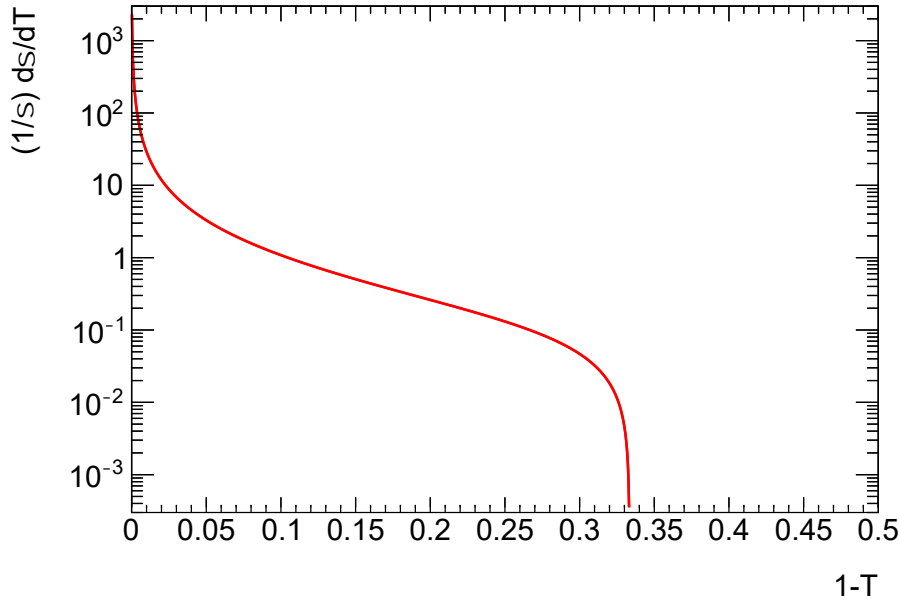


Figure 2.4: Thrust distribution at LO calculated using pQCD in the massless limit with the strong coupling constant at the same order for a number of active flavours $n_f = 6$ and a renormalization scale value of $\ln(\mu_R^2/\Lambda_{\text{QCD}}^2) = 20$.

The main event-shape variables extracted from here are the sphericity S and the aplanarity A . Larger values of the sphericity indicate more spherical events, while the aplanarity is a measure of the extent to which the radiation is contained in the plane defined by the two first eigenvectors of the sphericity tensor, larger values indicate less planar events. Its definitions can be found below along with other relevant factors:

$$S = \frac{3}{2}(\lambda_2 + \lambda_3); \quad A = \frac{3}{2}\lambda_3; \quad C = 3(\lambda_1\lambda_2 + \lambda_1\lambda_3 + \lambda_2\lambda_3); \quad D = 27(\lambda_1\lambda_2\lambda_3).$$

Since the C -factor is defined by products of eigenvalue pairs, it vanishes for pencil-like events, while the D -factor, which is defined by multiplying the three eigenvalues, vanishes for events in which all particle momenta lie on the same plane.

Energy-Energy Correlations

A particularly interesting infrared safe event-shape observable is the energy-energy correlation (EEC) function which was originally introduced in 1979 in Refs. [27, 28] to provide a quantitative test of QCD in e^+e^- annihilation experiments. The EEC function and its associated azimuthal angular asymmetry (AEEC) can be calculated in pQCD and their measurements have had significant impact on the early precision tests of QCD and in the determination of the strong coupling constant.

The EEC function is defined as the energy-energy-weighted azimuthal angular dis-

tribution of produced particle pairs in the final state:

$$\frac{1}{\sigma} \frac{d\Sigma}{d \cos \phi} = \frac{1}{\sigma} \sum_{i,j} \int d\sigma \frac{E_i E_j}{Q^2} \delta(\cos \phi - \cos \Delta\varphi_{ij})$$

where the indices i and j run over all outgoing particles in a given event, Q is the invariant mass of the system, E_i is the energy of the outgoing particle i , and $\Delta\varphi_{ij}$ is the angle in the transverse plane between particles i and j .

The Dirac delta function ensures that $\phi = \Delta\varphi_{ij}$ and the normalization to the effective cross section $\sigma = \int d\sigma$ ensures that the integral of the function over all the azimuthal range $\cos \phi$ is unity by definition, as the invariant mass Q is the total sum of the outgoing energies. The observable is by definition invariant under collinear splitting and soft emissions do not contribute. Hence, this weighting of the cross section prevents from infrared divergences.

In addition, the AEEC function is defined as the difference between the forward ($\cos \phi > 0$) and the backward ($\cos \phi < 0$) part of the EEC function to cancel constant contributions over $\cos \phi$. Thus, it is insensitive to isotropic radiation:

$$\frac{1}{\sigma} \frac{d\Sigma^{\text{asym}}}{d \cos \phi} = \frac{1}{\sigma} \frac{d\Sigma}{d \cos \phi}_\phi - \frac{1}{\sigma} \frac{d\Sigma}{d \cos \phi}_{\pi-\phi}.$$

The main features of the EEC function is a peak at $\cos \phi = 1$ associated to self-correlations, another peak at $\cos \phi = -1$ associated to back-to-back configurations and a central plateau between them coming from the strong radiation and therefore sensitive to the strong coupling. The AEEC function presents a strong fall-off with the first value taking a negative value due to self-correlations. These contributions vanish when using alternative weights like $p_i \cdot p_j / Q^2$ which are Lorentz invariant.

For e^+e^- experiments, the EEC function calculated at LO using pQCD in the massless limit is given by Eq. (2.3) where the kinematic variable $\chi = (1 - \cos \phi)/2$ is implemented to simplify notation. This analytical expression is represented in Figure 2.5 where the features mentioned before can be clearly identified.

$$\frac{1}{\sigma_0} \frac{d\Sigma}{d \cos \phi} = a(\mu_R^2) C_F \frac{3 - 2\chi}{2\chi^5(1 - \chi)} [2(3 - 6\chi + 2\chi^2) \ln(1 - \chi) + 3\chi(2 - 3\chi)] \quad (2.3)$$

The transverse energy-energy correlation was proposed in 1984 as the appropriate generalization for hadron collider experiments in Ref. [29]. Longitudinally invariant quantities must be considered instead whilst keeping the infrared collinear safety. Then, the transverse energy-energy correlation function is given by

$$\frac{1}{\sigma} \frac{d\Sigma}{d \cos \phi} = \frac{1}{\sigma} \sum_{i,j} \int d\sigma \frac{E_{Ti} E_{Tj}}{E_T^2} \delta(\cos \phi - \cos \Delta\varphi_{ij})$$

where the variable E_T is the total sum of the transverse energies of the outgoing particles so that the integral over the whole range is still unity.

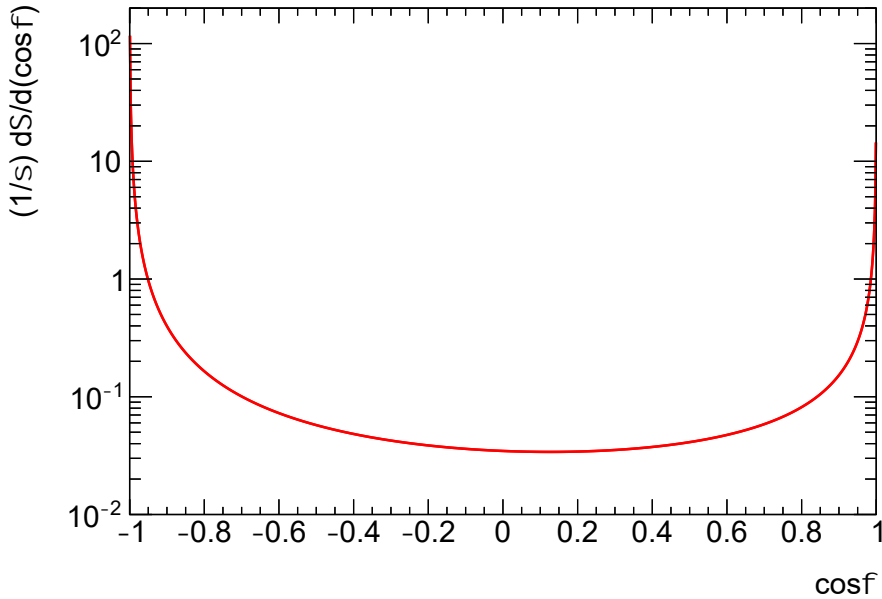


Figure 2.5: Energy-energy correlation at LO calculated using pQCD in the massless limit with the strong coupling constant at the same order for a number of active flavours $n_f = 6$ and a renormalization scale value of $\ln(\mu_R^2/\Lambda_{\text{QCD}}^2) = 20$.

2.2.5 Jet algorithms

In hard interactions, hadrons appear predominantly in collimated bunches, which are generically called jets. Consequently, physical observables can consider a set of jets in the final state instead of the individually observed particles. To a first approximation, a jet can be thought of as a hard parton that has undergone soft and collinear showering, and then hadronization. So as to map observed hadrons onto a set of jets, one uses a jet definition. The main jet definitions are cone algorithms and sequential recombination algorithms, both jet clustering algorithms are infrared safe and preserve the infrared safety of observables.

The first jet definition was a cone algorithm proposed by George Sterman and Steven Weinberg in 1977 to test pQCD calculations in e^+e^- experiments [30]. The algorithm classified an event as having two jets if at least a fraction of the event's energy was contained in two cones of opening half-angle. Afterwards, sequential recombination algorithms started to abound due to their simplicity. They go beyond finding jets and implicitly assign a clustering sequence to an event. The first one was introduced by the JADE collaboration. For each pair of particles i,j in the final state, it computes their distance as $d_{ij} = 2E_i E_j (1 - \cos \theta_{ij})/Q^2$ where θ_{ij} is the angle between them. If the minimum of all distances is below a certain threshold d_{cut} , then both particles are recombined into a new pseudo-particle and the process repeats again until remaining particles are declared jets and the iteration terminates. The recombination scheme and other properties of jet definitions were set out in the Snowmass accord from 1990 [31].

The anti- k_t clustering algorithm is a sequential recombination algorithm introduced in 2008 as a generalization for jet definitions in experiments with incoming hadrons [32]. It has become the de-facto standard for the LHC experiments. In addition to the distance between a pair of outgoing particles i,j , there is a distance between a particle i and the beam direction:

$$d_{ij} = \min(p_{Ti}^{2r}, p_{Tj}^{2r}) \frac{\Delta R_{ij}^2}{R^2}; \quad d_{iB} = p_{Ti}^{2r};$$

$$\Delta R_{ij}^2 = 2(\cosh \Delta y_{ij} - \cos \Delta \varphi_{ij}) = \Delta y_{ij}^2 + \Delta \varphi_{ij}^2.$$

Here, $p_{Ti,j}$ are their transverse momenta, ΔR_{ij} is their separation in the rapidity-azimuthal plane and R is a free parameter acting as a threshold for the jet radius.

The proper anti- k_t algorithm takes the parameter $r = -1$ and favours clusterings that involve hard particles rather than the ones involving soft particles. If one takes the parameter $r = 1$ the k_t algorithm is recovered instead, whereas for $r = 0$ one has the Cambridge/Aachen one (C/A). The former prefers to cluster soft particles first; the latter was introduced in 1999 as an energy-independent clustering following a sequence based only on angular separations.

To merge a list of particles into a set of jets one identifies the smallest of all the d_{ij} and d_{iB} , and if it is a d_{ij} , then i and j are merged into a new pseudo-particle. The recombination scheme to merge them is the E -scheme, or 4-vector recombination scheme, that just adds their 4-vectors, producing massive jets. Nevertheless, if the smallest distance is a d_{iB} , then i is removed from the list and declared a jet.

Jet substructure

As mentioned before, a jet can be thought of as hard parton that has undergone showering and then hadronization. However, collimated hadronic decays of boosted particles can also be reconstructed as a single jet. Jet substructure techniques were born to distinguish signal jets from background. The first ones were jet tagging algorithms that classify jets based on either their parton flavour or their collimated hadronic decay. Later, other techniques like jet grooming algorithms were developed to remove underlying-event contamination.

In 2008 the Butterworth-Davison-Rubin-Salam (BDRS) Mass Drop plus filtering technique was presented to split large signal jets from boosted hadronic decays whilst removing the underlying-event [33]. Other techniques like trimming and pruning were later introduced to improve jet tagging algorithms.

In 2014 the Soft Drop technique was presented to remove constituents at wide angle and relatively soft within reconstructed jets [34]. First, jets are clustered using the anti- k_t algorithm and later each one is reclustered again using the C/A algorithm to transverse the angular sequence backwards. At each point in the sequence two branches merge where i is the harder and j is the softer. The softer branch is

removed if it satisfies the condition:

$$z_{ij} = \frac{p_{Ti}}{p_{Ti} + p_{Tj}} > z_{\text{cut}} \frac{\Delta R_{ij}^\beta}{R^\beta}$$

where z_{cut} is a threshold and β is the parameter that characterize the algorithm. Then the process continues down the harder branch until the end of the sequence.

The Lund jet plane encodes this emission pattern in the angular sequence of a jet. It is based on the transverse momentum fraction of the emitted gluon z_{ij} and the opening angle of the emission $\Delta R_{ij}/R$. The number of emissions within regions provides discrimination between quark and gluon jets. [35]

In addition, jet-shape variables have been introduced to study the hadronic structure within jets. These variables can be a powerful discriminant in jet algorithms. The classical one is called N -subjettiness and was designed in 2010 to identify boosted hadronically-decaying objects like electroweak bosons and top quarks [36]. One takes a reconstructed jet and identifies N candidate subjets using a specific subjet finding procedure. Then, the jet-shape variable is calculated via

$$\tau_N^{(\beta)} = \frac{\sum_i p_{Ti} \min(\Delta R_{1i}^\beta, \dots, \Delta R_{Ni}^\beta)}{\sum_i p_{Ti} R^\beta}$$

where both sums run over all constituents in the jet and for each of them one considers the minimal distance between a candidate subjet and that constituent.

There is also a family of jet-shape variables called N -point energy correlation functions (ECF) presented in 2013 as a powerful probe of jet substructure [37, 38]. These observables have utility for quark-gluon discrimination using 2-point correlators, for boosted electroweak boson identification using 3-point correlators and for boosted top quark identification using 4-point correlators. In hadron colliders, their natural definition is as transverse momentum correlation functions:

$$\text{ECF}(N, \beta) = \sum_{i_1 < \dots < i_N} \left(\prod_{a=1}^N p_{Ti_a} \right) \left(\prod_{b=1}^{N-1} \prod_{c=b+1}^N (\Delta R_{i_b i_c}^\beta) \right)$$

where the sum runs over all constituents within the reconstructed jet. These functions can be combined to form different dimensionless ratios that are good observables to study jet substructure. Thus, one has extra jet-shape variables like

$$C_N^{(\beta)} = \frac{\text{ECF}(N+1, \beta) \text{ECF}(N-1, \beta)}{\text{ECF}(N, \beta)^2}.$$

2.2.6 Underlying event

In hadron collider events that contain a hard interaction, there is extra hadron production that cannot be ascribed to showering from partons participating in the main interaction. This extra activity is called underlying event (UE) and arises mainly

from collisions between those partons in the incoming hadrons that do not directly participate in the hard interaction. These soft collisions are called multiple-parton interactions (MPI). Although there are other sources like beam-beam remnants, asymptotic radiation, pile-up, and noise. The events where the hard interaction is not identifiable are called minimum-bias events.

Models that account for both underlying event and minimum-bias events are based on multiple-parton interactions with relatively small momentum transfer. The most common one is the elastic gluon-gluon scattering which is highly probable in hadron collisions and leads to extra hadron production. This production is simulated using different tunes where an impact parameter characterizes the structure of the collision. Bear in mind that the presence of a hard interaction in the collision is correlated with more multiple interactions and a higher level of underlying event activity.

Pile-up mitigation

Pile-up is a situation frequently observed in collider experiments where a particle detector is affected by several events at the same time. Hence, background signals that occur in the same time gate as the signal of interest add to the event. These signals correspond with multiple-hadron collisions happening during a single bunch crossing. These soft and simultaneous proton-proton collisions complicate the extraction of precise information from the hard interaction in LHC experiments.

In 2008 a novel technique was proposed to mitigate this effect in hadron collider experiments. This technique is called $\rho \times A^{\text{jet}}$ subtraction method and it is based on background densities and jet areas to provide jet-by-jet corrections for pile-up and underlying-event [39]. In 2015 the ATLAS collaboration developed its own algorithm to correct for the impact of pile-up on jet energy and jet shapes using subtraction and grooming procedures, the so-called jet vertex tagger (JVT) algorithm [40].

Nowadays, one can still find new techniques to face the pile-up major challenge. The iterative constituent subtraction (ICS) method was proposed in 2019 to improve the background mitigation in hadron collisions [41]. This method is an extension to the jet area-based pile-up subtraction method with an iteratively implementation to equilibrate the background subtraction across the entire event.

2.2.7 Monte Carlo methods

Monte Carlo (MC) methods are a broad class of computational algorithms that rely on repeated random sampling to obtain numerical theoretical results. The random sampling follows a certain density distribution of a random variable.

In 1946 Stanislaw Ulam and John von Neumann invented the first modern version of a Monte Carlo method at the Los Alamos National Laboratory. The aim was to solve problems in nuclear weapons projects using random sampling instead of

deterministic mathematical methods. Later, these algorithms were improved and implemented in different fields thanks to the development of computing machinery.

In the first place, the middle-square method was used for generating pseudo-random numbers which act as seeds for Monte Carlo algorithms. For instance, the acceptance-rejection algorithm that returns random numbers distributed according to a density function from random numbers generated following a uniform distribution.

More worldly methods appeared later to generate the initial pseudo-random numbers. In 1958 the linear congruential generator was presented, producing a set of pseudo-random numbers $u \in [0, 1)$ following an uniform distribution $h(u) = 1$ according to the sequence:

$$u_{n+1} = (au_n + c) \bmod m$$

where the initial seed is u_0 , the modulo is m and the mod operator returns the remainder of the division. The parameters are the multiplier a and the increment c .

Once the pseudo-random numbers u have been generated, one can compute the set of pseudo-random numbers x following a certain invertible distribution $f(x)$ using the transformation method $\int dx f(x) = du h(u)$. Then, the outcome values are determined by inverting the equation:

$$\int_{-\infty}^x dx f(x) = u.$$

The definite integral may have intricate boundary conditions and a conventional solution is limited to a few scenarios. Monte Carlo integration must employ a non-deterministic approach to provide the outcome values. Thus, the final outcome is an approximation of the correct value with respective error bars, where the correct value is likely to be found.

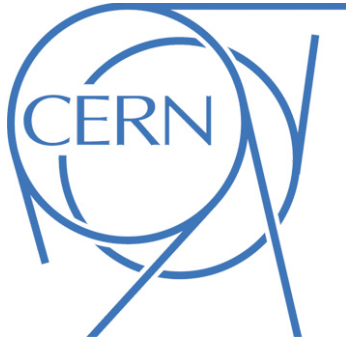
In particle physics, Monte Carlo methods are used to generate events. These simulated events allow obtaining theoretical predictions for physical observables when analytical calculations cannot be performed. In order to do that, observables are computed as histograms where each bin is filled with simulated events.

CHAPTER 3

Experimental setup

CERN operates a wide range of particle and nuclear facilities used by experiments covering a wealth of topics in physics. For instance, nuclear fixed-target experiments at ISOLDE, antimatter experiments at AD, and particle collider experiments at LHC.

In this chapter, a description of the experimental setup is given, with special attention to the LHC accelerator and the ATLAS detector. The LHC accelerator is the largest particle accelerator in the world. Its circular tunnel was originally constructed for the LEP machine between 1984 and 1989. It has 26.7 km of circumference and is buried 100 m under the franco-swiss border in Geneva. The LHC facilities are run by several experimental collaborations, mainly, ATLAS and CMS which are general-purpose particle detectors, whereas LHCb focus primarily on flavour physics and ALICE specializes on heavy ion collisions.



3.1 The LHC accelerator

The LHC accelerator [42] accelerates two proton beams moving in opposite directions up to a nominal centre-of-mass energy taking the value $\sqrt{s} = 13$ TeV since 2015. Once the nominal energy is reached, both beams collide inside the particle detectors, which are distributed along the accelerator circumference. The purpose of the LHC is to produce these proton-proton collisions which are then recorded by detectors and used for physical analyses, like the one presented in this thesis.

Although the initial proton beams were injected into the LHC in 2008, the first successful collision occurred in 2010 at 7 TeV. The collision energy was increased to 8 TeV during the 2012 data-taking period, delivering a luminosity of 22.8 fb^{-1} . Thereafter, the LHC was deactivated for a two-year maintenance period, restarting in 2015 with a collision energy of 13 TeV. This was the beginning of the LHC Run 2, which extended until 2018 and delivered a total luminosity of 156 fb^{-1} .

Additionally, the LHC also recorded proton-lead collisions to study the quark-gluon plasma. Nowadays, the LHC remains deactivated for its second long shutdown.

The proton beams accelerated by the LHC are extracted from Hydrogen gas and drift in a smaller system of accelerators. The injection complex pushes beams from the 50 MeV obtained with Linac 2, to 1.4 GeV in the Proton Synchrotron Booster (PSB), to 25 GeV in the Proton Synchrotron (PS) and 450 GeV in the Super Proton Synchrotron (SPS). Proton beams reaching the LHC travel in two separate rings inside vacuum chambers passing through 1232 superconducting dipole magnets and 392 quadrupole magnet distributed around the circumference. Figure 3.1 depicts the layout of this accelerator chain.

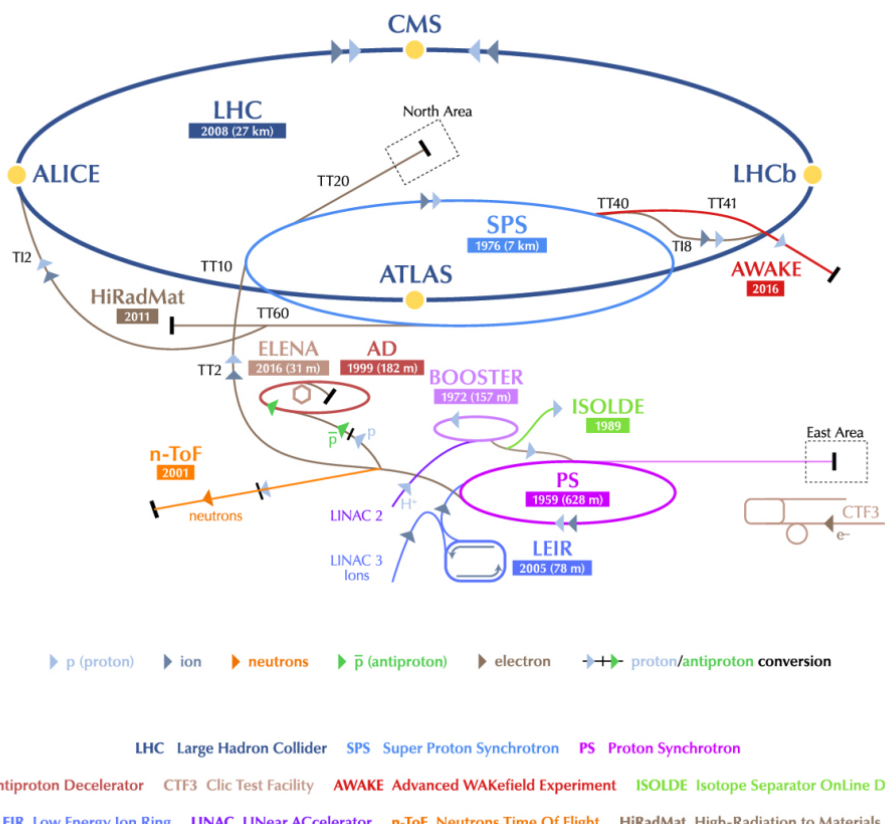


Figure 3.1: Distribution of the CERN accelerator complex, including particle and nuclear experiments along with other additional information [43].

As previously mentioned in Section 2.2, every physics process has a probability to occur parametrized by the process cross section. The LHC provides millions of pp collisions per second, giving an expected event rate proportional to its cross section:

$$\frac{dN_{\text{ev}}}{dt} = \sigma \mathcal{L} \quad \Rightarrow \quad N_{\text{ev}}(t_0, t_1) = \sigma \int_{t_0}^{t_1} dt \mathcal{L} = \sigma L$$

where the proportionality factor corresponds to the differential luminosity. Consequently, the total number of events recorded is the product of the process cross

section and the differential luminosity integrated over time. This key quantity is called integrated luminosity and needs to be precisely measured by both the accelerator (delivered luminosity) and each experimental detector (recorded luminosity) when the data taking is ready. Figure 3.2 shows the integrated luminosity delivered to ATLAS as a function of the month in years from 2011 to 2018.

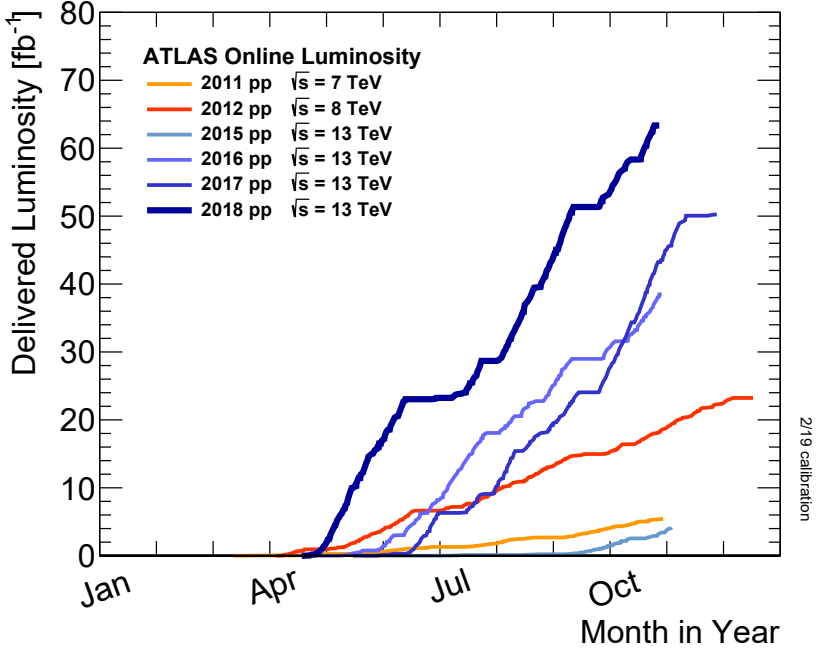


Figure 3.2: Cumulative luminosity versus day delivered to ATLAS during stable beams and for high-energy pp collisions only between 2011 and 2018 [44].

The differential luminosity is defined as the number of protons crossing the unit area per unit time. Assuming a gaussian distribution of the proton density inside the beam, it can be calculated from beam parameters like σ_x and σ_y , characterizing the beam transverse profiles. Proton beams have a bunch train structure with each bunch containing a high number of protons to maximize the probability of interaction for each bunch crossing. Then, if two proton bunches cross with numbers of particles N_1 and N_2 collide at a frequency f , the differential luminosity is simply given by

$$\mathcal{L} = f \frac{N_1 N_2}{4\pi\sigma_x\sigma_y}.$$

The average bunch crossing rate is given by the product of the number of bunches per beam and the revolution frequency, $f_{\text{rev}} N_{\text{bunch}}$. Hence, one can use this result to obtain the number of interactions per bunch crossing as

$$\mu = \frac{N_{\text{ev}}}{f_{\text{rev}} N_{\text{bunch}}}.$$

Figure 3.3 presents the mean number of interactions per bunch crossing registered in pp collisions for each of the yearly data-taking periods during the Run 2. The nominal value for the bunch spacing is always 25 ns. This number of interactions

per bunch crossing is a powerful indicator of the pile-up effects in measurements. As also mentioned in Section 2.2, pile-up is a situation where a particle detector is affected by several events at the same time. Attending to the time difference between interactions, one can distinguish two types of pile-up collisions. On the one hand, the in-time pile-up occurs when the pile-up signal in the detector corresponds to the same bunch crossing as the hard-scattering signal, and therefore, both are recorded in the same data taking window. On the other hand, the out-of-time pile-up is the effect of collisions which have produced in a different bunch crossing has the hard-scattering signal recorded in the detector.

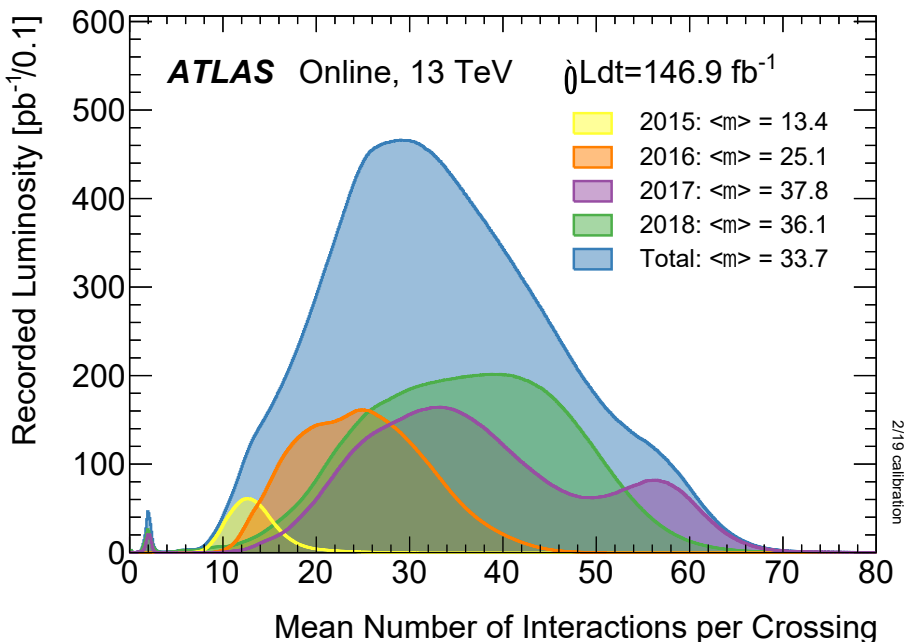


Figure 3.3: Mean number of interactions per bunch crossing μ , showing the 13 TeV data recorded by ATLAS from 2015 to 2018 [44].

3.2 The ATLAS detector

The ATLAS detector [45] is a multi-purpose particle detector located at Point-1, near CERN Meyrin site, whose name derives from the expression A Toroidal LHC ApparatuS. This cylindrical apparatus is designed to detect the outgoing products of hadron collisions occurring along the beam pipe. The coordinate system is exactly the same as the one presented in Section 2.2.

From the nominal IP outwards, it contains an inner detector (ID), designed to precisely measure the momentum of charged particle tracks, a calorimeter system for measuring the energy deposition of electrons and photons, along with strong-interacting particles, and a



muon spectrometer based on toroidal magnets for measuring the energy and momentum of muons. A schematic representation of the detector is shown in Figure 3.4. Moreover, the detector is equipped with an excellent trigger and data-acquisition system (TDAQ).

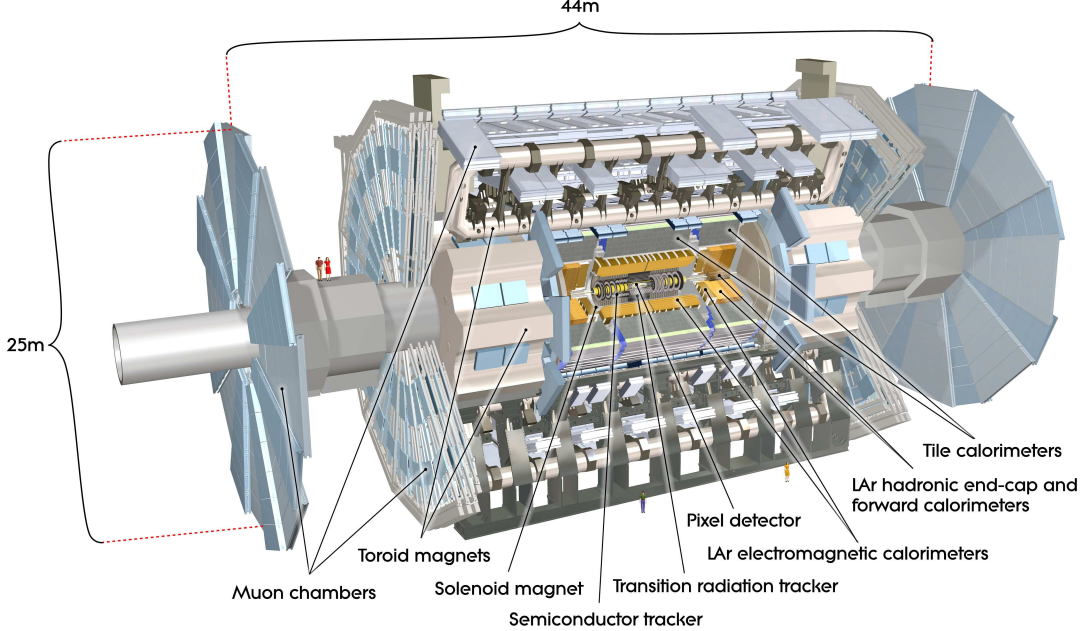


Figure 3.4: Cut-away view of the ATLAS detector. The dimensions of the detector are 25 m in height and 44 m in length. The overall weight of the detector is approximately 7000 tonnes [45].

3.2.1 Inner Detector

The ATLAS ID [46, 47] is designed to precisely measure the momentum of charged particles produced in the collisions, as well as for primary and secondary vertex identification. Thus, it is expected to give an excellent tracking performance, covering the full azimuthal range $-\pi < \varphi \leq \pi$ and the pseudorapidity region $|\eta| < 2.5$. It is able to track particles with transverse momentum above 500 MeV, except for some minimum bias analyses where the threshold is 100 MeV. The ID is immersed in an axial magnetic field of 2 T which bends the trajectory of charged particles and allows for a measurement of the charge. The overall transverse momentum resolution of the ID is required to be

$$\frac{\sigma_{p_T}}{p_T} = 0.05\% p_T[\text{GeV}] \oplus 1\%.$$

The inner detector consists of three different systems, starting from the nearest to the IP is the Pixel detector, followed by the Semiconductor Tracker (SCT) and then the Transition Radiation Tracker (TRT). Figure 3.5 depicts a cut-away view of this structure, and Table 3.1 provides the main parameters of each system.

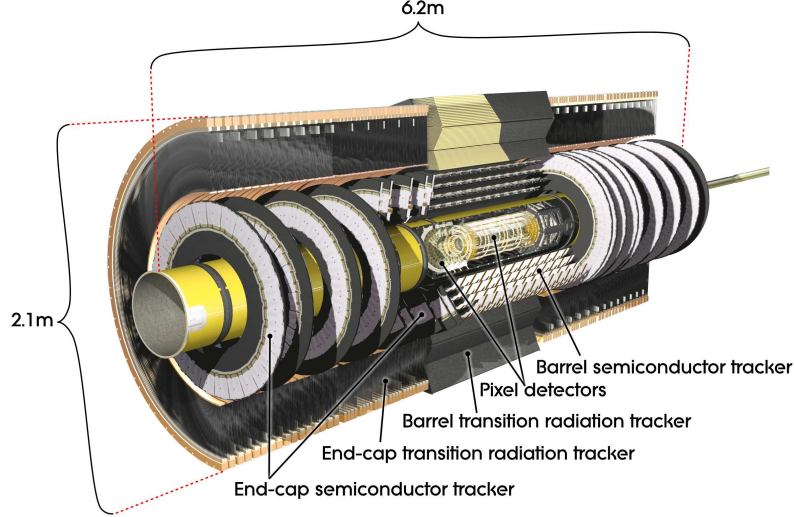


Figure 3.5: Cut-away view of the ATLAS inner detector [45].

System and position	Coverage	Channels ($\times 10^6$)	Resolution (μm)
Pixel	4 barrel cylindrical layers	$ \eta < 2.5$	10 ($R - \varphi$), 115 (z)
	2×3 end-cap disks		10 ($R - \varphi$), 115 (R)
SCT	4 barrel cylindrical layers	$ \eta < 1.4$	17 ($R - \varphi$), 580 (z)
	2×9 end-cap disks		17 ($R - \varphi$), 580 (R)
TRT	73 barrel straw planes	$ \eta < 0.625$	0.105
	160 end-cap straw planes		0.246
			170 ($R - \varphi$)
			170 ($R - \varphi$)

Table 3.1: Main parameters of the systems conforming the inner detector. The resolutions quoted are the typical intrinsic accuracies per module or straw. Note that the channels in the pixel system were increased from 80.4 to 92 millions during the first long shutdown thanks to an additional barrel cylindrical layer.

Pixel Detector

The main advantage of the pixel detector is its high granularity close to the IP. It determines the performance of the ID at finding short-lived particles such as b -quarks and τ -leptons. The system is designed to be highly modular, with four barrel cylindrical layers containing 1736 identical sensor modules, plus three end-cap disks on each side containing 288 modules. The whole system uses just one type of support structure in the barrel and one in the disks. The pixel modules are designed very similarly for the disks and layer modules. Each module contains 61440 pixel elements, with a read-out system consisting of 16 chips.

Semiconductor Tracker

The SCT is designed to provide four independent measurements per track in the intermediate radial range, contributing to the measurement of the track momentum,

impact parameter and vertex position. The SCT contains four layers of silicon microstrip detectors in the barrel and nine end-cap disks on each side. A silicon microstrip tracker consisting of 4,088 two-sided modules and over 6 million implanted read-out strips, so as to allow precision measurements of the track coordinates.

Transition Radiation Tracker

The TRT consists on gaseous straw detectors, measuring the track radial and azimuthal coordinates. Each straw tube is 4 mm in diameter, with a gold-plated tungsten wire of diameter 0.03 mm in the centre, providing fast response and good mechanical properties. The barrel is formed 50,000 straws, each of 144 cm long and placed parallel to the beam direction, with their wires divided in two halves approximately at $\eta = 0$. In both end-cap regions, there are 250,000 straws, each of 39 cm long and arranged radially in wheels.

3.2.2 Calorimeter System

The ATLAS calorimeter system is made of a Liquid Argon (LAr) calorimeter [48] and a Tile calorimeter [49]. These calorimeters cover the pseudorapidity region $|\eta| < 4.9$ and are designed for a good containment of electromagnetic and hadronic showers, also providing punch-through containment into the muon system. The fine granularity of the LAr electromagnetic calorimeter is ideally suited for precision measurements of electrons and photons, within the $|\eta|$ range matched to the inner detector. The coarser granularity of hadronic calorimeters is sufficient to satisfy the physics requirements for jet and missing transverse energy reconstruction. Figure 3.6 presents a view of the systems composing the calorimeter system, and Tables 3.2 and 3.3 detail their main parameters.

LAr electromagnetic calorimeter

The electromagnetic calorimeter is a lead-LAr detector with accordion-shaped kapton electrodes and lead absorber plates over its full coverage. The accordion geometry provides a complete azimuthal symmetry without cracks, while the lead thickness in the absorber plates is optimised in terms of energy resolution performance. The energy resolution for the LAr electromagnetic calorimeter is required to be

$$\frac{\sigma_E}{E} = \frac{10\%}{\sqrt{E[\text{GeV}]}} \oplus 0.7\%.$$

The system is divided into a barrel part covering the range $|\eta| < 1.475$, and two end-caps covering $1.375 < |\eta| < 3.2$, both made of several layers of active material. The barrel calorimeter consists of two identical half-barrels, separated by a small gap, and each end-cap is divided into two coaxial wheels.

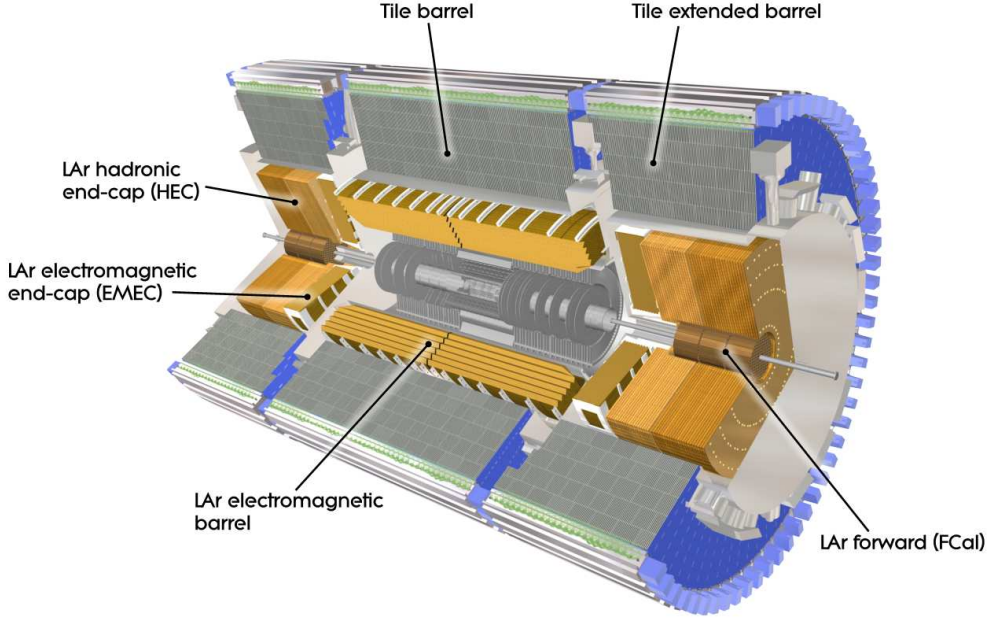


Figure 3.6: Cut-away view of the ATLAS calorimeter system [45].

The granularity $\Delta\eta \times \Delta\varphi$ depends on the layer but also on the $|\eta|$ range, being the finest in the central region of the barrel, where maximum precision is required. In addition, a presampler detector made of an active LAr layer is used within $|\eta| < 1.8$ to correct for the energy lost by electrons and photons upstream of the calorimeter. Table 3.2 specifies the main parameters of the electromagnetic calorimeter.

System and position		Coverage	Channels ($\times 10^0$)	Granularity $\Delta\eta \times \Delta\varphi$
Presampler	1 barrel layer	$ \eta < 1.52$	7808	0.025×0.1
	1 end-cap layer	$1.5 < \eta < 1.8$	1536	0.025×0.1
Calorimeter	5 barrel layers	$ \eta < 1.475$	101760	0.075×0.025
	5 inner end-cap layers	$1.375 < \eta < 2.5$	62208	0.050×0.1
	2 outer end-cap layers	$2.5 < \eta < 3.2$		0.1×0.1

 Table 3.2: Main parameters of the LAr electromagnetic calorimeter. The quoted values for the granularity are the larger ones within that layer and $|\eta|$ range.

Hadronic calorimeters

The hadronic part of the ATLAS calorimeter is composed of several systems, namely the scintillator tile calorimeter (TileCal), the LAr hadronic end-cap (HEC), and the LAr forward calorimeter (FCal), with their parameters specified in Table 3.3. The energy resolution for the calorimeters varies with the system and is required to be

$$\frac{\sigma_E}{E} = \frac{50\%}{\sqrt{E[\text{GeV}]}} \oplus 3\% \text{ (barrel \& end-cap)}; \quad \frac{\sigma_E}{E} = \frac{100\%}{\sqrt{E[\text{GeV}]}} \oplus 10\% \text{ (forward)}.$$

Therefore, the forward calorimeter has a poorer resolution compared to the barrel and end-cap calorimeters. A brief description of the different hadronic calorimeters is presented below.

TileCal: The scintillator tile hadronic calorimeter is a sampling calorimeter using layers of steel as absorber and around 500,000 plastic scintillating tiles as active material. It is the heaviest part of the experiment, weighing almost 2900 tons. Its barrel covers the region $|\eta| < 1.0$ and its two extended barrels the range $0.8 < |\eta| < 1.7$. The central barrel and each of the two extended barrels are made of 64 wedges extended azimuthally.

HEC: The LAr hadronic end-cap consists of two independent wheels per end-cap, located directly behind the end-cap electromagnetic calorimeter and sharing the same LAr cryostats. It overlaps with the forward calorimeter to reduce the drop in the material density at the transition region around $|\eta| = 3.1$, extending up to $|\eta| = 3.2$. Each wheel is built from 32 identical wedge-shaped modules, assembled with fixtures at the periphery and at the central bored. Each wheel is divided into two segments in depth for a total of four layers per end-cap.

FCal: The LAr forward calorimeter is integrated into the end-cap cryostats, as this provides clear benefits in terms of uniformity of the coverage as well as reduced radiation levels in the muon spectrometer. It is approximately 10 interaction lengths deep, and consists of three modules in each end-cap: the first, made of copper, is optimised for electromagnetic measurements, while the other two, made of tungsten, measure predominantly the energy of hadronic interactions.

System and position		Coverage	Channels ($\times 10^0$)	Granularity $\Delta\eta \times \Delta\varphi$
TileCal	3 barrel layers	$ \eta < 1.0$	5760	0.2×0.1
	3 extended barrel layers	$0.8 < \eta < 1.7$	4092	0.2×0.1
HEC	4 end-cap layers	$1.5 < \eta < 3.2$	5632	0.2×0.2
FCal	3 end-cap layers	$3.1 < \eta < 4.9$	3524	5.4×4.7

Table 3.3: Main parameters of the hadronic calorimeters. The quoted values for the granularity are the larger ones within that layer and $|\eta|$ range.

3.2.3 Muon Spectrometer

The ATLAS muon system [50] exploits the magnetic deflection of muon tracks in the large superconducting air-core toroid magnets. In the barrel region $|\eta| < 1.4$, the bending is provided by a large barrel toroid with a bending power between 1.5 and 5.5 Tm, while for the end-cap region $1.6 < |\eta| < 2.7$, the muon trajectories are deflected by two smaller end-cap magnets inserted into both ends of the barrel toroid, providing a bending power between 1 and 7.5 Tm. In the so called transition region $1.4 < |\eta| < 1.6$, the deflection is provided by a combination of barrel and end-cap fields. This configuration provides a field which is mostly orthogonal to the muon trajectories, while minimising the degradation of resolution due to multiple

scattering. The tracks are measured in chambers arranged in three cylindrical layers located either around the beam axis for the barrel region, or in planes perpendicular to the beam for the transition and end-cap regions. The overall transverse momentum resolution of the muon system is required to be

$$\frac{\sigma_{p_T}}{p_T} = 10\% \text{ at } p_T = 1 \text{ TeV.}$$

Note that, for high- p_T muons, the muon-spectrometer performance is independent of the inner-detector system.

The muon spectrometer is a collection of four different systems, namely the Monitored Drift Tubes (MDT), the Cathode Strip Chambers (CSC), the Resistive Plate Chambers (RPC) and the Thin Gap Chambers (TGC). The two former are used for precision tracking purposes, whereas the two latter provide triggering capabilities. Figure 3.7 depicts a general view of the muon spectrometer, including toroid magnets, and Table 3.4 provides the main parameters of each system.

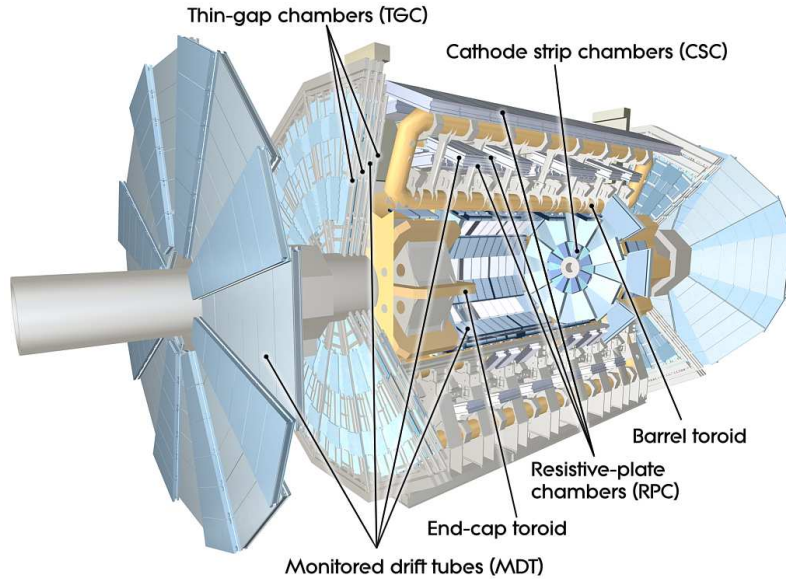


Figure 3.7: Cut-away view of the ATLAS muon system [45].

System	Function	Coverage	Chambers ($\times 10^0$)	Channels ($\times 10^3$)
MDT	Precision tracking	$ \eta < 2.7$	1150	354
CSC		$2.0 < \eta < 2.7$	32	31
RPC	Triggering, second coordinate	$ \eta < 1.05$	606	373
TGC		$1.05 < \eta < 2.7$	3588	318

Table 3.4: Main parameters of the systems conforming the muon spectrometer, along with the function that each system fulfils in the detection.

Precision tracking chambers

The MDT chambers are made of three to eight drift tube layers, operated at an absolute pressure of 3 bar, achieving an average resolution of $80 \mu\text{m}$ per tube, or about $35 \mu\text{m}$ per chamber. The MDTs perform the precision momentum measurement and cover the pseudorapidity range $|\eta| < 2.7$, except in the innermost end-cap layer, where their coverage is limited to $|\eta| < 2.0$.

The CSCs are multiwire proportional chambers with cathode planes segmented into strips in orthogonal directions, allowing the measurement of both coordinates from the induced-charge distribution. The achieved resolution of a chamber is $40 \mu\text{m}$ in the bending plane, and about 5 mm in the transverse plane. They are used in the innermost tracking layer due to their higher rate capability and time resolution, covering the pseudorapidity region $2.0 < |\eta| < 2.7$.

Triggering chambers

The precision-tracking chambers are complemented by a system of fast trigger chambers capable of delivering track information with a spread of 15 to 25 ns. In the barrel region $|\eta| < 1.05$, the RPCs were selected for this purpose, whereas in the end-cap region $1.05 < |\eta| < 2.4$, the TGCs were chosen. In addition, they are designed to measure both coordinates of the track, one in the bending plane, in the η direction, and another one in the non-bending azimuthal plane. Here, the end-cap range extends up to $|\eta| < 2.7$.

The purpose of the precision-tracking chambers is to determine the coordinate of the track in the bending plane. After matching of the MDT and trigger chamber hits in the bending plane, the trigger chamber's coordinate in the non-bending plane is adopted as the second coordinate of the MDT measurement. This method assumes that in any MDT/trigger chamber pair a maximum of one track per event be present, since with two or more tracks the η and φ hits cannot be combined in an unambiguous way.

3.2.4 Trigger and Data-Acquisition System

The ATLAS TDAQ system [51], upgraded for Run 2 [52], is deisgned to select with high efficiency signal events, while rejecting the overwhelming background processes. Its aim is to reduce the storage event rate to approximately 1 kHz from the nominal bunch crossing rate, happening with a frequency of 40 MHz, every 25 ns. In order to achive it, the trigger decision chain uses a hardware-based first level trigger (Level-1) and a software-based high-level trigger (HLT). The former reduces the storage rate to 100 kHz, and then, the latter down to the limit of 1 kHz. The performance of the trigger system during the whole Run 2 is presented in Ref. [53]

Level-1 Trigger

The Level-1 trigger performs the initial event selection based on the information from the calorimeter and muon systems, searching for high-transverse momentum objects. This process reduces the event rate to about 100 kHz and makes use of custom electronics to determine Regions-of-Interest (RoIs), characterized by a position in the $\eta\text{-}\varphi$ plane where the selection process has identified interesting features. It requires about 2.5 μs to reach its decision, including the propagation delays on cables between the detector and the underground computing farm where the trigger logic is located.

The information provided by the calorimeter system allows the Level-1 trigger to identify high-transverse energy objects such as electrons, photons, hadronically decaying τ -leptons or jet clusters, as well as events with large missing transverse energy. Each of the determined RoIs consists of 4×4 trigger towers with a reduced granularity of $\Delta\eta \times \Delta\varphi = 0.1 \times 0.1$, and a η -dependent p_{T} requirement to account for energy losses and the geometry of the detector. In addition, the triggering capabilities of muon chambers also bring information into the decision chain by tracking the trajectory of high-transverse momentum muons.

High Level Trigger

The HLT is mainly based on the same regions identified by the Level-1 trigger and runs on an underground computing farm at Point-1. The RoIs are used to construct a seed for each formed object, consisting of a p_{T} threshold and a position in the $\eta\text{-}\varphi$ plane. Later, for the final trigger decision, sophisticated selection algorithms are run using full granularity detector information, including the ID. That way, the HLT reduces the storage event rate to around 1 kHz on average, within a processing time of approximately 200 ms, which is the one required to take the decision of either keeping or rejecting the event. At the end of the trigger decision chain, data registered in disk are prepared through a processing chain that promptly reconstructs objects using calibration and validation algorithms, so as to provide data samples for physical analyses.

CHAPTER 4

Computing projects

In addition to the experimental setup, physical analyses achieve high precision thanks to a gigantic computing infrastructure that increases information processing speed and handles the prodigious volume of data produced by LHC experiments. CERN designed a grid-based computer network infrastructure called Worldwide LHC Computing Grid to cope with the situation.

Nowadays, this international collaborative project works with an operation system called CentOS Linux 7 equipped with a GNU bash shell and a gcc compiler by default. CERN users operate the same software when running in local machines. So as to access these machines, a valid user within the LXPLUS service is required. Each user has a user and a work area operating with the distributed file system AFS with Kerberos for authentication. The work area stores up to 100 giga-bytes. However, if more quota is required one can save up to 1 tera-byte at the CERN storage system called EOS, which was created for the extreme LHC computing requirements and is connected to the cloud storage CERNBox. Other machines have been used to perform analyses like the UIs machines at DFT UAM which provide a large number of computer cores. Point out that none of the results presented would have been possible without this whole computing power.

To provide computing power for their machines, the CERN Batch service has the aim to share the resources fairly and as agreed between all users of the system. Local jobs are supported via HTCondor which is a software framework for parallelization of computationally intensive tasks. Other services provided by the IT department are Indico to organize events, JIRA to track issues, VOMS to sort users into group hierarchies and CDS to archive documents, among others.

There are other tools that have been essential to carry out the analysis and therefore this thesis. For instance, GitLab which is a mainstream tool that provides a repository for code and documentation, Docker which is set of products used to deliver software in packages, and LaTeX which is a system for document preparation designed for the production of technical and scientific documentation thanks to a large number of features. In this framework, the writer uses a plain text that later generates the formatted version, displaying always a professional-looking. ROOT is another relevant tool for this analysis, discussed below owing to its importance.

ROOT is a data analysis framework widely used in particle physics [54]. The aim of this software is to analyse and visualize large amounts of data. It is mainly written in C++ which is one of the foremost general-purpose programming languages along with Python. The great advantage of this framework is the vast set of libraries provided. They are linked at the macro file and allow working with a wide range of objects and functionalities. This macro file contains the code that one want to run. In most scenarios, it reads data from an input file to return an output one. These ROOT files generally contains histograms and trees. The latter were designed for managing data held in a relational database system, therefore providing the perfect objects for storing relevant information at particle collisions.



ROOT is open source and can be directly downloaded form their website which also provide tutorials and courses to improve user skills. Additionally, users can create their own packages to implement new techniques in the software. The central external packages employed in this analysis are `BOOTSTRAPGENERATOR` for managing the boostrapping technique and `ROOUNFOLD` for performing the Iterative Bayesian unfolding. They can be respectively downloaded from their repositories:

<https://gitlab.cern.ch/cjmeyer/BootstrapGenerator.git>
<https://gitlab.cern.ch/RooUnfold/RooUnfold.git>

Moreover, the `MINUIT` package used to minimize the χ^2 function in the fit is already included, while the one for the Gaussian kernel smoothing is implemented manually.

4.1 Monte Carlo Event Generators

Monte Carlo algorithms in particle physics are applied to MC event generators. These programs simulate particle collisions based on a theoretical framework and a random number generator with an input seed, allowing for comparison with data and validating the theory. Most of them either belong to the HEPForge project or are externally hosted by it. This project constitutes a development environment for high energy physics software projects.

The main general-purpose event generators like `HERWIG`, `SHERPA`, and `PYTHIA` can be found at HEPForge. They are implemented in a C++ routine using `RIVET` which is a widespread system for validation of MC event generators [55, 56]. This system reads the event information from HepMC to return YODA files containing the simulated distributions.

In order to obtain physical simulations, additional programs have to be linked in the routine. For instance, the LHAPDF 6 interpolator used for evaluation of PDFs from discretised data [57]. This library comes from “Les Houches Accord” and contains a wide range of official PDF groups which are supported and available at their website. For jet-based simulations the `FASTJET` library is required to find jets in the final

state given a certain jet definition [58]. Furthermore, other software packages like the UE+MPI tunes may be necessary to take into account extra features.

There are also tools designed to display events for the visual investigation and the understanding of particle physics. Figure 4.1 shows two multi-jet events simulated for the ATLAS detector with the Atlantis event display.

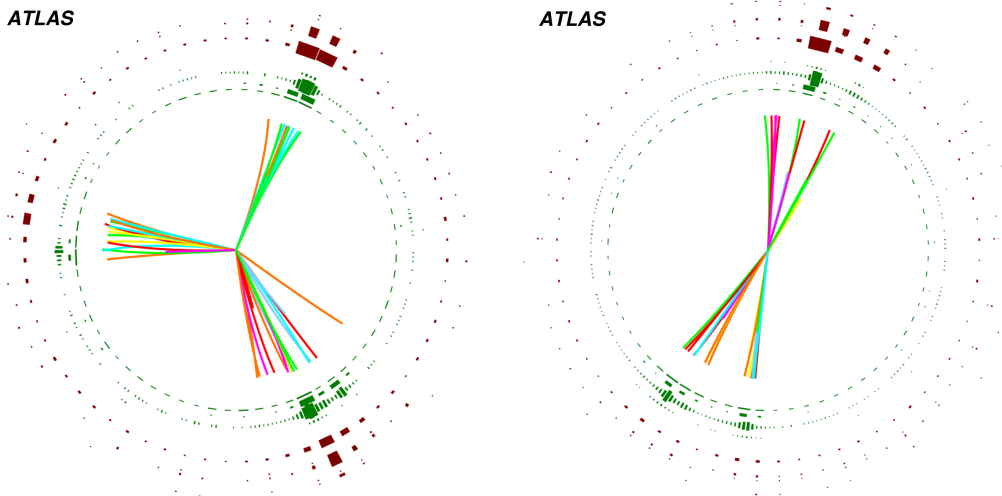


Figure 4.1: Transverse plane projection of two final states in multi-jet events created with the Atlantis event display. The colours are chosen for illustrative purposes [59].

4.1.1 Fixed-order generators

Fixed-order generators allow reliable theoretical predictions for infrared-safe physical observables at a given order in perturbative theory. They calculate the matrix-elements that contribute so as to get the expected cross section that weights the random-generated event. The first non-trivial contribution is the LO one but when increasing to NLO a subtraction scheme is required in the calculation.

The Catani-Seymour subtraction scheme based on the dipole factorization formulae has become the major scheme for NLO QCD corrections [60]. This scheme is used to construct the NLOJET++ program presented by Zoltan Nagy [61, 62]. This fixed-order event generator was one of the firsts to reproduce three-jet events in hadron collisions at NLO accuracy in pQCD. Therefore, initiating the accurate study of geometrical properties of the hadronic final state thanks to a considerable reduction of the theoretical scale uncertainty.

Nowadays, novel subtraction schemes have been developed to achieve NNLO accuracy in pQCD like the antenna subtraction method. Another example is the STRIPPER subtraction scheme which was extended in Ref. [63] to arbitrary processes with any number of coloured partons in the final state, and up to two partons in the initial state. The last scheme allows the calculation of NNLO QCD corrections to three-jet

events and has been used to construct a MC event generator, providing today the perfect tool to study physical observables in hadron collisions [64, 65].

This MC event generator requires libraries from OPENLOOPS 2 to calculate the matrix-elements [66], which is a program that allows for fast and stable numerical evaluation of tree and one-loop matrix-elements for any process at NLO QCD. Consequently, it has become one of the core libraries in many general-purpose event generators. In addition, the FIVEPOINTAMPLITUDES library has to be considered for evaluation of analytic expressions for finite remainders of two-loop five-point scattering amplitudes [67]. The library is meant to provide so-called double-virtual contributions using PENTAGONFUNCTIONS++ [68].

4.1.2 General-purpose generators

There are other MC event generators called general-purpose generators which are used to describe multi-jet production in hadron collisions by the convolution of the production cross sections for parton-parton scattering, given by pQCD, with the corresponding PDFs. In addition to the matrix-elements calculations, a parton shower is incorporated here to consider higher-order real emissions along with a matching procedure between them. Moreover, they can provide particle-level predictions when a fragmentation model and a UE+MPI tune are considered to account for long-distance effects.

QCD-based MC event generators differ between them in the approximations used to calculate the underlying short-distance hard processes, in the way parton showers are built to take into account higher-order effects and in the fragmentation scheme responsible for long-distance effects. In multi-jet production in hadron colliders, the baseline MC simulated samples are generated with the PYTHIA 8.235 [69] event generator which is generally used to unfold the measured distributions from the detector to the particle level, as well as the theoretical predictions from the parton to the particle level. Alternatively, MC simulated samples with the HERWIG 7.1.3 [70, 71], SHERPA 2.1.1 [72], and SHERPA 2.2.5 event generators are also considered.

The PYTHIA 8.235 event generator uses LO matrix elements to calculate the $2 \rightarrow 2$ hard processes matched to a p_T -ordered parton shower to simulate higher-order processes. The hadronization follows the Lund string fragmentation model and the ATLAS A14 tune [73] has been used to simulate the underlying-event. The HERWIG 7.1.3 event generator calculates matrix elements for $2 \rightarrow 2$ hard processes at NLO with MATCHBOX [74], higher-order processes are simulated with a dipole showering or an angular-ordered parton shower, both interfaced to the matrix element calculation using the MC@NLO matching scheme. The fragmentation follows the cluster hadronization model [75]. Finally, SHERPA 2.1.1 calculates matrix elements for $2 \rightarrow 2$ and $2 \rightarrow 3$ hard processes at LO, using the CKKW [76] method for the parton shower matching, while SHERPA 2.2.5 calculates only $2 \rightarrow 2$ matrix elements. The fragmentation follows a phenomenological cluster hadronization model. However, the latest version also includes the Lund string fragmentation model. These MC event generators used different PDF groups; namely, NNPDF 2.3 LO [77] for

PYTHIA 8.235, MMHT 2014 NLO [78] for HERWIG 7.1.3, CT10 [79] for SHERPA 2.1.1, and CT14 [80] for SHERPA 2.2.5.

4.2 The Worldwide LHC Computing Grid

The Worldwide LHC Computing Grid (WLCG) is a global computing infrastructure whose mission is to provide computing resources to store, distribute and analyse the data generated by the LHC, making data equally available to all partners, regardless of their physical location. This project is a global collaboration of around 170 computing centres in 42 countries, supported by many national and international grid infrastructures across the world. It has become the largest computing grid in the globe, managed and operated by a worldwide collaboration between the LHC experiments and the participating computer centres.

The WLCG consists of sophisticated data-taking & analysis systems dealing with rates of data production of approximately 25 penta-bytes per year, providing physicists around the world with near real-time access to LHC data, and the power to process it. This ground-breaking infrastructure is made up of almost 1 million computer cores and has a quota of 1 exa-bytes of storage. Bear in mind that these numbers will increase as computing resources and new technologies will become ever more available in the future. These computing resources include not only data storage capacity and processing power, but also a wide range of tools.

In LHC experiments, produced raw data passing TDAQ system requirements are promptly analysed and stored in the Tier-0 of the computing grid, which corresponds with the CPU farm at the CERN Data Centre. Then, data are sent out from CERN to thirteen Tier-1 academic institutions in Europe, Asia, and America, via the LHC Optical Private Network. A larger number of Tier-2 institutions are connected to Tier-1 centres by general-purpose national research and education networks. The national Spanish Tier-1 centre is Port d'Informació Científica (PIC) at Barcelona, while my institution holds a Tier-2 centre at Madrid called UAM-LCG2.

4.3 ATLAS Computing and Software

LHC experiments design software to analyse produced data. So as to accomplish the goal, ATLAS uses a common Gaudi framework called Athena whose repository contains any and all code that could be built into an ATLAS software release. The repository is hosted in <https://gitlab.cern.ch/atlas/athena.git>.

Athena contains a wide range of projects with difference purposes. For instance, the AnalysisBase one used in ROOT-based analyses. When a particular build of an Athena project is deemed ready for production it is installed as a numbered release onto the ATLAS production server. In this case, the analysis has been carried out with the `AnalysisBase,21.2.139` release.

Users can access to this software with `setupATLAS` which also grant access to other programs like PanDa and Rucio. The former sends tasks to run in the WLCG, the latter downloads their output samples. In order to access WLCG resources ATLAS users require a valid certificate and their tasks can be monitorized at the website <https://bigpanda.cern.ch/>.

Information about any ATLAS resources or recommendations are usually found in specific Twiki pages that are only going to be mentioned in this thesis if necessary.

4.3.1 Data preparation

Data collected by the ATLAS detector need to be stored in files that can be read by users in their local analyses. The processing chain that prepares data registered at detectors for analyses works with the ATLAS software framework called Athena. The first step is to provide a sample with all data written in disk after being selected by triggers. The data sample used in this analysis corresponds to the full dataset with 25 ns bunch-crossing space taken during the pp Run 2. In this case, the LHC delivers up to 40 MHz for each bunch crossing. The Level-1 trigger implemented in hardware reduces rate to 100 kHz, then the High Level trigger implemented in software running on Point-1 machines reduces rate to 1 kHz.

The next step in the processing chain is object reconstruction which runs at the WLCG with Athena to produce the Analysis Object Data (AOD) samples. Firstly, raw data stored at Point-1 machines are promptly reconstructed at the Tier-0 using fast calibrations and validation software. Data Quality algorithms check operation of detectors and performance of physical objects to decide which data should be accepted. The All Good Data Quality criteria require all reconstructed physics objects to be of good data quality [81]. Only events labelled as “Good for Physics” enter the sample and therefore the real luminosity is slightly lower than the delivered one by the LHC. The delivered luminosity accounts for the luminosity delivered from the start of stable beams until the LHC requests ATLAS to put the detector in a safe standby mode to allow a beam dump or beam studies. The total integrated luminosity and data quality in the 2015-2018 period is shown in Figure 4.2.

The total integrated luminosity during the pp Run 2 that can be considered in physical analyses reaches up to 139 fb^{-1} . For each data-taking period the integrated luminosities are 36.2 fb^{-1} for 2015+2016, 44.3 fb^{-1} for 2017 and 58.5 fb^{-1} for 2018. The luminosity blocks labelled as “Good for Physics” are given in the official precomputed Good Run Lists (GRLs) which are taken from the following path:

`/cvmfs/atlas.cern.ch/repo/sw/database/GroupData/GoodRunsLists/`.

4.3.2 Monte Carlo production

The ATLAS Collaboration produces its own official MC simulations which are available for all users. These samples also undergo a processing chain with Athena at

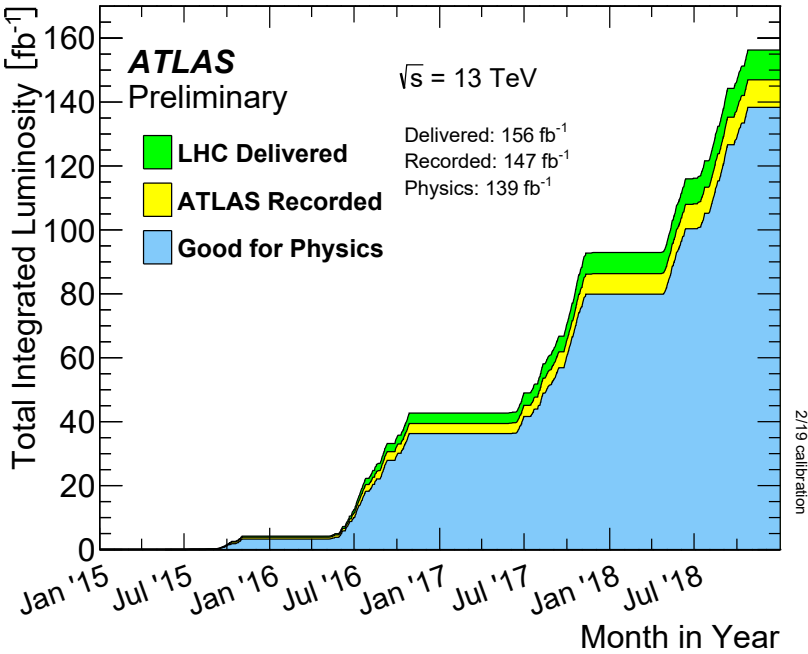


Figure 4.2: Cumulative luminosity versus time delivered to ATLAS, recorded by ATLAS, and certified to be good quality data during stable beams for pp collisions at 13 TeV centre-of-mass energy in the 2015–2018 period [44].

the WLC Grid until they are ready to be considered in local ROOT-based analyses. They can be found along with data samples at the ATLAS Metadata Interface (AMI). A Grid certificate is required to access its website <https://ami.in2p3.fr/> where one can search for all the official samples available.

The first step in the processing chain is event generation where all events in the sample are created using MC programs like the ones described before. Generated samples at this point are called EVNT. The next step is detector simulation where the performance of the detector is taken into account. The generated events are processed with the ATLAS full detector simulation [82] based on GEANT4 [83]. Output samples once the simulated detector deposits are included are called HITS. To compare with real data, one must assume that simulated collisions would be collected by the same electronics. The simulated deposits have then to be turned into a detector response comparable to the one of the raw data from the real detector. This step is digitalization and output samples are called RDO.

The last steps are the same for data and simulation, and provide the samples that are going to be processed in the analysis routine. The first one is called object reconstruction and returns the already mentioned AOD samples. To better handle these huge samples one should apply a derivation to save only certain event information within them. The derivation frameworks considered in here for multi-jet production are JETM1 and STDM11. These Derived Analysis Object Data (DAOD) samples are then validated by the corresponding Physics Modelling Group (PMG) before using them. To conclude, validated DAOD samples are processed by users to get their ROOT input files. In this step, users build a set of trees with the main information

required in their local ROOT-based analyses. Figure 4.3 shows a diagram of the whole software processing chain for MC production and data preparation.

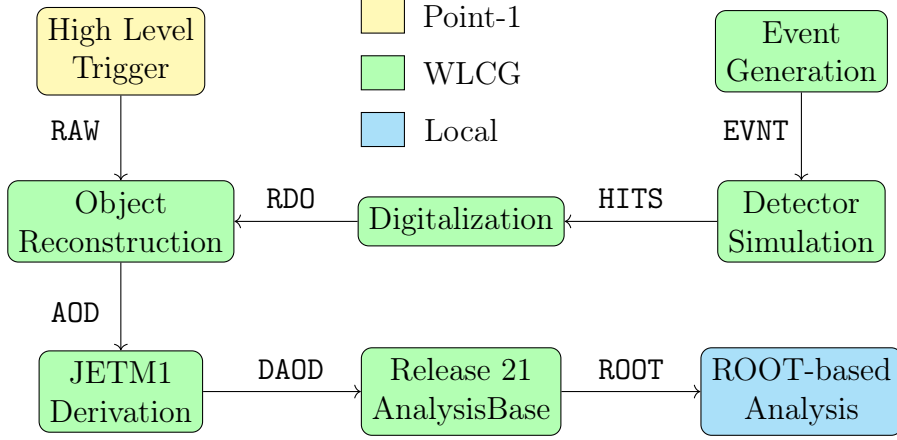


Figure 4.3: Software processing chain for official data and MC simulation samples at the ATLAS experiment. The name of the output samples after each step in the chain is included and arrows indicates the direction of the processing chain.

The official MC simulations are produced in MC16 campaigns that match the data collected by detectors. Hence, making a comparison between data and simulation suitable. MC16 campaigns are divided in different subcampaigns depending on the period of time they try to simulate. The aim is to have the same pile-up distribution in data and simulation for each data collecting period. The MC16a subcampaign matches the 2015-2016 period, MC16d the 2017 period, and MC16e the 2018 period.

In order to compensate for the steeply falling p_T spectrum, each subcampaign in multi-jet production is generated in difference intervals of the leading transverse momentum of the generated outgoing partons \hat{p}_T . These slices are called JZ slices and are merged together in analyses using the luminosity weights that reproduce the expected leading-jet p_T distribution.

Luminosity weights are given by the ratio $w_{\text{lumi}} = L_{\text{phys}}/L_{\text{MC}}$. This is the ratio of integrated luminosity in the simulated data-taking period L_{phys} and the MC sample luminosity L_{MC} which is computed for each JZ slice of the subcampaign as

$$L_{\text{MC}} = \frac{\sum_{A=1}^{N_{\text{ev}}} w_{\text{ev}}^{(A)}}{\sigma F_{\text{eff}}}$$

where σ is the cross section and F_{eff} is the filter efficiency for each slice in a subcampaign. Note that each slice contains N_{ev} events with different event weights w_{ev} . Finally, all MC simulated samples are subject to a reweighting algorithm in order to match exactly with the average number of pp interactions per bunch-crossing observed in the associated data-taking period divided by a factor 1.03.

CHAPTER 5

Object reconstruction and calibration

This chapter discusses the performance of the ATLAS detector in terms of object reconstruction and calibration, including vertices and jets originated from them. The latter are collimated bunches of hadrons, reconstructed from tracks in the inner detector and calibrated following certain criteria. Jet systematic uncertainties associated to the calibration procedure, namely, jet energy scale (JES) and jet energy resolution (JER), are also discussed in the chapter, along with jet quality criteria.

5.1 Tracks and vertices

Tracks are charged-particle trajectories reconstructed from global fits and Kalman-filter techniques [84] in the inner detector, which are later considered in the reconstruction of other objects, mainly, vertices and jets. Track seeds are formed by combining space-points from clusters in the pixel and first SCT layer, which are then extended throughout the whole SCT and fitted to form track candidates. The latter are extended into the TRT to associate the drift-circle information and fitted again including information from all the ID. Track candidates passing certain kinematic cuts and quality criteria are taken as input for vertex and jet reconstruction:

- Kinematic cuts $|\eta| < 2.5$ and $p_T > 400$ MeV, plus $p_T > 500$ MeV for jets.
- Number of silicon hits ≥ 9 , plus silicon hits ≥ 11 for vertices if $|\eta| > 1.65$.
- Pixel holes = 0, plus SCT holes ≤ 1 for vertices.
- IBL hits + B-layer hits ≥ 1 for vertices.

Moreover, tracks selected for jet reconstruction must be associated with a primary vertex so as to suppress the effects of pile-up. Primary vertex reconstruction [85] in a LHC collision is essential for determining the full kinematic properties of a hard-scatter event and of soft interactions. The procedure of primary vertex reconstruction from tracks passing these selection criteria is divided in two stages: vertex finding and vertex fitting. The best vertex position is iteratively derived from the selected tracks and a seed position. Thereafter, incompatible tracks with the vertex

are removed from it and allowed to be used in the determination of another one. The procedure is repeated again until no unassociated tracks are left in the event or no additional vertex can be found in the remaining set of tracks. Note that a vertex requires at least two selected tracks to be formed as a candidate vertex.

5.2 Jet reconstruction

Jets are collimated bunches of hadrons in an attempt to reconstruct the kinematic properties of the hard partons from which they originated. As already discussed in Section 2.2, a jet definition is required to map observed hadrons onto a set of jets. In this case, jets are defined using the anti- k_t clustering algorithm with radius $R = 0.4$, conforming the main objects used in the analyses presented in this thesis.

Nowadays, based on the input four-vector objects considered for the jet reconstruction, one can identify two different schemes. The old-fashioned procedure builds jets from calorimeter energy deposits through a set of topological clusters (EMtopo) [86], whereas the current one builds jets including also charged-particle tracks into the particle-flow (PFlow) reconstruction technique [87]. Both algorithms are properly discussed at the end of this section.

A detailed explanation for the whole procedure of jet reconstruction and calibration is found in Ref. [88]. This is carried out with the latest version of the ATLAS software as discussed in Section 4.3. Specific analysis recommendations for Release 21 MC16 are provided by the ATLAS Jet and Emiss Combined Performance Group at the twiki.cern.ch webpage:

[/twiki/bin/view/AtlasProtected/JetEtmissRecommendationsR21](https://twiki/bin/view/AtlasProtected/JetEtmissRecommendationsR21)

These recommendations are supported for jet collections with transverse momentum $p_T > 20$ GeV and pseudorapidity $|\eta| < 4.5$. The PFlow jet collection is the one recommended by default. The main analysis uses this collection for jet reconstruction in data and MC, along with a detailed jet calibration scheme: calibration for data or FullSim (JES MC \oplus *in situ*) \oplus nominal JER MC-smearing \oplus JMS calibration. Table 5.1 summarizes the main information of the jet calibration procedure:

AntiKt4EMPFlow
Configuration file: .config
<u>JES_JMS_MC16Recommendation_Consolidated_MC_only_PFlow_July2019_Rel21</u>
<u>JES_JMS_MC16Recommendation_Consolidated_data_only_PFlow_July2019_Rel21</u>
Calibration sequence:
JetArea_Residual_EtaJES_GSC_Smear_JMS
JetArea_Residual_EtaJES_GSC_JMS_Insitu
Calibration area: 00-04-82

Table 5.1: Main parameters of the jet calibration procedure for PFlow jets reconstructed using the anti- k_t algorithm with radius parameter $R = 0.4$. The files above in the cell apply to MC, `isData=false`, and the ones below to data, `isData=true`.

5.2.1 Topological clusters

The EMtopo jet reconstruction [86] is based on clustering of individual calorimeter cells following their signal-significance patterns generated by electromagnetic and hadronic showers. These cells are first clustered into three-dimensional topological clusters using a nearest-neighbour algorithm. These massless clusters are called topo-clusters and their formation is depicted in Figure 5.1. Then, calorimeter cells are added to a topo-cluster according to the ratio of the cell energy to the expected noise in each cell, removing cells with insignificant signals which are not in close proximity to significant cells in order to suppress the noise contribution.

The resulting topological cell clusters have shape and location information, which is required for local energy calibration. Moreover, the resulting energy is given at the electromagnetic scale, which is the one that correctly measures energy depositions from electromagnetic showers. Thereafter, positive-energy topo-clusters are used as inputs to the jet reconstruction. These topo-clusters are corrected to account for the position of the primary vertex in each event, defined as the reconstructed vertex with at least two associated tracks and the largest sum of squared track momentum. This step is referred to as origin correction. In addition, topo-clusters are also used to represent the energy flow from softer particles, required for the reconstruction of observables like the missing transverse momentum.

Jets reconstructed using only calorimeter-based energy information from origin-corrected topo-clusters are referred to as EMtopo jets. This was the primary method used for jet reconstruction in ATLAS before the emerge of particle-flow reconstruction techniques. EMtopo jets exhibit robust energy scale and resolution characteristics across a wide kinematic range, and are independent of other reconstruction algorithms such as tracking at the jet-building stage.

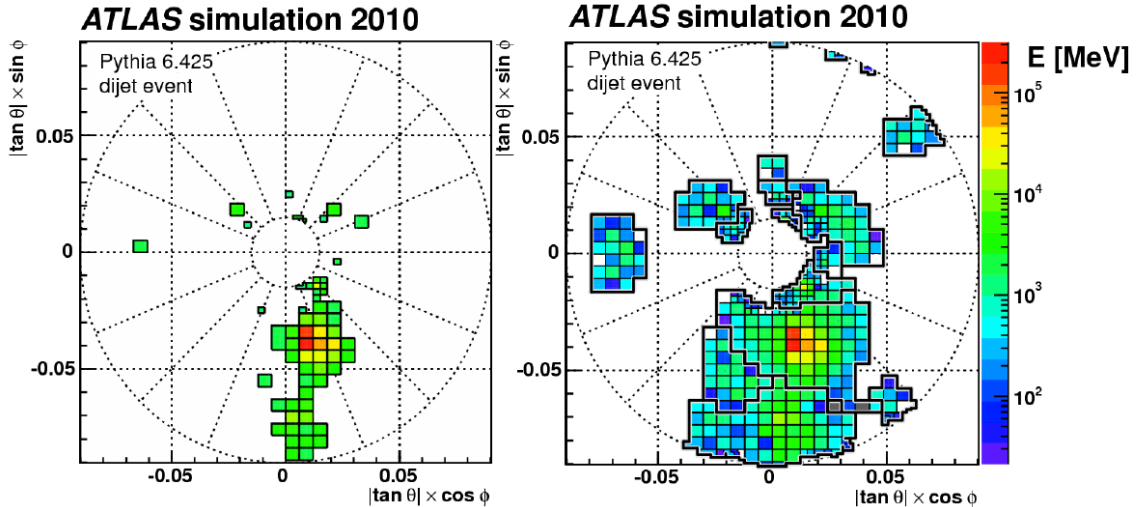


Figure 5.1: Stages of topo-cluster formation in the FCAL calorimeter for a simulated dijet event with at least one jet entering this calorimeter. The left figure shows cells with signal significance $|E_{EM}|/\sigma > 4$ that can seed topo-clusters, while the right one shows all clustered cells and the outline of topo-clusters in this module [86].

5.2.2 Particle-flow reconstruction technique

The PFlow algorithm [87] makes a more complete use of the information from both the tracking and calorimeter systems to form the input signals, which are intended to approximate individual particles. This algorithm subtracts energy deposited in the calorimeter by charged particles from the observed topo-clusters, and replaces it by the momenta of tracks that are matched to those topo-clusters. Jet reconstruction is then performed on an ensemble of particle-flow objects consisting of the remaining calorimeter energy and tracks which are matched to the hard interaction. These resulting PFlow jets exhibit improved energy and angular resolution, reconstruction efficiency, and pile-up stability compared to EMtopo jets.

For the Run 2 jet calibration, the alternative particle-flow approach superseded the previous clustering of individual calorimeter cells. A combination of the tracking and calorimeter systems is preferred for optimal event reconstruction, as the capabilities of the tracker in reconstructing charged particles are complemented by the reconstruction of both charged and neutral particles provided by the calorimeter. The algorithm provides a list of tracks and a list of topo-clusters containing also a set of new topo-clusters resulting from the energy subtraction procedure. Figure 5.2 sketches the whole technique. First, well-measured tracks are selected, and then, each track is matched to a single topo-cluster in the calorimeter. However, it is quite common for a single particle to deposit energy in multiple topo-clusters, so the algorithm has to decide if it is necessary to add more topo-clusters so as to recover the full shower energy. In this case, the expected energy is now subtracted cell by cell from the set of matched topo-clusters. Finally, the topo-cluster remnants are removed. Figure 5.3 illustrates this methodology for several cases.

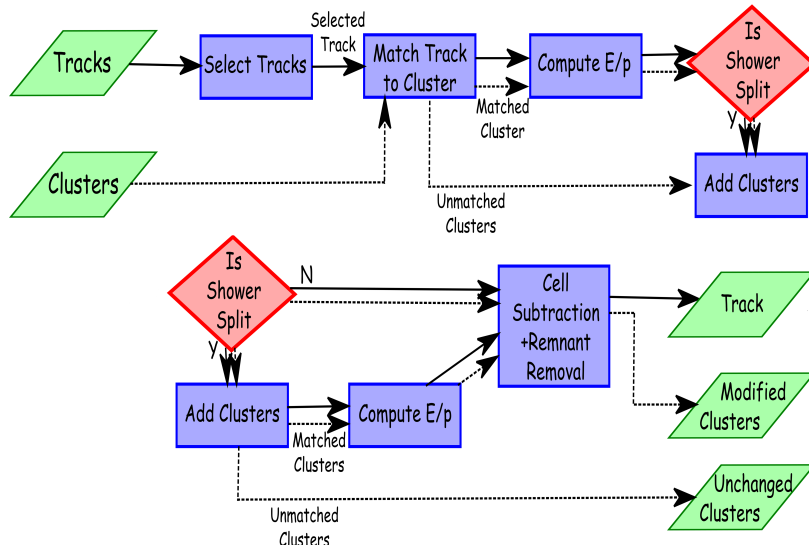


Figure 5.2: A flow chart of how the particle flow algorithm proceeds, starting with track selection and continuing until the energy associated with the selected tracks has been removed from the calorimeter. At the end, charged particles, topo-clusters which have not been modified by the algorithm, and remnants of topo-clusters which have had part of their energy removed remain [87].

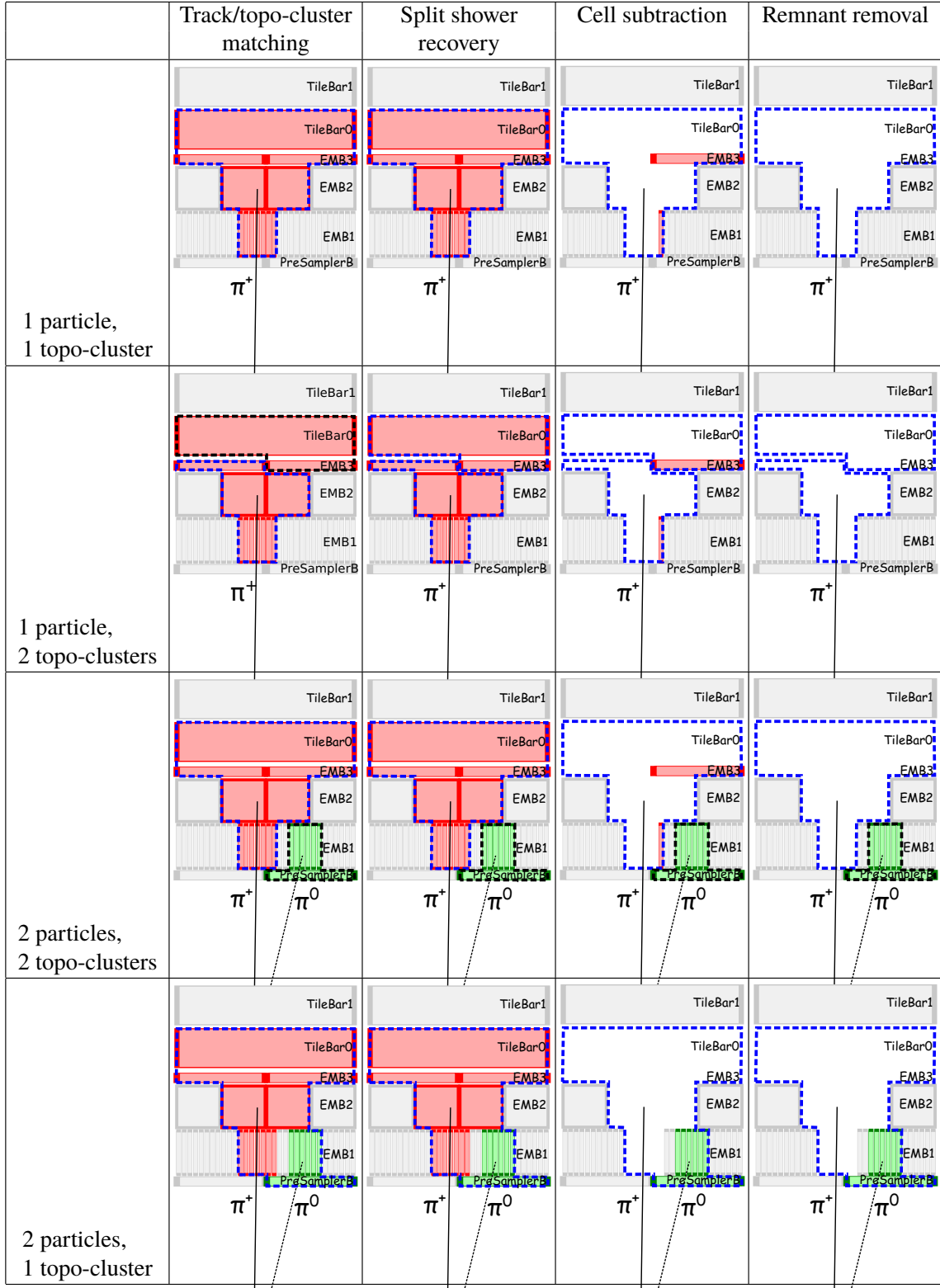


Figure 5.3: Idealised examples of how the algorithm is designed to deal with several different cases. The red cells are those which have energy from the π^+ , the green cells energy from the photons from the π^0 decay, the dotted lines represent the original topo-cluster boundaries with those outlined in blue having been matched by the algorithm to the π^+ , while those in black are yet to be selected. The different layers in the electromagnetic calorimeter are indicated [87].

5.3 Jet energy scale calibration

Thereafter PFlow jets are reconstructed, a MC simulation is used to determine the energy scale and resolution of jets by comparing those jets with particle-level jets. The latter are reconstructed using stable final-state particles and excluding muons, neutrinos, and particles from pile-up interactions. The so-called *truth* jets must fulfil the same kinematic cuts and are geometrically matched to PFlow jets using the angular distance with the requirement $\Delta R < 0.3$ in the y - φ plane.

The procedure that restores the jet energy to that of jets reconstructed at the particle level is called jet energy scale calibration. At each stage of the calibration chain, the four-momentum of the jet is corrected, scaling certain kinematic variables, such as transverse momentum, energy, and mass. Figure 5.4 illustrates the full chain of corrections for the JES calibration.

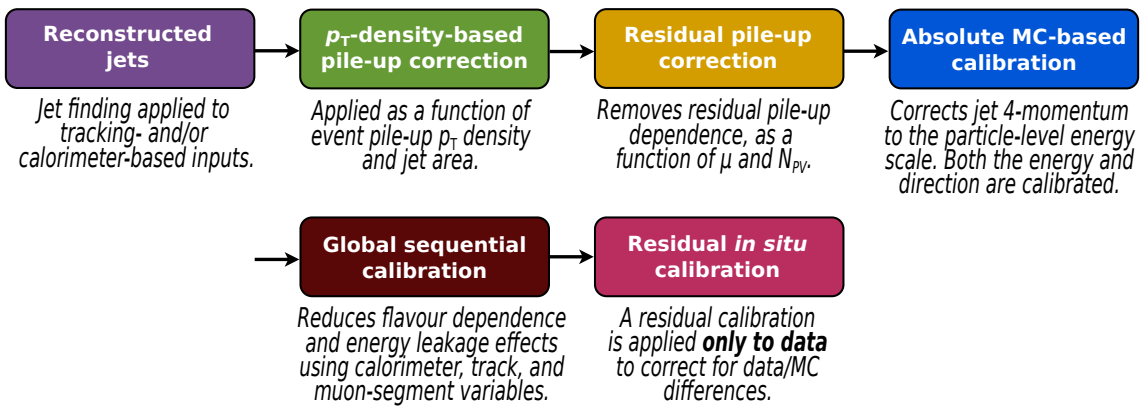


Figure 5.4: Stages of jet energy scale calibrations. Each one is applied to the jet four-momentum in order to restore the jet energy to the one at particle level [88].

The first two steps in the calibration chain are pile-up corrections, removing the excess energy due to additional pp interactions within the same or nearby bunch crossings. The main correction is based on the jet area and transverse momentum density of the event, while the residual one is derived from MC simulation and parameterized as a function of the mean number of interactions per bunch crossing, μ , and the number of reconstructed primary vertices in the event, N_{PV} . The absolute JES calibration occurs in the next step, correcting the four-momentum of jets so that it agrees in energy and direction with the one of truth jets from dijet MC events. The same MC simulation is later used to improve the transverse momentum resolution. This step is called global sequential calibration and it associates uncertainties by removing the dependence of the reconstructed jet response on observables constructed using information from the detector systems. Finally, a residual *in situ* calibration is applied only to data to correct for remaining differences between data and MC simulation. All of the stages of the chain are discussed in this section. Furthermore, the full treatment of the systematic uncertainties coming from the calibration procedure is included at the end of the section.

5.3.1 Simulation-based calibration

Pile-up corrections

As explained in Section 2.2, pile-up effects are mitigated using the so-called $\rho \times A^{\text{jet}}$ subtraction method. The jet area is considered as a measure of the susceptibility of the jet to pile-up and is calculated by determining the relative number of ghost particles associated with a jet after clustering. Note that tracks are matched to jets using ghost association [39]. Next, the background p_T density is calculated from jets in the central region so as to estimate the pile-up contribution. A subtraction of this pile-up contribution to the transverse momentum is then performed, applying the ratio of the subtracted to the uncorrected jet p_T as a scale factor to the jet four-momentum. The computation of ρ in the central region $|\eta| < 2.0$ gives a more meaningful measure of the pile-up activity than the median over the entire detector acceptance. In this case, jets are reconstructed from positive-energy topo-clusters using the k_t algorithm with radius parameter $R = 0.4$. The main reason to consider this jet definition is that the algorithm has a tendency to naturally reconstruct jets including an uniform soft background.

After the main pile-up correction, effects of the pile-up activity remains in the jet p_T , mainly, due to the fact that the pile-up sensitivity in the forward calorimeter region or in higher-occupancy core of high p_T jets is not described. Therefore, a residual correction is introduced as the difference between the reconstructed and truth jet p_T as a function of both N_{PV} and μ . The final corrected jet p_T is then given by

$$p_T^{\text{corr}} = p_T^{\text{reco}} - \rho \times A^{\text{jet}} - \alpha \times (N_{\text{PV}} - 1) - \beta \times \mu.$$

where α and β are fitted coefficients. The residual p_T dependences on N_{PV} and μ are observed to be fairly linear and independent of one another. Their coefficients are derived in $|\eta_{\text{det}}|$ and p_T^{truth} bins, where the former is the jet η pointing from the geometric centre of the detector, and the latter is the p_T of the truth jet that matches the reconstructed jet. Four systematic uncertainties are introduced to account for MC mis-modelling of N_{PV} , μ , the ρ topology, and the p_T dependence of the residual pile-up corrections.

Absolute MC-based calibration

The next stage in the chain is the absolute MC-based calibration of the energy and direction of reconstructed jets. Hence, the four-momentum of the jet is corrected to the particle-level energy scale accounting for non-compensating calorimeter response, energy losses in dead material, out-of-cone effects and biases in the jet direction reconstruction. Those bias are primarily caused by the transition between different calorimeter technologies and sudden changes in calorimeter granularity. In addition, at this point, the jet mass scale (JMS) calibration may be also considered to improve reliability of jet kinematics, which is recommended for low-energy measurements.

The calibration is derived from a PYTHIA 8 simulation of dijet events after the

application of the pile-up corrections. The reconstructed jets are defined using the anti- k_t algorithm with radius parameter $R = 0.4$. Then, they are geometrically matched to truth jets within $\Delta R = 0.3$ and a numerical inversion procedure is used. The relation between the different jet calibration variables for the reconstructed jet and the truth jet matched to it provides the correction parameters:

$$E^{\text{reco}} = c_{\text{JES}} E^{\text{truth}}, \quad m^{\text{reco}} = c_{\text{JES}} c_{\text{JMS}} m^{\text{truth}}, \quad \eta^{\text{reco}} = \eta^{\text{truth}} + \Delta\eta.$$

The mean of a Gaussian fit to the core of the $E^{\text{reco}}/E^{\text{truth}}$ distribution returns the average jet energy response \mathcal{R} which is measured in η_{det} and E^{reco} bins. However, changes in calorimeter geometry or technology cause different energy responses. A second correction is therefore derived as the difference between the reconstructed and truth directions parametrized in η_{det} and E^{truth} bins.

Global sequential calibration

Nevertheless, the response can still vary from jet to jet depending on the flavour and energy distribution of the constituent particles, their transverse distribution, and the fluctuations of the jet development in the calorimeter. As discussed in Section 2.2, jet's features are determined by the hard parton originating the showering. For instance, the average particle composition and shower shape, which vary most notably between quark- and gluon-initiated jets. A quark-initiated jet will often include hadrons with a higher fraction of the jet p_T that penetrate further into the calorimeter, whereas a gluon-initiated jet will typically contain more particles of softer p_T , leading to a lower calorimeter response and a wider transverse profile.

The global sequential calibration (GSC) reduces the effects from these fluctuations and improve the jet resolution without changing the average jet energy response. This procedure is based on global jet observables such as the longitudinal structure of the energy depositions within the calorimeters, tracking information associated with the jet, and information related to the activity in the muon chambers behind a jet. In total, six observables are parametrized as a function of $|\eta_{\text{det}}|$ and p_T^{truth} . Then, corrections for each observable are applied independently and sequentially to the jet four-momentum for jets with $|\eta| < 3.2$. The six observables that account for the dependence of the jet response in the GSC are given in Table 5.2.

Obser.	Description
f_{charged}	fraction of jet p_T measured from ghost-associated tracks
f_{Tile0}	fraction of jet E measured in the first layer of the TileCal
f_{LAr3}	fraction of jet E measured in the third layer of the LAr EMCAL
n_{trk}	number of tracks with $p_T > 1$ GeV ghost-associated with the jet
w_{trk}	average p_T -weighted transverse distance in the η - φ plane between the jet axis and all tracks of $p_T > 1$ GeV ghost-associated with the jet
n_{segments}	number of muon track segments ghost-associated with the jet

Table 5.2: Observables parametrized during the GSC to improve the jet response.

5.3.2 *In situ* calibration

The absolute MC-based JES calibration and the GSC do not account for differences between the jet response in data and MC simulation. Therefore, one final calibration stage must be applied only to data to correct for these differences. This last step is the so-called residual *in situ* calibration, which measures the jet response in data and MC simulation separately and uses the ratio as an additional correction in data.

The differences between data and MC simulation arises by imperfect simulation of both the detector materials and the physics processes involved. These imperfections translate into the jet response, which must then be calculated by balancing the p_T of a jet against that of a well-calibrated reference object or system. The response is given by the average ratio of the jet p_T to the reference object p_T in bins of reference object p_T . In order to avoid sensitivity to secondary effects, the double ratio from the response in data and MC simulation is computed as a reliable measure of the jet energy scale difference between them. In the final step of the *in situ* calibration, this quantity is transformed via a numerical inversion to a function of the jet p_T .

There are three stages of *in situ* analyses and they are performed sequentially, namely, η intercalibration, $Z/\gamma + \text{jet}$ MPDF, and MJB. Each of them based on a well-calibrated reference object or system. A set of systematic uncertainties is introduced for each analysis, which arise from three sources: modelling of physics processes in simulation, uncertainties in the measurement of the reference object, and uncertainties in the expected p_T balance due to the event's topology.

The first step is the η intercalibration analysis where the energy scale of forward jets is corrected to match those of central jets thanks to the p_T balance presented in dijet events. Afterwards, the $Z+\text{jet}$ and $\gamma+\text{jet}$ analyses balance the hadronic recoil of a jet in an event against the p_T of a calibrated Z boson or photon. So as to help mitigate effects of pile-up in low- p_T measurements, the missing- E_T projection fraction (MPF) method uses the full hadronic recoil to compute the balance [89]. Finally, the multi-jet balance (MJB) analysis uses a system of well-calibrated low- p_T jets to calibrate a single high- p_T jet [90]. Even though the last two analysis are computed only for central jets, they still apply to forward jets due to the effect of the η intercalibration. Additionally, they provide a single smooth calibration that covers the full transverse momentum range.

The three *in situ* analyses require some common selection criteria. For instance, each event must have a reconstructed vertex with at least two associated tracks of $p_T > 500$ MeV. Moreover, each jet with $20 \text{ GeV} < p_T < 60 \text{ GeV}$ and $|\eta| < 2.4$ must pass the jet vertex tagging (JVT) criteria. These requirements for tagging and suppressing pile-up jets are constructed as a multivariate combination of the fraction of the total momentum of tracks in the jet which is associated with the primary vertex and the number of reconstructed primary vertices in the event [91]. In analyses working with the PFlow jet collection, the Tight threshold is $\text{JVT} > 0.5$. In addition, there is a forward pile-up jet vertex tagging (fJVT) algorithm that covers the rest of the supported range $2.5 < |\eta| < 4.5$. In this case, the Loose threshold is $\text{fJVT} < 0.5$ with the additional timing cut < 10 .

5.3.3 Systematic uncertainties

The full systematic uncertainty in the jet energy scale consists of 113 sources with variations up and down. They are summarized in Table 5.3 and, as mentioned before, they are derived from the in situ measurements, pile-up effects, flavour dependence, and other additional effects. Figure 5.5 shows the fractional jet energy scale uncertainty as a function of the jet p_T and jet η when considering PFlow jets.

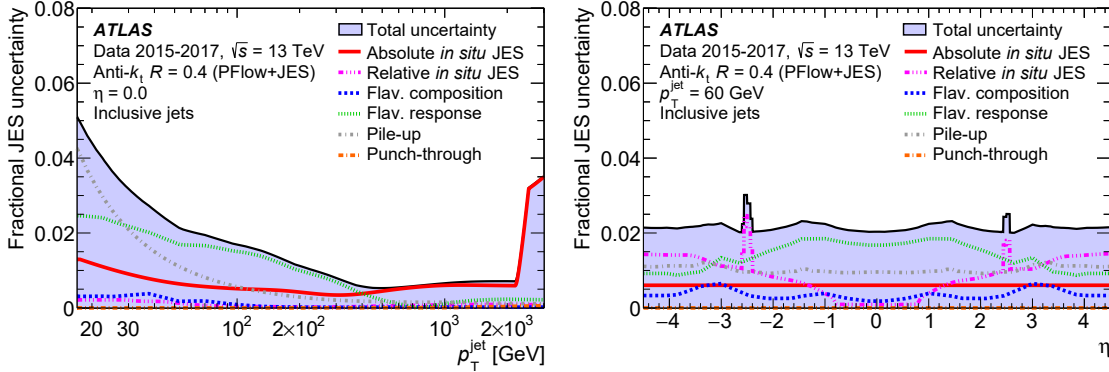


Figure 5.5: Fractional jet energy scale systematic uncertainty components for anti- k_t $R = 0.4$ jets reconstructed from particle-flow objects as a function of jet p_T at $\eta = 0$ in the left figure, and as a function of η at $p_T = 60$ GeV in the right one. Flavour-dependent components shown here assume a dijet flavour composition [88].

These JES uncertainties are extended to other analyses following the official recommendations. In this case, the variations are computed for the baseline MC simulation using the parameters given in Table 5.4. Note that this procedure takes into account the 34 sources parametrizing the JER uncertainties discussed in Section 5.4.

AntiKt4EMPFlow

Configuration file:
`rel21/Summer2019/R4_AllNuisanceParameters_AllJERNP.config`

Analysysis file:
`/path/to/FlavourComposition.root`

Calibration area: CalibArea-08

Table 5.4: Main parameters of the jet uncertainty procedure for PFlow jets reconstructed using the anti- k_t algorithm with radius parameter $R = 0.4$. It applies to MC, `isData=false`, but also to pseudo-data in JER variations, `isData=true`.

The file `FlavourComposition` provides the flavour composition expected in the sample as a function of the jet p_T and jet $|\eta|$. Otherwise, the fraction of quark- and gluon-initiated jets is assumed 0.5 ± 0.5 by default in both cases. Therefore, as the topology differs, the gluon fraction f_g and its uncertainty Δf_g must be derived for each analysis. These two parameters determine the flavour composition uncertainty, $\Delta f_g \times (\mathcal{R}_q - \mathcal{R}_g)$, and flavour response uncertainty, $f_g \times \Delta \mathcal{R}_g$, where \mathcal{R}_q and \mathcal{R}_g are the response for quark- and gluon initiated jets, respectively.

Component	Description
	η intercalibration
Systematic mis-modelling	Envelope of the generator, pile-up, and event topology var.
Statistical component	Statistical component (single component)
Non-closure	Three components at high energy and at $\eta \sim \pm 2.4$
Non-closure, 2018 only	Single component at $\eta \sim \pm 1.5$ due to Tile calibration
	Z + jet
Electron scale	Uncertainty in the electron energy scale
Electron resolution	Uncertainty in the electron energy resolution
Muon scale	Uncertainty in the muon momentum scale
Muon resolution (ID)	Uncertainty in the muon resolution in the ID
Muon resolution (MS)	Uncertainty in the muon resolution in the MS
MC generator	Difference between MC event generators
JVT cut	Jet vertex tagger uncertainty
$\Delta\phi$ cut	Variation of $\Delta\phi$ between the jet and Z boson
Subleading jet veto	Radiation suppression though second-jet veto
Showering & topology	Modelling energy flow and distribution in and around a jet
Statistical	Statistical uncertainty in 28 discrete p_T terms
	$\gamma + \text{jet}$
Photon scale	Uncertainty in the photon energy scale
Photon resolution	Uncertainty in the photon energy resolution
MC generator	Difference between MC event generators
JVT cut	Jet vertex tagger uncertainty
$\Delta\phi$ cut	Variation of $\Delta\phi$ between the jet and photon
Subleading jet veto	Radiation suppression though second-jet veto
Showering & topology	Modelling energy flow and distribution in and around a jet
Photon purity	Purity of sample used for $\gamma + \text{jet}$ balance
Statistical	Statistical uncertainty in 16 discrete p_T terms
	Multi-jet balance
$\Delta\phi$ (lead, recoil system)	Angle between leading jet and recoil system
$\Delta\phi$ (lead, any sublead)	Angle between leading jet and closest subleading jet
MC generator	Difference between MC event generators
p_T^{asym} selection	Second jet's p_T contribution to the recoil system
Jet p_T	Jet p_T threshold
Statistical	Statistical uncertainty in 28 discrete p_T terms
	Pile-up
μ offset	Uncertainty in the μ modelling in MC simulation
M_{PV} offset	Uncertainty in the N_{PV} modelling in MC simulation
ρ topology	Uncertainty in the ρ density modelling in MC sim.
p_T dependence	Uncertainty in the residual p_T dependence
	Jet flavour
Flavour composition	Uncertainty in the prop. sample composition of partons
Flavour response	Uncertainty in the response of gluon-initiated jets
b-jets	Uncertainty in the response of b-quark initiated jets
Punch-through	Uncertainty in GSC punch-through correction
Single-particle response	High- p_T jet unc. from single-particle and test-beam meas.

Table 5.3: Sources of systematic uncertainty in the jet energy scale [88].

5.4 Jet energy resolution

In this section, the details of the JER are discussed. This information together with the one from the JES calibration are required for precise measurements with jets in the final state. In order to measure the JER, jet momentum must be measured precisely. This implies that the jets must either recoil against a reference object, or be balanced against one another in a well-defined dijet system.

The relative JER has a dependence on the transverse momentum of the jet, which may be parameterized using a functional with three independent contributions, namely, the noise (N), stochastic (S) and constant (C) terms [92]:

$$\frac{\sigma_{p_T}}{p_T} = \frac{N}{p_T} \oplus \frac{S}{\sqrt{p_T}} \oplus C.$$

Consequently, the dominant contribution at low- p_T is the noise term, whereas at high- p_T is the constant term. The noise term comes from the contribution of electronic noise to the signal measured by the detector front-end electronics, but also from the pile-up. The stochastic captures the statistical fluctuations in the amount of energy deposited and represents the limiting term in the resolution. Finally, the constant term corresponds to fluctuations that are a constant fraction of the jet p_T , such as energy depositions in passive material, the starting point of the hadron showers, and non-uniformities of response across the calorimeter.

5.4.1 Resolution measurement

The resolution measurement is generally performed using well-defined jet systems. In this case, the procedure relies on the approximate scalar balance between the transverse momenta of the two leading jets. The so-called dijet balance method measures the deviation from the exact balance due to a combination of experimental resolution, the presence of additional radiation in the event, and biases due to the event selection used in the measurement. This imbalance in the system is qualified via the assymetry given by

$$\mathcal{A} = 2 \frac{p_T^{\text{probe}} - p_T^{\text{ref}}}{p_T^{\text{probe}} + p_T^{\text{ref}}}.$$

The p_T of a reference jet ref is required to be located in the well-calibrated, central region of the detector and the probe jet is the jet for which the resolution is to be measured. Taken the standard deviations of both p_T , the standard deviation of the assymetry can be expressed as

$$\sigma_{\mathcal{A}} = \left\langle \frac{\sigma_{p_T}}{p_T} \right\rangle^{\text{probe}} \oplus \left\langle \frac{\sigma_{p_T}}{p_T} \right\rangle^{\text{ref}}.$$

The determination of this deviation must account for effects such as additional radiation, non-perturbative processes including hadronization and multi-parton interactions, and others that may lead to particle losses and additions in the measured jets.

Therefore, a baseline MC simulation modelling this effects needs to be considered.

5.4.2 Noise measurement

The noise contribution from the pile-up to the resolution is estimated by measuring the fluctuations in the energy deposits due to pile-up using data samples that are collected by random unbiased triggers.

These measurements are performed using the random cones method in which energy deposits in the calorimeter are summed at the energy scale of the constituents in circular areas analogous to the jet area. The imbalance between two of these random cones within opposite pseudo-rapidity regions is given by Δp_T^{RC} , whose distribution provides an estimator of noise $N^{\text{PU}} = \sigma_{\text{RC}}/2\sqrt{2}$.

The total noise contribution to the JER includes also electronic noise, to which the random cones are not sensitive due to the topo-clustering process. This electronic contribution is estimated through fits to the JER measured in a dedicated MC simulation with no pile-up effects $\mu = 0$. The total noise term used is therefore taken to be $N = N^{\text{PU}} \oplus N^{\mu=0}$.

5.4.3 Total *in situ* combination

The implementation of the total *in situ* combination is performed in a manner nearly identical for the JES and JER sources, propagating uncertainties from the dijet measurement and using an eigenvalue decomposition to reduce the final number of nuisance parameters. Nevertheless, the JES combination uses polynomial splines to interpolate across the jet p_T , while the JER combination uses the functional introduced at the beginning of Section 5.4. In this case, its combined measurement is obtained by performing a fit to the dijet balance measurements using a constraint on the noise term derived as previously explained.

5.4.4 Systematic uncertainties

There are 34 JER sources with variations up and down, each of them computed as pseudo-data and MC simulation. Added to the 113 JES sources with variations up and down, the total number of variations needed to describe the jet systematic uncertainties is 360. Moreover, one also has to consider the effect of other sources, such as, the jet angular resolution (JAR) or the choice of a MC model in the unfolding procedure. Figure 5.6 shows the resulting combined JER measurement and the absolute uncertainties on it as a function of the jet p_T at a fixed jet η when considering PFlow jets.

A smearing procedure is recommended to ensure that the resolution of the jet energy scale in MC simulation matches that in data. For regions of phase space in which the resolution in data is larger than in MC simulation, the simulation sample should

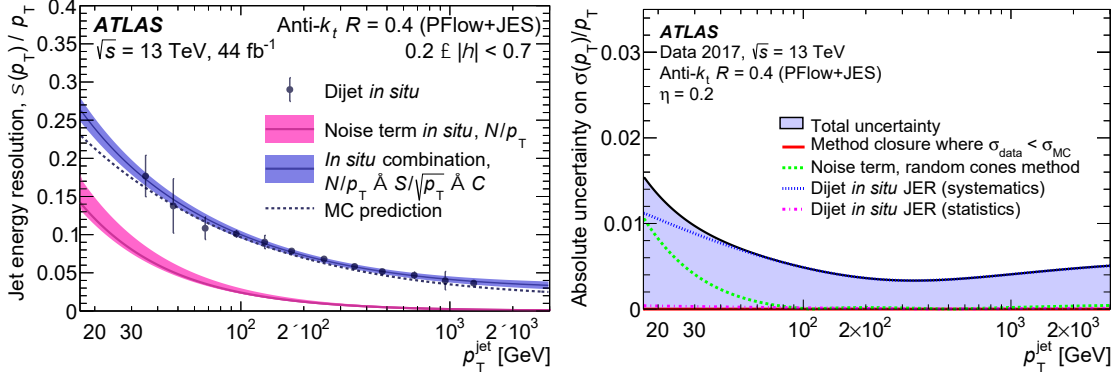


Figure 5.6: Relative jet energy resolution as a function of p_T for fully calibrated PFflow+JES jets in the left figure, and absolute uncertainty on the relative jet energy resolution as a function of jet p_T in the right one. Uncertainties from the two *in situ* measurements and from the data/MC simulation difference are shown separately [88].

be smeared until its average resolution matches that of data. However, data should always remain unaltered, even if resolution in data is smaller than in simulation. JER systematic uncertainties are propagated through analyses by smearing jets according to a Gaussian function with width $\sigma_{\text{smear}}^2 = (\sigma_{\text{nom}} - |\sigma_{\text{NP}}|)^2 - \sigma_{\text{nom}}^2$ where σ_{nom} is the nominal JER of the sample and the one-standard-deviation variation in the uncertainty component to be evaluated is given by σ_{NP} .

Application of JER systematic uncertainties must account for anti-correlations across a single uncertainty component and differences in resolution between data and MC simulation. Therefore, the uncertainty is calculated for each JER source as the difference between the varied values computed as pseudo-data and MC simulation, while, for each JES source, it is just the difference between the varied value and the nominal value, both computed as MC simulation.

5.5 Jet quality criteria

The quality criteria for the selection of reconstructed anti- k_t jets with radius parameter $R = 0.4$ is described in Ref. [93]. There are two selection criteria used for a jet-based event cleaning, namely, Loose and Tight. The cleaning recommendation is to remove the whole event from the sample if either a pre-selected jet within it is tagged as BadLoose, or one of the two leading jets is tagged as BadTight.

These selection criteria are designed to distinguish signal jets from misidentified jets of non-collision origin. The Loose selection is proposed by default, whereas the Tight selection is designed to further reject background jets for analyses sensitive to non-collision backgrounds. The main background jets comes from these sources:

- Beam-induced background due to proton losses upstream of the interaction point that can induce secondary cascades leading to muons that can reach the

detector and are reconstructed as jets.

- Cosmic-ray showers produced in the atmosphere overlapping with collision events. The particles reaching the ATLAS detector are predominantly muons.
- Calorimeter noise from large scale coherent noise or isolated pathological cells. Thankfully, most of the noise is already identified and rejected by the data quality inspection mentioned in Section 4.3 and performed shortly after the data taking.

These jet candidates coming from the background are referred to as fake jets, while jets produced in collision events are called good jets. The jet selection criteria should efficiently identify the nature of the jet candidate so as to reject jets from background processes while keeping the highest efficiency selection for jets. Jet quality variables help to perform this task. They can be divided into three categories: variables based on signal pulse shape in the LAr calorimeters, energy ratio variables, and track-based variables. The last two categories provide a good discrimination against noise in the LAr and Tile calorimeters, rejecting beam-induced background and cosmic muon showers at the same time.

CHAPTER 6

Asymptotic freedom beyond the TeV scale

In this chapter, measurements of transverse energy-energy correlations and their associated azimuthal asymmetries in multi-jet events are presented. The data sample with integrated luminosity of 139 fb^{-1} corresponds to proton-proton collisions at a centre-of-mass energy of $\sqrt{s} = 13 \text{ TeV}$, collected with the ATLAS detector at the LHC. The measurements are presented in bins of the scalar sum of the transverse momenta of the two leading jets, compared with simulations from Monte Carlo event generators and unfolded to the particle level. The unfolded distributions are fitted to NNLO pQCD calculations. The agreement between data and theory is excellent, thus providing a precision test of QCD at large momentum transfers. The strong coupling constant has been extracted from these fits at different scale regimes, studying asymptotic freedom beyond the TeV scale.

The transverse energy-energy correlation (TEEC) and its associated azimuthal angular asymmetry (ATEEC) were proposed as the appropriate generalization of the EEC function for hadron collider experiments in Ref. [29], where LO predictions were also presented. The EEC function was originally introduced in Refs. [27, 28] to provide a quantitative test of QCD in e^+e^- annihilation experiments. It can be calculated in pQCD and in fact the $\mathcal{O}(\alpha_s^2)$ corrections were found to be modest [94–98] and studied also in the nearly back-to-back limit [99]. Their measurements [100–112] have had significant impact on the early precision tests of QCD and in the determination of the strong coupling constant.

The EEC function has attracted significant recent attention. Analytical calculations at NLO using pQCD [113, 114] and $\mathcal{N} = 4$ SYM [115, 116] have been performed. Moreover, resummation of the EEC function in the back-to-back limit has been improved [117, 118] and numerical results with NNLL+NNLO accuracy have been computed [119, 120] and used to determine the strong coupling [121]. Most recently, a factorization formula to describe the collinear limit of the EEC function has been presented [122].

In experiments with incoming hadrons, longitudinally invariant expressions along the direction of the beams are required. Therefore, as jet-based observables, the TEEC and ATEEC make use of the jet transverse energy E_T . Both observables are sensitive to QCD radiation and present a clear dependence with the strong coupling.

Numerical results at NLO for the jet-based TEEC function were obtained [123] by using the NLOJET++ program [61, 62], which provides the LO and NLO corrections to the three-jet production. Furthermore, numerical results for the hadron-based TEEC function with NLO+NNLL accuracy were computed [124]. Recently, the NNLO corrections to the 3-jet cross sections have been calculated [65] and they have been used to obtain predictions for the TEEC function at NNLO accuracy.

The TEEC function is defined as the transverse energy-weighted azimuthal angular distribution of produced jet pairs in the final state [125], i.e.

$$\frac{1}{\sigma} \frac{d\Sigma}{d \cos \phi} = \frac{1}{\sigma} \sum_{i,j} \int \frac{d\sigma}{dx_{Ti} dx_{Tj} d \cos \phi} x_{Ti} x_{Tj} dx_{Ti} dx_{Tj}$$

where the indices i and j run over all jets in a given event, $x_{Ti} = E_{Ti}/E_T$ is the jet i normalized transverse energy, E_T is the sum of the jet transverse energies, $\Delta\varphi_{ij}$ is the angle in the transverse plane between the jets i and j , and the Dirac delta function ensures that $\phi = \Delta\varphi_{ij}$. The normalization to the effective cross section $\sigma = \int d\sigma$ guarantees that the integral of the TEEC function over $\cos \phi$ is unity.

In order to cancel uncertainties which are constant over $\cos \phi$, the ATEEC function is defined as the difference between the forward ($\cos \phi > 0$) and the backward ($\cos \phi < 0$) part of the TEEC function, i.e.

$$\frac{1}{\sigma} \frac{d\Sigma^{\text{asym}}}{d \cos \phi} = \frac{1}{\sigma} \frac{d\Sigma}{d \cos \phi}_{\phi} - \frac{1}{\sigma} \frac{d\Sigma}{d \cos \phi}_{\pi-\phi}.$$

In pp collisions observables are not totally inclusive over all coloured particles in the initial state. However, finite predictions can still be obtained at any order in pQCD when infrared divergences due to collinear emissions from incoming partons are factorized out of the perturbative computation. The hadron-parton transition is then factorized into the PDFs. Furthermore, ultraviolet divergences arise in any perturbative calculation. The bare coupling is then renormalized to the physical coupling which is an indicative of the effective strength of the interaction when the unphysical scale is taken close to the interaction scale Q . The evolution of $\alpha_s(Q)$ is given by the solution to the RGE for α_s [126].

Recently, the ATLAS Collaboration presented a measurement of the TEEC and ATEEC functions at $\sqrt{s} = 7$ TeV [1] and at $\sqrt{s} = 8$ TeV [2], determining $\alpha_s(Q)$ in each of the scale regimes and using these determinations to test the running of α_s predicted by the RGE for α_s . The existence of new coloured fermions would imply modifications to the QCD β -function [127, 128]. Therefore, the running of α_s is not only important as a precision test of QCD at large scales but also as a test for new physics. An interpretation of these measurements in terms of constraints on new coloured particles through their impact on the running of α_s has been presented in Ref. [129].

This analysis extends previous measurements to higher scales Q and with a significantly improved precision. It also makes comparisons to NNLO pQCD predic-

tions, providing a quantitative test of the running of α_s beyond the TeV scale, thus measuring asymptotic freedom. In addition, these measurements provide a tighter constraint for new physics.

6.1 Data and Monte Carlo samples

The treatment of data and MC samples is explained in Section 4.3. In both cases, jets are reconstructed using the anti- k_t EMPFlow algorithm with jet radius $R = 0.4$. Hence, any arbitrarily soft particle emitted at a larger distance than R will become a jet in its own. Therefore, a jet p_T threshold is specified for jets to be of interest, $p_T > 60$ GeV. They are also required to lie within $|\eta| < 2.4$. A more restrictive cut in jet p_T reduces significantly the amount of hard radiation, increasing the effect of unbalanced 2-jet events in the nearly back-to-back limit of the TEEC function. On the other hand, one is exposed to pile-up effects when reducing the jet p_T threshold.

Events are collected using the HLT _j460 unprescaled single-jet trigger. The single-jet trigger requires at least one jet with a jet transverse energy measured by the trigger system greater than 460 GeV at the trigger level. The trigger efficiency is computed as the fraction of events passing the probe and the reference trigger with respect to the total number of events passing the reference trigger. Figure 6.1 shows the trigger efficiency as a function of the two leading jets' calibrated transverse momenta for the data and the baseline MC event generator. The trigger is fully efficient for values above 1.0 TeV.

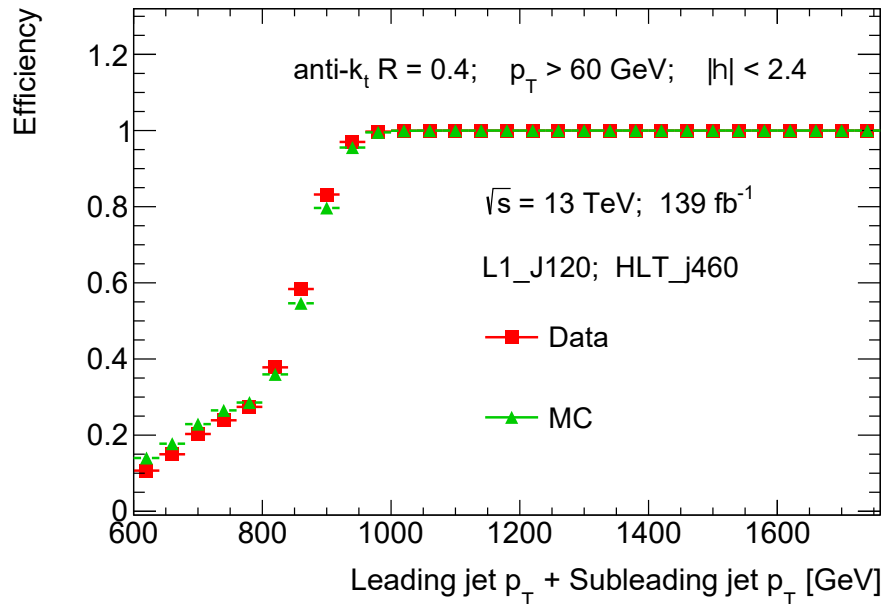


Figure 6.1: Trigger efficiency of the HLT _j460 trigger using the HLT _j100 trigger as the reference one for the data and the baseline MC event generator.

For this analysis, events with at least two jets are selected and the two leading

jets are required to fulfil $H_{\mathrm{T}2} > 1.0$ TeV where $H_{\mathrm{T}2}$ is defined as the sum of the two leading jets' transverse momenta $p_{\mathrm{T}1} + p_{\mathrm{T}2}$. Thus, the HLT_j460 unprescaled single-jet used to collect the data is fully efficient. In addition, all events with at least one jet passing the experimental requirements and tagged as TIGHTBAD are removed.

In order to study the energy scale dependence of observables, the phase space is binned in $H_{\mathrm{T}2}$. This has the main advantage not to underestimate the scale of the hard process as taking only the leading jet p_{T} does. Additionally, it does not introduce a discontinuous behaviour with the jet p_{T} cut for multi-jet events. Furthermore, $H_{\mathrm{T}2}$ has been proved to be significantly stable against higher-order perturbative corrections [130]. Table 6.1 summarizes the number of events in each $H_{\mathrm{T}2}$ bin, N_{ev} , along with the corresponding average scale value, $\langle H_{\mathrm{T}2} \rangle$.

$H_{\mathrm{T}2}$ range [GeV]	$\langle H_{\mathrm{T}2} \rangle$ [GeV]	N_{ev}
[1000,1200]	1082	36447484
[1200,1400]	1284	12526282
[1400,1600]	1485	4885650
[1600,1800]	1687	2093521
[1800,2000]	1888	958406
[2000,2300]	2125	602846
[2300,2600]	2427	226740
[2600,3000]	2762	107920
[3000,3500]	3197	39888
[3500,8000]	3919	15931

Table 6.1: Summary of the $H_{\mathrm{T}2}$ intervals in the analysis, together with the average scale value for each bin, $\langle H_{\mathrm{T}2} \rangle$, and the number of events in each bin, N_{ev} .

The QCD-based MC event generators are described in Section 4.1. As stated above, the baseline MC simulated samples are generated with the PYTHIA 8.235 [69] event generator and used to unfold the measured distributions from the detector to the particle level, as well as the theoretical predictions from the parton to the particle level. Table 6.2 summarizes the main properties of the PYTHIA 8.235 sample, mainly, the \hat{p}_{T} range of each JZ slice and the parameters required to merge them properly. Table 6.3 shows the equivalent information for HERWIG 7.1.3 with dipole showering, while Table 6.4 does it for HERWIG 7.1.3 with angular-ordered parton shower [70, 71]. Table 6.5 summarizes the properties of the SHERPA 2.1.1 sample [72]. All these samples are sliced using the anti- k_t jet \hat{p}_{T} with jet radius $R = 0.6$.

6.1.1 Control plots for MC predictions

To test the global quality of the description of the data made by the baseline MC predictions, a comparison between data and MC is performed for some relevant jet-based variables as shown in Figure 6.2, where the MC predictions are normalized to have the same area as the data distributions. The description of the shape of the distributions is good in general for all the variables considered.

DSID	$\hat{p_T}$ range [GeV]	σ [nb]	F_{eff}	N_{ev}
364704	[400,800]	2.5461E+02	1.3369E-02	61872800
364705	[800,1300]	4.5529E+00	1.4529E-02	31933284
364706	[1300,1800]	2.5754E-01	9.4734E-03	31961550
364707	[1800,2500]	1.6215E-02	1.1099E-02	15875000
364708	[2500,3200]	6.2506E-04	1.0156E-02	15963000
364709	[3200,3900]	1.9639E-05	1.2057E-02	7691000

Table 6.2: The PYTHIA 8.235 samples used in the analysis, along with their cross sections σ , filter efficiencies F_{eff} , and number of events N_{ev} .

DSID	$\hat{p_T}$ range [GeV]	σ [nb]	F_{eff}	N_{ev}
364904	[400,800]	3.5330E+02	6.9838E-03	58664000
364905	[800,1300]	6.0335E+00	7.9876E-03	58047000
364906	[1300,1800]	3.2247E-01	5.4909E-03	19560000
364907	[1800,2500]	1.9162E-02	6.8314E-03	7837000
364908	[2500,3200]	7.0036E-04	6.6438E-03	3916000
364909	[3200,3900]	2.1234E-05	8.2304E-03	3918000

Table 6.3: The HERWIG 7.1.3 samples with dipole showering used in the analysis, along with their cross sections σ , filter efficiencies F_{eff} , and number of events N_{ev} .

DSID	$\hat{p_T}$ range [GeV]	σ [nb]	F_{eff}	N_{ev}
364924	[400,800]	3.5358E+02	7.4221E-03	58718000
364925	[800,1300]	6.0311E+00	8.4244E-03	58740000
364926	[1300,1800]	3.2251E-01	5.7101E-03	19582000
364927	[1800,2500]	1.9148E-02	7.0547E-03	7799000
364928	[2500,3200]	7.0005E-04	6.7417E-03	3910000
364929	[3200,3900]	2.1245E-05	8.1723E-03	3913000

Table 6.4: The HERWIG 7.1.3 samples with angular-ordered parton shower used in the analysis, along with their cross sections σ , filter efficiencies F_{eff} , and number of events N_{ev} .

DSID	$\hat{p_T}$ range [GeV]	σ [nb]	F_{eff}	N_{ev}
426134	[400,800]	9.6079E+01	2.7790E-02	29200600
426135	[800,1300]	2.7250E+00	1.8421E-02	29257400
426136	[1300,1800]	2.0862E-01	8.7435E-03	7179200
426137	[1800,2500]	4.3732E-02	3.1001E-03	7217000
426138	[2500,3200]	3.3372E-04	1.4573E-02	7311800
426139	[3200,3900]	5.8948E-05	3.0994E-03	7263900

Table 6.5: The SHERPA 2.1.1 samples used in the analysis, along with their cross sections σ , filter efficiencies F_{eff} , and number of events N_{ev} .

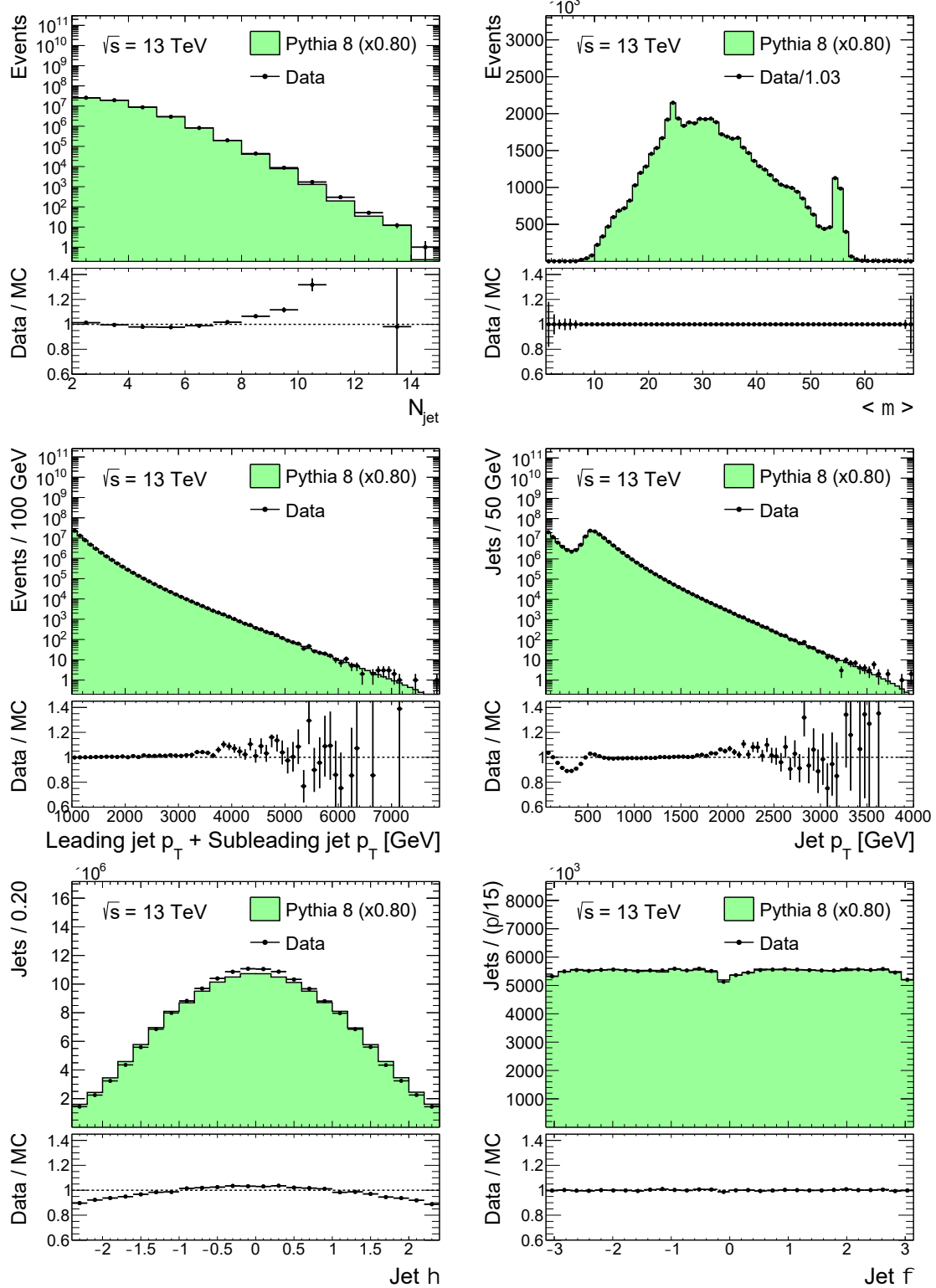


Figure 6.2: Distributions, measured in the inclusive $H_{\text{T}2}$ sample, for jet multiplicity (top left), $\langle \mu \rangle / 1.03$ (top right), $H_{\text{T}2}$ (middle left), jet p_{T} (middle right), jet η (bottom left) and jet φ (bottom right), along with normalized PYTHIA 8.235 simulations.

6.2 Detector-level results

In practical terms, for a data sample fulfilling the requirements described in Section 6.1, the transverse energy-energy correlations are measured as distributions in $\cos \phi$ bins of width $\Delta \cos \phi$ following Eq. (6.1).

$$\frac{1}{\sigma} \frac{d\Sigma}{d \cos \phi} = \frac{1}{N_{\text{ev}} \Delta \cos \phi} \sum_{A=1}^{N_{\text{ev}}} \sum_{i,j}^{\text{jets}} \left(\frac{E_{T,i}^{(A)} E_{T,j}^{(A)}}{\left(\sum_k E_{T,k}^{(A)} \right)^2} \right) \quad (6.1)$$

Only jet pairs with azimuthal angular differences within the bin limits contribute, i.e. $\cos \Delta \varphi_{ij}^{(A)} \in (\cos \phi - (\Delta \cos \phi)/2, \cos \phi + (\Delta \cos \phi)/2)$, and the total number of multi-jet events in the data sample is N_{ev} . The fully inclusive TEEC distribution, $H_{T2} > 1.0$ TeV, is measured considering 100 bins of width $\Delta \cos \phi = 0.02$. The TEEC distributions in the H_{T2} intervals introduced in Table 6.1 have to be measured with a coarser binning because statistical fluctuations increase as the number of events steeply falls with increasing H_{T2} . Nevertheless, for $|\cos \phi| > 0.90$ the bin width is kept at $\Delta \cos \phi = 0.02$ in all the H_{T2} bins to provide detailed measurements of the nearly back-to-back limit at different scale regimes.

Figure 6.3 compares the TEEC and ATEEC distributions, measured in the first H_{T2} bin, for two different jet transverse momentum thresholds, including the nominal one. The ATEEC distributions are less sensitive to the effects of the jet p_T threshold, allowing measurements slightly affected by the jet selection cuts.

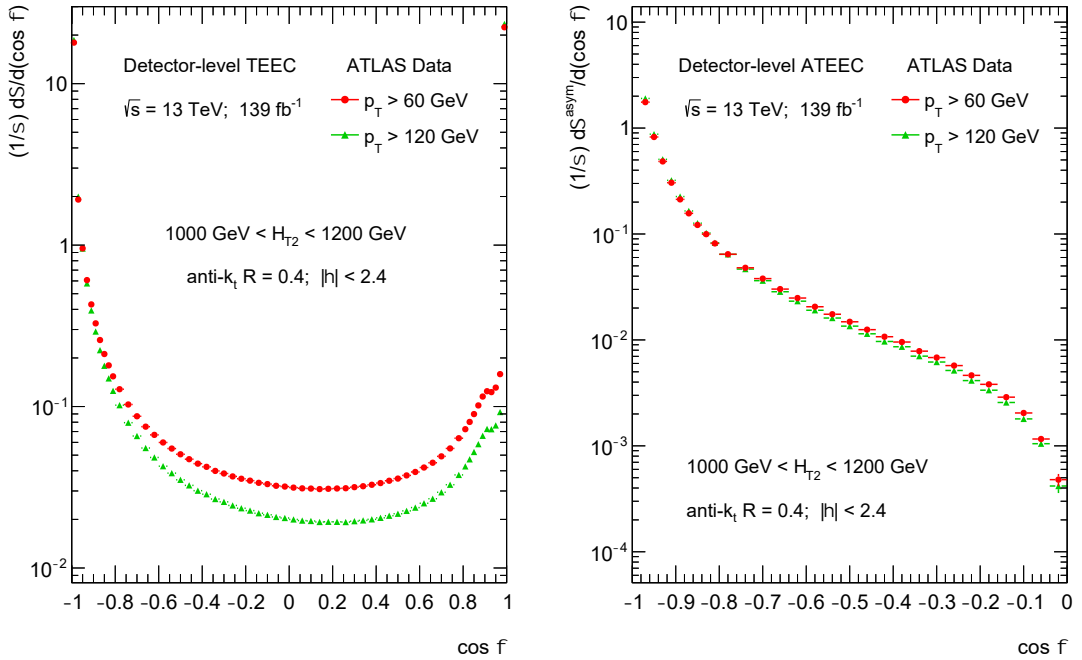


Figure 6.3: Detector-level TEEC (left) and ATEEC (right) distributions, measured in the first H_{T2} bin, for two jet p_T thresholds: $p_T > 60$ GeV and $p_T > 120$ GeV.

The TEEC distributions show two peaks in the regions close to the kinematical endpoints $\cos\phi = \pm 1$. The first one, at $\cos\phi = -1$ is due to the back-to-back configuration in 2-jet events, while the second peak at $\cos\phi = +1$ is due to the self-correlations of one jet with itself. These self-correlations are included in Eq. (6.1) and are necessary for the correct normalization of the TEEC function. The effect of the jet radius R is seen as a kink in the TEEC distributions at $\cos\phi \simeq 0.92$. Furthermore, the TEEC distributions present a central plateau dominated by jets arising from hard gluon radiation, which is decorrelated from the main event axis as predicted by QCD and measured in Refs. [131, 132]. The ATEEC distributions show a fall-off from $\cos\phi \simeq -1$ to $\cos\phi = 0$, with the value at $\cos\phi = -1$ being negative, and therefore, not represented using a logarithmic scale.

In order to see possible effects due to pile-up, the TEEC and ATEEC distributions are measured for two separated samples depending on whether the average number of pp interactions per bunch crossing lies above or below the median which is found to be 33. This is illustrated in Figure 6.4 where the TEEC and ATEEC distributions are shown in the first H_{T2} bin. The differences are below the statistical uncertainty for most of the phase space, and therefore, pile-up effects are almost negligible.

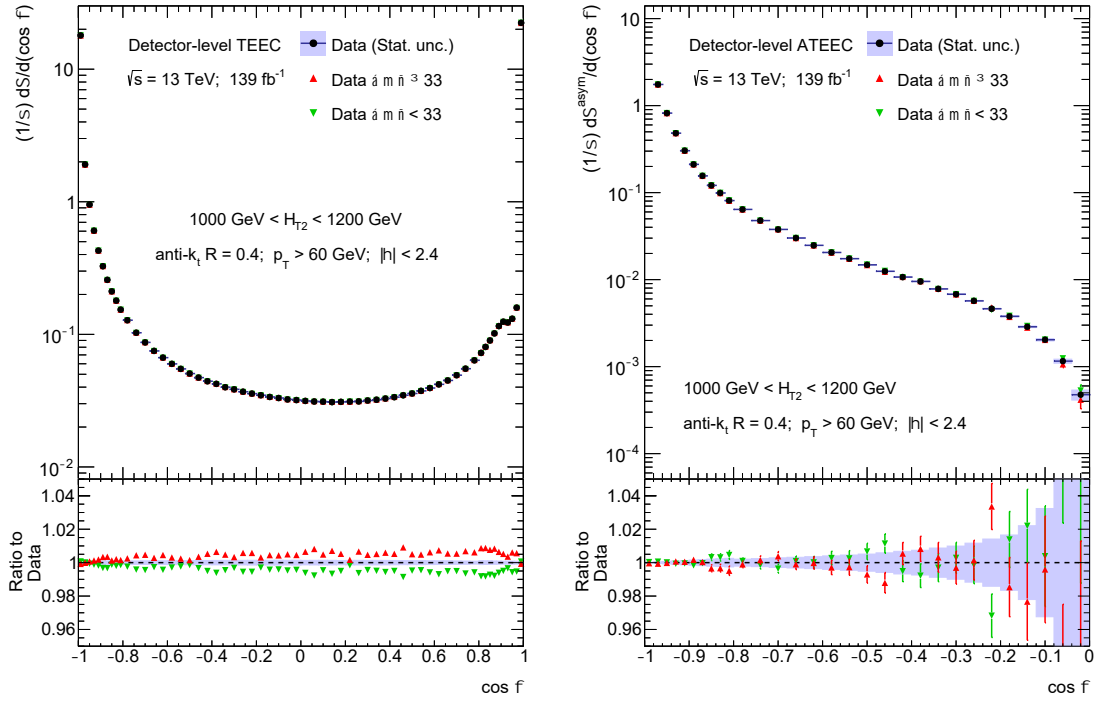


Figure 6.4: Detector-level TEEC (left) and ATEEC (right) distributions for low, $\langle\mu\rangle < 33$, and high, $\langle\mu\rangle \geq 33$, average number of interactions per bunch-crossing.

The results at detector level for the TEEC and ATEEC distributions, compared with the MC predictions from the PYTHIA 8.235, HERWIG 7.1.3 and SHERPA 2.1.1 event generators, are shown in Figures 6.5 to 6.10. The agreement of the detector-level predictions with data is good in general for PYTHIA 8.235, SHERPA 2.1.1, and HERWIG 7.1.3 with angular-ordered parton shower.

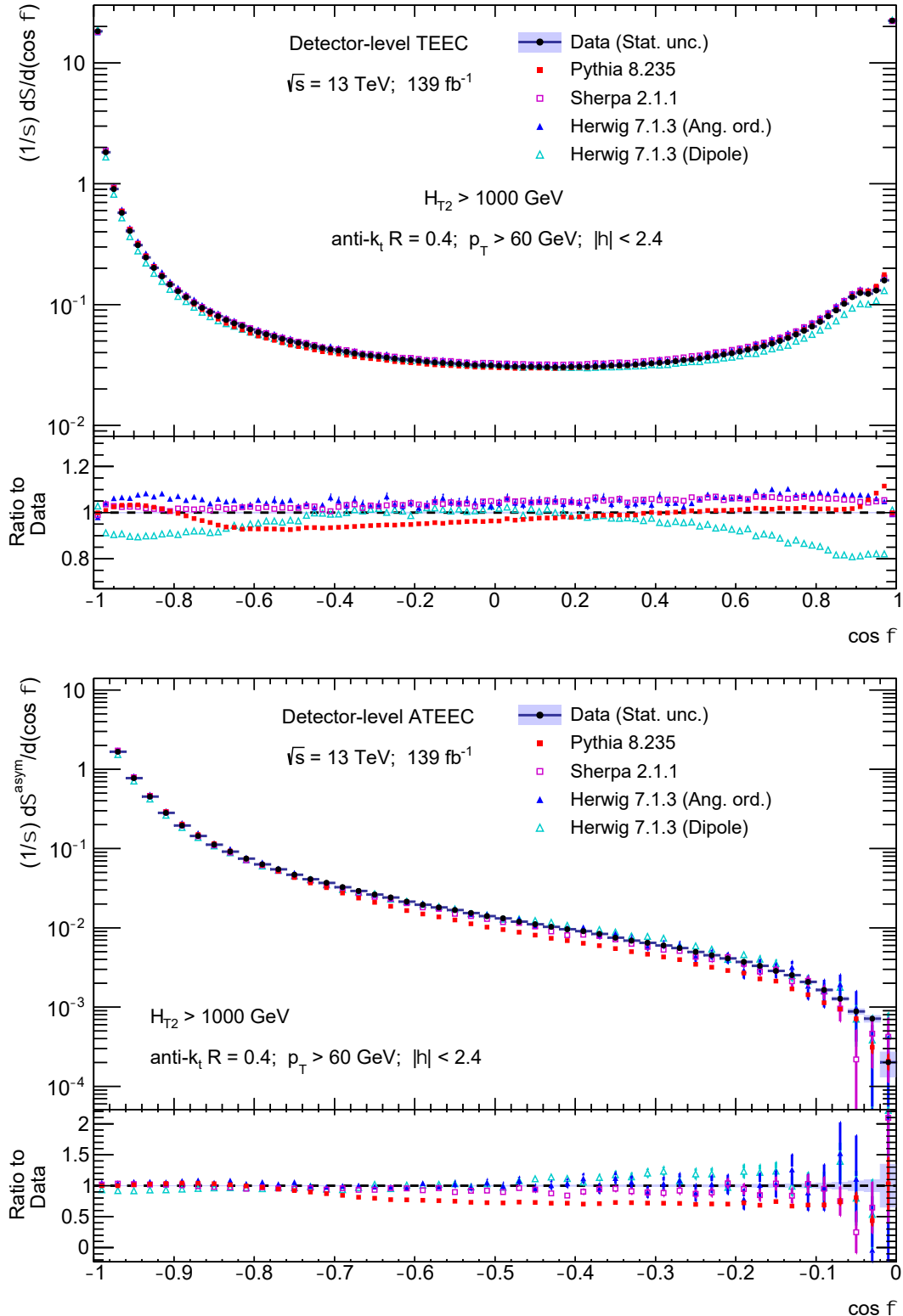


Figure 6.5: Detector-level TEEC (top) and ATEEC (bottom) distribution for the inclusive H_{T2} sample with the statistical uncertainty (shaded area), along with detector-level MC predictions. The ratio pad below compares the measured data and the MC predictions.

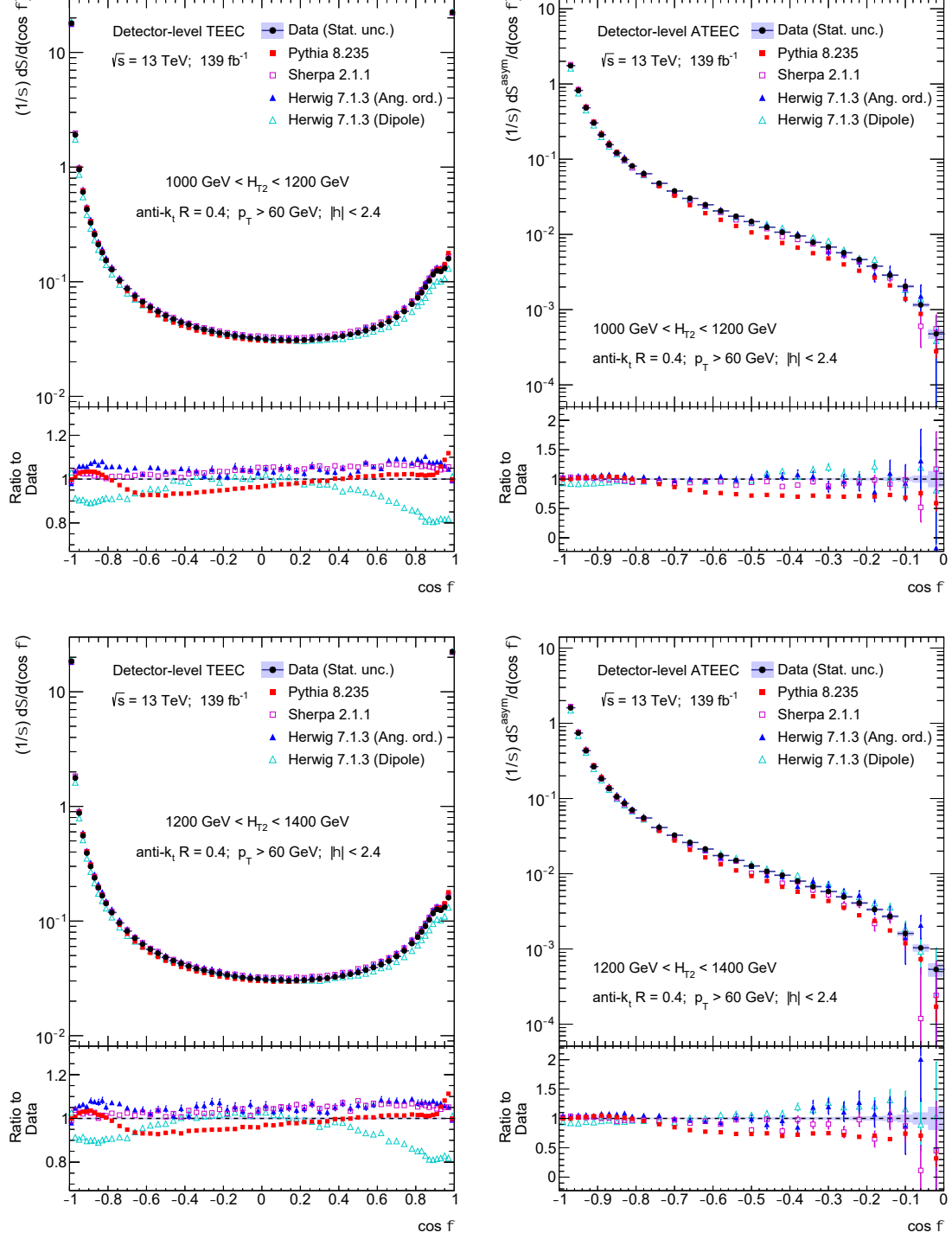


Figure 6.6: Detector-level TEEC (left) and ATEEC (right) distributions in two exclusive H_{T2} bins with the statistical uncertainty (shaded area), along with detector-level MC predictions. The ratio pad below compares the measured data and the MC predictions.

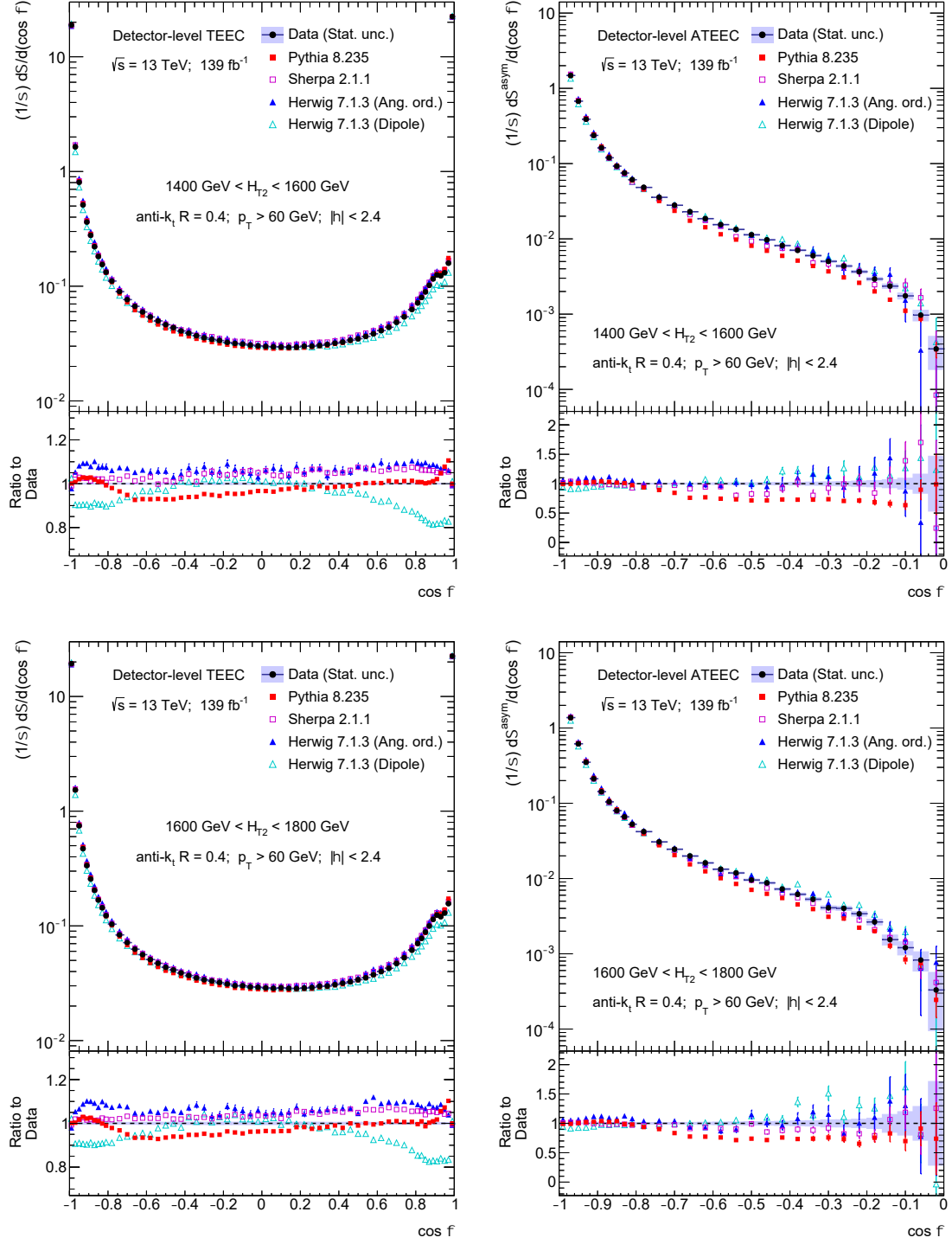


Figure 6.7: Detector-level TEEC (left) and ATEEC (right) distributions in two exclusive H_{T2} bins with the statistical uncertainty (shaded area), along with detector-level MC predictions. The ratio pad below compares the measured data and the MC predictions.

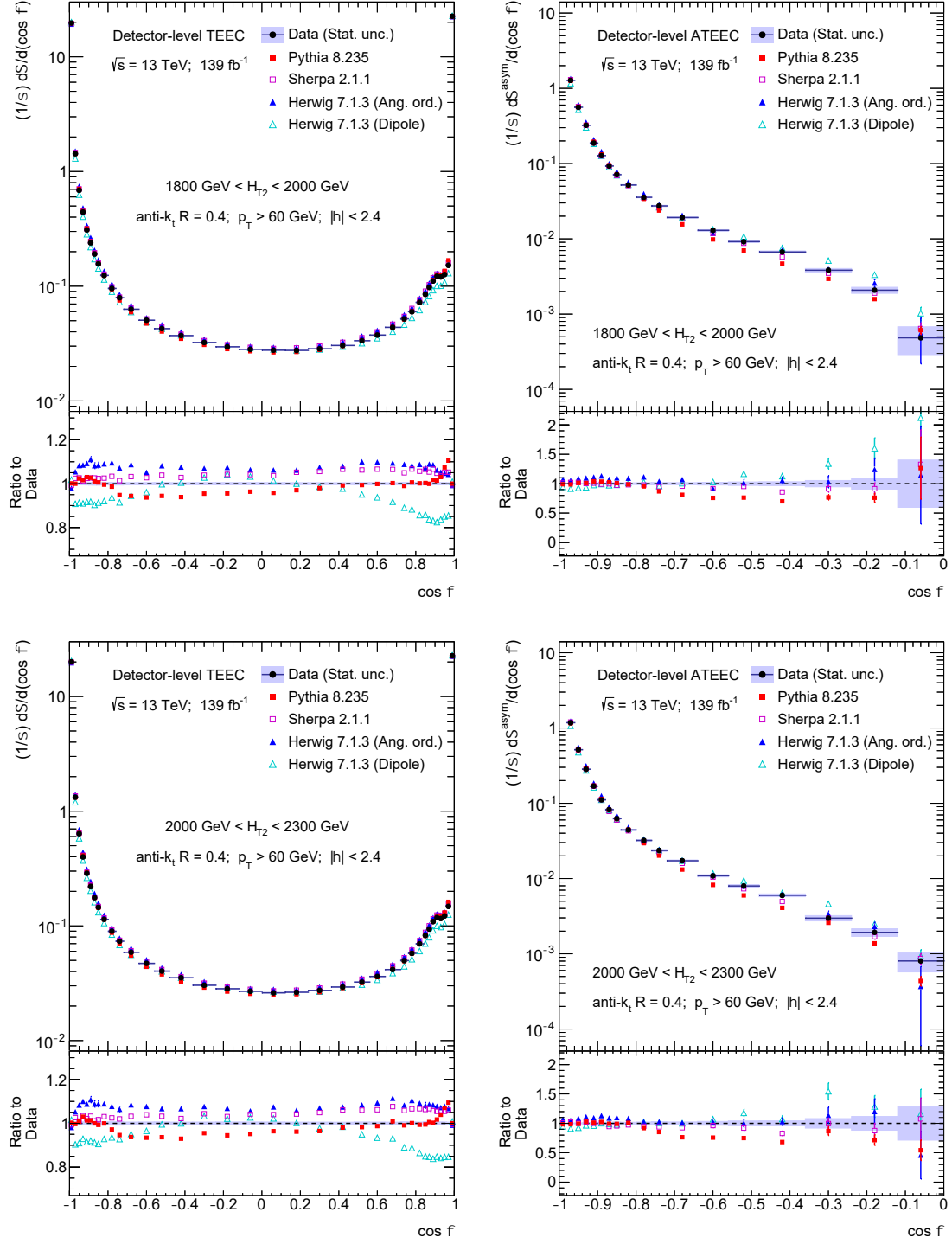


Figure 6.8: Detector-level TEEC (left) and ATEEC (right) distributions in two exclusive H_{T2} bins with the statistical uncertainty (shaded area), along with detector-level MC predictions. The ratio pad below compares the measured data and the MC predictions.

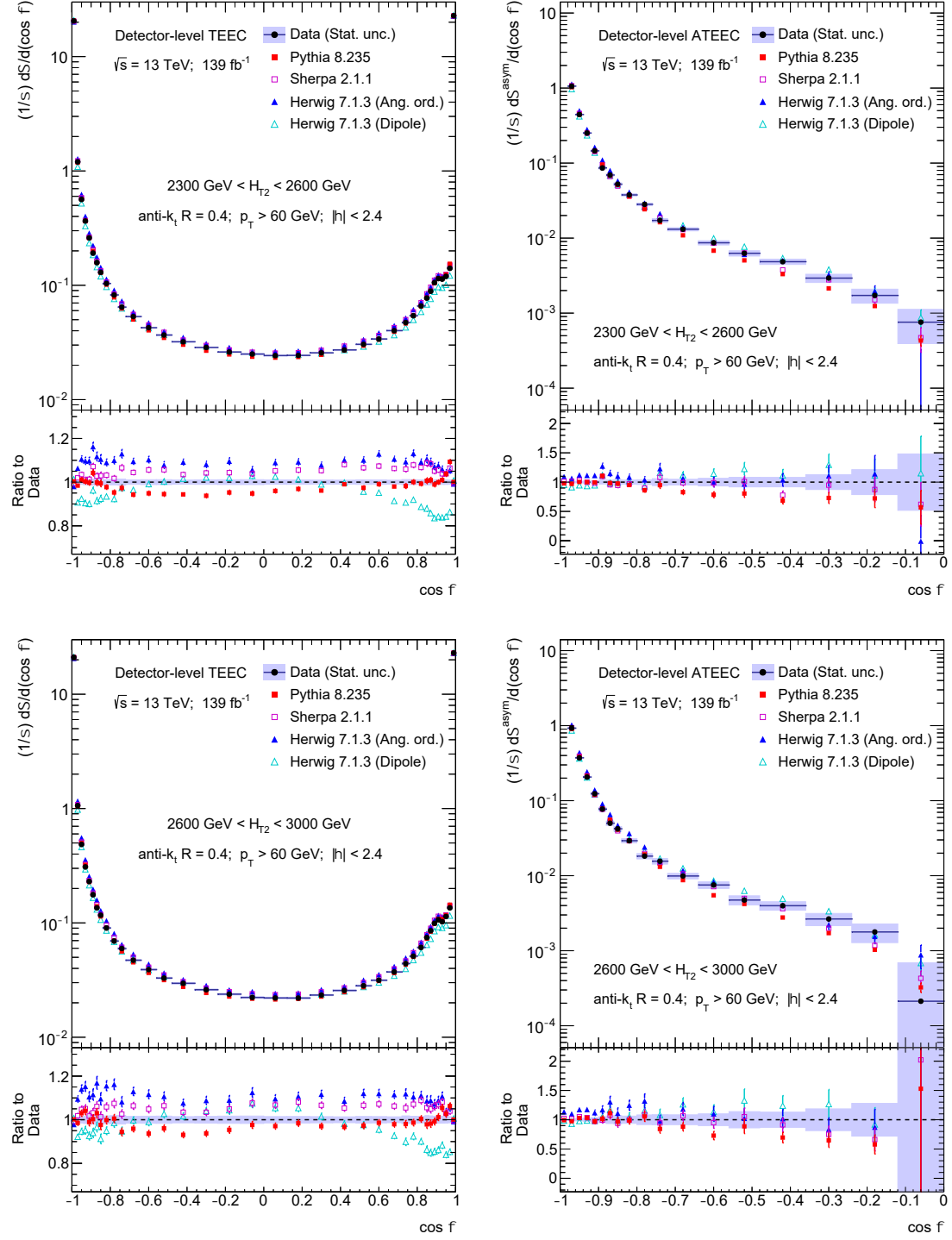


Figure 6.9: Detector-level TEEC (left) and ATEEC (right) distributions in two exclusive H_{T2} bins with the statistical uncertainty (shaded area), along with detector-level MC predictions. The ratio pad below compares the measured data and the MC predictions.

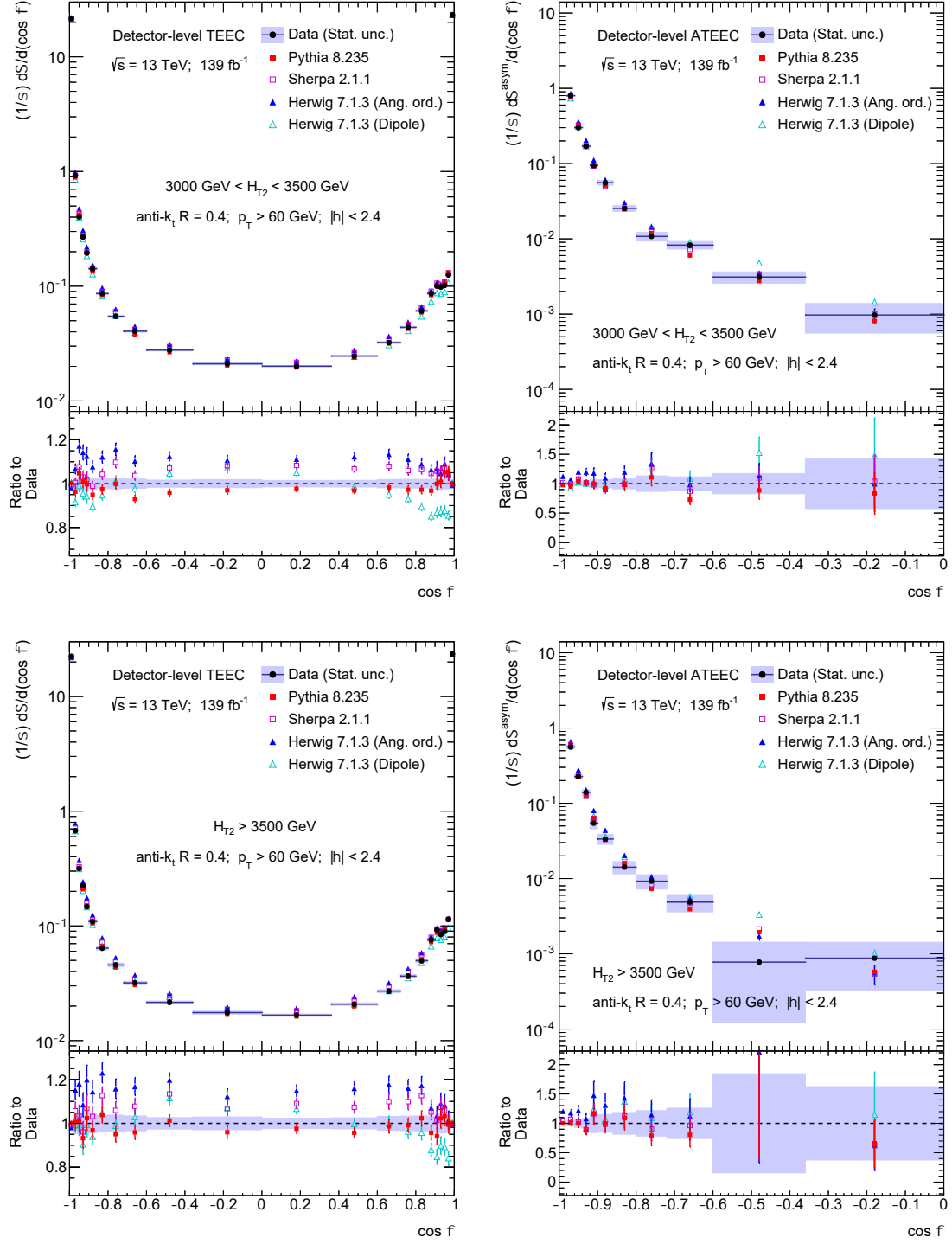


Figure 6.10: Detector-level TEEC (left) and ATEEC (right) distributions in two exclusive H_{T2} bins with the statistical uncertainty (shaded area), along with detector-level MC predictions. The ratio pad below compares the measured data and the MC predictions.

6.3 Iterative Bayesian unfolding

The measured histograms differ from their true quantities due to the fact that the detectors are not perfect. Thus, and in order to allow comparisons with theoretical predictions, the TEEC and ATEEC distributions shown in Section 6.2 need to be corrected for detector effects. An Iterative Bayesian (IB) unfolding procedure [133], as implemented in ROOUNFOLD [134], is used to correct for these distortions so as to extract the true distributions.

This technique uses Monte Carlo simulations to determine the detector response. The IB unfolding algorithm takes as input the transfer matrix M_{ij} parametrizing the bin-by-bin migrations in $\cos\phi$ due to the finite resolution of the detector response. The transfer matrix encodes the probability of reconstructing a value of $\cos\phi$ in bin i when the generated one is in bin j , which is called response matrix $P(\text{reco}_i|\text{gen}_j)$. The matrix projection can thus be written as

$$\mathcal{P}_i R_i = \sum_j M_{ij} = \sum_j \mathcal{E}_j T_j P(\text{reco}_i|\text{gen}_j) \quad \text{with} \quad \sum_i P(\text{reco}_i|\text{gen}_j) = 1.$$

The quantities R_i and T_j are the reconstructed or measured content in bin i (detector level) and the true generated quantity at bin j (particle level), respectively, whereas the factors \mathcal{E}_j and \mathcal{P}_i are the efficiency and the purity corrections due to the matching inefficiency involved in the transfer matrix. For instance, it can be reconstructed in bin i an entry that was not generated in any j bin and vice versa. Therefore, the value M_{ij} is the number of entries selected at detector level and measured in bin i matched to entries selected at particle level and generated in bin j .

At this point, the probability of generating a vale of $\cos\phi$ in bin j when the reconstructed one is in bin i is obviously unknown. Fortunately, probabilities are though related in the Bayes formula as

$$P(\text{gen}_j|\text{reco}_i) = \frac{\mathcal{E}_j T_j P(\text{reco}_i|\text{gen}_j)}{\sum_k \mathcal{E}_k T_k P(\text{reco}_i|\text{gen}_k)}.$$

The IB unfolding method calculates the “inverse” of the response matrix using an iterative algorithm that converges after five iterations. The aim is to get the true distributions which are not affected by detector effects anymore:

$$\text{unf}_j(R) = T_j = \frac{1}{\mathcal{E}_j} \sum_i \mathcal{P}_i R_i P(\text{gen}_j|\text{reco}_i).$$

This procedure is implemented for the baseline MC predictions generated with PYTHIA 8.235, and thereafter, a closure test is performed to validate it. Then, it can be applied to data so that their true quantities are extracted from the measured ones.

In Monte Carlo predictions, jets are reconstructed using the anti- k_t algorithm with radius $R = 0.4$ and applied to final-state particles with average lifetime $\tau > 10^{-11}$ s.

The selection criteria for jets and events at particle level are the same as for those at detector level. Afterwards, the transfer matrices are obtained by matching detector and particle-level jets by requiring them to be within $\Delta R = 0.3$ in the $\eta\phi$ plane. This procedure ensures that every detector-level jet entering the matrix has always a particle-level counterpart and therefore, a detector-level jet pair enters the transfer matrix if both jets in the pair are matched to the corresponding particle-level jets. Each jet pair enters in the matrix with the generated weight, i.e. the one at particle-level, as by definition the matrix parameterizes the probability of a jet pair generated in one bin to be reconstructed in another one. Figures 6.11 and 6.12 show the transfer matrices, normalizing each row. The excellent azimuthal resolution of the ATLAS detector, together with the reduction of the energy scale and resolution effects by the weighting involved in the definition of the TEEC function, are reflected in the fact that the transfer matrices have very small off-diagonal terms leading to very small migrations between $\cos\phi$ bins.

However, the matching procedure used for the calculation of the transfer matrices has an inherent inefficiency, mainly, due to the arbitrariness of the ΔR cut. Thus, not all jets at the detector level have a counterpart at the particle level and vice versa. Pairs of jets not entering the transfer matrices are accounted for using inefficiency correction factors. These factors are defined as the ratio between the TEEC distribution obtained using only the detector-level jets matched to a particle-level jet, i.e. the x -projection of the transfer matrix normalized to area unity, and the TEEC distribution obtained using all detector-level jets, regardless of whether they are matched or not to a particle-level jet. The detector-level data distribution is then multiplied by these correction factors before using it as an input to the IB unfolding algorithm. Figures 6.13 and 6.14 show the calculated inefficiency correction factors. These factors correspond with the purity correction and are above one for $\cos\phi = \pm 1$ due to the normalization of the distributions. The efficiency correction factors are also considered accordingly in the unfolding procedure.

As a cross-check of the IB procedure, a bin-by-bin correcting method based on correction factors from detector level to particle level is also tested. The differences between the two approaches are below the statistical uncertainties, pointing to a very small dependence on the unfolding procedure.

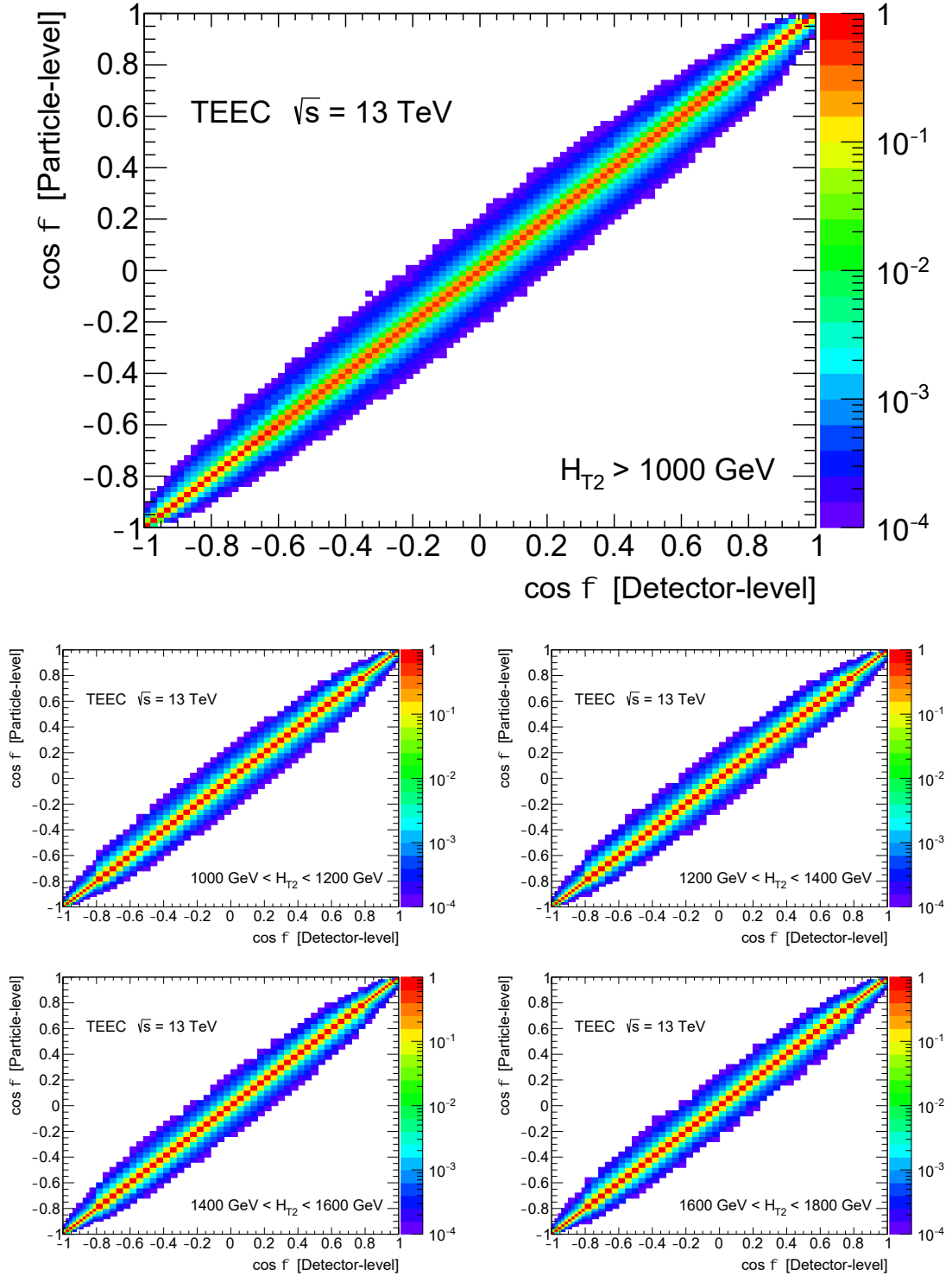


Figure 6.11: Transfer matrices normalizing each row, in inclusive (top) and exclusive (bottom) H_{T2} bins, for the TEEC function obtained from the MC simulated sample with the PYTHIA 8.235 event generator. The off-diagonal terms are negligible since the excellent azimuthal resolution of the detector leads to very small migrations between $\cos \phi$ bins.

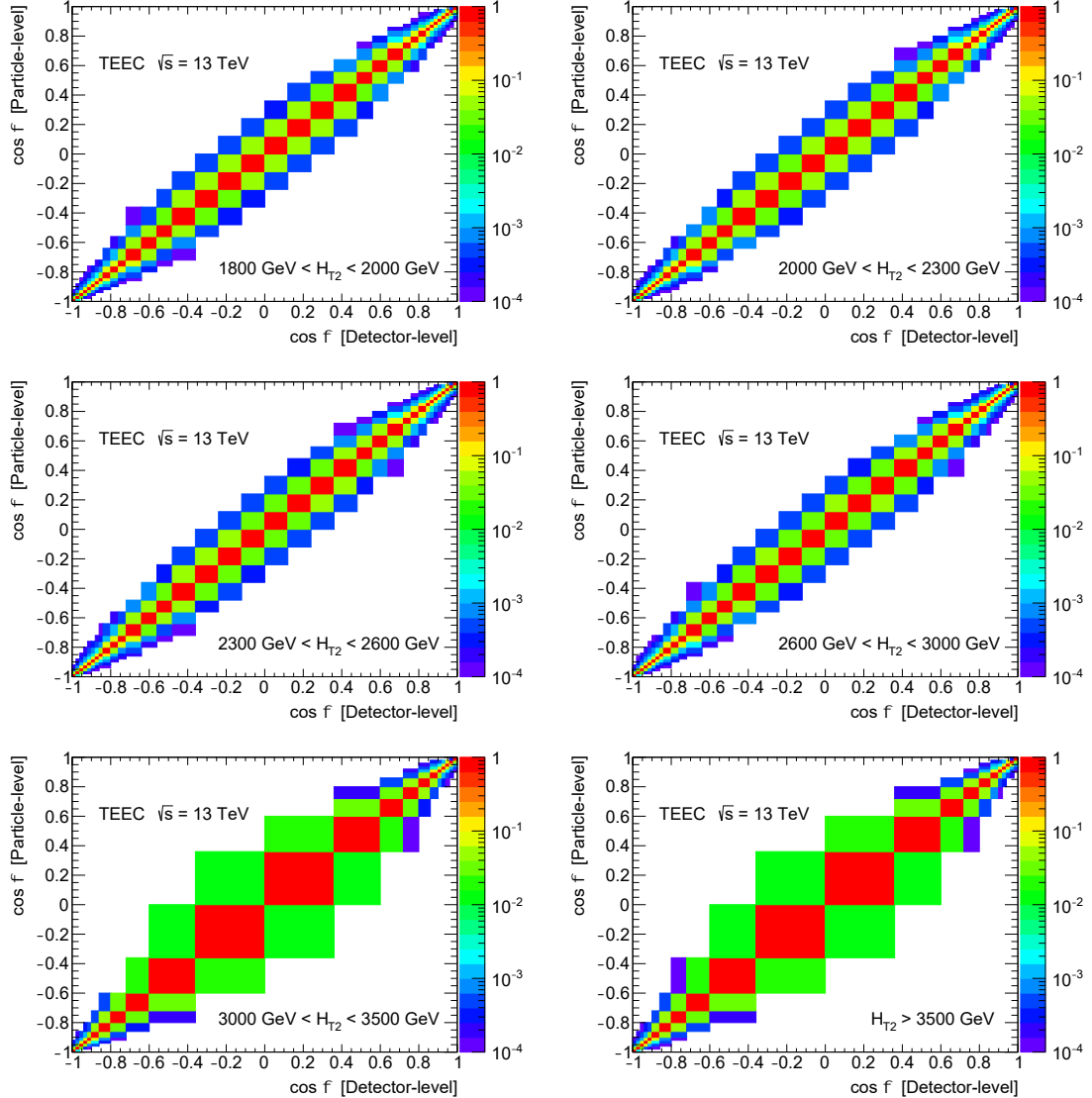


Figure 6.12: Transfer matrices normalizing each row, in exclusive H_{T2} bins, for the TEEC function obtained from the MC simulated sample with the PYTHIA 8.235 event generator. The off-diagonal terms are negligible since the excellent azimuthal resolution of the detector leads to very small migrations between $\cos \phi$ bins.

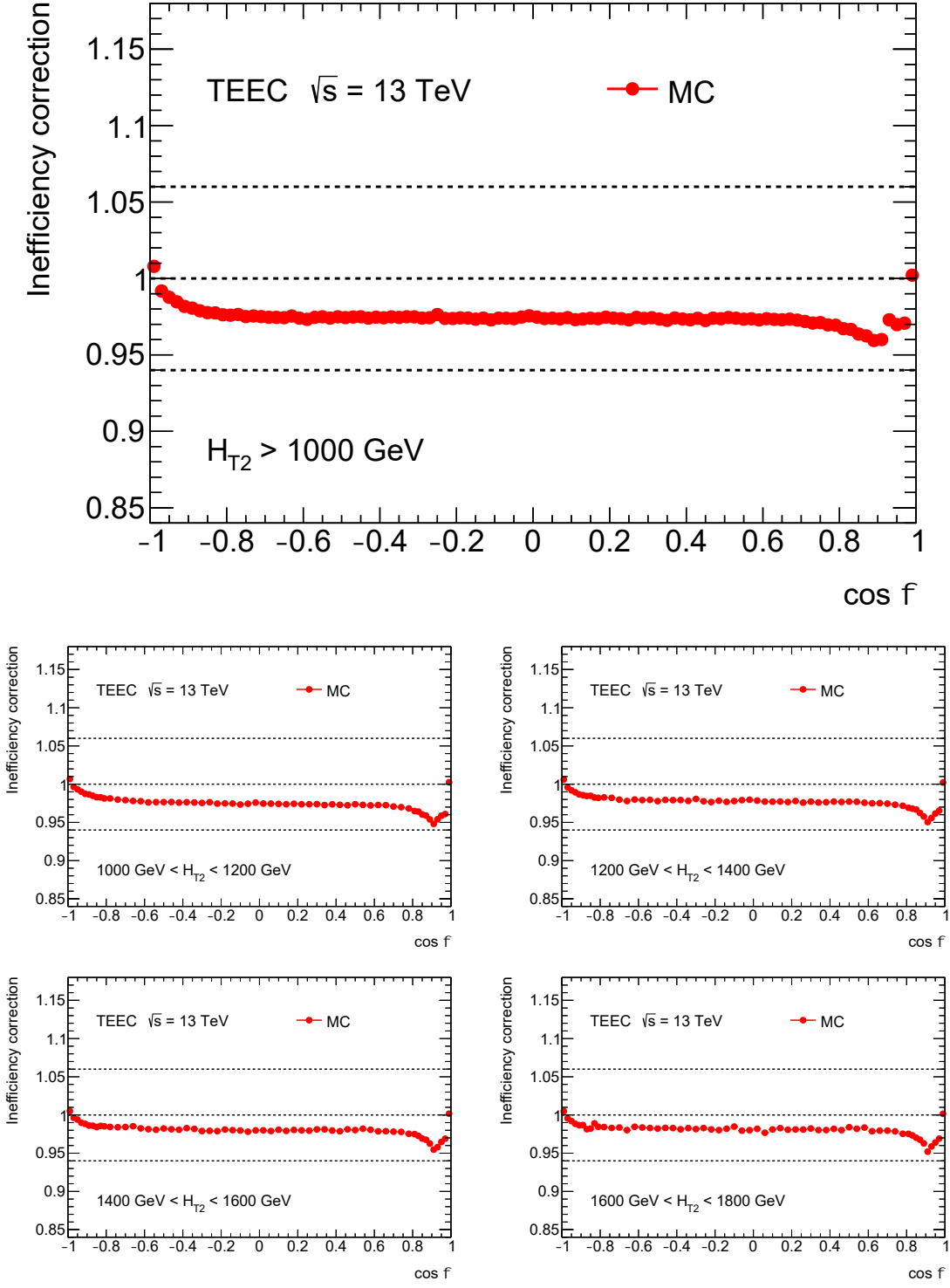


Figure 6.13: Inefficiency correction factors, in inclusive (top) and exclusive (bottom) H_{T2} bins, for the TEEC function obtained from the MC simulated sample with the PYTHIA 8.235 event generator. These factors correspond with the purity correction and are above one for $\cos \phi = \pm 1$ due to the normalization of the distributions.

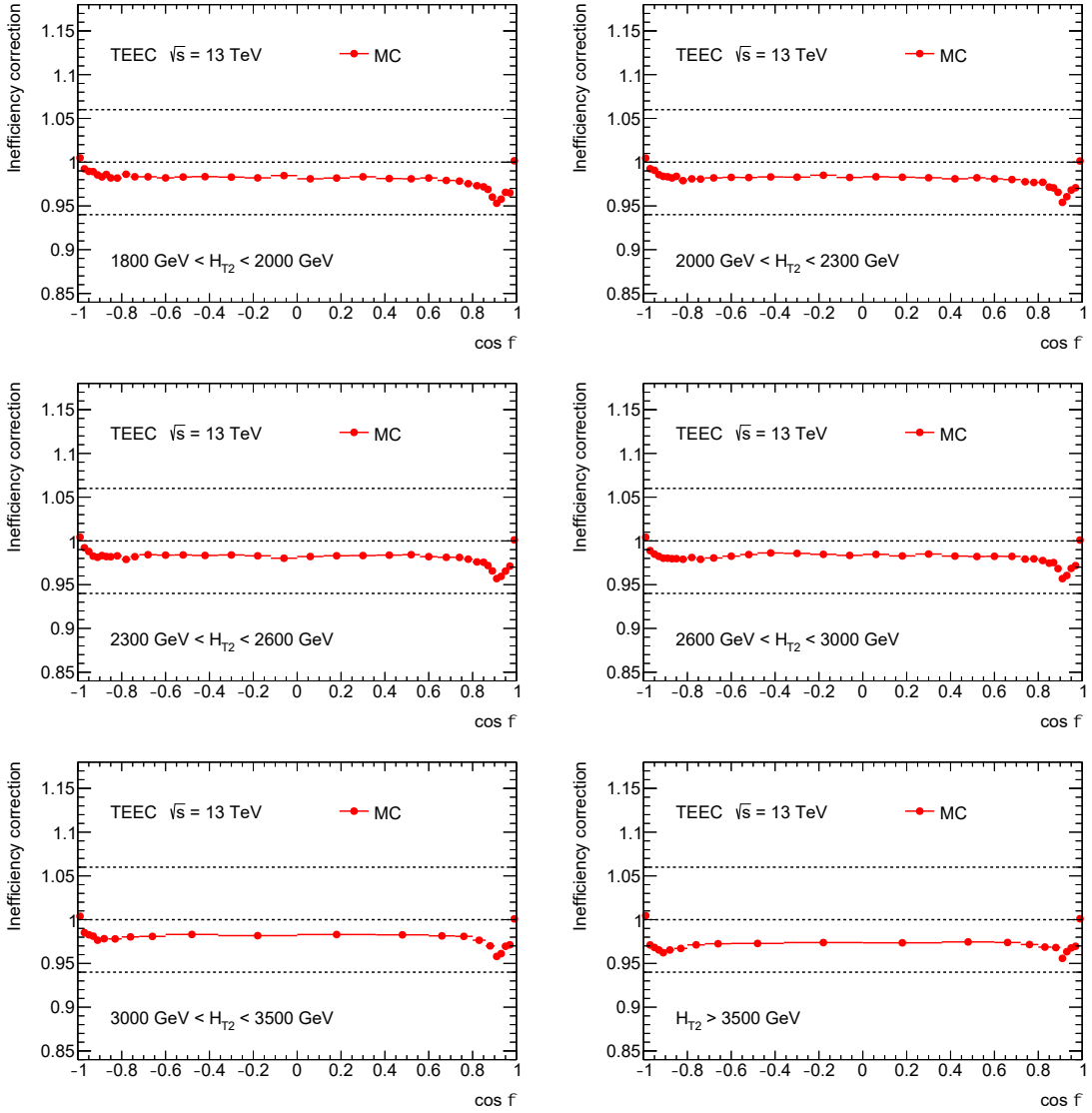


Figure 6.14: Inefficiency correction factors, in exclusive H_{T2} bins, for the TEEC function obtained from the MC simulated sample with the PYTHIA 8.235 event generator. These factors correspond with the purity correction and are above one for $\cos \phi = \pm 1$ due to the normalization of the distributions.

6.4 Statistical uncertainty

In collider experiments, there is a large number of hadrons involved in each bunch crossing but the probability to have inelastic scattering between them is low. Therefore, events follow a Poisson discrete probability distribution:

$$f(k; \lambda) = \frac{\lambda^k e^{-\lambda}}{k!}$$

where k is the number of times an event occurs and the parameter the λ is both the mean and the variance. Hence, a bin that has been filled with N_{ev} events would have a relative statistical uncertainty that goes like $1/\sqrt{N_{\text{ev}}}$. As expected, more precise results are obtained as the number of events filling the bin increases.

For observables like the TEEC function, the same event enters weighted in different bins of the histogram at the same time. Moreover, correlations between histograms are presented when deriving new ones. In order to take into account correlations and to improve accuracy of statistical uncertainties, the bootstrapping technique, as implemented in `BOOTSTRAPGENERATOR`, is widely used. This method generates a large number of replicas, 10^3 , whilst filling the histogram, by weighting each event with Poisson-distributed weights with $\lambda = 1$. For the resulting histogram, the value and statistical uncertainty on each bin are defined as the mean and the standard deviation, respectively, of all the bootstrap generated replicas.

The statistical uncertainty in the unfolded distributions is also calculated with the bootstrapping technique, after performing the IB unfolding method for each replica, thus taking into account the correlations between the particle and detector-level distributions. This statistical uncertainty is therefore determined by those in the detector-level data distribution and in the MC sample which are required as inputs in the unfolding method.

Figures 6.15 to 6.18 show the relative difference of each bootstrap replica with respect to the nominal distribution, i.e. the one which has not been weighted using the Poisson-distributed weights described above, for the TEEC and ATEEC distributions. The resulting statistical uncertainty is also shown as a red line.

Furthermore, the bin-by-bin correlations in $\cos \phi$ of the TEEC and ATEEC distributions are studied. Figures 6.19 to 6.22 show the correlation coefficient for each $\cos \phi$ bin pair, by considering the differences between the bootstrap replicas with respect to the nominal distribution. The correlations for $\cos \phi$ bin pairs is found to be negligible, with the exception of the correlation between the bins $\cos \phi = +1$ and $\cos \phi = -1$ due to the normalization of the TEEC distributions.

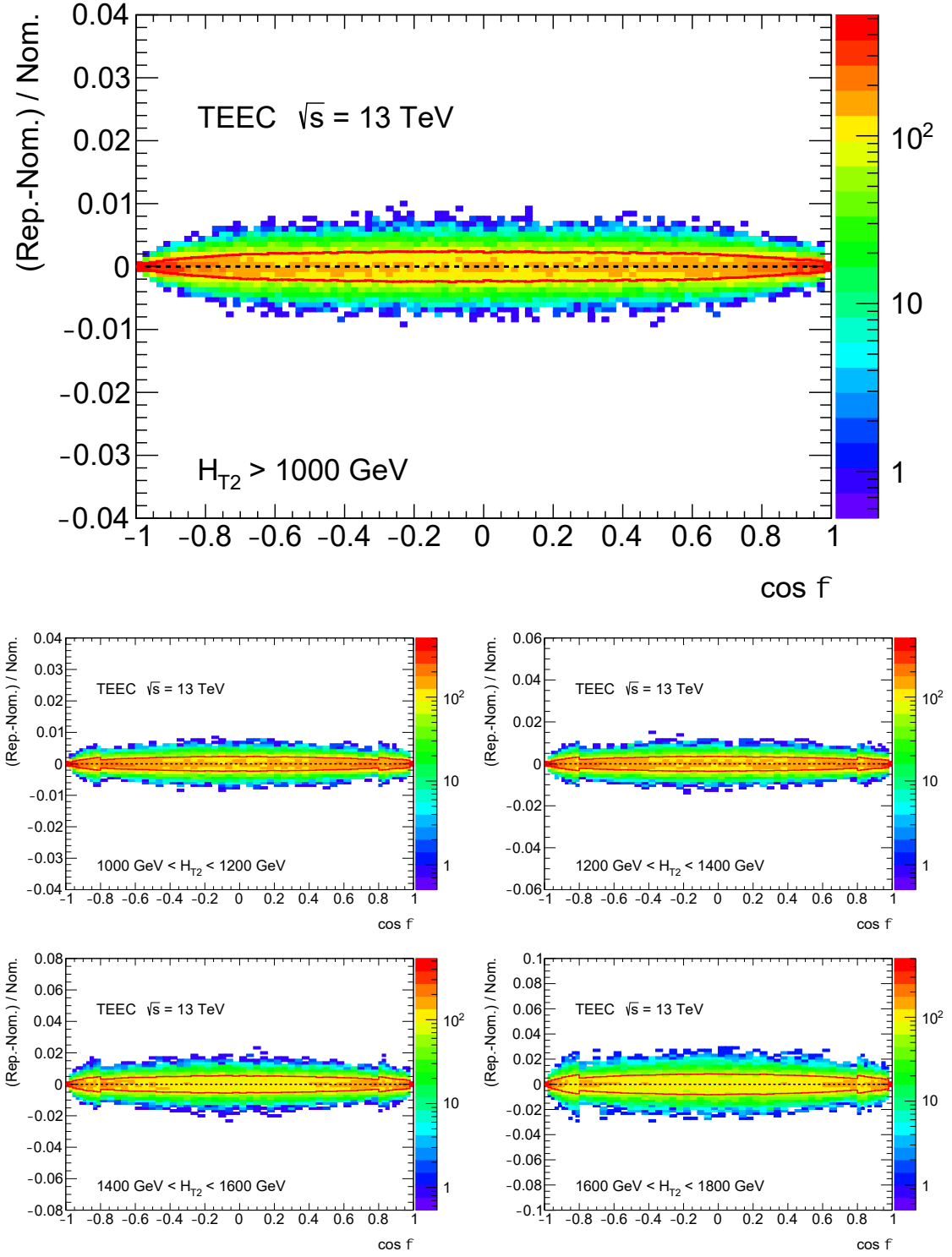


Figure 6.15: Relative difference of the bootstrap replicas with respect to the nominal distribution, in inclusive (top) and exclusive (bottom) H_{T2} bins, for the TEEC function obtained from the MC simulated sample with the PYTHIA 8.235 event generator. The resulting statistical uncertainty, derived as the RMS of these differences, is shown with a red line.

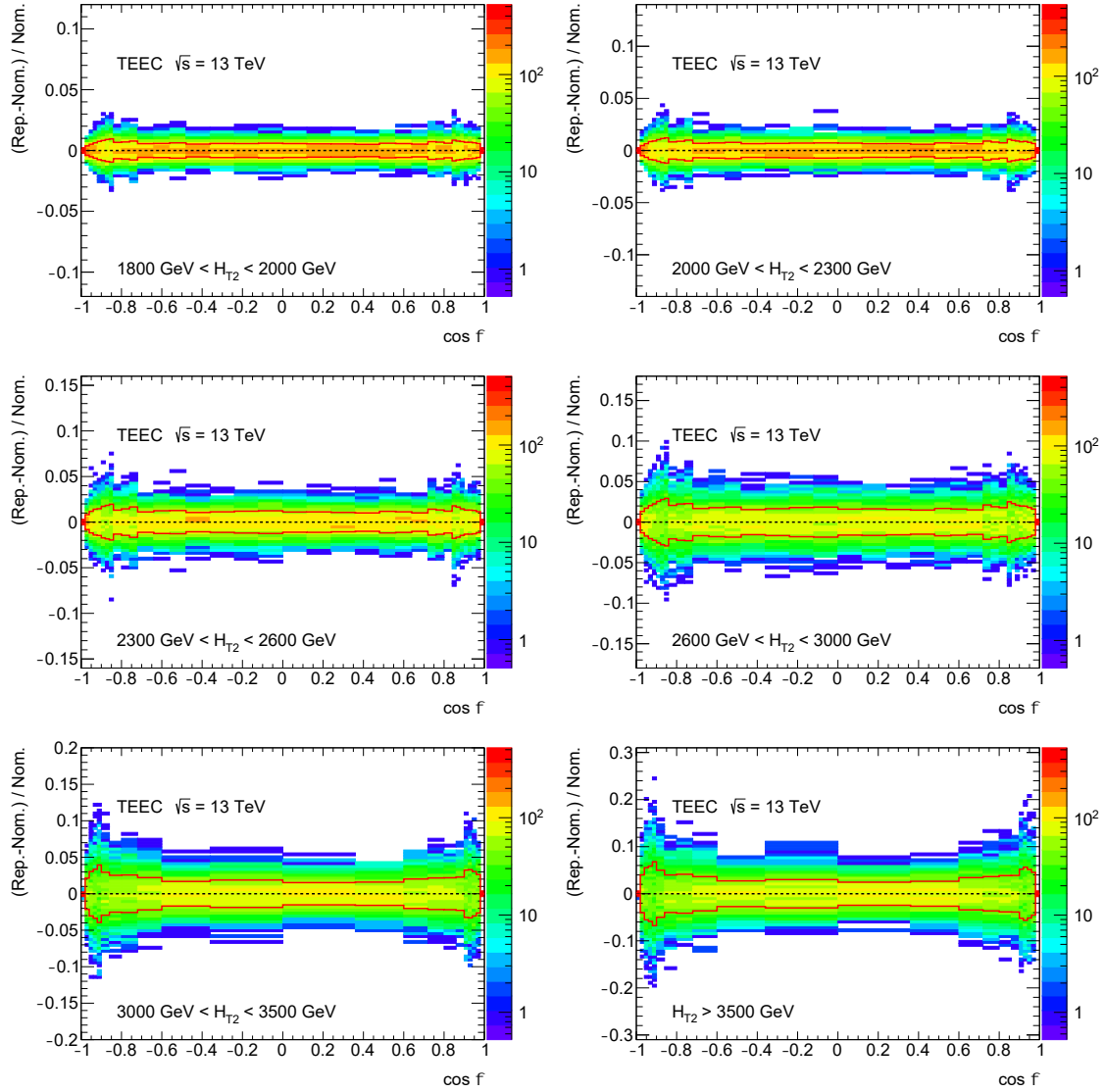


Figure 6.16: Relative difference of the bootstrap replicas with respect to the nominal distribution, in exclusive H_{T2} bins, for the TEEC function obtained from the MC simulated sample with the PYTHIA 8.235 event generator. The resulting statistical uncertainty, derived as the RMS of these differences, is shown with a red line.

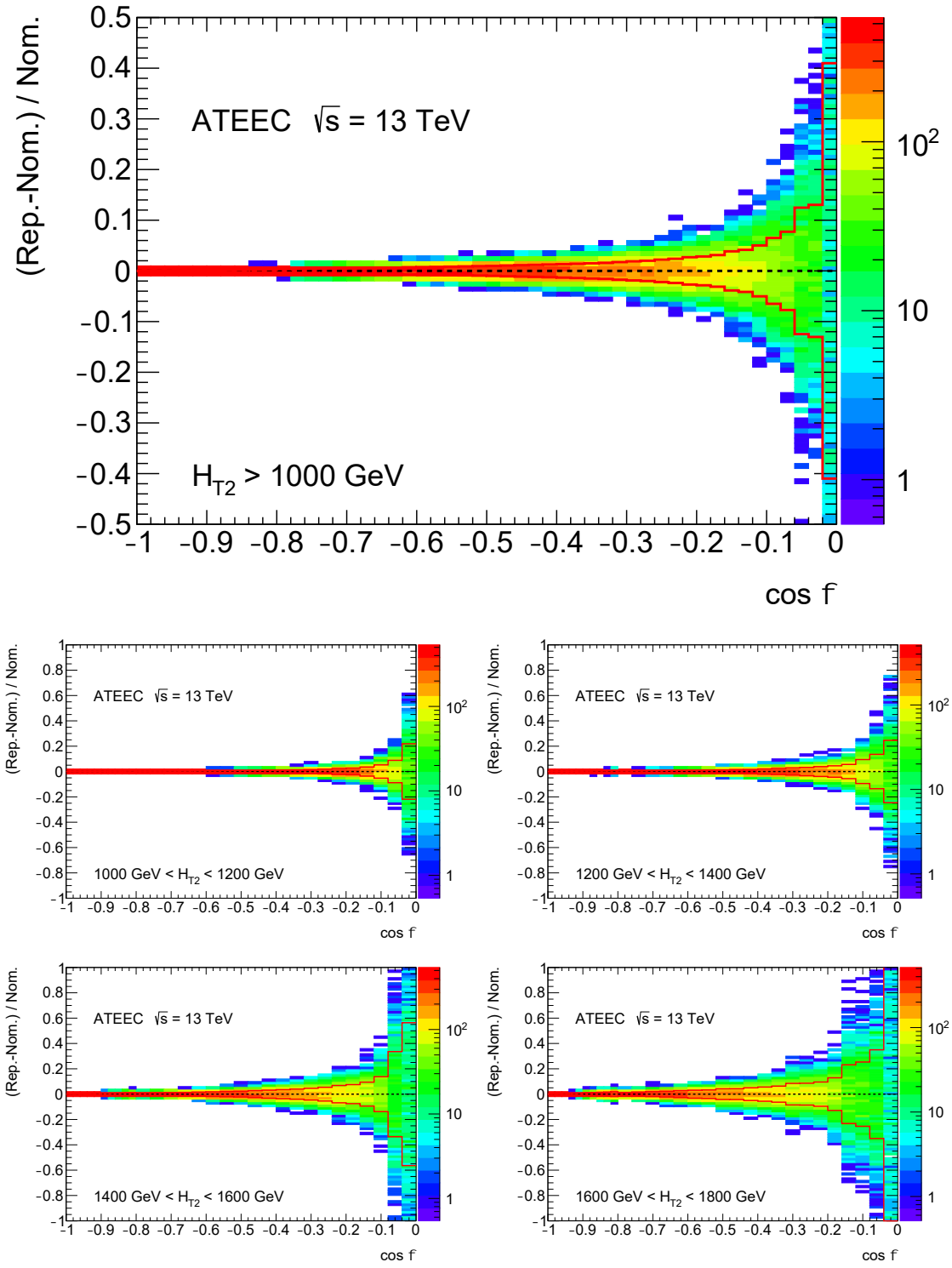


Figure 6.17: Relative difference of the bootstrap replicas with respect to the nominal distribution, in inclusive (top) and exclusive (bottom) H_{T2} bins, for the ATEEC function obtained from the MC simulated sample with the PYTHIA 8.235 event generator. The resulting statistical uncertainty, derived as the RMS of these differences, is shown with a red line.

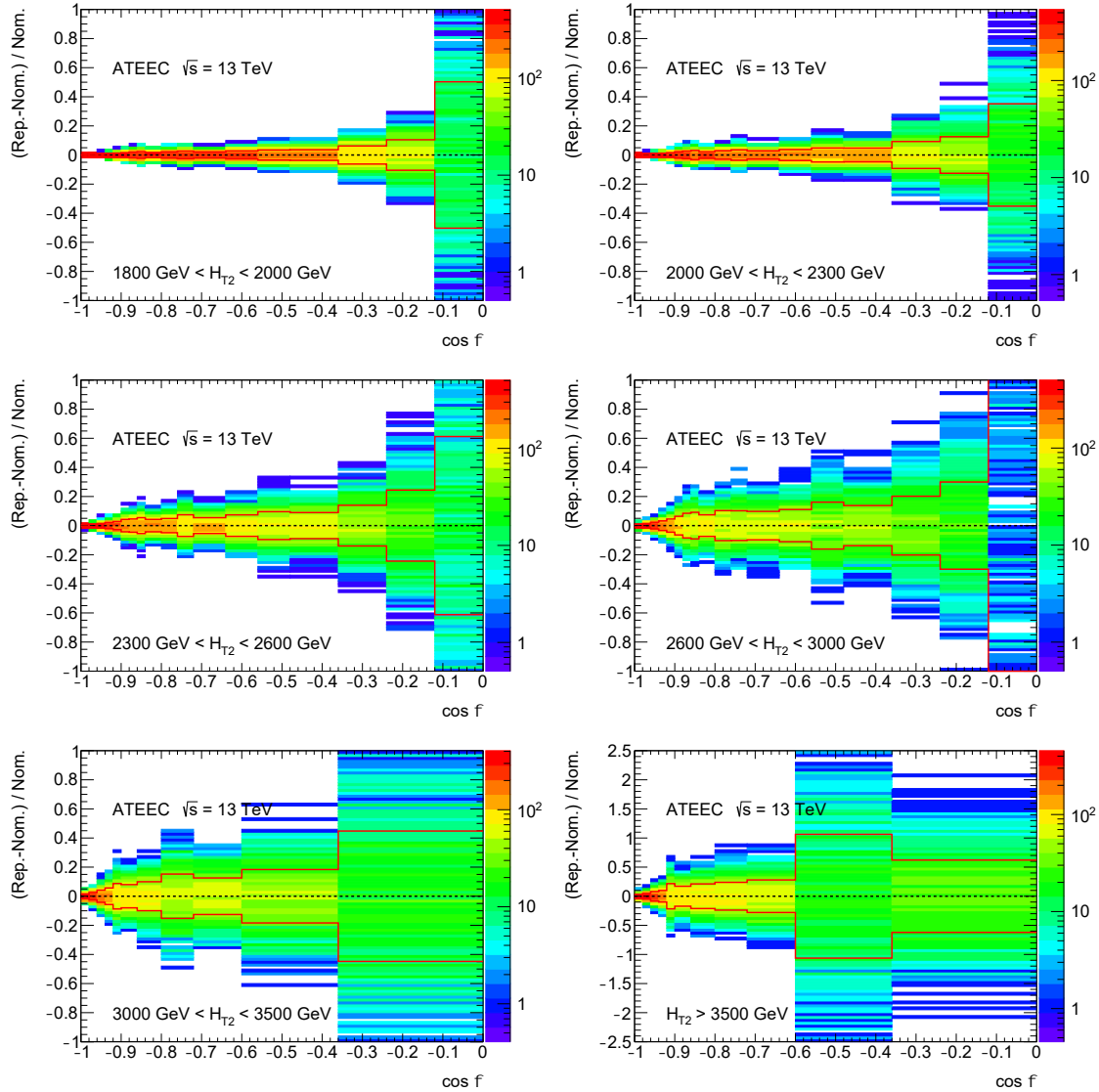


Figure 6.18: Relative difference of the bootstrap replicas with respect to the nominal distribution, in exclusive H_{T2} bins, for the ATEEC function obtained from the MC simulated sample with the PYTHIA 8.235 event generator. The resulting statistical uncertainty, derived as the RMS of these differences, is shown with a red line.

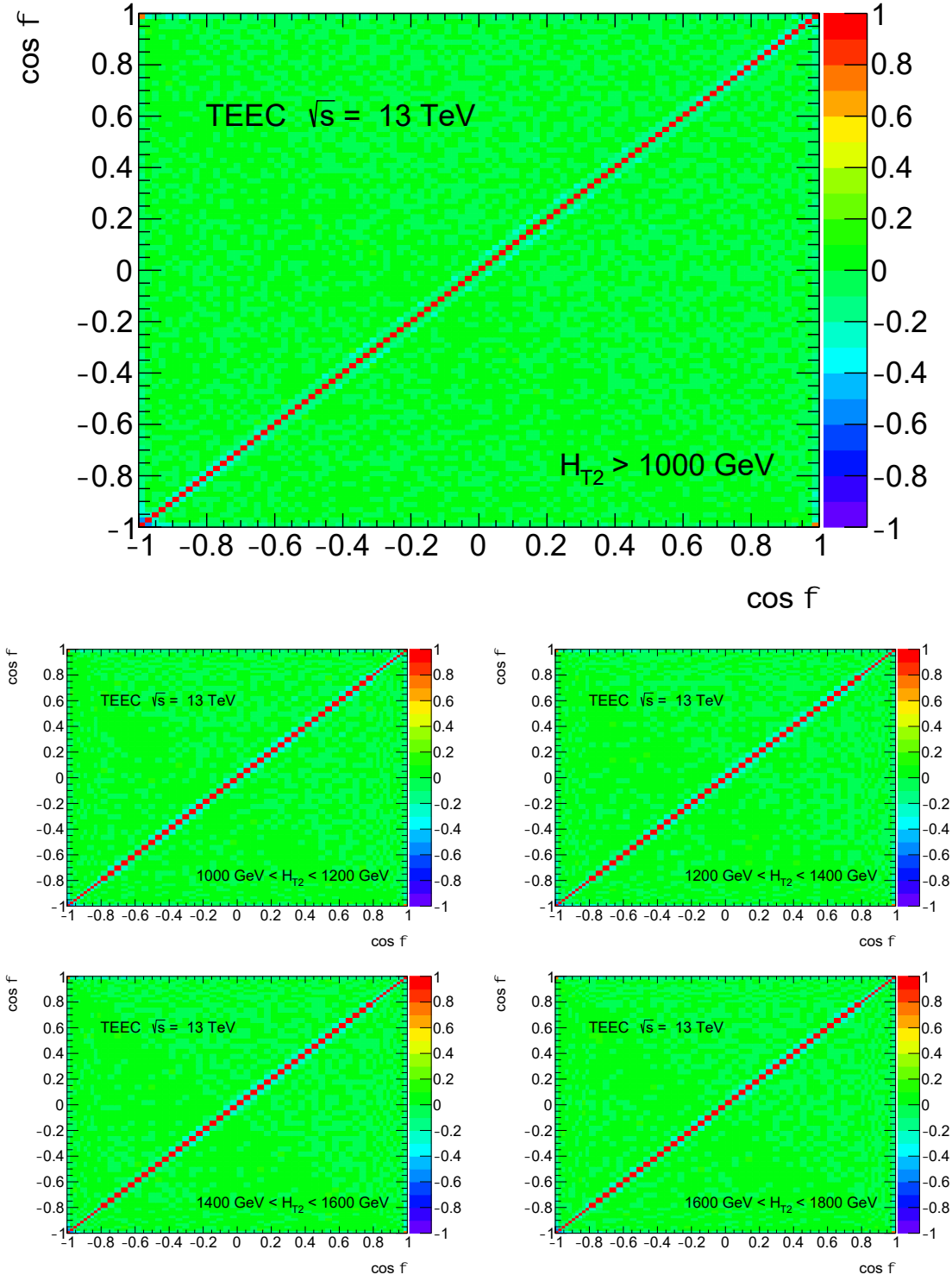


Figure 6.19: Bin-by-bin $\cos \phi$ correlation matrices, in inclusive (top) and exclusive (bottom) H_{T2} bins, for the TEEC function obtained from the MC simulated sample with the PYTHIA 8.235 event generator. The correlations for bin pairs is negligible, with the exception of the correlation between the bins $\cos \phi \pm 1$ due to the normalization of the distributions. The first two bins are also found to be anti-correlated.

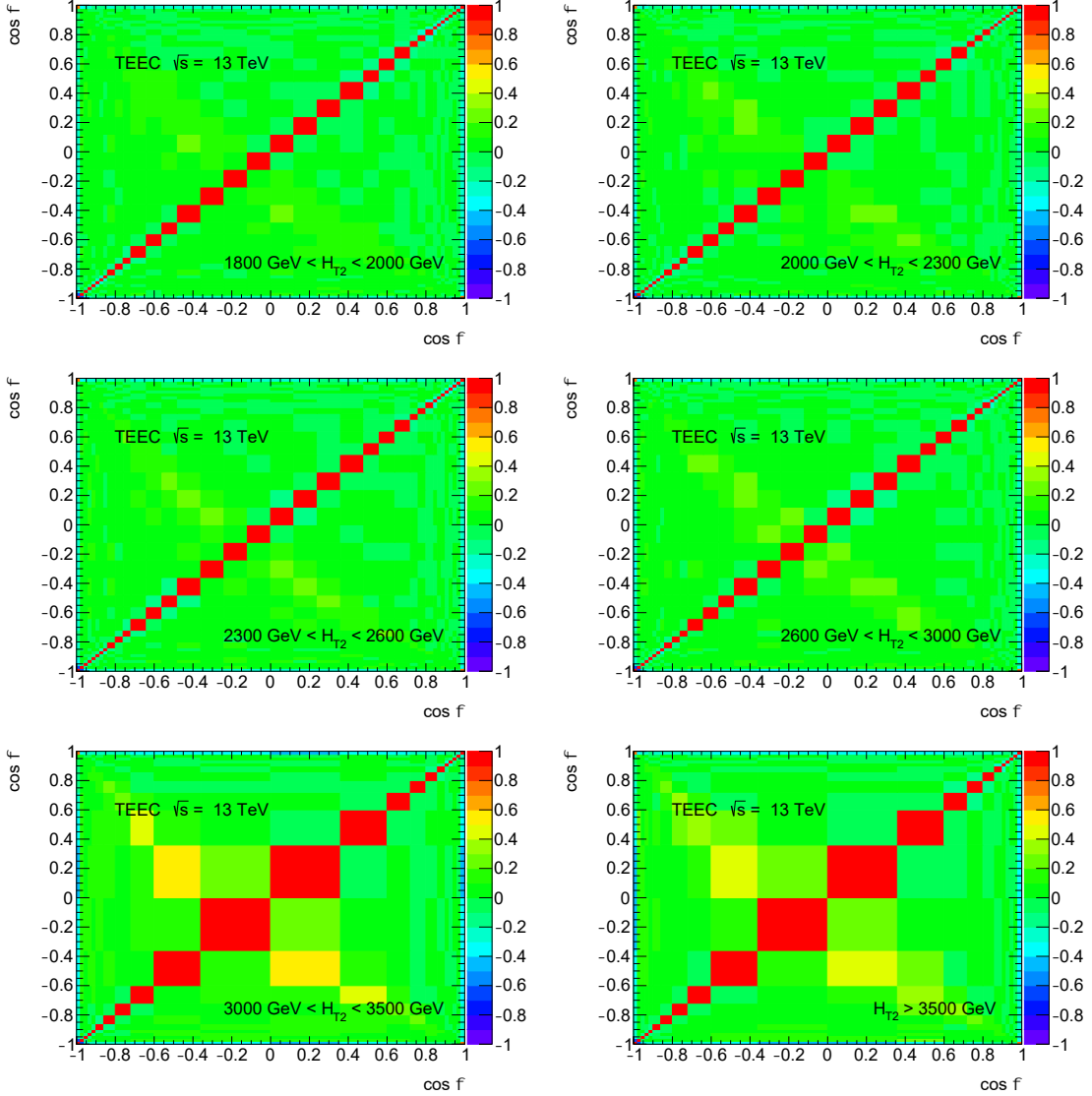


Figure 6.20: Bin-by-bin $\cos \phi$ correlation matrices, in exclusive H_{T2} bins, for the TEEC function obtained from the MC simulated sample with the PYTHIA 8.235 event generator. The correlations for bin pairs is negligible, with the exception of the correlation between the bins $\cos \phi \pm 1$ due to the normalization of the distributions. The first two bins are also found to be anti-correlated.

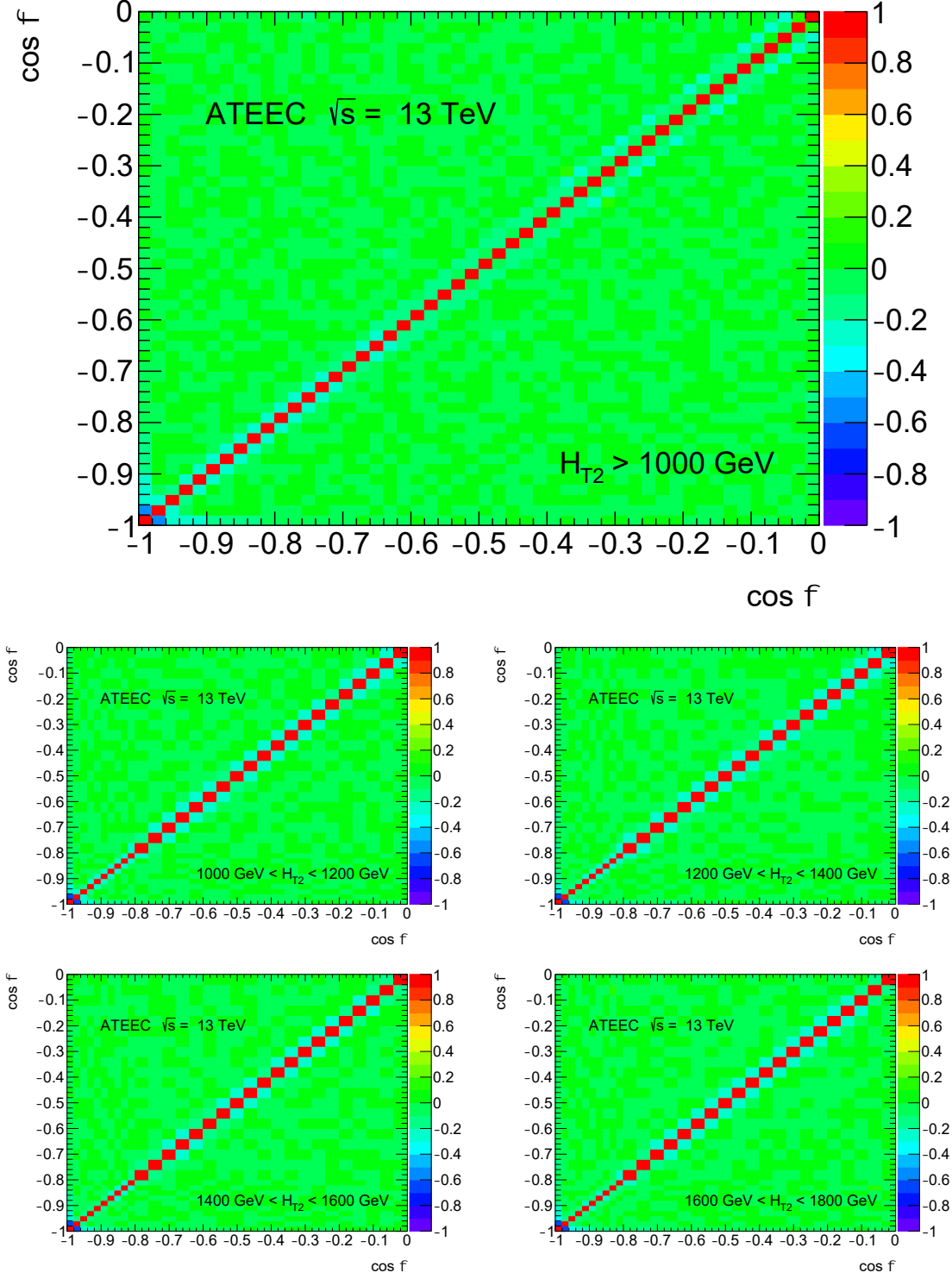


Figure 6.21: Bin-by-bin $\cos\phi$ correlation matrices, in inclusive (top) and exclusive (bottom) H_{T2} bins, for the ATEEC function obtained from the MC simulated sample with the PYTHIA 8.235 event generator. The correlations for bin pairs is negligible, with the exception of the correlation between the first two bins in $\cos\phi$ which are found to be anti-correlated.

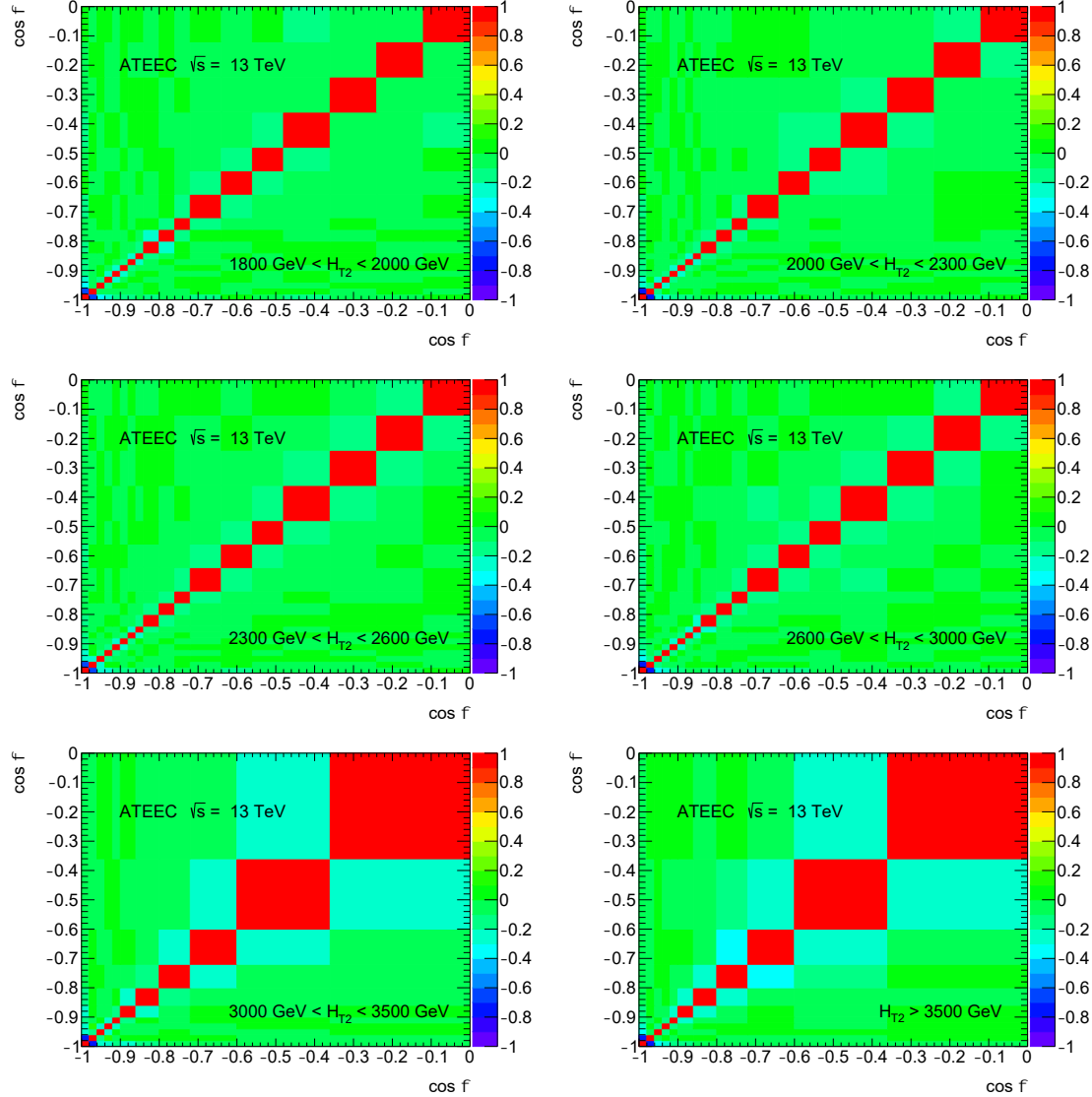


Figure 6.22: Bin-by-bin $\cos \phi$ correlation matrices, in exclusive H_{T2} bins, for the ATTEC function obtained from the MC simulated sample with the PYTHIA 8.235 event generator. The correlations for bin pairs is negligible, with the exception of the correlation between the first two bins in $\cos \phi$ which are found to be anti-correlated.

6.5 Systematic uncertainties

The main sources of systematic uncertainty for the measurements include the jet energy scale, the jet energy resolution, the jet angular resolution, the mismodelling of the data by the MC in the unfolding (non-closure), and an additional uncertainty due to the choice of the MC model used for the unfolding. All systematics uncertainties are estimated together with their statistical uncertainties using the bootstrap technique and added together in quadrature.

In order to mitigate statistical fluctuations in a set of bins that follow a curve, a smoothing technique is applied to the resulting systematic uncertainties combining adjacent bins until they have statistical significance over 2σ . Adjacent bins are then combined starting from left to right and from right to left, selecting the combination with a higher number of bins.

This smoothing technique is called Gaussian kernel smoothing and it calculates each bin content as a weighted average of the contents in all bins in the distribution. Eq. (6.2) defines the estimated content \hat{H} for a value $\cos \phi$ in a given bin.

$$\hat{H}_i = \hat{H}(\cos \phi_i) = \frac{\sum_j K_{ij} H_j}{\sum_j K_{ij}}; \quad K_{ij} = \exp \left[-\frac{(\cos \phi_i - \cos \phi_j)^2}{2b_i^2} \right] \quad (6.2)$$

The quantity H_j is the original content in bin j and K_{ij} are the Gaussian kernels. They take into account the distance between each pair of bins to weight their contribution accordingly. The free parameter b is the length scale controlling the smoothness of the distribution, larger values imply smoother averaged distributions. In this case, it is parametrized for each bin as $b_i = \mathcal{A}[1 - (\cos \phi_i)^2]$. The value of \mathcal{A} is adequately set for each source of uncertainty.

The total relative systematic uncertainty for the TEEC and ATEEC distributions is shown in Figures 6.23 to 6.26, together with a breakdown of the general source uncertainties: JES, JER, JAR, MC modelling and unfolding closure. The dominant systematic sources for the TEEC distributions are due to the JES and the choice of the MC model used in the IB unfolding. The former is dominated by the Flavour Response nuisance parameters from the JES; the latter is computed as the symmetric envelope of the differences between the distributions unfolded with SHERPA 2.1.1 and HERWIG 7.1.3, with respect to those unfolded with PYTHIA 8.235. They are found to be around 2% in the central plateau. This deviation arises from the two hadronization schemes considered, namely, cluster hadronization and Lund string fragmentation. Figures 6.27 to 6.30 show the relative systematic uncertainty of the TEEC and ATEEC distributions associated to the MC model.

The jet systematic uncertainties are introduced in Sections 5.3 and 5.4. The JES, JER and JAR sources are considered propagating the uncertainty to the TEEC and ATEEC distributions by varying certain jet variables by their uncertainties in the MC simulated sample obtained with the PYTHIA 8.235 event generator. The varied distributions associated to each source are computed at detector level, unfolded to the particle level with the nominal PYTHIA 8.235 and compared with the associated

unfolded nominal PYTHIA 8.235 distribution at particle level. In the case of the JER sources, the unfolded varied distributions are compared with the associated unfolded varied distribution generated as data. In the case of the Flavour Composition and Flavour Response sources, the varied distributions consider the gluon fraction of the jet as the one obtained from the MC simulation as a function of the p_T and the $|\eta|$ of the jet. The gluon fraction is determined using PYTHIA 8.235, while its uncertainty is defined as the difference between PYTHIA 8.235, SHERPA 2.1.1, and HERWIG 7.1.3. They are depicted in Figures 6.31 and 6.32.

For the JES and JER sources, the uncertainty in the jet calibration procedure [135] is propagated by varying up and down each jet energy and transverse momentum by one standard deviation of each of the 113 nuisance parameters of the JES uncertainty and the 34 nuisance parameters of JER uncertainty. The dominant contribution to the JES systematic uncertainty for the TEEC distributions comes from the Flavour Response nuisance parameters. Figures 6.33 to 6.36 show the relative systematic uncertainty of the TEEC and ATEEC distributions associated to the variations of the Flavour Response nuisance parameter. The dominant contribution for the ATEEC distributions comes from the Gjet GamESZee for the JES uncertainties and from the JER dijet closure for the JER uncertainties. Figures 6.37 to 6.44 show the relative systematic uncertainty of the TEEC and ATEEC distributions associated to these last two sources.

For the JAR source, the jet azimuthal coordinate is smeared by a factor defined as the azimuthal angular resolution estimated in the MC simulated sample as a function of the p_T and the $|\eta|$ of the jet. This resolution is calculated by using the same matching approach as in the calculation of the transfer matrices. A detector-level jet is matched to a particle-level jet if the latter is the closest jet to the former within $\Delta R = 0.3$. Figures 6.45 and 6.46 show the distribution of the azimuthal differences $\varphi(\text{reco}) - \varphi(\text{gen})$ along with a fit to a Gaussian distribution, that yields a standard deviation considered as the azimuthal angular resolution. The angular resolution for the inclusive sample is well below the binning used in the TEEC and ATEEC measurements which is always greater than or equal to $\Delta \cos \phi = 0.02$. Indeed, Figures 6.47 and 6.48 show the $\cos \phi$ resolution for the central plateau and a fit to a Gaussian distribution yields a standard deviation of $\sigma = 0.01$. The minimum width used in the $\cos \phi$ binning approximately corresponds to this $\pm 1\sigma$ contour. Figures 6.49 to 6.52 show the relative systematic uncertainty of the TEEC and ATEEC distributions associated to the JAR.

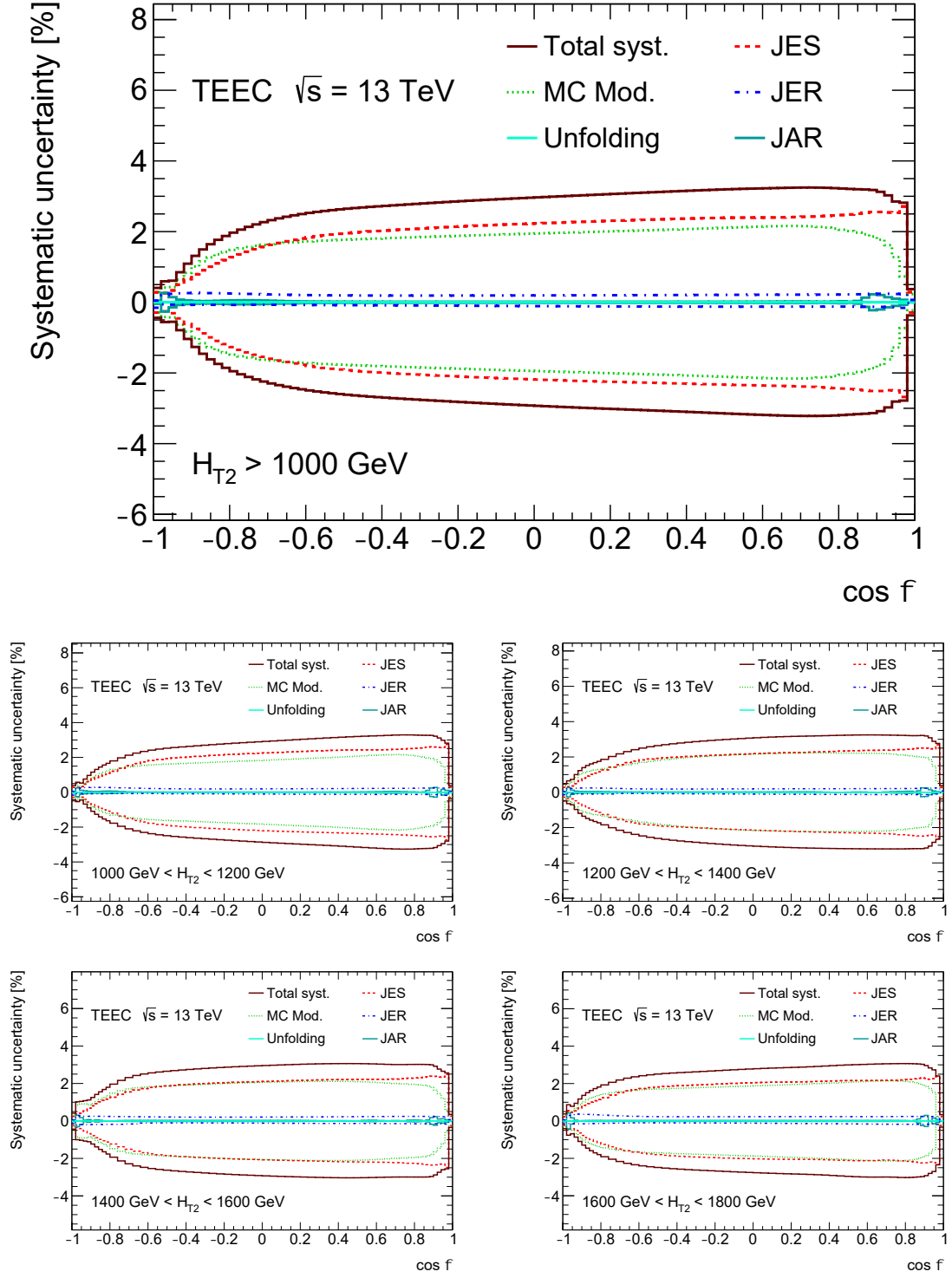


Figure 6.23: Total relative systematic uncertainty for the TEEC distribution, in inclusive (top) and exclusive (bottom) H_{T2} bins, together with a breakdown on the general source uncertainties: JES, JER, JAR, MC model and unfolding closure. These sources are added together in quadrature, with the JES and the choice of the MC model being the dominant ones.

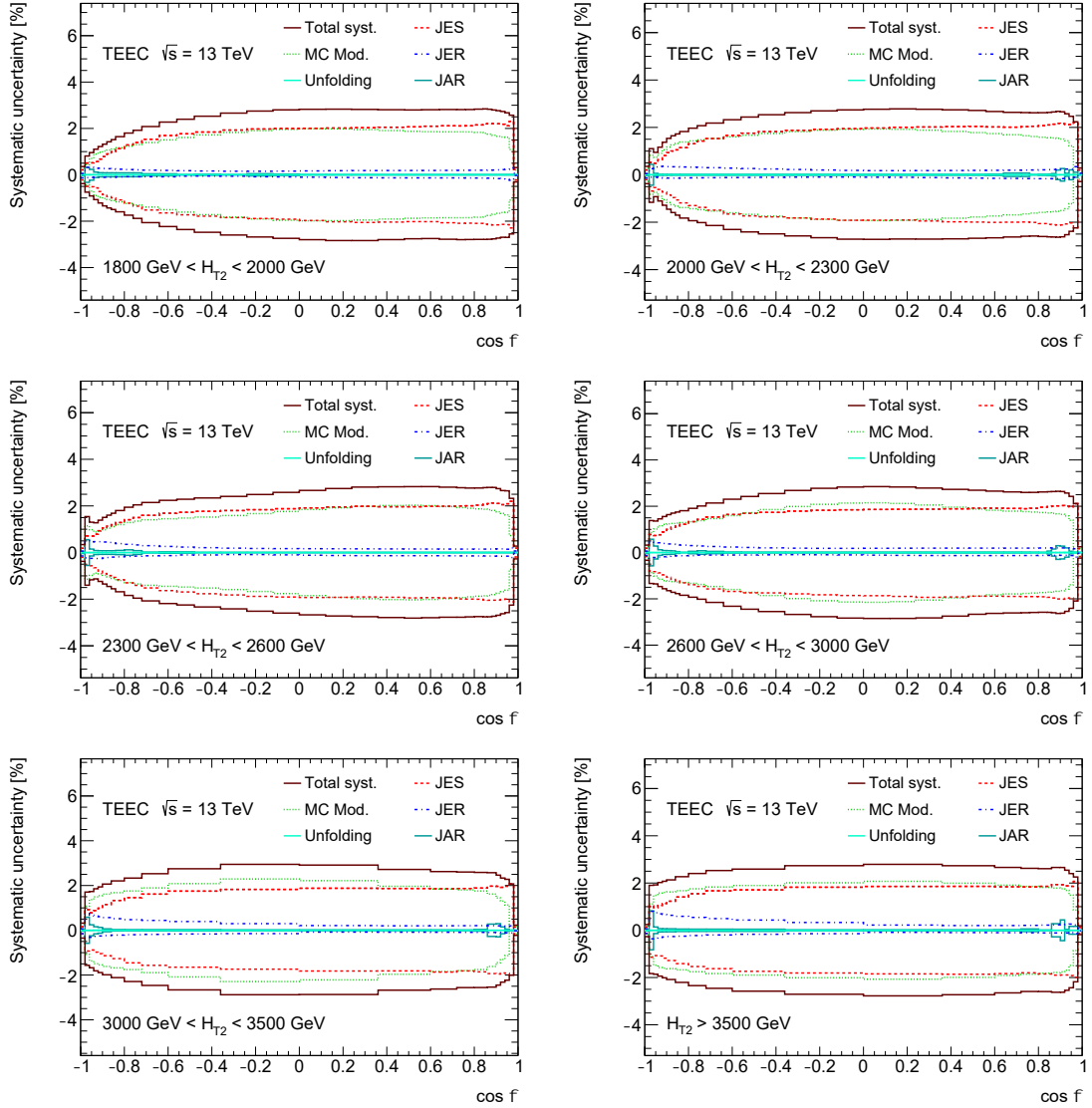


Figure 6.24: Total relative systematic uncertainty for the TEEC distribution, in exclusive H_{T2} bins, together with a breakdown on the general source uncertainties: JES, JER, JAR, MC model and unfolding closure. These sources are added together in quadrature, with the JES and the choice of the MC model being the dominant ones.

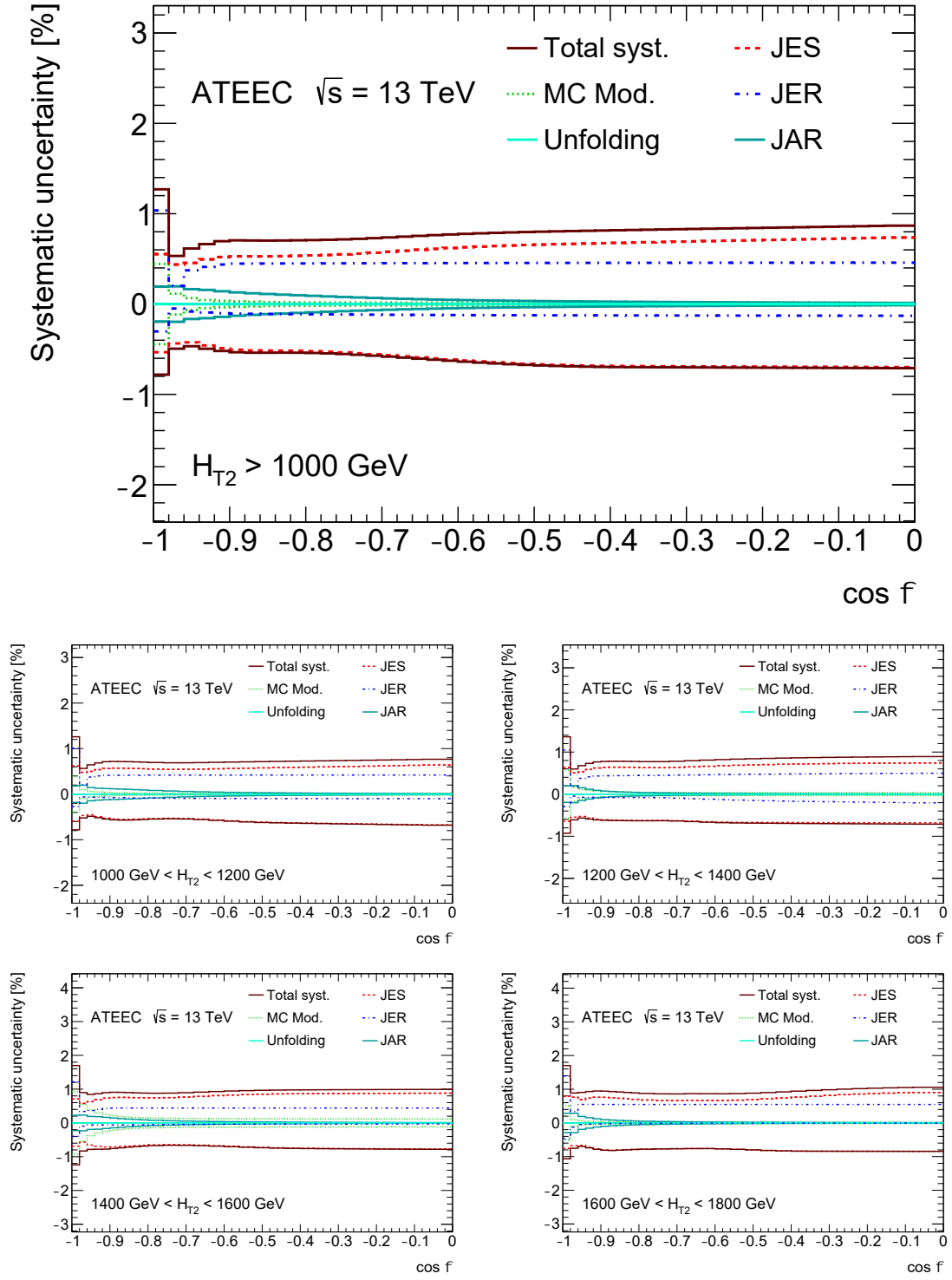


Figure 6.25: Total relative systematic uncertainty for the ATEEC distribution, in inclusive (top) and exclusive (bottom) H_{T2} bins, together with a breakdown on the general source uncertainties: JES, JER, JAR, MC model and unfolding closure. These sources are added together in quadrature, with the JES and the JER being the dominant ones.

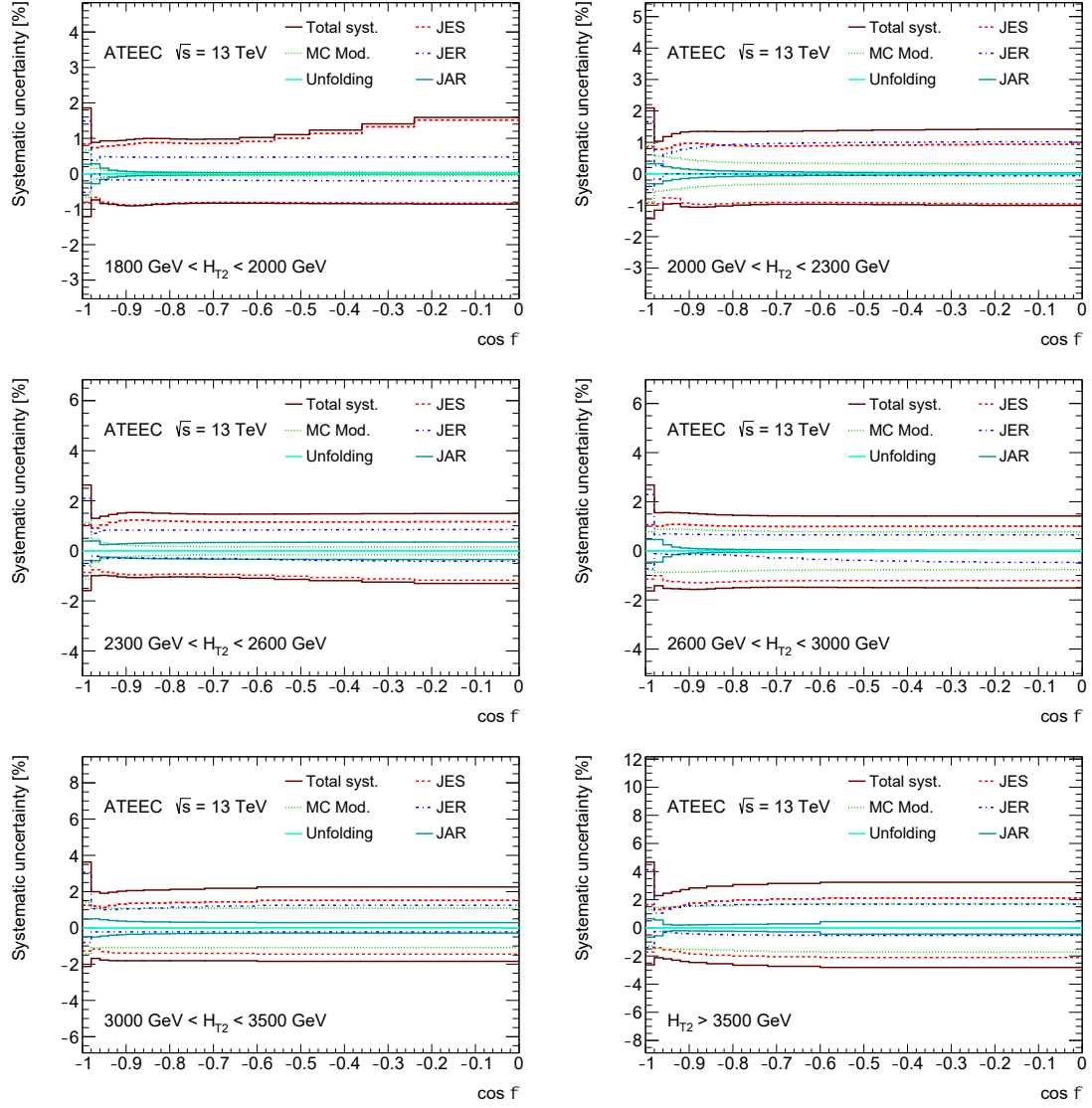


Figure 6.26: Total relative systematic uncertainty for the ATEEC distribution, in exclusive H_{T2} bins, together with a breakdown on the general source uncertainties: JES, JER, JAR, MC model and unfolding closure. These sources are added together in quadrature, with the JES and the JER being the dominant ones.

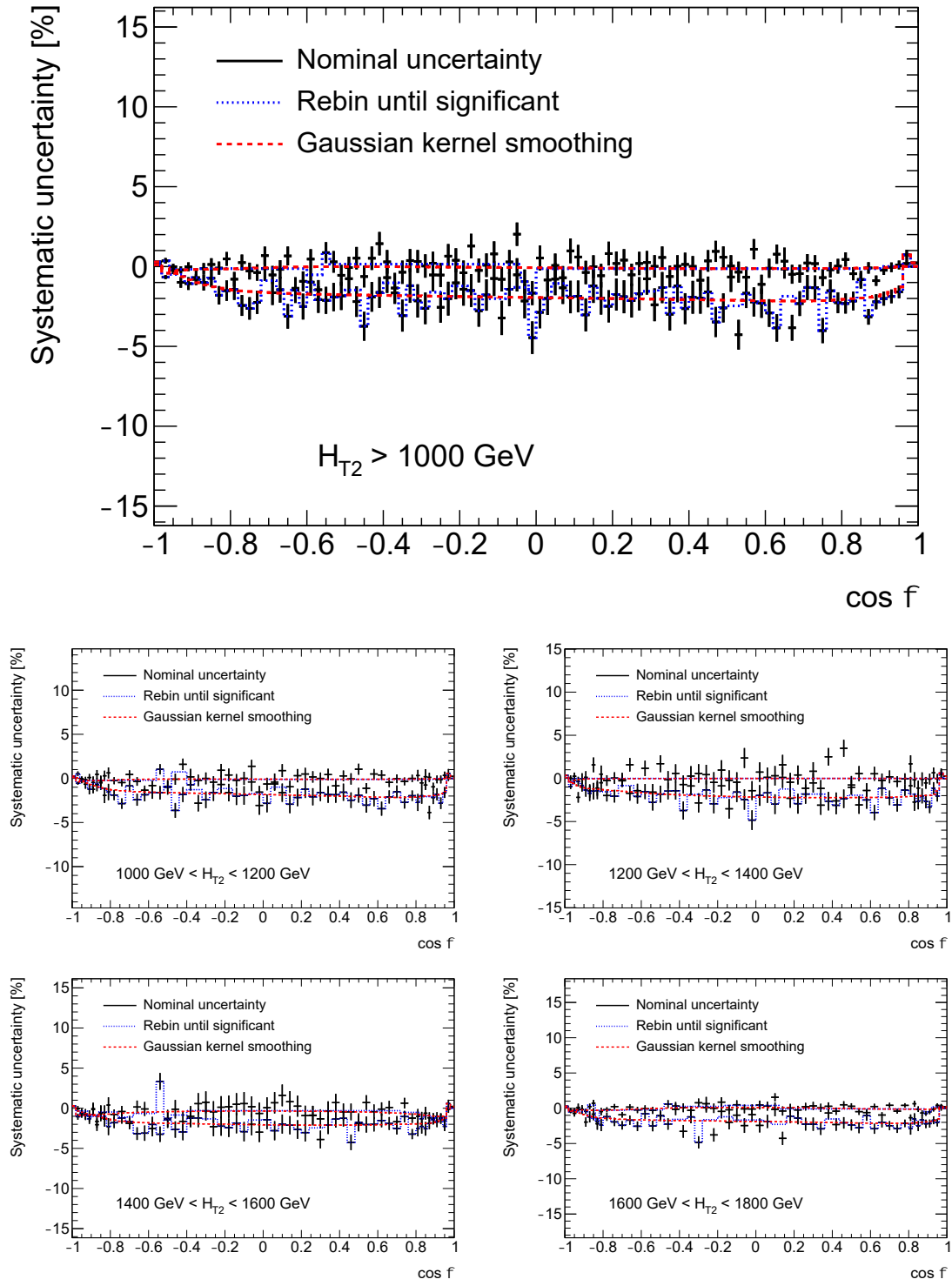


Figure 6.27: Relative systematic uncertainty due to the MC model used in the IB unfolding, in inclusive (top) and exclusive (bottom) H_{T2} bins, for the TEEC function obtained from MC simulated samples with PYTHIA 8.235, HERWIG 7.1.3, and SHERPA 2.1.1 event generators. It arises from the two hadronization schemes considered: cluster hadronization and Lund string fragmentation.

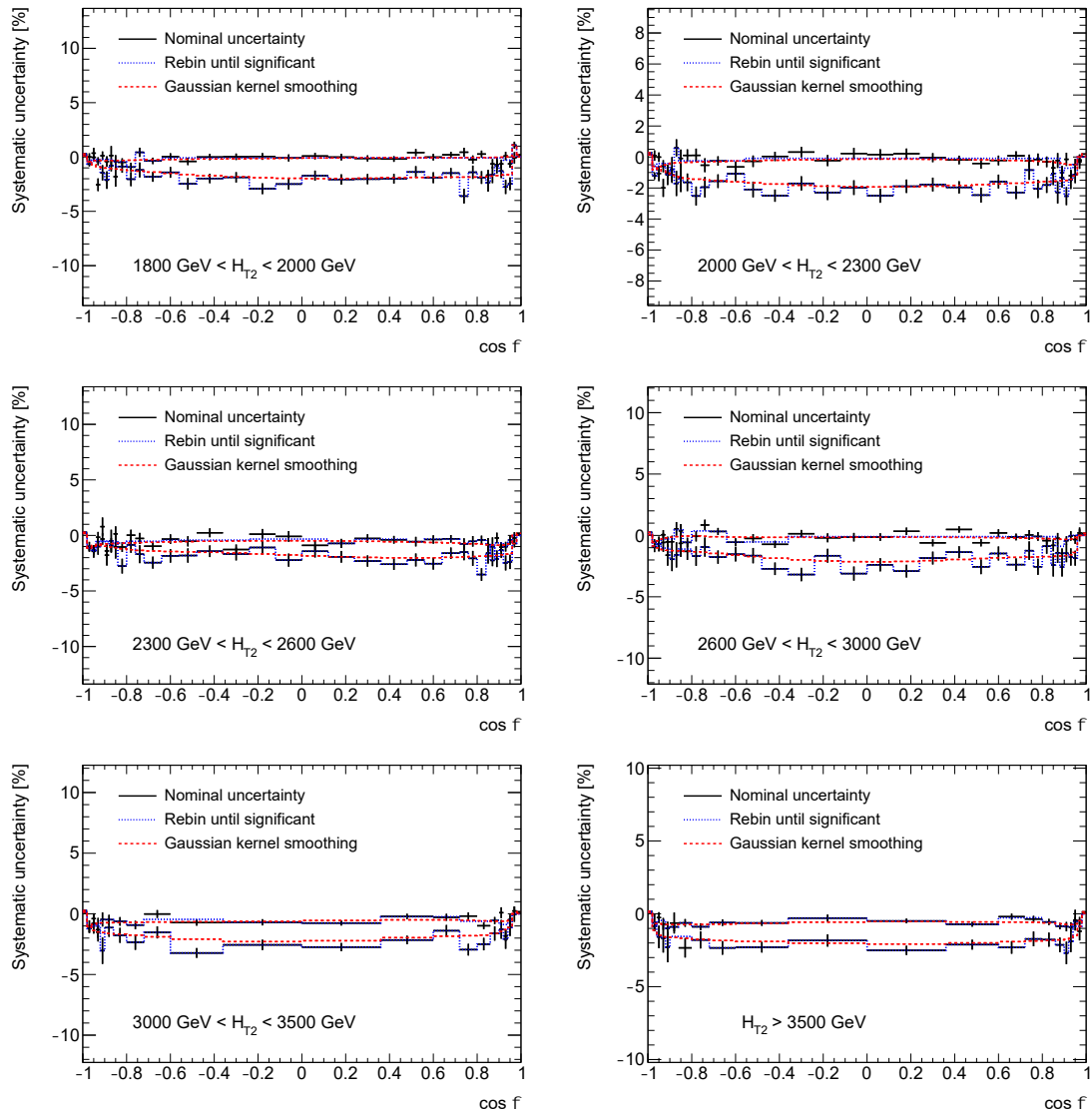


Figure 6.28: Relative systematic uncertainty due to the MC model used in the IB unfolding, in exclusive H_{T2} bins, for the TEEC function obtained from MC simulated samples with PYTHIA 8.235, HERWIG 7.1.3, and SHERPA 2.1.1 event generators. It arises from the two hadronization schemes considered: cluster hadronization and Lund string fragmentation.

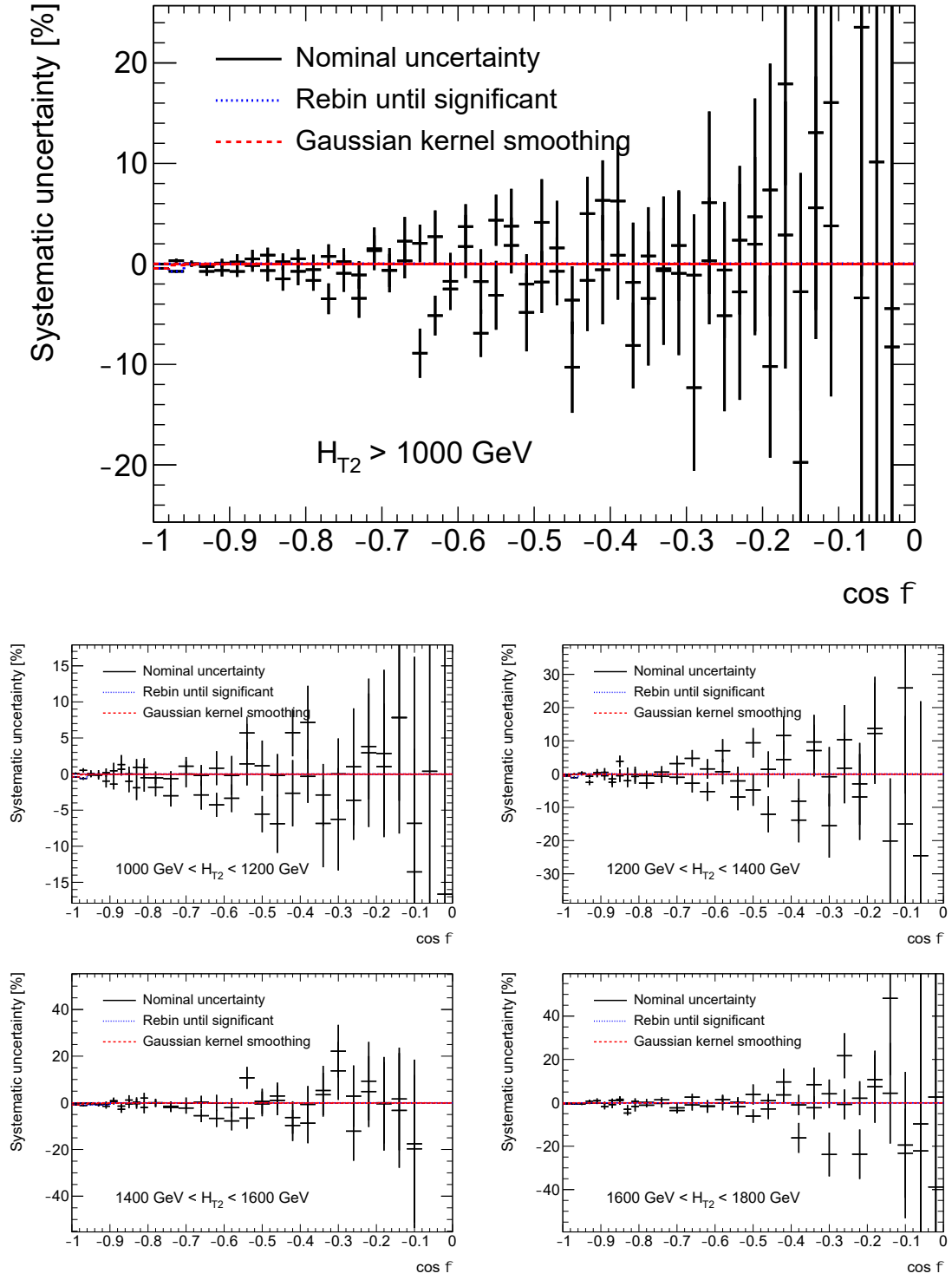


Figure 6.29: Relative systematic uncertainty due to the MC model used in the IB unfolding, in inclusive (top) and exclusive (bottom) H_{T2} bins, for the ATEEC function obtained from MC simulated samples with PYTHIA 8.235, HERWIG 7.1.3, and SHERPA 2.1.1 event generators. It arises from the two hadronization schemes considered: cluster hadronization and Lund string fragmentation.

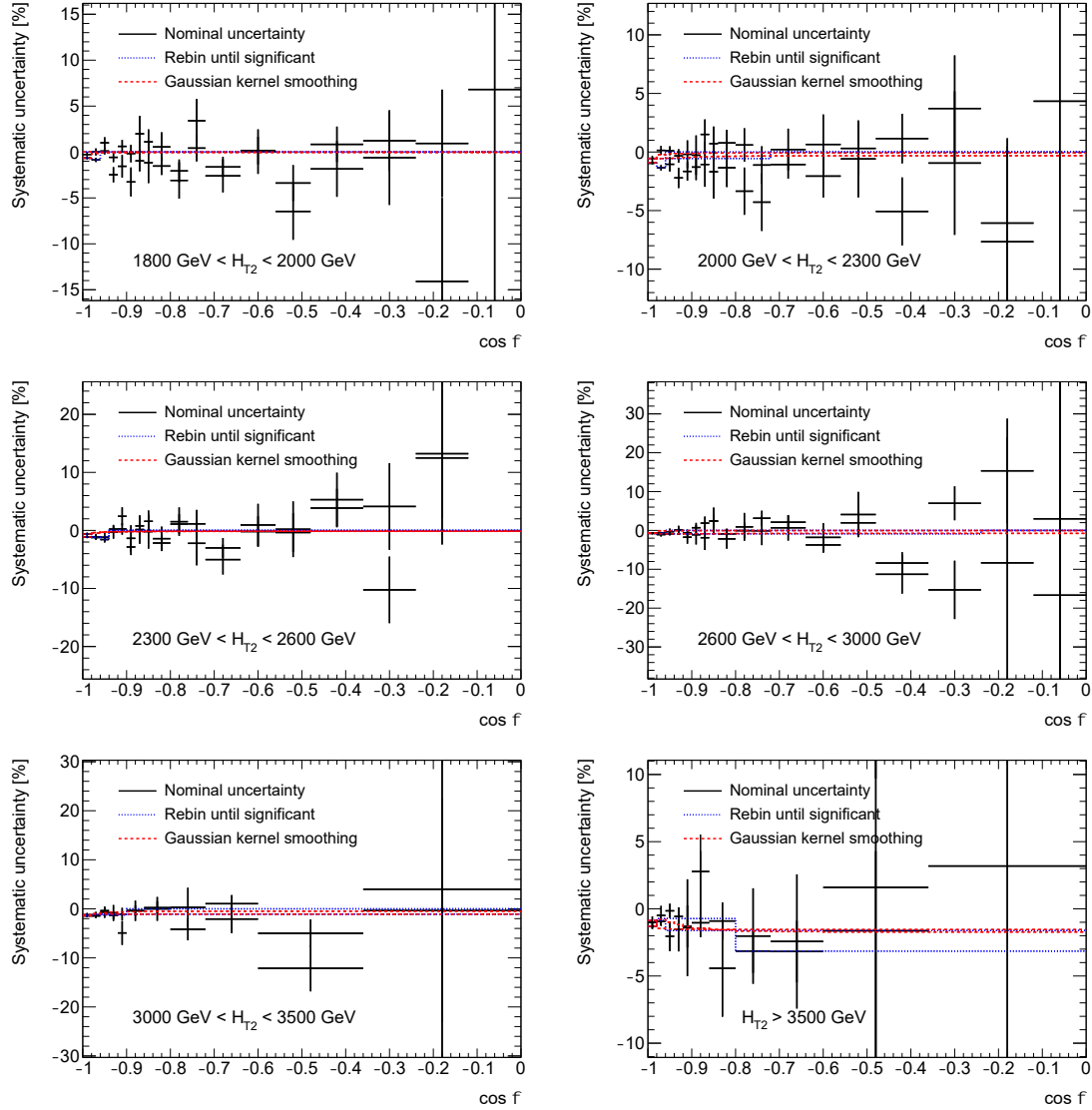


Figure 6.30: Relative systematic uncertainty due to the MC model used in the IB unfolding, in exclusive H_{T2} bins, for the ATEEC function obtained from MC simulated samples with PYTHIA 8.235, HERWIG 7.1.3, and SHERPA 2.1.1 event generators. It arises from the two hadronization schemes considered: cluster hadronization and Lund string fragmentation.

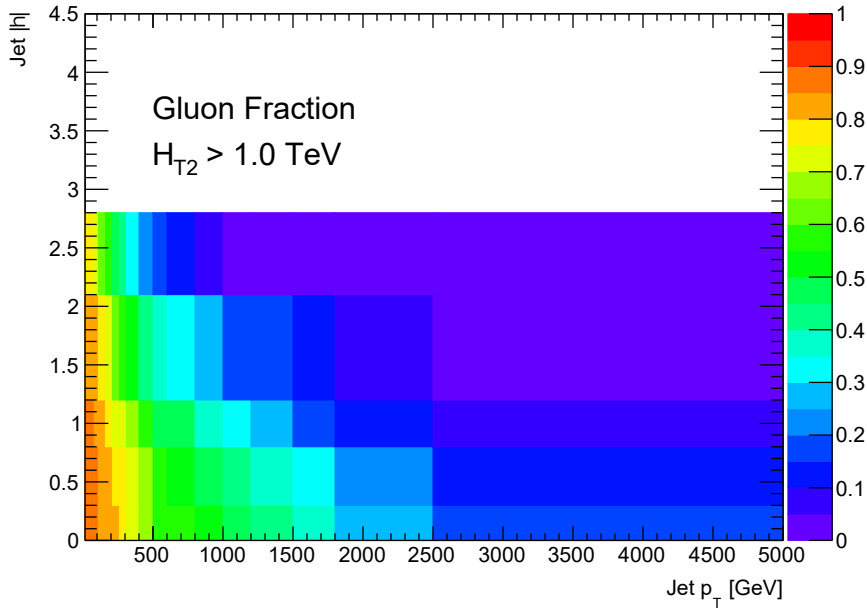


Figure 6.31: Gluon jet fraction determined as a function of the p_T and the $|\eta|$ of the jet. The distribution is determined using the PYTHIA 8.235 simulated sample and used to constrain the Flavour Response uncertainty.

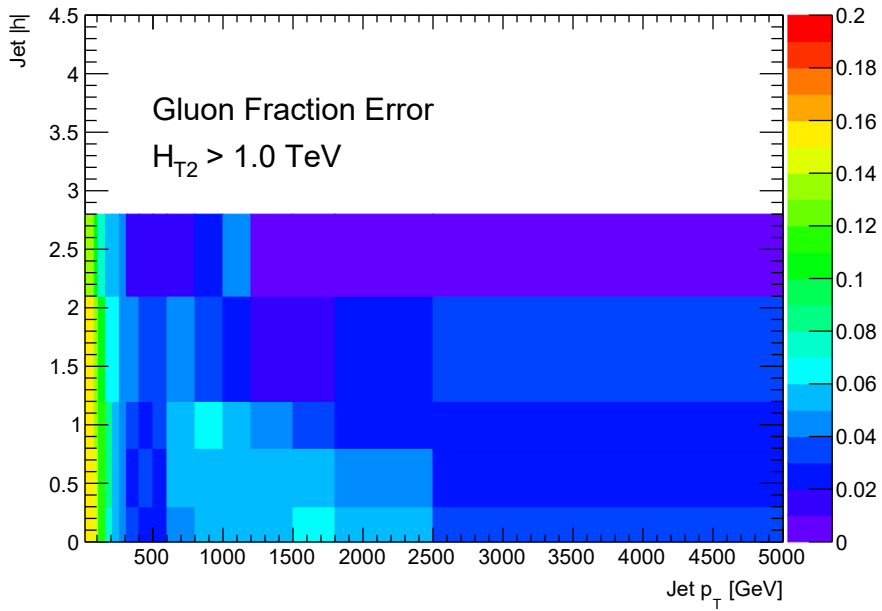


Figure 6.32: Uncertainty in the determination of the gluon jet fraction defined as the difference between PYTHIA 8.235, SHERPA 2.1.1, and HERWIG 7.1.3 simulated samples. The distribution is used to constrain the Flavour Composition uncertainty.

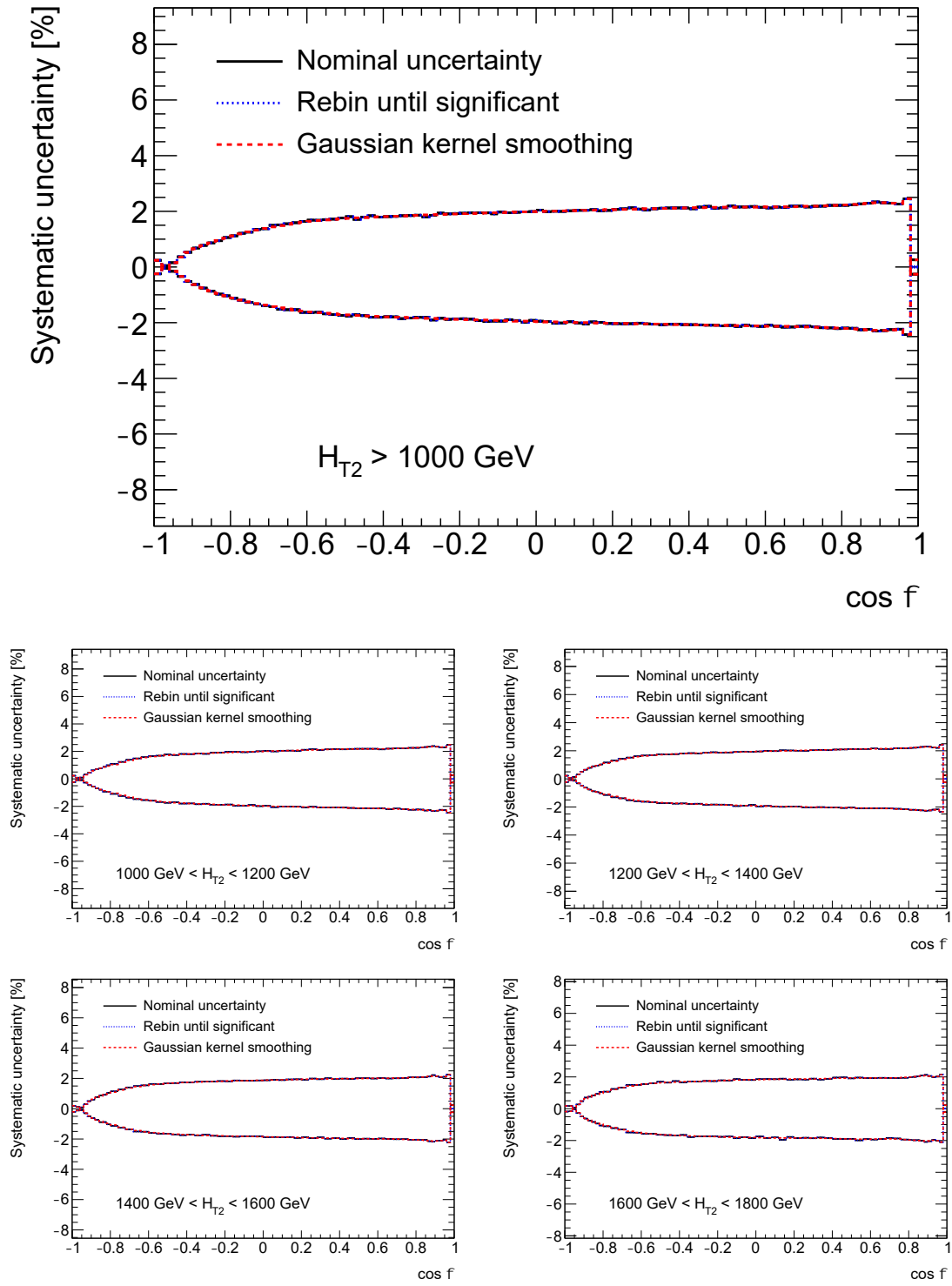


Figure 6.33: Relative systematic uncertainty due to the Flavour Response, in inclusive (top) and exclusive (bottom) H_{T2} bins, for the TEEC function obtained from the MC simulated sample with the PYTHIA 8.235 event generator.

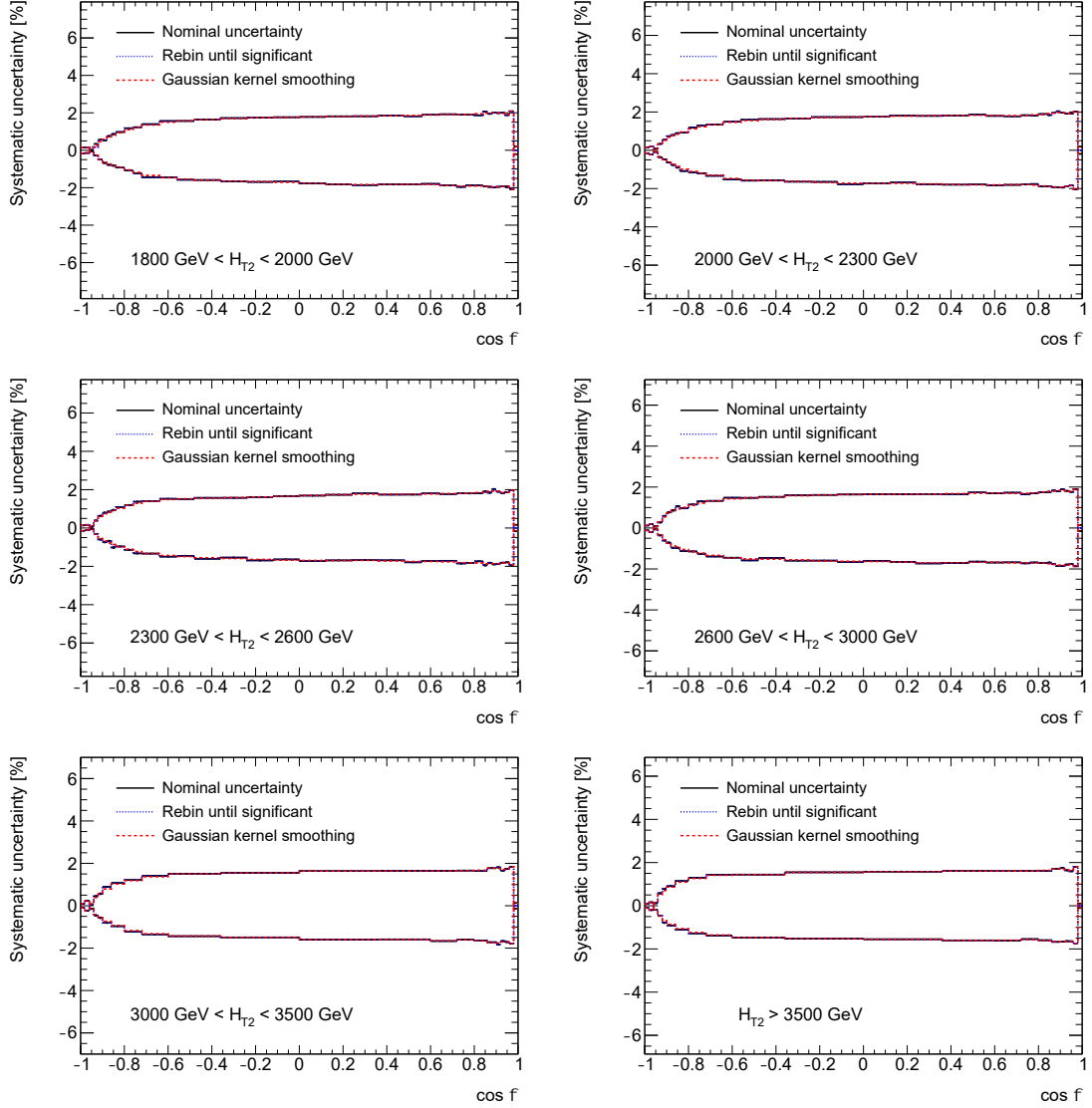


Figure 6.34: Relative systematic uncertainty due to the Flavour Response, in exclusive H_{T2} bins, for the TEEC function obtained from the MC simulated sample with the PYTHIA 8.235 event generator.

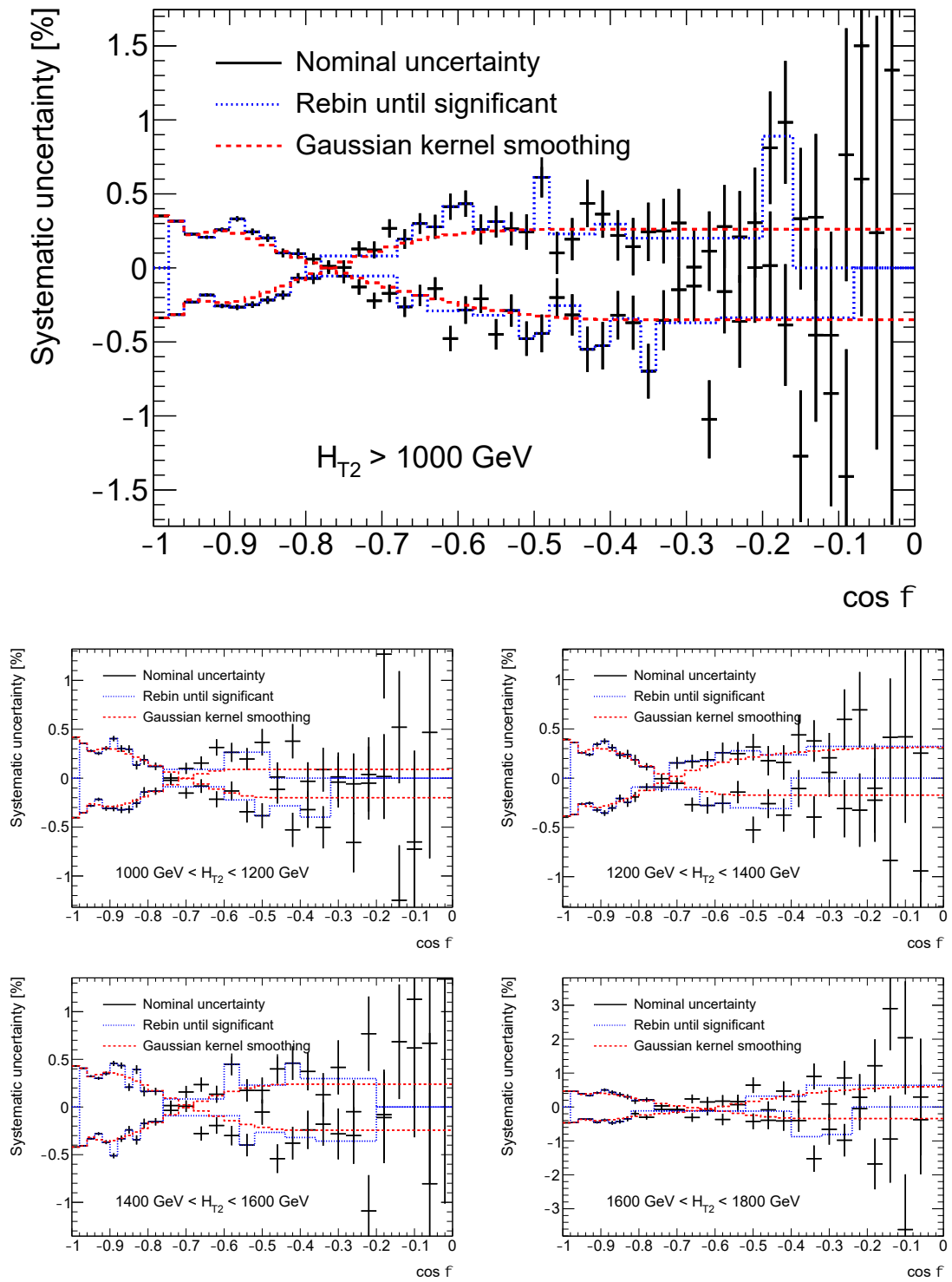


Figure 6.35: Relative systematic uncertainty due to the Flavour Response, in inclusive (top) and exclusive (bottom) H_{T2} bins, for the ATEEC function obtained from the MC simulated sample with the PYTHIA 8.235 event generator.

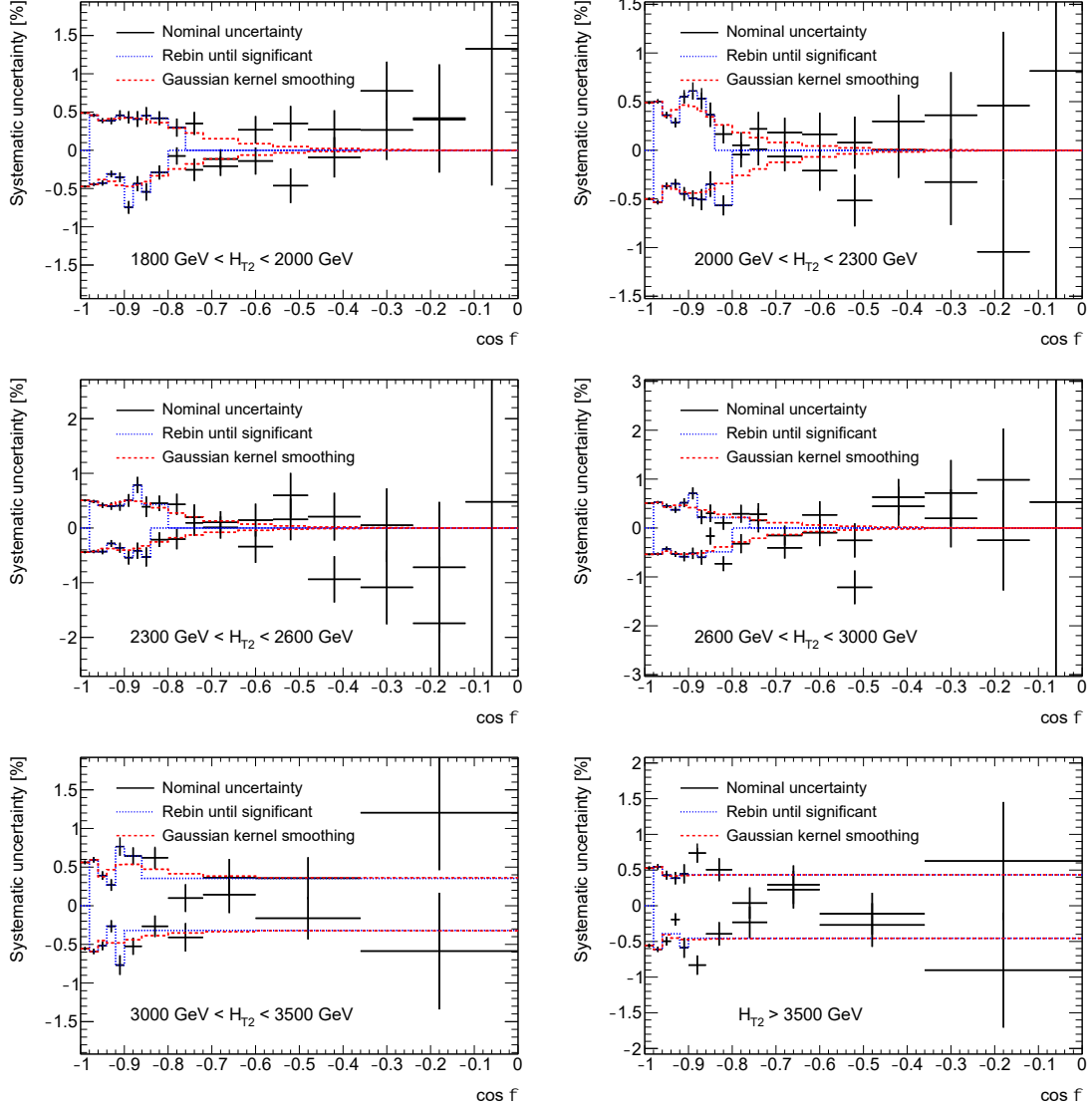


Figure 6.36: Relative systematic uncertainty due to the Flavour Response, in exclusive H_{T2} bins, for the ATEEC function obtained from the MC simulated sample with the PYTHIA 8.235 event generator.

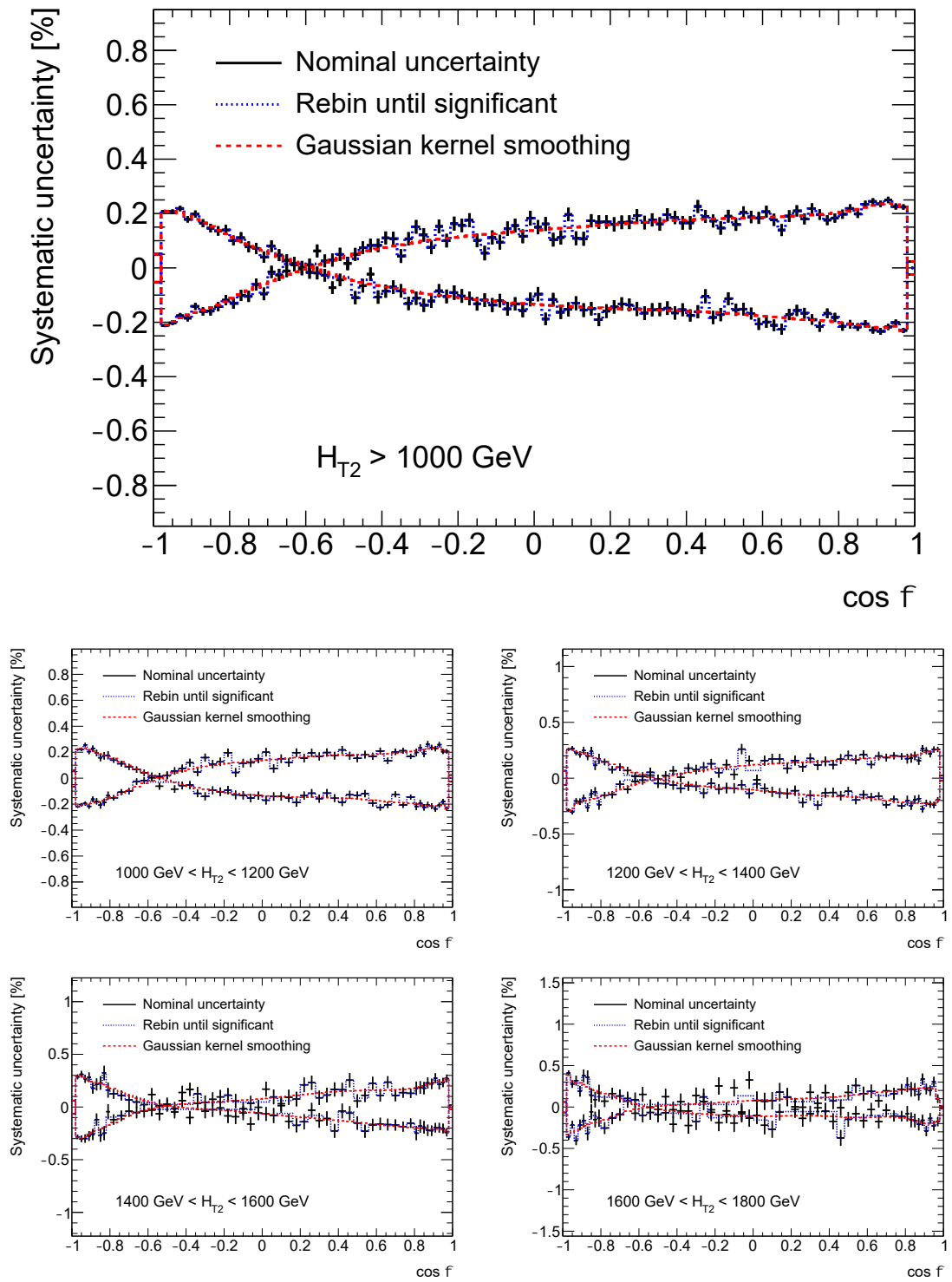


Figure 6.37: Relative systematic uncertainty due to the Gjet GamESZee, in inclusive (top) and exclusive (bottom) H_{T2} bins, for the TEEC function obtained from the MC simulated sample with the PYTHIA 8.235 event generator.

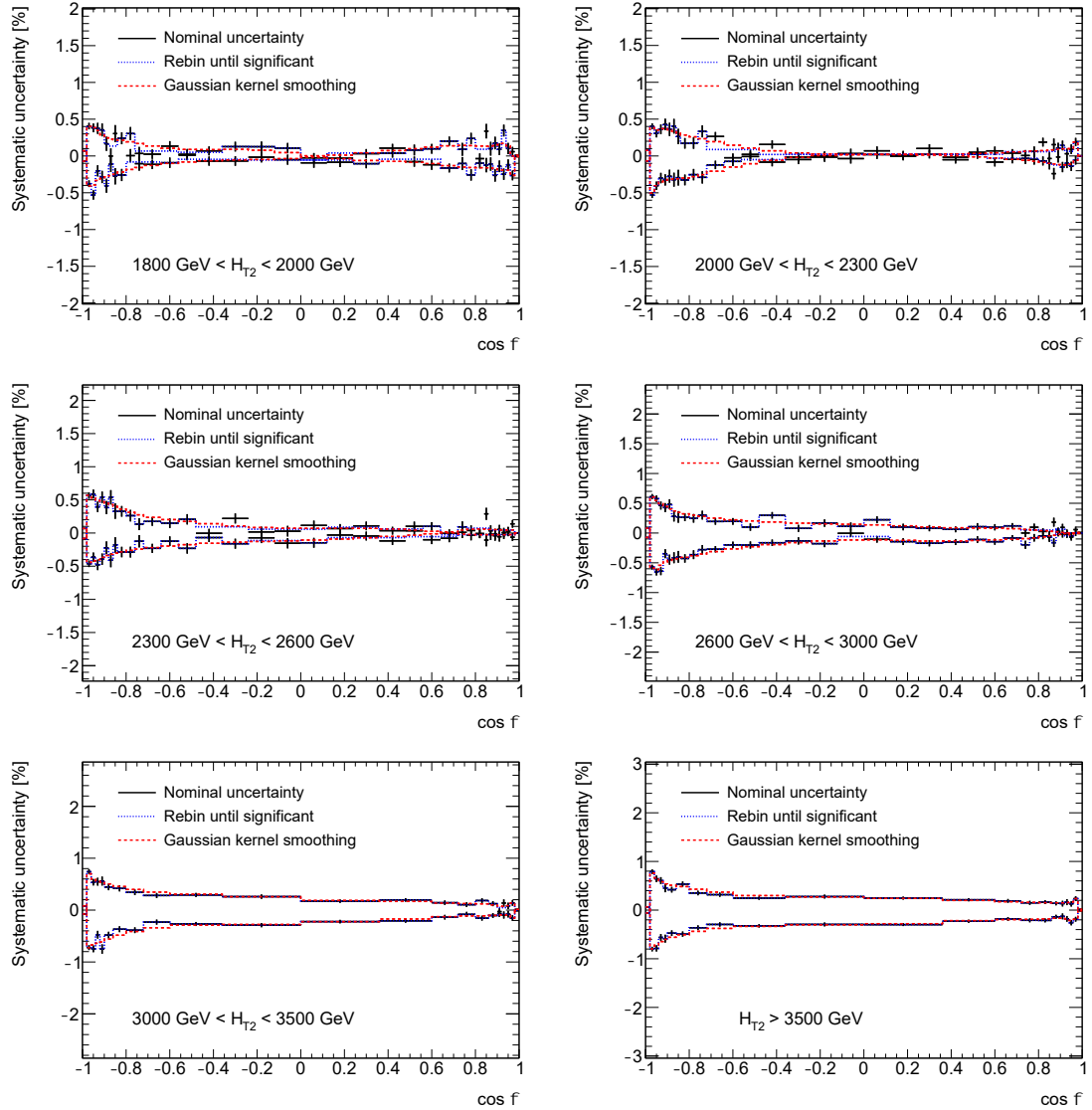


Figure 6.38: Relative systematic uncertainty due to the Gjet GamESZee, in exclusive H_{T2} bins, for the TEEC function obtained from the MC simulated sample with the PYTHIA 8.235 event generator.

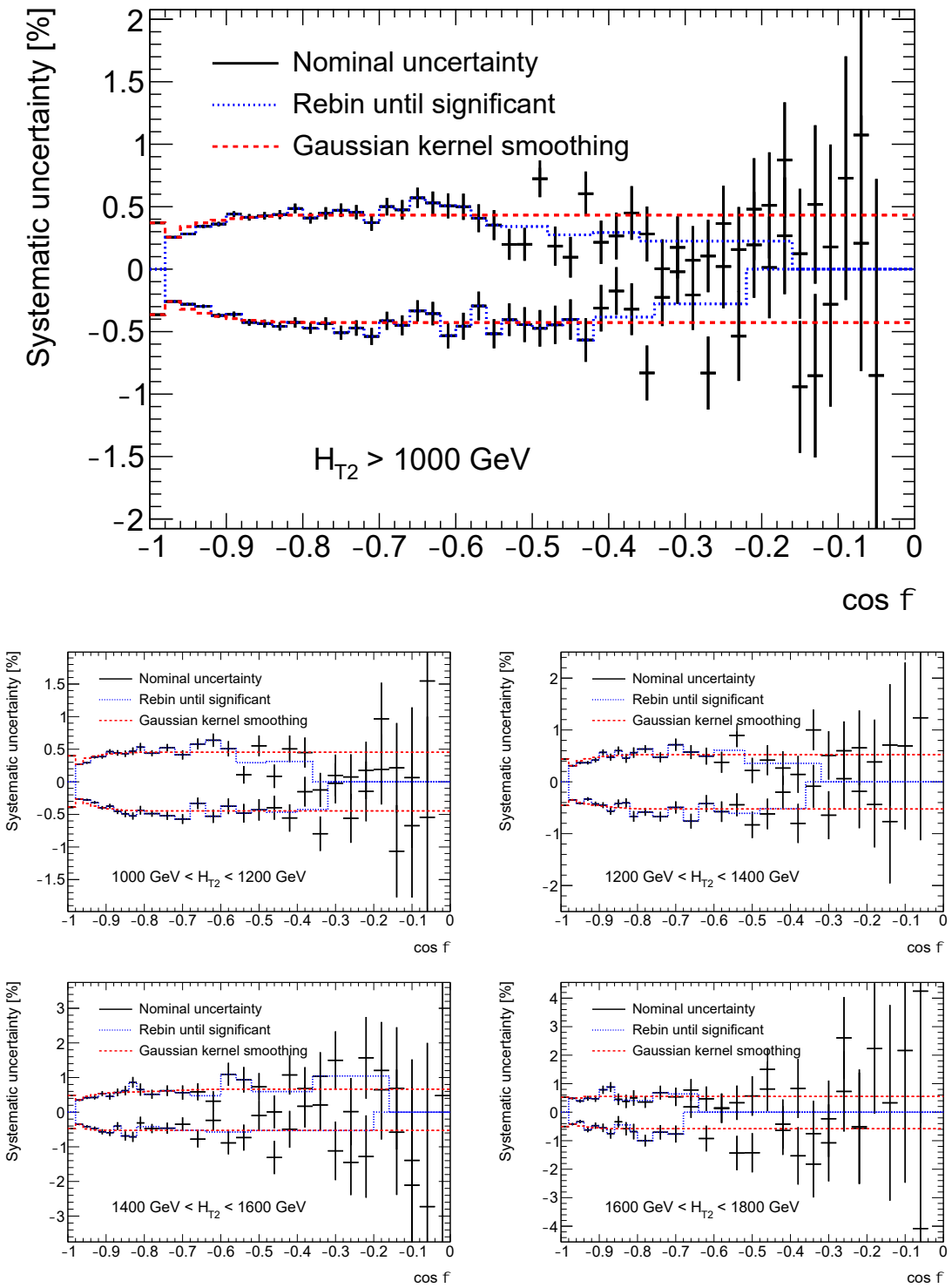


Figure 6.39: Relative systematic uncertainty due to the Gjet GamESZee, in inclusive (top) and exclusive (bottom) H_{T2} bins, for the ATEEC function obtained from the MC simulated sample with the PYTHIA 8.235 event generator.

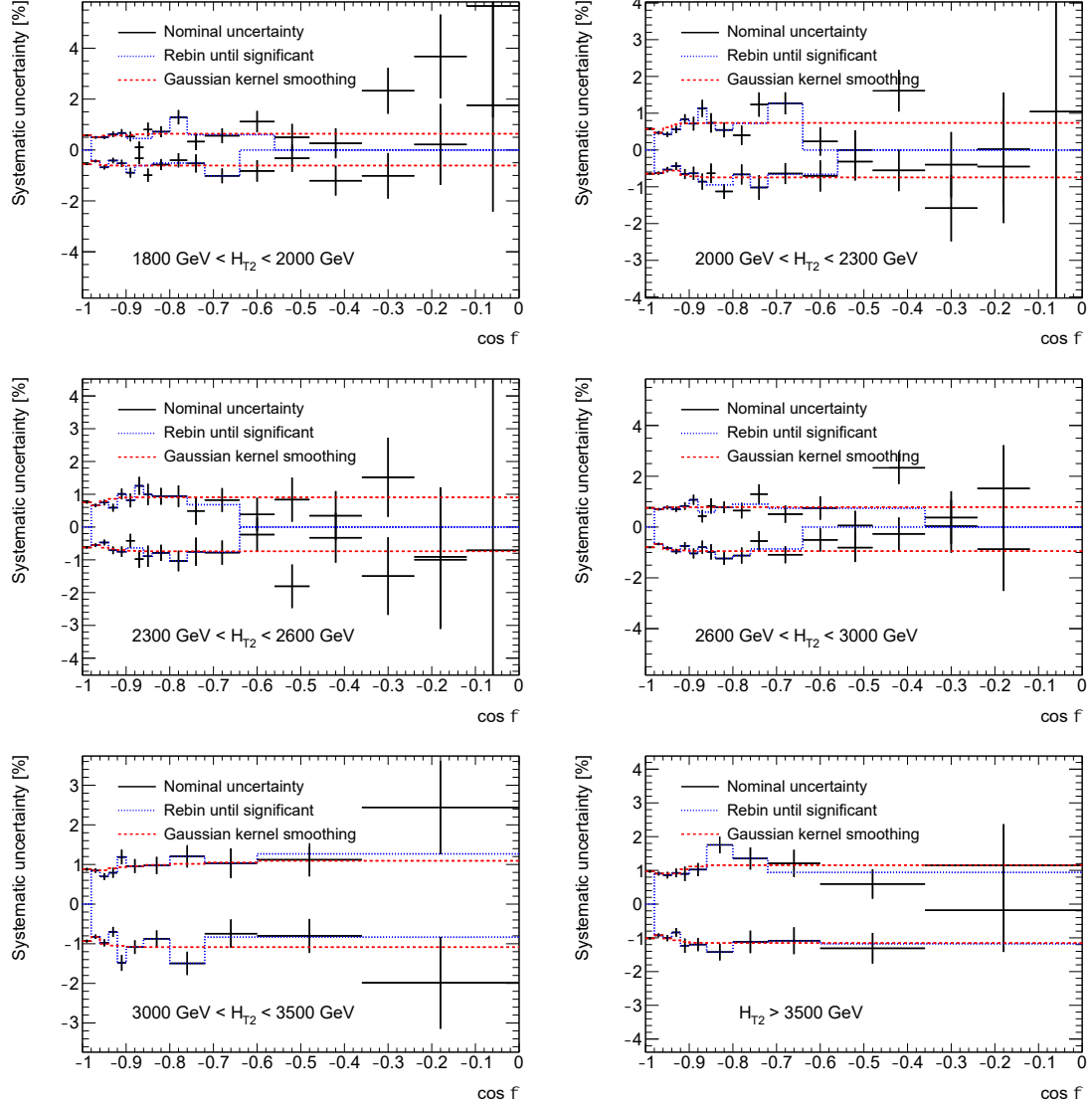


Figure 6.40: Relative systematic uncertainty due to the Gjet GamESZee, in exclusive H_{T2} bins, for the ATEEC function obtained from the MC simulated sample with the PYTHIA 8.235 event generator.

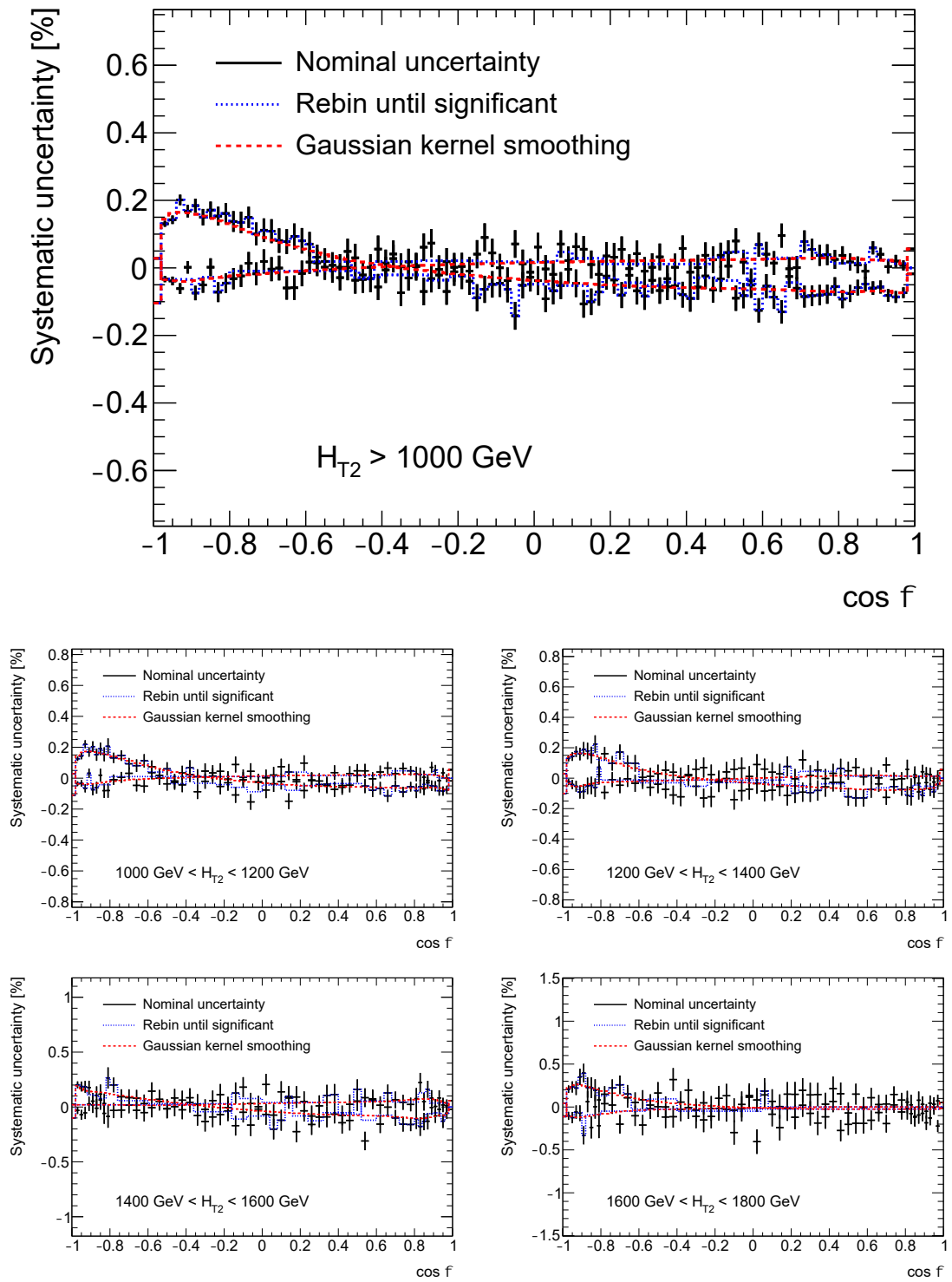


Figure 6.41: Relative systematic uncertainty due to the JER dijet closure, in inclusive (top) and exclusive (bottom) H_{T2} bins, for the TEEC function obtained from the MC simulated sample with the PYTHIA 8.235 event generator.

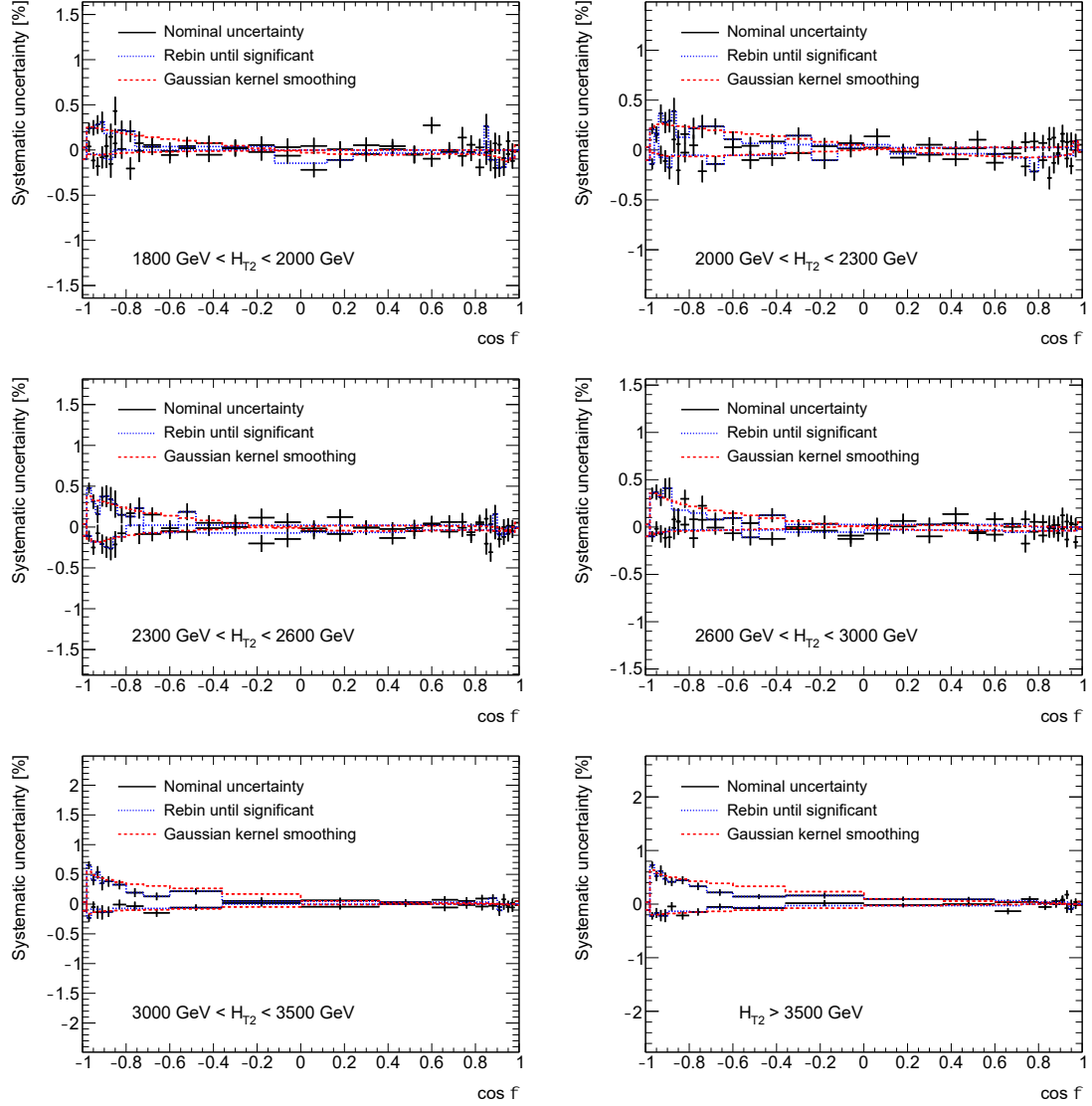


Figure 6.42: Relative systematic uncertainty due to the JER dijet closure, in exclusive H_{T2} bins, for the TEEC function obtained from the MC simulated sample with the PYTHIA 8.235 event generator.

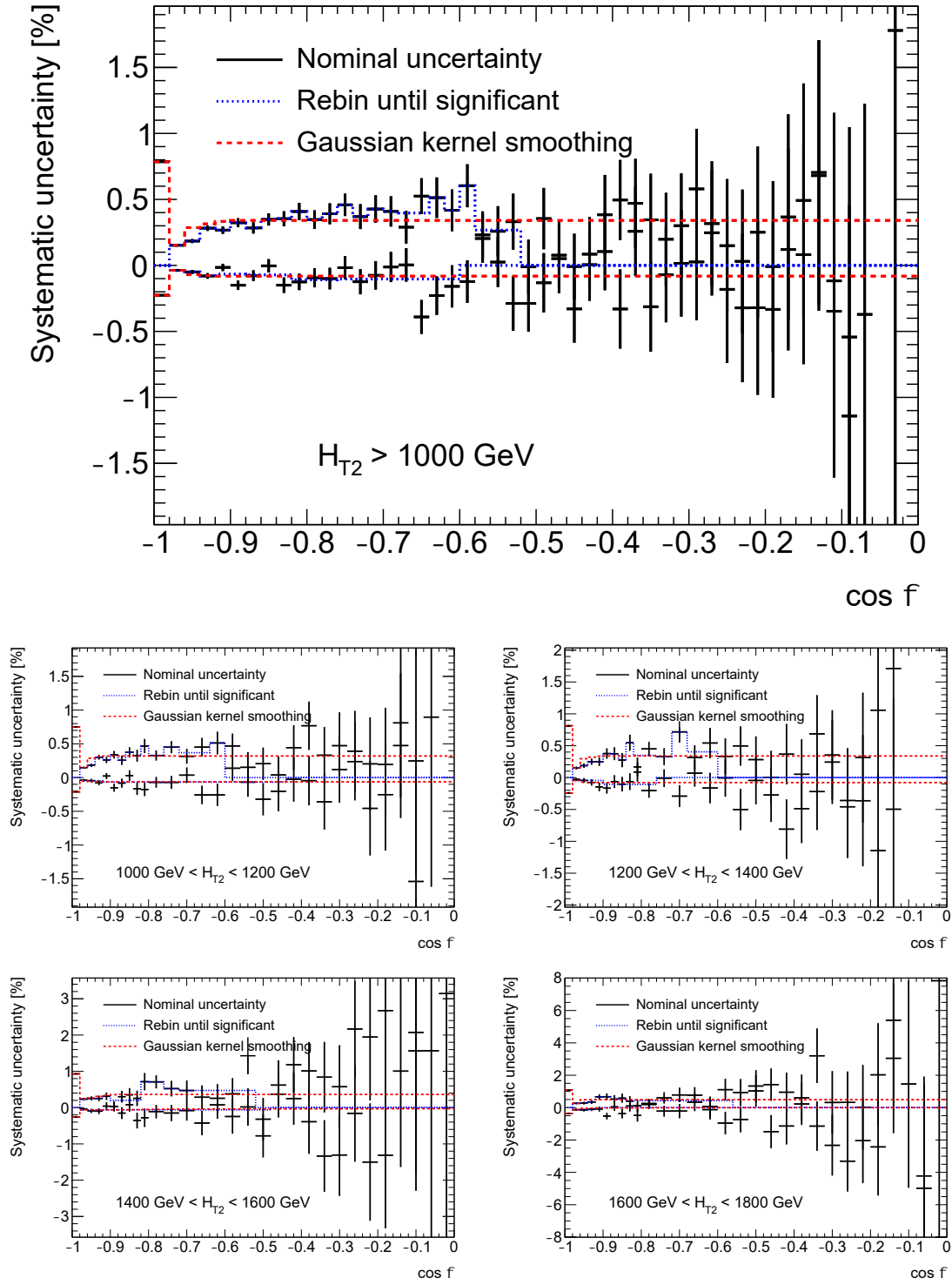


Figure 6.43: Relative systematic uncertainty due to the JER dijet closure, in inclusive (top) and exclusive (bottom) H_{T2} bins, for the ATEEC function obtained from the MC simulated sample with the PYTHIA 8.235 event generator.

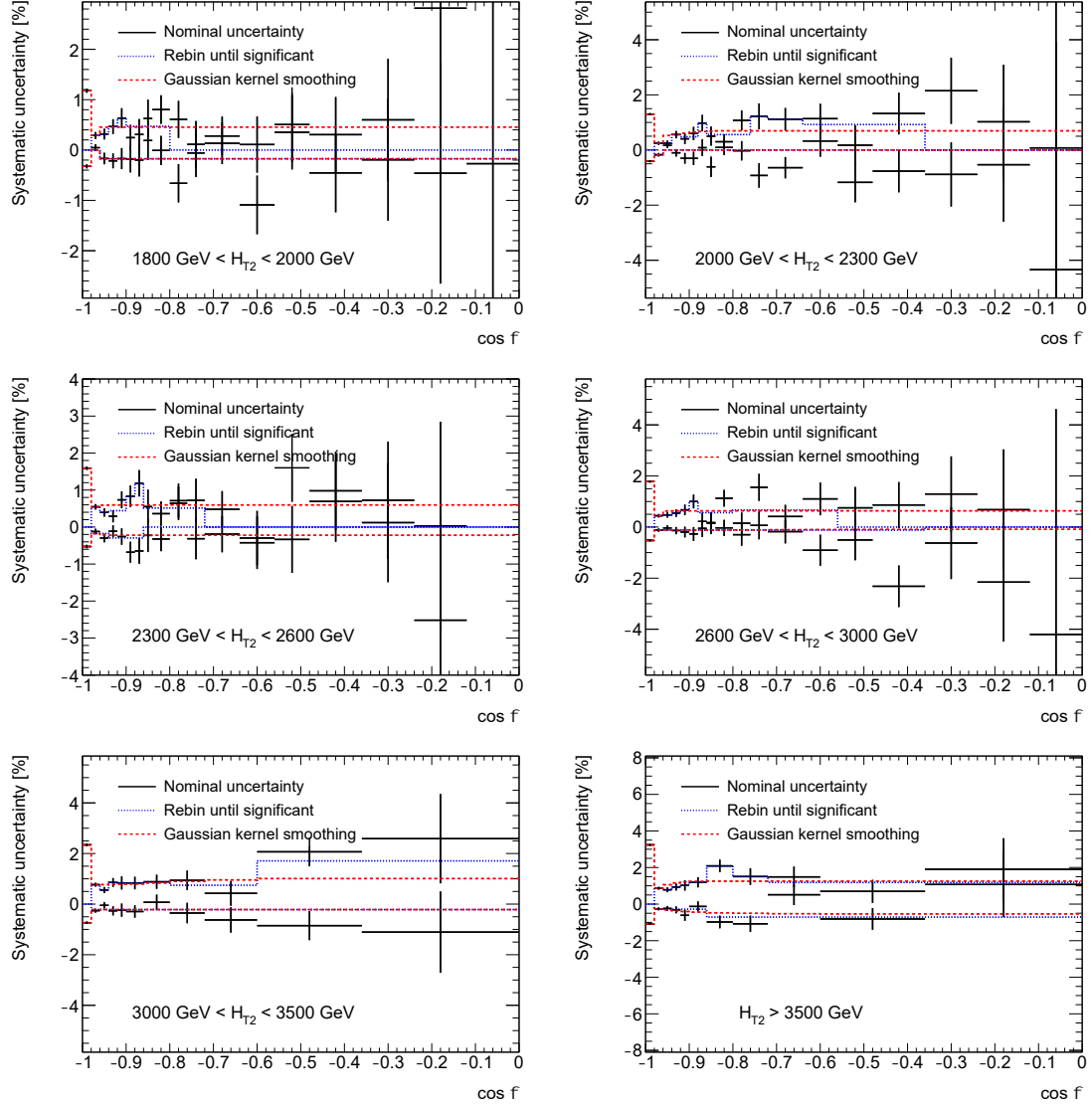


Figure 6.44: Relative systematic uncertainty due to the JER dijet closure, in exclusive H_{T2} bins, for the ATEEC function obtained from the MC simulated sample with the PYTHIA 8.235 event generator.

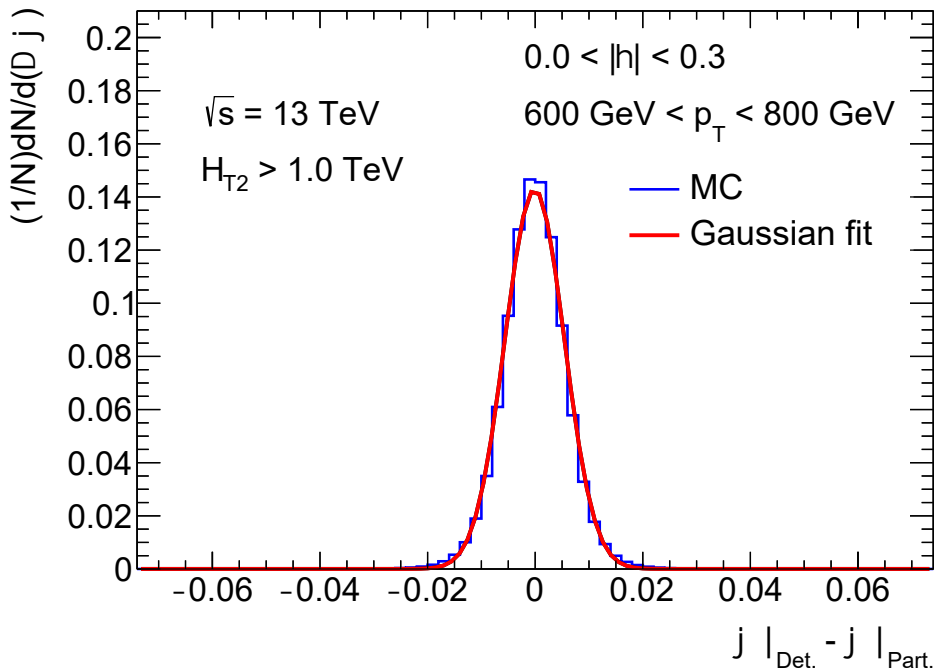


Figure 6.45: Azimuthal angular resolution in the PYTHIA 8.235 simulated sample for $600 \text{ GeV} < p_T < 800 \text{ GeV}$ and $|\eta| < 0.3$. A fit to a Gaussian distribution yields a standard deviation of $\sigma = 5.6 \times 10^{-3}$.

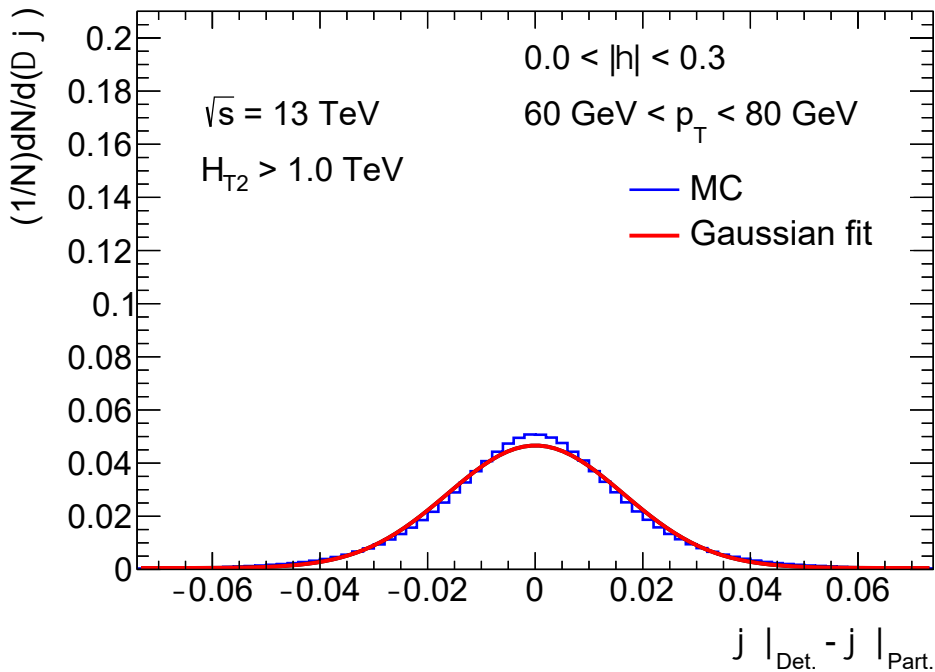
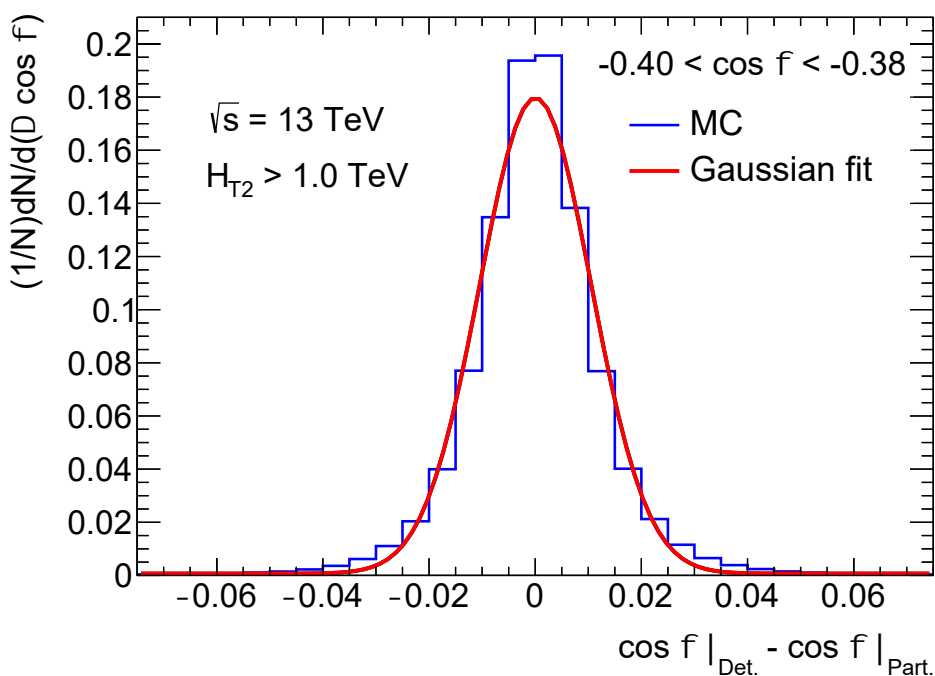
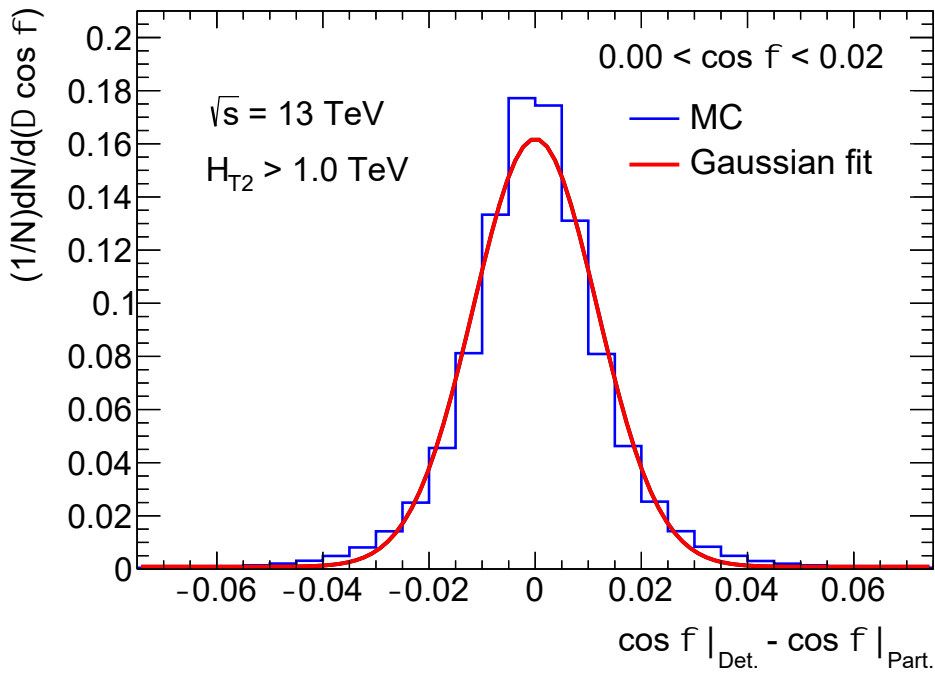


Figure 6.46: Azimuthal angular resolution in the PYTHIA 8.235 simulated sample for $60 \text{ GeV} < p_T < 80 \text{ GeV}$ and $|\eta| < 0.3$. A fit to a Gaussian distribution yields a standard deviation of $\sigma = 16.0 \times 10^{-3}$.



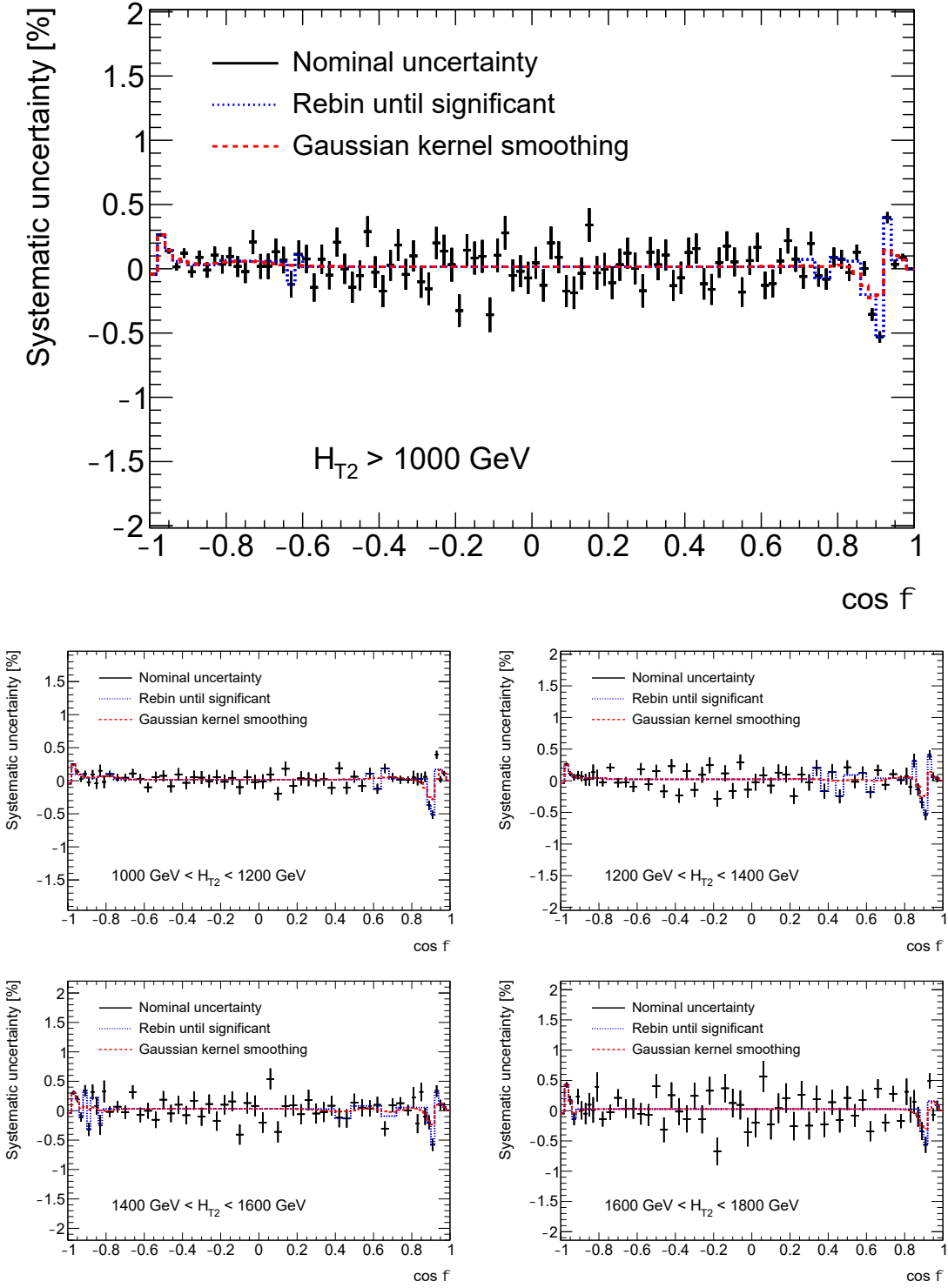


Figure 6.49: Relative systematic uncertainty due to the JAR, in inclusive (top) and exclusive (bottom) H_{T2} bins, for the TEEC function obtained from the MC simulated sample with the PYTHIA 8.235 event generator.

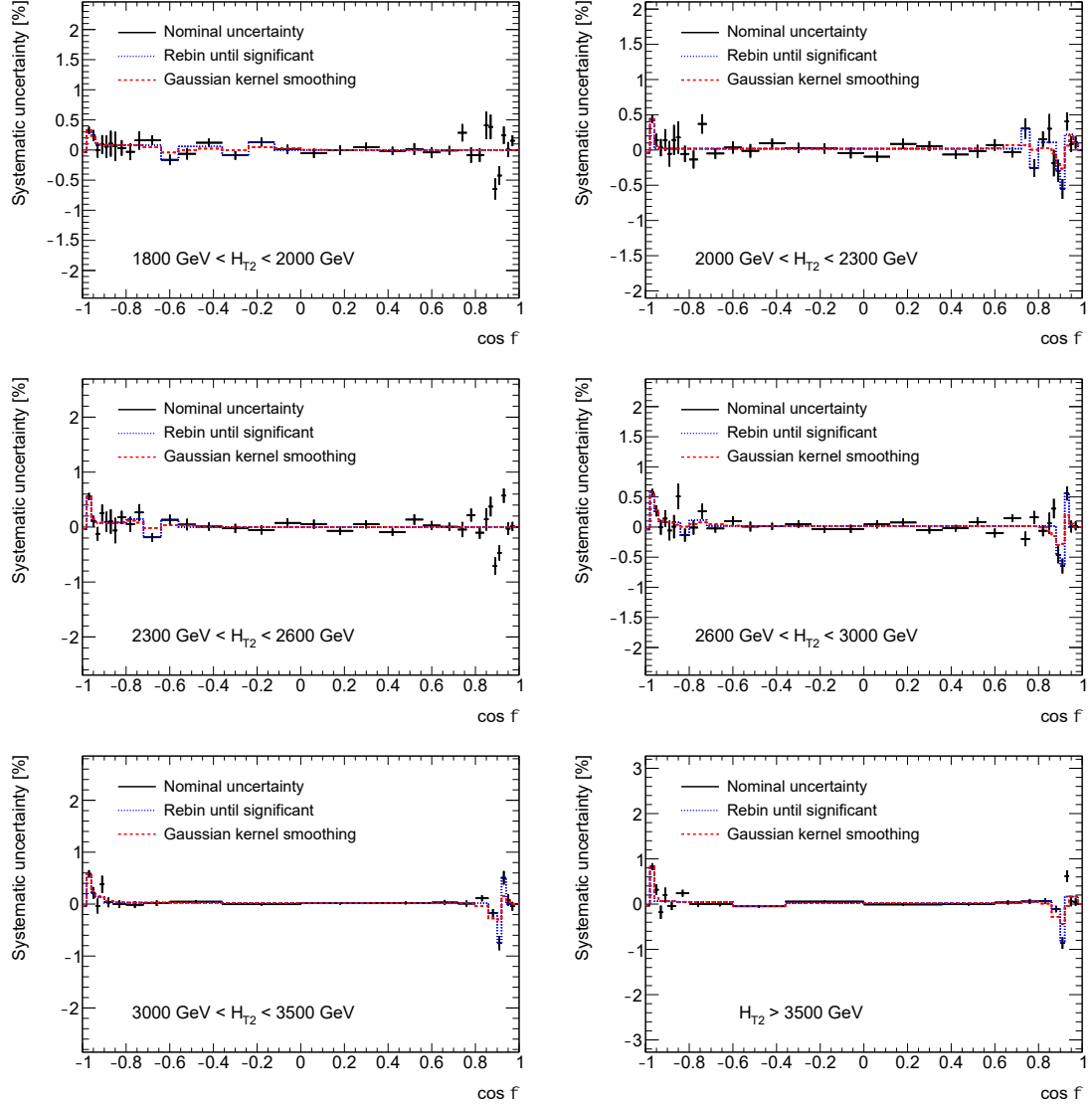


Figure 6.50: Relative systematic uncertainty due to the JAR, in exclusive H_{T2} bins, for the TEEC function obtained from the MC simulated sample with the PYTHIA 8.235 event generator.

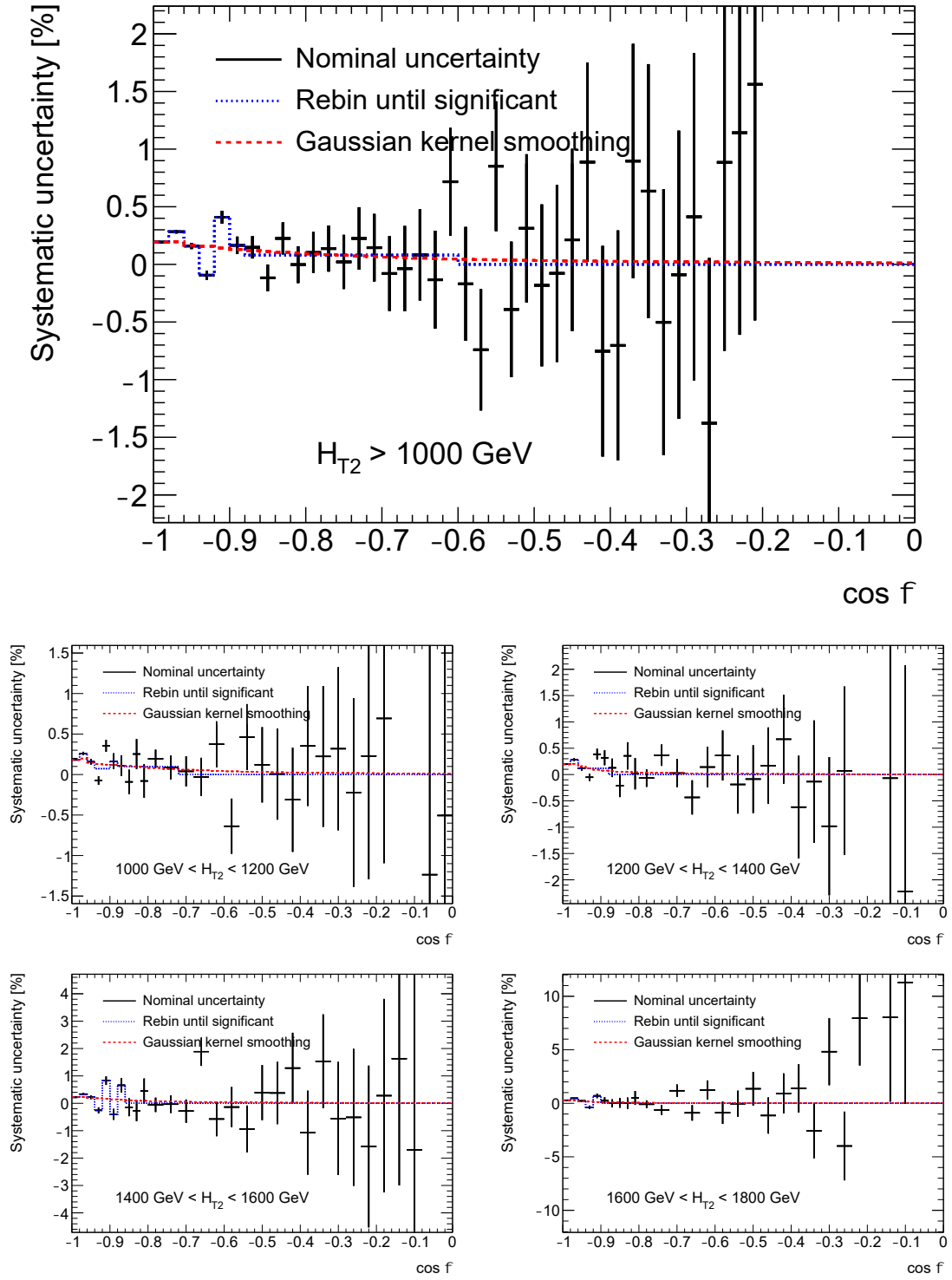


Figure 6.51: Relative systematic uncertainty due to the JAR, in inclusive (top) and exclusive (bottom) H_{T2} bins, for the ATEEC function obtained from the MC simulated sample with the PYTHIA 8.235 event generator.

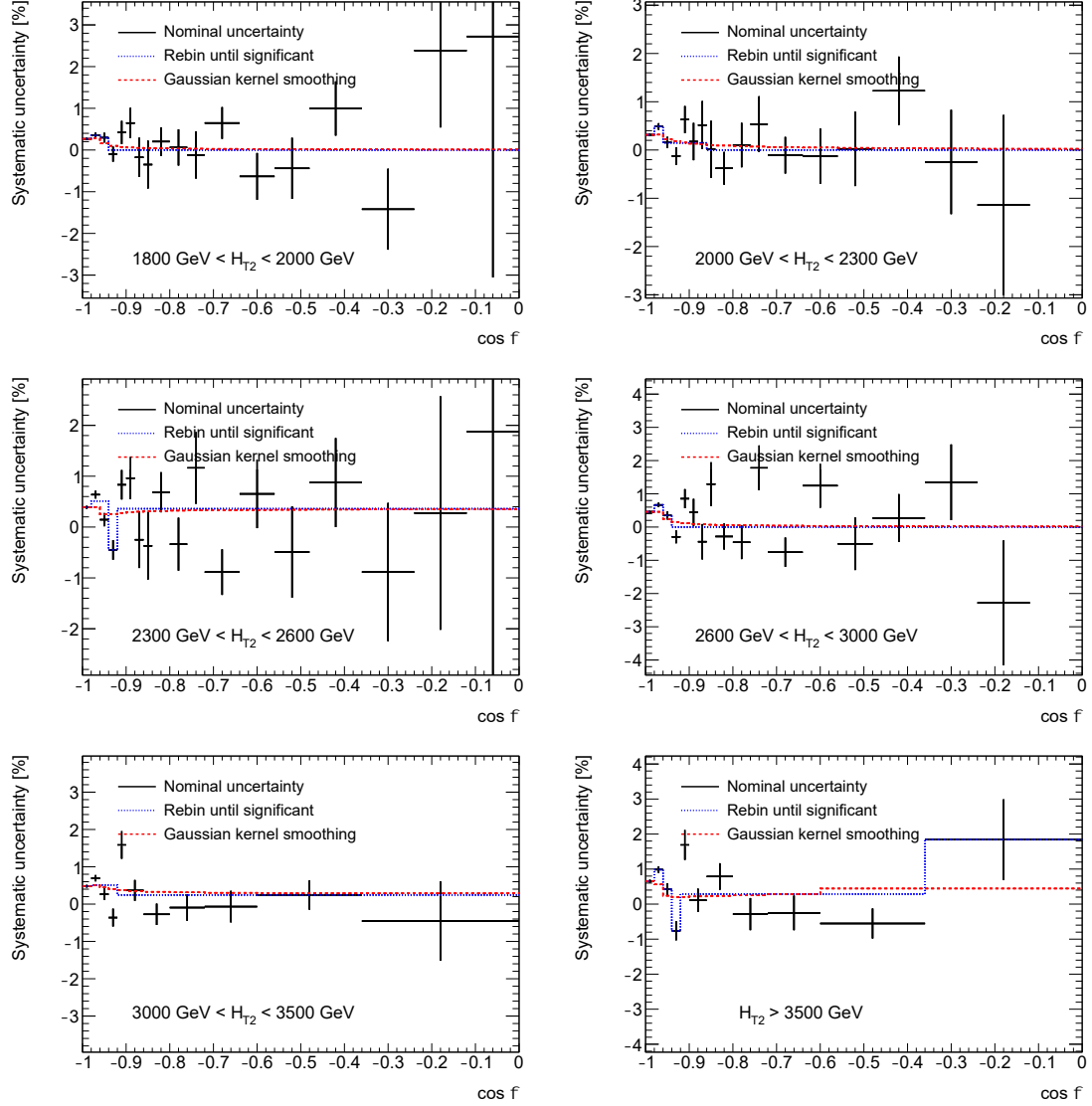


Figure 6.52: Relative systematic uncertainty due to the JAR, in exclusive H_{T2} bins, for the ATEEC function obtained from the MC simulated sample with the PYTHIA 8.235 event generator.

6.5.1 Unfolding Closure Test

The unfolding uncertainty takes into account the mismodelling of the data made by the MC simulated sample (non-closure). The method relies on the row-by-row weighting of the transfer matrices, shown in Figures 6.11 and 6.12, to enhance the agreement between the detector-level data and MC, given by the x -projection of the transfer matrices. The weights are therefore estimated as the ratio between the detector-level data and MC distributions:

$$w_j = \frac{D_j}{R_j}; \quad \tilde{M}_{ij} = w_j M_{ij}.$$

where D_j is the measured content in bin j for the data sample. The values of the weighted transfer matrix are represented by \tilde{M}_{ij} .

Figures 6.53 and 6.54 show the ratio of the detector-level MC and data distributions for the TEEC function before and after the weights are applied. Once the transfer matrices have been weighted, the detector-level MC distributions, defined as the x -projections of the weighted transfer matrices, are unfolded using the nominal transfer matrices and taking into account matching inefficiencies:

$$\tilde{R}_i = \frac{1}{\mathcal{P}_i} \sum_j \tilde{M}_{ij}; \quad \text{unf}_j(\tilde{R}) = \frac{1}{\mathcal{E}_j} \sum_i \mathcal{P}_i \tilde{R}_i P(\text{gen}_j | \text{reco}_i);$$

Afterwards, they are compared to the particle-level MC distributions, given by the y -projections of the weighted transfer matrices:

$$\tilde{T}_j = w_j T_j = \frac{1}{\mathcal{E}_j} \sum_i \tilde{M}_{ij}.$$

The differences between both distributions define the unfolding systematic uncertainty. Figures 6.55 to 6.58 show the relative systematic uncertainty of the TEEC and ATEEC distributions associated to the unfolding uncertainty. As expected, this uncertainty is negligible within the statistical uncertainties for the whole phase space owing to the reliability of the Iterative Bayesian unfolding procedure.

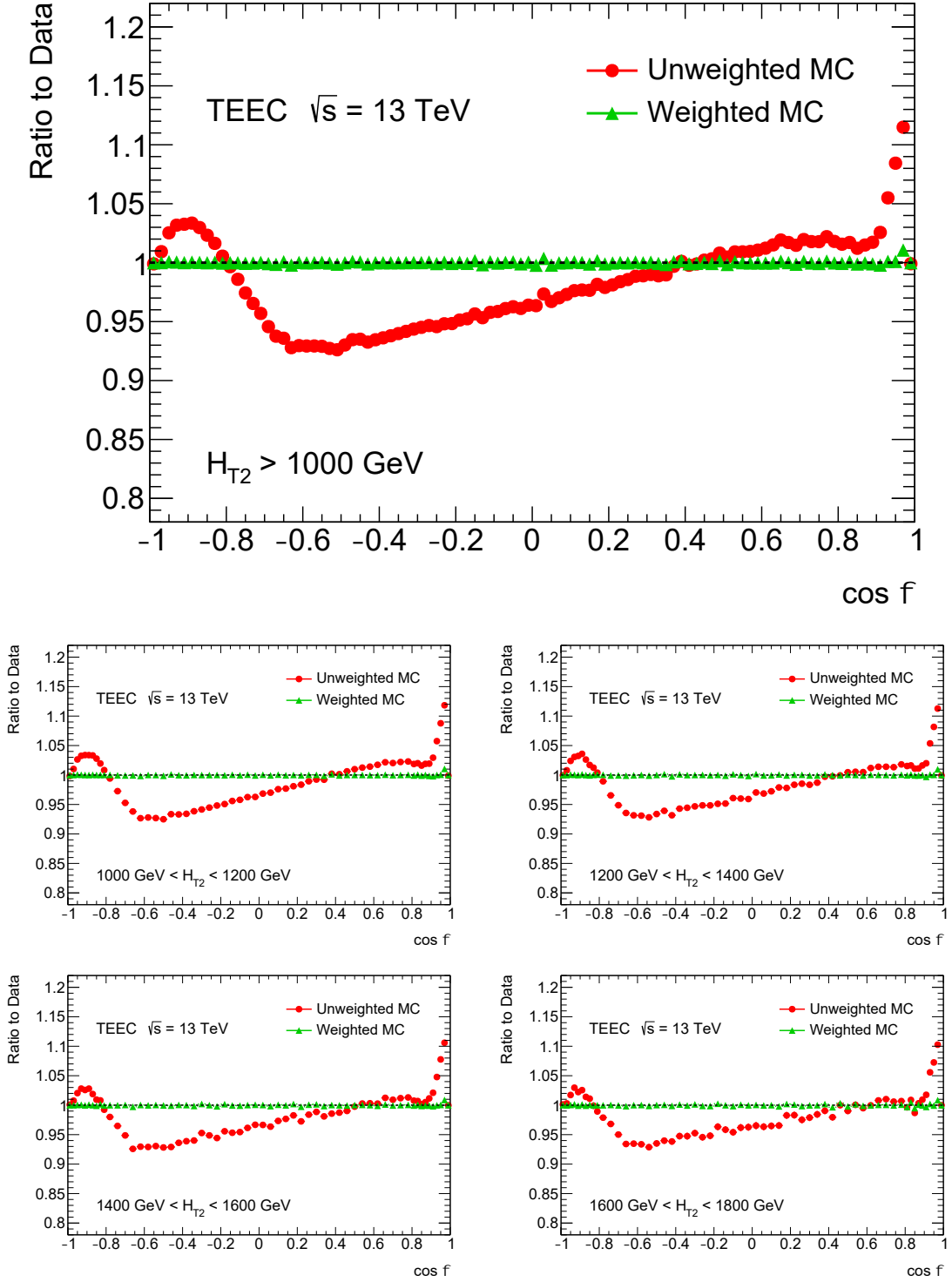


Figure 6.53: Ratios of the detector-level data to the detector-level MC TEEC distributions obtained from the MC simulated sample with the PYTHIA 8.235 event generator before (red) and after (green) the row-by-row weighting procedure, in inclusive (top) and exclusive (bottom) H_{T2} bins.

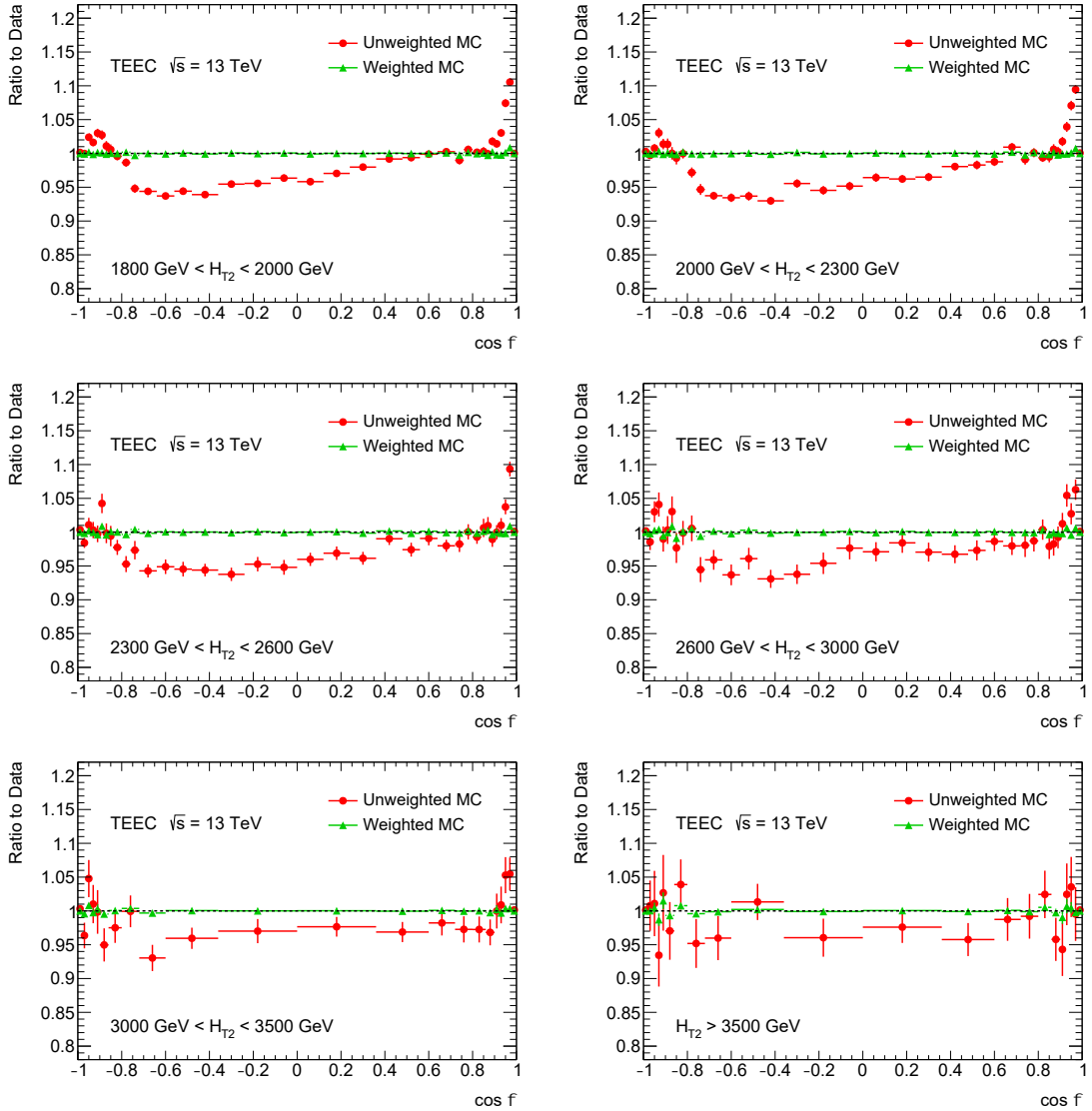


Figure 6.54: Ratios of the detector-level data to the detector-level MC TEEC distributions obtained from the MC simulated sample with the PYTHIA 8.235 event generator before (red) and after (green) the row-by-row weighting procedure, in exclusive H_{T2} bins.

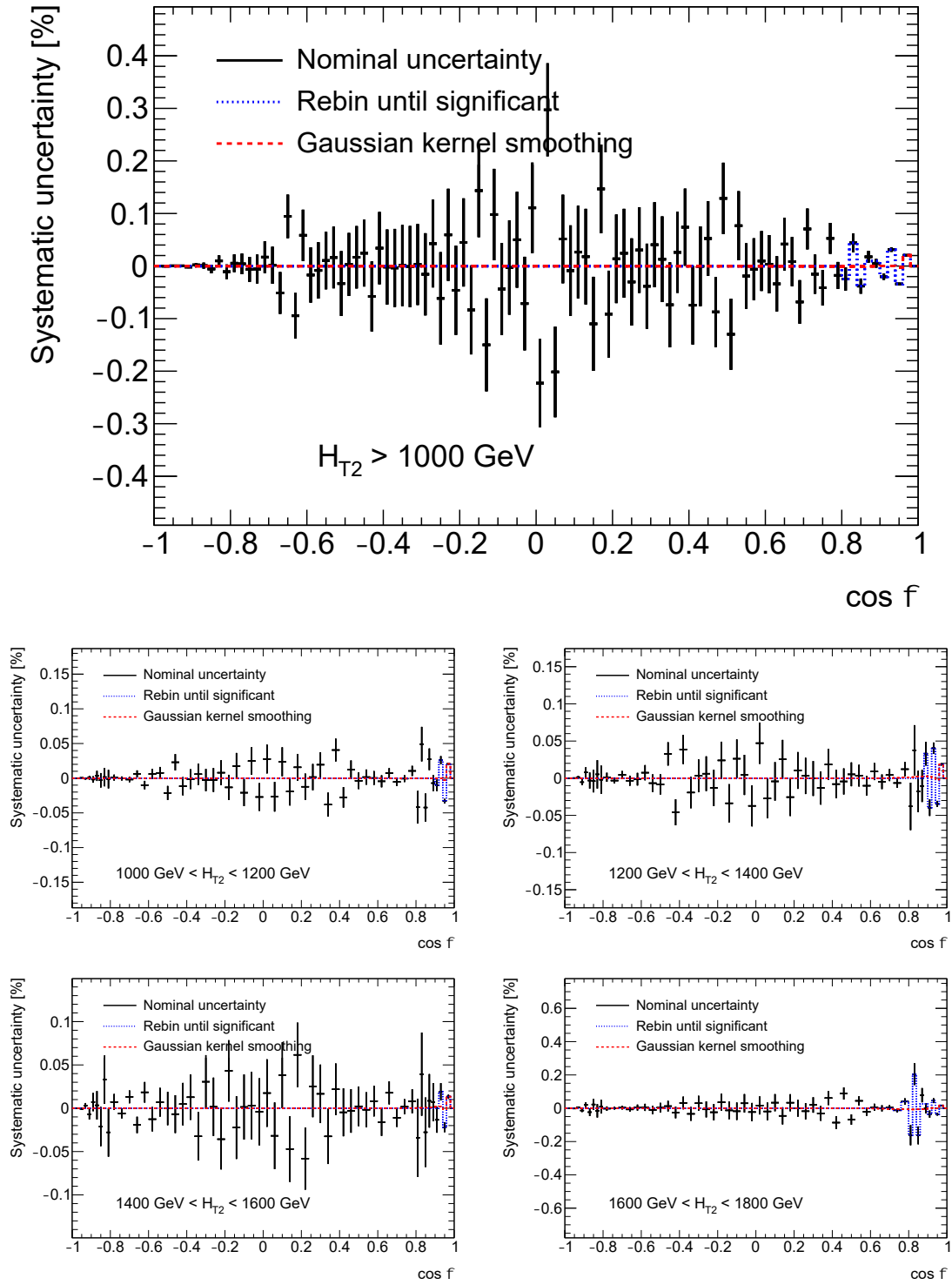


Figure 6.55: Relative systematic uncertainty due to the unfolding, in inclusive (top) and exclusive (bottom) H_{T2} bins, for the TEEC function obtained from the MC simulated sample with the PYTHIA 8.235 event generator. It is found to be compatible with zero within the statistical fluctuations.

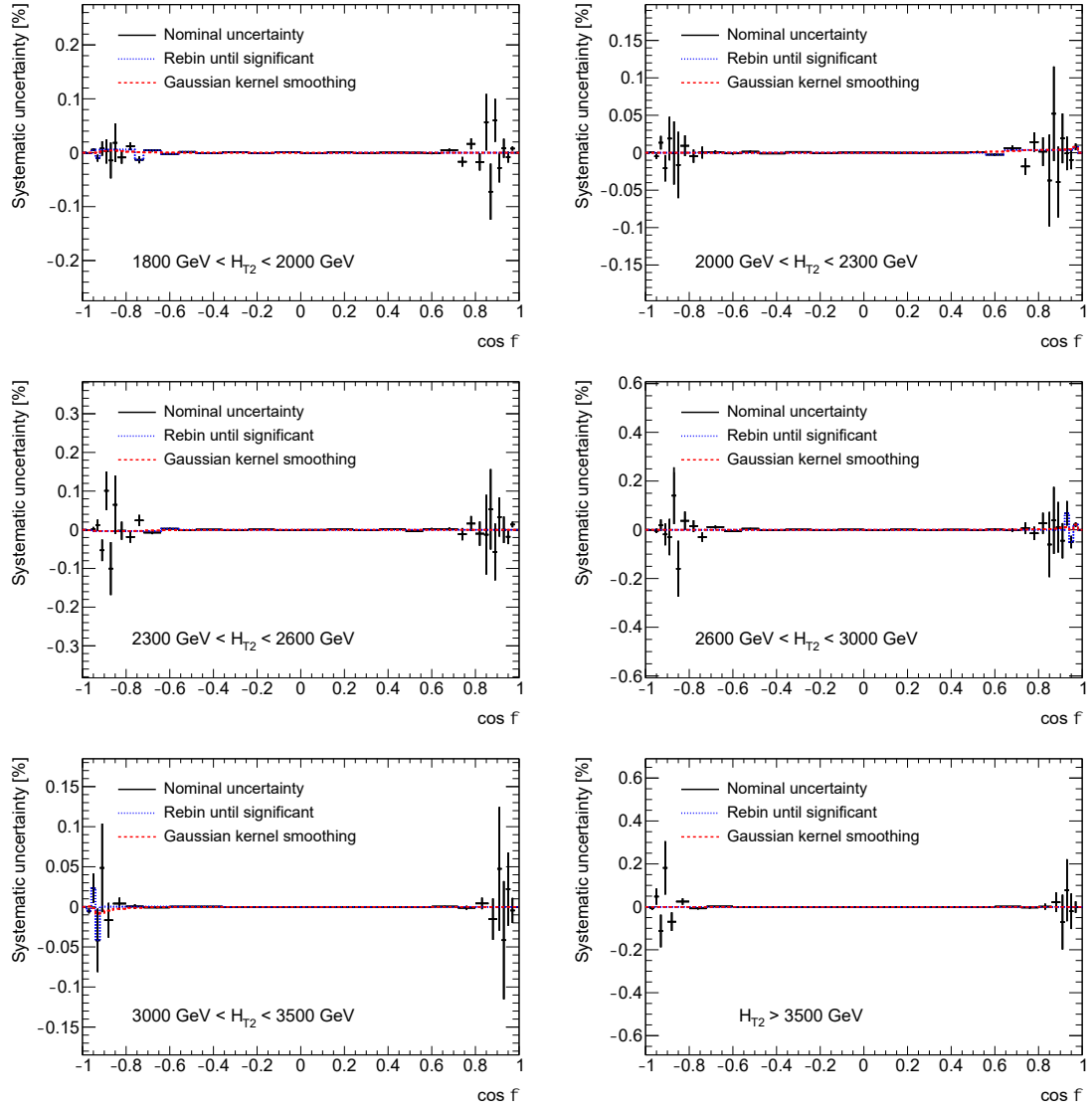


Figure 6.56: Relative systematic uncertainty due to the unfolding, in exclusive H_{T2} bins, for the TEEC function obtained from the MC simulated sample with the PYTHIA 8.235 event generator. It is found to be compatible with zero within the statistical fluctuations.

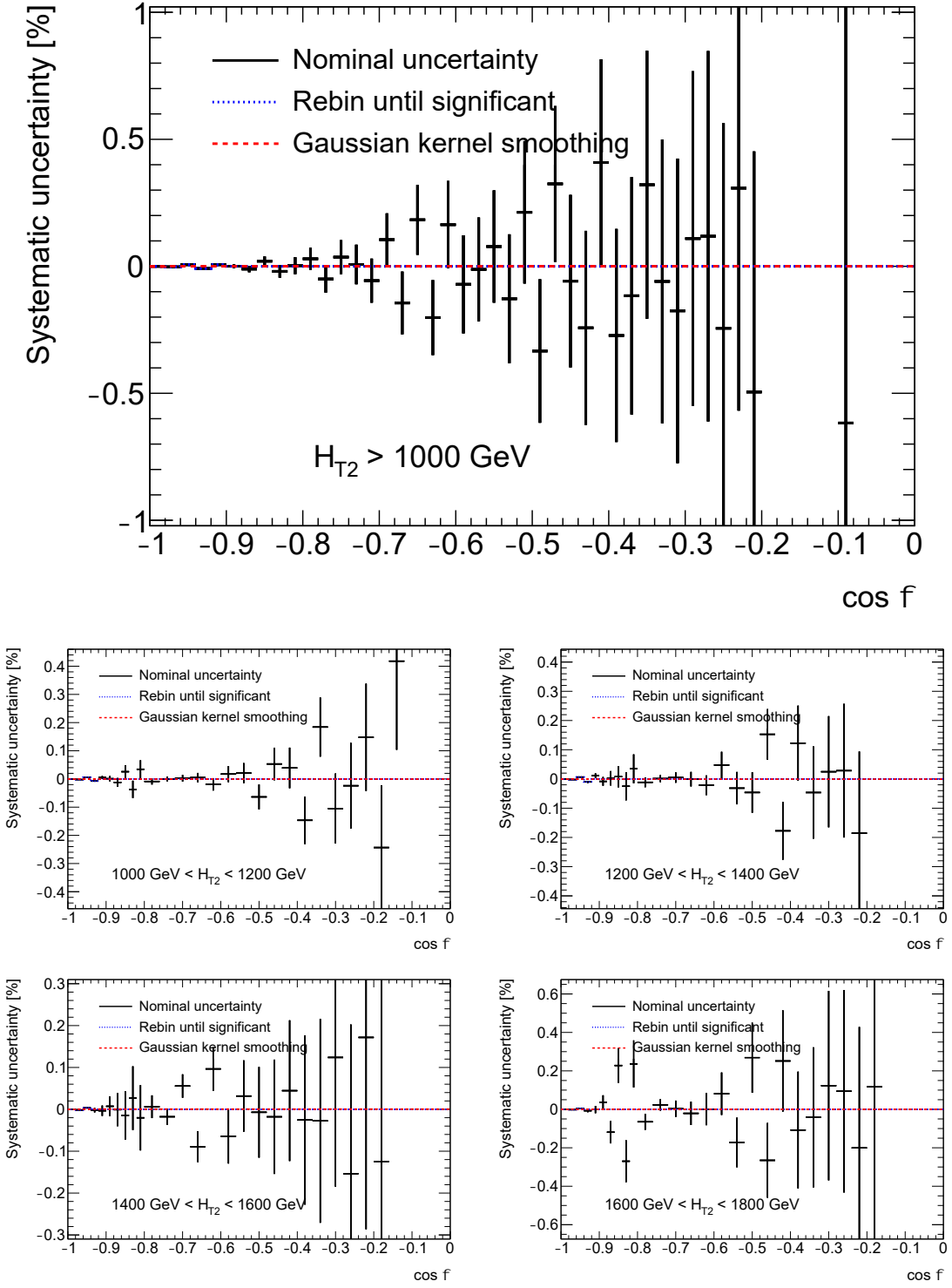


Figure 6.57: Relative systematic uncertainty due to the unfolding, in inclusive (top) and exclusive (bottom) H_{T2} bins, for the ATEEC function obtained from the MC simulated sample with the PYTHIA 8.235 event generator. It is found to be compatible with zero within the statistical fluctuations.

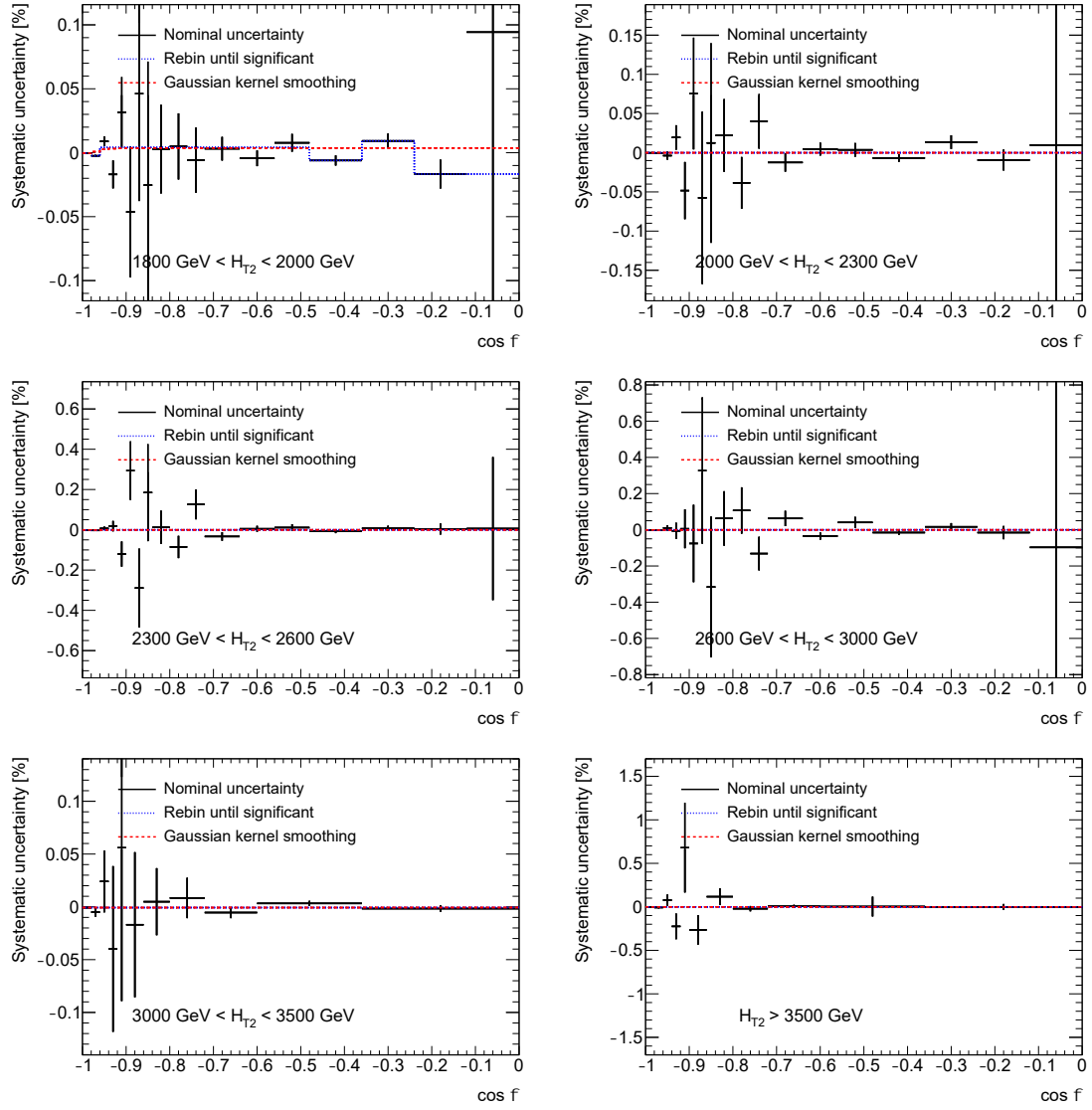


Figure 6.58: Relative systematic uncertainty due to the unfolding, in exclusive H_{T2} bins, for the ATEEC function obtained from the MC simulated sample with the PYTHIA 8.235 event generator. It is found to be compatible with zero within the statistical fluctuations.

6.6 Experimental results

The unfolded data including the estimated systematic uncertainties are compared with particle-level MC predictions. Figures 6.59 to 6.64 show this comparison for the TEEC and ATEEC distributions with particle-level MC predictions from PYTHIA 8.235, HERWIG 7.1.3 and SHERPA 2.1.1 event generators. Tables 6.6 to 6.27 present the numerical values for the TEEC and ATEEC functions, together with their statistical and systematic uncertainties.

The agreement of the particle-level predictions with data is good in general for all the MC event generators considered. However, SHERPA 2.1.1 which includes contributions due to $2 \rightarrow 3$ hard processes at LO describes the large angle ATEEC distributions a bit better than PYTHIA 8.235 which is a $2 \rightarrow 2$ event generator. HERWIG 7.1.3 exhibits some discrepancies but the improvement over older versions is very visible [1, 2]. In fact HERWIG 7.1.3 with angular-ordered parton shower is superior to the dipole version which fails to reproduce the large $|\cos \phi|$ region of the TEEC distributions in all H_{T2} bins.

To sum up, the following comments are in order:

- PYTHIA 8.235, SHERPA 2.1.1 and HERWIG 7.1.3 with angular-ordered parton shower give a similar and fairly good description of the correlations.
- PYTHIA 8.235 clearly underestimates the $\cos \phi > -0.70$ region of the asymmetries while SHERPA 2.1.1 provides a better agreement with data.
- HERWIG 7.1.3 with the dipole showering shows some discrepancies with the data in particular for $|\cos \phi| > 0.80$ regions of the correlations.

After comparing the experimental results with predictions from general-purpose event generators, the unfolded distributions are fitted to finite fixed-order pQCD calculations in order to extract the value of the strong coupling constant at different scale regimes. Thus, measuring asymptotic freedom at high-energy scales.

The predictions for the transverse energy-energy correlations and their asymmetries are also computed using the SHERPA 2.2.5 generated sample with the CT14 PDF group and the default CSS parton shower. The calculation only contains matrix elements for $2 \rightarrow 2$ hard processes at LO but the fragmentation follows two different hadronization schemes, the AHADIC model and the Lund string model. The results are found in Section A.1 and include a SHERPA 2.2.11 generated sample with a second parton shower called DIRE. Additionally, the distributions are computed using the POWHEG + PYTHIA 8.245 + EVTGEN 1.7.0 and the POWHEG + HERWIG 7.1.6 + EVTGEN 1.7.0 generated samples. Nevertheless, there is no improvement in the description of data when considering these two generated samples.

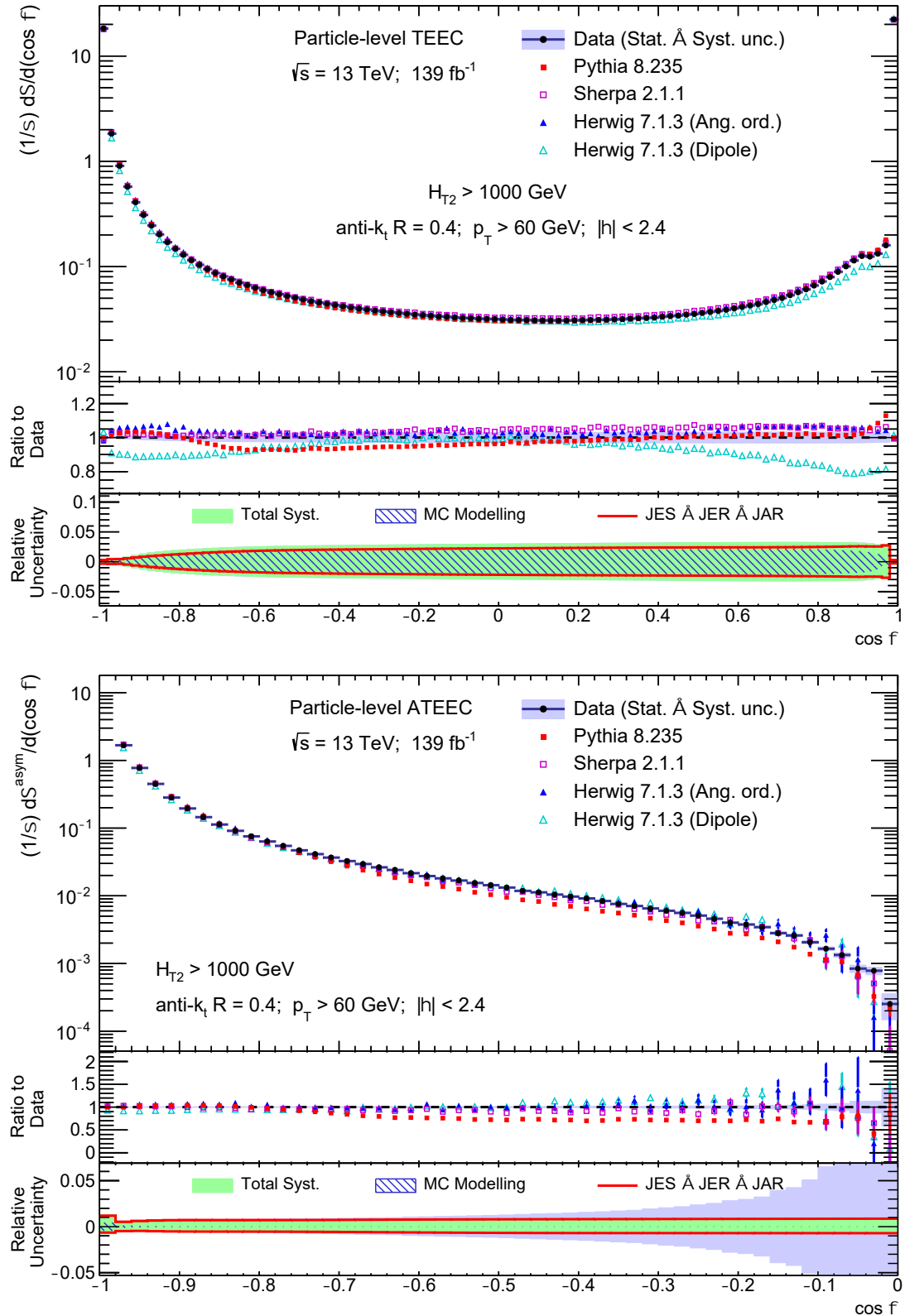


Figure 6.59: Particle-level TEEC (top) and ATEEC (bottom) distribution for the inclusive H_{T2} sample with the total experimental uncertainty (blue area), along with particle-level MC predictions. The relative systematic uncertainties (green area) are shown in the ratio pad below, while the ratio pad above compares the unfolded data and the MC predictions.

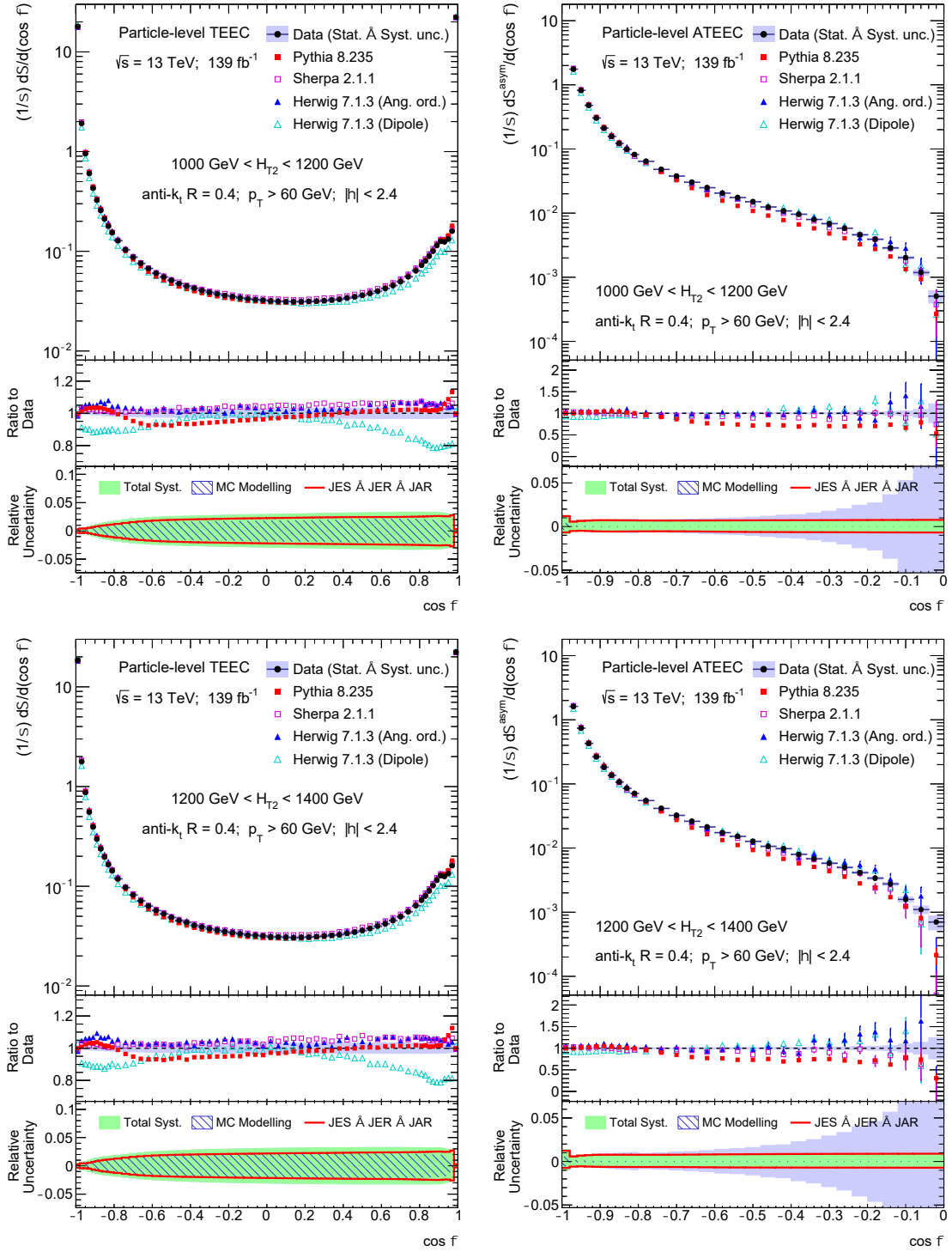


Figure 6.60: Particle-level TEEC (left) and ATEEC (right) distributions in two exclusive H_{T2} bins with the total experimental uncertainty (blue area), along with particle-level MC predictions. The relative systematic uncertainties (green area) are shown in the ratio pad below, while the ratio pad above compares the unfolded data and the MC predictions.

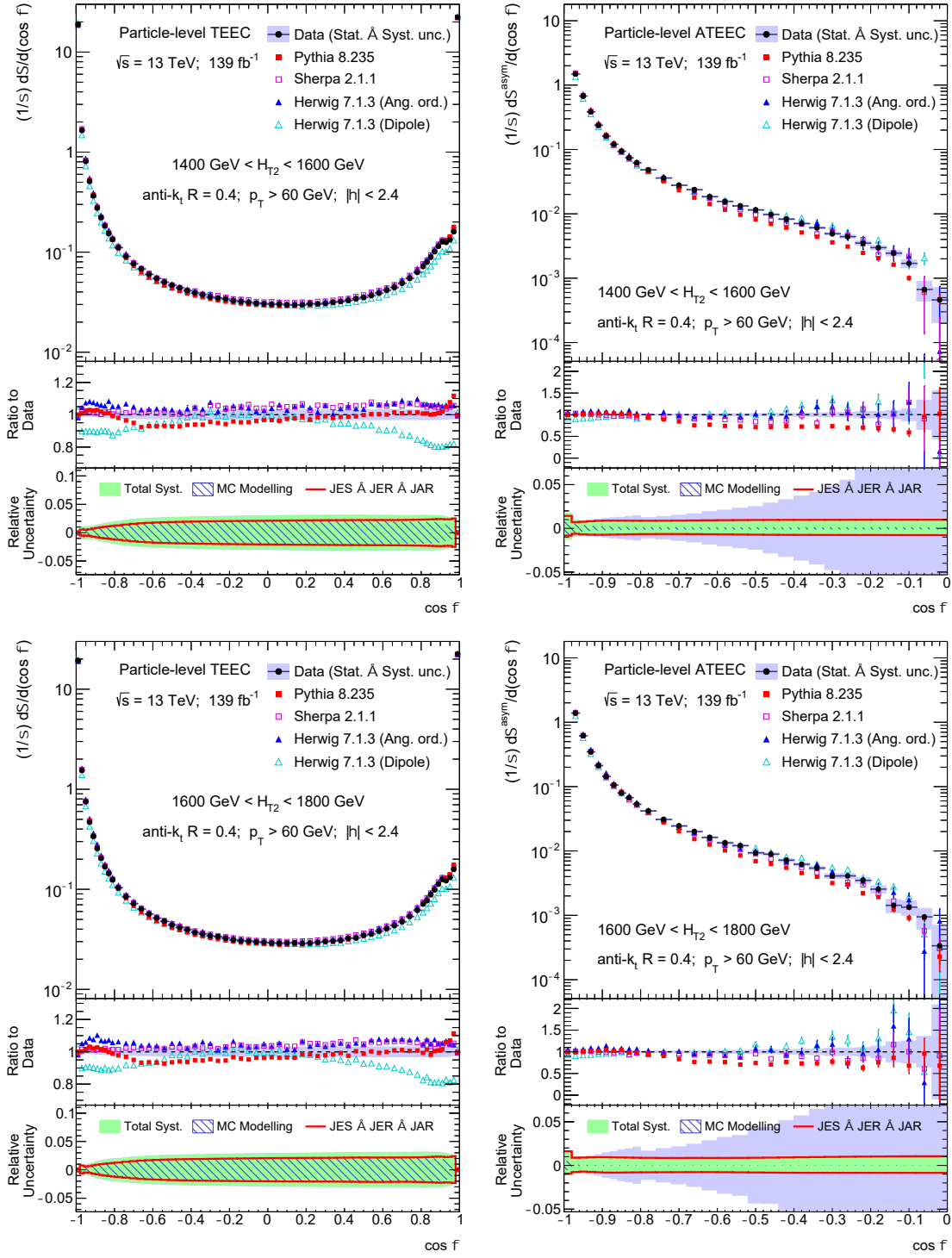


Figure 6.61: Particle-level TEEC (left) and ATEEC (right) distributions in two exclusive H_{T2} bins with the total experimental uncertainty (blue area), along with particle-level MC predictions. The relative systematic uncertainties (green area) are shown in the ratio pad below, while the ratio pad above compares the unfolded data and the MC predictions.

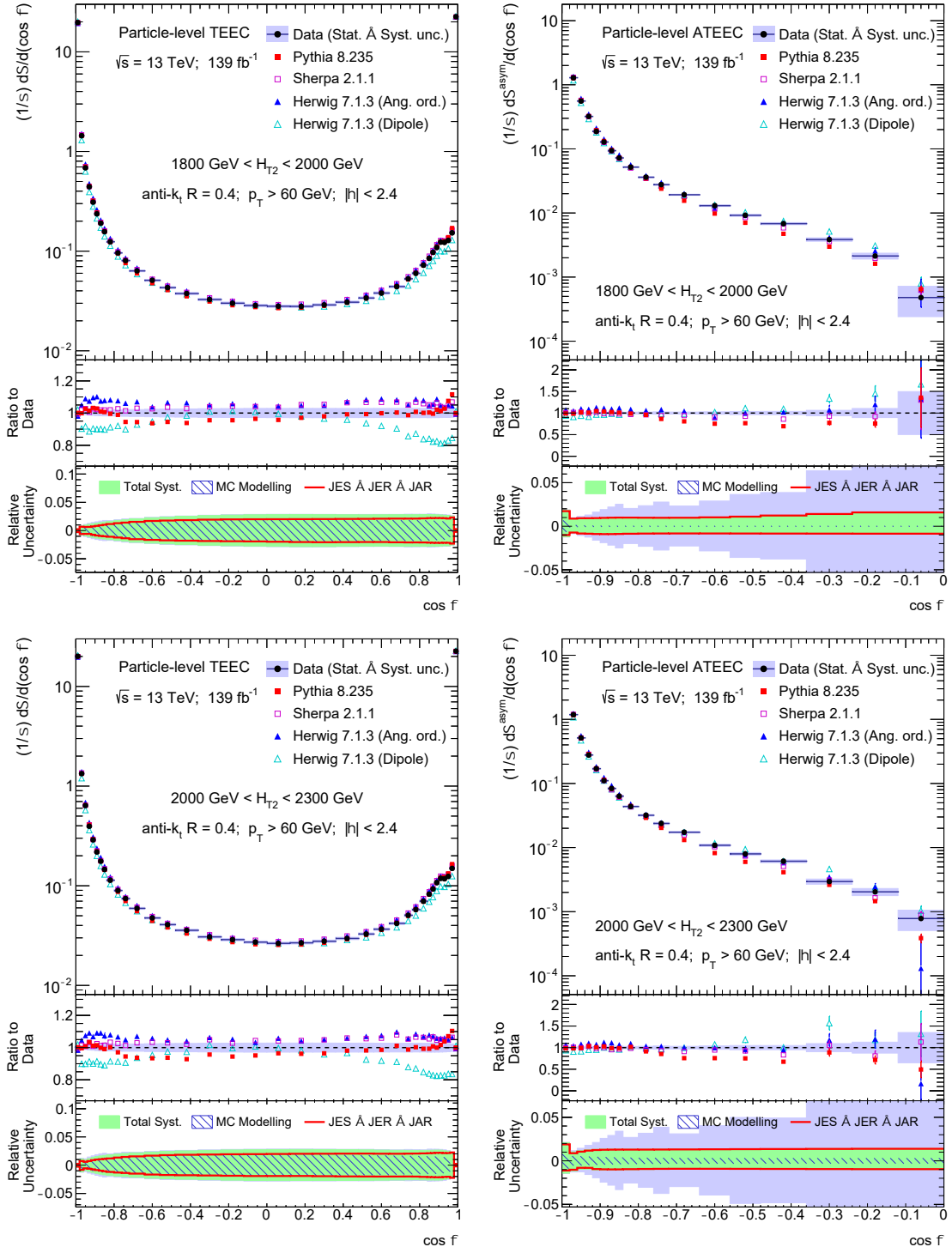


Figure 6.62: Particle-level TEEC (left) and ATEEC (right) distributions in two exclusive H_{T2} bins with the total experimental uncertainty (blue area), along with particle-level MC predictions. The relative systematic uncertainties (green area) are shown in the ratio pad below, while the ratio pad above compares the unfolded data and the MC predictions.

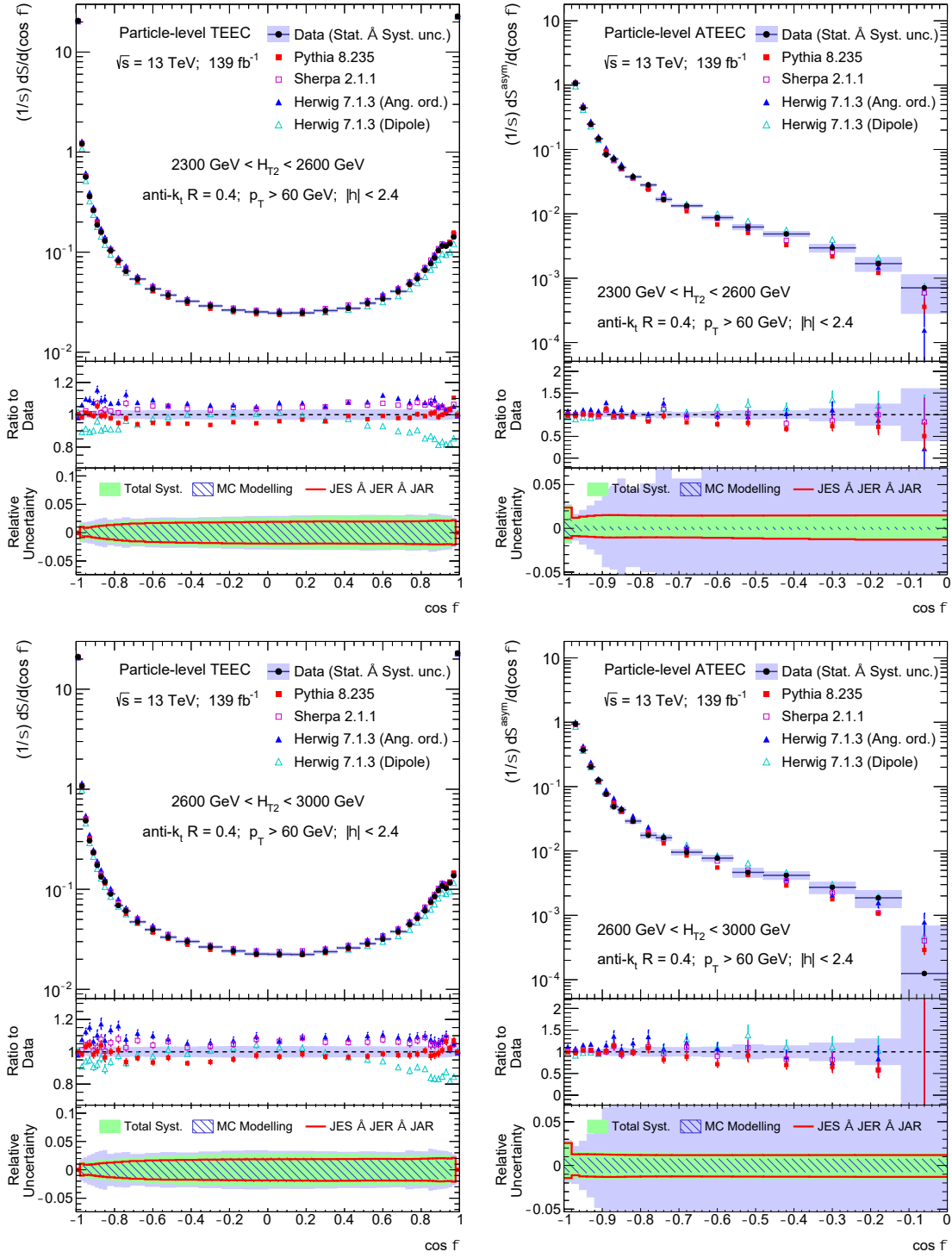


Figure 6.63: Particle-level TEEC (left) and ATEEC (right) distributions in two exclusive H_{T2} bins with the total experimental uncertainty (blue area), along with particle-level MC predictions. The relative systematic uncertainties (green area) are shown in the ratio pad below, while the ratio pad above compares the unfolded data and the MC predictions.

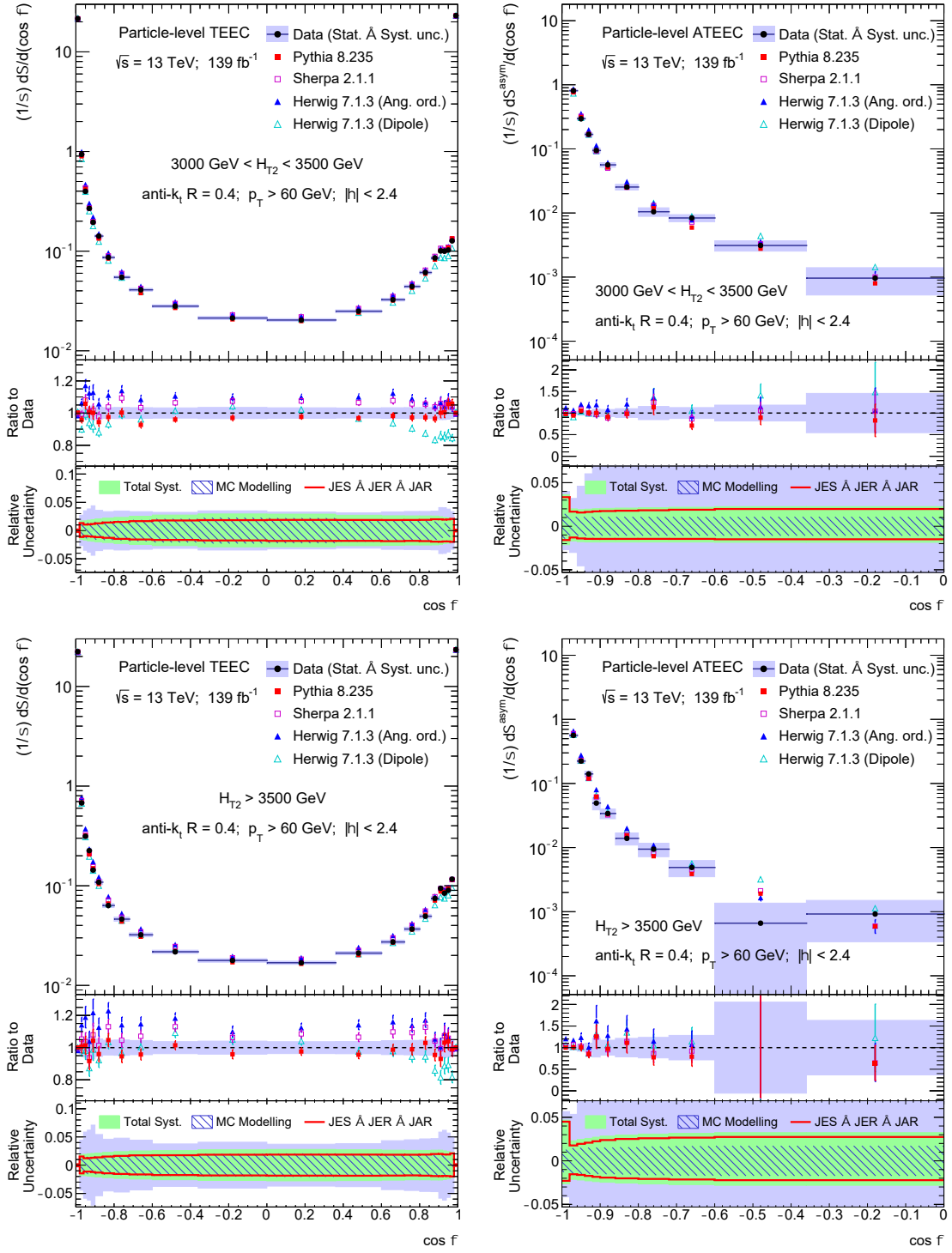


Figure 6.64: Particle-level TEEC (left) and ATEEC (right) distributions in two exclusive H_{T2} bins with the total experimental uncertainty (blue area), along with particle-level MC predictions. The relative systematic uncertainties (green area) are shown in the ratio pad below, while the ratio pad above compares the unfolded data and the MC predictions.

$\cos \phi$	Value	Stat.	JES	JER	JAR	MC Mod.
(-1.00 , -0.98)	18.29026	0.00140	+0.05145 -0.05324	+0.00874 -0.02827	0.00778	0.05232
(-0.98 , -0.96)	1.83224	0.00088	+0.00473 -0.00469	+0.00371 -0.00104	0.00483	0.00767
(-0.96 , -0.94)	0.90569	0.00062	+0.00303 -0.00281	+0.00215 -0.00062	0.00130	0.00388
(-0.94 , -0.92)	0.57387	0.00049	+0.00286 -0.00262	+0.00145 -0.00042	0.00043	0.00365
(-0.92 , -0.90)	0.40849	0.00042	+0.00268 -0.00251	+0.00106 -0.00030	0.00022	0.00340
(-0.90 , -0.88)	0.30922	0.00034	+0.00245 -0.00232	+0.00081 -0.00022	0.00012	0.00313
(-0.88 , -0.86)	0.24559	0.00030	+0.00223 -0.00216	+0.00064 -0.00018	0.00008	0.00285
(-0.86 , -0.84)	0.20211	0.00027	+0.00203 -0.00201	+0.00052 -0.00014	0.00007	0.00257
(-0.84 , -0.82)	0.17066	0.00025	+0.00188 -0.00187	+0.00044 -0.00012	0.00007	0.00232
(-0.82 , -0.80)	0.14768	0.00022	+0.00176 -0.00175	+0.00037 -0.00011	0.00007	0.00211
(-0.80 , -0.78)	0.12948	0.00021	+0.00165 -0.00164	+0.00032 -0.00010	0.00007	0.00192
(-0.78 , -0.76)	0.11535	0.00019	+0.00156 -0.00155	+0.00028 -0.00009	0.00007	0.00176
(-0.76 , -0.74)	0.10402	0.00018	+0.00149 -0.00147	+0.00025 -0.00007	0.00006	0.00163
(-0.74 , -0.72)	0.09473	0.00017	+0.00142 -0.00141	+0.00022 -0.00006	0.00005	0.00151
(-0.72 , -0.70)	0.08693	0.00016	+0.00136 -0.00134	+0.00020 -0.00006	0.00004	0.00141
(-0.70 , -0.68)	0.08072	0.00016	+0.00131 -0.00129	+0.00018 -0.00006	0.00004	0.00133
(-0.68 , -0.66)	0.07547	0.00015	+0.00127 -0.00124	+0.00016 -0.00005	0.00003	0.00126
(-0.66 , -0.64)	0.07034	0.00014	+0.00121 -0.00119	+0.00015 -0.00005	0.00002	0.00119
(-0.64 , -0.62)	0.06674	0.00013	+0.00118 -0.00116	+0.00014 -0.00005	0.00002	0.00113
(-0.62 , -0.60)	0.06290	0.00013	+0.00114 -0.00111	+0.00013 -0.00005	0.00002	0.00108
(-0.60 , -0.58)	0.05969	0.00013	+0.00110 -0.00107	+0.00012 -0.00005	0.00001	0.00103
(-0.58 , -0.56)	0.05696	0.00012	+0.00106 -0.00104	+0.00011 -0.00004	0.00001	0.00099
(-0.56 , -0.54)	0.05471	0.00012	+0.00104 -0.00102	+0.00011 -0.00004	0.00001	0.00096
(-0.54 , -0.52)	0.05253	0.00011	+0.00101 -0.00099	+0.00010 -0.00004	0.00001	0.00092
(-0.52 , -0.50)	0.05064	0.00011	+0.00098 -0.00096	+0.00010 -0.00004	0.00001	0.00089
(-0.50 , -0.48)	0.04867	0.00011	+0.00095 -0.00094	+0.00009 -0.00004	0.00001	0.00086
(-0.48 , -0.46)	0.04681	0.00010	+0.00092 -0.00091	+0.00009 -0.00004	0.00001	0.00083
(-0.46 , -0.44)	0.04550	0.00010	+0.00091 -0.00089	+0.00009 -0.00004	0.00001	0.00081
(-0.44 , -0.42)	0.04434	0.00010	+0.00089 -0.00087	+0.00008 -0.00004	0.00001	0.00080
(-0.42 , -0.40)	0.04313	0.00010	+0.00087 -0.00086	+0.00008 -0.00004	0.00001	0.00078
(-0.40 , -0.38)	0.04190	0.00010	+0.00085 -0.00084	+0.00008 -0.00004	0.00001	0.00076
(-0.38 , -0.36)	0.04090	0.00009	+0.00084 -0.00082	+0.00008 -0.00004	0.00001	0.00074
(-0.36 , -0.34)	0.03989	0.00009	+0.00082 -0.00081	+0.00008 -0.00004	0.00001	0.00073
(-0.34 , -0.32)	0.03910	0.00009	+0.00081 -0.00079	+0.00007 -0.00004	0.00001	0.00072
(-0.32 , -0.30)	0.03816	0.00009	+0.00079 -0.00078	+0.00007 -0.00003	0.00001	0.00070
(-0.30 , -0.28)	0.03750	0.00009	+0.00078 -0.00077	+0.00007 -0.00003	0.00001	0.00069
(-0.28 , -0.26)	0.03683	0.00009	+0.00077 -0.00076	+0.00007 -0.00003	0.00001	0.00068
(-0.26 , -0.24)	0.03625	0.00009	+0.00077 -0.00075	+0.00007 -0.00003	0.00001	0.00067
(-0.24 , -0.22)	0.03563	0.00008	+0.00076 -0.00074	+0.00007 -0.00003	0.00001	0.00067
(-0.22 , -0.20)	0.03499	0.00008	+0.00075 -0.00073	+0.00007 -0.00003	0.00001	0.00066
(-0.20 , -0.18)	0.03457	0.00008	+0.00074 -0.00073	+0.00007 -0.00003	0.00001	0.00065
(-0.18 , -0.16)	0.03415	0.00008	+0.00074 -0.00072	+0.00007 -0.00003	0.00001	0.00065
(-0.16 , -0.14)	0.03355	0.00008	+0.00073 -0.00071	+0.00006 -0.00003	0.00001	0.00064
(-0.14 , -0.12)	0.03335	0.00008	+0.00073 -0.00071	+0.00006 -0.00003	0.00001	0.00063

(-0.12 , -0.10)	0.03283	0.00008	+0.00072	+0.00006	0.00001	0.00063
(-0.10 , -0.08)	0.03249	0.00008	+0.00071	+0.00006	0.00001	0.00062
(-0.08 , -0.06)	0.03236	0.00008	+0.00071	+0.00006	0.00001	0.00062
(-0.06 , -0.04)	0.03194	0.00008	+0.00071	+0.00006	0.00001	0.00062
(-0.04 , -0.02)	0.03184	0.00007	+0.00071	+0.00006	0.00000	0.00062
(-0.02 , 0.00)	0.03167	0.00008	+0.00070	+0.00006	0.00000	0.00061
(0.00 , 0.02)	0.03142	0.00007	+0.00070	+0.00006	0.00000	0.00061
(0.02 , 0.04)	0.03106	0.00007	+0.00070	+0.00006	0.00000	0.00061
(0.04 , 0.06)	0.03110	0.00007	+0.00070	+0.00006	0.00000	0.00061
(0.06 , 0.08)	0.03102	0.00007	+0.00070	+0.00006	0.00000	0.00061
(0.08 , 0.10)	0.03083	0.00007	+0.00070	+0.00006	0.00000	0.00061
(0.10 , 0.12)	0.03077	0.00007	+0.00070	+0.00006	0.00000	0.00061
(0.12 , 0.14)	0.03075	0.00007	+0.00070	+0.00006	0.00000	0.00061
(0.14 , 0.16)	0.03074	0.00007	+0.00070	+0.00006	0.00000	0.00061
(0.16 , 0.18)	0.03070	0.00007	+0.00070	+0.00006	0.00000	0.00061
(0.18 , 0.20)	0.03080	0.00007	+0.00071	+0.00006	0.00000	0.00062
(0.20 , 0.22)	0.03099	0.00007	+0.00071	+0.00006	0.00000	0.00062
(0.22 , 0.24)	0.03105	0.00007	+0.00072	+0.00006	0.00000	0.00063
(0.24 , 0.26)	0.03115	0.00007	+0.00072	+0.00006	0.00000	0.00063
(0.26 , 0.28)	0.03124	0.00007	+0.00073	+0.00006	0.00000	0.00063
(0.28 , 0.30)	0.03149	0.00007	+0.00074	+0.00006	0.00000	0.00064
(0.30 , 0.32)	0.03166	0.00007	+0.00074	+0.00006	0.00000	0.00065
(0.32 , 0.34)	0.03203	0.00007	+0.00075	+0.00007	0.00001	0.00066
(0.34 , 0.36)	0.03231	0.00007	+0.00076	+0.00007	0.00001	0.00066
(0.36 , 0.38)	0.03252	0.00007	+0.00077	+0.00007	0.00001	0.00067
(0.38 , 0.40)	0.03274	0.00007	+0.00077	+0.00007	0.00001	0.00068
(0.40 , 0.42)	0.03339	0.00007	+0.00079	+0.00007	0.00001	0.00069
(0.42 , 0.44)	0.03392	0.00008	+0.00081	+0.00007	0.00001	0.00071
(0.44 , 0.46)	0.03425	0.00007	+0.00082	+0.00007	0.00001	0.00072
(0.46 , 0.48)	0.03498	0.00007	+0.00083	+0.00007	0.00001	0.00073
(0.48 , 0.50)	0.03543	0.00007	+0.00085	+0.00007	0.00001	0.00075
(0.50 , 0.52)	0.03629	0.00008	+0.00087	+0.00008	0.00001	0.00077
(0.52 , 0.54)	0.03708	0.00008	+0.00089	+0.00008	0.00001	0.00079
(0.54 , 0.56)	0.03790	0.00008	+0.00091	+0.00008	0.00001	0.00081
(0.56 , 0.58)	0.03886	0.00008	+0.00093	+0.00008	0.00001	0.00083
(0.58 , 0.60)	0.04013	0.00008	+0.00096	+0.00009	0.00001	0.00086
(0.60 , 0.62)	0.04132	0.00009	+0.00099	+0.00009	0.00001	0.00089
(0.62 , 0.64)	0.04266	0.00008	+0.00102	+0.00009	0.00001	0.00092
(0.64 , 0.66)	0.04402	0.00009	+0.00106	+0.00009	0.00001	0.00095
(0.66 , 0.68)	0.04601	0.00009	+0.00111	+0.00010	0.00001	0.00099
(0.68 , 0.70)	0.04815	0.00009	+0.00116	+0.00010	0.00001	0.00104
(0.70 , 0.72)	0.05025	0.00009	+0.00122	+0.00011	0.00001	0.00108
(0.72 , 0.74)	0.05346	0.00009	+0.00130	+0.00012	0.00001	0.00115
(0.74 , 0.76)	0.05705	0.00010	+0.00128	-0.00007	0.00001	0.00122
(0.76 , 0.78)	0.06077	0.00010	+0.00139	+0.00012	0.00001	0.00128
(0.78 , 0.80)	0.06608	0.00010	+0.00162	+0.00014	0.00001	0.00138

(0.80 , 0.82)	0.07218	0.00011	+0.00178 -0.00176	+0.00016 -0.00009	0.00002	0.00148
(0.82 , 0.84)	0.07957	0.00011	+0.00198 -0.00195	+0.00018 -0.00010	0.00001	0.00160
(0.84 , 0.86)	0.08921	0.00012	+0.00224 -0.00221	+0.00020 -0.00011	0.00003	0.00176
(0.86 , 0.88)	0.10050	0.00012	+0.00255 -0.00251	+0.00023 -0.00013	0.00013	0.00193
(0.88 , 0.90)	0.11423	0.00013	+0.00292 -0.00287	+0.00027 -0.00015	0.00026	0.00213
(0.90 , 0.92)	0.12626	0.00013	+0.00323 -0.00317	+0.00031 -0.00016	0.00026	0.00224
(0.92 , 0.94)	0.12456	0.00014	+0.00317 -0.00310	+0.00030 -0.00017	0.00018	0.00202
(0.94 , 0.96)	0.13282	0.00013	+0.00337 -0.00331	+0.00031 -0.00019	0.00013	0.00170
(0.96 , 0.98)	0.15937	0.00014	+0.00432 -0.00427	+0.00038 -0.00025	0.00011	0.00116
(0.98 , 1.00)	22.31758	0.00047	+0.06378 -0.06466	+0.01507 -0.00487	0.00003	0.05145

Table 6.6: Numerical values of the TEEC function together with statistical and systematic uncertainties for $H_{T2} > 1000$ GeV.

$\cos \phi$	Value	Stat.	JES	JER	JAR	MC Mod.
(-1.00 , -0.98)	17.99154	0.00190	+0.04996 -0.05221	+0.00952 -0.02999	0.00781	0.04782
(-0.98 , -0.96)	1.91746	0.00117	+0.00529 -0.00508	+0.00403 -0.00156	0.00473	0.00748
(-0.96 , -0.94)	0.95296	0.00083	+0.00306 -0.00266	+0.00236 -0.00078	0.00109	0.00303
(-0.94 , -0.92)	0.60412	0.00066	+0.00281 -0.00247	+0.00161 -0.00050	0.00054	0.00319
(-0.92 , -0.90)	0.42989	0.00055	+0.00262 -0.00240	+0.00118 -0.00036	0.00026	0.00298
(-0.90 , -0.88)	0.32565	0.00047	+0.00240 -0.00225	+0.00091 -0.00028	0.00016	0.00274
(-0.88 , -0.86)	0.25755	0.00041	+0.00217 -0.00209	+0.00072 -0.00022	0.00013	0.00249
(-0.86 , -0.84)	0.21147	0.00037	+0.00197 -0.00195	+0.00059 -0.00019	0.00012	0.00226
(-0.84 , -0.82)	0.17881	0.00034	+0.00181 -0.00180	+0.00049 -0.00016	0.00011	0.00206
(-0.82 , -0.80)	0.15430	0.00031	+0.00168 -0.00167	+0.00042 -0.00014	0.00011	0.00189
(-0.80 , -0.76)	0.12796	0.00017	+0.00154 -0.00153	+0.00034 -0.00009	0.00008	0.00167
(-0.76 , -0.72)	0.10354	0.00015	+0.00142 -0.00141	+0.00026 -0.00008	0.00005	0.00145
(-0.72 , -0.68)	0.08730	0.00014	+0.00133 -0.00131	+0.00021 -0.00007	0.00002	0.00128
(-0.68 , -0.64)	0.07563	0.00013	+0.00125 -0.00122	+0.00018 -0.00006	0.00002	0.00114
(-0.64 , -0.60)	0.06726	0.00012	+0.00117 -0.00115	+0.00015 -0.00005	0.00001	0.00104
(-0.60 , -0.56)	0.06026	0.00011	+0.00110 -0.00107	+0.00013 -0.00004	0.00001	0.00095
(-0.56 , -0.52)	0.05530	0.00010	+0.00104 -0.00102	+0.00012 -0.00004	0.00001	0.00088
(-0.52 , -0.48)	0.05126	0.00010	+0.00099 -0.00097	+0.00010 -0.00005	0.00001	0.00083
(-0.48 , -0.44)	0.04742	0.00010	+0.00093 -0.00092	+0.00009 -0.00004	0.00001	0.00077
(-0.44 , -0.40)	0.04484	0.00009	+0.00090 -0.00088	+0.00009 -0.00004	0.00001	0.00074
(-0.40 , -0.36)	0.04261	0.00009	+0.00087 -0.00085	+0.00008 -0.00004	0.00001	0.00071
(-0.36 , -0.32)	0.04049	0.00009	+0.00083 -0.00082	+0.00008 -0.00004	0.00001	0.00068
(-0.32 , -0.28)	0.03882	0.00008	+0.00081 -0.00080	+0.00007 -0.00003	0.00001	0.00066
(-0.28 , -0.24)	0.03740	0.00008	+0.00079 -0.00078	+0.00007 -0.00003	0.00001	0.00064
(-0.24 , -0.20)	0.03606	0.00008	+0.00077 -0.00076	+0.00007 -0.00003	0.00001	0.00063
(-0.20 , -0.16)	0.03514	0.00008	+0.00076 -0.00074	+0.00007 -0.00003	0.00001	0.00062
(-0.16 , -0.12)	0.03410	0.00008	+0.00075 -0.00073	+0.00007 -0.00003	0.00001	0.00060
(-0.12 , -0.08)	0.03331	0.00008	+0.00073 -0.00072	+0.00006 -0.00003	0.00001	0.00060
(-0.08 , -0.04)	0.03273	0.00007	+0.00073 -0.00071	+0.00006 -0.00003	0.00001	0.00059
(-0.04 , 0.00)	0.03232	0.00007	+0.00072 -0.00071	+0.00006 -0.00003	0.00001	0.00059
(0.00 , 0.04)	0.03182	0.00007	+0.00072 -0.00070	+0.00006 -0.00003	0.00001	0.00059

(0.04 , 0.08)	0.03154	0.00007	+0.00072 -0.00070	+0.00006 -0.00003	0.00001	0.00059
(0.08 , 0.12)	0.03129	0.00007	+0.00072 -0.00070	+0.00006 -0.00003	0.00001	0.00059
(0.12 , 0.16)	0.03124	0.00007	+0.00072 -0.00070	+0.00006 -0.00004	0.00001	0.00059
(0.16 , 0.20)	0.03123	0.00007	+0.00073 -0.00071	+0.00006 -0.00004	0.00001	0.00060
(0.20 , 0.24)	0.03147	0.00007	+0.00074 -0.00072	+0.00006 -0.00004	0.00001	0.00061
(0.24 , 0.28)	0.03159	0.00007	+0.00075 -0.00072	+0.00006 -0.00004	0.00001	0.00062
(0.28 , 0.32)	0.03197	0.00007	+0.00076 -0.00074	+0.00007 -0.00004	0.00001	0.00063
(0.32 , 0.36)	0.03253	0.00007	+0.00078 -0.00075	+0.00007 -0.00004	0.00001	0.00065
(0.36 , 0.40)	0.03301	0.00007	+0.00079 -0.00077	+0.00007 -0.00004	0.00001	0.00066
(0.40 , 0.44)	0.03403	0.00007	+0.00082 -0.00080	+0.00007 -0.00004	0.00001	0.00069
(0.44 , 0.48)	0.03496	0.00007	+0.00085 -0.00082	+0.00007 -0.00004	0.00001	0.00072
(0.48 , 0.52)	0.03618	0.00007	+0.00088 -0.00086	+0.00008 -0.00004	0.00001	0.00075
(0.52 , 0.56)	0.03783	0.00007	+0.00092 -0.00090	+0.00008 -0.00005	0.00001	0.00079
(0.56 , 0.60)	0.03978	0.00007	+0.00097 -0.00095	+0.00009 -0.00005	0.00001	0.00084
(0.60 , 0.64)	0.04235	0.00008	+0.00103 -0.00102	+0.00009 -0.00005	0.00002	0.00090
(0.64 , 0.68)	0.04536	0.00008	+0.00111 -0.00110	+0.00010 -0.00006	0.00002	0.00098
(0.68 , 0.72)	0.04952	0.00008	+0.00122 -0.00120	+0.00011 -0.00006	0.00003	0.00107
(0.72 , 0.76)	0.05556	0.00008	+0.00138 -0.00136	+0.00013 -0.00007	0.00002	0.00120
(0.76 , 0.80)	0.06378	0.00008	+0.00160 -0.00158	+0.00015 -0.00008	0.00002	0.00135
(0.80 , 0.82)	0.07249	0.00014	+0.00183 -0.00181	+0.00017 -0.00009	0.00001	0.00151
(0.82 , 0.84)	0.07994	0.00015	+0.00203 -0.00200	+0.00019 -0.00010	0.00001	0.00164
(0.84 , 0.86)	0.08940	0.00016	+0.00229 -0.00225	+0.00021 -0.00011	0.00002	0.00180
(0.86 , 0.88)	0.10047	0.00016	+0.00260 -0.00255	+0.00024 -0.00013	0.00011	0.00199
(0.88 , 0.90)	0.11438	0.00017	+0.00298 -0.00292	+0.00028 -0.00015	0.00028	0.00221
(0.90 , 0.92)	0.12585	0.00018	+0.00327 -0.00321	+0.00031 -0.00017	0.00035	0.00234
(0.92 , 0.94)	0.12470	0.00018	+0.00321 -0.00314	+0.00031 -0.00017	0.00004	0.00217
(0.94 , 0.96)	0.13293	0.00017	+0.00342 -0.00338	+0.00031 -0.00019	0.00022	0.00197
(0.96 , 0.98)	0.15945	0.00019	+0.00439 -0.00437	+0.00040 -0.00028	0.00018	0.00089
(0.98 , 1.00)	22.29510	0.00064	+0.06586 -0.06676	+0.01502 -0.00496	0.00004	0.05192

Table 6.7: Numerical values of the TEEC function together with statistical and systematic uncertainties for $1000 \text{ GeV} < H_{\text{T2}} < 1200 \text{ GeV}$.

$\cos \phi$	Value	Stat.	JES	JER	JAR	MC Mod.
(-1.00 , -0.98)	18.47755	0.00286	+0.05078 -0.05143	+0.00883 -0.02613	0.00739	0.06643
(-0.98 , -0.96)	1.77902	0.00179	+0.00557 -0.00629	+0.00330 -0.00103	0.00460	0.00833
(-0.96 , -0.94)	0.87397	0.00124	+0.00311 -0.00326	+0.00188 -0.00069	0.00106	0.00511
(-0.94 , -0.92)	0.55446	0.00097	+0.00271 -0.00267	+0.00128 -0.00051	0.00036	0.00466
(-0.92 , -0.90)	0.39347	0.00081	+0.00257 -0.00246	+0.00094 -0.00037	0.00019	0.00398
(-0.90 , -0.88)	0.29732	0.00068	+0.00237 -0.00228	+0.00072 -0.00028	0.00013	0.00332
(-0.88 , -0.86)	0.23771	0.00062	+0.00218 -0.00212	+0.00058 -0.00023	0.00010	0.00281
(-0.86 , -0.84)	0.19686	0.00055	+0.00199 -0.00195	+0.00048 -0.00019	0.00009	0.00241
(-0.84 , -0.82)	0.16548	0.00050	+0.00180 -0.00178	+0.00040 -0.00017	0.00007	0.00208
(-0.82 , -0.80)	0.14349	0.00046	+0.00166 -0.00164	+0.00034 -0.00015	0.00006	0.00185
(-0.80 , -0.76)	0.11876	0.00026	+0.00151 -0.00150	+0.00028 -0.00012	0.00005	0.00160
(-0.76 , -0.72)	0.09705	0.00022	+0.00139 -0.00137	+0.00022 -0.00010	0.00003	0.00138

(-0.72 , -0.68)	0.08183	0.00020	+0.00128	+0.00017	0.00002	0.00122
(-0.68 , -0.64)	0.07138	0.00018	+0.00120	+0.00014	0.00002	0.00112
(-0.64 , -0.60)	0.06333	0.00017	-0.00118	-0.00005	0.00002	0.00103
(-0.60 , -0.56)	0.05720	0.00017	+0.00112	+0.00012	0.00001	0.00097
(-0.56 , -0.52)	0.05292	0.00015	+0.00100	+0.00010	0.00001	0.00093
(-0.52 , -0.48)	0.04869	0.00014	+0.00094	+0.00009	0.00001	0.00088
(-0.48 , -0.44)	0.04538	0.00014	+0.00089	+0.00008	0.00001	0.00084
(-0.44 , -0.40)	0.04350	0.00013	+0.00086	+0.00008	0.00001	0.00082
(-0.40 , -0.36)	0.04059	0.00014	-0.00085	-0.00004	0.00001	0.00078
(-0.36 , -0.32)	0.03907	0.00013	+0.00078	-0.00003	0.00001	0.00077
(-0.32 , -0.28)	0.03749	0.00013	+0.00077	+0.00007	0.00001	0.00075
(-0.28 , -0.24)	0.03621	0.00012	+0.00075	+0.00007	0.00001	0.00073
(-0.24 , -0.20)	0.03503	0.00012	-0.00072	-0.00003	0.00001	0.00072
(-0.20 , -0.16)	0.03416	0.00012	+0.00072	+0.00006	0.00001	0.00071
(-0.16 , -0.12)	0.03335	0.00011	+0.00071	-0.00003	0.00001	0.00070
(-0.12 , -0.08)	0.03238	0.00011	+0.00069	+0.00006	0.00001	0.00069
(-0.08 , -0.04)	0.03212	0.00011	+0.00069	+0.00006	0.00001	0.00069
(-0.04 , 0.00)	0.03177	0.00011	+0.00069	+0.00006	0.00001	0.00068
(0.00 , 0.04)	0.03106	0.00011	+0.00068	+0.00006	0.00001	0.00067
(0.04 , 0.08)	0.03102	0.00011	-0.00067	-0.00003	0.00001	0.00068
(0.08 , 0.12)	0.03079	0.00010	+0.00068	+0.00006	0.00001	0.00068
(0.12 , 0.16)	0.03059	0.00011	+0.00068	+0.00006	0.00001	0.00067
(0.16 , 0.20)	0.03076	0.00010	-0.00068	-0.00004	0.00001	0.00068
(0.20 , 0.24)	0.03090	0.00010	+0.00070	+0.00006	0.00001	0.00069
(0.24 , 0.28)	0.03122	0.00010	+0.00071	+0.00006	0.00001	0.00069
(0.28 , 0.32)	0.03169	0.00010	+0.00072	+0.00006	0.00001	0.00070
(0.32 , 0.36)	0.03226	0.00010	+0.00074	+0.00006	0.00001	0.00072
(0.36 , 0.40)	0.03261	0.00011	-0.00073	-0.00004	0.00000	0.00073
(0.40 , 0.44)	0.03371	0.00010	+0.00078	+0.00007	0.00000	0.00075
(0.44 , 0.48)	0.03474	0.00011	-0.00077	-0.00004	0.00000	0.00077
(0.48 , 0.52)	0.03595	0.00010	+0.00084	+0.00007	0.00000	0.00080
(0.52 , 0.56)	0.03769	0.00011	-0.00082	-0.00005	0.00001	0.00084
(0.56 , 0.60)	0.03979	0.00011	+0.00089	+0.00008	0.00001	0.00084
(0.60 , 0.64)	0.04201	0.00011	-0.00092	-0.00005	0.00001	0.00088
(0.64 , 0.68)	0.04524	0.00012	+0.00100	+0.00009	0.00000	0.00093
(0.68 , 0.72)	0.04950	0.00012	-0.00097	-0.00006	0.00000	0.00100
(0.72 , 0.76)	0.05553	0.00012	+0.00107	+0.00009	0.00000	0.00105
(0.76 , 0.80)	0.06378	0.00013	-0.00105	-0.00006	0.00000	0.00110
(0.80 , 0.82)	0.07249	0.00023	+0.00118	+0.00010	0.00001	0.00108
(0.82 , 0.84)	0.07993	0.00023	-0.00116	-0.00007	0.00000	0.00118
(0.84 , 0.86)	0.08986	0.00024	+0.00133	+0.00012	0.00002	0.00120
(0.86 , 0.88)	0.10167	0.00025	-0.00132	-0.00007	0.00002	0.00125
(0.88 , 0.90)	0.11505	0.00026	+0.00154	+0.00013	0.00003	0.00135
(0.90 , 0.92)	0.12824	0.00028	-0.00153	-0.00009	0.00004	0.00151
(0.92 , 0.94)	0.12567	0.00028	+0.00176	+0.00015	0.00005	0.00164
(0.94 , 0.96)	0.13415	0.00026	-0.00176	-0.00010	0.00002	0.00183

(0.96 , 0.98)	0.16115	0.00028	+0.00433 -0.00418	+0.00040 -0.00016	0.00007	0.00099
(0.98 , 1.00)	22.30639	0.00098	+0.06241 -0.06319	+0.01507 -0.00516	0.00006	0.05547

Table 6.8: Numerical values of the TEEC function together with statistical and systematic uncertainties for $1200 \text{ GeV} < H_{\text{T2}} < 1400 \text{ GeV}$.

$\cos \phi$	Value	Stat.	JES	JER	JAR	MC Mod.
(-1.00 , -0.98)	18.90289	0.00447	+0.04695 -0.04834	+0.01168 -0.02768	0.00788	0.06090
(-0.98 , -0.96)	1.65177	0.00272	+0.00618 -0.00594	+0.00463 -0.00358	0.00505	0.01416
(-0.96 , -0.94)	0.80954	0.00189	+0.00331 -0.00330	+0.00213 -0.00163	0.00146	0.00735
(-0.94 , -0.92)	0.51042	0.00146	+0.00273 -0.00277	+0.00128 -0.00098	0.00021	0.00463
(-0.92 , -0.90)	0.36525	0.00115	+0.00246 -0.00247	+0.00091 -0.00069	0.00026	0.00313
(-0.90 , -0.88)	0.27613	0.00105	+0.00223 -0.00218	+0.00069 -0.00053	0.00005	0.00256
(-0.88 , -0.86)	0.22170	0.00092	+0.00205 -0.00198	+0.00055 -0.00042	0.00012	0.00230
(-0.86 , -0.84)	0.18271	0.00076	+0.00186 -0.00180	+0.00045 -0.00034	0.00007	0.00209
(-0.84 , -0.82)	0.15356	0.00070	+0.00168 -0.00162	+0.00038 -0.00029	0.00001	0.00192
(-0.82 , -0.80)	0.13415	0.00065	+0.00156 -0.00151	+0.00033 -0.00025	0.00000	0.00181
(-0.80 , -0.76)	0.11117	0.00037	+0.00141 -0.00137	+0.00027 -0.00020	0.00001	0.00165
(-0.76 , -0.72)	0.09073	0.00031	+0.00129 -0.00125	+0.00021 -0.00016	0.00002	0.00147
(-0.72 , -0.68)	0.07665	0.00030	+0.00119 -0.00116	+0.00018 -0.00013	0.00002	0.00131
(-0.68 , -0.64)	0.06806	0.00028	+0.00112 -0.00110	+0.00015 -0.00011	0.00002	0.00120
(-0.64 , -0.60)	0.06006	0.00026	+0.00104 -0.00102	+0.00013 -0.00007	0.00002	0.00108
(-0.60 , -0.56)	0.05459	0.00024	+0.00097 -0.00096	+0.00012 -0.00006	0.00002	0.00100
(-0.56 , -0.52)	0.05011	0.00022	+0.00092 -0.00090	+0.00011 -0.00005	0.00001	0.00093
(-0.52 , -0.48)	0.04680	0.00021	+0.00087 -0.00086	+0.00010 -0.00005	0.00001	0.00088
(-0.48 , -0.44)	0.04404	0.00021	+0.00084 -0.00083	+0.00009 -0.00005	0.00001	0.00083
(-0.44 , -0.40)	0.04129	0.00020	+0.00080 -0.00079	+0.00008 -0.00004	0.00001	0.00079
(-0.40 , -0.36)	0.03926	0.00019	+0.00077 -0.00076	+0.00008 -0.00004	0.00001	0.00075
(-0.36 , -0.32)	0.03771	0.00019	+0.00075 -0.00073	+0.00008 -0.00004	0.00001	0.00073
(-0.32 , -0.28)	0.03563	0.00018	+0.00071 -0.00070	+0.00007 -0.00004	0.00001	0.00070
(-0.28 , -0.24)	0.03480	0.00019	+0.00070 -0.00069	+0.00007 -0.00004	0.00001	0.00069
(-0.24 , -0.20)	0.03405	0.00018	+0.00069 -0.00068	+0.00007 -0.00004	0.00001	0.00068
(-0.20 , -0.16)	0.03273	0.00017	+0.00067 -0.00066	+0.00007 -0.00004	0.00001	0.00066
(-0.16 , -0.12)	0.03222	0.00017	+0.00066 -0.00065	+0.00007 -0.00004	0.00001	0.00065
(-0.12 , -0.08)	0.03151	0.00017	+0.00065 -0.00064	+0.00006 -0.00004	0.00001	0.00064
(-0.08 , -0.04)	0.03088	0.00017	+0.00064 -0.00063	+0.00006 -0.00004	0.00001	0.00063
(-0.04 , 0.00)	0.03056	0.00016	+0.00064 -0.00063	+0.00006 -0.00004	0.00001	0.00063
(0.00 , 0.04)	0.03010	0.00017	+0.00063 -0.00062	+0.00006 -0.00004	0.00001	0.00062
(0.04 , 0.08)	0.03021	0.00016	+0.00064 -0.00063	+0.00006 -0.00004	0.00001	0.00063
(0.08 , 0.12)	0.02981	0.00016	+0.00064 -0.00063	+0.00006 -0.00004	0.00001	0.00062
(0.12 , 0.16)	0.02977	0.00016	+0.00064 -0.00063	+0.00006 -0.00004	0.00001	0.00062
(0.16 , 0.20)	0.02974	0.00016	+0.00064 -0.00063	+0.00006 -0.00004	0.00001	0.00062
(0.20 , 0.24)	0.03054	0.00016	+0.00066 -0.00065	+0.00007 -0.00004	0.00001	0.00064
(0.24 , 0.28)	0.03038	0.00015	+0.00066 -0.00065	+0.00007 -0.00004	0.00001	0.00064
(0.28 , 0.32)	0.03072	0.00015	+0.00067 -0.00066	+0.00007 -0.00004	0.00000	0.00065
(0.32 , 0.36)	0.03164	0.00016	+0.00070 -0.00068	+0.00007 -0.00004	0.00000	0.00067

(0.36 , 0.40)	0.03219	0.00016	+0.00071	+0.00007	0.00000	0.00068
(0.40 , 0.44)	0.03301	0.00016	+0.00073	+0.00007	-0.00004	0.00070
(0.44 , 0.48)	0.03426	0.00015	+0.00072	-0.00007	-0.00004	0.00001
(0.48 , 0.52)	0.03530	0.00016	+0.00076	+0.00008	0.00000	0.00072
(0.52 , 0.56)	0.03684	0.00017	+0.00082	+0.00009	-0.00005	0.00001
(0.56 , 0.60)	0.03899	0.00016	+0.00087	+0.00009	0.00002	0.00081
(0.60 , 0.64)	0.04159	0.00017	+0.00093	+0.00010	0.00001	0.00085
(0.64 , 0.68)	0.04433	0.00018	+0.00099	+0.00011	-0.00006	0.00090
(0.68 , 0.72)	0.04890	0.00018	+0.00109	+0.00012	-0.00006	0.00098
(0.72 , 0.76)	0.05470	0.00019	+0.00123	+0.00013	-0.00008	0.00001
(0.76 , 0.80)	0.06288	0.00020	+0.00144	+0.00015	-0.00009	0.00003
(0.80 , 0.82)	0.07201	0.00034	+0.00166	+0.00018	-0.00011	0.00003
(0.82 , 0.84)	0.07952	0.00035	+0.00184	+0.00019	-0.00012	0.00003
(0.84 , 0.86)	0.08912	0.00036	+0.00207	+0.00022	-0.00013	0.00001
(0.86 , 0.88)	0.10118	0.00038	+0.00238	+0.00025	-0.00015	0.00006
(0.88 , 0.90)	0.11457	0.00040	+0.00273	+0.00028	-0.00017	0.00020
(0.90 , 0.92)	0.12728	0.00041	+0.00303	+0.00031	-0.00019	0.00030
(0.92 , 0.94)	0.12550	0.00040	+0.00293	+0.00030	-0.00019	0.00013
(0.94 , 0.96)	0.13330	0.00040	+0.00313	+0.00030	-0.00021	0.00016
(0.96 , 0.98)	0.16034	0.00042	+0.00398	+0.00043	-0.00027	0.00011
(0.98 , 1.00)	22.35160	0.00154	+0.05788	+0.01538	-0.00657	0.00008

Table 6.9: Numerical values of the TEEC function together with statistical and systematic uncertainties for $1400 \text{ GeV} < H_{\text{T2}} < 1600 \text{ GeV}$.

$\cos \phi$	Value	Stat.	JES	JER	JAR	MC Mod.
(-1.00 , -0.98)	19.30135	0.00657	+0.04367 -0.04576	+0.01177 -0.02978	0.00884	0.05601
(-0.98 , -0.96)	1.54676	0.00386	+0.00845 -0.00692	+0.00458 -0.00210	0.00661	0.00659
(-0.96 , -0.94)	0.74968	0.00263	+0.00346 -0.00306	+0.00257 -0.00106	0.00125	0.00377
(-0.94 , -0.92)	0.46953	0.00198	+0.00252 -0.00238	+0.00173 -0.00072	0.00018	0.00320
(-0.92 , -0.90)	0.33807	0.00160	+0.00235 -0.00218	+0.00123 -0.00052	0.00002	0.00295
(-0.90 , -0.88)	0.25610	0.00147	+0.00214 -0.00199	+0.00091 -0.00039	0.00004	0.00262
(-0.88 , -0.86)	0.20445	0.00125	+0.00190 -0.00183	+0.00071 -0.00030	0.00005	0.00232
(-0.86 , -0.84)	0.16823	0.00111	+0.00170 -0.00168	+0.00058 -0.00024	0.00004	0.00207
(-0.84 , -0.82)	0.14449	0.00104	+0.00156 -0.00157	+0.00048 -0.00020	0.00004	0.00189
(-0.82 , -0.80)	0.12453	0.00093	+0.00143 -0.00144	+0.00041 -0.00017	0.00003	0.00170
(-0.80 , -0.76)	0.10358	0.00052	+0.00129 -0.00130	+0.00032 -0.00013	0.00003	0.00149
(-0.76 , -0.72)	0.08434	0.00046	+0.00117 -0.00116	+0.00025 -0.00010	0.00002	0.00127
(-0.72 , -0.68)	0.07188	0.00042	+0.00109 -0.00108	+0.00020 -0.00008	0.00002	0.00112
(-0.68 , -0.64)	0.06340	0.00038	+0.00102 -0.00101	+0.00016 -0.00007	0.00002	0.00102
(-0.64 , -0.60)	0.05662	0.00036	+0.00095 -0.00094	+0.00014 -0.00006	0.00001	0.00093
(-0.60 , -0.56)	0.05156	0.00034	+0.00089 -0.00089	+0.00012 -0.00005	0.00001	0.00086
(-0.56 , -0.52)	0.04787	0.00033	+0.00085 -0.00085	+0.00011 -0.00005	0.00001	0.00081
(-0.52 , -0.48)	0.04402	0.00031	+0.00080 -0.00079	+0.00010 -0.00004	0.00001	0.00075
(-0.48 , -0.44)	0.04157	0.00030	+0.00077 -0.00076	+0.00009 -0.00004	0.00001	0.00072
(-0.44 , -0.40)	0.03952	0.00029	+0.00074 -0.00074	+0.00009 -0.00004	0.00001	0.00069

(-0.40 , -0.36)	0.03706	0.00027	+0.00070 -0.00070	+0.00008 -0.00004	0.00001	0.00065
(-0.36 , -0.32)	0.03580	0.00027	+0.00068 -0.00068	+0.00008 -0.00004	0.00001	0.00063
(-0.32 , -0.28)	0.03419	0.00027	+0.00066 -0.00066	+0.00008 -0.00004	0.00001	0.00061
(-0.28 , -0.24)	0.03361	0.00026	+0.00065 -0.00065	+0.00008 -0.00004	0.00001	0.00060
(-0.24 , -0.20)	0.03253	0.00026	+0.00064 -0.00064	+0.00007 -0.00004	0.00001	0.00059
(-0.20 , -0.16)	0.03121	0.00025	+0.00062 -0.00061	+0.00007 -0.00004	0.00001	0.00057
(-0.16 , -0.12)	0.03063	0.00024	+0.00061 -0.00061	+0.00007 -0.00004	0.00001	0.00056
(-0.12 , -0.08)	0.03040	0.00024	+0.00061 -0.00061	+0.00007 -0.00003	0.00001	0.00056
(-0.08 , -0.04)	0.02986	0.00025	+0.00060 -0.00060	+0.00007 -0.00003	0.00001	0.00055
(-0.04 , 0.00)	0.02947	0.00024	+0.00060 -0.00059	+0.00007 -0.00003	0.00001	0.00055
(0.00 , 0.04)	0.02913	0.00024	+0.00060 -0.00059	+0.00007 -0.00003	0.00001	0.00055
(0.04 , 0.08)	0.02892	0.00023	+0.00060 -0.00059	+0.00007 -0.00004	0.00001	0.00055
(0.08 , 0.12)	0.02906	0.00023	+0.00060 -0.00059	+0.00007 -0.00004	0.00001	0.00056
(0.12 , 0.16)	0.02920	0.00022	+0.00061 -0.00060	+0.00007 -0.00004	0.00001	0.00056
(0.16 , 0.20)	0.02866	0.00022	+0.00060 -0.00059	+0.00007 -0.00004	0.00001	0.00056
(0.20 , 0.24)	0.02904	0.00022	+0.00061 -0.00060	+0.00007 -0.00004	0.00001	0.00057
(0.24 , 0.28)	0.02951	0.00024	+0.00062 -0.00061	+0.00007 -0.00004	0.00001	0.00058
(0.28 , 0.32)	0.03011	0.00023	+0.00063 -0.00062	+0.00007 -0.00004	0.00001	0.00060
(0.32 , 0.36)	0.03039	0.00022	+0.00064 -0.00063	+0.00007 -0.00004	0.00001	0.00061
(0.36 , 0.40)	0.03085	0.00022	+0.00066 -0.00064	+0.00007 -0.00004	0.00001	0.00062
(0.40 , 0.44)	0.03234	0.00023	+0.00069 -0.00067	+0.00007 -0.00005	0.00001	0.00066
(0.44 , 0.48)	0.03264	0.00023	+0.00070 -0.00069	+0.00008 -0.00005	0.00001	0.00067
(0.48 , 0.52)	0.03466	0.00024	+0.00075 -0.00073	+0.00008 -0.00005	0.00001	0.00072
(0.52 , 0.56)	0.03577	0.00024	+0.00077 -0.00076	+0.00008 -0.00006	0.00001	0.00075
(0.56 , 0.60)	0.03819	0.00024	+0.00082 -0.00081	+0.00009 -0.00006	0.00001	0.00080
(0.60 , 0.64)	0.04039	0.00025	+0.00087 -0.00086	+0.00009 -0.00007	0.00001	0.00086
(0.64 , 0.68)	0.04340	0.00026	+0.00094 -0.00091	+0.00010 -0.00007	0.00001	0.00092
(0.68 , 0.72)	0.04739	0.00026	+0.00103 -0.00099	+0.00011 -0.00008	0.00001	0.00101
(0.72 , 0.76)	0.05351	0.00027	+0.00116 -0.00112	+0.00013 -0.00009	0.00001	0.00115
(0.76 , 0.80)	0.06172	0.00029	+0.00135 -0.00132	+0.00015 -0.00011	0.00001	0.00132
(0.80 , 0.82)	0.07130	0.00050	+0.00158 -0.00154	+0.00017 -0.00013	0.00001	0.00150
(0.82 , 0.84)	0.07712	0.00051	+0.00172 -0.00168	+0.00019 -0.00014	0.00000	0.00161
(0.84 , 0.86)	0.08884	0.00054	+0.00200 -0.00195	+0.00021 -0.00016	0.00002	0.00182
(0.86 , 0.88)	0.09891	0.00057	+0.00226 -0.00219	+0.00024 -0.00018	0.00011	0.00198
(0.88 , 0.90)	0.11279	0.00059	+0.00260 -0.00253	+0.00027 -0.00020	0.00028	0.00218
(0.90 , 0.92)	0.12575	0.00061	+0.00287 -0.00281	+0.00029 -0.00022	0.00038	0.00233
(0.92 , 0.94)	0.12207	0.00059	+0.00272 -0.00268	+0.00028 -0.00021	0.00001	0.00212
(0.94 , 0.96)	0.13180	0.00058	+0.00297 -0.00293	+0.00032 -0.00021	0.00020	0.00201
(0.96 , 0.98)	0.15830	0.00060	+0.00377 -0.00368	+0.00038 -0.00029	0.00014	0.00033
(0.98 , 1.00)	22.42199	0.00223	+0.05369 -0.05461	+0.01464 -0.00643	0.00002	0.04970

Table 6.10: Numerical values of the TEEC function together with statistical and systematic uncertainties for $1600 \text{ GeV} < H_{\text{T2}} < 1800 \text{ GeV}$.

$\cos \phi$	Value	Stat.	JES	JER	JAR	MC Mod.
(-1.00 , -0.98)	19.67682	0.00909	+0.04230 -0.04351	+0.01157 -0.02617	0.00758	0.05404

(-0.98 , -0.96)	1.44149	0.00549	+0.00731 -0.00717	+0.00462 -0.00177	0.00469	0.00632
(-0.96 , -0.94)	0.68659	0.00354	+0.00355 -0.00354	+0.00215 -0.00078	0.00160	0.00484
(-0.94 , -0.92)	0.44341	0.00280	+0.00250 -0.00250	+0.00129 -0.00047	0.00051	0.00397
(-0.92 , -0.90)	0.31042	0.00234	+0.00210 -0.00224	+0.00087 -0.00034	0.00027	0.00301
(-0.90 , -0.88)	0.23697	0.00196	+0.00186 -0.00203	+0.00064 -0.00025	0.00020	0.00242
(-0.88 , -0.86)	0.19100	0.00173	+0.00172 -0.00180	+0.00050 -0.00021	0.00016	0.00204
(-0.86 , -0.84)	0.15700	0.00149	+0.00157 -0.00156	+0.00040 -0.00017	0.00013	0.00174
(-0.84 , -0.80)	0.12432	0.00083	+0.00141 -0.00135	+0.00030 -0.00011	0.00010	0.00145
(-0.80 , -0.76)	0.09605	0.00067	+0.00124 -0.00117	+0.00022 -0.00008	0.00008	0.00119
(-0.76 , -0.72)	0.08046	0.00062	+0.00112 -0.00109	+0.00017 -0.00007	0.00007	0.00105
(-0.72 , -0.64)	0.06339	0.00036	+0.00097 -0.00096	+0.00013 -0.00005	0.00003	0.00088
(-0.64 , -0.56)	0.05098	0.00030	+0.00086 -0.00084	+0.00010 -0.00004	0.00002	0.00077
(-0.56 , -0.48)	0.04306	0.00027	+0.00076 -0.00074	+0.00008 -0.00003	0.00000	0.00069
(-0.48 , -0.36)	0.03756	0.00020	+0.00069 -0.00067	+0.00006 -0.00002	0.00001	0.00065
(-0.36 , -0.24)	0.03273	0.00019	+0.00063 -0.00060	+0.00005 -0.00002	0.00000	0.00060
(-0.24 , -0.12)	0.03004	0.00017	+0.00059 -0.00057	+0.00005 -0.00003	0.00001	0.00057
(-0.12 , 0.00)	0.02850	0.00017	+0.00057 -0.00055	+0.00005 -0.00003	0.00001	0.00056
(0.00 , 0.12)	0.02802	0.00016	+0.00056 -0.00055	+0.00005 -0.00003	0.00000	0.00056
(0.12 , 0.24)	0.02790	0.00015	+0.00056 -0.00057	+0.00005 -0.00003	0.00000	0.00055
(0.24 , 0.36)	0.02888	0.00016	+0.00059 -0.00059	+0.00005 -0.00004	0.00000	0.00056
(0.36 , 0.48)	0.03075	0.00016	+0.00063 -0.00063	+0.00006 -0.00004	0.00000	0.00059
(0.48 , 0.56)	0.03386	0.00020	+0.00070 -0.00068	+0.00006 -0.00004	0.00000	0.00063
(0.56 , 0.64)	0.03798	0.00022	+0.00080 -0.00077	+0.00007 -0.00005	0.00000	0.00071
(0.64 , 0.72)	0.04415	0.00023	+0.00093 -0.00091	+0.00008 -0.00006	0.00000	0.00082
(0.72 , 0.76)	0.05277	0.00038	+0.00111 -0.00110	+0.00010 -0.00007	0.00000	0.00098
(0.76 , 0.80)	0.05996	0.00041	+0.00127 -0.00125	+0.00012 -0.00008	0.00000	0.00111
(0.80 , 0.84)	0.07235	0.00043	+0.00156 -0.00152	+0.00014 -0.00010	0.00000	0.00132
(0.84 , 0.86)	0.08477	0.00072	+0.00186 -0.00180	+0.00017 -0.00012	0.00000	0.00152
(0.86 , 0.88)	0.09728	0.00075	+0.00215 -0.00209	+0.00020 -0.00014	0.00000	0.00171
(0.88 , 0.90)	0.10899	0.00080	+0.00240 -0.00236	+0.00022 -0.00016	0.00000	0.00186
(0.90 , 0.92)	0.12330	0.00083	+0.00271 -0.00266	+0.00026 -0.00020	0.00000	0.00205
(0.92 , 0.94)	0.12272	0.00083	+0.00268 -0.00262	+0.00028 -0.00022	0.00000	0.00200
(0.94 , 0.96)	0.12838	0.00082	+0.00271 -0.00276	+0.00030 -0.00025	0.00000	0.00208
(0.96 , 0.98)	0.15289	0.00087	+0.00353 -0.00351	+0.00047 -0.00036	0.00000	0.00167
(0.98 , 1.00)	22.50616	0.00305	+0.05026 -0.05099	+0.01588 -0.00624	0.00011	0.04632

Table 6.11: Numerical values of the TEEC function together with statistical and systematic uncertainties for $1800 \text{ GeV} < H_{\text{T2}} < 2000 \text{ GeV}$.

$\cos \phi$	Value	Stat.	JES	JER	JAR	MC Mod.
(-1.00 , -0.98)	20.05806	0.01053	+0.04132 -0.04076	+0.01034 -0.02687	0.00796	0.05639
(-0.98 , -0.96)	1.33519	0.00632	+0.00707 -0.00914	+0.00345 -0.00135	0.00585	0.01099
(-0.96 , -0.94)	0.63864	0.00417	+0.00310 -0.00344	+0.00211 -0.00064	0.00038	0.00473
(-0.94 , -0.92)	0.39574	0.00340	+0.00252 -0.00245	+0.00142 -0.00050	0.00008	0.00359
(-0.92 , -0.90)	0.28893	0.00263	+0.00234 -0.00210	+0.00102 -0.00039	0.00005	0.00304
(-0.90 , -0.88)	0.21814	0.00227	+0.00203 -0.00185	+0.00075 -0.00030	0.00004	0.00255

(-0.88 , -0.86)	0.17638	0.00204	+0.00177 -0.00170	+0.00060 -0.00025	0.00003	0.00223
(-0.86 , -0.84)	0.14579	0.00177	+0.00153 -0.00155	+0.00049 -0.00021	0.00003	0.00193
(-0.84 , -0.80)	0.11363	0.00094	+0.00130 -0.00135	+0.00037 -0.00015	0.00002	0.00157
(-0.80 , -0.76)	0.08957	0.00079	+0.00117 -0.00116	+0.00029 -0.00011	0.00002	0.00128
(-0.76 , -0.72)	0.07435	0.00074	+0.00106 -0.00102	+0.00023 -0.00009	0.00001	0.00109
(-0.72 , -0.64)	0.05928	0.00041	+0.00091 -0.00088	+0.00018 -0.00007	0.00001	0.00091
(-0.64 , -0.56)	0.04753	0.00035	+0.00079 -0.00079	+0.00013 -0.00006	0.00001	0.00076
(-0.56 , -0.48)	0.04074	0.00032	+0.00072 -0.00071	+0.00011 -0.00005	0.00001	0.00068
(-0.48 , -0.36)	0.03572	0.00023	+0.00065 -0.00063	+0.00009 -0.00004	0.00001	0.00062
(-0.36 , -0.24)	0.03070	0.00021	+0.00058 -0.00056	+0.00007 -0.00003	0.00001	0.00056
(-0.24 , -0.12)	0.02880	0.00021	+0.00055 -0.00054	+0.00006 -0.00003	0.00001	0.00054
(-0.12 , 0.00)	0.02720	0.00020	+0.00053 -0.00052	+0.00005 -0.00003	0.00000	0.00052
(0.00 , 0.12)	0.02642	0.00019	+0.00052 -0.00051	+0.00005 -0.00003	0.00000	0.00051
(0.12 , 0.24)	0.02676	0.00017	+0.00054 -0.00051	+0.00005 -0.00003	0.00000	0.00051
(0.24 , 0.36)	0.02775	0.00018	+0.00056 -0.00054	+0.00005 -0.00003	0.00001	0.00052
(0.36 , 0.48)	0.02960	0.00018	+0.00060 -0.00059	+0.00005 -0.00004	0.00001	0.00054
(0.48 , 0.56)	0.03277	0.00024	+0.00067 -0.00065	+0.00006 -0.00005	0.00001	0.00058
(0.56 , 0.64)	0.03667	0.00026	+0.00074 -0.00074	+0.00007 -0.00005	0.00001	0.00064
(0.64 , 0.72)	0.04193	0.00027	+0.00084 -0.00084	+0.00008 -0.00006	0.00003	0.00071
(0.72 , 0.76)	0.05055	0.00046	+0.00103 -0.00101	+0.00010 -0.00008	0.00004	0.00083
(0.76 , 0.80)	0.05768	0.00047	+0.00118 -0.00116	+0.00012 -0.00009	0.00000	0.00093
(0.80 , 0.84)	0.06992	0.00051	+0.00145 -0.00144	+0.00015 -0.00012	0.00002	0.00111
(0.84 , 0.86)	0.08240	0.00088	+0.00173 -0.00172	+0.00018 -0.00014	0.00002	0.00129
(0.86 , 0.88)	0.09275	0.00091	+0.00198 -0.00195	+0.00021 -0.00015	0.00005	0.00144
(0.88 , 0.90)	0.10757	0.00098	+0.00233 -0.00228	+0.00025 -0.00018	0.00022	0.00166
(0.90 , 0.92)	0.11876	0.00099	+0.00256 -0.00251	+0.00028 -0.00019	0.00031	0.00179
(0.92 , 0.94)	0.11757	0.00103	+0.00250 -0.00244	+0.00028 -0.00018	0.00007	0.00169
(0.94 , 0.96)	0.12420	0.00097	+0.00264 -0.00252	+0.00030 -0.00019	0.00026	0.00152
(0.96 , 0.98)	0.14944	0.00100	+0.00330 -0.00334	+0.00051 -0.00016	0.00016	0.00000
(0.98 , 1.00)	22.60561	0.00373	+0.04670 -0.04748	+0.01503 -0.00723	0.00010	0.04262

Table 6.12: Numerical values of the TEEC function together with statistical and systematic uncertainties for $2000 \text{ GeV} < H_{\text{T2}} < 2300 \text{ GeV}$.

$\cos \phi$	Value	Stat.	JES	JER	JAR	MC Mod.
(-1.00 , -0.98)	20.52361	0.01637	+0.03751 -0.04181	+0.01285 -0.03017	0.00835	0.05735
(-0.98 , -0.96)	1.21439	0.00991	+0.00865 -0.00660	+0.00612 -0.00279	0.00672	0.01390
(-0.96 , -0.94)	0.56514	0.00668	+0.00399 -0.00321	+0.00259 -0.00141	0.00084	0.00554
(-0.94 , -0.92)	0.36187	0.00512	+0.00285 -0.00236	+0.00169 -0.00093	0.00031	0.00320
(-0.92 , -0.90)	0.26252	0.00386	+0.00245 -0.00209	+0.00122 -0.00067	0.00021	0.00239
(-0.90 , -0.88)	0.18718	0.00324	+0.00197 -0.00168	+0.00084 -0.00044	0.00014	0.00183
(-0.88 , -0.86)	0.15877	0.00292	+0.00180 -0.00157	+0.00069 -0.00034	0.00012	0.00166
(-0.86 , -0.84)	0.12960	0.00254	+0.00155 -0.00138	+0.00053 -0.00025	0.00010	0.00144
(-0.84 , -0.80)	0.10388	0.00136	+0.00134 -0.00121	+0.00040 -0.00019	0.00009	0.00124
(-0.80 , -0.76)	0.08244	0.00120	+0.00116 -0.00107	+0.00029 -0.00014	0.00010	0.00106
(-0.76 , -0.72)	0.06473	0.00108	+0.00097 -0.00091	+0.00021 -0.00010	0.00005	0.00087

(-0.72 , -0.64)	0.05389	0.00060	+0.00086 -0.00082	+0.00016 -0.00008	0.00001	0.00076
(-0.64 , -0.56)	0.04293	0.00054	+0.00072 -0.00070	+0.00011 -0.00006	0.00001	0.00062
(-0.56 , -0.48)	0.03721	0.00047	+0.00064 -0.00063	+0.00009 -0.00004	0.00001	0.00055
(-0.48 , -0.36)	0.03233	0.00034	+0.00057 -0.00057	+0.00007 -0.00003	0.00000	0.00049
(-0.36 , -0.24)	0.02902	0.00033	+0.00052 -0.00053	+0.00005 -0.00003	0.00000	0.00046
(-0.24 , -0.12)	0.02639	0.00032	+0.00049 -0.00050	+0.00005 -0.00002	0.00000	0.00044
(-0.12 , 0.00)	0.02530	0.00031	+0.00048 -0.00048	+0.00004 -0.00003	0.00000	0.00045
(0.00 , 0.12)	0.02459	0.00027	+0.00047 -0.00047	+0.00004 -0.00003	0.00000	0.00045
(0.12 , 0.24)	0.02471	0.00028	+0.00048 -0.00047	+0.00004 -0.00003	0.00000	0.00047
(0.24 , 0.36)	0.02607	0.00028	+0.00052 -0.00050	+0.00004 -0.00003	0.00000	0.00052
(0.36 , 0.48)	0.02747	0.00028	+0.00054 -0.00053	+0.00004 -0.00004	0.00000	0.00055
(0.48 , 0.56)	0.03097	0.00037	+0.00061 -0.00060	+0.00005 -0.00004	0.00000	0.00063
(0.56 , 0.64)	0.03419	0.00039	+0.00068 -0.00066	+0.00005 -0.00005	0.00000	0.00069
(0.64 , 0.72)	0.04055	0.00041	+0.00081 -0.00079	+0.00006 -0.00006	0.00000	0.00080
(0.72 , 0.76)	0.04798	0.00068	+0.00096 -0.00095	+0.00007 -0.00007	0.00000	0.00093
(0.76 , 0.80)	0.05432	0.00072	+0.00109 -0.00108	+0.00008 -0.00008	0.00000	0.00103
(0.80 , 0.84)	0.06628	0.00079	+0.00135 -0.00133	+0.00010 -0.00010	0.00000	0.00124
(0.84 , 0.86)	0.07710	0.00138	+0.00160 -0.00157	+0.00011 -0.00011	0.00000	0.00143
(0.86 , 0.88)	0.08764	0.00145	+0.00184 -0.00179	+0.00013 -0.00013	0.00000	0.00161
(0.88 , 0.90)	0.10387	0.00151	+0.00221 -0.00212	+0.00016 -0.00016	0.00000	0.00188
(0.90 , 0.92)	0.11536	0.00152	+0.00243 -0.00235	+0.00018 -0.00018	0.00000	0.00202
(0.92 , 0.94)	0.11514	0.00152	+0.00236 -0.00232	+0.00018 -0.00018	0.00000	0.00193
(0.94 , 0.96)	0.12164	0.00155	+0.00254 -0.00243	+0.00017 -0.00019	0.00000	0.00197
(0.96 , 0.98)	0.14212	0.00163	+0.00312 -0.00302	+0.00028 -0.00030	0.00000	0.00103
(0.98 , 1.00)	22.74054	0.00570	+0.04268 -0.04358	+0.01551 -0.00597	0.00001	0.04312

Table 6.13: Numerical values of the TEEC function together with statistical and systematic uncertainties for $2300 \text{ GeV} < H_{\text{T2}} < 2600 \text{ GeV}$.

$\cos \phi$	Value	Stat.	JES	JER	JAR	MC Mod.
(-1.00 , -0.98)	21.03794	0.02244	+0.03860 -0.03652	+0.01297 -0.02702	0.00840	0.05301
(-0.98 , -0.96)	1.07362	0.01413	+0.00836 -0.00859	+0.00507 -0.00270	0.00617	0.00930
(-0.96 , -0.94)	0.48589	0.00835	+0.00357 -0.00401	+0.00218 -0.00104	0.00136	0.00493
(-0.94 , -0.92)	0.30605	0.00625	+0.00235 -0.00269	+0.00129 -0.00059	0.00037	0.00353
(-0.92 , -0.90)	0.23336	0.00525	+0.00207 -0.00225	+0.00092 -0.00042	0.00020	0.00283
(-0.90 , -0.88)	0.17424	0.00447	+0.00174 -0.00186	+0.00065 -0.00028	0.00014	0.00216
(-0.88 , -0.86)	0.13354	0.00373	+0.00146 -0.00155	+0.00047 -0.00019	0.00009	0.00168
(-0.86 , -0.84)	0.11856	0.00347	+0.00137 -0.00146	+0.00040 -0.00017	0.00005	0.00151
(-0.84 , -0.80)	0.09004	0.00186	+0.00110 -0.00118	+0.00029 -0.00012	0.00001	0.00116
(-0.80 , -0.76)	0.06903	0.00155	+0.00092 -0.00096	+0.00021 -0.00009	0.00004	0.00092
(-0.76 , -0.72)	0.06068	0.00139	+0.00087 -0.00089	+0.00017 -0.00007	0.00005	0.00084
(-0.72 , -0.64)	0.04731	0.00079	+0.00073 -0.00074	+0.00012 -0.00005	0.00002	0.00069
(-0.64 , -0.56)	0.03956	0.00071	+0.00065 -0.00066	+0.00009 -0.00004	0.00001	0.00063
(-0.56 , -0.48)	0.03325	0.00062	+0.00056 -0.00058	+0.00007 -0.00004	0.00001	0.00057
(-0.48 , -0.36)	0.03010	0.00046	+0.00052 -0.00052	+0.00006 -0.00003	0.00001	0.00056
(-0.36 , -0.24)	0.02652	0.00044	+0.00047 -0.00047	+0.00005 -0.00002	0.00000	0.00053

(-0.24 , -0.12)	0.02420	0.00044	+0.00044 -0.00044	+0.00004 -0.00002	0.00000	0.00050
(-0.12 , 0.00)	0.02253	0.00042	+0.00042 -0.00042	+0.00004 -0.00002	0.00000	0.00048
(0.00 , 0.12)	0.02241	0.00036	+0.00042 -0.00042	+0.00004 -0.00003	0.00000	0.00048
(0.12 , 0.24)	0.02233	0.00037	+0.00042 -0.00042	+0.00004 -0.00003	0.00000	0.00047
(0.24 , 0.36)	0.02379	0.00037	+0.00045 -0.00046	+0.00005 -0.00003	0.00000	0.00049
(0.36 , 0.48)	0.02592	0.00039	+0.00049 -0.00050	+0.00005 -0.00003	0.00000	0.00051
(0.48 , 0.56)	0.02860	0.00048	+0.00055 -0.00054	+0.00005 -0.00004	0.00000	0.00054
(0.56 , 0.64)	0.03183	0.00051	+0.00061 -0.00060	+0.00006 -0.00004	0.00001	0.00058
(0.64 , 0.72)	0.03774	0.00057	+0.00072 -0.00072	+0.00007 -0.00005	0.00001	0.00067
(0.72 , 0.76)	0.04464	0.00095	+0.00084 -0.00085	+0.00009 -0.00006	0.00001	0.00079
(0.76 , 0.80)	0.05153	0.00098	+0.00099 -0.00098	+0.00010 -0.00007	0.00001	0.00090
(0.80 , 0.84)	0.06090	0.00109	-0.00116 +0.00119	-0.00008 +0.00012	0.00000	0.00105
(0.84 , 0.86)	0.07478	0.00188	+0.00149 -0.00145	+0.00015 -0.00009	0.00005	0.00128
(0.86 , 0.88)	0.08488	0.00194	+0.00170 -0.00167	+0.00017 -0.00010	0.00013	0.00144
(0.88 , 0.90)	0.09762	0.00203	+0.00197 -0.00196	+0.00019 -0.00012	0.00029	0.00164
(0.90 , 0.92)	0.10786	0.00214	+0.00219 -0.00217	+0.00022 -0.00013	0.00030	0.00178
(0.92 , 0.94)	0.10271	0.00202	+0.00206 -0.00203	+0.00020 -0.00012	0.00020	0.00162
(0.94 , 0.96)	0.11608	0.00209	+0.00229 -0.00228	+0.00022 -0.00015	0.00006	0.00162
(0.96 , 0.98)	0.13712	0.00222	+0.00289 -0.00286	+0.00022 -0.00027	0.00000	0.00000
(0.98 , 1.00)	22.90232	0.00769	+0.03884 -0.03885	+0.01560 -0.00618	0.00007	0.03860

Table 6.14: Numerical values of the TEEC function together with statistical and systematic uncertainties for $2600 \text{ GeV} < H_{\text{T2}} < 3000 \text{ GeV}$.

$\cos \phi$	Value	Stat.	JES	JER	JAR	MC Mod.
(-1.00 , -0.98)	21.55663	0.03324	+0.03438 -0.03489	+0.01416 -0.03281	0.00703	0.05749
(-0.98 , -0.96)	0.93558	0.02005	+0.00863 -0.00867	+0.00705 -0.00287	0.00544	0.01007
(-0.96 , -0.94)	0.39890	0.01217	+0.00312 -0.00351	+0.00269 -0.00125	0.00098	0.00546
(-0.94 , -0.92)	0.26852	0.00902	+0.00237 -0.00262	+0.00171 -0.00073	0.00042	0.00401
(-0.92 , -0.90)	0.19507	0.00769	+0.00192 -0.00204	+0.00118 -0.00050	0.00025	0.00302
(-0.90 , -0.86)	0.14170	0.00416	+0.00163 -0.00161	+0.00080 -0.00033	0.00009	0.00229
(-0.86 , -0.80)	0.08646	0.00219	+0.00115 -0.00110	+0.00045 -0.00019	0.00003	0.00145
(-0.80 , -0.72)	0.05468	0.00140	+0.00080 -0.00080	+0.00026 -0.00011	0.00002	0.00096
(-0.72 , -0.60)	0.04095	0.00091	+0.00066 -0.00064	+0.00018 -0.00008	0.00001	0.00078
(-0.60 , -0.36)	0.02808	0.00047	+0.00049 -0.00046	+0.00011 -0.00005	0.00001	0.00059
(-0.36 , 0.00)	0.02133	0.00040	+0.00039 -0.00037	+0.00006 -0.00003	0.00000	0.00049
(0.00 , 0.36)	0.02037	0.00031	+0.00038 -0.00037	+0.00004 -0.00002	0.00000	0.00045
(0.36 , 0.60)	0.02496	0.00040	+0.00047 -0.00045	+0.00005 -0.00002	0.00000	0.00049
(0.60 , 0.72)	0.03259	0.00066	+0.00060 -0.00061	+0.00007 -0.00003	0.00001	0.00060
(0.72 , 0.80)	0.04422	0.00096	+0.00083 -0.00080	+0.00009 -0.00004	0.00001	0.00080
(0.80 , 0.86)	0.06105	0.00134	+0.00115 -0.00113	+0.00013 -0.00006	0.00002	0.00107
(0.86 , 0.90)	0.08534	0.00195	+0.00168 -0.00165	+0.00018 -0.00008	0.00024	0.00138
(0.90 , 0.92)	0.10070	0.00326	+0.00198 -0.00197	+0.00020 -0.00010	0.00030	0.00145
(0.92 , 0.94)	0.10007	0.00331	+0.00192 -0.00191	+0.00019 -0.00011	0.00015	0.00130
(0.94 , 0.96)	0.10276	0.00314	+0.00202 -0.00197	+0.00018 -0.00012	0.00005	0.00116
(0.96 , 0.98)	0.12725	0.00336	+0.00263 -0.00255	+0.00025 -0.00015	0.00000	0.00000

(0.98 , 1.00)	23.09402	0.01179	+0.03377 -0.03457	+0.01328 -0.00534	0.00014	0.03876
-----------------	----------	---------	----------------------	----------------------	---------	---------

Table 6.15: Numerical values of the TEEC function together with statistical and systematic uncertainties for $3000 \text{ GeV} < H_{\text{T2}} < 3500 \text{ GeV}$.

$\cos \phi$	Value	Stat.	JES	JER	JAR	MC Mod.
(-1.00 , -0.98)	22.33047	0.04458	+0.03110 -0.02998	+0.01468 -0.03022	0.00696	0.04168
(-0.98 , -0.96)	0.67872	0.02730	+0.00696 -0.00774	+0.00543 -0.00245	0.00560	0.00758
(-0.96 , -0.94)	0.31362	0.01738	+0.00302 -0.00336	+0.00233 -0.00103	0.00043	0.00464
(-0.94 , -0.92)	0.22504	0.01320	+0.00237 -0.00244	+0.00157 -0.00068	0.00016	0.00355
(-0.92 , -0.90)	0.14365	0.00974	+0.00163 -0.00170	+0.00096 -0.00041	0.00009	0.00230
(-0.90 , -0.86)	0.10856	0.00542	+0.00134 -0.00139	+0.00069 -0.00029	0.00007	0.00176
(-0.86 , -0.80)	0.06336	0.00253	+0.00089 -0.00089	+0.00037 -0.00016	0.00003	0.00106
(-0.80 , -0.72)	0.04624	0.00191	+0.00072 -0.00071	+0.00025 -0.00010	0.00002	0.00081
(-0.72 , -0.60)	0.03219	0.00117	+0.00054 -0.00052	+0.00016 -0.00006	0.00002	0.00059
(-0.60 , -0.36)	0.02175	0.00059	+0.00037 -0.00038	+0.00009 -0.00004	0.00001	0.00041
(-0.36 , 0.00)	0.01781	0.00054	+0.00032 -0.00032	+0.00006 -0.00003	0.00000	0.00036
(0.00 , 0.36)	0.01689	0.00041	+0.00031 -0.00031	+0.00004 -0.00001	0.00000	0.00035
(0.36 , 0.60)	0.02109	0.00056	+0.00039 -0.00039	+0.00004 -0.00002	0.00000	0.00042
(0.60 , 0.72)	0.02729	0.00093	+0.00050 -0.00050	+0.00005 -0.00003	0.00001	0.00052
(0.72 , 0.80)	0.03679	0.00134	+0.00068 -0.00066	+0.00008 -0.00004	0.00002	0.00068
(0.80 , 0.86)	0.04944	0.00191	+0.00092 -0.00091	+0.00011 -0.00005	0.00001	0.00090
(0.86 , 0.90)	0.07453	0.00290	+0.00144 -0.00142	+0.00017 -0.00008	0.00021	0.00133
(0.90 , 0.92)	0.09419	0.00491	+0.00182 -0.00178	+0.00023 -0.00010	0.00041	0.00166
(0.92 , 0.94)	0.08416	0.00474	+0.00158 -0.00159	+0.00021 -0.00010	0.00003	0.00142
(0.94 , 0.96)	0.09007	0.00465	+0.00168 -0.00173	+0.00024 -0.00009	0.00015	0.00134
(0.96 , 0.98)	0.11638	0.00529	+0.00241 -0.00232	+0.00026 -0.00017	0.00019	0.00100
(0.98 , 1.00)	23.39142	0.01647	+0.02887 -0.02891	+0.01392 -0.00549	0.00001	0.03099

Table 6.16: Numerical values of the TEEC function together with statistical and systematic uncertainties for $H_{\text{T2}} > 3500 \text{ GeV}$.

$\cos \phi$	Value	Stat.	JES	JER	JAR	MC Mod.
(-1.00 , -0.98)	-4.02732	0.00110	+0.02227 -0.02147	+0.04173 -0.01220	0.00775	0.01788
(-0.98 , -0.96)	1.67287	0.00088	+0.00732 -0.00729	+0.00337 -0.00083	0.00328	0.00193
(-0.96 , -0.94)	0.77286	0.00063	+0.00352 -0.00327	+0.00289 -0.00064	0.00128	0.00050
(-0.94 , -0.92)	0.44932	0.00050	+0.00222 -0.00206	+0.00185 -0.00042	0.00070	0.00020
(-0.92 , -0.90)	0.28223	0.00044	+0.00147 -0.00138	+0.00124 -0.00029	0.00040	0.00010
(-0.90 , -0.88)	0.19498	0.00036	+0.00103 -0.00099	+0.00087 -0.00020	0.00025	0.00006
(-0.88 , -0.86)	0.14509	0.00032	+0.00077 -0.00074	+0.00065 -0.00016	0.00017	0.00004
(-0.86 , -0.84)	0.11290	0.00030	+0.00060 -0.00058	+0.00051 -0.00012	0.00013	0.00002
(-0.84 , -0.82)	0.09109	0.00027	+0.00048 -0.00047	+0.00041 -0.00010	0.00010	0.00002
(-0.82 , -0.80)	0.07550	0.00024	+0.00040 -0.00039	+0.00034 -0.00008	0.00007	0.00001
(-0.80 , -0.78)	0.06339	0.00023	+0.00034 -0.00033	+0.00029 -0.00007	0.00006	0.00001
(-0.78 , -0.76)	0.05458	0.00022	+0.00030 -0.00029	+0.00025 -0.00006	0.00005	0.00001
(-0.76 , -0.74)	0.04697	0.00020	+0.00026 -0.00025	+0.00021 -0.00005	0.00004	0.00001

(-0.74 , -0.72)	0.04126	0.00019	+0.00023 -0.00022	+0.00019 -0.00005	0.00003	0.00001
(-0.72 , -0.70)	0.03668	0.00018	+0.00021 -0.00020	+0.00017 -0.00004	0.00002	0.00001
(-0.70 , -0.68)	0.03257	0.00018	+0.00019 -0.00018	+0.00015 -0.00004	0.00002	0.00001
(-0.68 , -0.66)	0.02947	0.00017	+0.00017 -0.00017	+0.00013 -0.00004	0.00002	0.00000
(-0.66 , -0.64)	0.02633	0.00016	+0.00016 -0.00016	+0.00012 -0.00003	0.00001	0.00000
(-0.64 , -0.62)	0.02408	0.00015	+0.00015 -0.00014	+0.00011 -0.00003	0.00001	0.00000
(-0.62 , -0.60)	0.02158	0.00016	+0.00013 -0.00013	+0.00010 -0.00003	0.00001	0.00000
(-0.60 , -0.58)	0.01956	0.00015	+0.00012 -0.00012	+0.00009 -0.00002	0.00001	0.00000
(-0.58 , -0.56)	0.01810	0.00014	+0.00012 -0.00011	+0.00008 -0.00002	0.00001	0.00000
(-0.56 , -0.54)	0.01680	0.00014	+0.00011 -0.00011	+0.00008 -0.00002	0.00001	0.00000
(-0.54 , -0.52)	0.01546	0.00014	+0.00010 -0.00010	+0.00007 -0.00002	0.00001	0.00000
(-0.52 , -0.50)	0.01435	0.00013	+0.00009 -0.00009	+0.00007 -0.00002	0.00000	0.00000
(-0.50 , -0.48)	0.01323	0.00013	+0.00009 -0.00009	+0.00006 -0.00002	0.00000	0.00000
(-0.48 , -0.46)	0.01182	0.00013	+0.00008 -0.00008	+0.00005 -0.00001	0.00000	0.00000
(-0.46 , -0.44)	0.01125	0.00013	+0.00007 -0.00008	+0.00005 -0.00001	0.00000	0.00000
(-0.44 , -0.42)	0.01042	0.00012	+0.00007 -0.00007	+0.00005 -0.00001	0.00000	0.00000
(-0.42 , -0.40)	0.00974	0.00012	+0.00007 -0.00007	+0.00004 -0.00001	0.00000	0.00000
(-0.40 , -0.38)	0.00915	0.00012	+0.00006 -0.00006	+0.00004 -0.00001	0.00000	0.00000
(-0.38 , -0.36)	0.00838	0.00012	+0.00006 -0.00006	+0.00004 -0.00001	0.00000	0.00000
(-0.36 , -0.34)	0.00758	0.00011	+0.00005 -0.00005	+0.00003 -0.00001	0.00000	0.00000
(-0.34 , -0.32)	0.00706	0.00011	+0.00005 -0.00005	+0.00003 -0.00001	0.00000	0.00000
(-0.32 , -0.30)	0.00650	0.00011	+0.00004 -0.00004	+0.00003 -0.00001	0.00000	0.00000
(-0.30 , -0.28)	0.00601	0.00011	+0.00004 -0.00004	+0.00003 -0.00001	0.00000	0.00000
(-0.28 , -0.26)	0.00559	0.00011	+0.00004 -0.00004	+0.00003 -0.00001	0.00000	0.00000
(-0.26 , -0.24)	0.00510	0.00011	+0.00004 -0.00004	+0.00002 -0.00001	0.00000	0.00000
(-0.24 , -0.22)	0.00458	0.00011	+0.00003 -0.00003	+0.00002 -0.00001	0.00000	0.00000
(-0.22 , -0.20)	0.00400	0.00011	+0.00003 -0.00003	+0.00002 -0.00001	0.00000	0.00000
(-0.20 , -0.18)	0.00377	0.00011	+0.00003 -0.00003	+0.00002 -0.00000	0.00000	0.00000
(-0.18 , -0.16)	0.00344	0.00011	+0.00002 -0.00002	+0.00002 -0.00000	0.00000	0.00000
(-0.16 , -0.14)	0.00281	0.00011	+0.00002 -0.00002	+0.00001 -0.00000	0.00000	0.00000
(-0.14 , -0.12)	0.00259	0.00011	+0.00002 -0.00002	+0.00001 -0.00000	0.00000	0.00000
(-0.12 , -0.10)	0.00206	0.00010	+0.00001 -0.00001	+0.00001 -0.00000	0.00000	0.00000
(-0.10 , -0.08)	0.00165	0.00011	+0.00001 -0.00001	+0.00001 -0.00000	0.00000	0.00000
(-0.08 , -0.06)	0.00134	0.00010	+0.00001 -0.00001	+0.00001 -0.00000	0.00000	0.00000
(-0.06 , -0.04)	0.00084	0.00011	+0.00001 -0.00001	+0.00000 -0.00000	0.00000	0.00000
(-0.04 , -0.02)	0.00078	0.00010	+0.00001 -0.00001	+0.00000 -0.00000	0.00000	0.00000
(-0.02 , 0.00)	0.00025	0.00010	+0.00000 -0.00000	+0.00000 -0.00000	0.00000	0.00000

Table 6.17: Numerical values of the ATEEC function together with statistical and systematic uncertainties for $H_{\text{T2}} > 1000$ GeV.

$\cos \phi$	Value	Stat.	JES	JER	JAR	MC Mod.
(-1.00 , -0.98)	-4.30357	0.00150	+0.02665 -0.02543	+0.04332 -0.01168	0.00775	0.01710
(-0.98 , -0.96)	1.75801	0.00118	+0.00841 -0.00825	+0.00359 -0.00106	0.00348	0.00172
(-0.96 , -0.94)	0.82003	0.00085	+0.00409 -0.00372	+0.00308 -0.00056	0.00120	0.00051
(-0.94 , -0.92)	0.47942	0.00068	+0.00258 -0.00236	+0.00192 -0.00033	0.00063	0.00023

(-0.92 , -0.90)	0.30404	0.00058	+0.00172 -0.00160	+0.00126 -0.00022	0.00037	0.00012
(-0.90 , -0.88)	0.21126	0.00050	+0.00121 -0.00115	+0.00088 -0.00016	0.00025	0.00007
(-0.88 , -0.86)	0.15708	0.00044	+0.00090 -0.00087	+0.00065 -0.00012	0.00018	0.00005
(-0.86 , -0.84)	0.12207	0.00040	+0.00069 -0.00067	+0.00051 -0.00010	0.00013	0.00003
(-0.84 , -0.82)	0.09887	0.00037	+0.00056 -0.00054	+0.00041 -0.00008	0.00010	0.00003
(-0.82 , -0.80)	0.08180	0.00034	+0.00046 -0.00044	+0.00034 -0.00007	0.00007	0.00002
(-0.80 , -0.76)	0.06418	0.00019	+0.00035 -0.00034	+0.00027 -0.00006	0.00005	0.00002
(-0.76 , -0.72)	0.04798	0.00017	+0.00026 -0.00025	+0.00020 -0.00004	0.00003	0.00001
(-0.72 , -0.68)	0.03778	0.00016	+0.00021 -0.00020	+0.00016 -0.00003	0.00002	0.00001
(-0.68 , -0.64)	0.03027	0.00015	+0.00017 -0.00017	+0.00013 -0.00003	0.00002	0.00001
(-0.64 , -0.60)	0.02491	0.00014	+0.00014 -0.00014	+0.00010 -0.00002	0.00001	0.00001
(-0.60 , -0.56)	0.02049	0.00013	+0.00012 -0.00012	+0.00009 -0.00002	0.00001	0.00000
(-0.56 , -0.52)	0.01748	0.00012	+0.00010 -0.00011	+0.00007 -0.00002	0.00001	0.00000
(-0.52 , -0.48)	0.01507	0.00012	+0.00009 -0.00009	+0.00006 -0.00001	0.00000	0.00000
(-0.48 , -0.44)	0.01246	0.00012	+0.00007 -0.00008	+0.00005 -0.00001	0.00000	0.00000
(-0.44 , -0.40)	0.01081	0.00012	+0.00006 -0.00007	+0.00005 -0.00001	0.00000	0.00000
(-0.40 , -0.36)	0.00960	0.00011	+0.00006 -0.00006	+0.00004 -0.00001	0.00000	0.00000
(-0.36 , -0.32)	0.00796	0.00011	+0.00005 -0.00005	+0.00003 -0.00001	0.00000	0.00000
(-0.32 , -0.28)	0.00685	0.00011	+0.00004 -0.00004	+0.00003 -0.00001	0.00000	0.00000
(-0.28 , -0.24)	0.00581	0.00011	+0.00004 -0.00004	+0.00002 -0.00001	0.00000	0.00000
(-0.24 , -0.20)	0.00459	0.00011	+0.00003 -0.00003	+0.00002 -0.00000	0.00000	0.00000
(-0.20 , -0.16)	0.00391	0.00010	+0.00002 -0.00003	+0.00002 -0.00000	0.00000	0.00000
(-0.16 , -0.12)	0.00286	0.00010	+0.00002 -0.00002	+0.00001 -0.00000	0.00000	0.00000
(-0.12 , -0.08)	0.00202	0.00011	+0.00001 -0.00001	+0.00001 -0.00000	0.00000	0.00000
(-0.08 , -0.04)	0.00118	0.00010	+0.00001 -0.00001	+0.00000 -0.00000	0.00000	0.00000
(-0.04 , 0.00)	0.00051	0.00011	+0.00000 -0.00000	+0.00000 -0.00000	0.00000	0.00000

Table 6.18: Numerical values of the ATEEC function together with statistical and systematic uncertainties for $1000 \text{ GeV} < H_{\text{T2}} < 1200 \text{ GeV}$.

$\cos \phi$	Value	Stat.	JES	JER	JAR	MC Mod.
(-1.00 , -0.98)	-3.82885	0.00224	+0.02415 -0.02459	+0.04010 -0.01127	0.00746	0.02181
(-0.98 , -0.96)	1.61787	0.00178	+0.00815 -0.00884	+0.00285 -0.00077	0.00330	0.00278
(-0.96 , -0.94)	0.73982	0.00125	+0.00392 -0.00391	+0.00279 -0.00054	0.00113	0.00082
(-0.94 , -0.92)	0.42879	0.00100	+0.00252 -0.00243	+0.00176 -0.00033	0.00050	0.00037
(-0.92 , -0.90)	0.26523	0.00085	+0.00165 -0.00158	+0.00114 -0.00021	0.00024	0.00019
(-0.90 , -0.88)	0.18227	0.00072	+0.00116 -0.00111	+0.00080 -0.00014	0.00014	0.00011
(-0.88 , -0.86)	0.13604	0.00066	+0.00087 -0.00083	+0.00060 -0.00011	0.00009	0.00007
(-0.86 , -0.84)	0.10699	0.00060	+0.00069 -0.00066	+0.00047 -0.00009	0.00006	0.00005
(-0.84 , -0.82)	0.08554	0.00055	+0.00055 -0.00053	+0.00038 -0.00007	0.00004	0.00004
(-0.82 , -0.80)	0.07101	0.00050	+0.00045 -0.00044	+0.00031 -0.00006	0.00003	0.00003
(-0.80 , -0.76)	0.05497	0.00028	+0.00035 -0.00034	+0.00024 -0.00004	0.00002	0.00002
(-0.76 , -0.72)	0.04152	0.00025	+0.00026 -0.00026	+0.00019 -0.00004	0.00001	0.00002
(-0.72 , -0.68)	0.03234	0.00024	+0.00021 -0.00020	+0.00015 -0.00003	0.00001	0.00001
(-0.68 , -0.64)	0.02614	0.00021	+0.00017 -0.00017	+0.00012 -0.00003	0.00001	0.00001
(-0.64 , -0.60)	0.02132	0.00020	+0.00014 -0.00014	+0.00010 -0.00003	0.00000	0.00001

(-0.60 , -0.56)	0.01741	0.00020	+0.00012 -0.00012	+0.00008 -0.00002	0.00000	0.00001
(-0.56 , -0.52)	0.01523	0.00019	+0.00010 -0.00010	+0.00007 -0.00002	0.00000	0.00001
(-0.52 , -0.48)	0.01273	0.00017	+0.00009 -0.00009	+0.00006 -0.00002	0.00000	0.00000
(-0.48 , -0.44)	0.01065	0.00017	+0.00007 -0.00007	+0.00005 -0.00002	0.00000	0.00000
(-0.44 , -0.40)	0.00979	0.00017	+0.00007 -0.00007	+0.00005 -0.00002	0.00000	0.00000
(-0.40 , -0.36)	0.00798	0.00017	+0.00006 -0.00005	+0.00004 -0.00001	0.00000	0.00000
(-0.36 , -0.32)	0.00681	0.00016	+0.00005 -0.00005	+0.00003 -0.00001	0.00000	0.00000
(-0.32 , -0.28)	0.00580	0.00016	+0.00004 -0.00004	+0.00003 -0.00001	0.00000	0.00000
(-0.28 , -0.24)	0.00499	0.00016	+0.00004 -0.00003	+0.00002 -0.00001	0.00000	0.00000
(-0.24 , -0.20)	0.00413	0.00016	+0.00003 -0.00003	+0.00002 -0.00001	0.00000	0.00000
(-0.20 , -0.16)	0.00340	0.00015	+0.00002 -0.00002	+0.00002 -0.00001	0.00000	0.00000
(-0.16 , -0.12)	0.00276	0.00015	+0.00002 -0.00002	+0.00001 -0.00001	0.00000	0.00000
(-0.12 , -0.08)	0.00158	0.00015	+0.00001 -0.00001	+0.00001 -0.00000	0.00000	0.00000
(-0.08 , -0.04)	0.00110	0.00015	+0.00001 -0.00001	+0.00001 -0.00000	0.00000	0.00000
(-0.04 , 0.00)	0.00070	0.00017	+0.00001 -0.00000	+0.00000 -0.00000	0.00000	0.00000

Table 6.19: Numerical values of the ATEEC function together with statistical and systematic uncertainties for $1200 \text{ GeV} < H_{\text{T2}} < 1400 \text{ GeV}$.

$\cos \phi$	Value	Stat.	JES	JER	JAR	MC Mod.
(-1.00 , -0.98)	-3.44871	0.00344	+0.02441 -0.02370	+0.04192 -0.01373	0.00786	0.03190
(-0.98 , -0.96)	1.49143	0.00275	+0.00861 -0.00850	+0.00503 -0.00143	0.00346	0.00820
(-0.96 , -0.94)	0.67624	0.00192	+0.00426 -0.00443	+0.00249 -0.00042	0.00130	0.00255
(-0.94 , -0.92)	0.38492	0.00151	+0.00267 -0.00267	+0.00153 -0.00024	0.00071	0.00114
(-0.92 , -0.90)	0.23797	0.00124	+0.00174 -0.00170	+0.00101 -0.00015	0.00039	0.00059
(-0.90 , -0.88)	0.16156	0.00112	+0.00122 -0.00115	+0.00071 -0.00010	0.00023	0.00034
(-0.88 , -0.86)	0.12051	0.00098	+0.00091 -0.00084	+0.00053 -0.00007	0.00015	0.00023
(-0.86 , -0.84)	0.09358	0.00084	+0.00070 -0.00064	+0.00041 -0.00005	0.00011	0.00016
(-0.84 , -0.82)	0.07404	0.00077	+0.00055 -0.00050	+0.00033 -0.00004	0.00007	0.00012
(-0.82 , -0.80)	0.06213	0.00072	+0.00046 -0.00041	+0.00027 -0.00003	0.00006	0.00009
(-0.80 , -0.76)	0.04829	0.00041	+0.00036 -0.00031	+0.00021 -0.00002	0.00004	0.00007
(-0.76 , -0.72)	0.03602	0.00036	+0.00027 -0.00023	+0.00016 -0.00002	0.00002	0.00005
(-0.72 , -0.68)	0.02775	0.00033	+0.00021 -0.00018	+0.00012 -0.00001	0.00002	0.00004
(-0.68 , -0.64)	0.02372	0.00033	+0.00019 -0.00016	+0.00010 -0.00001	0.00001	0.00003
(-0.64 , -0.60)	0.01847	0.00031	+0.00015 -0.00012	+0.00008 -0.00001	0.00001	0.00002
(-0.60 , -0.56)	0.01561	0.00029	+0.00013 -0.00011	+0.00007 -0.00001	0.00001	0.00002
(-0.56 , -0.52)	0.01326	0.00028	+0.00011 -0.00009	+0.00006 -0.00000	0.00000	0.00002
(-0.52 , -0.48)	0.01150	0.00026	+0.00010 -0.00008	+0.00005 -0.00000	0.00000	0.00001
(-0.48 , -0.44)	0.00978	0.00027	+0.00008 -0.00007	+0.00004 -0.00000	0.00000	0.00001
(-0.44 , -0.40)	0.00828	0.00026	+0.00007 -0.00006	+0.00004 -0.00000	0.00000	0.00001
(-0.40 , -0.36)	0.00707	0.00025	+0.00006 -0.00005	+0.00003 -0.00000	0.00000	0.00001
(-0.36 , -0.32)	0.00607	0.00024	+0.00005 -0.00005	+0.00003 -0.00000	0.00000	0.00001
(-0.32 , -0.28)	0.00490	0.00023	+0.00004 -0.00004	+0.00002 -0.00000	0.00000	0.00001
(-0.28 , -0.24)	0.00443	0.00024	+0.00004 -0.00003	+0.00002 -0.00000	0.00000	0.00001
(-0.24 , -0.20)	0.00351	0.00024	+0.00003 -0.00003	+0.00002 -0.00000	0.00000	0.00000
(-0.20 , -0.16)	0.00298	0.00022	+0.00003 -0.00002	+0.00001 -0.00000	0.00000	0.00000

(-0.16 , -0.12)	0.00245	0.00023	+0.00002 -0.00002	+0.00001 -0.00000	0.00000	0.00000
(-0.12 , -0.08)	0.00170	0.00023	+0.00001 -0.00001	+0.00001 -0.00000	0.00000	0.00000
(-0.08 , -0.04)	0.00067	0.00023	+0.00001 -0.00001	+0.00000 -0.00000	0.00000	0.00000
(-0.04 , 0.00)	0.00046	0.00026	+0.00000 -0.00000	+0.00000 -0.00000	0.00000	0.00000

Table 6.20: Numerical values of the ATEEC function together with statistical and systematic uncertainties for $1400 \text{ GeV} < H_{\text{T2}} < 1600 \text{ GeV}$.

$\cos \phi$	Value	Stat.	JES	JER	JAR	MC Mod.
(-1.00 , -0.98)	-3.12065	0.00509	+0.02468 -0.02357	+0.04335 -0.01457	0.00895	0.01600
(-0.98 , -0.96)	1.38846	0.00390	+0.01058 -0.00940	+0.00472 -0.00178	0.00400	0.00133
(-0.96 , -0.94)	0.61788	0.00268	+0.00426 -0.00411	+0.00339 -0.00030	0.00118	0.00038
(-0.94 , -0.92)	0.34747	0.00205	+0.00256 -0.00251	+0.00191 -0.00012	0.00054	0.00016
(-0.92 , -0.90)	0.21232	0.00170	+0.00162 -0.00164	+0.00116 -0.00006	0.00026	0.00008
(-0.90 , -0.88)	0.14331	0.00158	+0.00109 -0.00115	+0.00079 -0.00003	0.00014	0.00005
(-0.88 , -0.86)	0.10554	0.00134	+0.00079 -0.00086	+0.00058 -0.00002	0.00009	0.00003
(-0.86 , -0.84)	0.07939	0.00121	+0.00058 -0.00064	+0.00043 -0.00001	0.00006	0.00002
(-0.84 , -0.82)	0.06738	0.00114	+0.00048 -0.00054	+0.00037 -0.00001	0.00004	0.00002
(-0.82 , -0.80)	0.05323	0.00102	+0.00037 -0.00042	+0.00029 -0.00001	0.00003	0.00001
(-0.80 , -0.76)	0.04186	0.00058	+0.00028 -0.00033	+0.00023 -0.00001	0.00002	0.00001
(-0.76 , -0.72)	0.03083	0.00053	+0.00021 -0.00024	+0.00017 -0.00000	0.00001	0.00001
(-0.72 , -0.68)	0.02449	0.00048	+0.00016 -0.00019	+0.00013 -0.00000	0.00001	0.00001
(-0.68 , -0.64)	0.02000	0.00045	+0.00013 -0.00015	+0.00011 -0.00000	0.00001	0.00000
(-0.64 , -0.60)	0.01623	0.00044	+0.00011 -0.00012	+0.00009 -0.00000	0.00000	0.00000
(-0.60 , -0.56)	0.01338	0.00041	+0.00009 -0.00010	+0.00007 -0.00000	0.00000	0.00000
(-0.56 , -0.52)	0.01210	0.00040	+0.00008 -0.00009	+0.00007 -0.00000	0.00000	0.00000
(-0.52 , -0.48)	0.00936	0.00039	+0.00006 -0.00007	+0.00005 -0.00000	0.00000	0.00000
(-0.48 , -0.44)	0.00893	0.00038	+0.00006 -0.00007	+0.00005 -0.00000	0.00000	0.00000
(-0.44 , -0.40)	0.00718	0.00036	+0.00005 -0.00006	+0.00004 -0.00000	0.00000	0.00000
(-0.40 , -0.36)	0.00622	0.00035	+0.00005 -0.00005	+0.00003 -0.00000	0.00000	0.00000
(-0.36 , -0.32)	0.00541	0.00034	+0.00004 -0.00005	+0.00003 -0.00000	0.00000	0.00000
(-0.32 , -0.28)	0.00409	0.00035	+0.00003 -0.00003	+0.00002 -0.00000	0.00000	0.00000
(-0.28 , -0.24)	0.00410	0.00035	+0.00003 -0.00003	+0.00002 -0.00000	0.00000	0.00000
(-0.24 , -0.20)	0.00349	0.00033	+0.00003 -0.00003	+0.00002 -0.00000	0.00000	0.00000
(-0.20 , -0.16)	0.00255	0.00033	+0.00002 -0.00002	+0.00001 -0.00000	0.00000	0.00000
(-0.16 , -0.12)	0.00143	0.00033	+0.00001 -0.00001	+0.00001 -0.00000	0.00000	0.00000
(-0.12 , -0.08)	0.00134	0.00034	+0.00001 -0.00001	+0.00001 -0.00000	0.00000	0.00000
(-0.08 , -0.04)	0.00095	0.00034	+0.00001 -0.00001	+0.00001 -0.00000	0.00000	0.00000
(-0.04 , 0.00)	0.00034	0.00037	+0.00000 -0.00000	+0.00000 -0.00000	0.00000	0.00000

Table 6.21: Numerical values of the ATEEC function together with statistical and systematic uncertainties for $1600 \text{ GeV} < H_{\text{T2}} < 1800 \text{ GeV}$.

$\cos \phi$	Value	Stat.	JES	JER	JAR	MC Mod.
(-1.00 , -0.98)	-2.82934	0.00705	+0.02390 -0.02332	+0.04216 -0.01477	0.00755	0.01882
(-0.98 , -0.96)	1.28860	0.00552	+0.00947 -0.00857	+0.00488 -0.00000	0.00362	0.00188

(-0.96 , -0.94)	0.55821	0.00360	+0.00430 -0.00447	+0.00271 -0.00097	0.00088	0.00056
(-0.94 , -0.92)	0.32070	0.00290	+0.00252 -0.00267	+0.00153 -0.00056	0.00032	0.00026
(-0.92 , -0.90)	0.18713	0.00248	+0.00150 -0.00163	+0.00088 -0.00032	0.00014	0.00014
(-0.90 , -0.88)	0.12798	0.00211	+0.00107 -0.00113	+0.00060 -0.00022	0.00008	0.00009
(-0.88 , -0.86)	0.09372	0.00185	+0.00081 -0.00082	+0.00044 -0.00016	0.00005	0.00006
(-0.86 , -0.84)	0.07223	0.00168	+0.00063 -0.00063	+0.00034 -0.00013	0.00003	0.00004
(-0.84 , -0.80)	0.05197	0.00093	+0.00046 -0.00044	+0.00024 -0.00009	0.00002	0.00003
(-0.80 , -0.76)	0.03609	0.00078	+0.00031 -0.00030	+0.00017 -0.00006	0.00001	0.00002
(-0.76 , -0.72)	0.02769	0.00072	+0.00024 -0.00022	+0.00013 -0.00005	0.00001	0.00001
(-0.72 , -0.64)	0.01924	0.00041	+0.00017 -0.00016	+0.00009 -0.00004	0.00001	0.00001
(-0.64 , -0.56)	0.01300	0.00035	+0.00012 -0.00011	+0.00006 -0.00002	0.00000	0.00001
(-0.56 , -0.48)	0.00919	0.00032	+0.00009 -0.00007	+0.00004 -0.00002	0.00000	0.00000
(-0.48 , -0.36)	0.00682	0.00025	+0.00008 -0.00006	+0.00003 -0.00001	0.00000	0.00000
(-0.36 , -0.24)	0.00385	0.00024	+0.00005 -0.00003	+0.00002 -0.00001	0.00000	0.00000
(-0.24 , -0.12)	0.00213	0.00022	+0.00003 -0.00002	+0.00001 -0.00000	0.00000	0.00000
(-0.12 , 0.00)	0.00048	0.00024	+0.00001 -0.00000	+0.00000 -0.00000	0.00000	0.00000

Table 6.22: Numerical values of the ATEEC function together with statistical and systematic uncertainties for $1800 \text{ GeV} < H_{\text{T2}} < 2000 \text{ GeV}$.

$\cos \phi$	Value	Stat.	JES	JER	JAR	MC Mod.
(-1.00 , -0.98)	-2.54755	0.00800	+0.02184 -0.02387	+0.04220 -0.01283	0.00801	0.02286
(-0.98 , -0.96)	1.18575	0.00637	+0.00916 -0.01130	+0.00308 -0.00204	0.00378	0.00656
(-0.96 , -0.94)	0.51443	0.00426	+0.00414 -0.00395	+0.00332 -0.00000	0.00115	0.00274
(-0.94 , -0.92)	0.27817	0.00348	+0.00255 -0.00218	+0.00198 -0.00000	0.00051	0.00138
(-0.92 , -0.90)	0.17017	0.00279	+0.00164 -0.00158	+0.00131 -0.00000	0.00026	0.00079
(-0.90 , -0.88)	0.11057	0.00244	+0.00107 -0.00107	+0.00090 -0.00000	0.00015	0.00048
(-0.88 , -0.86)	0.08363	0.00216	+0.00080 -0.00082	+0.00071 -0.00000	0.00010	0.00034
(-0.86 , -0.84)	0.06339	0.00198	+0.00059 -0.00062	+0.00056 -0.00000	0.00007	0.00025
(-0.84 , -0.80)	0.04371	0.00102	+0.00040 -0.00042	+0.00040 -0.00000	0.00004	0.00016
(-0.80 , -0.76)	0.03189	0.00092	+0.00028 -0.00030	+0.00030 -0.00000	0.00003	0.00011
(-0.76 , -0.72)	0.02380	0.00086	+0.00021 -0.00022	+0.00023 -0.00000	0.00002	0.00008
(-0.72 , -0.64)	0.01735	0.00049	+0.00015 -0.00016	+0.00017 -0.00001	0.00001	0.00006
(-0.64 , -0.56)	0.01086	0.00041	+0.00010 -0.00010	+0.00011 -0.00000	0.00001	0.00004
(-0.56 , -0.48)	0.00797	0.00038	+0.00007 -0.00007	+0.00008 -0.00000	0.00000	0.00003
(-0.48 , -0.36)	0.00612	0.00029	+0.00006 -0.00006	+0.00006 -0.00000	0.00000	0.00002
(-0.36 , -0.24)	0.00295	0.00027	+0.00003 -0.00003	+0.00003 -0.00000	0.00000	0.00001
(-0.24 , -0.12)	0.00204	0.00026	+0.00002 -0.00002	+0.00002 -0.00000	0.00000	0.00001
(-0.12 , 0.00)	0.00078	0.00027	+0.00001 -0.00001	+0.00001 -0.00000	0.00000	0.00000

Table 6.23: Numerical values of the ATEEC function together with statistical and systematic uncertainties for $2000 \text{ GeV} < H_{\text{T2}} < 2300 \text{ GeV}$.

$\cos \phi$	Value	Stat.	JES	JER	JAR	MC Mod.
(-1.00 , -0.98)	-2.21693	0.01240	+0.02310 -0.01914	+0.04652 -0.01311	0.00859	0.02504
(-0.98 , -0.96)	1.07228	0.00999	+0.00973 -0.00810	+0.00749 -0.00232	0.00422	0.00500

(-0.96 , -0.94)	0.44351	0.00681	+0.00459 -0.00373	+0.00362 -0.00130	0.00110	0.00144
(-0.94 , -0.92)	0.24673	0.00526	+0.00279 -0.00218	+0.00205 -0.00073	0.00064	0.00066
(-0.92 , -0.90)	0.14716	0.00406	+0.00177 -0.00137	+0.00122 -0.00043	0.00041	0.00035
(-0.90 , -0.88)	0.08331	0.00356	+0.00103 -0.00080	+0.00069 -0.00024	0.00024	0.00018
(-0.88 , -0.86)	0.07113	0.00323	+0.00088 -0.00069	+0.00059 -0.00021	0.00021	0.00014
(-0.86 , -0.84)	0.05249	0.00286	+0.00064 -0.00050	+0.00043 -0.00015	0.00016	0.00010
(-0.84 , -0.80)	0.03760	0.00160	+0.00045 -0.00035	+0.00031 -0.00011	0.00012	0.00007
(-0.80 , -0.76)	0.02812	0.00137	+0.00033 -0.00026	+0.00023 -0.00008	0.00009	0.00005
(-0.76 , -0.72)	0.01676	0.00124	+0.00019 -0.00016	+0.00014 -0.00005	0.00005	0.00003
(-0.72 , -0.64)	0.01334	0.00073	+0.00015 -0.00013	+0.00011 -0.00004	0.00004	0.00002
(-0.64 , -0.56)	0.00874	0.00065	+0.00010 -0.00009	+0.00007 -0.00003	0.00003	0.00001
(-0.56 , -0.48)	0.00624	0.00060	+0.00007 -0.00006	+0.00005 -0.00002	0.00002	0.00001
(-0.48 , -0.36)	0.00487	0.00044	+0.00006 -0.00005	+0.00004 -0.00002	0.00002	0.00001
(-0.36 , -0.24)	0.00296	0.00041	+0.00003 -0.00003	+0.00003 -0.00001	0.00001	0.00000
(-0.24 , -0.12)	0.00169	0.00041	+0.00002 -0.00002	+0.00001 -0.00001	0.00001	0.00000
(-0.12 , 0.00)	0.00071	0.00042	+0.00001 -0.00001	+0.00001 -0.00000	0.00000	0.00000

Table 6.24: Numerical values of the ATEEC function together with statistical and systematic uncertainties for $2300 \text{ GeV} < H_{\text{T2}} < 2600 \text{ GeV}$.

$\cos \phi$	Value	Stat.	JES	JER	JAR	MC Mod.
(-1.00 , -0.98)	-1.86438	0.01737	+0.01978 -0.02155	+0.04272 -0.01356	0.00856	0.01440
(-0.98 , -0.96)	0.93649	0.01411	+0.00935 -0.00948	+0.00613 -0.00110	0.00430	0.00821
(-0.96 , -0.94)	0.36981	0.00848	+0.00392 -0.00451	+0.00257 -0.00052	0.00090	0.00324
(-0.94 , -0.92)	0.20334	0.00660	+0.00218 -0.00255	+0.00139 -0.00029	0.00031	0.00178
(-0.92 , -0.90)	0.12550	0.00569	+0.00134 -0.00161	+0.00085 -0.00018	0.00014	0.00110
(-0.90 , -0.88)	0.07662	0.00492	+0.00081 -0.00099	+0.00051 -0.00011	0.00007	0.00066
(-0.88 , -0.86)	0.04866	0.00414	+0.00050 -0.00063	+0.00032 -0.00007	0.00004	0.00042
(-0.86 , -0.84)	0.04378	0.00397	+0.00045 -0.00056	+0.00029 -0.00007	0.00003	0.00037
(-0.84 , -0.80)	0.02913	0.00215	+0.00029 -0.00037	+0.00019 -0.00005	0.00002	0.00024
(-0.80 , -0.76)	0.01750	0.00181	+0.00017 -0.00022	+0.00011 -0.00003	0.00001	0.00014
(-0.76 , -0.72)	0.01604	0.00163	+0.00016 -0.00020	+0.00010 -0.00004	0.00001	0.00013
(-0.72 , -0.64)	0.00956	0.00093	+0.00009 -0.00012	+0.00006 -0.00003	0.00000	0.00008
(-0.64 , -0.56)	0.00773	0.00085	+0.00008 -0.00009	+0.00005 -0.00003	0.00000	0.00006
(-0.56 , -0.48)	0.00465	0.00075	+0.00005 -0.00006	+0.00003 -0.00002	0.00000	0.00004
(-0.48 , -0.36)	0.00418	0.00058	+0.00004 -0.00005	+0.00003 -0.00002	0.00000	0.00003
(-0.36 , -0.24)	0.00273	0.00055	+0.00003 -0.00003	+0.00002 -0.00001	0.00000	0.00002
(-0.24 , -0.12)	0.00187	0.00055	+0.00002 -0.00002	+0.00001 -0.00001	0.00000	0.00001
(-0.12 , 0.00)	0.00012	0.00056	+0.00000 -0.00000	+0.00000 -0.00000	0.00000	0.00000

Table 6.25: Numerical values of the ATEEC function together with statistical and systematic uncertainties for $2600 \text{ GeV} < H_{\text{T2}} < 3000 \text{ GeV}$.

$\cos \phi$	Value	Stat.	JES	JER	JAR	MC Mod.
(-1.00 , -0.98)	-1.53739	0.02549	+0.01909 -0.01958	+0.04707 -0.01239	0.00737	0.02188

(-0.98 , -0.96)	0.80833	0.02020	+0.00970 -0.00943	+0.00854 -0.00179	0.00408	0.00873
(-0.96 , -0.94)	0.29614	0.01240	+0.00334 -0.00388	+0.00297 -0.00066	0.00133	0.00320
(-0.94 , -0.92)	0.16845	0.00959	+0.00207 -0.00231	+0.00170 -0.00037	0.00068	0.00182
(-0.92 , -0.90)	0.09437	0.00827	+0.00124 -0.00131	+0.00097 -0.00021	0.00036	0.00102
(-0.90 , -0.86)	0.05636	0.00450	+0.00076 -0.00079	+0.00059 -0.00013	0.00020	0.00061
(-0.86 , -0.80)	0.02541	0.00253	+0.00035 -0.00036	+0.00028 -0.00006	0.00008	0.00027
(-0.80 , -0.72)	0.01046	0.00158	+0.00015 -0.00015	+0.00012 -0.00002	0.00003	0.00011
(-0.72 , -0.60)	0.00836	0.00105	+0.00012 -0.00012	+0.00010 -0.00002	0.00003	0.00009
(-0.60 , -0.36)	0.00311	0.00057	+0.00005 -0.00005	+0.00004 -0.00001	0.00001	0.00003
(-0.36 , 0.00)	0.00096	0.00044	+0.00001 -0.00001	+0.00001 -0.00000	0.00000	0.00001

Table 6.26: Numerical values of the ATEEC function together with statistical and systematic uncertainties for $3000 \text{ GeV} < H_{\text{T2}} < 3500 \text{ GeV}$.

$\cos \phi$	Value	Stat.	JES	JER	JAR	MC Mod.
(-1.00 , -0.98)	-1.06094	0.03387	+0.01747 -0.01808	+0.04384 -0.01477	0.00696	0.01366
(-0.98 , -0.96)	0.56234	0.02713	+0.00733 -0.00792	+0.00593 -0.00146	0.00316	0.00821
(-0.96 , -0.94)	0.22355	0.01786	+0.00315 -0.00350	+0.00297 -0.00071	0.00054	0.00335
(-0.94 , -0.92)	0.14089	0.01393	+0.00208 -0.00236	+0.00205 -0.00052	0.00028	0.00213
(-0.92 , -0.90)	0.04946	0.01068	+0.00081 -0.00088	+0.00076 -0.00020	0.00010	0.00075
(-0.90 , -0.86)	0.03403	0.00582	+0.00060 -0.00063	+0.00054 -0.00015	0.00007	0.00052
(-0.86 , -0.80)	0.01392	0.00296	+0.00026 -0.00027	+0.00023 -0.00007	0.00003	0.00022
(-0.80 , -0.72)	0.00945	0.00223	+0.00019 -0.00019	+0.00016 -0.00005	0.00002	0.00016
(-0.72 , -0.60)	0.00489	0.00138	+0.00010 -0.00010	+0.00008 -0.00003	0.00001	0.00008
(-0.60 , -0.36)	0.00066	0.00070	+0.00001 -0.00001	+0.00001 -0.00000	0.00000	0.00001
(-0.36 , 0.00)	0.00092	0.00058	+0.00002 -0.00002	+0.00002 -0.00000	0.00000	0.00002

Table 6.27: Numerical values of the ATEEC function together with statistical and systematic uncertainties for $H_{\text{T2}} > 3500 \text{ GeV}$.

6.7 Theoretical predictions

The theoretical predictions for the TEEC function are calculated from the NNLO 3-jet cross sections obtained by M. Czakon, A. Mitov and R. Poncelet using pQCD in powers of the strong coupling constant, $\alpha_s(\mu_R)$, [65]. Their calculations at NNLO include NLO corrections and LO predictions compatible with the ones provided by NLOJET++ [61, 62]. The value of $\alpha_s(\mu_R)$ which enters in the partonic matrix-element calculation is obtained by evolving the α_s values provided by the PDF at the Z boson mass scale, $m_Z = 91$ GeV. Jets are reconstructed using the anti- k_t algorithm with $R = 0.4$ as implemented in FASTJET [58], and the NNLO PDF groups used to convolute the partonic cross sections are provided in the LHAPDF [57] package, namely MMHT 2014 [78], NNPDF 3.0 [136], and CT14 [80]. It has been proved that the calculations obtained with CT18 [137] coincide with those of MMHT 2014 when evolving the nominal value $\alpha_s(m_Z) = 0.1180$. They use the $\overline{\text{MS}}$ scheme in the fixed-flavour number scheme for $n_f = 5$.

The STRIPPER scheme [63, 64] introduced in Section 4.1 allows the calculation of NNLO QCD corrections to 3-jet events. For this subtraction scheme, higher order corrections are decomposed in different contributions which are calculated separately and then added all together to the LO prediction. The NLO correction is built with the virtual-finite term VF, the real-finite term RF, and the unresolved terms and convolutions UC. In addition, the NNLO correction is made of the double-virtual finite term VVF, the double-real finite term RRF, the single-unresolved term SU, the double-unresolved term DU, the real-virtual-finite term RVF, and finite remainders FR. Figure 6.65 displays certain configurations of NNLO corrections to 3-jet events for illustrative purposes only.

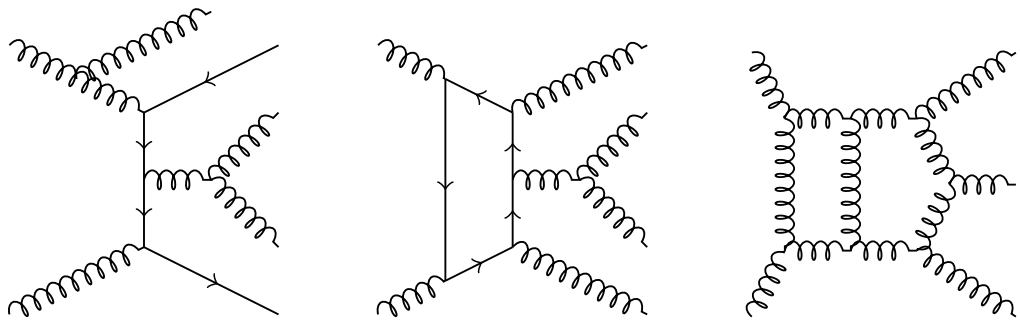


Figure 6.65: Feynman diagrams for gluon-gluon processes at 3-jet NNLO accuracy in pQCD. These particular configurations contribute to the RRF (left), RVF (middle), and VVF (right) terms. They are depicted for illustrative purposes only and have been provided through the courtesy of R. Poncelet.

Finite theoretical predictions for processes with incoming hadrons and totally inclusive in the final state can be obtained at any order in pQCD. The cross section is factorized into the partonic cross sections, $\hat{\sigma}_{ab}$, and the PDFs, $f_{a/p}(x_a)$ and $f_{b/p}(x_b)$, where x_a and x_b are the fractional momenta carried by the incoming partons a and b , respectively. The azimuthal angular range in the calculation is restricted in the

calculation to $|\cos\phi| < 0.92$ due to the finite resolution for the angular difference between jet pairs introduced by the jet algorithm. In the pQCD framework at NNLO, the differential partonic cross section for a $2 \rightarrow m$ partonic process is given by

$$d\hat{\sigma}_{ab \rightarrow m} = d\sigma_{ab}^{B(m)} + d\sigma_{ab}^{VF(m)} + d\sigma_{ab}^{RF(m+1)} + d\sigma_{ab}^{UC(m)} + d\sigma_{ab}^{VVF(m)} + \\ d\sigma_{ab}^{RRF(m+2)} + d\sigma_{ab}^{SU(m+1)} + d\sigma_{ab}^{DU(m)} + d\sigma_{ab}^{RVF(m+1)} + d\sigma_{ab}^{FR(m)}.$$

The azimuthal cut avoids calculating the $2 \rightarrow 2$ partonic processes at Born level and their virtual corrections for $\cos\phi$ distributions. Moreover, the contribution of unbalanced 2-jet events in the range $|\cos\phi| < 0.92$ is highly suppressed. Therefore, the TEEC function can be simply calculated as the transverse energy-weighted 3-jet cross section of produced jet pairs in $\cos\phi$ normalized to the 2-jet cross section. The former is computed in this framework as

$$\frac{d\Sigma^{3\text{jet}}}{d\cos\phi} = \sum_{i,j}^{\text{jets}} \int \left(\sum_{a,b}^{\text{part.}} f_{a/p} f_{b/p} \otimes d\hat{\sigma}_{ab \rightarrow 3} \frac{E_{Ti} E_{Tj}}{E_T^2} \delta(\cos\phi - \cos\Delta\varphi_{ij}) \right)$$

where \otimes denotes the convolution of the partonic cross sections with the parton distribution functions. See more details in Section 2.1.

The renormalization and factorization scales, $\mu_{R,F}$, inherent in any pQCD calculation with incoming hadrons, contribute to the cross section computation with logarithmic terms as $\ln(\mu_{R,F}^2/Q^2)$ where Q is a physical hard scale. In order to keep the perturbative framework reliable, these scales are taken to reflect the physical hard scale Q . Therefore, the renormalization and factorization scales are set for each event to the interaction scale of the partonic process given by the sum of the transverse momentum of the outgoing partons, $\mu_{R,F} = \hat{H}_T$.

In that situation, the strong coupling becomes indicative of the effective strength of the short-distance interaction between partons. Furthermore, this scale choice is event based, infrared safe and independent of the analysis constraints. In Born kinematics, \hat{H}_T coincides with the event based scale, H_{T2} . Recently, the authors of Ref. [138] have found the central scale choice $\mu_R = \hat{H}_T$ to be clearly favoured in terms of stability and convergence of the perturbative expansion for single jet inclusive production and encourage to use it for precision determination of QCD parameters.

The treatment of the number of active flavours follows a mixed scheme in this analysis. On the one hand the fixed-order predictions are calculated in the fixed-flavour number scheme for $n_f = 5$, but on the other hand the strong coupling α_s includes the top-quark flavour in the running. The proper transition rules for $n_f = 5$ to $n_f = 6$ are applied, so that the running of α_s is a continuous function across top quark mass threshold. Despite the lack of the top-quark flavour in the fixed-order predictions, the effects from top-quark loops are not expected to be sizeable when everything is treated consistently and the fraction of $t\bar{t}$ dijets events is negligible for the inclusive sample.

In order to fit the theoretical predictions in pQCD to the experimental results mea-

sured by ATLAS, thus determining the strong coupling α_s , the former must be generated with precision. $5 \times \mathcal{O}(10^{13})$ events are generated for the calculation. In total, around 200M CPU hours in the WLCG infrastructure were required to produce the whole theoretical sample at NNLO in pQCD.

The pQCD predictions for the TEEC function are calculated at parton level only, i.e. considering jets as collimated bunches of partons instead of hadrons. Therefore, in order to compare with the experimental results at particle level, the predictions have to be unfolded from the parton to the hadron (particle) level, correcting them for non-pQCD effects, namely hadronization, underlying event (UE) and beam remnants. See more details in Section 2.2. A bin-by-bin correcting method based on correction factors is considered, where the factors are obtained using a PYTHIA 8.235 simulated sample with ATLAS A14 tune [73] and NNPDF 2.3 LO [77], which is the same one used to unfold the measurements from detector to particle level.

The non-pQCD correction factors are just the ratio between the predictions simulated at particle and parton level as implemented in RIVET, with the only difference that in the parton-level predictions effects due to hadronization, multi-parton interactions (MPI) and primordial k_t are turned off. These factors correct the pQCD prediction to the particle level by multiplying each $\cos\phi$ bin of the theoretical distributions. They are also calculated using other tunes like the default one and the tune 4C [139]. Moreover, they are calculated too using a HERWIG 7.2.1 simulated sample with the default tune. The other tunes available, namely, BaryonicReconnection and SoftTune, provide similar predictions. Figures 6.66 and 6.67 show the distributions of these correction factors for the TEEC function. The non-pQCD effects are only significant in the nearly self correlation limit, $\cos\phi > 0.86$ where the factors can reach a 5% deviation. In addition, to avoid statistical fluctuations spoiling the accuracy in the pQCD predictions, the Gaussian kernel smoothing technique, introduced in Section 6.5, is applied in the range $|\cos\phi| < 0.86$ to the non-pQCD correction factor distributions.

The statistical uncertainty is below the one from measurements at NLO and comes from two different sources. Namely, the one provided by the parton-level predictions and the one from MC simulations generated with PYTHIA 8.235, required for the bin-by-bin correcting method. The clear dependence of the predictions with the strong coupling value $\alpha_s(m_Z)$ for each H_{T2} interval makes these observables suitable to determine the fundamental QCD parameter at large scale regimes. Figures 6.68 to 6.73 show the particle-level pQCD predictions for the TEEC and ATEEC functions at NLO, along with their dependence upon the strong coupling $\alpha_s(m_Z)$, using MMHT 2014 as the nominal group of parton distribution functions. Unfortunately, the current statistical uncertainties in the NNLO predictions do not match the experimental accuracy. Therefore and in order to mitigate theoretical statistical fluctuations, theoretical predictions at NNLO are presented with a coarser binning.

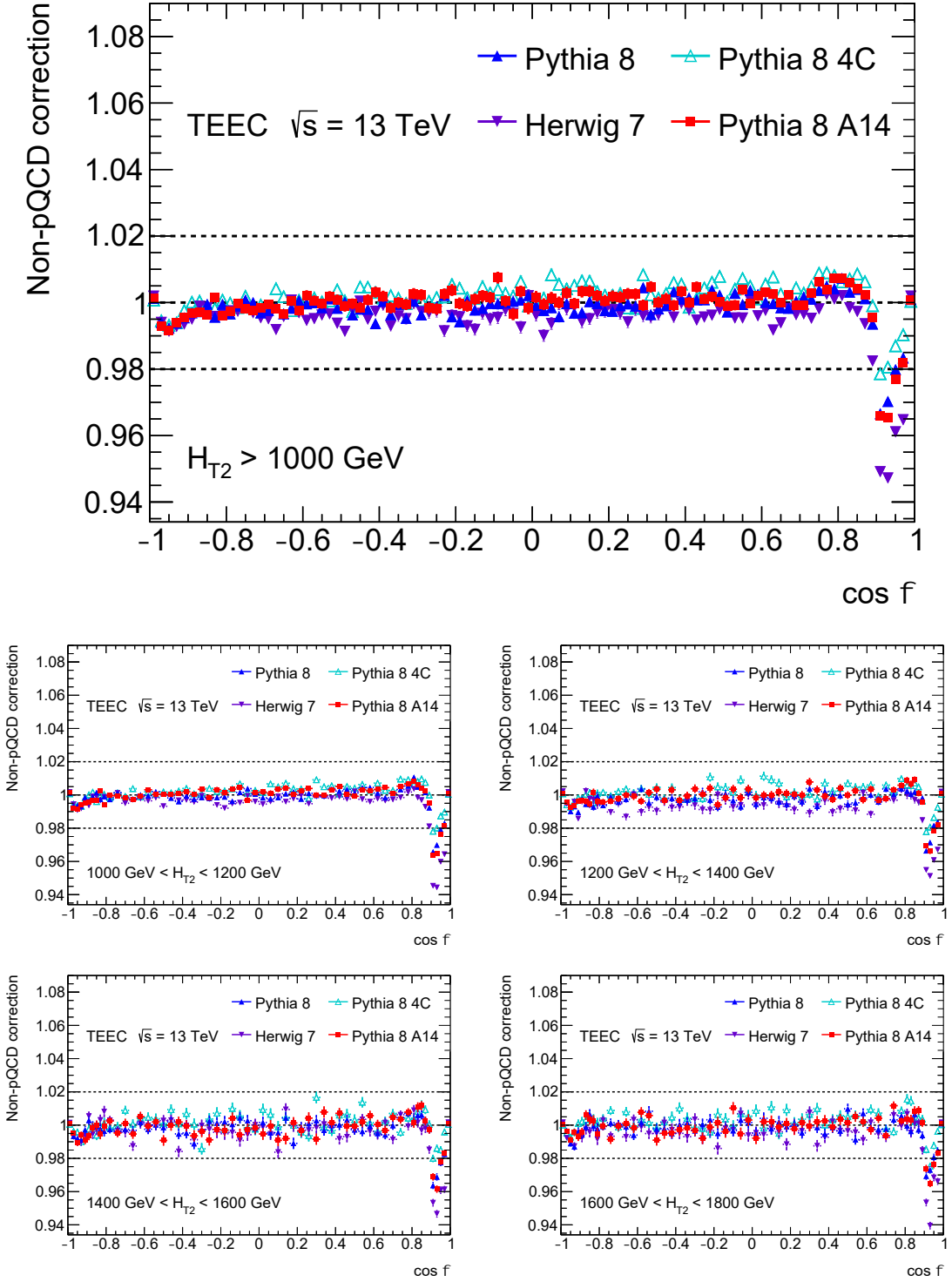


Figure 6.66: Non-perturbative QCD correction factors, in inclusive (top) and exclusive (bottom) H_{T2} bins, for the TEEC function obtained from MC simulated samples with PYTHIA 8.235 and HERWIG 7.2.1 event generator. They are only significant in the nearly self correlation limit.

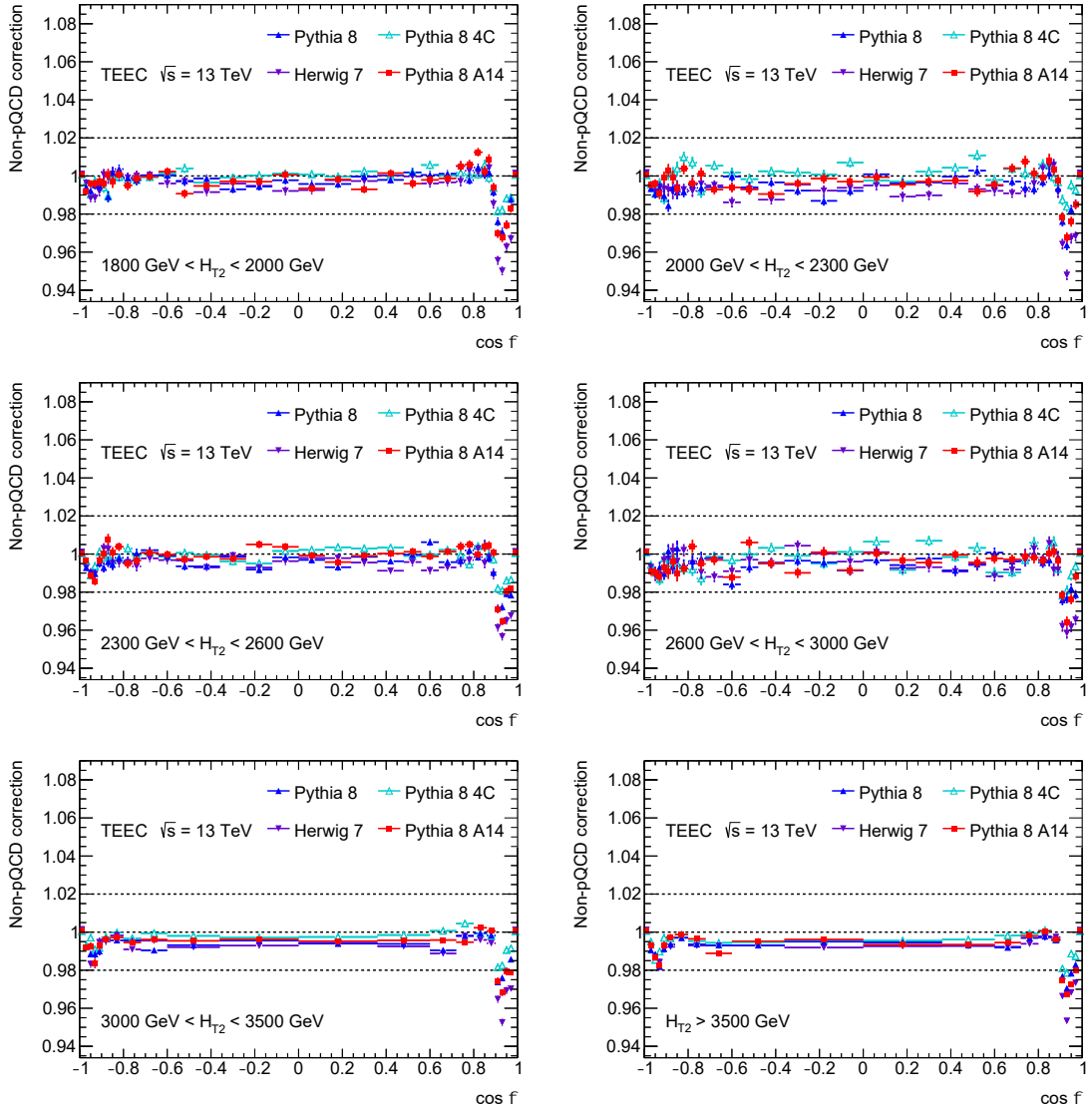


Figure 6.67: Non-perturbative QCD correction factors, in exclusive H_{T2} bins, for the TEEC function obtained from MC simulated samples with PYTHIA 8.235 and HERWIG 7.2.1 event generator. They are only significant in the nearly self correlation limit.

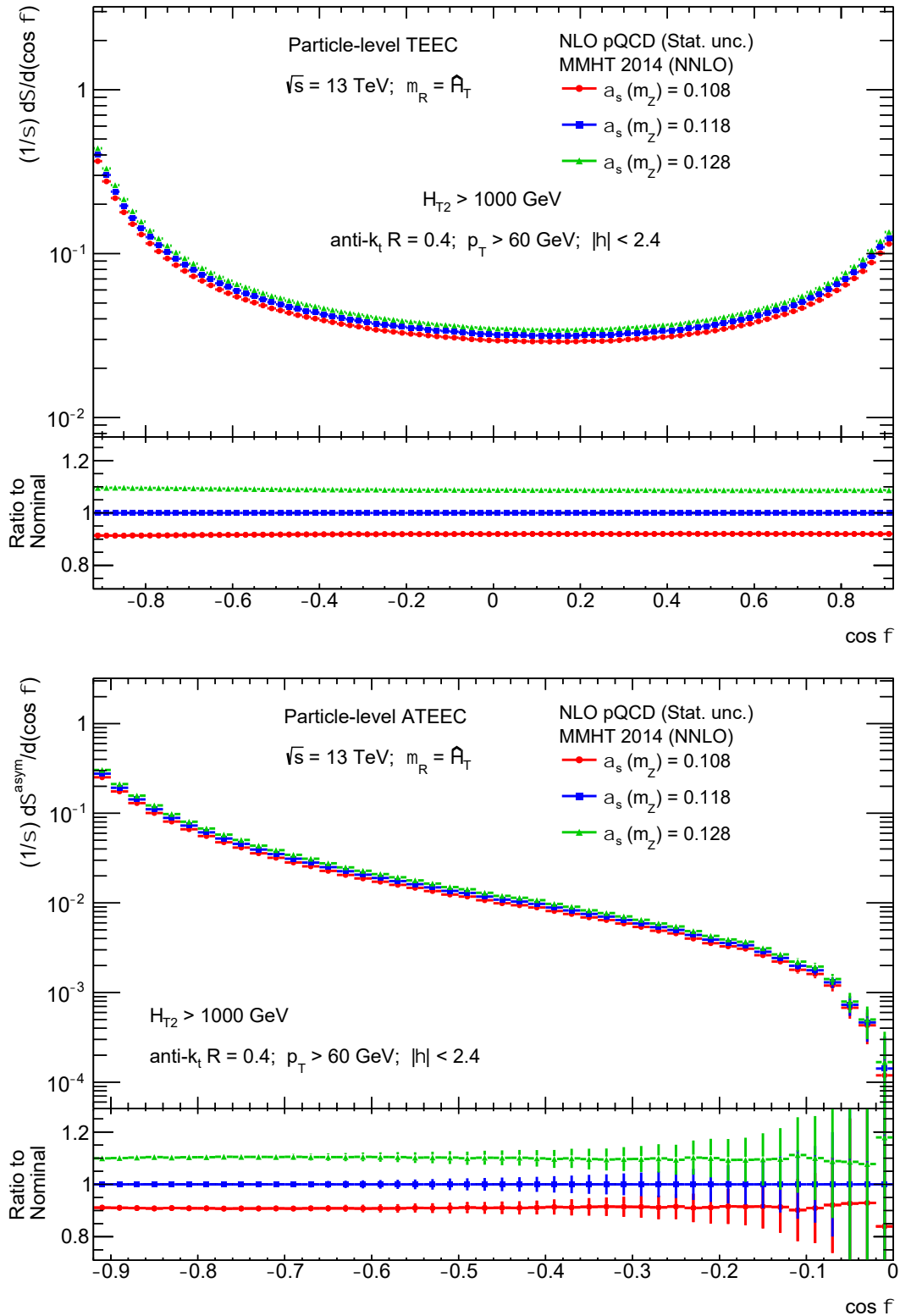


Figure 6.68: Dependence with $\alpha_s(m_Z)$ of the particle-level pQCD predictions at NLO for the TEEC (top) and ATEEC (bottom) functions in the inclusive H_{T2} sample using MMHT 2014 PDF group. The clear dependence of the predictions with the value $\alpha_s(m_Z)$ makes these observables suitable to determine the strong coupling.

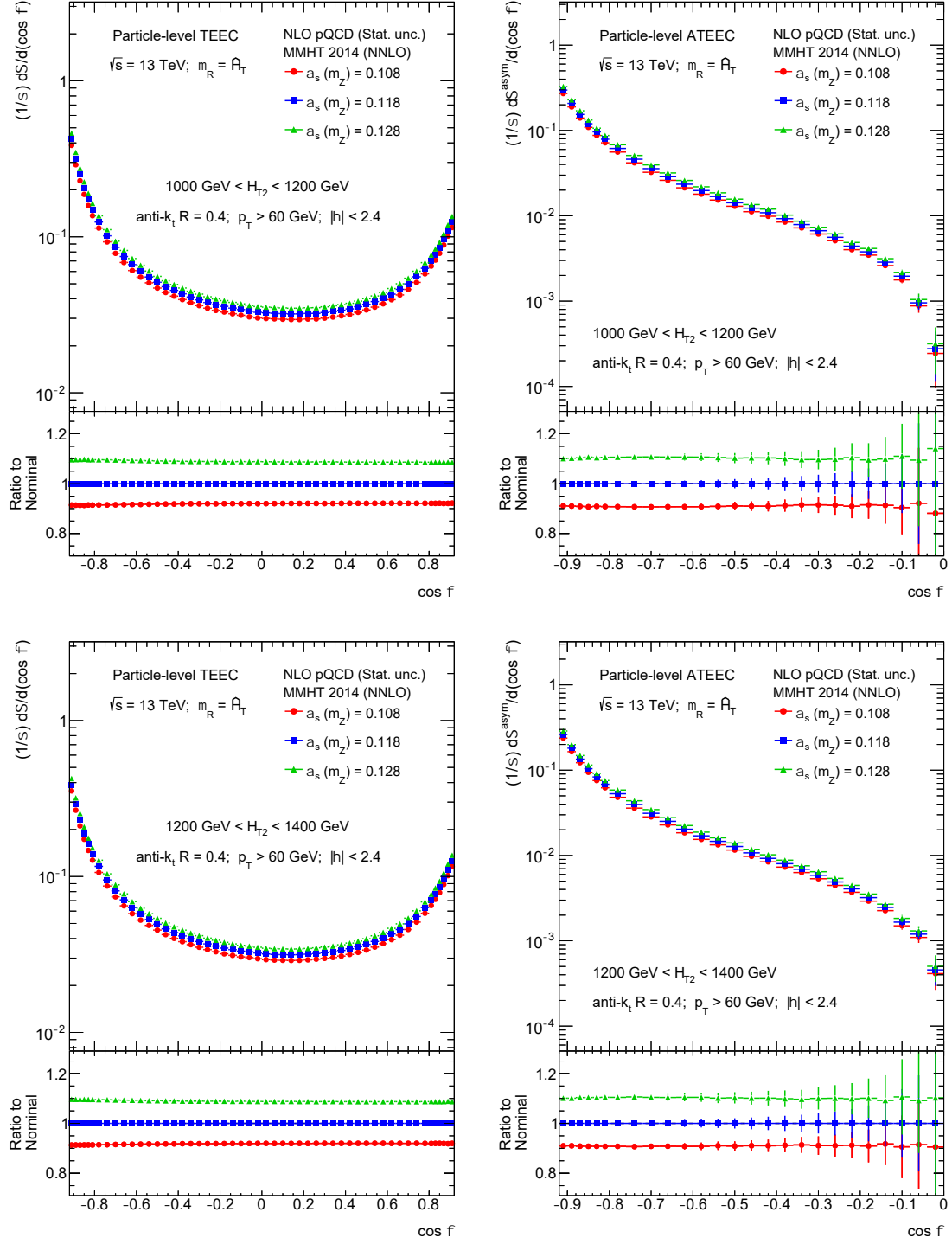


Figure 6.69: Dependence with $\alpha_s(m_Z)$ of the particle-level pQCD predictions at NLO for the TEEC (left) and ATEEC (right) functions in two exclusive H_{T2} bins using MMHT 2014 PDF group. The clear dependence of the predictions with the value $\alpha_s(m_Z)$ makes these observables suitable to determine the strong coupling.

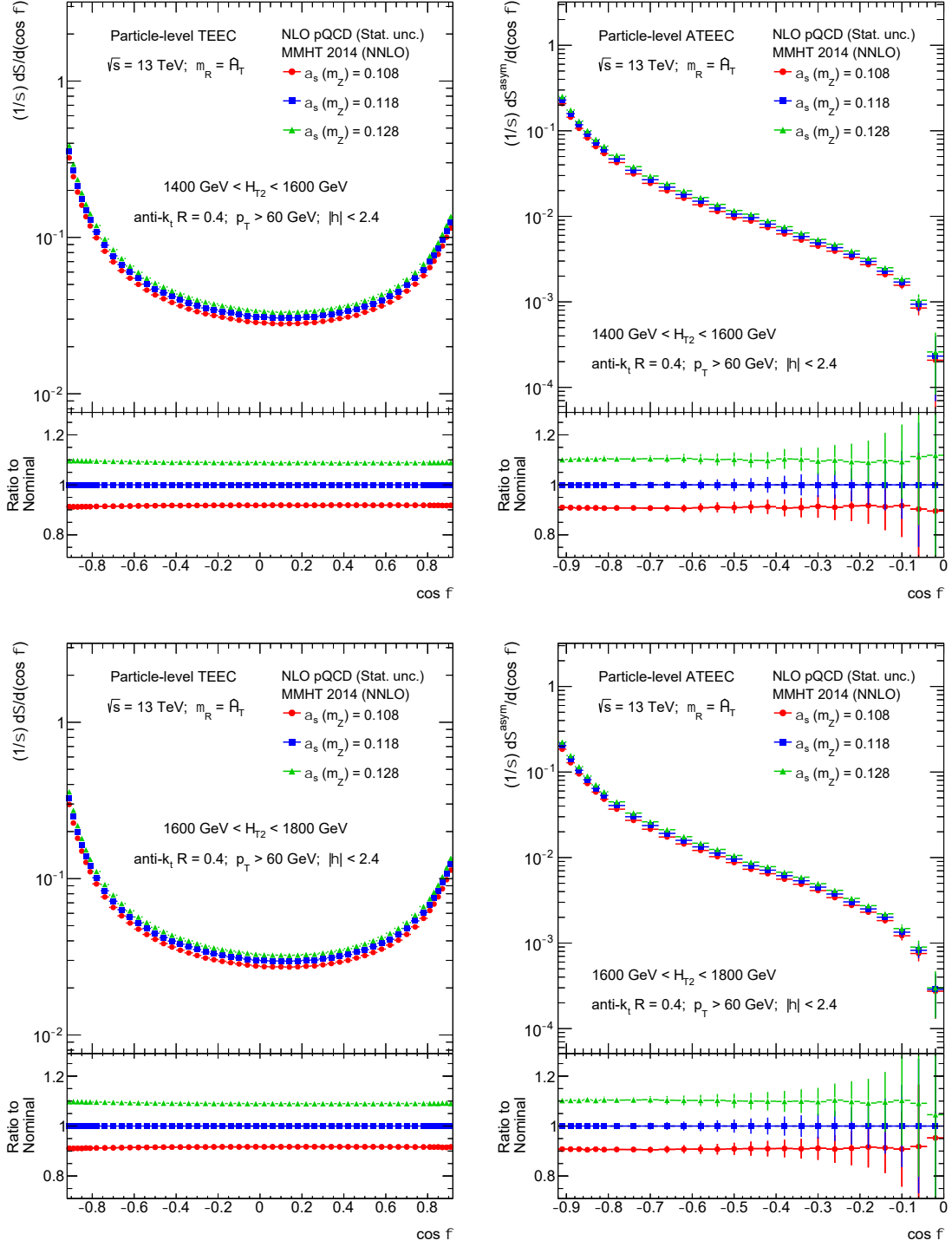


Figure 6.70: Dependence with $\alpha_s(m_Z)$ of the particle-level pQCD predictions at NLO for the TEEC (left) and ATEEC (right) functions in two exclusive H_{T2} bins using MMHT 2014 PDF group. The clear dependence of the predictions with the value $\alpha_s(m_Z)$ makes these observables suitable to determine the strong coupling.

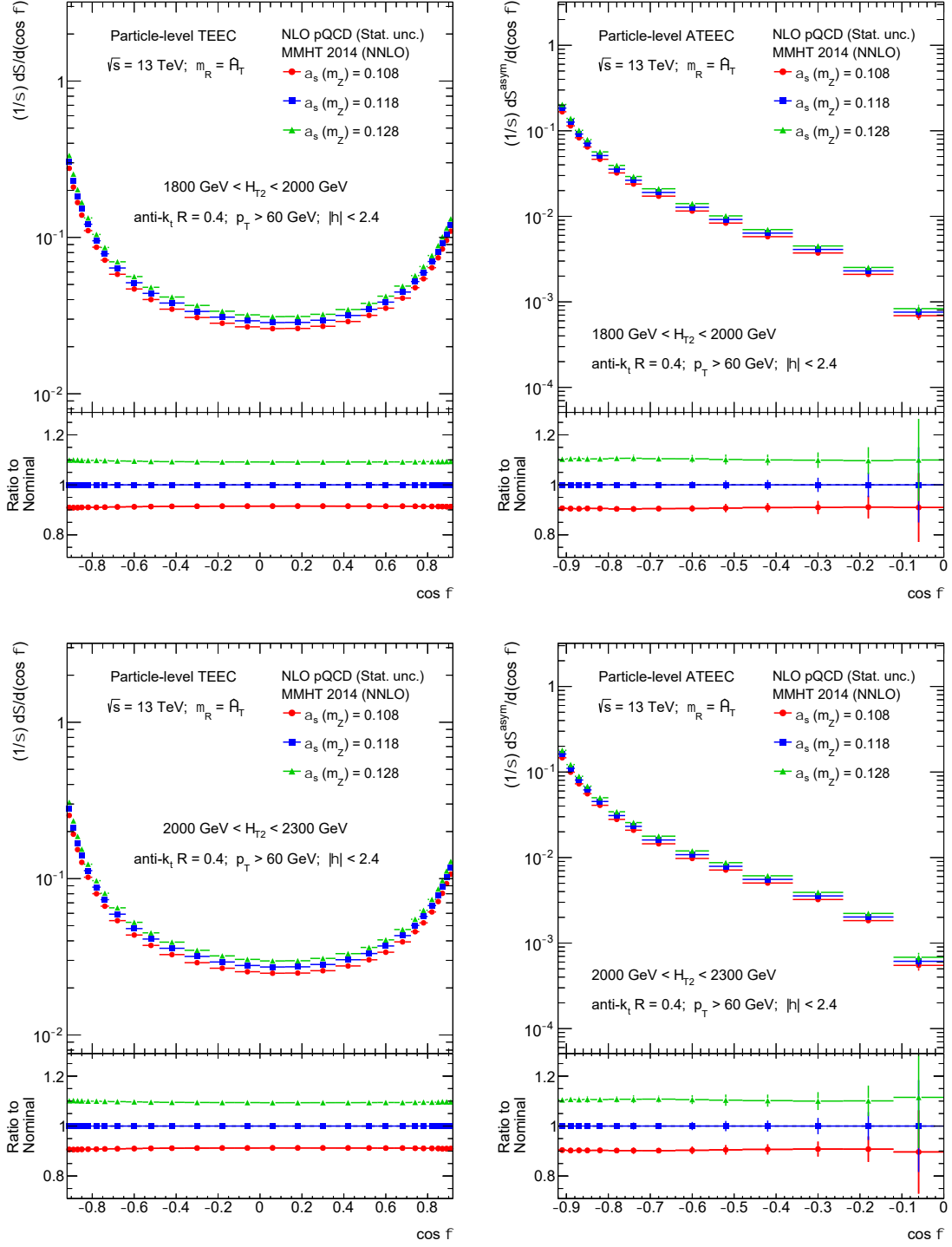


Figure 6.71: Dependence with $\alpha_s(m_Z)$ of the particle-level pQCD predictions at NLO for the TEEC (left) and ATEEC (right) functions in two exclusive H_{T2} bins using MMHT 2014 PDF group. The clear dependence of the predictions with the value $\alpha_s(m_Z)$ makes these observables suitable to determine the strong coupling.

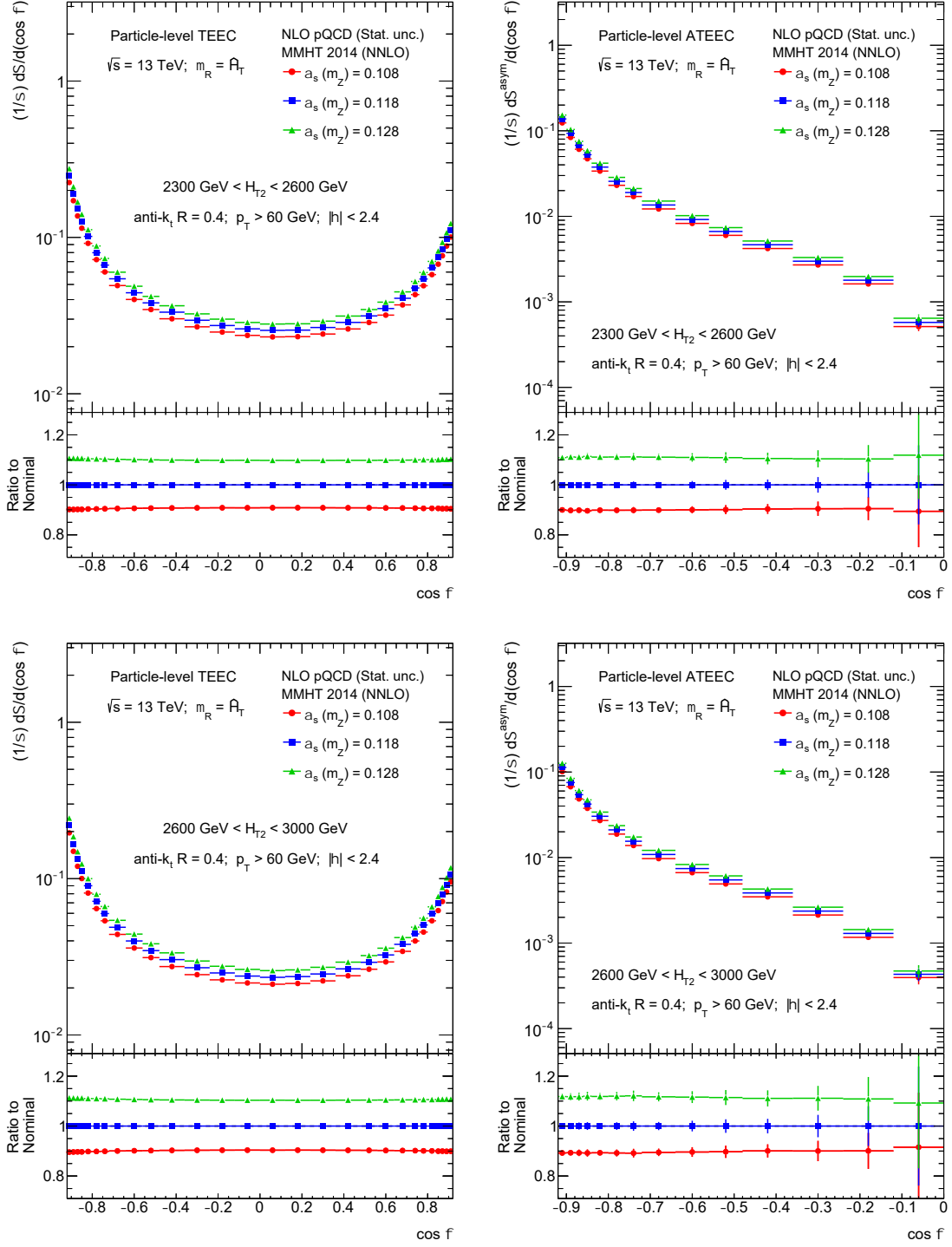


Figure 6.72: Dependence with $\alpha_s(m_Z)$ of the particle-level pQCD predictions at NLO for the TEEC (left) and ATEEC (right) functions in two exclusive H_{T2} bins using MMHT 2014 PDF group. The clear dependence of the predictions with the value $\alpha_s(m_Z)$ makes these observables suitable to determine the strong coupling.

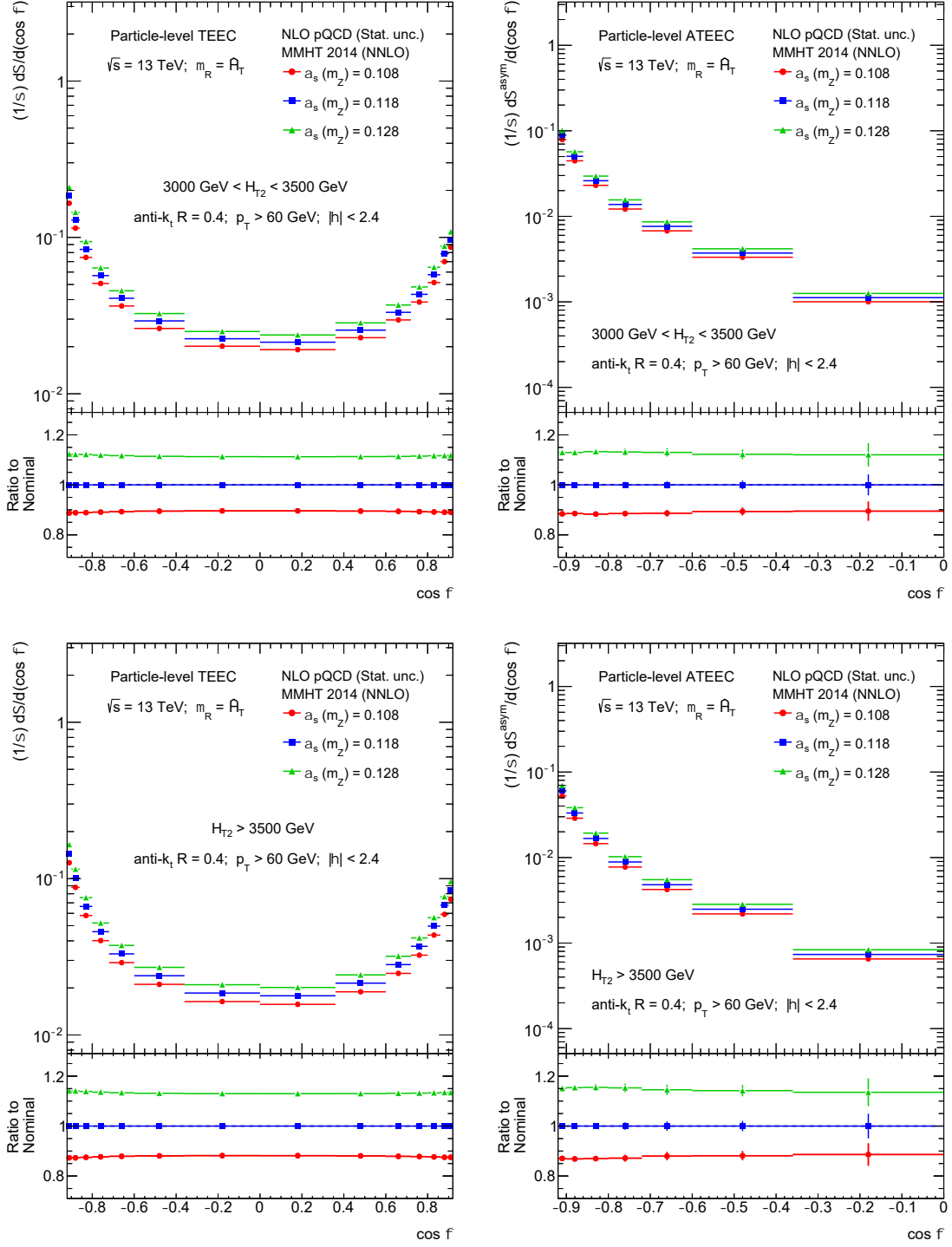


Figure 6.73: Dependence with $\alpha_s(m_Z)$ of the particle-level pQCD predictions at NLO for the TEEC (left) and ATEEC (right) functions in two exclusive H_{T2} bins using MMHT 2014 PDF group. The clear dependence of the predictions with the value $\alpha_s(m_Z)$ makes these observables suitable to determine the strong coupling.

6.7.1 Theoretical systematic uncertainties

The theoretical uncertainties are divided into statistical and systematic uncertainties. The systematic uncertainties sources include the PDF parametrization, the different MC tunes used to correct for non-pQCD effects, and the dependence of the unphysical scales introduced in Section 2.1.

The choice of the theoretical scales gives rise to a scale uncertainty, which is calculated varying the renormalization and factorization scales by a factor of two, $\mu_R = x_R \hat{H}_T$ and $\mu_F = x_F \hat{H}_T$, with the additional requirement $1/2 \leq x_R/x_F \leq 2$ to avoid large logarithmic contributions. This uncertainty improves significantly the accuracy in the pQCD predictions when compared to those in Refs. [1, 2] which reached up to 20% in the central plateau and were based on the choice $\mu_R = H_{T2}/2$.

The ambiguity in the MC tune used to correct for non-pQCD effects is computed as the envelope of the differences of the particle-level theoretical predictions corrected with the different tunes with respect to the nominal prediction, which uses ATLAS tune A14 for the non-pQCD correction. The value of this uncertainty is below 1% in the phase-space region where α_s is determined.

In order to take into account the uncertainty on the PDF parameters, the PDFs are varied following the set of replicas or eigenvectors of the covariance matrix provided by each group, which come from fitted parameters at a confidence level of 68% or 90%. The propagation of the corresponding uncertainty to the observables is done following the set of errors and combining them accordingly [78, 80, 136]. NNPDF 3.0 provides a set of $N = 100$ replicas; while MMHT 2014 and CT14 use a Hessian type of error, providing a set of $N = 25$ and $N = 28$ eigenvectors, respectively, with non-symmetric variations up and down.

The relative uncertainty at a confidence level of 68% for an observable H due to the uncertainty in PDF parameter k is defined in Eq. (6.3) for each PDF group:

$$\begin{aligned} \sigma_k^{\text{MMHT}} &= \frac{|H_k^{\text{up}} - H_k^{\text{down}}|}{2H}; & \sigma_k^{\text{NNPDF}} &= \frac{1}{\sqrt{N-1}} \frac{|H_k - \langle H \rangle|}{H}; \\ \sigma_k^{\text{CT14}} &= \frac{|H_k^{\text{up}} - H_k^{\text{down}}|}{1.645 \cdot 2H}. \end{aligned} \quad (6.3)$$

The PDF parametrization uncertainties are then added in quadrature. Figures 6.74 and 6.75 show these uncertainties for the TEEC distributions at LO and NLO. The relative uncertainty has a mild dependence with the perturbative order for all PDF groups considered. Thus, they are not explicitly computed at NNLO in order to save computational resources; instead, they are extrapolated from the NLO results.

The total theoretical uncertainty is then obtained by adding these uncertainties in quadrature and shown in Figures 6.76 and 6.77. The NNLO corrections for the scale choice $\mu_{R,F} = \hat{H}_T$ reduce the scale uncertainty down to 2% for the central plateau of the TEEC function. This is the dominant uncertainty of the analysis. However, the PDF parametrization uncertainty can increase up to 2% for high H_{T2} intervals.

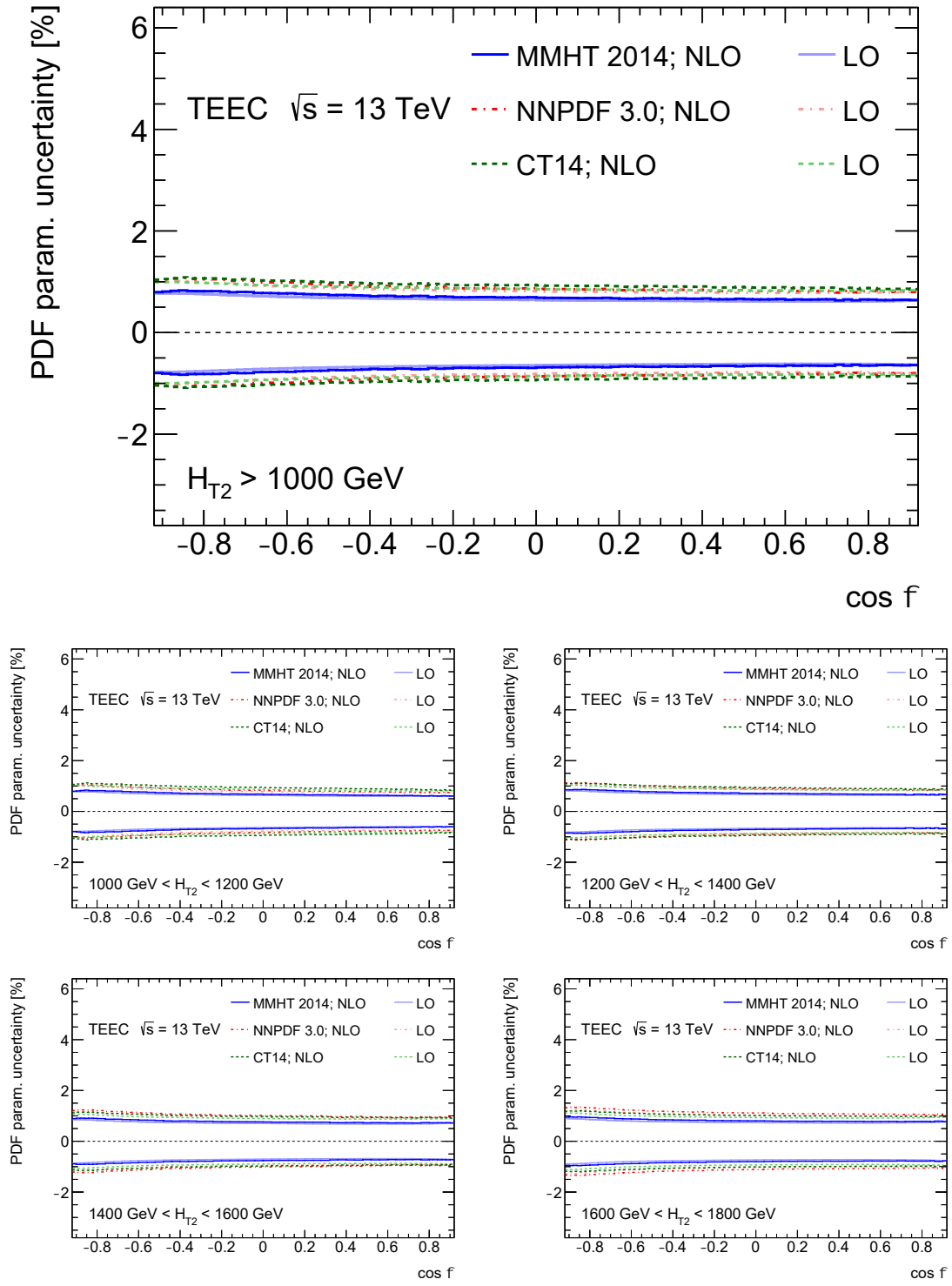


Figure 6.74: Theoretical relative uncertainty for the TEEC distributions at LO and NLO in pQCD obtained from the PDF parameters using the PDF groups available, in inclusive (top) and exclusive (bottom) H_{T2} bins. The PDF parametrization uncertainty at NNLO is extrapolated from the NLO results applying the same relative uncertainty to the NNLO nominal value.

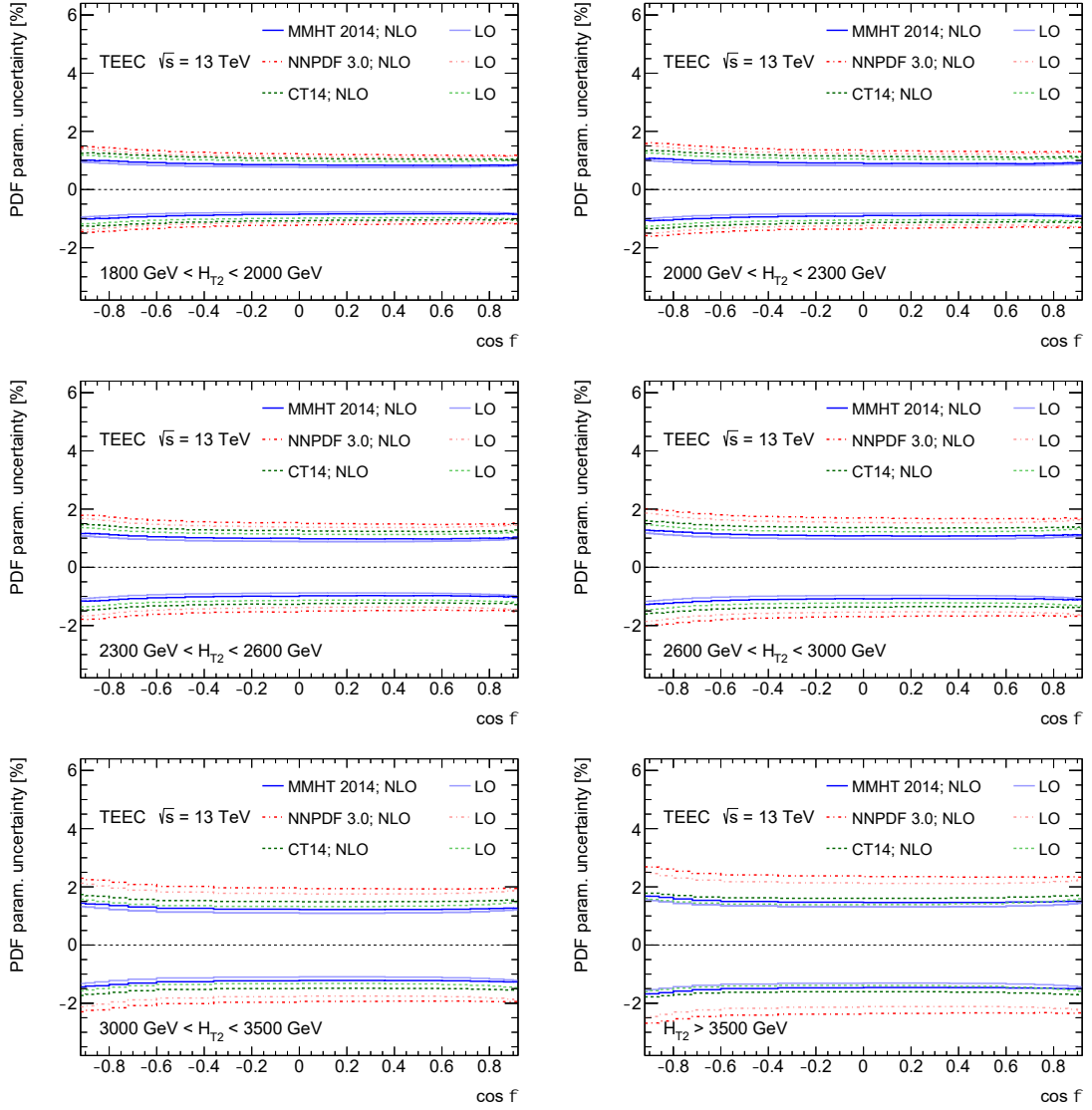


Figure 6.75: Theoretical relative uncertainty for the TEEC distributions at LO and NLO in pQCD obtained from the PDF parameters using the PDF groups available, in exclusive H_{T2} bins. The PDF parametrization uncertainty at NNLO is extrapolated from the NLO results applying the same relative uncertainty to the NNLO nominal value.

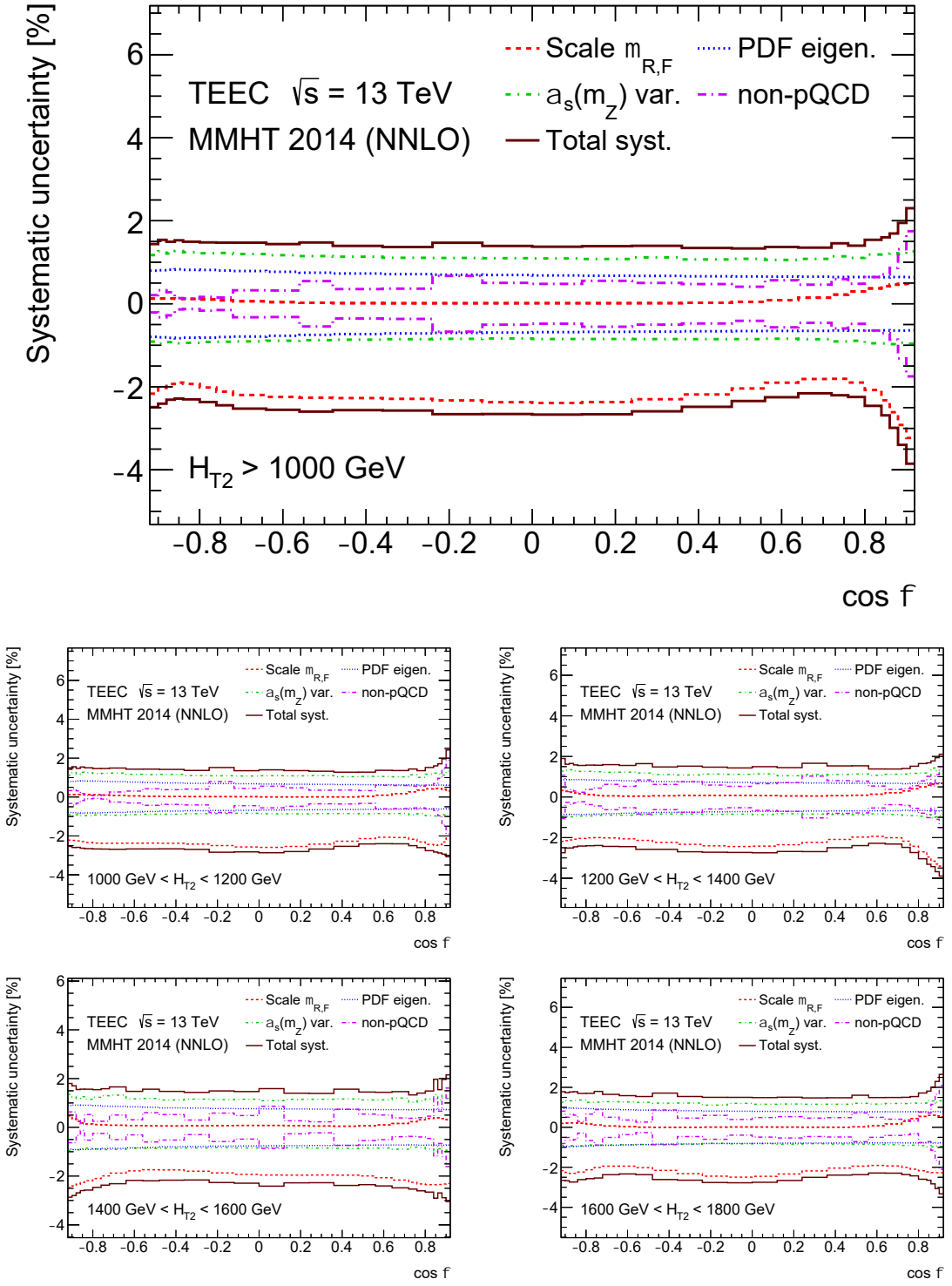


Figure 6.76: Total relative theoretical systematic uncertainty for the TEEC distribution using MMHT 2014 PDF group, in inclusive (top) and exclusive (bottom) H_{T2} bins, together with a breakdown on the general source uncertainties: PDF parametrization, theoretical scale, non-pQCD tune and $\alpha_s(m_Z)$ variation. These sources are added together in quadrature.

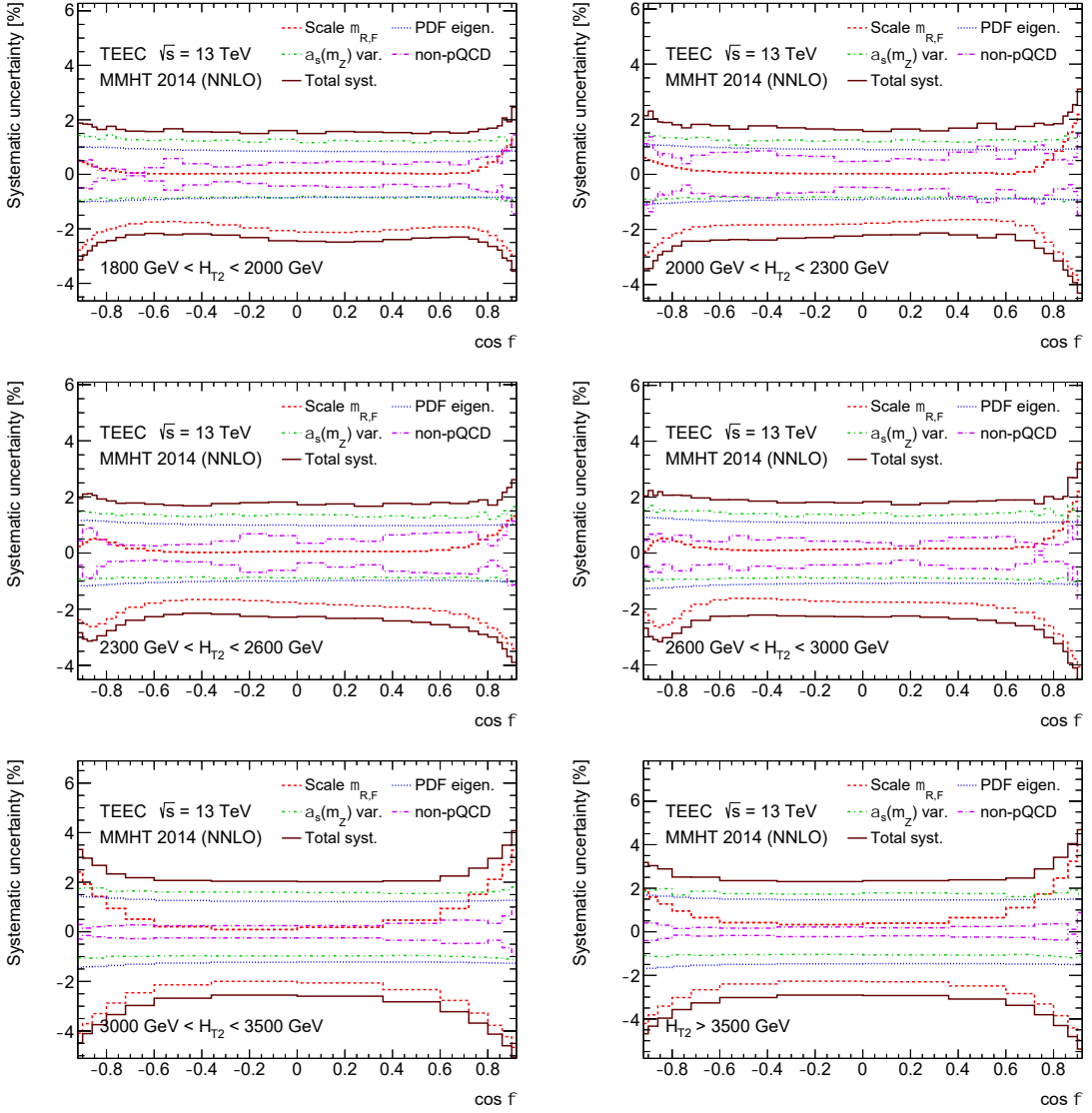


Figure 6.77: Total relative theoretical systematic uncertainty for the TEEC distribution using MMHT 2014 PDF group, in exclusive H_{T2} bins, together with a breakdown on the general source uncertainties: PDF parametrization, theoretical scale, non-pQCD tune and $\alpha_s(m_Z)$ variation. These sources are added together in quadrature.

6.8 Comparison of theory and experiment

The experimental results for the TEEC and ATEEC functions are compared to the pQCD predictions, once corrected for non-pQCD effects. Figures 6.78 to 6.83 show the ratio of the data to the theoretical predictions calculated using the PDF groups available at NNLO in pQCD with $\alpha_s(m_Z) = 0.1180$; taking into account all theoretical and experimental uncertainties. The theoretical uncertainty is dominated by the scale uncertainty in most of the phase space, therefore, all other sources are depicted together under the label of non-scale uncertainty.

In addition, Figures 6.84 to 6.89 compare the experimental data to the pQCD predictions for each of the PDF groups available. In order to have an idea about the size of the so called K-factors, a comparison between the LO and NNLO predictions to the NLO calculations is also presented. For higher perturbative orders the scale uncertainty is substantially reduced, improving the description of experimental data. The dependence of the other theoretical uncertainties with the perturbative order is mild, and therefore, they are not shown in the comparison. The statistical uncertainties are shown with a gray shaded band when larger than the scale ones.

The agreement between theoretical predictions at NNLO and experimental data is excellent over the whole phase space. The reduction of the scale uncertainties is made evident from these figures, as well as the improvement of the description. In particular, the collinear part, $\cos\phi > 0.80$, shows a great improvement for all H_{T2} bins. However, for the higher H_{T2} bins, and for some PDF sets, the NNLO theoretical predictions are slightly above the data.

This trend in normalization is understood to be due to the limited accuracy of the PDF determinations at high values of x , which are limited by the statistics and larger systematic uncertainties of the measurements used to constrain these regions. Indeed, the predictions for the TEEC functions vary less than 1% with the PDF set choice for lower H_{T2} intervals but around 2-3% for higher ones. Figure 6.90 compares the theoretical predictions at NLO for the TEEC function. Notice that their differences increase slightly at high-energy scales and that the results obtained with CT18 coincide with those of MMHT 2014 for the whole phase space. The ratios remain stable when higher order pQCD corrections are included in the calculations.

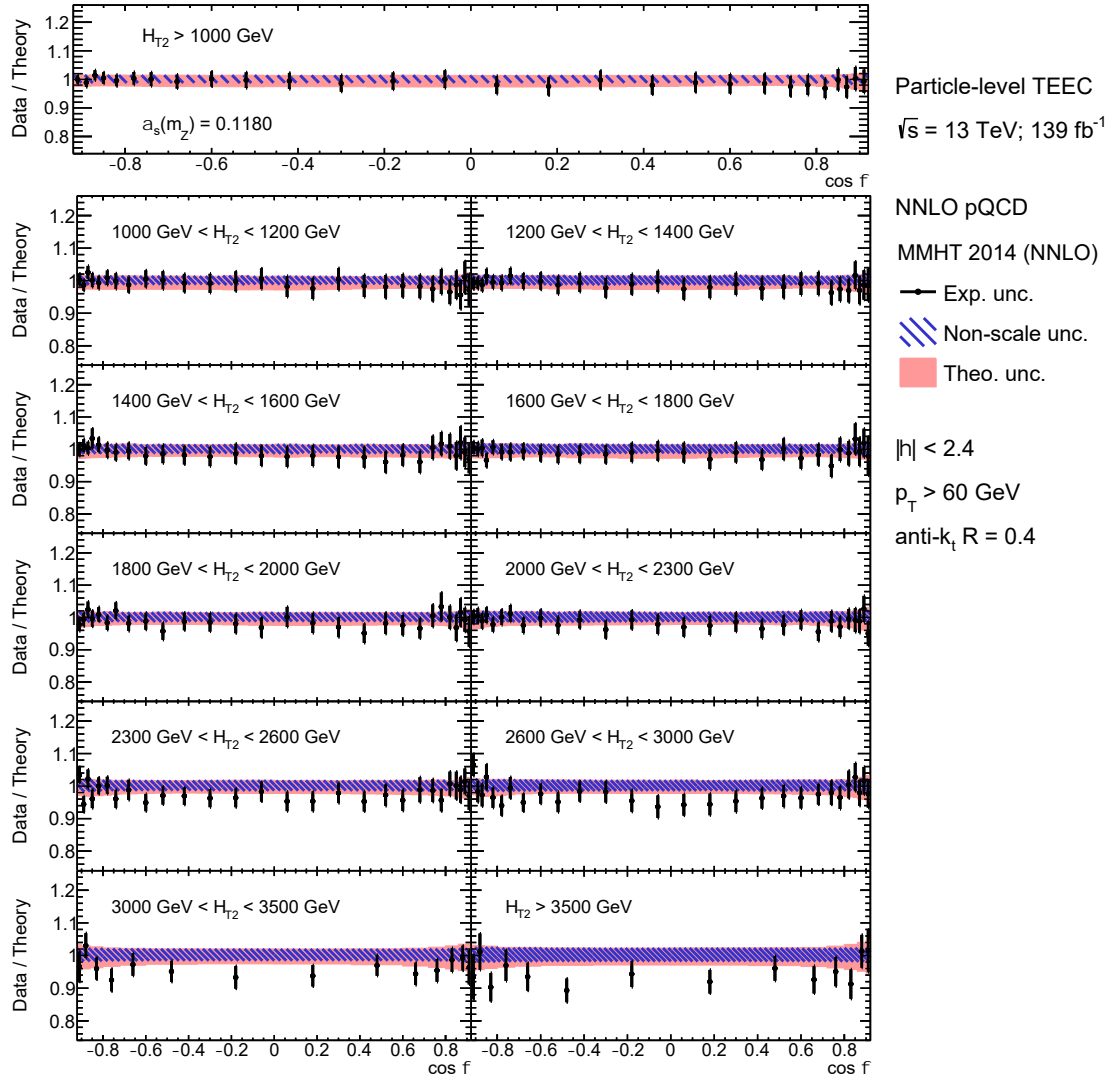


Figure 6.78: Ratios of the unfolded data to the particle-level NNLO pQCD predictions for the TEEC function obtained using MMHT 2014 PDF group, in inclusive and exclusive H_{T2} bins. The strong coupling constant is set to $\alpha_s(m_Z) = 0.1180$. The non-scale uncertainty corresponds to the PDF parametrization uncertainty, the $\alpha_s(m_Z)$ parameter uncertainty and the non-pQCD uncertainty from the MC model added in quadrature. The theoretical uncertainty includes both non-scale and scale uncertainties. The experimental uncertainty includes the statistical uncertainty.

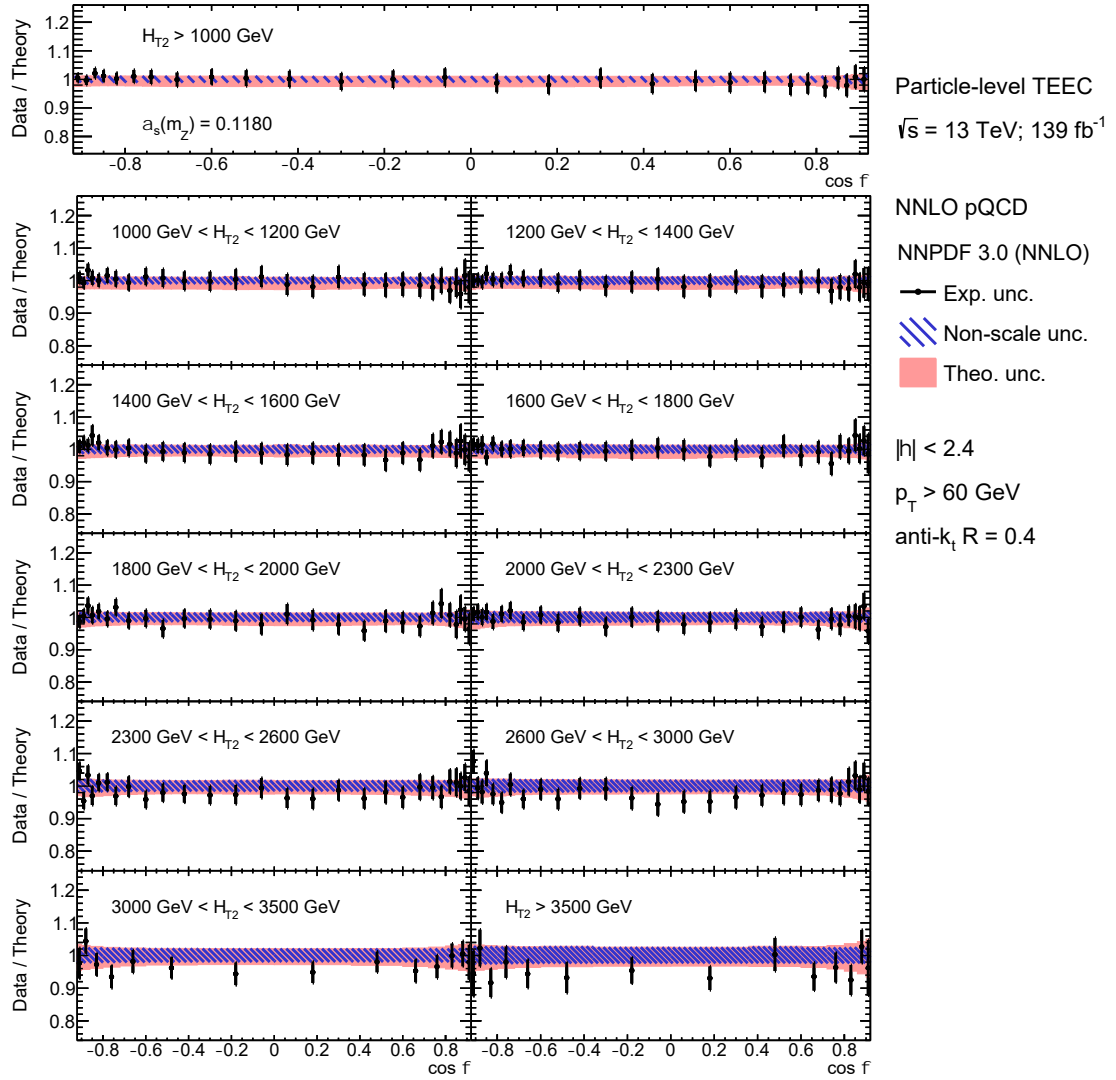


Figure 6.79: Ratios of the unfolded data to the particle-level NNLO pQCD predictions for the TEEC function obtained using NNPDF 3.0 PDF group, in inclusive and exclusive H_{T2} bins. The strong coupling constant is set to $\alpha_s(m_Z) = 0.1180$. The non-scale uncertainty corresponds to the PDF parametrization uncertainty, the $\alpha_s(m_Z)$ parameter uncertainty and the non-pQCD uncertainty from the MC model added in quadrature. The theoretical uncertainty includes both non-scale and scale uncertainties. The experimental uncertainty includes the statistical uncertainty.

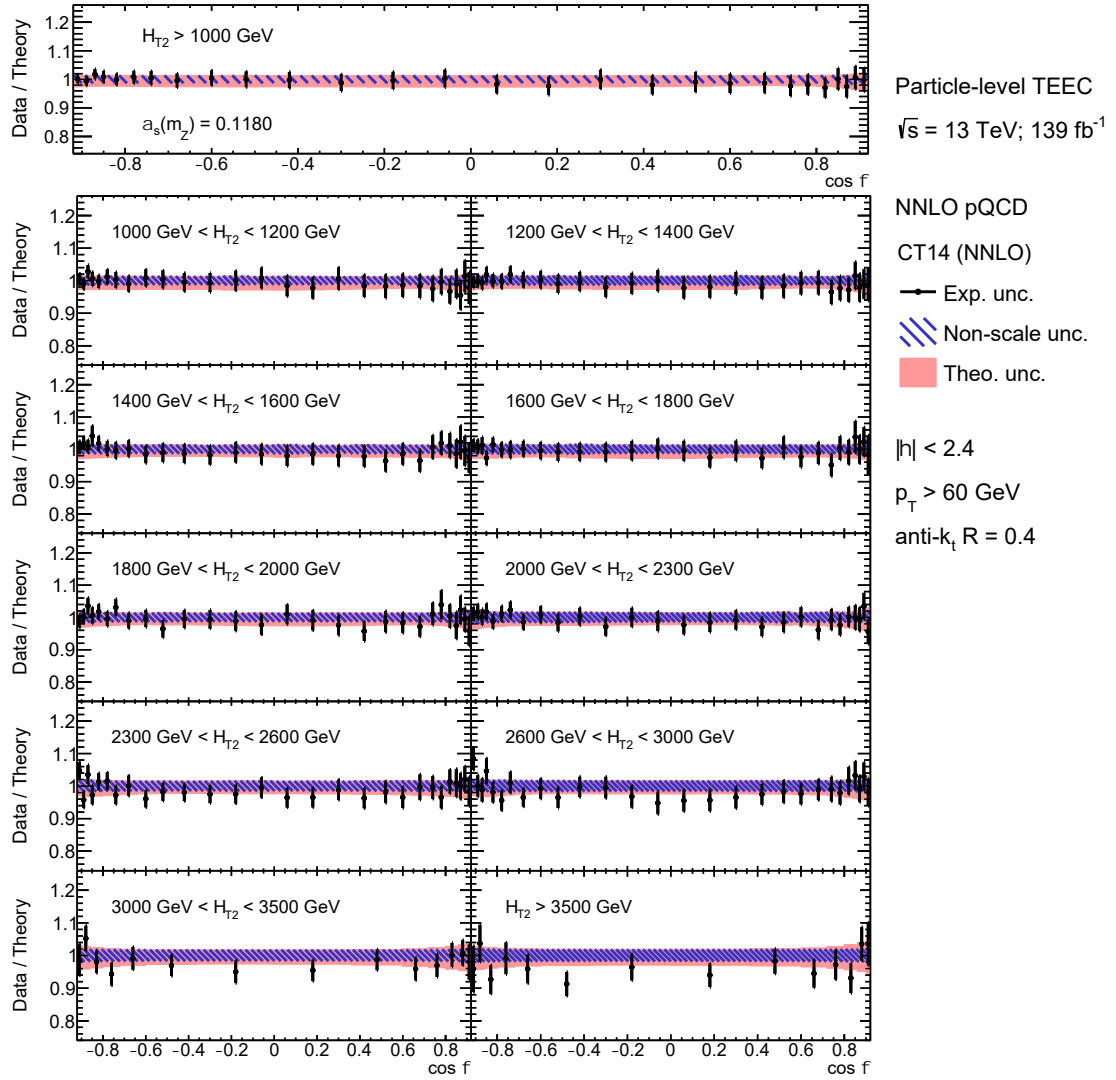


Figure 6.80: Ratios of the unfolded data to the particle-level NNLO pQCD predictions for the TEEC function obtained using CT14 PDF group, in inclusive and exclusive H_{T2} bins. The strong coupling constant is set to $\alpha_s(m_Z) = 0.1180$. The non-scale uncertainty corresponds to the PDF parametrization uncertainty, the $\alpha_s(m_Z)$ parameter uncertainty and the non-pQCD uncertainty from the MC model added in quadrature. The theoretical uncertainty includes both non-scale and scale uncertainties. The experimental uncertainty includes the statistical uncertainty.

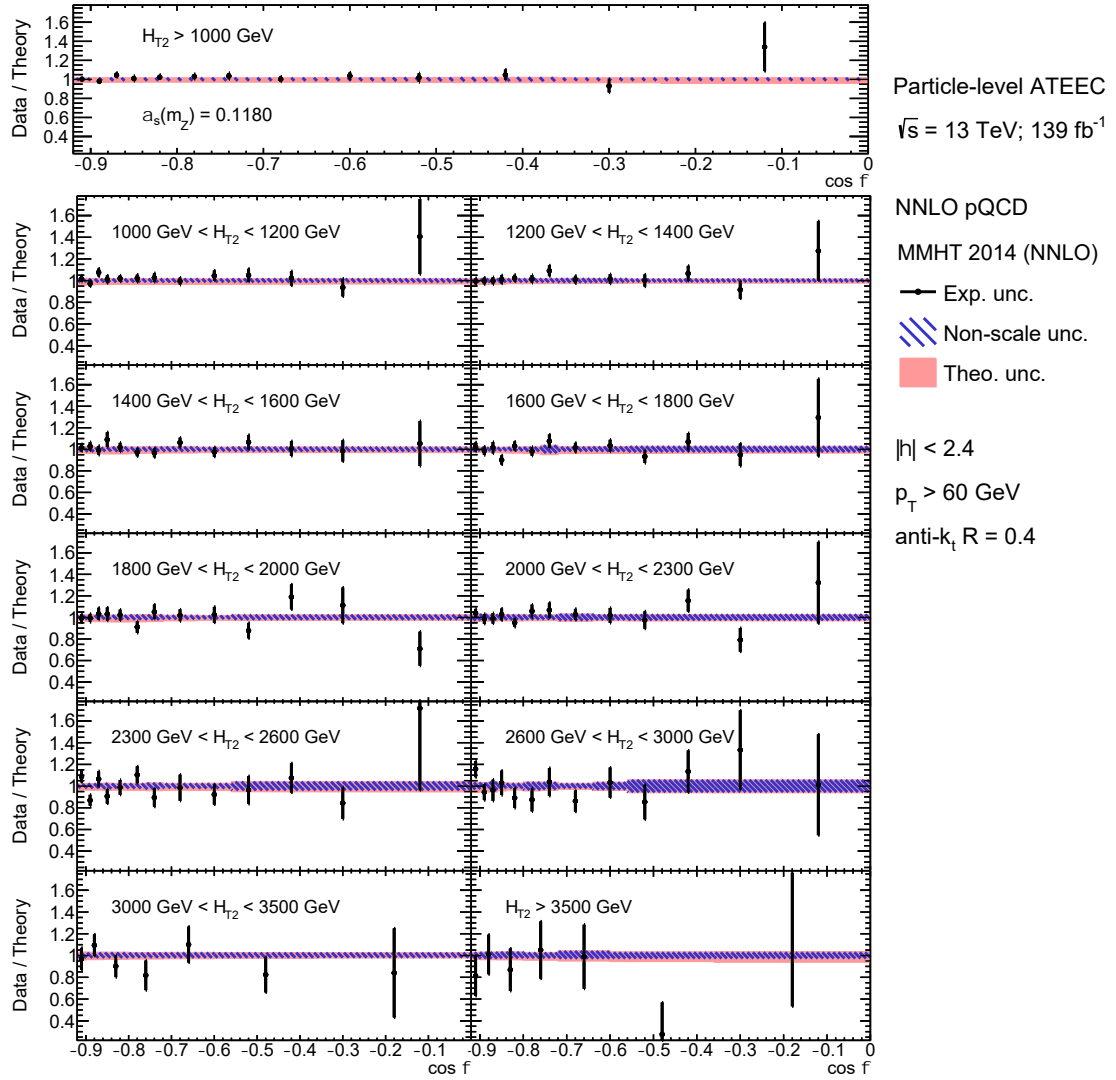


Figure 6.81: Ratios of the unfolded data to the particle-level NNLO pQCD predictions for the ATEEC function obtained using MMHT 2014 PDF group, in inclusive and exclusive H_{T2} bins. The strong coupling constant is set to $\alpha_s(m_Z) = 0.1180$. The non-scale uncertainty corresponds to the PDF parametrization uncertainty, the $\alpha_s(m_Z)$ parameter uncertainty and the non-pQCD uncertainty from the MC model added in quadrature. The theoretical uncertainty includes both non-scale and scale uncertainties. The experimental uncertainty includes the statistical uncertainty.

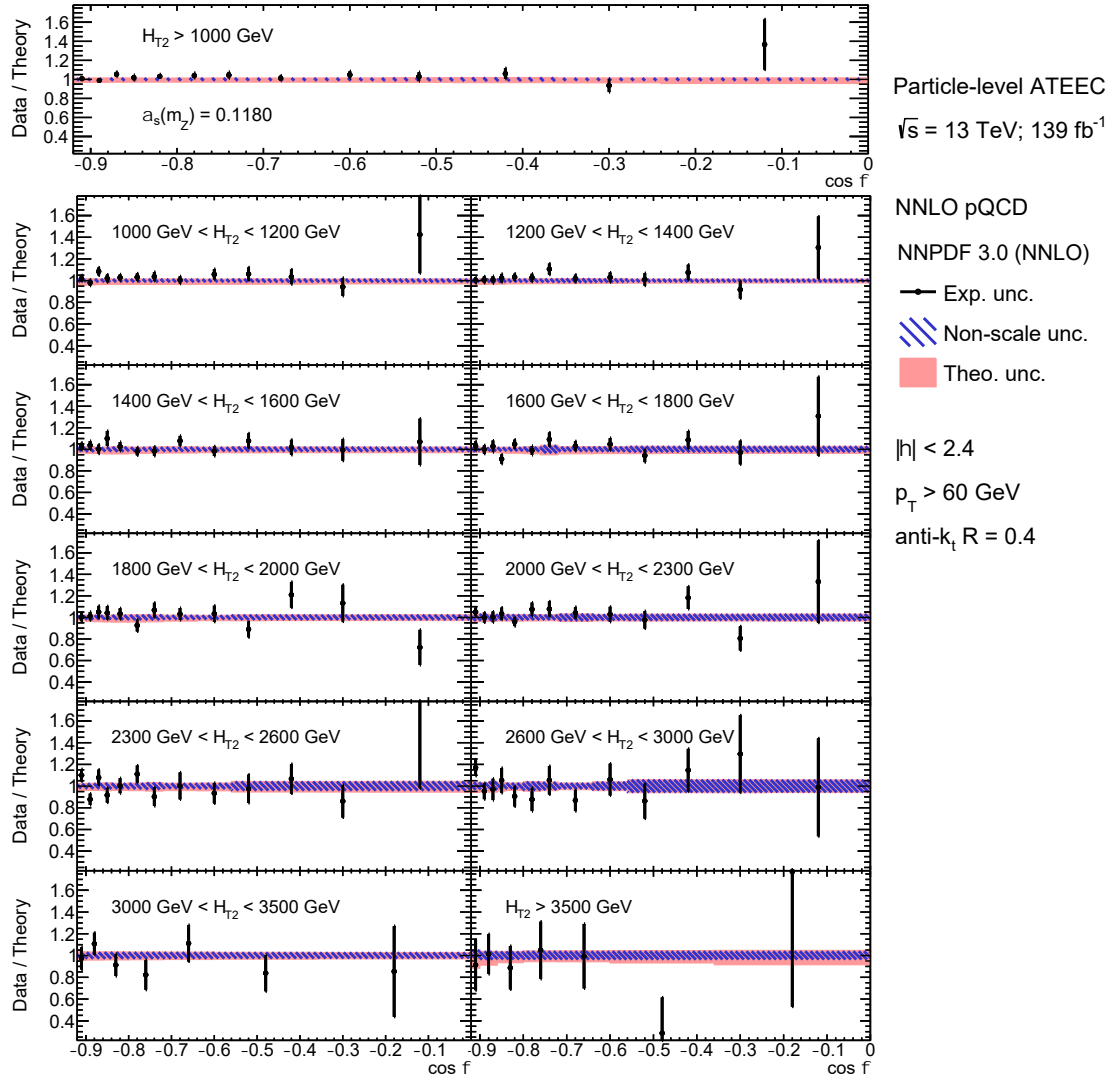


Figure 6.82: Ratios of the unfolded data to the particle-level NNLO pQCD predictions for the ATEEC function obtained using NNPDF 3.0 PDF group, in inclusive and exclusive H_{T2} bins. The strong coupling constant is set to $\alpha_s(m_Z) = 0.1180$. The non-scale uncertainty corresponds to the PDF parametrization uncertainty, the $\alpha_s(m_Z)$ parameter uncertainty and the non-pQCD uncertainty from the MC model added in quadrature. The theoretical uncertainty includes both non-scale and scale uncertainties. The experimental uncertainty includes the statistical uncertainty.

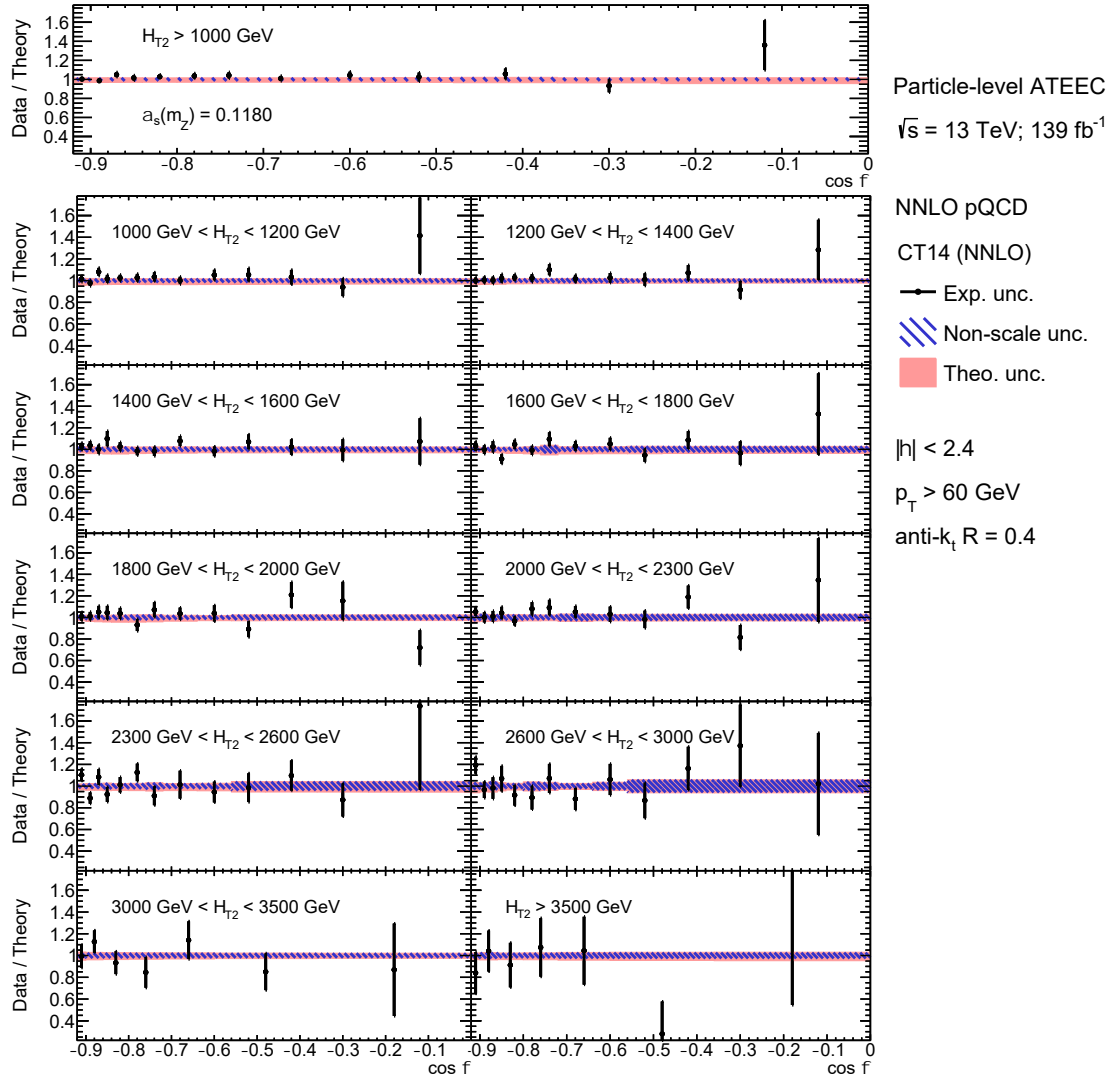


Figure 6.83: Ratios of the unfolded data to the particle-level NNLO pQCD predictions for the ATEEC function obtained using CT14 PDF group, in inclusive and exclusive H_{T2} bins. The strong coupling constant is set to $\alpha_s(m_Z) = 0.1180$. The non-scale uncertainty corresponds to the PDF parametrization uncertainty, the $\alpha_s(m_Z)$ parameter uncertainty and the non-pQCD uncertainty from the MC model added in quadrature. The theoretical uncertainty includes both non-scale and scale uncertainties. The experimental uncertainty includes the statistical uncertainty.

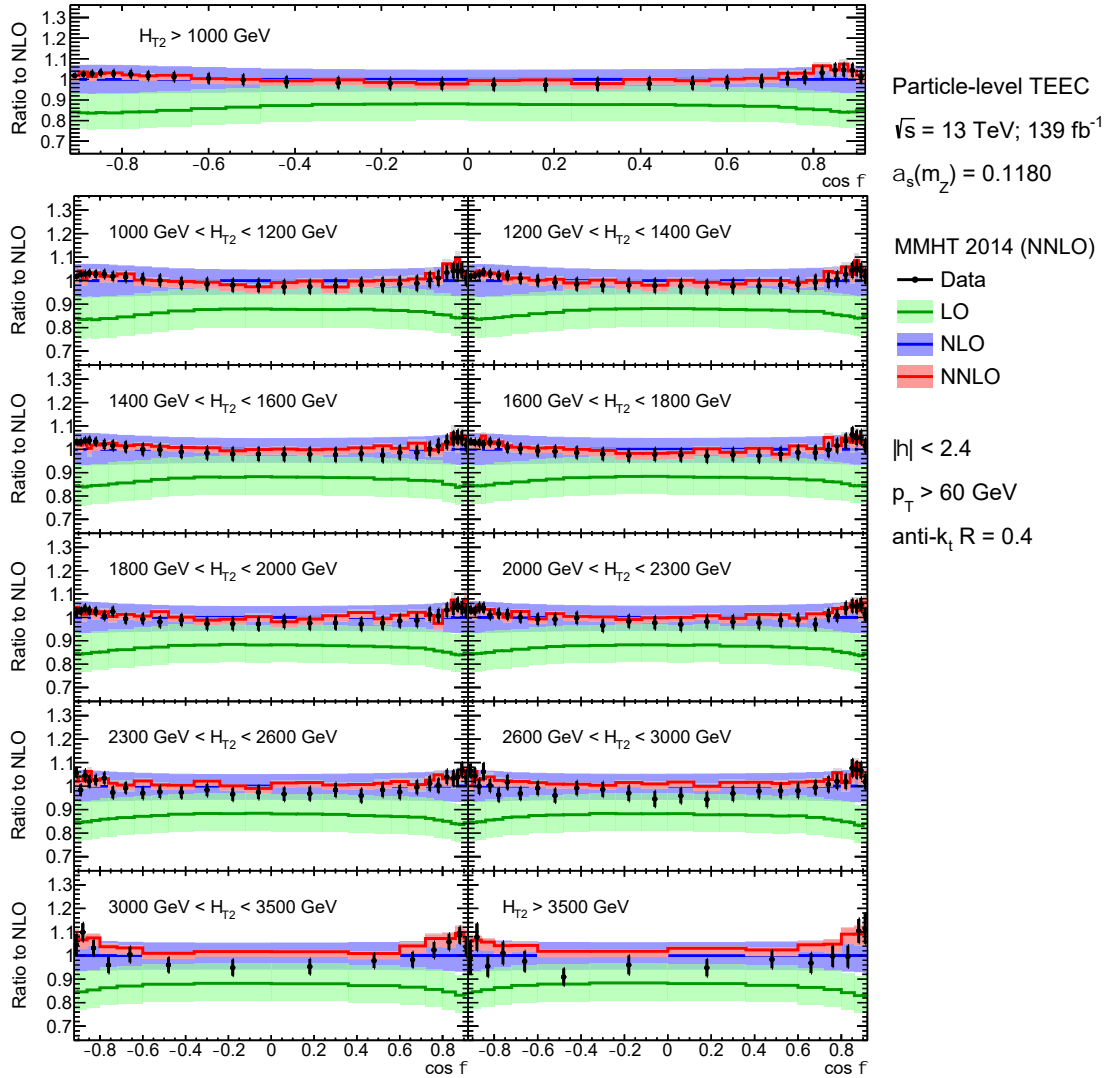


Figure 6.84: Theoretical predictions using MMHT 2014 PDF group for the TEEC functions at LO (green) and NNLO (red) compared to the NLO calculations (blue), in inclusive and exclusive H_{T2} bins. The strong coupling constant is set to $\alpha_s(m_Z) = 0.1180$, the coloured areas show the scale uncertainties, and the shaded area (gray) shows the statistical uncertainties in the ratios between theoretical predictions. A comparison of unfolded data to pQCD predictions is also presented, where the error bars correspond to the experimental uncertainties.

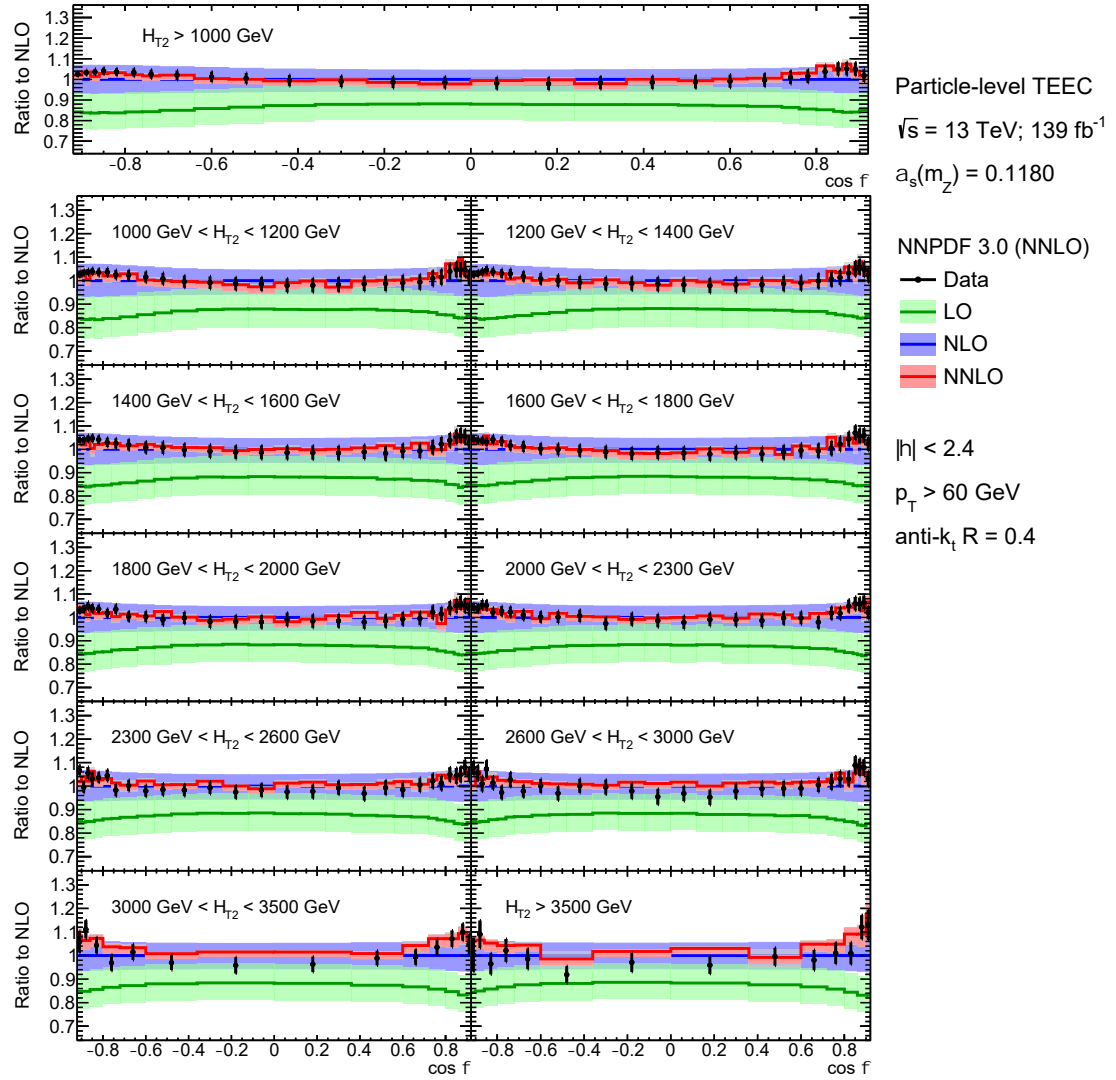


Figure 6.85: Theoretical predictions using NNPDF 3.0 PDF group for the TEEC functions at LO (green) and NNLO (red) compared to the NLO calculations (blue), in inclusive and exclusive H_{T2} bins. The strong coupling constant is set to $\alpha_s(m_Z) = 0.1180$, the coloured areas show the scale uncertainties, and the shaded area (gray) shows the statistical uncertainties in the ratios between theoretical predictions. A comparison of unfolded data to pQCD predictions is also presented, where the error bars correspond to the experimental uncertainties.

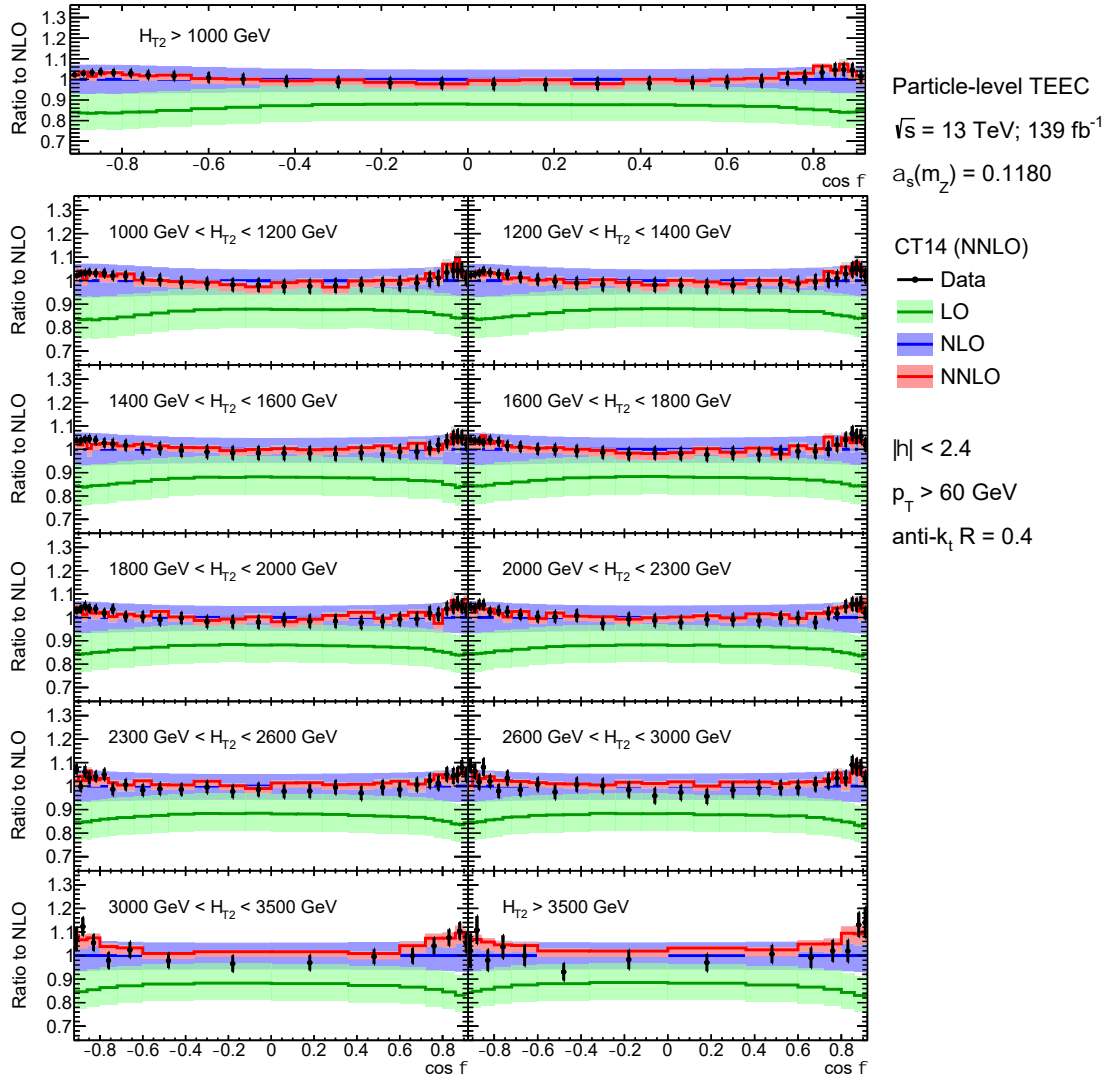


Figure 6.86: Theoretical predictions using CT14 PDF group for the TEEC functions at LO (green) and NNLO (red) compared to the NLO calculations (blue), in inclusive and exclusive H_{T2} bins. The strong coupling constant is set to $\alpha_s(m_Z) = 0.1180$, the coloured areas show the scale uncertainties, and the shaded area (gray) shows the statistical uncertainties in the ratios between theoretical predictions. A comparison of unfolded data to pQCD predictions is also presented, where the error bars correspond to the experimental uncertainties.

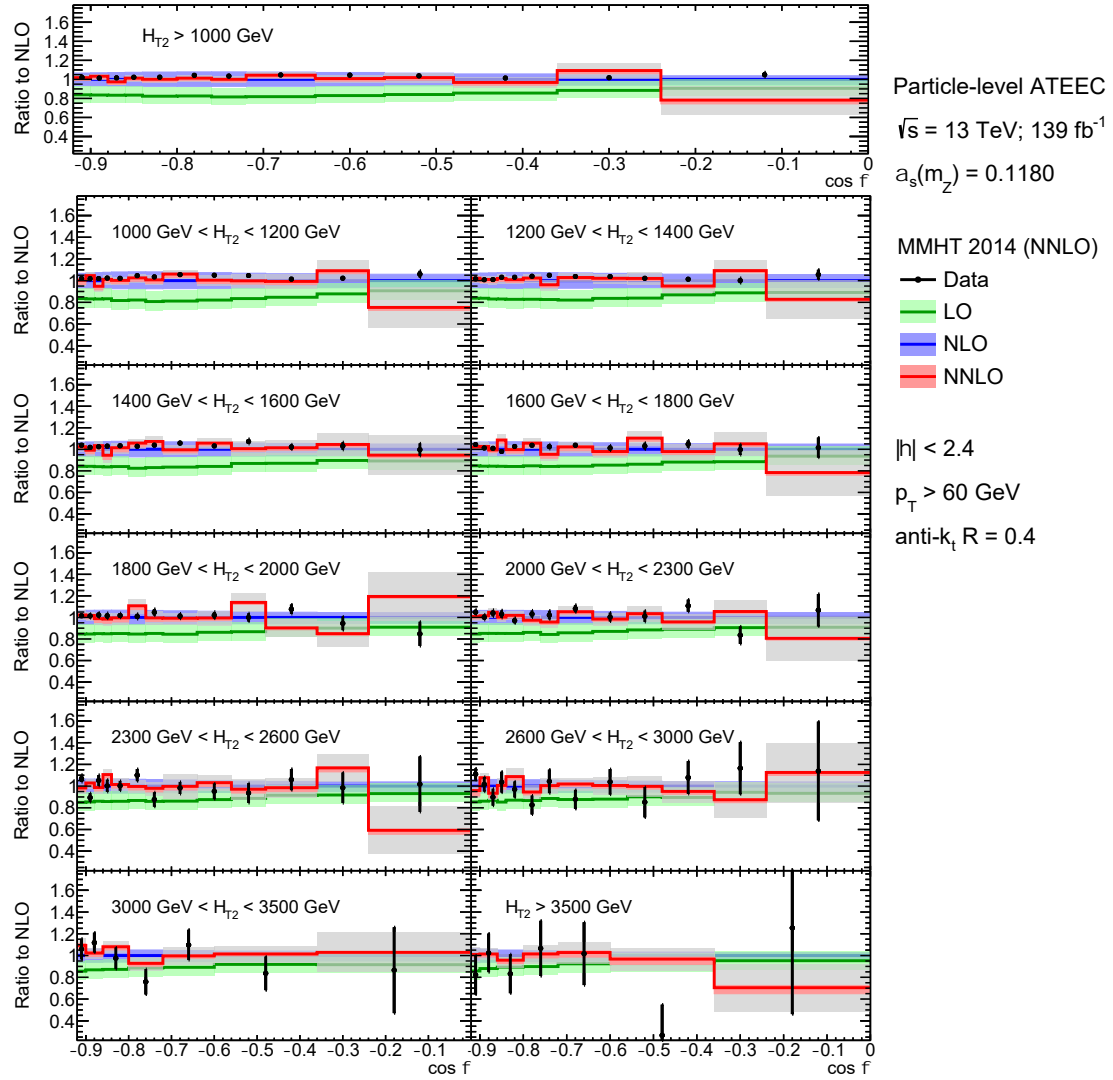


Figure 6.87: Theoretical predictions using MMHT 2014 PDF group for the ATEEC functions at LO (green) and NNLO (red) compared to the NLO calculations (blue), in inclusive and exclusive H_{T2} bins. The strong coupling constant is set to $\alpha_s(m_Z) = 0.1180$, the coloured areas show the scale uncertainties, and the shaded area (gray) shows the statistical uncertainties in the ratios between theoretical predictions. A comparison of unfolded data to pQCD predictions is also presented, where the error bars correspond to the experimental uncertainties.

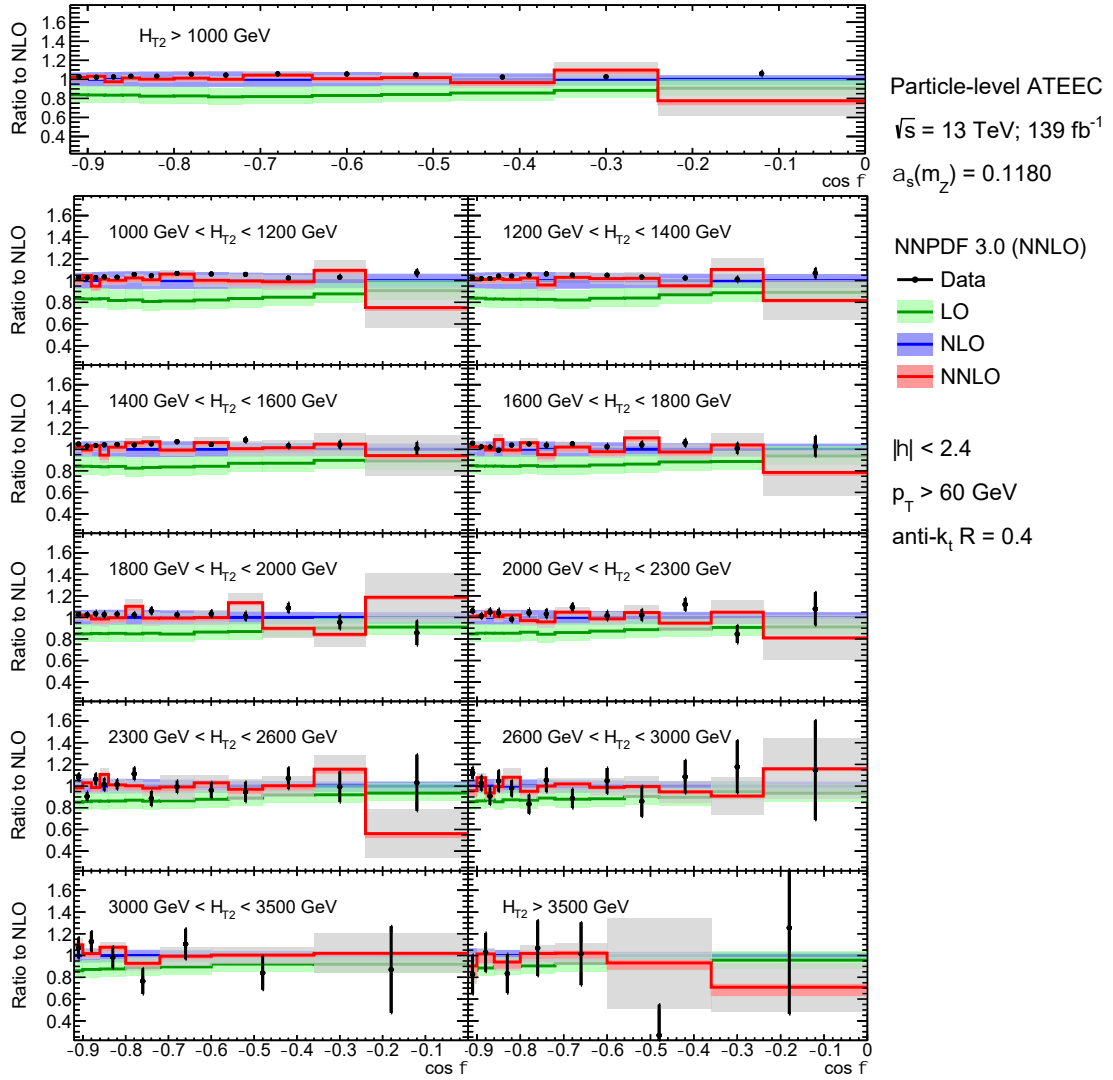


Figure 6.88: Theoretical predictions using NNPDF 3.0 PDF group for the ATEEC functions at LO (green) and NNLO (red) compared to the NLO calculations (blue), in inclusive and exclusive H_{T2} bins. The strong coupling constant is set to $\alpha_s(m_Z) = 0.1180$, the coloured areas show the scale uncertainties, and the shaded area (gray) shows the statistical uncertainties in the ratios between theoretical predictions. A comparison of unfolded data to pQCD predictions is also presented, where the error bars correspond to the experimental uncertainties.

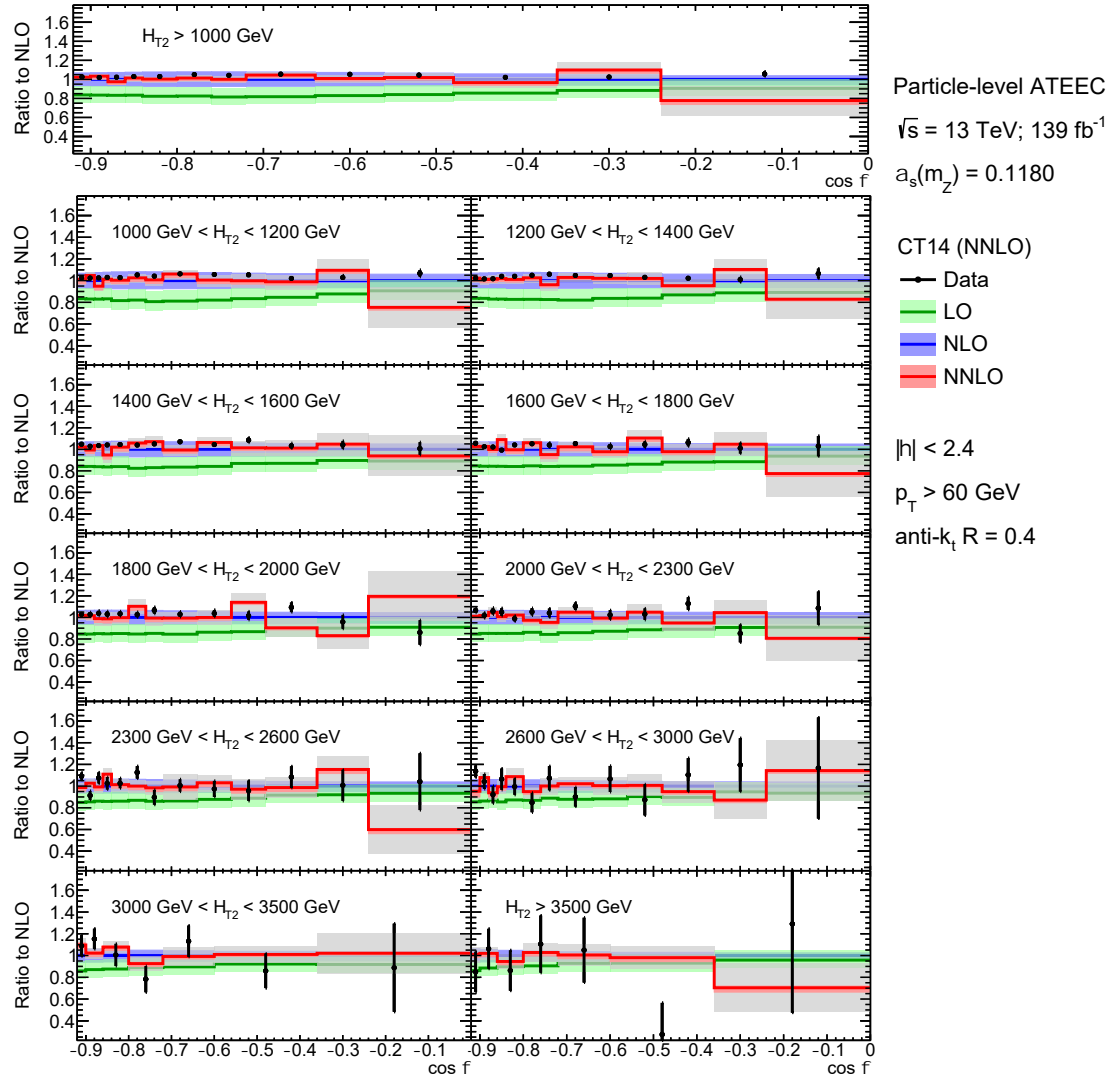


Figure 6.89: Theoretical predictions using the CT14 PDF group for the ATEEC functions at LO (green) and NNLO (red) compared to the NLO calculations (blue), in inclusive and exclusive H_{T2} bins. The strong coupling constant is set to $\alpha_s(m_Z) = 0.1180$, the coloured areas show the scale uncertainties, and the shaded area (gray) shows the statistical uncertainties in the ratios between theoretical predictions. A comparison of unfolded data to pQCD predictions is also presented, where the error bars correspond to the experimental uncertainties.

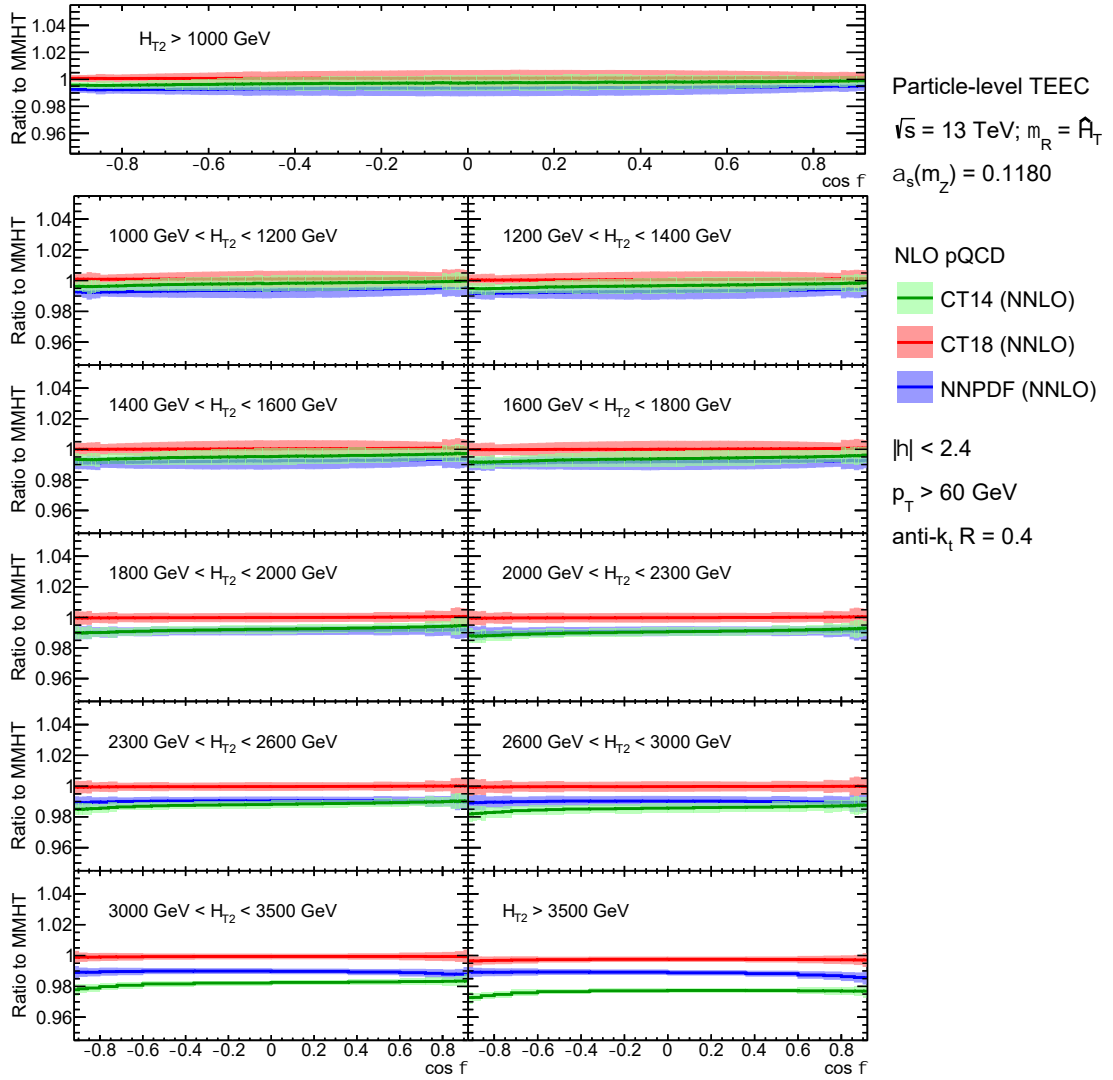


Figure 6.90: Theoretical predictions for the TEEC functions using NNPDF 3.0 (blue), CT14 (green), and CT18 (red) PDF groups compared to the calculations using MMHT 2014, in inclusive and exclusive H_{T2} bins. Their differences increase slightly at high-energy scales and that the results obtained with CT18 coincide with those of MMHT 2014 for the whole phase space. The strong coupling constant is set to $\alpha_s(m_Z) = 0.1180$, the theoretical scale choice is $\mu_{R,F} = \hat{H}_T$, and the shaded areas show the statistical uncertainties in the ratios between theoretical predictions.

6.9 Determination of the strong coupling

In physical analyses, there are fundamental parameters that characterize theoretical predictions. These parameters can be estimated from a fit theory to data, where the former carries an analytical dependence with the parameter. Thus, the value of the strong coupling is determined from the comparison of unfolded experimental results with their theoretical predictions at NNLO in pQCD.

This comparison requires an analytical expression for the dependence of the theoretical predictions with the $\alpha_s(m_Z)$ parameters provided by the PDFs. These functions are obtained at NNLO by fitting each $\cos \phi$ bin to a cubic polynomial, i.e.

$$t_i(\alpha_s) = t(\cos \phi_i; \alpha_s) = \sum_{n=0}^3 p_n(\cos \phi_i) \alpha_s^n.$$

Figure 6.91 shows the results of fitting the dependence with $\alpha_s(m_Z)$ for a couple of $\cos \phi$ bins in a given H_{T2} interval. Note that each group of PDFs provides different values for the parameter, with MMHT 2014 having the widest range.

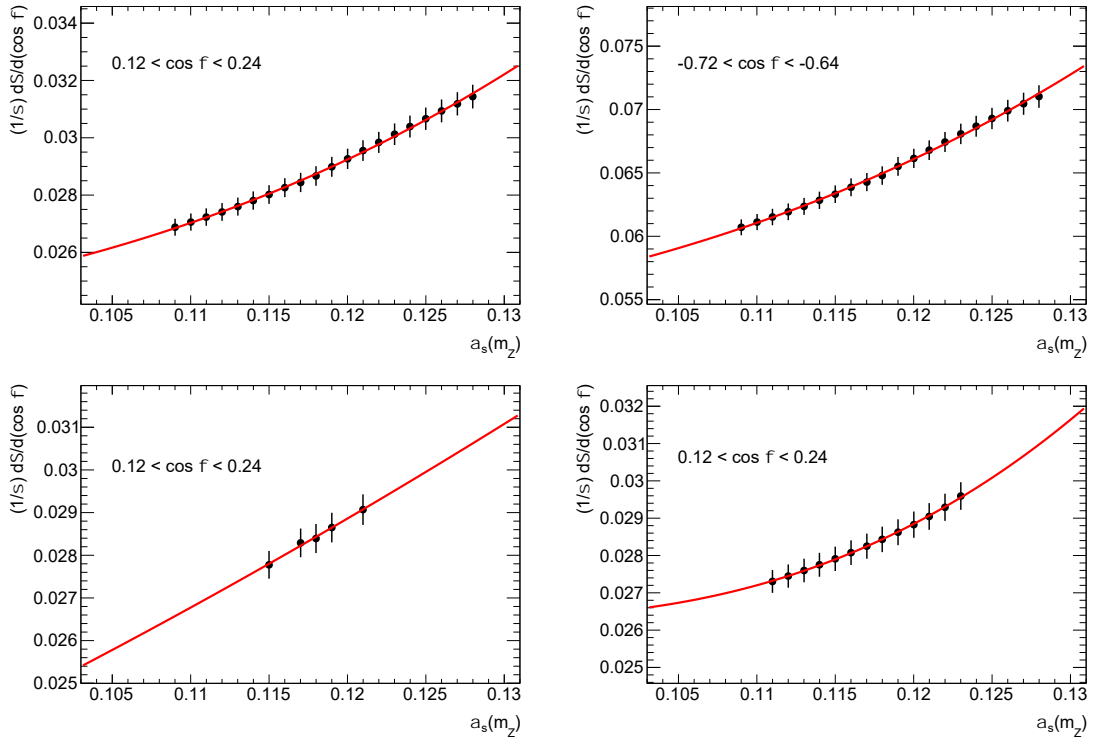


Figure 6.91: Fit to a third-order polynomial in $\alpha_s(m_Z)$ considering $\cos \phi$ bins in the $1.8 \text{ TeV} < H_{T2} < 2.0 \text{ TeV}$ interval of the TEEC functions at NNLO using MMHT 2014 (top), NNPDF 3.0 (bottom left), and CT14 (bottom right) PDF groups.

The value of the fundamental QCD parameter is then extracted at different H_{T2} intervals by fitting these analytical predictions on $\alpha_s(m_Z)$ to the unfolded experimental results for the TEEC functions, $d_i = d(\cos \phi_i)$. The estimator of the unknown

parameter α_s is the one maximizing the following likelihood function:

$$L(\vec{d}; \alpha_s) = \prod_{i=1}^{\text{bins}} f(d_i; \alpha_s); \quad f(d_i; \alpha_s) = \frac{1}{\sqrt{2\pi\Delta_i^2}} \exp\left[-\frac{(d_i - t_i(\alpha_s))^2}{2\Delta_i^2}\right];$$

where the product acts for all independent bins in the histogram with measured data points $\{d_i\}$. The value d_i is considered Gaussian distributed around the theoretical prediction $t_i(\alpha_s)$ with variance $\Delta_i^2 = \Delta d_i^2 + \Delta t_i^2$, where Δd_i is the experimental statistical uncertainty and Δt_i is the theoretical statistical uncertainty.

In order to compensate for the effect of correlated uncertainties in the shape of the distribution, nuisance parameters $\{\lambda_k\}$ are introduced, one for each source of correlated systematic uncertainty. These nuisance parameters shift the theory separately and are assumed to be normally distributed. The analytical prediction is varied to

$$\tilde{t}_i(\alpha_s) = t_i(\alpha_s) + \sum_{k=1}^{\text{corr.}} \lambda_k \Delta d_{i,k},$$

where $\Delta d_{i,k}$ is the systematic uncertainty of the experimental source k . It is important to note that, for those systematic sources which are asymmetric, the uncertainty $\Delta d_{i,k}$ is then defined as the average of the up and down variations. The JES, JER, JAR, and unfolding closure uncertainties are considered as correlated sources. Therefore, 149 nuisance parameters are introduced in total. The MC model uncertainty is not considered as a correlated source in order to extract the estimator with a well defined MC model. The final likelihood function is given by

$$L(\vec{d}; \alpha_s, \vec{\lambda}) = \left\{ \prod_{i=1}^{\text{bins}} \left(\frac{1}{\sqrt{2\pi\Delta_i^2}} \exp\left[-\frac{(d_i - \tilde{t}_i(\alpha_s))^2}{2\Delta_i^2}\right] \right) \right\} \left\{ \prod_{k=1}^{\text{corr.}} \left(\frac{1}{\sqrt{2\pi}} \exp\left[-\frac{\lambda_k^2}{2}\right] \right) \right\}$$

Maximising the likelihood function is tantamount to minimising the χ^2 function defined in Eq. (6.4). The minimum of the χ^2 function is found using techniques implemented in the MINUIT package and considering a 150-dimensional space, in which 149 correspond to the nuisance parameters $\{\lambda_k\}$ and one to the QCD parameter $\alpha_s(m_Z)$.

$$\chi^2(\alpha_s, \vec{\lambda}) = \sum_{i=1}^{\text{bins}} \frac{(d_i - \tilde{t}_i(\alpha_s))^2}{\Delta_i^2} + \sum_{k=1}^{\text{corr.}} \lambda_k^2 \quad (6.4)$$

For both the TEEC and ATEEC functions, the fits to extract $\alpha_s(m_Z)$ are repeated separately for each H_{T2} interval, thus determining a value of $\alpha_s(m_Z)$ for each energy bin. The theoretical uncertainties are determined by shifting the theory distributions by each of the uncertainties separately, recalculating the functions $t_i(\alpha_s)$ and determining a new value of $\alpha_s(m_Z)$. The uncertainty is determined by taking the difference between this value and the nominal one. The PDF parametrization uncertainties are combined following the recommendations introduced in Section 6.7 and the scale uncertainties are combined taking the envelope with respect to the nominal scale. The uncertainties due to the choice of the MC model in the unfolding and of

the MC tune in the non-perturbative correction are estimated by repeating the fit considering the data and theory distributions corrected with the other models and tunes, and taking the envelope with respect to the nominal fit. In addition, given the fact that the dependence of the TEEC and ATEEC functions on the PDF is small, a combined determination of α_s and the PDF is not attempted [140].

The quality of the fit and the validity of the estimator of $\alpha_s(m_Z)$ come from the χ^2 value. These values denoted with x follow the probability distribution:

$$f(x; N_{\text{dof}}) = \frac{x^{N_{\text{dof}}/2-1} e^{-x/2}}{2^{N_{\text{dof}}/2} \Gamma(N_{\text{dof}}/2)}$$

where the gamma function generalizes the concept $\Gamma(n) = (n - 1)!$ for $n \in \mathbb{N}$ to real numbers. The parameter N_{dof} corresponds with the number of degrees of freedom in the fit, which is the number of independent bins minus the number of parameters extracted. The goodness-of-fit test says that the fit must be rejected when the minimum χ^2 value lies in the boundary of its probability distribution, which translates into

$$\int_{\chi^2}^{+\infty} dx f(x; N_{\text{dof}}) \leq \alpha$$

where $\alpha = 0.05$ determines by convention the threshold area. As a general approximation, a good fit satisfies the requirement $\chi^2/N_{\text{dof}} \simeq 1$ to validate the estimator.

6.9.1 Scale evolution of the coupling

In order to obtain physical quantities, each of the estimated values of $\alpha_s(m_Z)$ has to be evolved to $\alpha_s(Q)$. The interaction scale Q is the one considered as the nominal renormalization and factorization scale in the calculation, $\mu_{\text{R,F}} = \hat{H}_{\text{T}}$. The average value of the scale $\langle \hat{H}_{\text{T}} \rangle$ is calculated at NNLO in pQCD for each of the H_{T2} intervals through the differential cross section:

$$\frac{d\sigma^{2\text{jet}}}{dQ} = \int \left(\sum_{a,b}^{\text{part.}} f_{a/p} f_{b/p} \otimes d\hat{\sigma}_{ab \rightarrow 2} \delta(Q - \hat{H}_{\text{T}}) \right).$$

The theoretical distributions are calculated using the PDF groups available with the nominal values of the strong coupling constant and the theoretical scales. Figure 6.92 shows the average value of the parton-level scale \hat{H}_{T} which is clearly correlated with detector-level scale H_{T2} .

The extracted values of $\alpha_s(m_Z)$ are then evolved to these average values using the approximate analytic solution to the RGE for α_s at NNLO in pQCD, formulated in Eq. (2.1). The value of the beta coefficients can be found in Eq. (6.5) where n_f is the number of flavours with mass far below the scale Q , i.e. active flavours.

$$\beta_0 = 11 - \frac{2}{3} n_f ; \quad \beta_1 = 102 - \frac{38}{3} n_f ; \quad \beta_2 = \frac{2857}{2} - \frac{5033}{18} n_f - \frac{325}{54} n_f^2 . \quad (6.5)$$

The proper transition rules for $n_f = 5$ to $n_f = 6$ are applied, so that the running of α_s is a continuous function across top quark mass threshold at scale $m_t = 173$ GeV. Additionally, the scale Λ_{QCD} is determined in each case from the fitted value of the strong coupling constant $\alpha_s(m_Z)$.

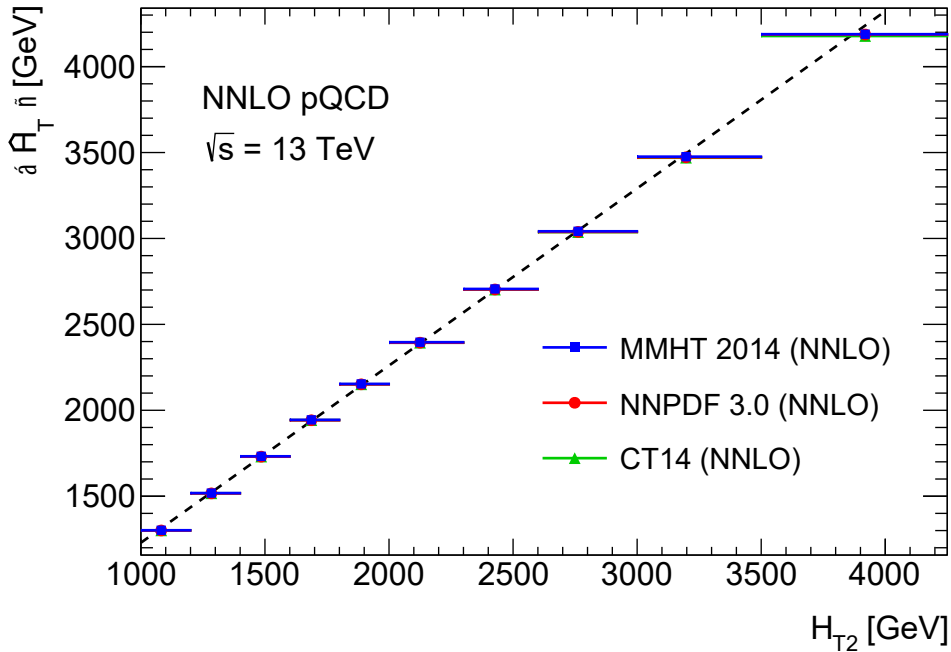


Figure 6.92: Values of the average interaction scale $\langle \hat{H}_T \rangle$, for each of the exclusive H_{T2} bins, calculated at NNLO in pQCD using the PDF groups available. The results are fitted to a straight line (dashed line) with slope 1.03 ± 0.07 , revealing that the parton-level scale \hat{H}_T is correlated with detector-level scale H_{T2} .

6.9.2 Correlations between fits

The correlations between the $\alpha_s(m_Z)$ results from the fit to the TEEC function and that from the ATEEC function are evaluated using the bootstrap method mentioned in Section 6.4. A set of 10^3 replicas of each distribution is obtained after the unfolding and the fit is repeated for each. Each replica of the ATEEC distributions is linked to the corresponding replica of the TEEC distribution, making the evaluation of the correlations straightforward. Figure 6.93 shows the distributions of the values of $\alpha_s(m_Z)$ obtained from fits to the set of replicas of the TEEC and ATEEC functions.

The evaluation of the correlation is done following the usual definition of the Pearson correlation coefficient given by Eq. (6.6). This equation defines the correlation coefficient between two populations X and Y with average values μ_X and μ_Y and standard deviations σ_X and σ_Y , respectively.

$$\rho_{XY} = \frac{\langle (X - \mu_X)(Y - \mu_Y) \rangle}{\sigma_X \sigma_Y} \quad (6.6)$$

Figure 6.94 shows the scatter plot for the values of $\alpha_s(m_Z)$ obtained from fits to the TEEC function on the x-axis and those from fits to the ATEEC function on y-axis, together with a linear fit to the scatter data. The result for the Pearson correlation coefficient for the inclusive sample in H_{T2} is $\rho = 0.86 \pm 0.02$. Thus, the values determined from the TEEC and ATEEC functions are strongly correlated.

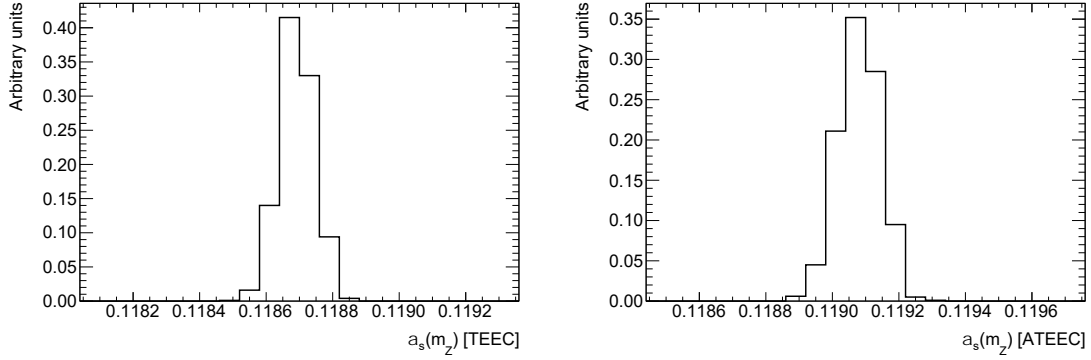


Figure 6.93: Distributions of the values of $\alpha_s(m_Z)$ obtained from fitting each of the 10^3 replicas of the inclusive TEEC (left) and ATEEC (right) distributions to the theoretical predictions using MMHT 2014 PDF group.

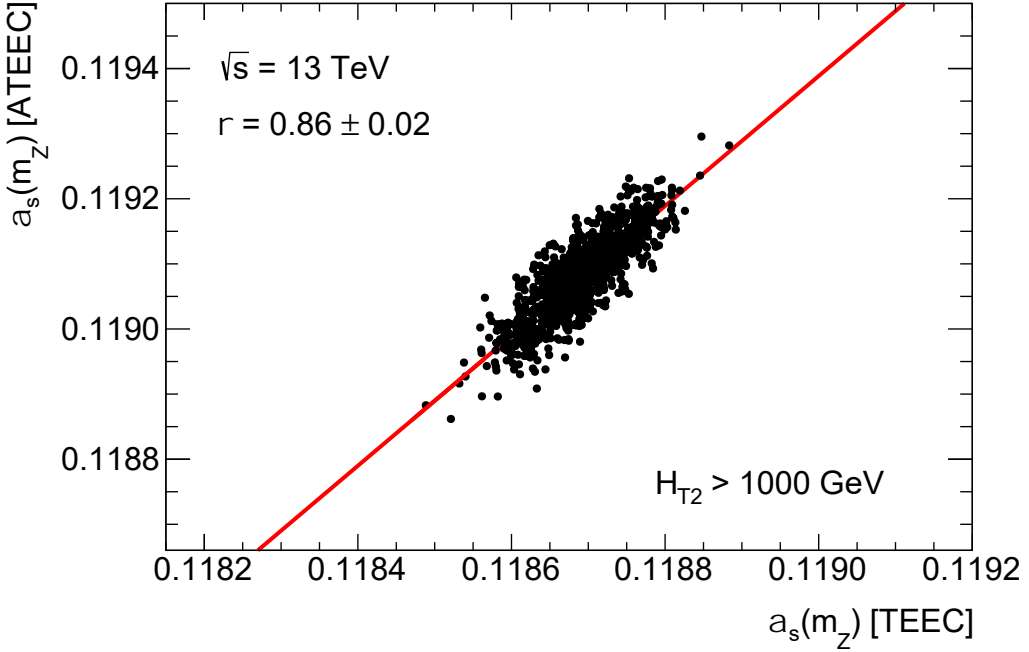


Figure 6.94: Scatter plot of the values of $\alpha_s(m_Z)$ obtained from the H_{T2} -inclusive TEEC (x -axis) and ATEEC (y -axis) fit using MMHT 2014 PDF group. The points are fitted to a first order polynomial, shown as a red line across the data. The result for the Pearson correlation coefficient is $\rho = 0.86 \pm 0.02$.

6.9.3 Fits to the TEEC function

The values of $\alpha_s(m_Z)$ extracted from a global fit to the TEEC function at NNLO as well as the individual fits in each exclusive H_{T2} bin and in the fully inclusive sample are summarized in Table 6.28. The theoretical predictions used for this extraction use MMHT 2014 as the nominal PDF group, which is the one providing a wider range of variations for $\alpha_s(m_Z)$. In addition, the extracted values using NNPDF 3.0 and CT14 as the PDF group are also presented in Tables 6.29 and 6.30, respectively. The uncertainty derived from the χ^2 fit includes both experimental and theoretical statistical uncertainties, along with the experimental systematic uncertainties constrained by the nuisance parameters.

The χ^2 values indicate that the agreement between the data and the theoretical predictions is good in each exclusive H_{T2} bin and in the fully inclusive sample. The critical value with a significance level of $\alpha = 0.05$ for the global fit is $\chi^2 = 289.0$. Thus, a slight tension arises in the global fit for certain PDF groups. This tension comes from the drop at high energy scales of the fitted values of α_s in exclusive bins. However, this effect is not found when using CT14 PDF. The nuisance parameters from the TEEC function fits are shown in Figures 6.95 and 6.96 and generally they are found to be compatible with zero. Nevertheless, there are few exceptions like the one associated to Flavour Response ($i = 9$), which is largely pulled, enhancing the agreement between data and theory. The nuisance parameters which are usually slightly pulled correspond to EtaIntercalibration Modelling ($i = 2$), Gjet GamESZee ($i = 10$), and JAR ($i = 148$).

The correlation coefficients between nuisance parameters are shown in Figures 6.97 and 6.98. The fact that the correlation matrices have very small off-diagonal terms indicates that the systematic sources are not significantly correlated between them. Nevertheless, the nuisance parameters associated to Flavour Composition ($i = 8$) and Flavour Response ($i = 9$) are slightly anticorrelated. This anticorrelation is only significant when evaluating the uncertainties assuming the fraction of quark- and gluon-initiated jets 0.5 ± 0.5 by default. Figures 6.102 to 6.101 compare the experimental results with fitted theoretical predictions; the ones where the fitted values of $\alpha_s(m_Z)$ and the nuisance parameters are already constrained.

The extracted values of the strong coupling constant $\alpha_s(m_Z)$ are in good agreement with the 2022 world average value $\alpha_s(m_Z) = 0.1179 \pm 0.0009$ [11]. A comparison of the results of α_s is shown in Figure 6.105. The results from previous extractions using LHC data [1, 2, 141–145] and Tevatron data [146, 147] are also shown, together with the world average band [11]. The values of α_s are evolved from m_Z to the corresponding scale Q using the three-loop solution of the RGE, introduced in Eq. (2.1), where the interaction scale is evaluated for each analysis at the central value of the renormalization scale. Tables 6.31 to 6.33 summarize the extracted values of the physical strong coupling constant $\alpha_s(Q)$ that enter the matrix elements in the calculation.

$\langle Q \rangle$ [GeV]		$\alpha_s(m_Z)$	value (MMHT 2014)	χ^2/N_{dof}
Global	0.1175 ± 0.0001 (stat.) ± 0.0006 (syst.)	$+0.0032$ (scale) -0.0011 (param.)	± 0.0002 (tune) ± 0.0005 (model)	$317.8 / 251$
Inclusive	0.1188 ± 0.0002 (stat.) ± 0.0007 (syst.)	$+0.0030$ (scale) -0.0002 (param.)	± 0.0002 (tune) ± 0.0008 (model)	$16.0 / 27$
1302	0.1186 ± 0.0003 (stat.) ± 0.0009 (syst.)	$+0.0031$ (scale) -0.0010 (param.)	± 0.0003 (tune) ± 0.0007 (model)	$16.4 / 27$
1518	0.1182 ± 0.0003 (stat.) ± 0.0009 (syst.)	$+0.0027$ (scale) -0.0005 (param.)	± 0.0003 (tune) ± 0.0008 (model)	$15.1 / 27$
1732	0.1191 ± 0.0003 (stat.) ± 0.0011 (syst.)	$+0.0030$ (scale) -0.0005 (param.)	± 0.0005 (tune) ± 0.0010 (model)	$19.8 / 27$
1944	0.1179 ± 0.0003 (stat.) ± 0.0011 (syst.)	$+0.0030$ (scale) -0.0011 (param.)	± 0.0005 (tune) ± 0.0009 (model)	$21.3 / 27$
2153	0.1175 ± 0.0004 (stat.) ± 0.0012 (syst.)	$+0.0029$ (scale) -0.0004 (param.)	± 0.0003 (tune) ± 0.0009 (model)	$32.9 / 27$
2396	0.1179 ± 0.0003 (stat.) ± 0.0012 (syst.)	$+0.0029$ (scale) -0.0005 (param.)	± 0.0012 (tune) ± 0.0012 (model)	$27.5 / 27$
2706	0.1164 ± 0.0004 (stat.) ± 0.0015 (syst.)	$+0.0030$ (scale) -0.0013 (param.)	± 0.0005 (tune) ± 0.0011 (model)	$35.1 / 27$
3042	0.1162 ± 0.0005 (stat.) ± 0.0017 (syst.)	$+0.0031$ (scale) -0.0005 (param.)	± 0.0002 (tune) ± 0.0015 (model)	$33.1 / 27$
3476	0.1141 ± 0.0007 (stat.) ± 0.0017 (syst.)	$+0.0033$ (scale) -0.0011 (param.)	± 0.0002 (tune) ± 0.0020 (model)	$15.1 / 13$
4189	0.1116 ± 0.0011 (stat.) ± 0.0018 (syst.)	$+0.0030$ (scale) -0.0009 (param.)	± 0.0002 (tune) ± 0.0020 (model)	$14.0 / 13$

Table 6.28: Values of the strong coupling constant at the Z boson mass scale, $\alpha_s(m_Z)$, obtained from fits to the TEEC function at NNLO using MMHT 2014 PDF group. The values of the average interaction scale $\langle Q \rangle$ are shown in the first column, while the values of the χ^2 function at the minimum are shown in the third column. The label (stat.) includes the experimental and theoretical statistical uncertainties, whereas the label (syst.) indicates only the experimental systematic uncertainties added in quadrature. The uncertainty related to the MC model in the IB unfolding is displayed separately as (model) and the one referred to as (tune) is related to the non-pQCD corrections.

$\langle Q \rangle$ [GeV]		$\alpha_s(m_Z)$	value (NNPDF 3.0)	$\chi^2/\text{N}_{\text{dof}}$
Global	0.1191 ± 0.0001 (stat.) ± 0.0006 (syst.)	$+0.00040$ (scale) -0.0011 (param.)	± 0.00020 (param.) ± 0.0003 (tune) ± 0.0007 (model)	299.9 / 251
Inclusive	0.1199 ± 0.0003 (stat.) ± 0.0008 (syst.)	$+0.00035$ (scale) -0.0003 (param.)	± 0.00015 (param.) ± 0.0002 (tune) ± 0.0009 (model)	17.6 / 27
1302	0.1196 ± 0.0004 (stat.) ± 0.0010 (syst.)	$+0.00036$ (scale) -0.0002 (param.)	± 0.00014 (param.) ± 0.0003 (tune) ± 0.0008 (model)	17.4 / 27
1518	0.1194 ± 0.0003 (stat.) ± 0.0010 (syst.)	$+0.00031$ (scale) -0.0005 (param.)	± 0.00015 (param.) ± 0.0004 (tune) ± 0.0008 (model)	16.0 / 27
1732	0.1206 ± 0.0004 (stat.) ± 0.0012 (syst.)	$+0.00036$ (scale) -0.0005 (param.)	± 0.00017 (param.) ± 0.0006 (tune) ± 0.0011 (model)	19.7 / 27
1944	0.1193 ± 0.0004 (stat.) ± 0.0012 (syst.)	$+0.00034$ (scale) -0.0005 (param.)	± 0.00018 (param.) ± 0.0006 (tune) ± 0.0010 (model)	22.5 / 27
2153	0.1189 ± 0.0004 (stat.) ± 0.0013 (syst.)	$+0.00033$ (scale) -0.0005 (param.)	± 0.00018 (param.) ± 0.0003 (tune) ± 0.0010 (model)	33.8 / 27
2396	0.1193 ± 0.0003 (stat.) ± 0.0014 (syst.)	$+0.00035$ (scale) -0.0005 (param.)	± 0.00020 (param.) ± 0.0011 (tune) ± 0.0014 (model)	28.7 / 27
2706	0.1175 ± 0.0004 (stat.) ± 0.0016 (syst.)	$+0.00033$ (scale) -0.0005 (param.)	± 0.00021 (param.) ± 0.0005 (tune) ± 0.0012 (model)	35.1 / 27
3042	0.1173 ± 0.0005 (stat.) ± 0.0018 (syst.)	$+0.00032$ (scale) -0.0004 (param.)	± 0.00022 (param.) ± 0.0003 (tune) ± 0.0016 (model)	33.0 / 27
3476	0.1151 ± 0.0007 (stat.) ± 0.0018 (syst.)	$+0.00035$ (scale) -0.0011 (param.)	± 0.00023 (param.) ± 0.0002 (tune) ± 0.0020 (model)	15.4 / 13
4189	0.1135 ± 0.0010 (stat.) ± 0.0014 (syst.)	$+0.0021$ (scale) -0.0008 (param.)	± 0.00019 (param.) ± 0.0001 (tune) ± 0.0015 (model)	10.5 / 13

Table 6.29: Values of the strong coupling constant at the Z boson mass scale, $\alpha_s(m_Z)$, obtained from fits to the TEEC function at NNLO using NNPDF 3.0 PDF group. The values of the average interaction scale $\langle Q \rangle$ are shown in the first column, while the values of the χ^2 function at the minimum are shown in the third column. The label (stat.) includes the experimental and theoretical statistical uncertainties, whereas the label (syst.) indicates only the experimental systematic uncertainties added in quadrature. The uncertainty related to the MC model in the IB unfolding is displayed separately as (model) and the one referred to as (tune) is related to the non-pQCD corrections.

$\langle Q \rangle$ [GeV]		$\alpha_s(m_Z)$ value (CT14)	χ^2/N_{dof}
Global	0.1196 ± 0.0001 (stat.) ± 0.0006 (syst.)	$+0.0035$ (scale) -0.0010 (param.)	0.0002 (tune) ± 0.0006 (model)
Inclusive	0.1197 ± 0.0003 (stat.) ± 0.0008 (syst.)	$+0.0034$ (scale) -0.0003 (param.)	0.0010 (model)
1302	0.1193 ± 0.0004 (stat.) ± 0.0010 (syst.)	$+0.0036$ (scale) -0.0015 (param.)	0.0002 (tune) ± 0.0010 (model)
1518	0.1193 ± 0.0003 (stat.) ± 0.0010 (syst.)	$+0.0032$ (scale) -0.0002 (param.)	0.0008 (model)
1732	0.1206 ± 0.0003 (stat.) ± 0.0012 (syst.)	$+0.0036$ (scale) -0.0006 (param.)	0.0003 (tune) ± 0.0008 (model)
1944	0.1193 ± 0.0004 (stat.) ± 0.0013 (syst.)	$+0.0033$ (scale) -0.0005 (param.)	0.0004 (tune) ± 0.0009 (model)
2153	0.1192 ± 0.0004 (stat.) ± 0.0014 (syst.)	$+0.0036$ (scale) -0.0007 (param.)	0.0005 (tune) ± 0.0010 (model)
2396	0.1199 ± 0.0004 (stat.) ± 0.0014 (syst.)	$+0.0037$ (scale) -0.0006 (param.)	0.0005 (tune) ± 0.0012 (model)
2706	0.1185 ± 0.0005 (stat.) ± 0.0018 (syst.)	$+0.0034$ (scale) -0.0007 (param.)	0.0006 (tune) ± 0.0012 (model)
3042	0.1184 ± 0.0006 (stat.) ± 0.0019 (syst.)	$+0.0035$ (scale) -0.0008 (param.)	0.0004 (tune) ± 0.0011 (model)
3476	0.1161 ± 0.0009 (stat.) ± 0.0024 (syst.)	$+0.0041$ (scale) -0.0019 (param.)	0.0003 (tune) ± 0.0028 (model)
4189	0.1123 ± 0.0019 (stat.) ± 0.0029 (syst.)	$+0.0047$ (scale) -0.0025 (param.)	0.0004 (tune) ± 0.0042 (model)

Table 6.30: Values of the strong coupling constant at the Z boson mass scale, $\alpha_s(m_Z)$, obtained from fits to the TEEC function at NNLO using CT14 PDF group. The values of the average interaction scale $\langle Q \rangle$ are shown in the first column, while the values of the χ^2 function at the minimum are shown in the third column. The label (stat.) includes the experimental and theoretical statistical uncertainties, whereas the label (syst.) indicates only the experimental systematic uncertainties added in quadrature. The uncertainty related to the MC model in the IB unfolding is displayed separately as (model) and the one referred to as (tune) is related to the non-pQCD corrections.

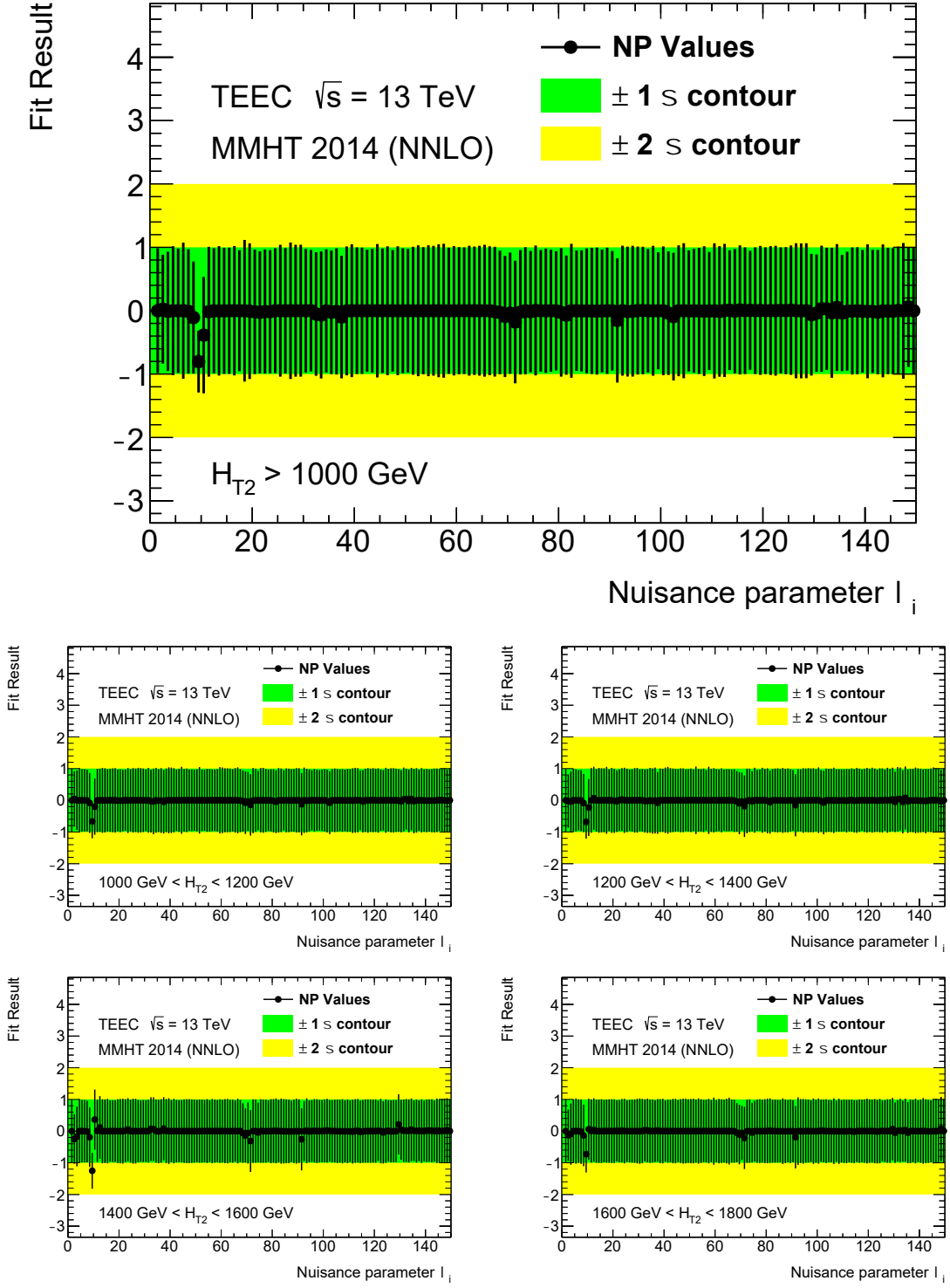


Figure 6.95: Values of the nuisance parameters obtained from individual fits, in inclusive (top) and exclusive (bottom) H_{T2} bins, to the TEEC function at NNLO using MMHT 2014 PDF group. They lie within the $\pm 1\sigma$ contour (green band) or $\pm 2\sigma$ contour (yellow band), and are generally found to be compatible with zero.

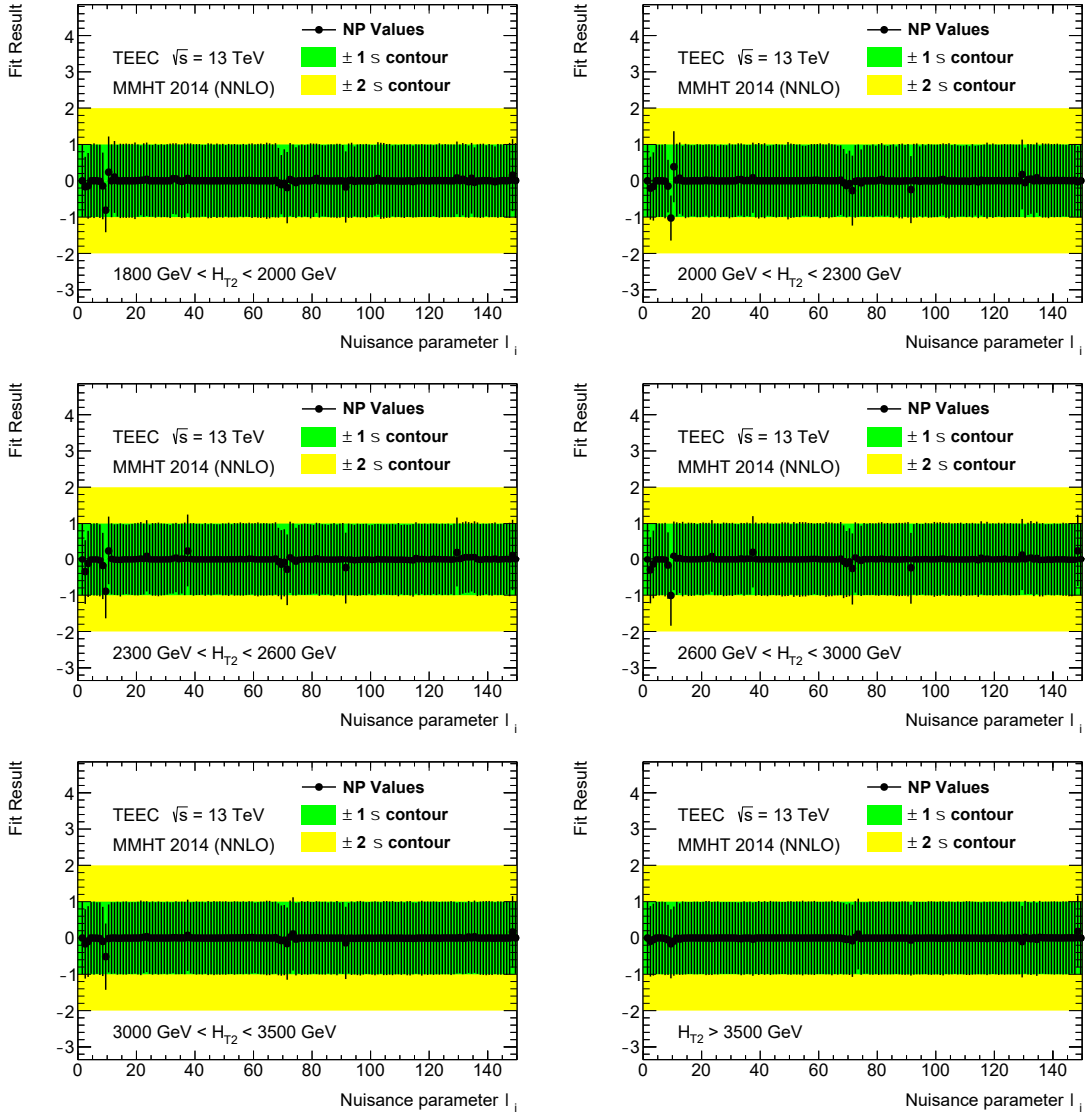


Figure 6.96: Values of the nuisance parameters obtained from individual fits, in exclusive H_{T2} bins, to the TEEC function at NNLO using MMHT 2014 PDF group. They lie within the $\pm 1\sigma$ contour (green band) or $\pm 2\sigma$ contour (yellow band), and are generally found to be compatible with zero.

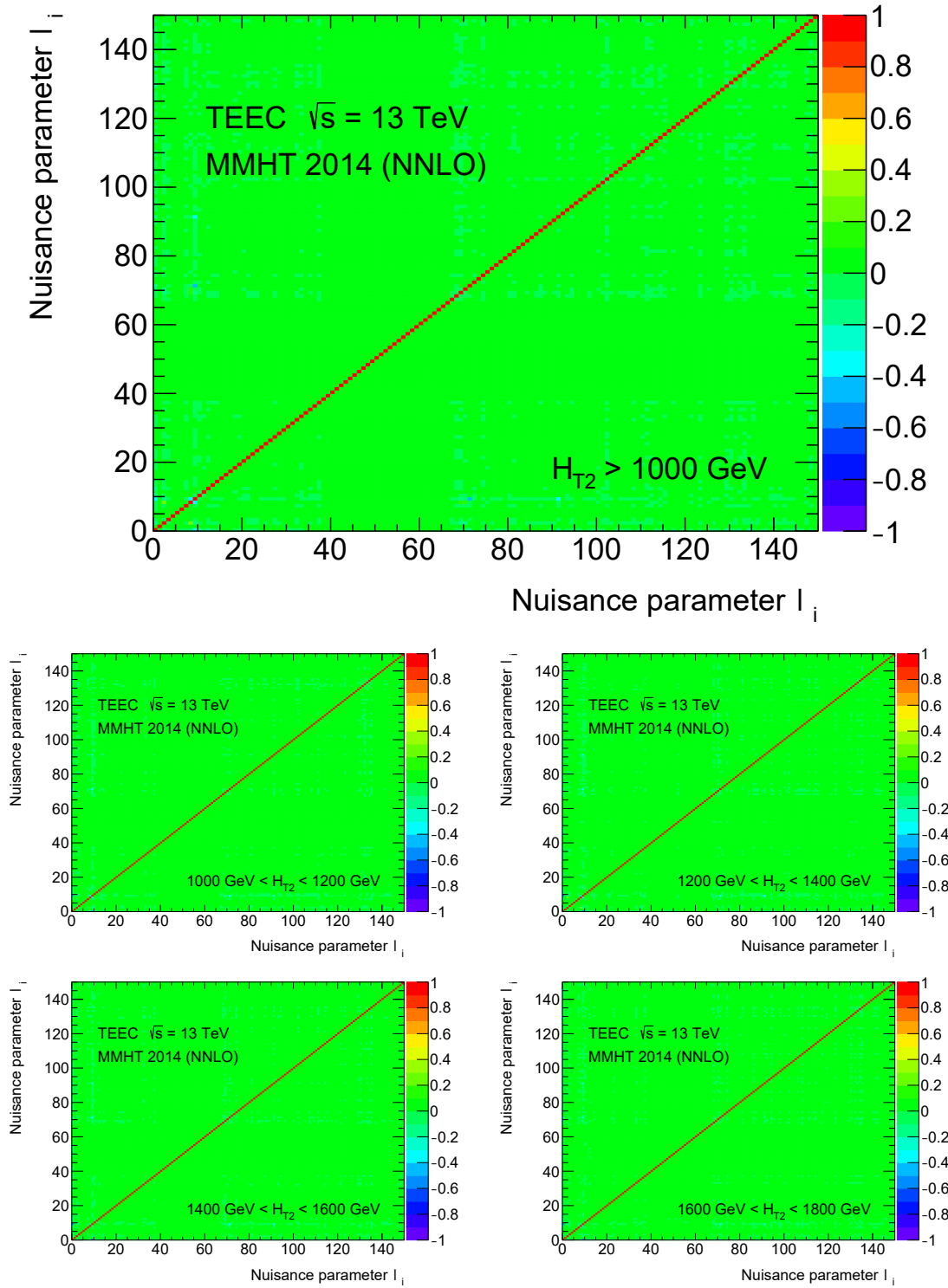


Figure 6.97: Correlation coefficients between the nuisance parameters obtained from individual fits, in inclusive (top) and exclusive (bottom) H_{T2} bins, to the TEEC function at NNLO using MMHT 2014 PDF group. The fact that the correlation matrices have very small off-diagonal terms indicates that the systematic sources are not significantly correlated between them.

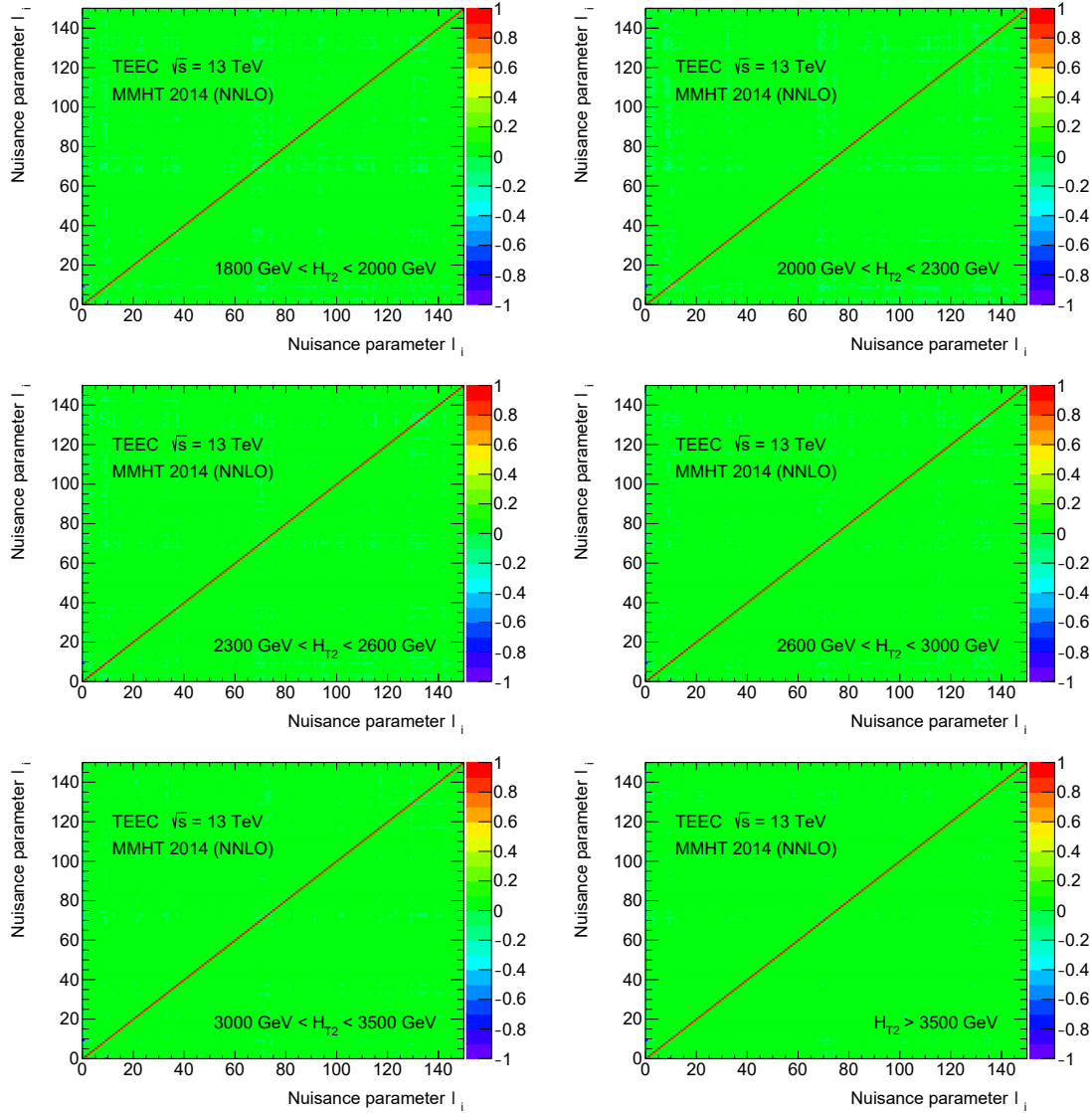


Figure 6.98: Correlation coefficients between the nuisance parameters obtained from individual fits, in exclusive H_{T2} bins, to the TEEC function at NNLO using MMHT 2014 PDF group. The fact that the correlation matrices have very small off-diagonal terms indicates that the systematic sources are not significantly correlated between them.

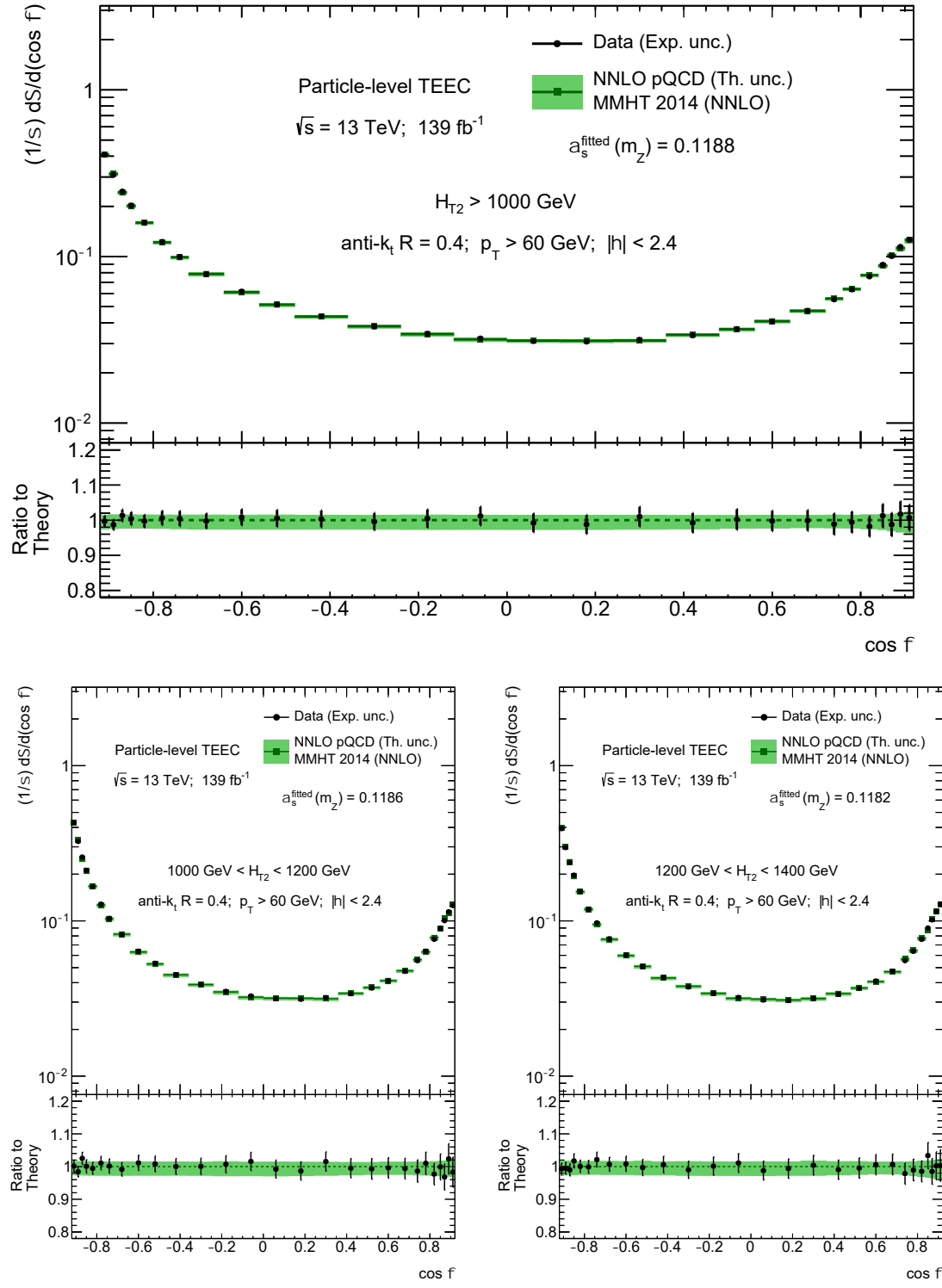


Figure 6.99: Comparison of the experimental results for the TEEC function, in inclusive and exclusive H_{T2} bins, and their fitted theoretical predictions at NNLO in pQCD using MMHT 2014 PDF group. The green band shows the theoretical uncertainties while the error bars show the experimental uncertainties, where correlations between the fit parameters have been taken into account.

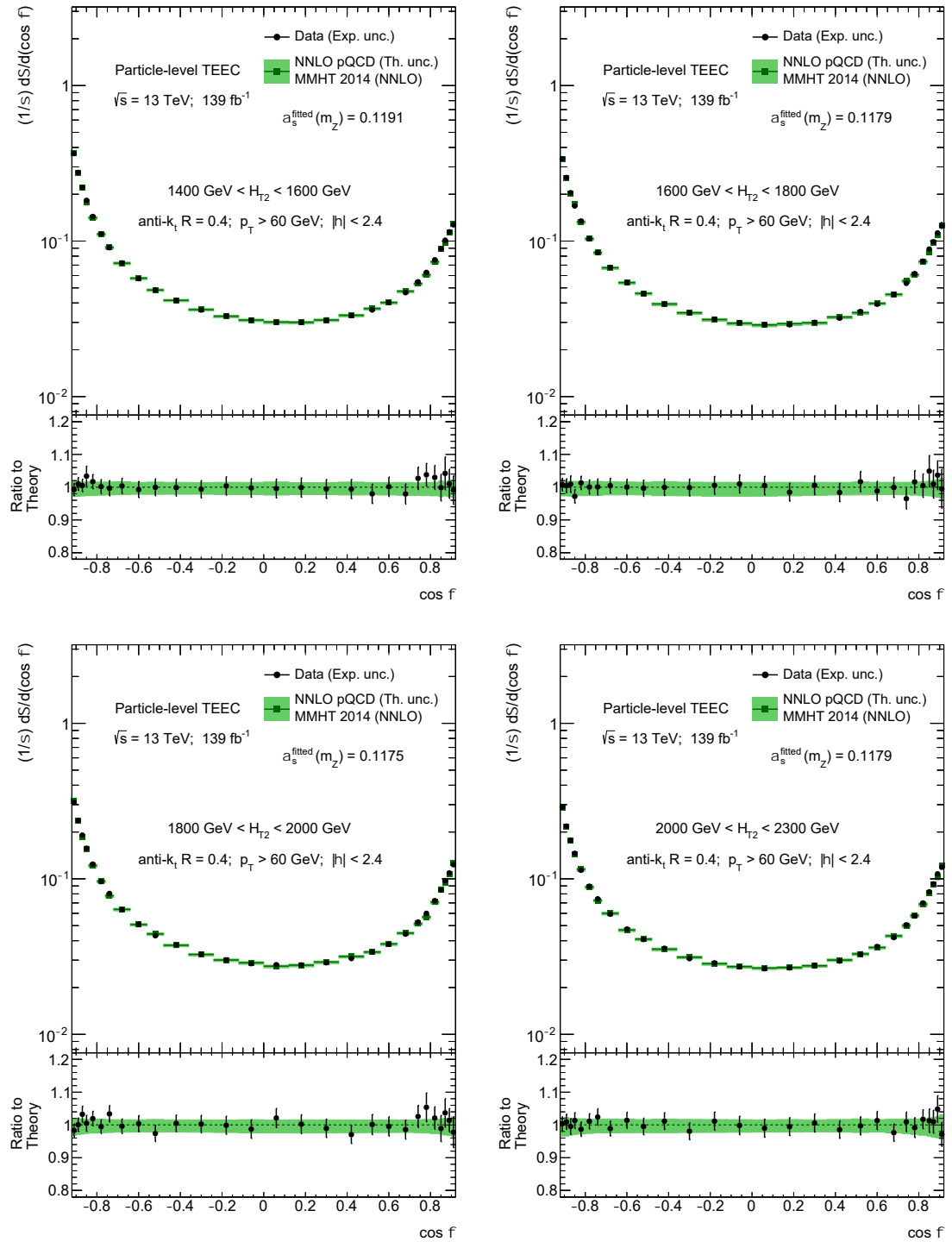


Figure 6.100: Comparison of the experimental results for the TEEC function, in exclusive H_{T2} bins, and their fitted theoretical predictions at NNLO in pQCD using MMHT 2014 PDF group. The green band shows the theoretical uncertainties while the error bars show the experimental uncertainties, where correlations between the fit parameters have been taken into account.

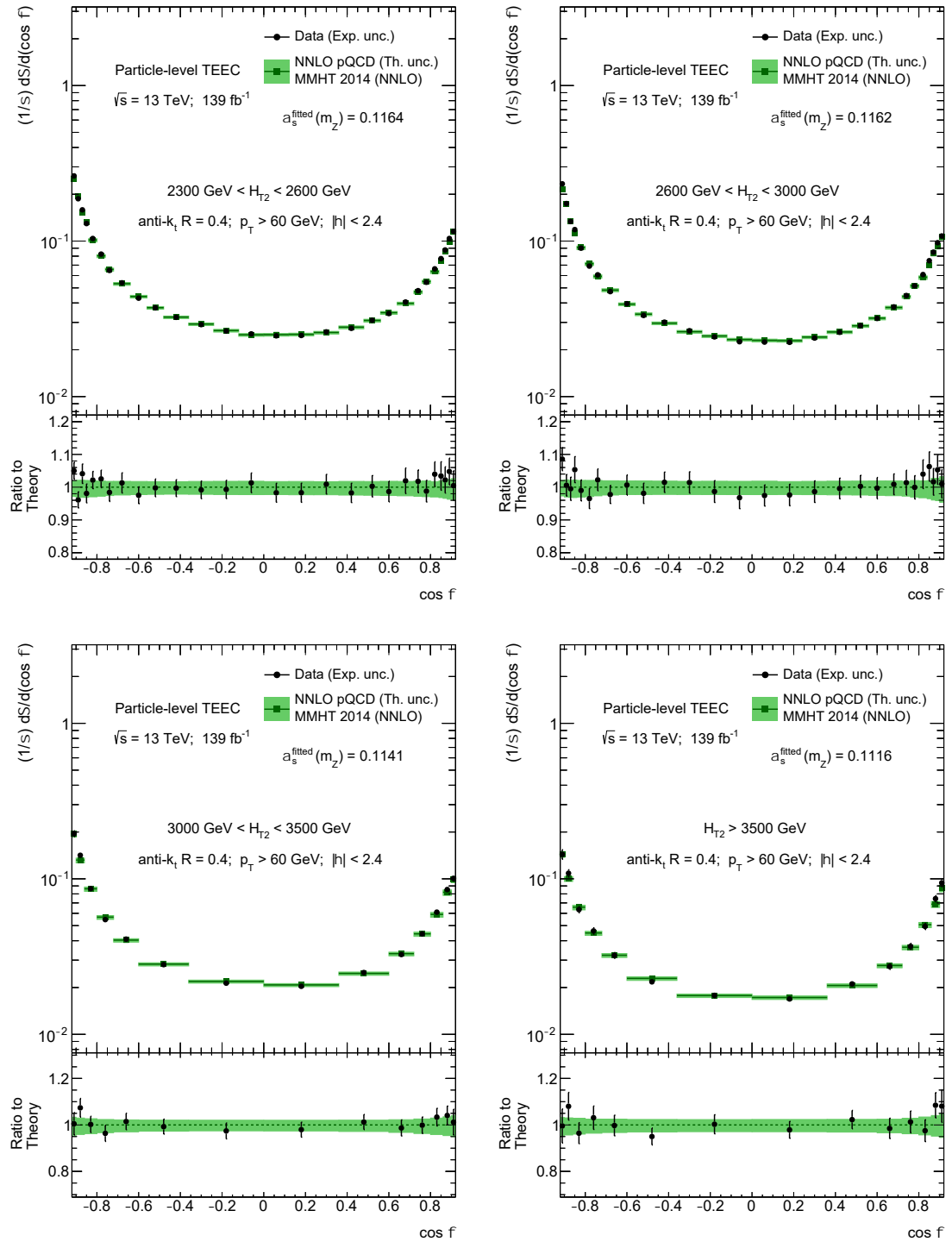


Figure 6.101: Comparison of the experimental results for the TEEC function, in exclusive H_{T2} bins, and their fitted theoretical predictions at NNLO in pQCD using MMHT 2014 PDF group. The green band shows the theoretical uncertainties while the error bars show the experimental uncertainties, where correlations between the fit parameters have been taken into account.

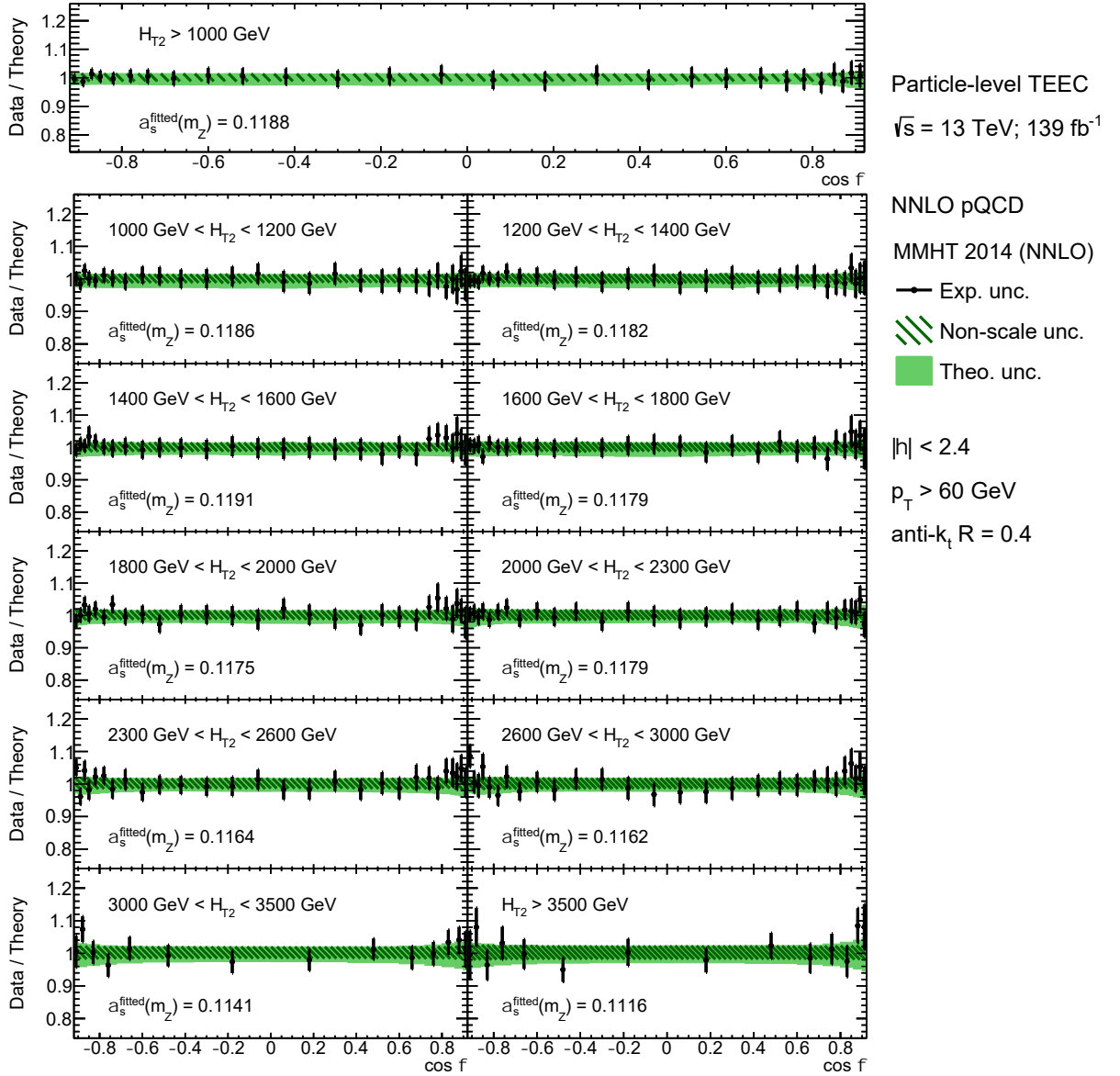


Figure 6.102: Ratios of the data to the fitted theoretical predictions at NNLO for the TEEC measurements, obtained using MMHT 2014 PDF group, in inclusive and exclusive H_{T2} bins. The green band shows the theoretical uncertainties, dominated by the scale variations, while the error bars show the experimental uncertainties, where correlations between the fit parameters have been taken into account.

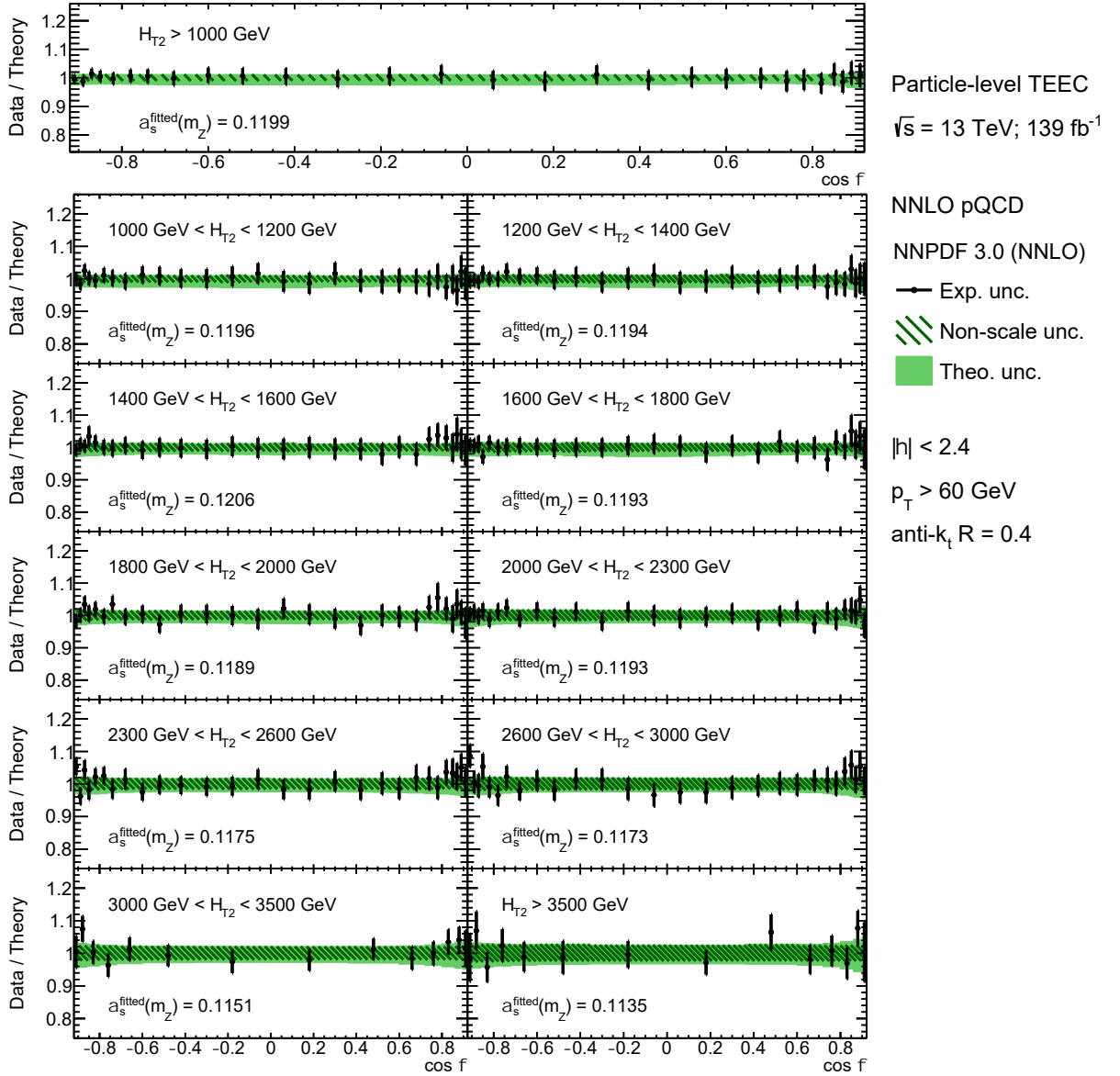


Figure 6.103: Ratios of the data to the fitted theoretical predictions at NNLO for the TEEC measurements, obtained using NNPDF 3.0 PDF group, in inclusive and exclusive H_{T2} bins. The green band shows the theoretical uncertainties, dominated by the scale variations, while the error bars show the experimental uncertainties, where correlations between the fit parameters have been taken into account.

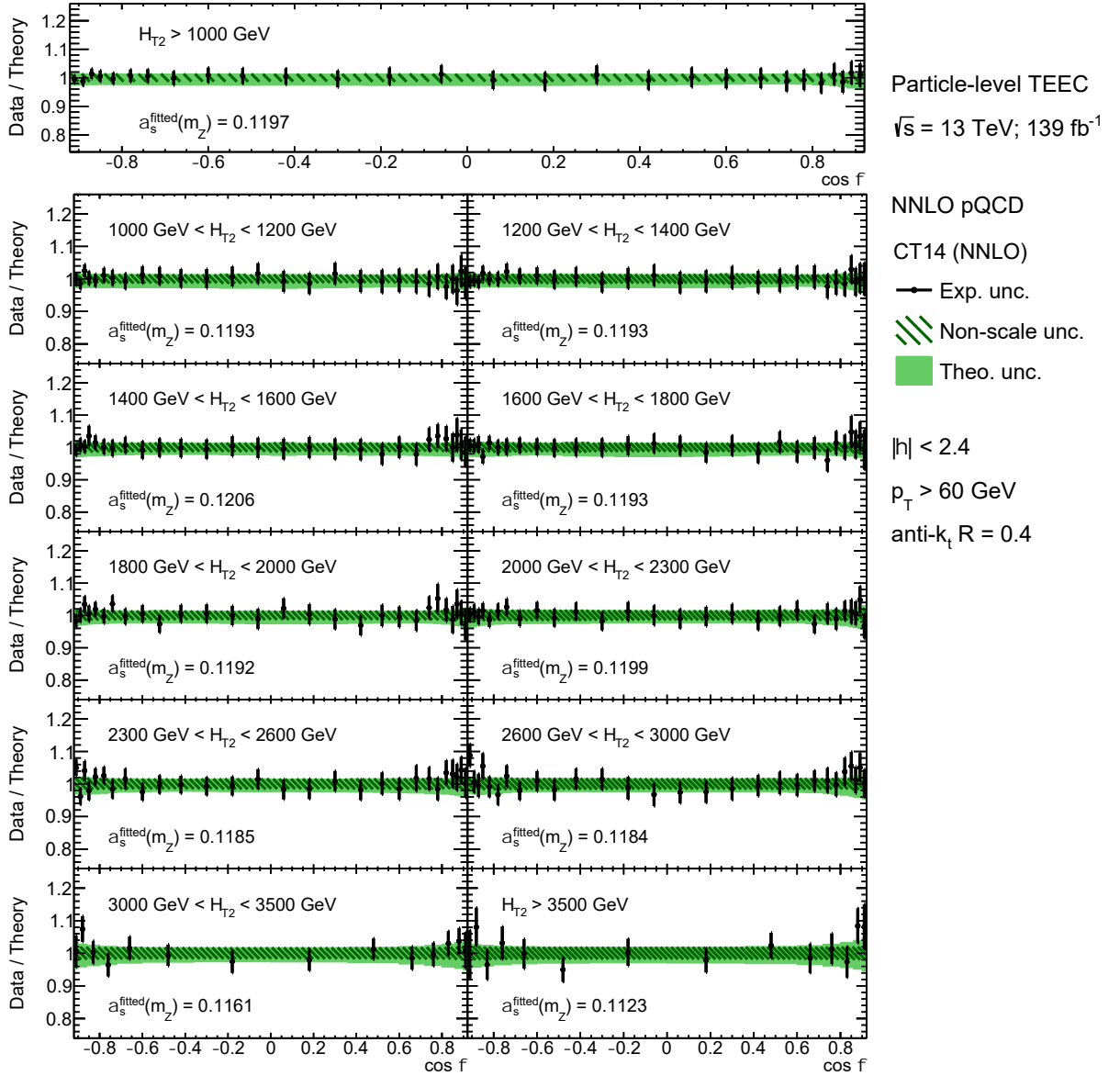


Figure 6.104: Ratios of the data to the fitted theoretical predictions at NNLO for the TEEC measurements, obtained using CT14 PDF group, in inclusive and exclusive H_{T2} bins. The green band shows the theoretical uncertainties, dominated by the scale variations, while the error bars show the experimental uncertainties, where correlations between the fit parameters have been taken into account.

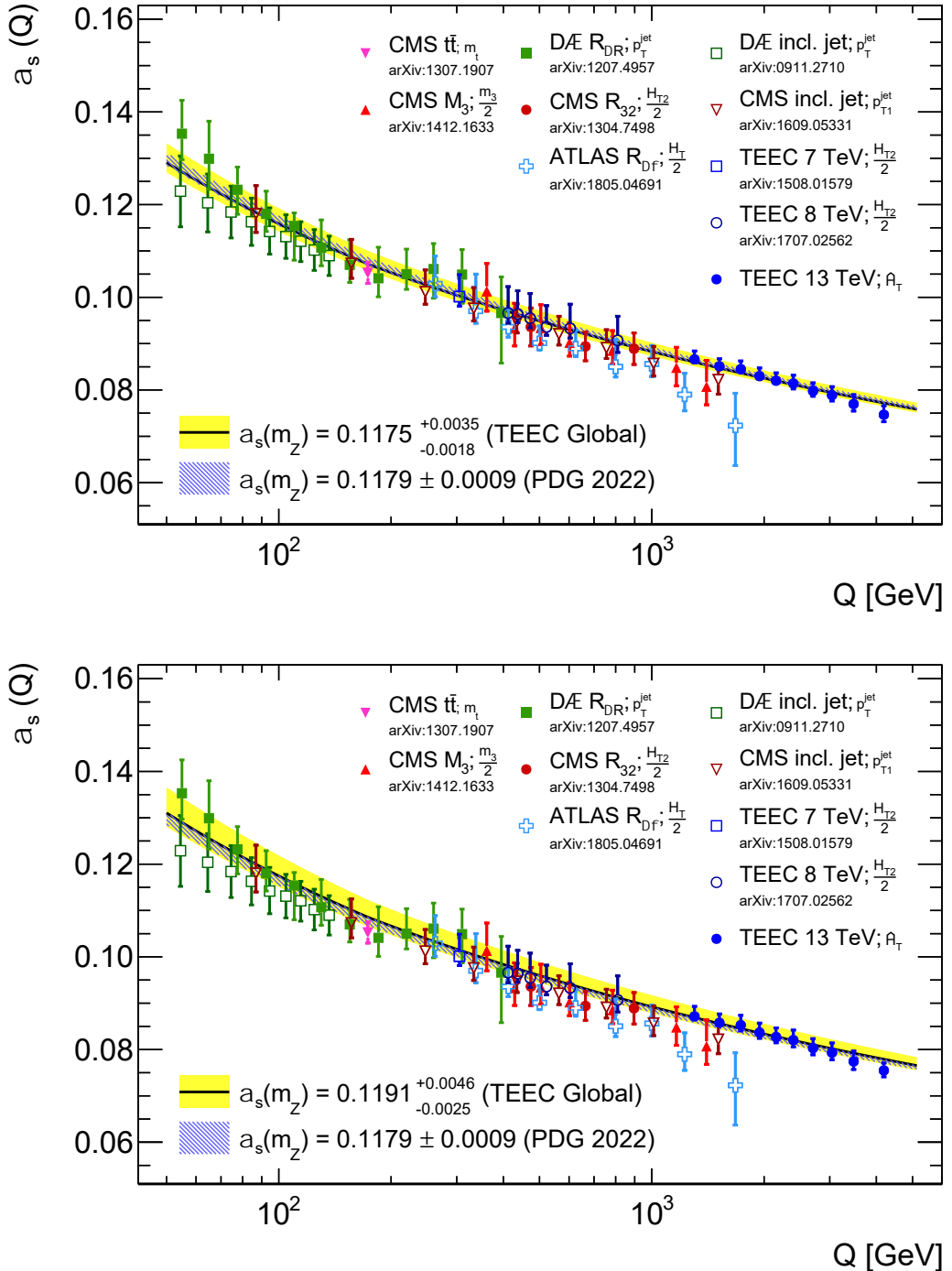


Figure 6.105: Comparison of the values of $\alpha_s(Q)$ obtained from fits to the TEEC function at NNLO in pQCD with the RGE prediction using the world average provided by the PDG (blue band) and with the value obtained from the global fit to all H_{T2} bins of the TEEC function (yellow band). Results from previous analyses, both from ATLAS and from other experiments, are also included, showing a very good agreement with the current measurements and with the world average. The interaction scale choice considered for each analysis is specified in the legend. The fits are performed using MMHT 2014 (top) and NNPDF 3.0 (bottom) PDF groups for the theoretical predictions.

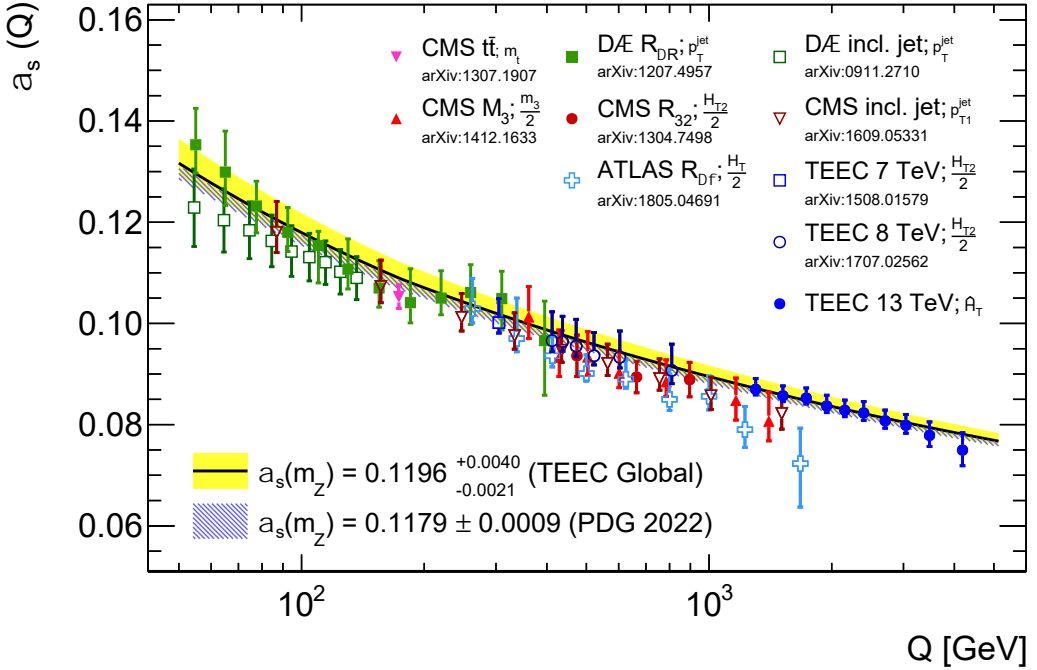


Figure 6.106: Comparison of the values of $\alpha_s(Q)$ obtained from fits to the TEEC function at NNLO in pQCD with the RGE prediction using the world average provided by the PDG (blue band) and with the value obtained from the global fit to all H_{T2} bins of the TEEC function (yellow band). Results from previous analyses, both from ATLAS and from other experiments, are also included, showing a very good agreement with the current measurements and with the world average. The interaction scale choice considered for each analysis is specified in the legend. The fits are performed using CT14 PDF group for the theoretical predictions.

$\langle Q \rangle$	$\alpha_s(Q)$ value (MMHT 2014)					
1302	0.0866 ± 0.0005 (fit)	$+0.0016$	(scale)	± 0.0005 (par.)	± 0.0001 (tune)	± 0.0004 (model)
1518	0.0851 ± 0.0005 (fit)	$+0.0014$	(scale)	± 0.0005 (par.)	± 0.0002 (tune)	± 0.0004 (model)
1732	0.0845 ± 0.0006 (fit)	$+0.0015$	(scale)	± 0.0005 (par.)	± 0.0002 (tune)	± 0.0005 (model)
1944	0.0830 ± 0.0006 (fit)	$+0.0015$	(scale)	± 0.0006 (par.)	± 0.0003 (tune)	± 0.0005 (model)
2153	0.0820 ± 0.0006 (fit)	$+0.0014$	(scale)	± 0.0006 (par.)	± 0.0001 (tune)	± 0.0004 (model)
2396	0.0814 ± 0.0006 (fit)	$+0.0014$	(scale)	± 0.0006 (par.)	± 0.0005 (tune)	± 0.0006 (model)
2706	0.0798 ± 0.0007 (fit)	$+0.0014$	(scale)	± 0.0006 (par.)	± 0.0002 (tune)	± 0.0005 (model)
3042	0.0789 ± 0.0008 (fit)	$+0.0014$	(scale)	± 0.0006 (par.)	± 0.0001 (tune)	± 0.0007 (model)
3476	0.0770 ± 0.0008 (fit)	$+0.0015$	(scale)	± 0.0006 (par.)	± 0.0001 (tune)	± 0.0009 (model)
4189	0.0747 ± 0.0009 (fit)	$+0.0013$	(scale)	± 0.0007 (par.)	± 0.0001 (tune)	± 0.0009 (model)

Table 6.31: Values of the strong coupling constant at the interaction scale, $\alpha_s(Q)$, obtained from fits to the TEEC function for each H_{T2} interval using MMHT 2014. The label (fit) indicates the statistical and experimental systematic uncertainties added in quadrature. The uncertainty related to the MC model in the IB unfolding is displayed separately as (model) and the one referred to as (tune) is related to the non-pQCD corrections. The average values of the scale are given in GeV.

$\langle Q \rangle$	$\alpha_s(Q)$ value (NNPDF 3.0)
1302	0.0872 ± 0.0006 (fit) $^{+0.0019}_{-0.0001}$ (scale) ± 0.0007 (par.) ± 0.0002 (tune) ± 0.0004 (model)
1518	0.0858 ± 0.0005 (fit) $^{+0.0016}_{-0.0003}$ (scale) ± 0.0008 (par.) ± 0.0002 (tune) ± 0.0004 (model)
1732	0.0853 ± 0.0006 (fit) $^{+0.0018}_{-0.0002}$ (scale) ± 0.0008 (par.) ± 0.0003 (tune) ± 0.0005 (model)
1944	0.0837 ± 0.0006 (fit) $^{+0.0017}_{-0.0003}$ (scale) ± 0.0009 (par.) ± 0.0003 (tune) ± 0.0005 (model)
2153	0.0827 ± 0.0006 (fit) $^{+0.0016}_{-0.0002}$ (scale) ± 0.0009 (par.) ± 0.0002 (tune) ± 0.0005 (model)
2396	0.0820 ± 0.0007 (fit) $^{+0.0016}_{-0.0002}$ (scale) ± 0.0010 (par.) ± 0.0005 (tune) ± 0.0006 (model)
2706	0.0803 ± 0.0008 (fit) $^{+0.0015}_{-0.0003}$ (scale) ± 0.0010 (par.) ± 0.0002 (tune) ± 0.0005 (model)
3042	0.0793 ± 0.0008 (fit) $^{+0.0014}_{-0.0002}$ (scale) ± 0.0010 (par.) ± 0.0001 (tune) ± 0.0007 (model)
3476	0.0774 ± 0.0009 (fit) $^{+0.0016}_{-0.0005}$ (scale) ± 0.0010 (par.) ± 0.0001 (tune) ± 0.0009 (model)
4189	0.0755 ± 0.0008 (fit) $^{+0.0009}_{-0.0003}$ (scale) ± 0.0008 (par.) ± 0.0001 (tune) ± 0.0007 (model)

Table 6.32: Values of the strong coupling constant at the interaction scale, $\alpha_s(Q)$, obtained from fits to the TEEC function for each H_{T2} interval using NNPDF 3.0. The label (fit) indicates the statistical and experimental systematic uncertainties added in quadrature. The uncertainty related to the MC model in the IB unfolding is displayed separately as (model) and the one referred to as (tune) is related to the non-pQCD corrections. The average values of the scale are given in GeV.

$\langle Q \rangle$	$\alpha_s(Q)$ value (CT14)
1302	0.0870 ± 0.0006 (fit) $^{+0.0018}_{-0.0001}$ (scale) ± 0.0008 (par.) ± 0.0002 (tune) ± 0.0004 (model)
1518	0.0857 ± 0.0006 (fit) $^{+0.0016}_{-0.0003}$ (scale) ± 0.0008 (par.) ± 0.0002 (tune) ± 0.0005 (model)
1732	0.0853 ± 0.0006 (fit) $^{+0.0016}_{-0.0003}$ (scale) ± 0.0007 (par.) ± 0.0003 (tune) ± 0.0005 (model)
1944	0.0837 ± 0.0007 (fit) $^{+0.0017}_{-0.0003}$ (scale) ± 0.0008 (par.) ± 0.0003 (tune) ± 0.0006 (model)
2153	0.0828 ± 0.0007 (fit) $^{+0.0016}_{-0.0003}$ (scale) ± 0.0008 (par.) ± 0.0002 (tune) ± 0.0005 (model)
2396	0.0823 ± 0.0007 (fit) $^{+0.0017}_{-0.0003}$ (scale) ± 0.0009 (par.) ± 0.0006 (tune) ± 0.0007 (model)
2706	0.0808 ± 0.0008 (fit) $^{+0.0016}_{-0.0004}$ (scale) ± 0.0009 (par.) ± 0.0003 (tune) ± 0.0006 (model)
3042	0.0799 ± 0.0009 (fit) $^{+0.0015}_{-0.0003}$ (scale) ± 0.0009 (par.) ± 0.0001 (tune) ± 0.0009 (model)
3476	0.0779 ± 0.0011 (fit) $^{+0.0018}_{-0.0009}$ (scale) ± 0.0010 (par.) ± 0.0001 (tune) ± 0.0013 (model)
4189	0.0750 ± 0.0015 (fit) $^{+0.0021}_{-0.0011}$ (scale) ± 0.0014 (par.) ± 0.0002 (tune) ± 0.0018 (model)

Table 6.33: Values of the strong coupling constant at the interaction scale, $\alpha_s(Q)$, obtained from fits to the TEEC function for each H_{T2} interval using CT14. The label (fit) indicates the statistical and experimental systematic uncertainties added in quadrature. The uncertainty related to the MC model in the IB unfolding is displayed separately as (model) and the one referred to as (tune) is related to the non-pQCD corrections. The average values of the scale are given in GeV.

6.9.4 Fits to the ATEEC function

The values of $\alpha_s(m_Z)$ extracted from a global fit to the ATEEC function at NNLO as well as to those individual fits in each exclusive H_{T2} bin and in the fully inclusive sample are summarized in Table 6.34. The theoretical predictions used for this extraction use MMHT 2014 as the nominal PDF group, which is the one providing a wider range of variations for $\alpha_s(m_Z)$. In addition, the extracted values using NNPDF 3.0 and CT14 as the PDF group are also presented in Tables 6.35 and 6.36, respectively. The uncertainty derived from the χ^2 fit includes both experimental and theoretical statistical uncertainties, along with the experimental systematic uncertainties constrained by the nuisance parameters.

The χ^2 values indicate that the agreement between the data and the theoretical predictions is good in each exclusive H_{T2} bin and in the fully inclusive sample. The critical value with a significance level of $\alpha = 0.05$ for the global fit is $\chi^2 = 143.2$. Thus, the tension found in the correlations is not presented, mainly due to the statistical fluctuations that partially cover the drop at high energy scales of the fitted values of α_s . The nuisance parameters from the ATEEC function fits are shown in Figures 6.107 and 6.108. The large theoretical statistical uncertainties prevent from constraining the nuisance parameters, thus they are all found to be compatible with zero. Nevertheless, for small theoretical statistical uncertainties, the nuisance parameters which are usually slightly pulled correspond to EtaIntercalibration Modelling ($i = 2$), Flavour Response ($i = 9$), Pileup RhoTopology ($i = 71$), Zjet MC ($i = 91$), and JAR ($i = 148$).

The correlation coefficients between nuisance parameters are shown in Figures 6.109 and 6.110. The fact that the correlation matrices have very small off-diagonal terms indicates that the systematic sources are not significantly correlated between them when large statistical uncertainties are involved. Otherwise, the nuisance parameters associated to Flavour Composition ($i = 8$) and Flavour Response ($i = 9$) would be slightly anticorrelated. Figures 6.114 to 6.113 compare the experimental results with fitted theoretical predictions; the ones where the fitted values of $\alpha_s(m_Z)$ and the nuisance parameters are already constrained.

The extracted values of the strong coupling constant $\alpha_s(m_Z)$ are in good agreement with the 2022 world average value $\alpha_s(m_Z) = 0.1179 \pm 0.0009$ [11]. A comparison of the results of α_s is shown in Figures 6.117 and 6.118. The results from previous extractions using LHC data [1, 2, 141–145] and Tevatron data [146, 147] are also shown, together with the world average band [11]. The values of α_s are evolved from m_Z to the corresponding scale Q using the three-loop solution of the RGE, introduced in Eq. (2.1), where the interaction scale is evaluated for each analysis at the central value of the renormalization scale. Tables 6.37 to 6.39 summarize the extracted values of the physical strong coupling constant $\alpha_s(Q)$ that enter the matrix elements in the calculation.

$\langle Q \rangle$ [GeV]		$\alpha_s(m_Z)$	value (MMHT 2014)	χ^2/N_{dof}
Global	0.1185 ± 0.0005 (stat.) ± 0.0008 (syst.)	$+0.0022$ (scale) -0.0002	± 0.0011 (param.) ± 0.0004 (tune) ± 0.0001 (model)	$109.5 / 117$
Inclusive	0.1194 ± 0.0009 (stat.) ± 0.0007 (syst.)	$+0.0023$ (scale) -0.0000	± 0.0011 (param.) ± 0.0005 (tune) ± 0.0000 (model)	$10.7 / 12$
1302	0.1195 ± 0.0011 (stat.) ± 0.0006 (syst.)	$+0.0024$ (scale) -0.0000	± 0.0011 (param.) ± 0.0006 (tune) ± 0.0000 (model)	$10.6 / 12$
1518	0.1191 ± 0.0011 (stat.) ± 0.0007 (syst.)	$+0.0020$ (scale) -0.0001	± 0.0011 (param.) ± 0.0004 (tune) ± 0.0001 (model)	$7.2 / 12$
1732	0.1187 ± 0.0015 (stat.) ± 0.0009 (syst.)	$+0.0026$ (scale) -0.0003	± 0.0012 (param.) ± 0.0010 (tune) ± 0.0002 (model)	$7.2 / 12$
1944	0.1178 ± 0.0016 (stat.) ± 0.0009 (syst.)	$+0.0022$ (scale) -0.0003	± 0.0013 (param.) ± 0.0007 (tune) ± 0.0000 (model)	$11.2 / 12$
2153	0.1174 ± 0.0017 (stat.) ± 0.0009 (syst.)	$+0.0022$ (scale) -0.0002	± 0.0013 (param.) ± 0.0007 (tune) ± 0.0001 (model)	$12.8 / 12$
2396	0.1187 ± 0.0017 (stat.) ± 0.0010 (syst.)	$+0.0017$ (scale) -0.0000	± 0.0012 (param.) ± 0.0007 (tune) ± 0.0004 (model)	$11.7 / 12$
2706	0.1148 ± 0.0026 (stat.) ± 0.0014 (syst.)	$+0.0024$ (scale) -0.0000	± 0.0015 (param.) ± 0.0007 (tune) ± 0.0002 (model)	$18.3 / 12$
3042	0.1169 ± 0.0031 (stat.) ± 0.0012 (syst.)	$+0.0018$ (scale) -0.0000	± 0.0015 (param.) ± 0.0014 (tune) ± 0.0009 (model)	$13.0 / 12$
3476	0.1141 ± 0.0052 (stat.) ± 0.0016 (syst.)	$+0.0025$ (scale) -0.0007	± 0.0018 (param.) ± 0.0008 (tune) ± 0.0011 (model)	$4.9 / 6$
4189	0.1096 ± 0.0085 (stat.) ± 0.0009 (syst.)	$+0.0013$ (scale) -0.0000	± 0.0009 (param.) ± 0.0002 (tune) ± 0.0007 (model)	$6.2 / 6$

Table 6.34: Values of the strong coupling constant at the Z boson mass scale, $\alpha_s(m_Z)$, obtained from fits to the ATEEC function at NNLO using MMHT 2014 PDF group. The values of the average interaction scale $\langle Q \rangle$ are shown in the first column, while the values of the χ^2 function at the minimum are shown in the third column. The label (stat.) includes the experimental and theoretical statistical uncertainties, whereas the label (syst.) indicates only the experimental systematic uncertainties added in quadrature. The uncertainty related to the MC model in the IB unfolding is displayed separately as (model) and the one referred to as (tune) is related to the non-pQCD corrections.

$\langle Q \rangle$ [GeV]		$\alpha_s(m_Z)$	value (NNPDF 3.0)	χ^2/N_{dof}
Global	0.1199 ± 0.0006 (stat.) ± 0.0009 (syst.)	$+0.0027$ (scale) -0.0062 (param.)	± 0.0017 (param.) ± 0.0005 (tune) ± 0.0001 (model)	108.2 / 117
Inclusive	0.1206 ± 0.0010 (stat.) ± 0.0008 (syst.)	$+0.0027$ (scale) -0.0000 (param.)	± 0.0016 (param.) ± 0.0005 (tune) ± 0.0000 (model)	11.9 / 12
1302	0.1208 ± 0.0013 (stat.) ± 0.0007 (syst.)	$+0.0028$ (scale) -0.0016 (param.)	± 0.0016 (param.) ± 0.0007 (tune) ± 0.0000 (model)	11.2 / 12
1518	0.1205 ± 0.0013 (stat.) ± 0.0008 (syst.)	$+0.0023$ (scale) -0.0001 (param.)	± 0.0017 (param.) ± 0.0004 (tune) ± 0.0001 (model)	8.1 / 12
1732	0.1201 ± 0.0016 (stat.) ± 0.0009 (syst.)	$+0.0030$ (scale) -0.0003 (param.)	± 0.0018 (param.) ± 0.0011 (tune) ± 0.0002 (model)	7.7 / 12
1944	0.1193 ± 0.0017 (stat.) ± 0.0010 (syst.)	$+0.0024$ (scale) -0.0020 (param.)	± 0.0008 (param.) ± 0.0008 (tune) ± 0.0000 (model)	12.1 / 12
2153	0.1192 ± 0.0019 (stat.) ± 0.0010 (syst.)	$+0.0023$ (scale) -0.0001 (param.)	± 0.0020 (param.) ± 0.0008 (tune) ± 0.0001 (model)	13.0 / 12
2396	0.1205 ± 0.0018 (stat.) ± 0.0012 (syst.)	$+0.0022$ (scale) -0.0000 (param.)	± 0.0023 (param.) ± 0.0011 (tune) ± 0.0005 (model)	12.3 / 12
2706	0.1162 ± 0.0026 (stat.) ± 0.0014 (syst.)	$+0.0024$ (scale) -0.0024 (param.)	± 0.0008 (param.) ± 0.0008 (tune) ± 0.0002 (model)	18.3 / 12
3042	0.1180 ± 0.0034 (stat.) ± 0.0013 (syst.)	$+0.0018$ (scale) -0.0002 (param.)	± 0.0027 (param.) ± 0.0015 (tune) ± 0.0009 (model)	13.2 / 12
3476	0.1149 ± 0.0050 (stat.) ± 0.0016 (syst.)	$+0.0024$ (scale) -0.0006 (param.)	± 0.0028 (param.) ± 0.0007 (tune) ± 0.0011 (model)	4.9 / 6
4189	0.1129 ± 0.0095 (stat.) ± 0.0019 (syst.)	$+0.0056$ (scale) -0.0056 (param.)	± 0.0031 (param.) ± 0.0003 (tune) ± 0.0014 (model)	2.5 / 6

Table 6.35: Values of the strong coupling constant at the Z boson mass scale, $\alpha_s(m_Z)$, obtained from fits to the ATEEC function at NNLO using NNPDF 3.0 PDF group. The values of the average interaction scale $\langle Q \rangle$ are shown in the first column, while the values of the χ^2 function at the minimum are shown in the third column. The label (stat.) includes the experimental and theoretical statistical uncertainties, whereas the label (syst.) indicates only the experimental systematic uncertainties added in quadrature. The uncertainty related to the MC model in the IB unfolding is displayed separately as (model) and the one referred to as (tune) is related to the non-pQCD corrections.

$\langle Q \rangle$ [GeV]		$\alpha_s(m_Z)$ value (CT14)	χ^2/N_{dof}
Global	0.1200 ± 0.0006 (stat.) ± 0.0009 (syst.)	$+0.0027$ (scale) ± 0.0018 (param.) ± 0.0006 (tune) ± 0.0001 (model)	$110.1 / 117$
Inclusive	0.1204 ± 0.0010 (stat.) ± 0.0008 (syst.)	-0.0001 (scale) ± 0.0016 (param.) ± 0.0005 (tune) ± 0.0000 (model)	$12.1 / 12$
1302	0.1205 ± 0.0013 (stat.) ± 0.0007 (syst.)	$+0.0027$ (scale) ± 0.0016 (param.) ± 0.0007 (tune) ± 0.0000 (model)	$11.3 / 12$
1518	0.1206 ± 0.0013 (stat.) ± 0.0009 (syst.)	-0.0000 (scale) ± 0.0017 (param.) ± 0.0004 (tune) ± 0.0001 (model)	$7.8 / 12$
1732	0.1203 ± 0.0016 (stat.) ± 0.0010 (syst.)	$+0.0030$ (scale) ± 0.0018 (param.) ± 0.0012 (tune) ± 0.0002 (model)	$7.4 / 12$
1944	0.1197 ± 0.0019 (stat.) ± 0.0011 (syst.)	$+0.0027$ (scale) ± 0.0021 (param.) ± 0.0009 (tune) ± 0.0000 (model)	$12.1 / 12$
2153	0.1196 ± 0.0021 (stat.) ± 0.0011 (syst.)	-0.0001 (scale) ± 0.0019 (param.) ± 0.0009 (tune) ± 0.0001 (model)	$13.5 / 12$
2396	0.1219 ± 0.0019 (stat.) ± 0.0013 (syst.)	$+0.0025$ (scale) ± 0.0022 (param.) ± 0.0012 (tune) ± 0.0005 (model)	$12.4 / 12$
2706	0.1171 ± 0.0035 (stat.) ± 0.0018 (syst.)	-0.0031 (scale) ± 0.0026 (param.) ± 0.0010 (tune) ± 0.0003 (model)	$18.2 / 12$
3042	0.1208 ± 0.0039 (stat.) ± 0.0016 (syst.)	-0.0003 (scale) ± 0.0020 (param.) ± 0.0020 (tune) ± 0.0011 (model)	$13.7 / 12$
3476	0.1180 ± 0.0072 (stat.) ± 0.0023 (syst.)	-0.0030 (scale) ± 0.0032 (param.) ± 0.0012 (tune) ± 0.0018 (model)	$4.8 / 6$
4189	0.1062 ± 0.0188 (stat.) ± 0.0004 (syst.)	-0.0004 (scale) ± 0.0000 (param.) ± 0.0001 (tune) ± 0.0000 (model)	$6.2 / 6$

Table 6.36: Values of the strong coupling constant at the Z boson mass scale, $\alpha_s(m_Z)$, obtained from fits to the ATTEC function at NNLO using CT14 PDF group. The values of the average interaction scale $\langle Q \rangle$ are shown in the first column, while the values of the χ^2 function at the minimum are shown in the third column. The label (stat.) includes the experimental and theoretical statistical uncertainties, whereas the label (syst.) indicates only the experimental systematic uncertainties added in quadrature. The uncertainty related to the MC model in the IB unfolding is displayed separately as (model) and the one referred to as (tune) is related to the non-pQCD corrections.

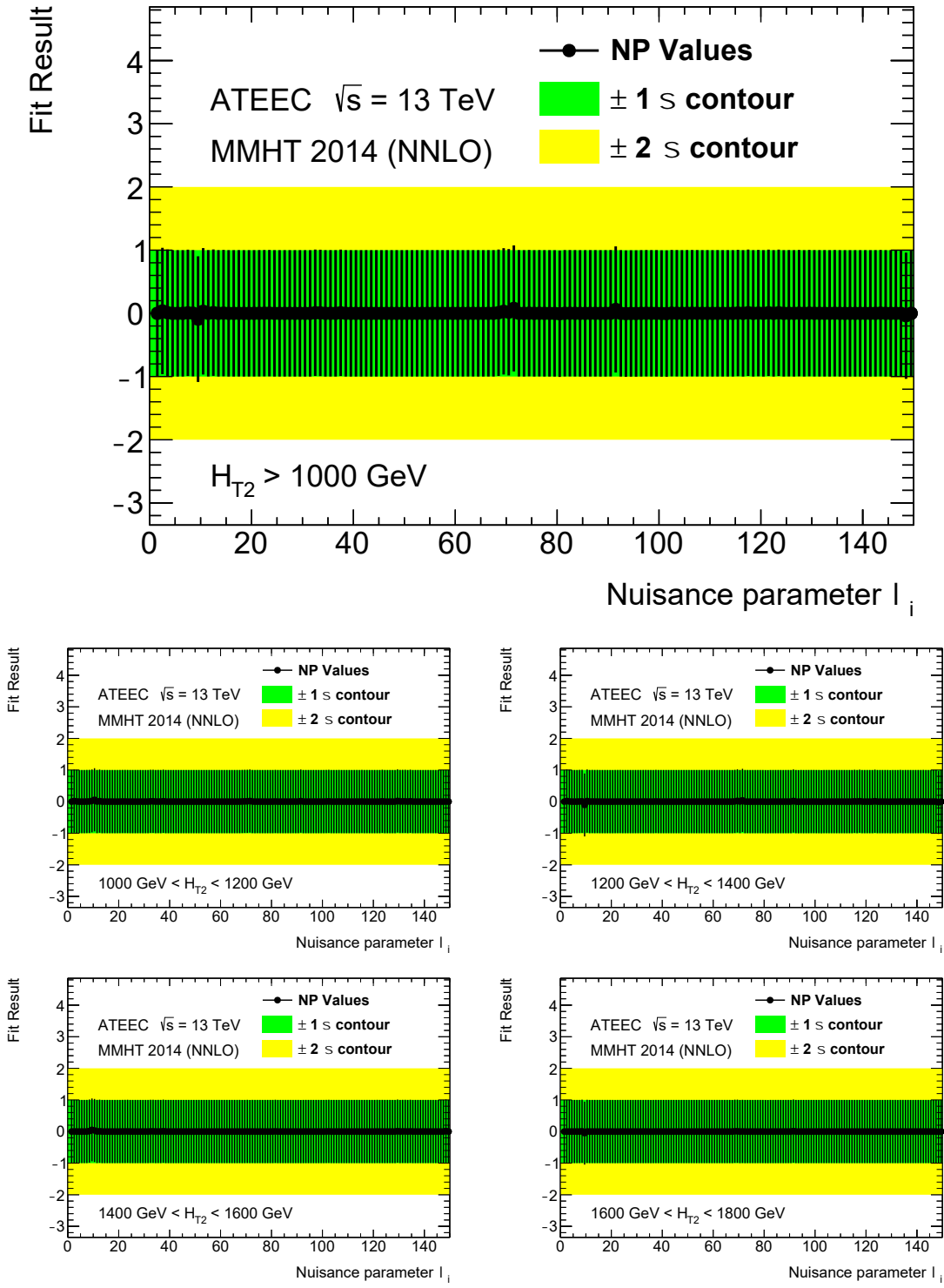


Figure 6.107: Values of the nuisance parameters obtained from individual fits, in inclusive (top) and exclusive (bottom) H_{T2} bins, to the ATEEC function at NNLO using MMHT 2014 PDF group. They lie within the $\pm 1\sigma$ contour (green band) or $\pm 2\sigma$ contour (yellow band), and are generally found to be compatible with zero.

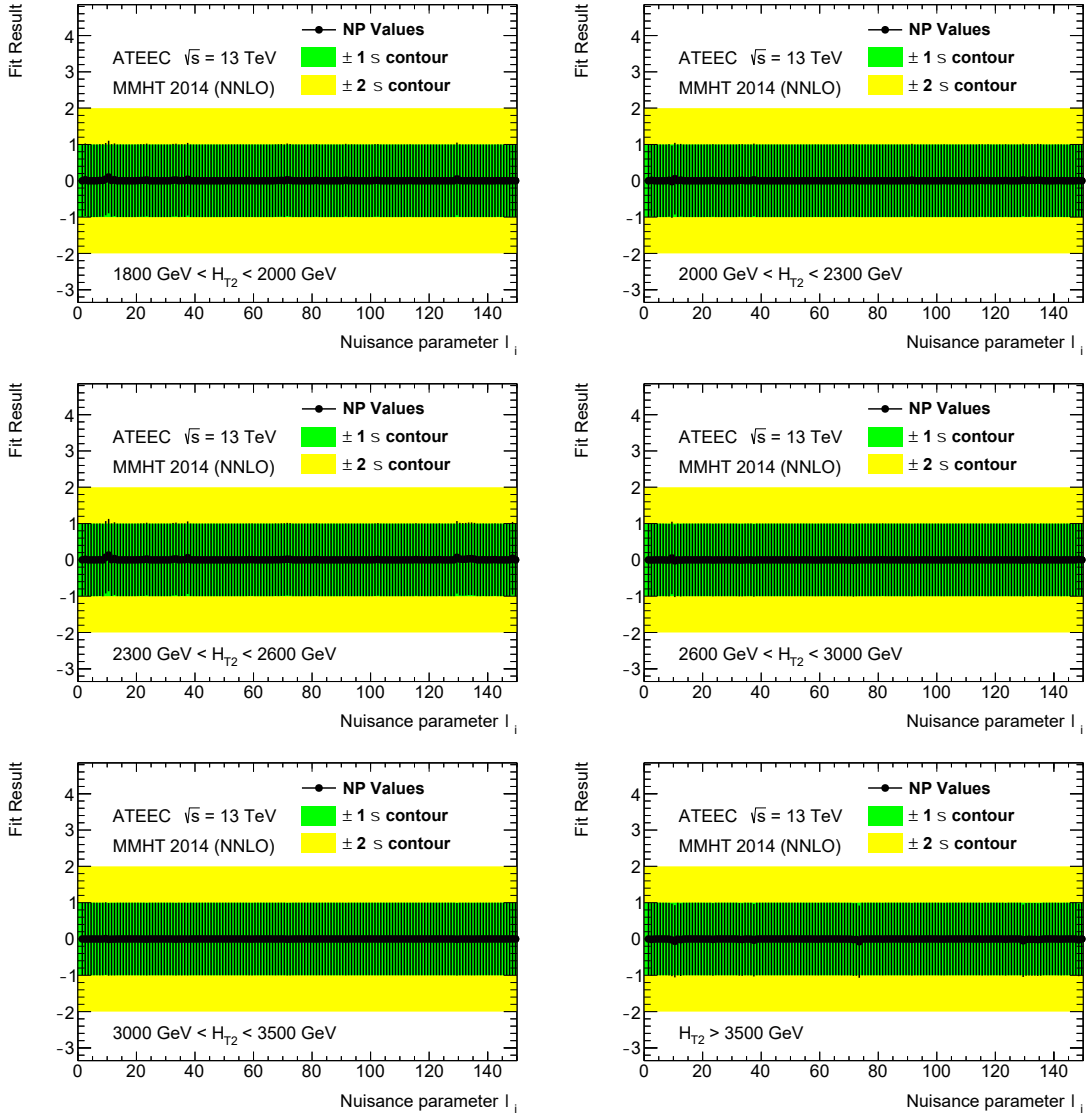


Figure 6.108: Values of the nuisance parameters obtained from individual fits, in exclusive H_{T2} bins, to the ATEEC function at NNLO using MMHT 2014 PDF group. They lie within the $\pm 1\sigma$ contour (green band) or $\pm 2\sigma$ contour (yellow band), and are generally found to be compatible with zero.

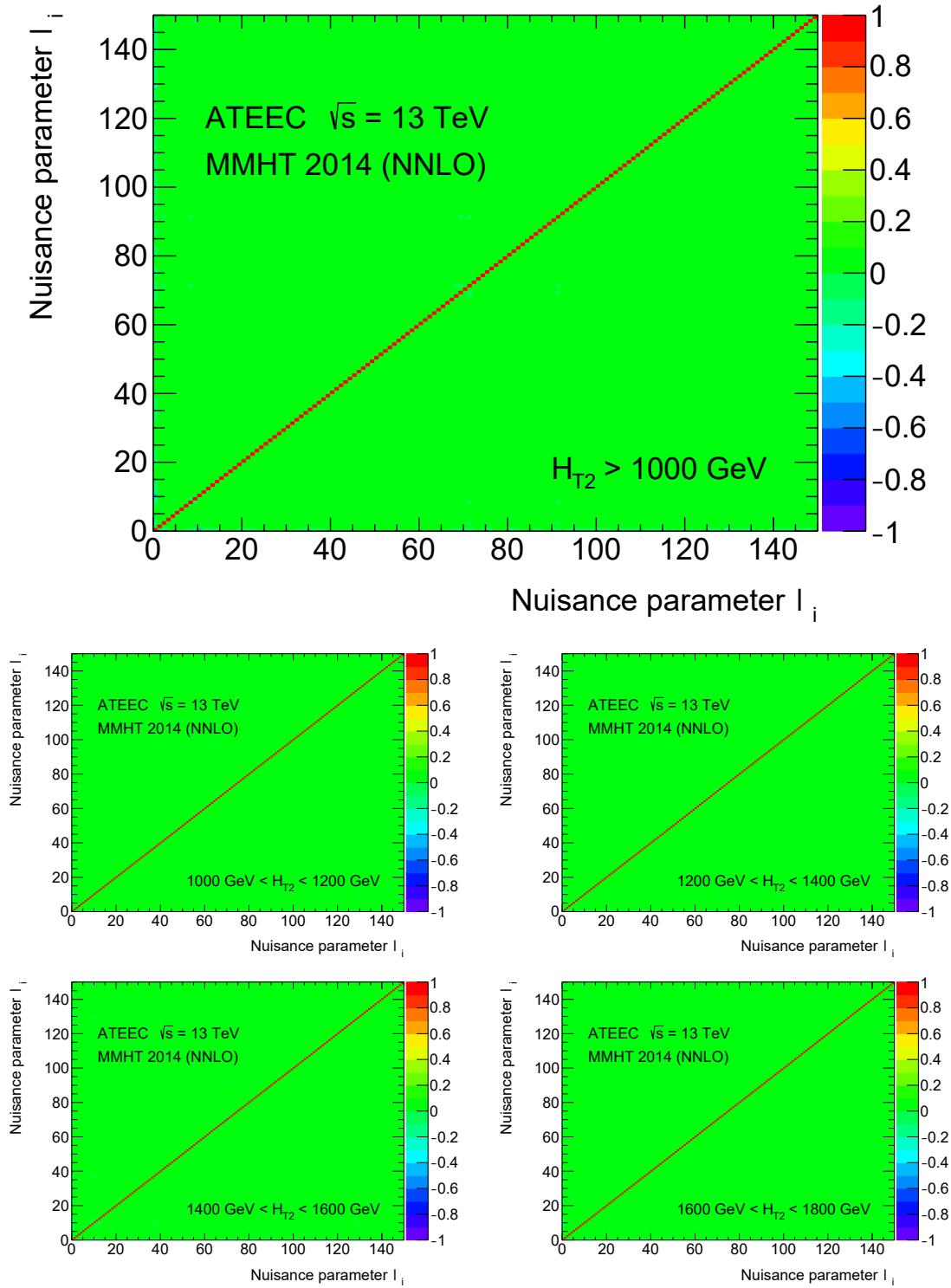


Figure 6.109: Correlation coefficients between the nuisance parameters obtained from individual fits, in inclusive (top) and exclusive (bottom) H_{T2} bins, to the ATEEC function at NNLO using MMHT 2014 PDF group. The fact that the correlation matrices have very small off-diagonal terms indicates that the systematic sources are not significantly correlated between them.

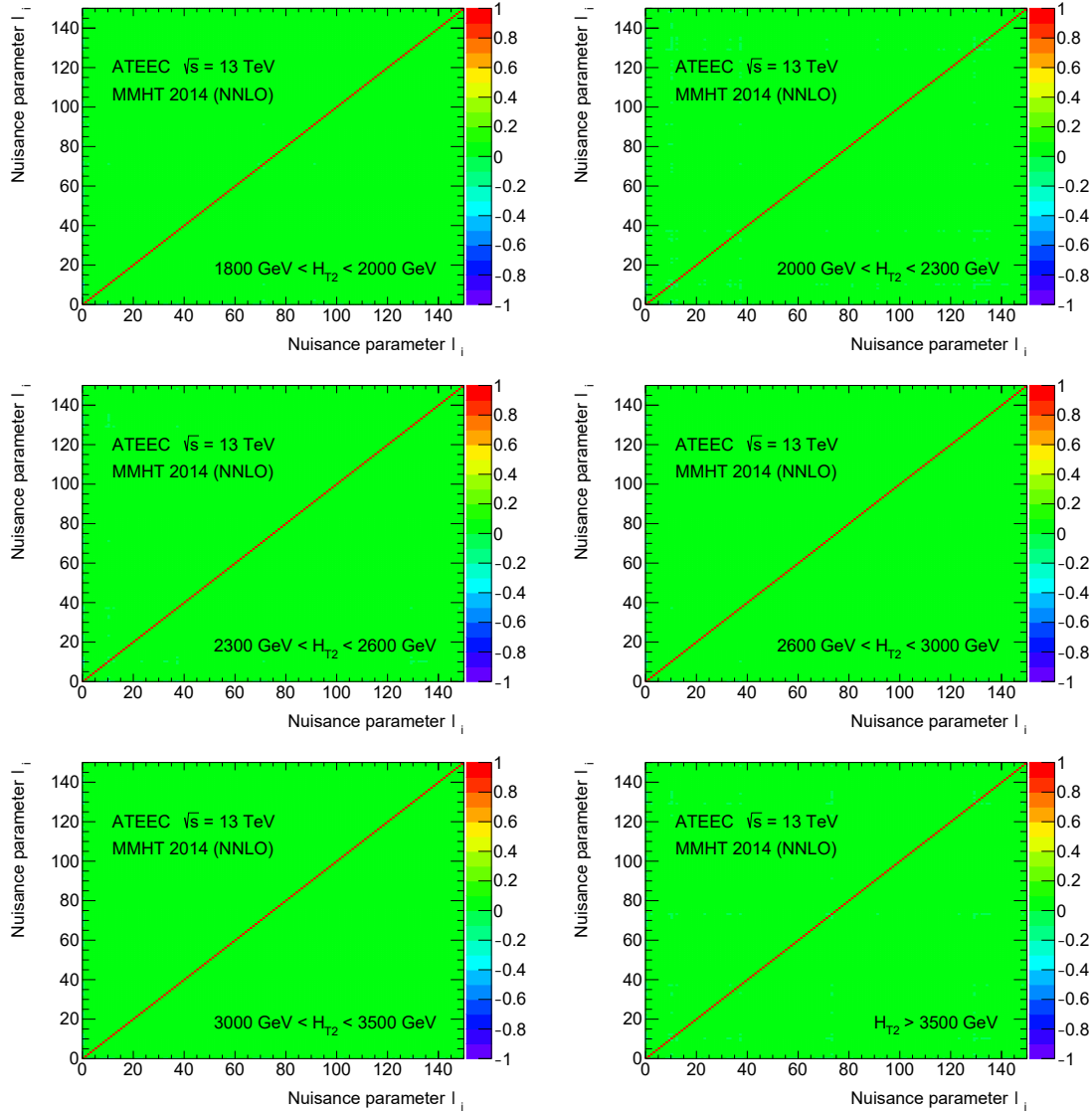


Figure 6.110: Correlation coefficients between the nuisance parameters obtained from individual fits, in exclusive H_{T2} bins, to the ATEEC function at NNLO using MMHT 2014 PDF group. The fact that the correlation matrices have very small off-diagonal terms indicates that the systematic sources are not significantly correlated between them.

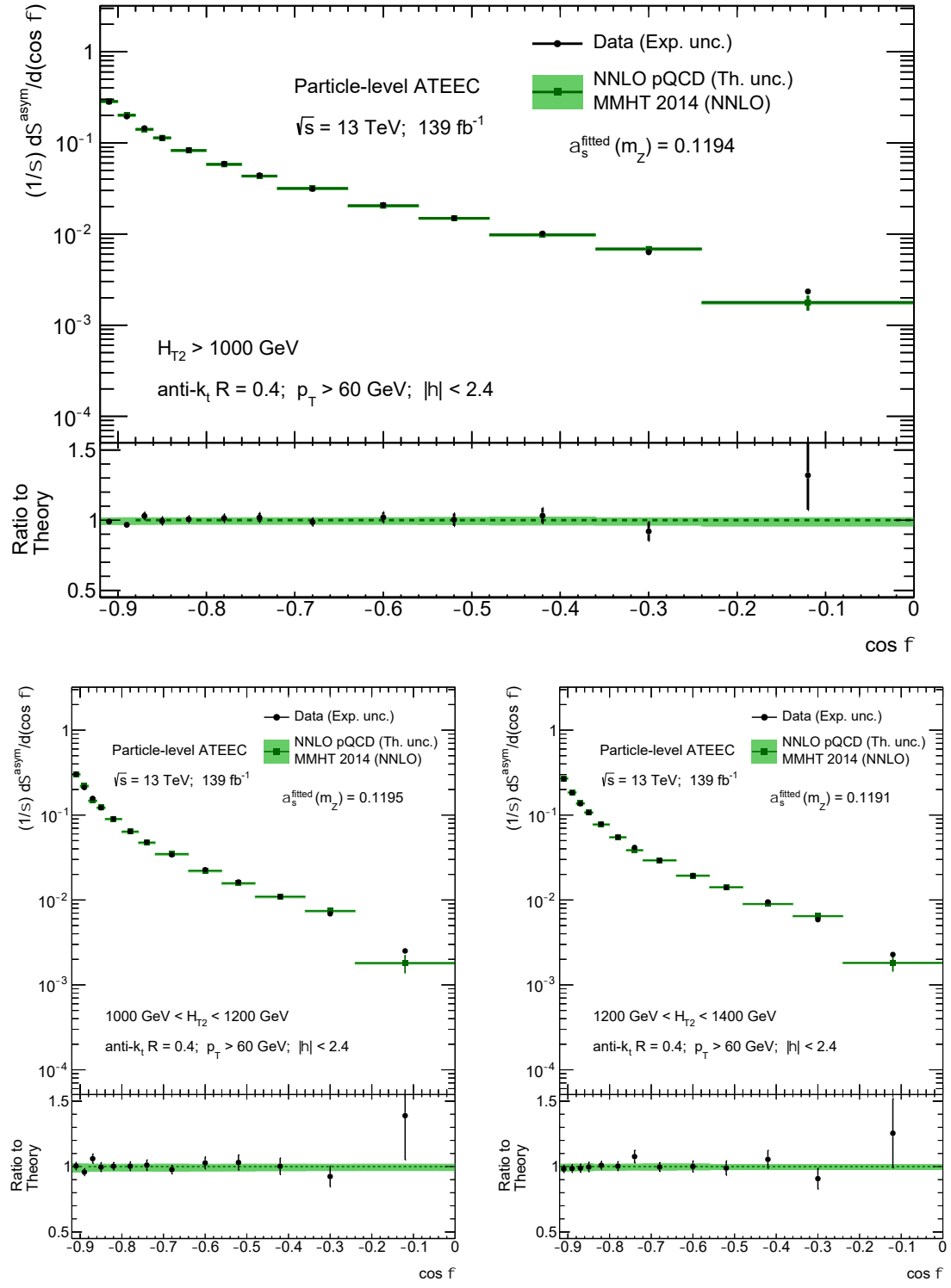


Figure 6.111: Comparison of the experimental results for the ATEEC function, in inclusive (top) and exclusive (bottom) H_{T2} bins, and their fitted theoretical predictions at NNLO in pQCD using MMHT 2014 PDF group. The green band shows the theoretical uncertainties while the error bars show the experimental uncertainties, where correlations between the fit parameters have been taken into account.

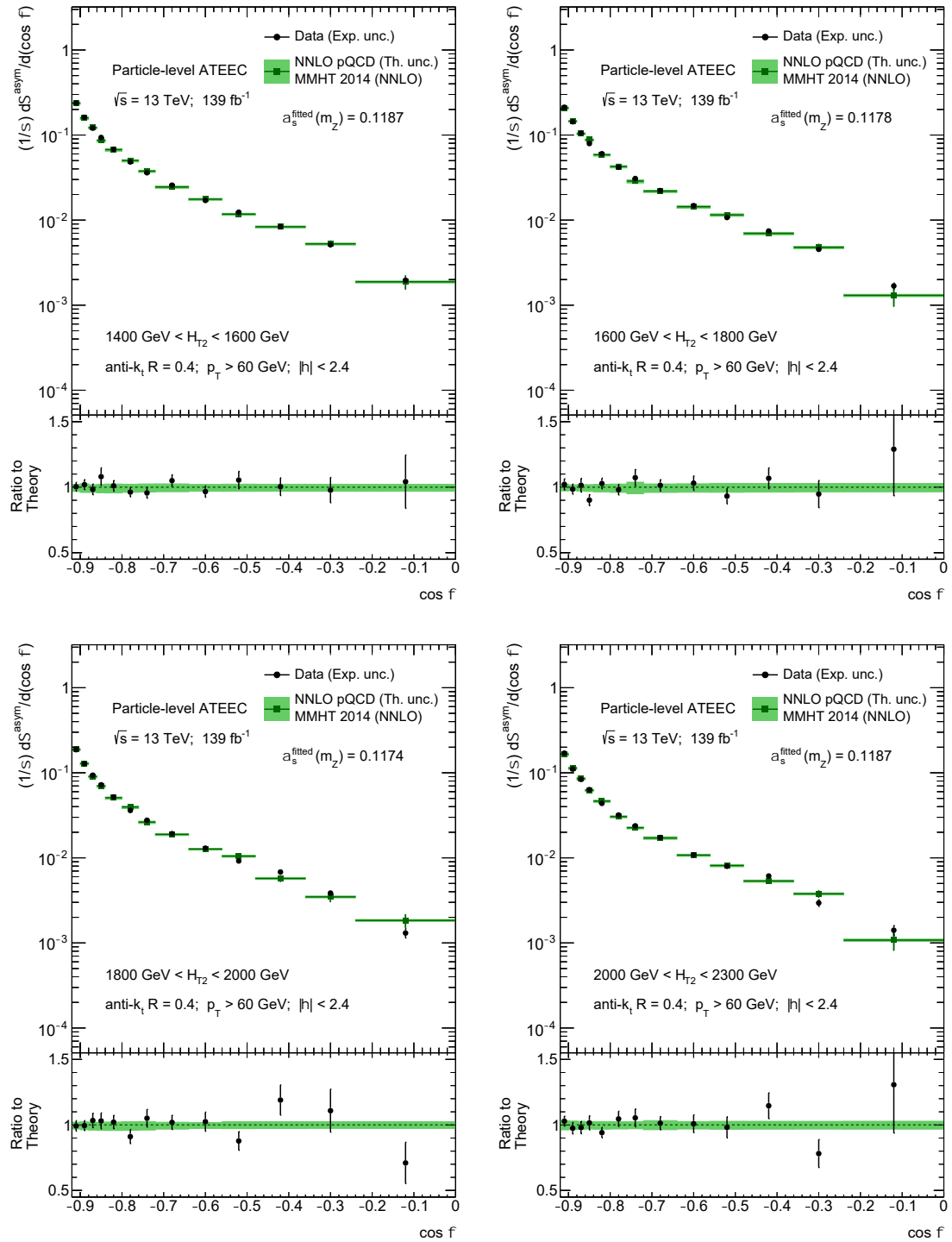


Figure 6.112: Comparison of the experimental results for the ATEEC function, in exclusive H_{T2} bins, and their fitted theoretical predictions at NNLO in pQCD using MMHT 2014 PDF group. The green band shows the theoretical uncertainties while the error bars show the experimental uncertainties, where correlations between the fit parameters have been taken into account.

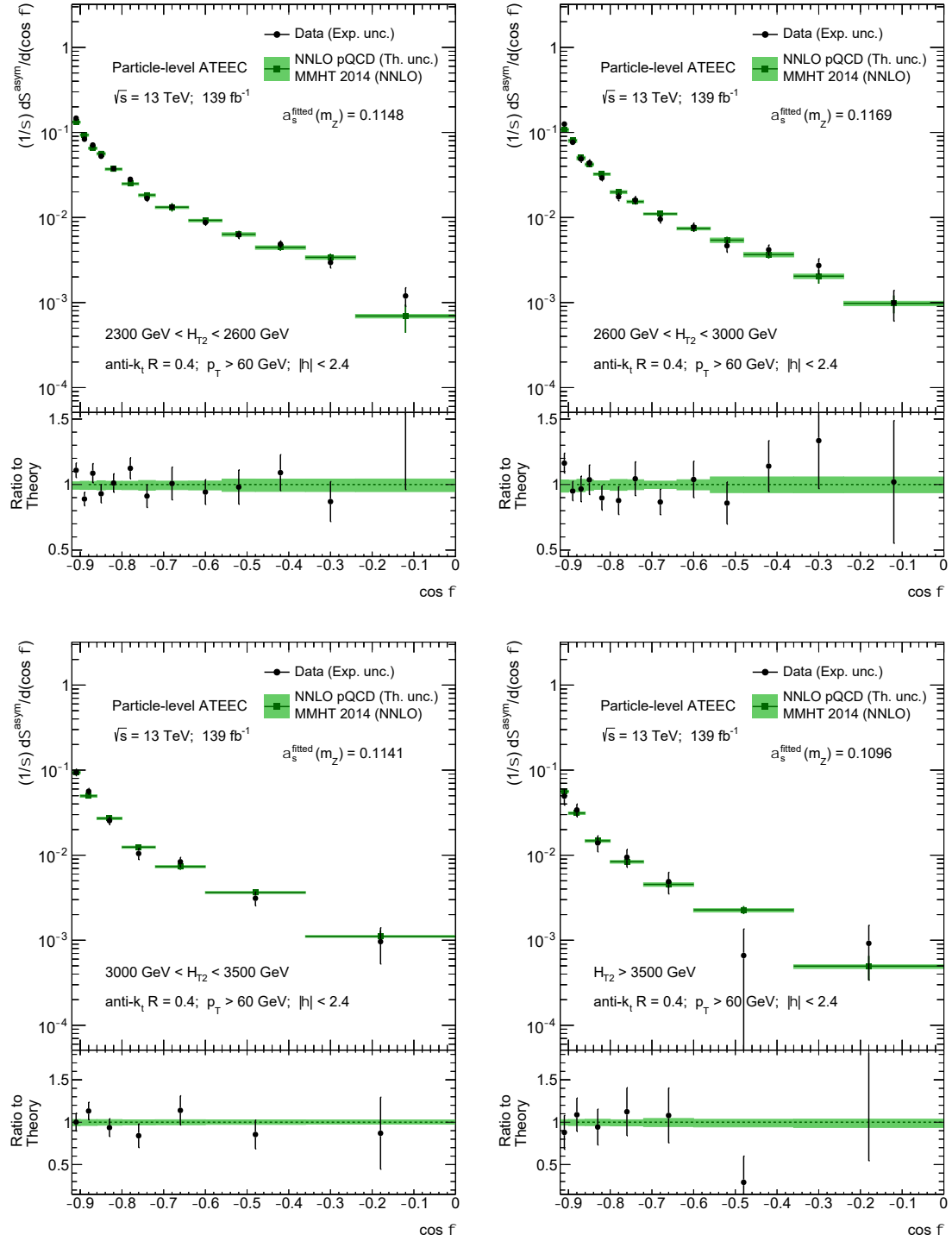


Figure 6.113: Comparison of the experimental results for the ATEEC function, in exclusive H_{T2} bins, and their fitted theoretical predictions at NNLO in pQCD using MMHT 2014 PDF group. The green band shows the theoretical uncertainties while the error bars show the experimental uncertainties, where correlations between the fit parameters have been taken into account.

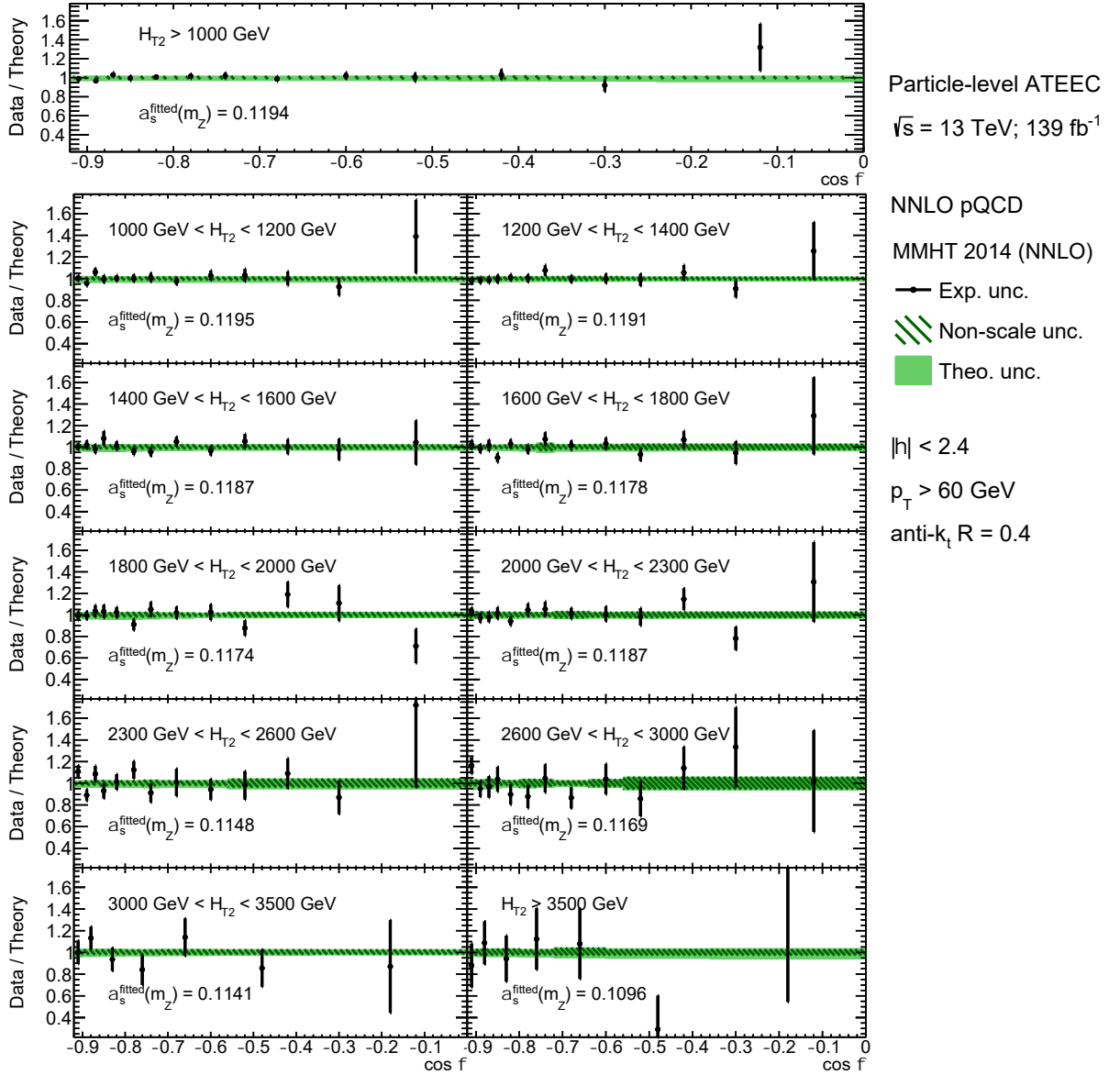


Figure 6.114: Ratios of the data to the fitted theoretical predictions at NNLO for the ATEEC measurements, obtained using MMHT 2014 PDF group, in inclusive and exclusive H_{T2} bins. The green band shows the theoretical uncertainties, dominated by the scale variations, while the error bars show the experimental uncertainties, where correlations between the fit parameters have been taken into account.

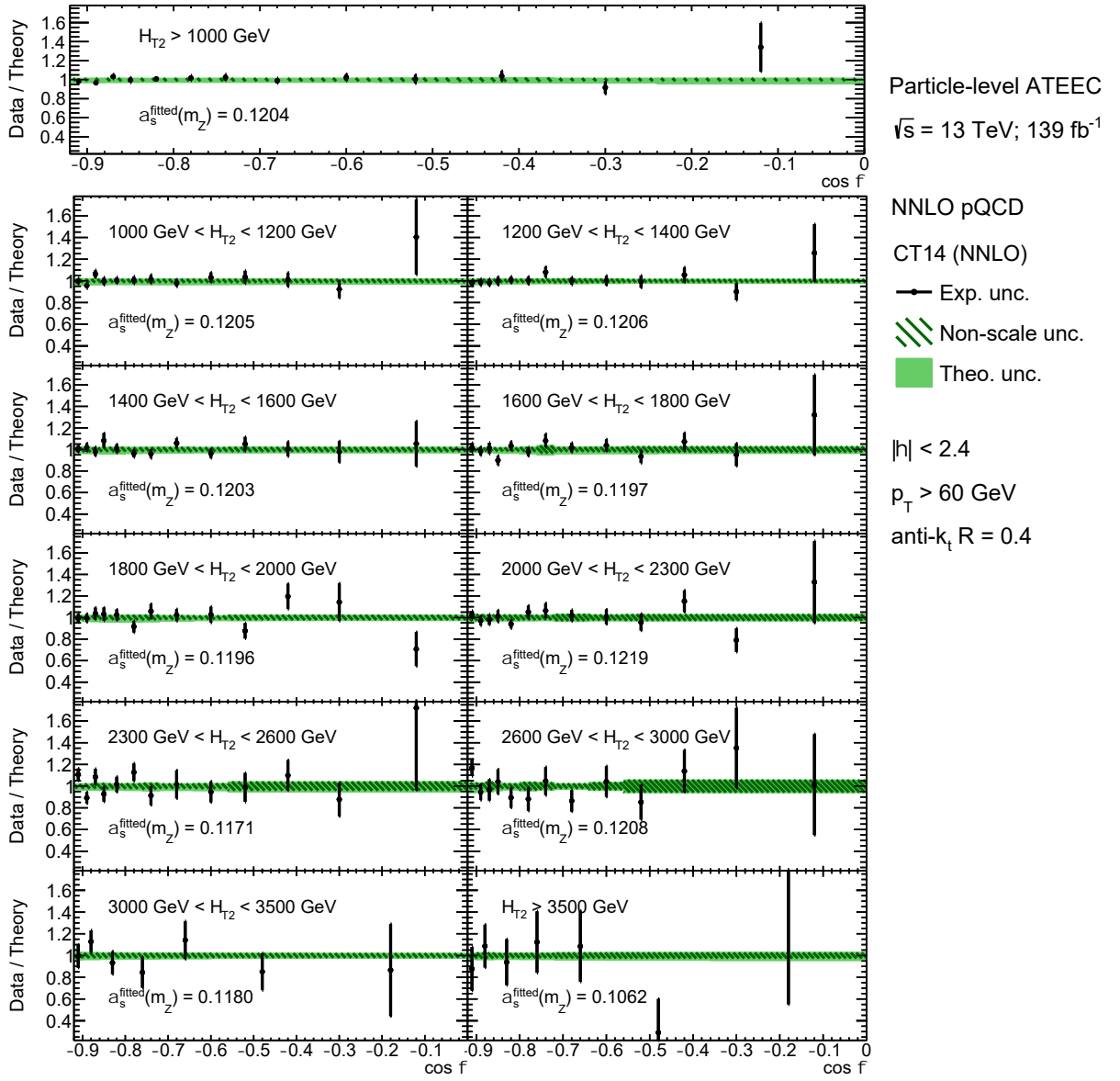


Figure 6.115: Ratios of the data to the fitted theoretical predictions at NNLO for the ATEEC measurements, obtained using CT14 PDF group, in inclusive and exclusive H_{T2} bins. The green band shows the theoretical uncertainties, dominated by the scale variations, while the error bars show the experimental uncertainties, where correlations between the fit parameters have been taken into account.

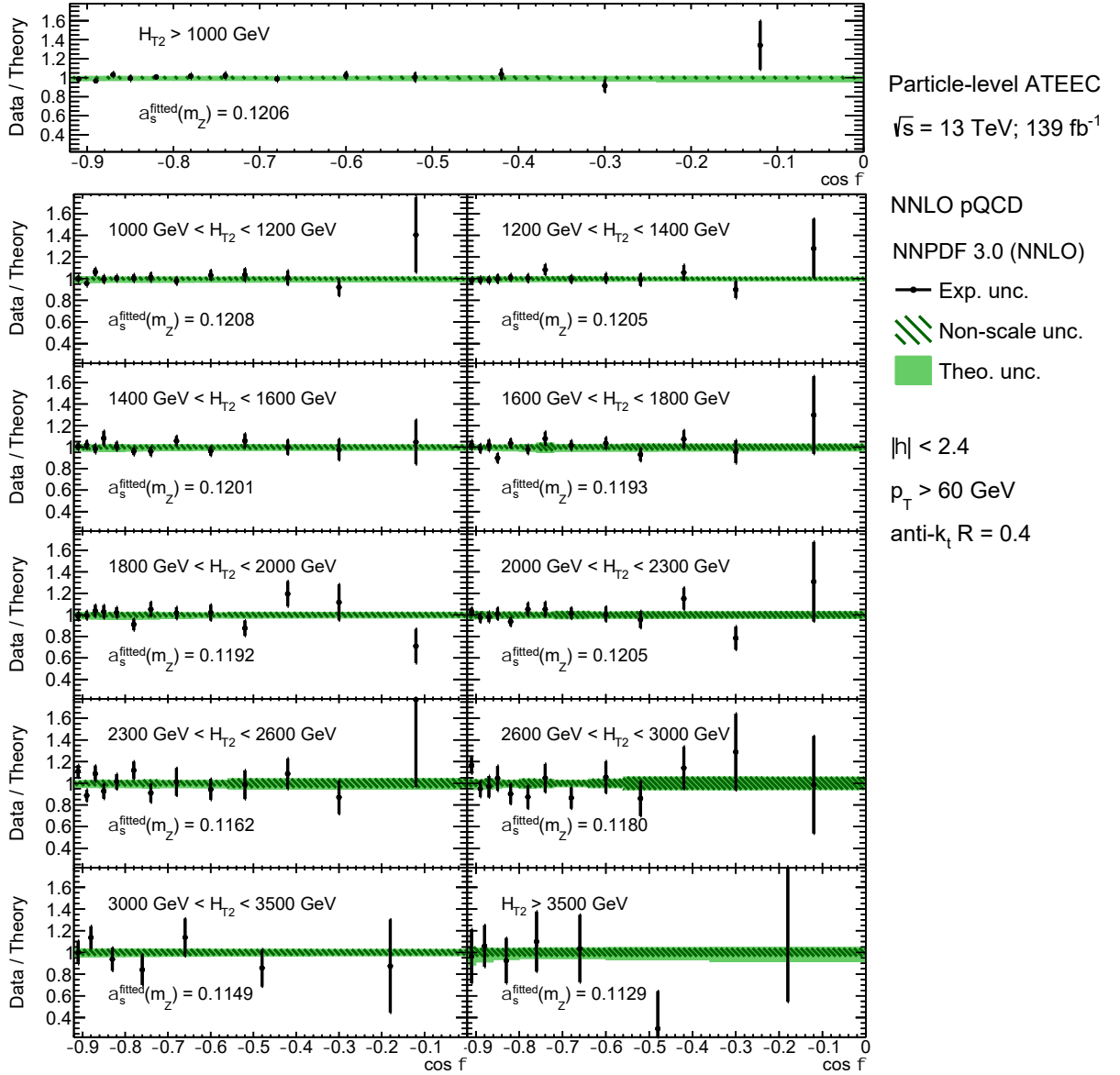


Figure 6.116: Ratios of the data to the fitted theoretical predictions at NNLO for the ATEEC measurements, obtained using NNPDF 3.0 PDF group, in inclusive and exclusive H_{T2} bins. The green band shows the theoretical uncertainties, dominated by the scale variations, while the error bars show the experimental uncertainties, where correlations between the fit parameters have been taken into account.

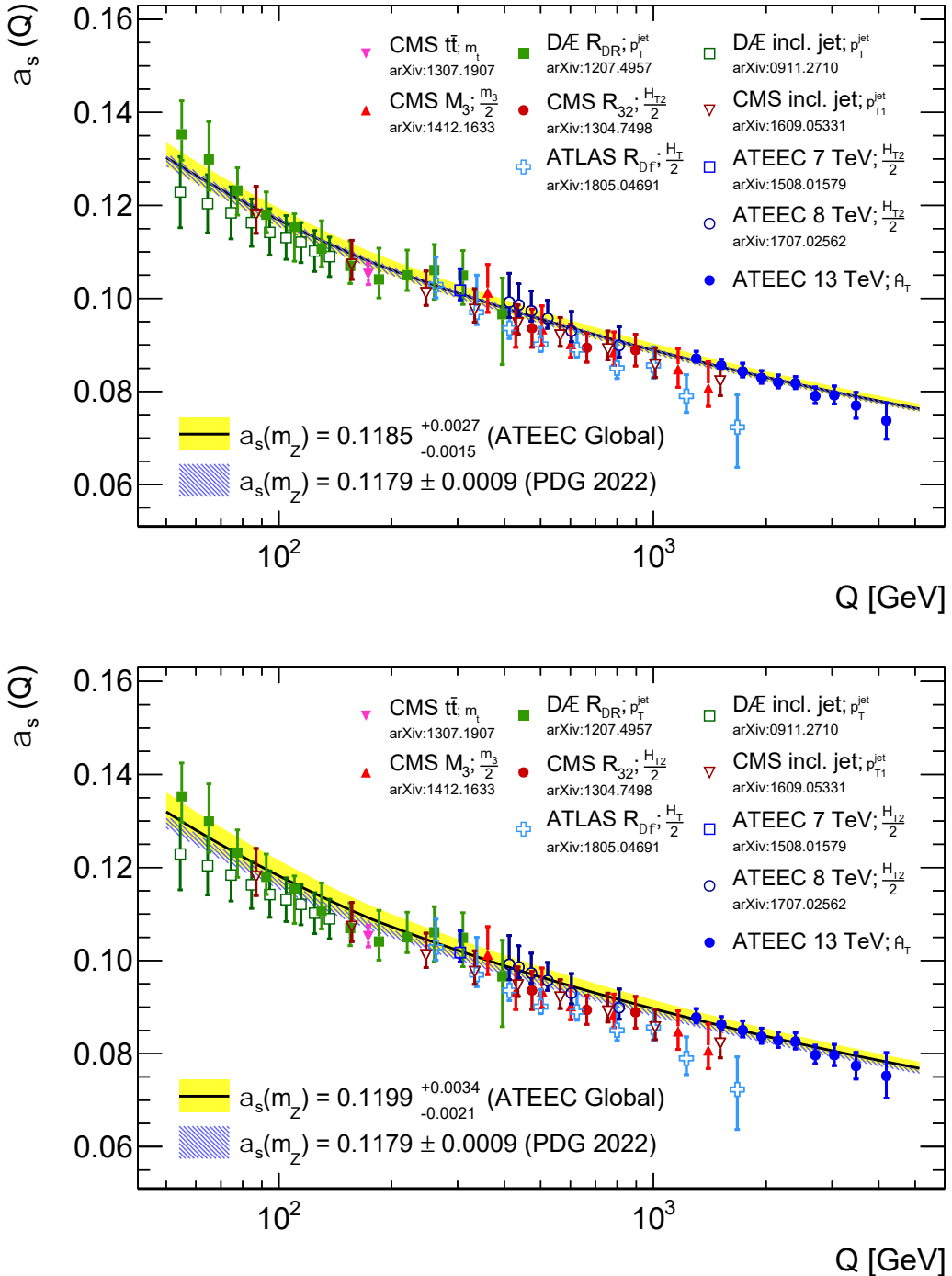


Figure 6.117: Comparison of the values of $\alpha_s(Q)$ obtained from fits to the ATEEC function at NNLO in pQCD with the RGE prediction using the world average provided by the PDG (blue band) and with the value obtained from the global fit to all H_{T2} bins of the ATEEC function (yellow band). Results from previous analyses, both from ATLAS and from other experiments, are also included, showing a very good agreement with the current measurements and with the world average. The interaction scale choice considered for each analysis is specified in the legend. The fits are performed using MMHT 2014 (top) and NNPDF 3.0 (bottom) PDF groups for the theoretical predictions.

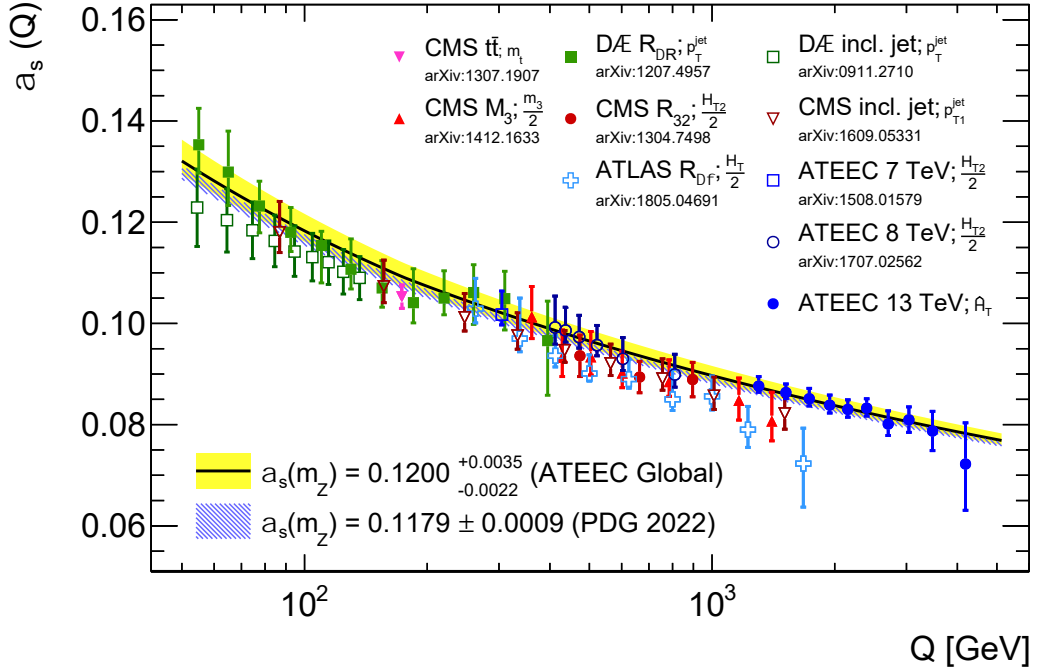


Figure 6.118: Comparison of the values of $\alpha_s(Q)$ obtained from fits to the ATEEC function at NNLO in pQCD with the RGE prediction using the world average provided by the PDG (blue band) and with the value obtained from the global fit to all H_{T2} bins of the ATEEC function (yellow band). Results from previous analyses, both from ATLAS and from other experiments, are also included, showing a very good agreement with the current measurements and with the world average. The interaction scale choice considered for each analysis is specified in the legend. The fits are performed using CT14 PDF group for the theoretical predictions.

$\langle Q \rangle$	$\alpha_s(Q)$ value (MMHT 2014)
1302	0.0871 ± 0.0007 (fit) $^{+0.0012}_{-0.0000}$ (scale) ± 0.0006 (par.) ± 0.0003 (tune) ± 0.0000 (model)
1518	0.0856 ± 0.0007 (fit) $^{+0.0010}_{-0.0000}$ (scale) ± 0.0006 (par.) ± 0.0002 (tune) ± 0.0000 (model)
1732	0.0843 ± 0.0009 (fit) $^{+0.0013}_{-0.0001}$ (scale) ± 0.0006 (par.) ± 0.0005 (tune) ± 0.0001 (model)
1944	0.0829 ± 0.0009 (fit) $^{+0.0011}_{-0.0000}$ (scale) ± 0.0006 (par.) ± 0.0004 (tune) ± 0.0000 (model)
2153	0.0820 ± 0.0009 (fit) $^{+0.0010}_{-0.0001}$ (scale) ± 0.0006 (par.) ± 0.0004 (tune) ± 0.0000 (model)
2396	0.0818 ± 0.0009 (fit) $^{+0.0008}_{-0.0000}$ (scale) ± 0.0006 (par.) ± 0.0003 (tune) ± 0.0002 (model)
2706	0.0790 ± 0.0014 (fit) $^{+0.0011}_{-0.0001}$ (scale) ± 0.0007 (par.) ± 0.0004 (tune) ± 0.0001 (model)
3042	0.0792 ± 0.0015 (fit) $^{+0.0008}_{-0.0000}$ (scale) ± 0.0007 (par.) ± 0.0006 (tune) ± 0.0004 (model)
3476	0.0770 ± 0.0024 (fit) $^{+0.0011}_{-0.0003}$ (scale) ± 0.0008 (par.) ± 0.0003 (tune) ± 0.0005 (model)
4189	0.0737 ± 0.0037 (fit) $^{+0.0006}_{-0.0000}$ (scale) ± 0.0004 (par.) ± 0.0001 (tune) ± 0.0003 (model)

Table 6.37: Values of the strong coupling constant at the interaction scale, $\alpha_s(Q)$, obtained from fits to the ATEEC function for each H_{T2} interval using MMHT 2014. The label (fit) indicates the statistical and experimental systematic uncertainties added in quadrature. The uncertainty related to the MC model in the IB unfolding is displayed separately as (model) and the one referred to as (tune) is related to the non-pQCD corrections. The average values of the scale are given in GeV.

$\langle Q \rangle$	$\alpha_s(Q)$ value (NNPDF 3.0)
1302	0.0878 ± 0.0008 (fit) $^{+0.0015}_{-0.0000}$ (scale) ± 0.0008 (par.) ± 0.0003 (tune) ± 0.0000 (model)
1518	0.0863 ± 0.0008 (fit) $^{+0.0011}_{-0.0001}$ (scale) ± 0.0008 (par.) ± 0.0002 (tune) ± 0.0000 (model)
1732	0.0850 ± 0.0009 (fit) $^{+0.0015}_{-0.0001}$ (scale) ± 0.0009 (par.) ± 0.0005 (tune) ± 0.0001 (model)
1944	0.0837 ± 0.0010 (fit) $^{+0.0012}_{-0.0001}$ (scale) ± 0.0010 (par.) ± 0.0004 (tune) ± 0.0000 (model)
2153	0.0828 ± 0.0010 (fit) $^{+0.0011}_{-0.0001}$ (scale) ± 0.0010 (par.) ± 0.0004 (tune) ± 0.0000 (model)
2396	0.0826 ± 0.0010 (fit) $^{+0.0010}_{-0.0000}$ (scale) ± 0.0011 (par.) ± 0.0005 (tune) ± 0.0002 (model)
2706	0.0797 ± 0.0014 (fit) $^{+0.0011}_{-0.0001}$ (scale) ± 0.0011 (par.) ± 0.0004 (tune) ± 0.0001 (model)
3042	0.0797 ± 0.0016 (fit) $^{+0.0008}_{-0.0000}$ (scale) ± 0.0012 (par.) ± 0.0007 (tune) ± 0.0004 (model)
3476	0.0774 ± 0.0023 (fit) $^{+0.0011}_{-0.0003}$ (scale) ± 0.0013 (par.) ± 0.0003 (tune) ± 0.0005 (model)
4189	0.0752 ± 0.0042 (fit) $^{+0.0024}_{-0.0009}$ (scale) ± 0.0014 (par.) ± 0.0001 (tune) ± 0.0006 (model)

Table 6.38: Values of the strong coupling constant at the interaction scale, $\alpha_s(Q)$, obtained from fits to the ATEEC function for each H_{T2} interval using NNPDF 3.0. The label (fit) indicates the statistical and experimental systematic uncertainties added in quadrature. The uncertainty related to the MC model in the IB unfolding is displayed separately as (model) and the one referred to as (tune) is related to the non-pQCD corrections. The average values of the scale are given in GeV.

$\langle Q \rangle$	$\alpha_s(Q)$ value (CT14)
1302	0.0876 ± 0.0008 (fit) $^{+0.0014}_{-0.0000}$ (scale) ± 0.0009 (par.) ± 0.0004 (tune) ± 0.0000 (model)
1518	0.0864 ± 0.0008 (fit) $^{+0.0012}_{-0.0001}$ (scale) ± 0.0009 (par.) ± 0.0002 (tune) ± 0.0000 (model)
1732	0.0851 ± 0.0009 (fit) $^{+0.0015}_{-0.0002}$ (scale) ± 0.0009 (par.) ± 0.0006 (tune) ± 0.0001 (model)
1944	0.0839 ± 0.0011 (fit) $^{+0.0013}_{-0.0001}$ (scale) ± 0.0010 (par.) ± 0.0004 (tune) ± 0.0000 (model)
2153	0.0830 ± 0.0011 (fit) $^{+0.0012}_{-0.0001}$ (scale) ± 0.0009 (par.) ± 0.0004 (tune) ± 0.0000 (model)
2396	0.0833 ± 0.0011 (fit) $^{+0.0010}_{-0.0000}$ (scale) ± 0.0010 (par.) ± 0.0005 (tune) ± 0.0002 (model)
2706	0.0801 ± 0.0018 (fit) $^{+0.0014}_{-0.0001}$ (scale) ± 0.0012 (par.) ± 0.0005 (tune) ± 0.0001 (model)
3042	0.0809 ± 0.0019 (fit) $^{+0.0009}_{-0.0000}$ (scale) ± 0.0011 (par.) ± 0.0009 (tune) ± 0.0005 (model)
3476	0.0787 ± 0.0033 (fit) $^{+0.0014}_{-0.0005}$ (scale) ± 0.0014 (par.) ± 0.0005 (tune) ± 0.0008 (model)
4189	0.0722 ± 0.0081 (fit) $^{+0.0000}_{-0.0002}$ (scale) ± 0.0000 (par.) ± 0.0000 (tune) ± 0.0000 (model)

Table 6.39: Values of the strong coupling constant at the interaction scale, $\alpha_s(Q)$, obtained from fits to the ATEEC function for each H_{T2} interval using CT14. The label (fit) indicates the statistical and experimental systematic uncertainties added in quadrature. The uncertainty related to the MC model in the IB unfolding is displayed separately as (model) and the one referred to as (tune) is related to the non-pQCD corrections. The average values of the scale are given in GeV.

6.9.5 Comparison with previous extractions

This analysis contains the first determination of the strong coupling at NNLO in pQCD using the ATLAS detector. The extracted values are in good agreement with the latest measurements in collider experiments [2, 148–150], one of them also at NNLO in multi-jet production [151]. These values are depicted in Figure 6.119.

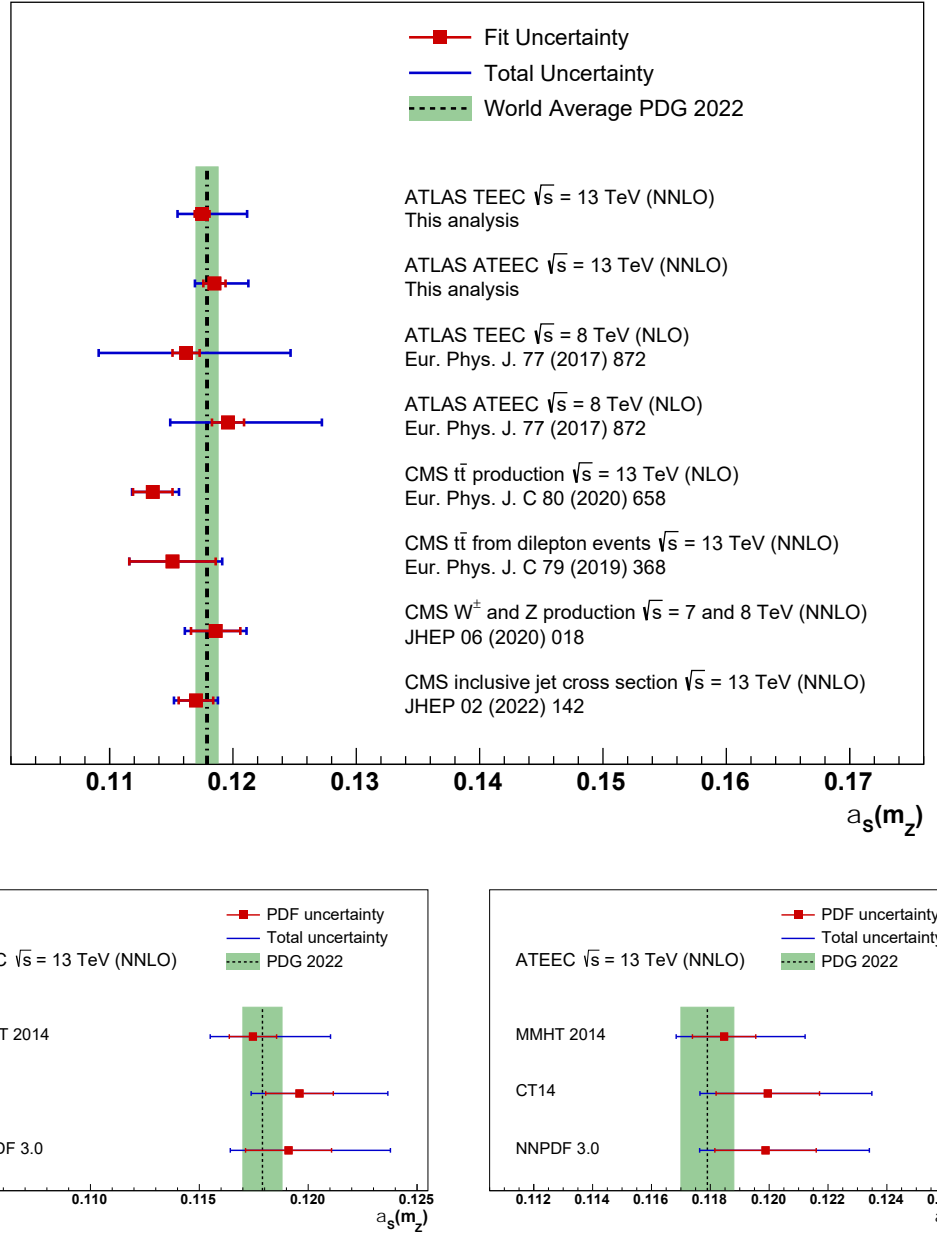


Figure 6.119: Values of the strong coupling constant $\alpha_s(m_Z)$ recently extracted and compared with the world average provided by the PDG (green band). Results from previous analyses, both from ATLAS and CMS experiments, are included, most of them extracted at NNLO in pQCD. The ATLAS analyses use MMHT 2014 as the nominal PDF. However, the results extracted using all PDF sets available for this analysis are depicted for the TEEC (bottom left) and the ATEEC (bottom right).

CHAPTER 7

Summary and conclusions

Multi-jet events produced by the LHC and registered with the ATLAS detector during the pp Run 2 are used to determine the strong coupling constant α_s from a particular event-shape measurement at high-energy scales. This gauge coupling is the fundamental parameter of the theory that describes strong interactions of gluons and coloured quarks. It is important to note that this study contains the first determination of the strong coupling constant from multi-jet events at next-to-next-to-leading-order accuracy in perturbative QCD. The information related to the analysis is summarized in the following paragraphs.

A measurement of transverse energy-energy correlations and their corresponding asymmetries in multi-jet events produced in pp collisions at a centre-of-mass energy $\sqrt{s} = 13$ TeV and registered with the ATLAS detector at the LHC is presented. The total integrated luminosity of the full data sample is 139.0 fb^{-1} . High-energy multijet events are selected by requiring the scalar sum of the two leading jets transverse momenta, $H_{\text{T}2} = p_{\text{T}1} + p_{\text{T}2}$, to be above 1.0 TeV; and the data are binned in ten intervals of this variable in order to study the scale dependence of these observables. The fully inclusive distribution is measured in bins of width $\Delta \cos \phi = 0.02$.

The data are corrected for detector effects and systematic uncertainties are evaluated. The experimental uncertainties are dominated by the uncertainty on the jet energy scale and the model used in the correction for detector effects. The total uncertainty is found to be of the order of 2% for the correlations and 1% for the asymmetries. The results are compared to Monte Carlo predictions by different generators, including PYTHIA 8.235, SHERPA 2.1.1, and HERWIG 7.1.3 with two different parton showers, one angle-ordered and one based on dipole radiation. Current MC event generators describe the gross features of the data fairly well. In particular, SHERPA and HERWIG 7 matched to the angle-ordered shower are found to give an overall good description of the data, while HERWIG 7 matched to the dipole parton shower is found to be disfavoured and PYTHIA 8 gives an intermediate description.

Finite theoretical predictions are calculated at parton level from the next-to-next-to-leading order 3-jet cross sections based on perturbative QCD with different PDF sets and corrected for non-perturbative effects such as hadronization and multi-

parton interaction effects. The agreement between data and theory is excellent, thus providing a precision test of QCD at large momentum transfers. The strong coupling constant α_s is determined from a χ^2 fit to the theoretical predictions for both the inclusive measurement and the different inclusive bins in H_{T2} ; along with its evolution with the interaction scale, studying asymptotic freedom beyond the TeV scale. Additionally, a global fit to all H_{T2} bins of each observable is performed, leading to the following values for the strong coupling constant:

$$\alpha_s(m_Z) = 0.1175 \pm 0.0006 \text{ (fit)} \quad {}^{+0.0034}_{-0.0017} \text{ (theo.) TEEC (NNLO pQCD)},$$

$$\alpha_s(m_Z) = 0.1185 \pm 0.0009 \text{ (fit)} \quad {}^{+0.0025}_{-0.0012} \text{ (theo.) ATEEC (NNLO pQCD).}$$

These two values are strongly correlated and obtained using MMHT 2014 PDF, as this set provides a wider range of α_s variations. The extracted values are in good agreement with the current world average $\alpha_s(m_Z) = 0.1179 \pm 0.0009$. The evolution of the values obtained from each of the exclusive fits to their corresponding physical scales leads to values of $\alpha_s(Q)$ which are compared to the solution of the renormalization group equation. The results show a good agreement with the current prediction up to the highest energy scales, as well as with previous measurements both in ATLAS and in other experiments.

The theoretical scale choice $\mu_{R,F} = \hat{H}_T$ and the inclusion of next-to-next-to-leading-order pQCD corrections reduce down to 2% the theoretical uncertainties on both the cross-section calculation for the correlations and their asymmetries, and on the determination of the strong coupling constant α_s . This is a significant improvement when compared with previous results at $\sqrt{s} = 7$ and 8 TeV. The resummation effects are expected to be negligible within the region where the coupling is determined, $|\cos \phi| < 0.92$; and electroweak corrections are not accounted for due to lack of knowledge, although their effect should be similar for three-jet and two-jet production and, thus, cancel to a large extent for these kind of observables.

These results provide a tighter constraint for new physics and are a milestone in QCD studies owing to the accuracy and precision achieved. Likewise, they not only supersed previous event-shape measurements but also previous α_s determinations in multi-jet production. The paper associated to this novel study is expected to be published soon with the approval of the ATLAS Collaboration.

Resumen y conclusiones en español

La constante de acople fuerte α_s ha sido extraída a altas energías usando sucesos multijet producidos en colisiones protón-protón y registrados por el detector ATLAS durante el LHC Run 2. Esto ha sido posible gracias a la medida de determinados observables pertenecientes a la familia de los *event shapes*. Esta constante de recalibración es el parámetro fundamental en la teoría que explica las interacciones entre gluones y quarks con carga de color. Tengamos también en cuenta que este estudio contiene la primera determinación de dicho parámetro usando sucesos multijet y con precisión *next-to-next-to-leading-order* en cromodinámica cuántica perturbativa. La información relativa al análisis se encuentra resumida en los siguientes párrafos.

Hemos presentado una medida de las correlaciones de energía-energía transversa y de sus asimetrías usando sucesos multijet producidos en colisiones protón-protón a una energía de centro-de-masas de $\sqrt{s} = 13$ TeV y registrados por el detector ATLAS en el LHC. La luminosidad integrada total es de $139,0 \text{ fb}^{-1}$. A altas energías, los sucesos multijet son seleccionados si la suma del momento transverso de los dos jets principales, $H_{T2} = p_{T1} + p_{T2}$, es mayor que 1,0 TeV. Estos sucesos se clasifican en diez intervalos en función de dicha variable; lo que permite estudiar la dependencia de los observables con la escala. A su vez, la distribución completamente inclusiva se mide con una anchura angular de $\Delta \cos \phi = 0,02$.

A continuación, la muestra experimental se corrige a partir de los efectos del detector y se evalúan las incertidumbres sistemáticas. Las incertidumbres experimentales están dominadas por la escala de energía del jet y el modelo usado en la corrección de los efectos del detector. La incertidumbre total resultante es del orden del 2 % para las correlaciones y del 1 % para las asimetrías. Los resultados han sido comparados con diferentes predicciones Monte Carlo generadas con PYTHIA 8.235, SHERPA 2.1.1 y HERWIG 7.1.3 con dos tipos de cascadas de radiación, una ordenada de forma angular y otra basada en la radiación dipolar. Estas predicciones describen bastante bien las características generales de los datos. En concreto, SHERPA and HERWIG 7 con una cascada ordenada de forma angular proporcionan una buena descripción a nivel general, mientras que HERWIG 7 con radiación dipolar está claramente en desventaja y PYTHIA 8 proporciona una descripción intermedia.

Las predicciones teóricas se han calculado a nivel de partones a partir de las secciones eficaces para tres jets evaluadas a *next-to-next-to-leading-order* en cromodinámica cuántica perturbativa. Estas secciones eficaces han sido convolucionadas con varios conjuntos de funciones PDF y corregidas a partir de los efectos no-perturbativos derivados de la hadronización y las interacciones multipartón. Los datos y la teoría

concuerdan perfectamente, lo que implica que la cromodinámica cuántica es válida en procesos que involucran grandes transferencias de momento. La constante de acople fuerte α_s se extrae a partir de un ajuste χ^2 a las predicciones teóricas, tanto para la medida inclusiva como para los diferentes intervalos de H_{T2} . También se estudia su evolución con la escala de interacción, estudiando la libertad asintótica más allá de la escala del teraelectronvoltio. Igualmente, se ha realizado un ajuste global para cada observable combinando todos los intervalos de H_{T2} y obteniendo los siguientes valores para la constante de acople fuerte:

$$\alpha_s(m_Z) = 0,1175 \pm 0,0006 \text{ (ajuste)} \quad {}^{+0,0034}_{-0,0017} \text{ (teoría) TEEC (NNLO pQCD)},$$

$$\alpha_s(m_Z) = 0,1185 \pm 0,0009 \text{ (ajuste)} \quad {}^{+0,0025}_{-0,0012} \text{ (teoría) ATEEC (NNLO pQCD)}.$$

Estos dos valores están fuertemente correlacionados y se han obtenido usando MMHT 2014 PDF, siendo estas funciones las que contienen el rango más amplio de variaciones de α_s . Además, estos valores concuerdan con el promedio mundial actual $\alpha_s(m_Z) = 0,1179 \pm 0,0009$. Los valores extraídos en cada uno de los ajustes son evolucionados hasta sus escalas físicas correspondientes. Estos nuevos valores $\alpha_s(Q)$ se han comparado con la solución de la ecuación de grupo de renormalización. Los resultados son compatibles con la predicción actual para todas las escalas de energía disponibles, así como con las mediciones anteriores realizadas tanto en ATLAS como en otros experimentos.

La elección de la escala teórica $\mu_{R,F} = \hat{H}_T$ y la inclusión de las correcciones *next-to-next-to-leading-order* en cromodinámica cuántica perturbativa han reducido hasta el 2% la incertidumbre teórica, tanto en el cálculo de las secciones eficaces de las correlaciones y sus asimetrías como en el valor de la constante de acople fuerte α_s . Esto constituye una mejora significativa si comparamos con los anteriores análisis realizados a $\sqrt{s} = 7$ y 8 TeV. Los efectos de la resumación parecen ser despreciables en la región donde se realiza el ajuste, $|\cos\phi| < 0,92$, y las correcciones electrodébiles no se han tenido en cuenta por desconocimiento. Sin embargo, sus efectos deben ser similares en sucesos con dos y tres jets, cancelándose prácticamente para este tipo de observables.

Estos resultados proporcionan límites más estrictos para las búsquedas de nueva física y constituyen un hito en los estudios de la fuerza fuerte, debido a la exactitud y a la precisión que se han alcanzado. Asimismo, no solo superan las medidas de *event shapes* realizadas hasta la fecha, sino que también mejoran las extracciones previas de α_s a partir de sucesos multijet. El artículo asociado a este innovador estudio será publicado tras la aprobación de la colaboración ATLAS.

APPENDIX A

Appendix

A.1 Complementary and additional studies

This section includes complementary and additional studies to the analysis in Chapter 6. These studies show how certain conditions can affect the measurement of the transverse energy-energy correlations and their asymmetries. Moreover, additional predictions are presented for these observables using Monte Carlo event generators with other parton showers and different hadronization schemes.

A.1.1 Dead tile modules

The ATLAS calorimeter system includes a scintillator tile calorimeter whose active material may turn unusable due to radiation exposure. The tile modules that suffer from this problem are labeled as “dead modules” and can affect the measurement. Thus, a study of the effect of the dead tile modules is performed. In this case, all events with at least one jet passing the experimental requirements and tagged by the TILETRIPREADER tool are removed at detector level. In order to avoid troubles close to the threshold, events are also removed if a jet with $p_T > 50$ GeV is tagged. The new selection criteria give rise to a difference of 0.4% in the central plateau of the correlations compared to the nominal distributions at detector level. Nevertheless, the unfolding procedure corrects for detector effects, and any difference at particle level is well below the statistical uncertainty, as it can be seen in Figure A.1.

A.1.2 Bin-by-bin migrations

The IB unfolding procedure introduced in Section 6.3 considers only bin-by-bin migrations in $\cos \phi$ since the effect of migrations in the variable H_{T2} is negligible. In order to prove this assertion, data are unfolded using a transfer matrix parametrizing the bin-by-bin migrations in $\cos \phi$ and H_{T2} . Figure A.2 shows the transfer matrices, normalizing each row. The phase space is binned in H_{T2} and then each interval in $\cos \phi$. The underflow bins correspond to the negative values. The transfer matrices

have very small off-diagonal terms leading to very small migrations between $\cos\phi$ bins and even smaller migrations between H_{T2} intervals. The unfolded data considering $\cos\phi$ and H_{T2} migrations are compared to the unfolded data considering only $\cos\phi$ migrations. The deviations are within the expected statistical uncertainty for the whole phase space, and therefore, both results are compatible.

A.1.3 Jets' collections

Particle-level jets are simulated in the MC samples using the Antikt4TruthJets collection. These samples are used to correct data for detector effects and compared to the unfolded results. In addition, we consider the Antikt4TruthWZJets collection in this study. This particular collection includes jets initiated by the hadronic decay of electroweak bosons which can alter the measurement. To estimate their effect, a sample is generated in PYTHIA 8.235 with both particle-level jet collections and used to compute the observables. Figures A.3 compares the TEEC and ATEEC predictions using both collections. The difference between both predictions in the central plateau is around 0.5% at low H_{T2} and increases to 1.0% at high H_{T2} . However, half of the deviation is explained through the difference in the non-pQCD correction factors using both jet collections. This result is shown in Figure A.4 for the first H_{T2} bins of the analysis.

A.1.4 Parton showers and hadronization schemes

The predictions for the transverse energy-energy correlations and their asymmetries are also computed using the SHERPA 2.2.5 generated sample with the CT14 PDF group and the default CSS parton shower. The calculation only contains matrix elements for $2 \rightarrow 2$ hard processes at LO but the fragmentation follows two different hadronization schemes, the AHADIC model used in the SHERPA 2.1.1 sample and the Lund string model. Figures A.5 to A.10 show the TEEC and the ATEEC unfolded results from Section 6.6 compared with the two SHERPA 2.2.5 predictions along with the previous predictions generated with SHERPA 2.1.1 and SHERPA 2.2.11 with a second parton shower called DIRE. SHERPA 2.2.5 with both hadronization schemes give a similar description for the distributions. Nevertheless, a systematic deviation in data arises after unfolding with the two hadronization schemes. This divergence is found to be around 2% in the central plateau of the correlations and coincides with the one found between PYTHIA 8.325 and HERWIG 7.1.3. Thus, it is already taken into account within the MC model uncertainty.

Appendix A. Appendix

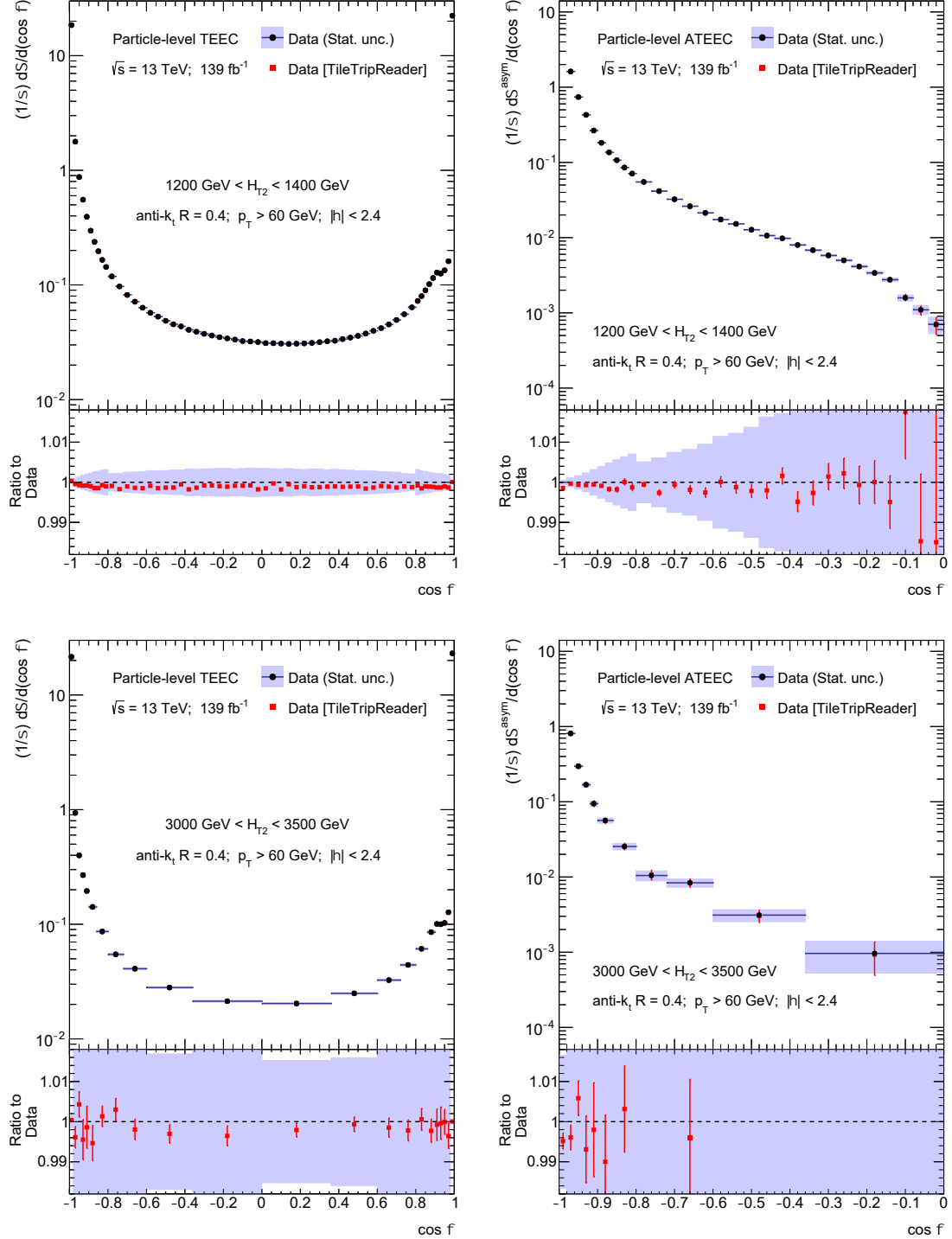


Figure A.1: Particle-level TEEC (left) and ATEEC (right) distributions in two exclusive H_{T2} bins for the nominal data sample and a new sample where events at detector level are removed if a jet tagged is by the TILETRIPREADER tool. The difference at particle level caused by dead tile modules is well below the statistical uncertainty (blue area).

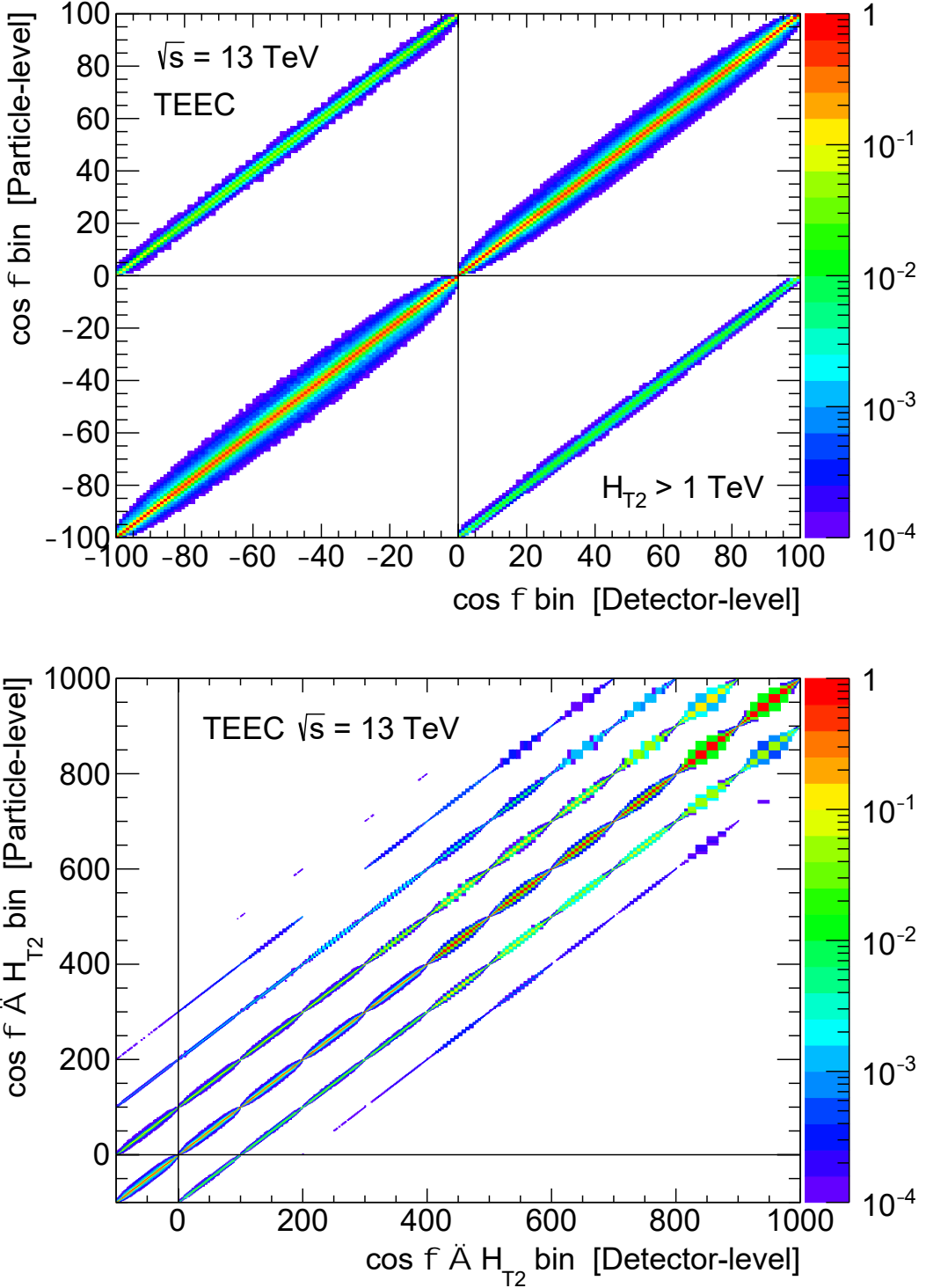


Figure A.2: Transfer matrices normalizing each row, in inclusive (top) and exclusive (bottom) H_{T2} bins, for the TEEC function obtained from the MC simulated sample with the PYTHIA 8.235 event generator. The phase space is binned in H_{T2} and then each interval in $\cos \phi$, where the underflow bins correspond to negative values. The off-diagonal terms are negligible since the excellent resolution of the detector leads to very small migrations between H_{T2} and $\cos \phi$ bins.

Appendix A. Appendix

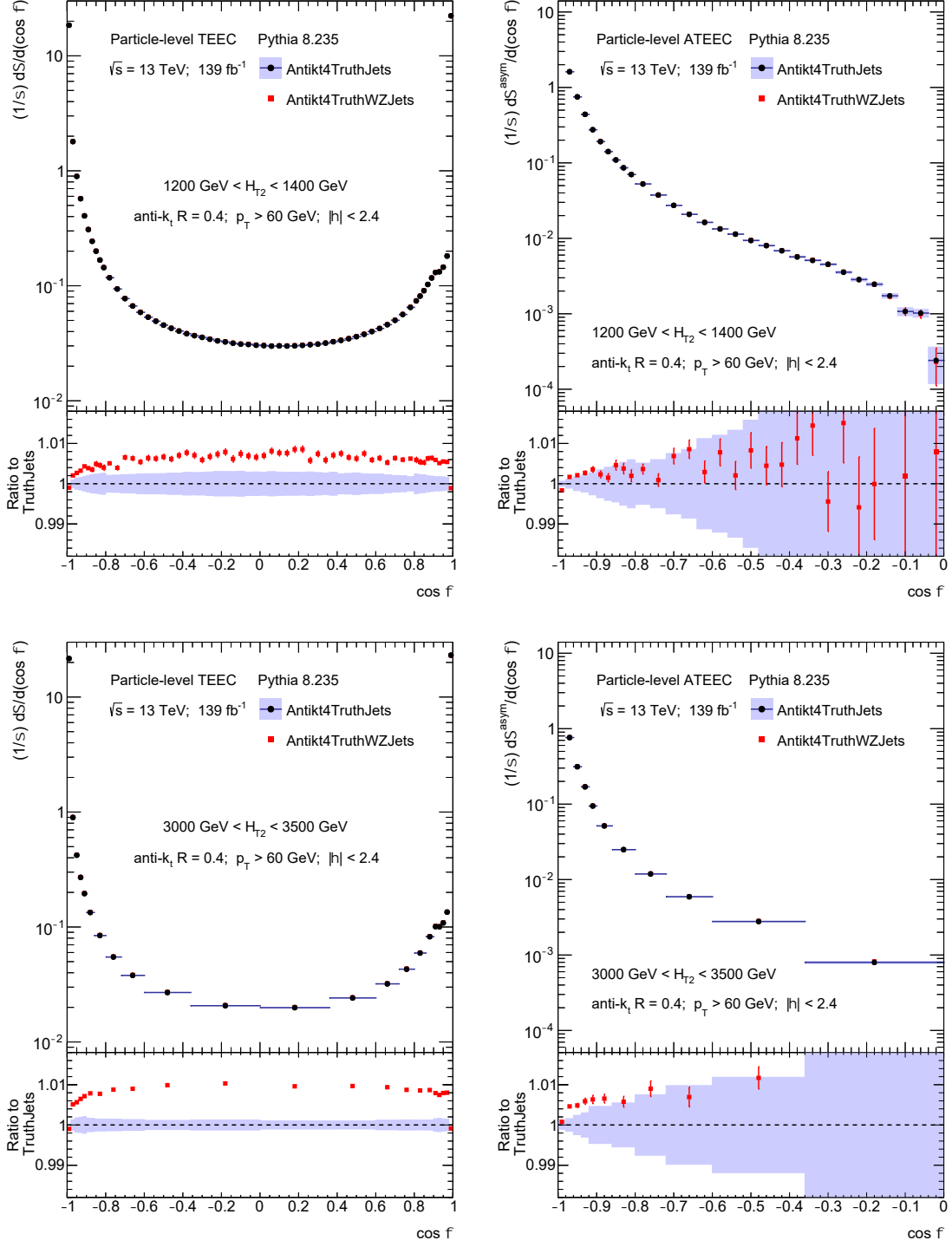


Figure A.3: Particle-level TEEC (left) and ATEEC (right) distributions in two exclusive H_{T2} bins for two simulated samples by PYTHIA 8.235 using the jets' collections Antikt4TruthJets and Antikt4TruthWZJets. The difference originated from jets initiated by the hadronic decay of electroweak bosons is partially explained through the difference in their non-pQCD correction factors.

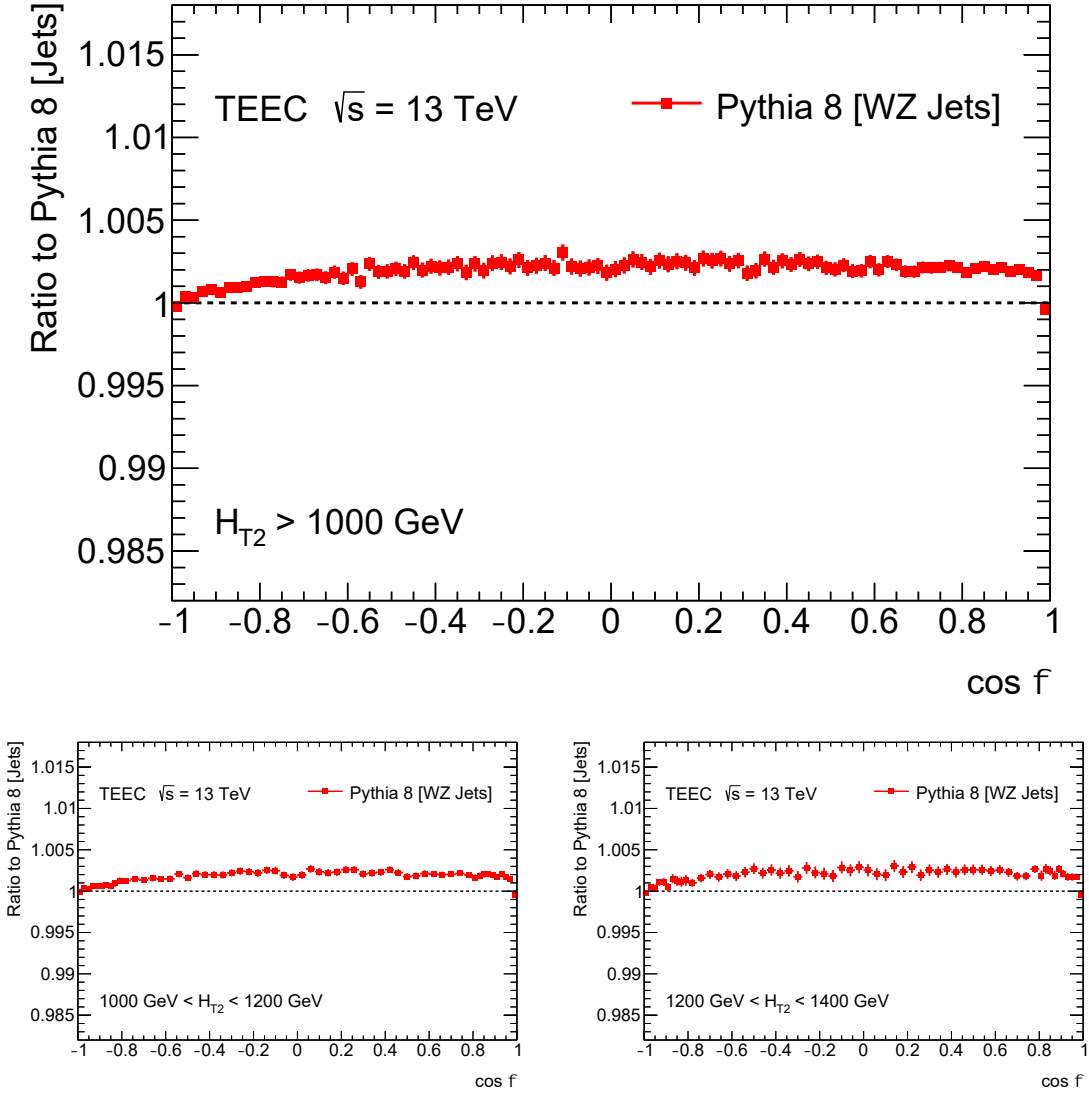


Figure A.4: Ratios of the non-perturbative QCD correction factors using the collection Antikt4TruthWZJets, in inclusive (top) and two exclusive (bottom) H_{T2} bins, compared with the factors using the nominal collection Antikt4TruthJets. The MC simulated samples are obtained with PYTHIA 8.235 event generator and partially compensate the differences observed at particle level for the TEEC distributions.

Appendix A. Appendix

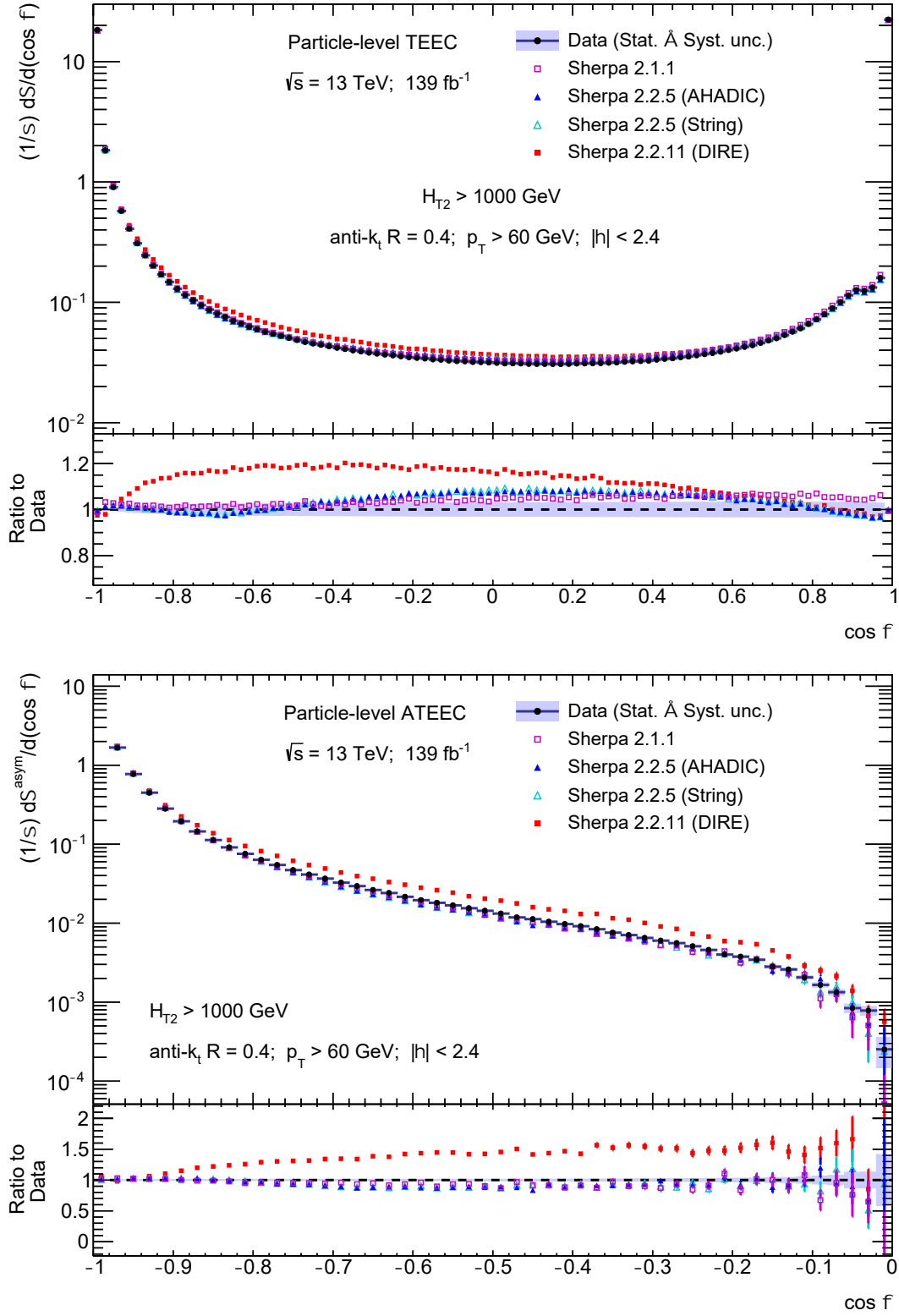


Figure A.5: Particle-level TEEC (top) and ATEEC (bottom) distribution for the inclusive H_{T2} sample with the total experimental uncertainty (blue area), along with particle-level MC predictions. The MC samples are simulated with SHERPA event generators and they differ in the parton shower, hadronization scheme, and matrix elements considered.

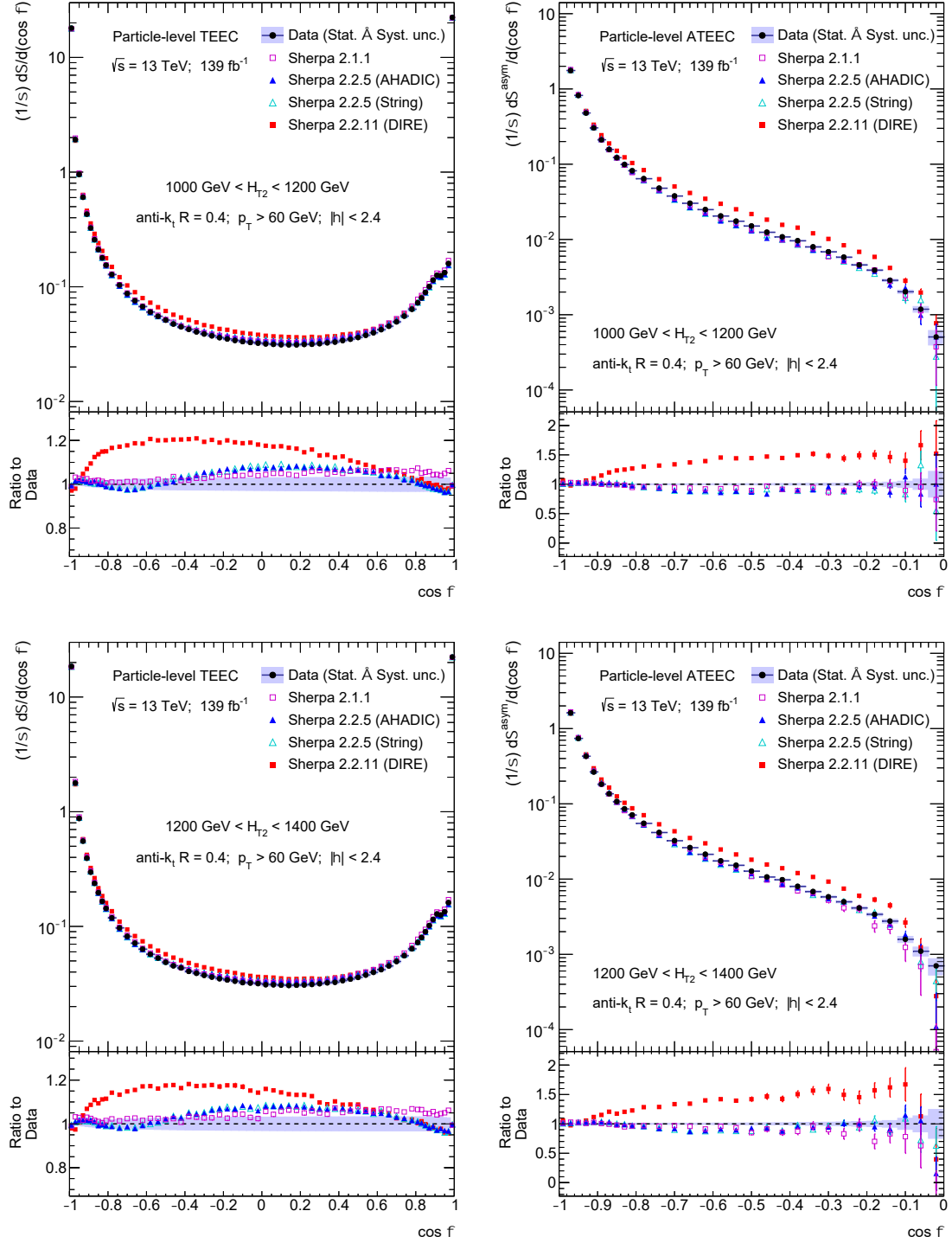


Figure A.6: Particle-level TEEC (left) and ATEEC (right) distributions in two exclusive H_{T2} bins with the total experimental uncertainty (blue area), along with particle-level MC predictions. The MC samples are simulated with SHERPA event generators and they differ in the parton shower, hadronization scheme, and matrix elements considered.

Appendix A. Appendix

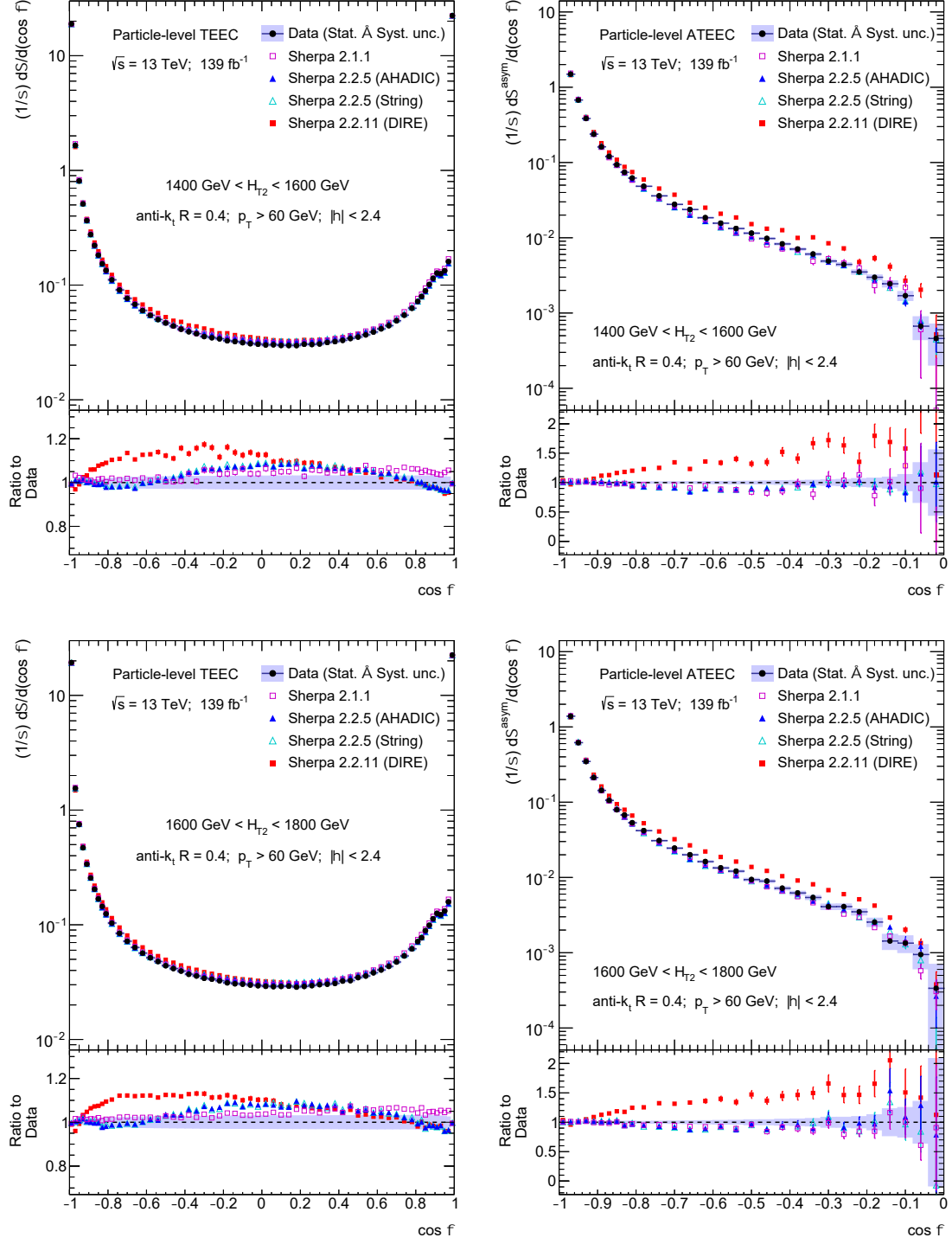


Figure A.7: Particle-level TEEC (left) and ATEEC (right) distributions in two exclusive H_{T2} bins with the total experimental uncertainty (blue area), along with particle-level MC predictions. The MC samples are simulated with SHERPA event generators and they differ in the parton shower, hadronization scheme, and matrix elements considered.

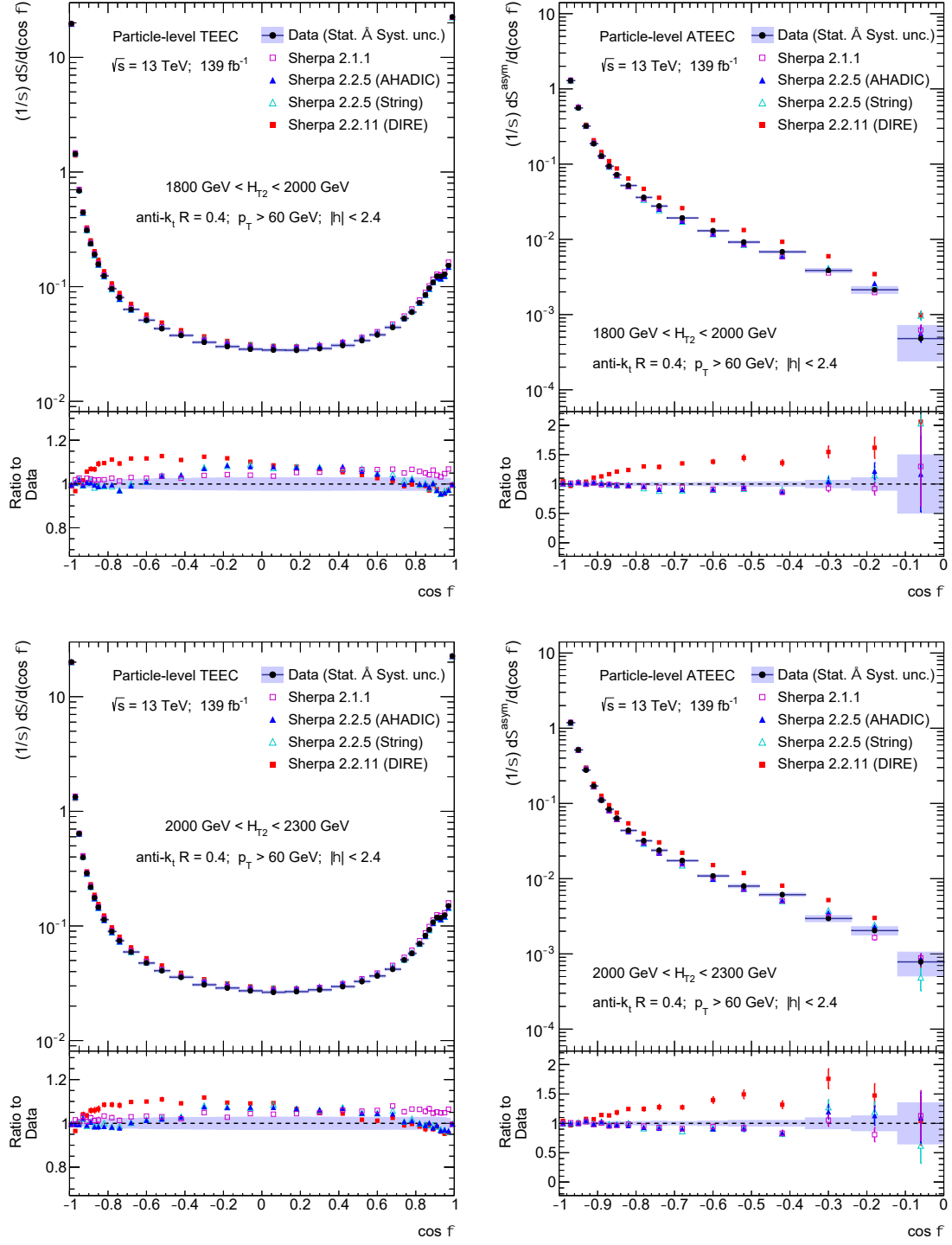


Figure A.8: Particle-level TEEC (left) and ATEEC (right) distributions in two exclusive H_{T2} bins with the total experimental uncertainty (blue area), along with particle-level MC predictions. The MC samples are simulated with SHERPA event generators and they differ in the parton shower, hadronization scheme, and matrix elements considered.

Appendix A. Appendix

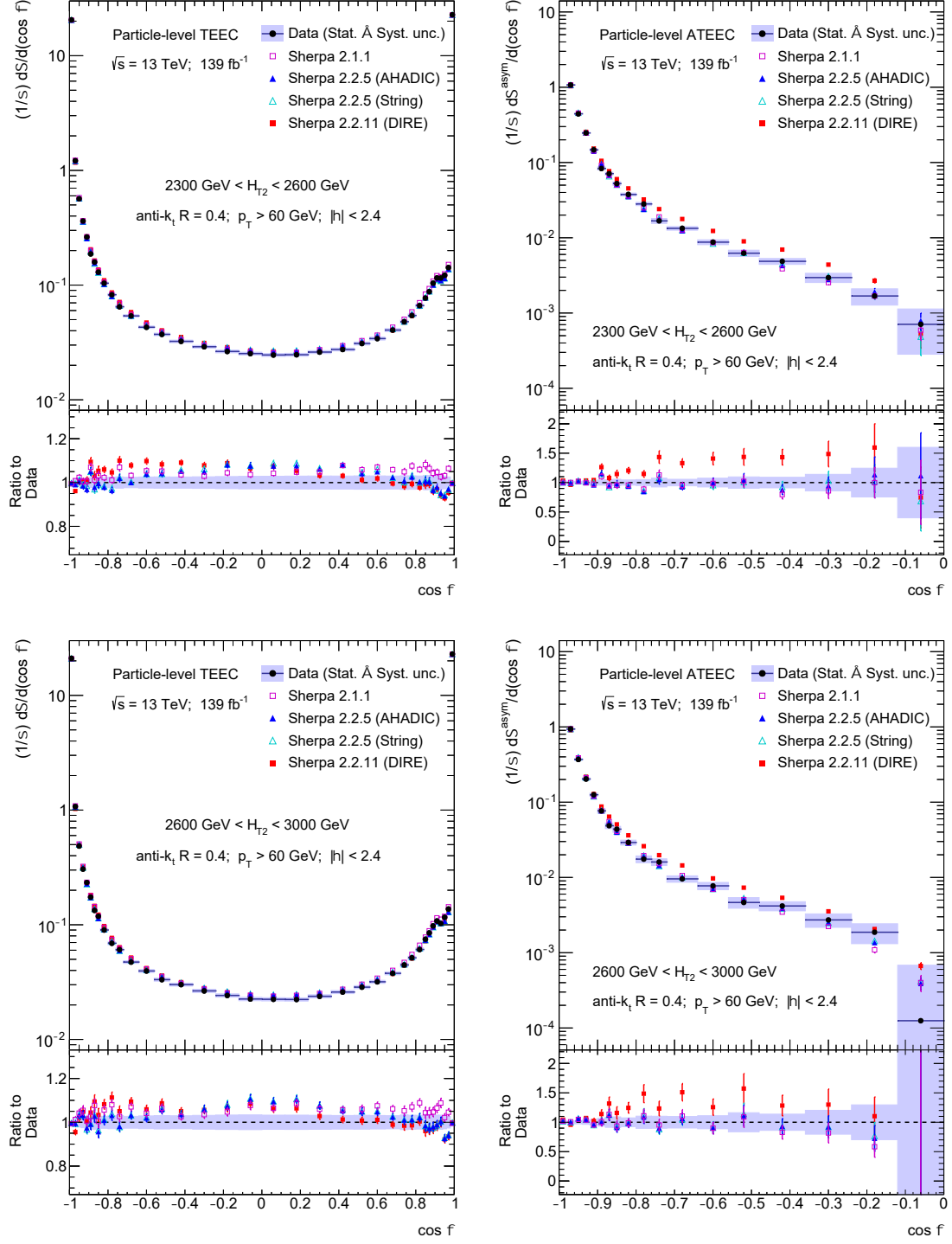


Figure A.9: Particle-level TEEC (left) and ATEEC (right) distributions in two exclusive H_{T2} bins with the total experimental uncertainty (blue area), along with particle-level MC predictions. The MC samples are simulated with SHERPA event generators and they differ in the parton shower, hadronization scheme, and matrix elements considered.

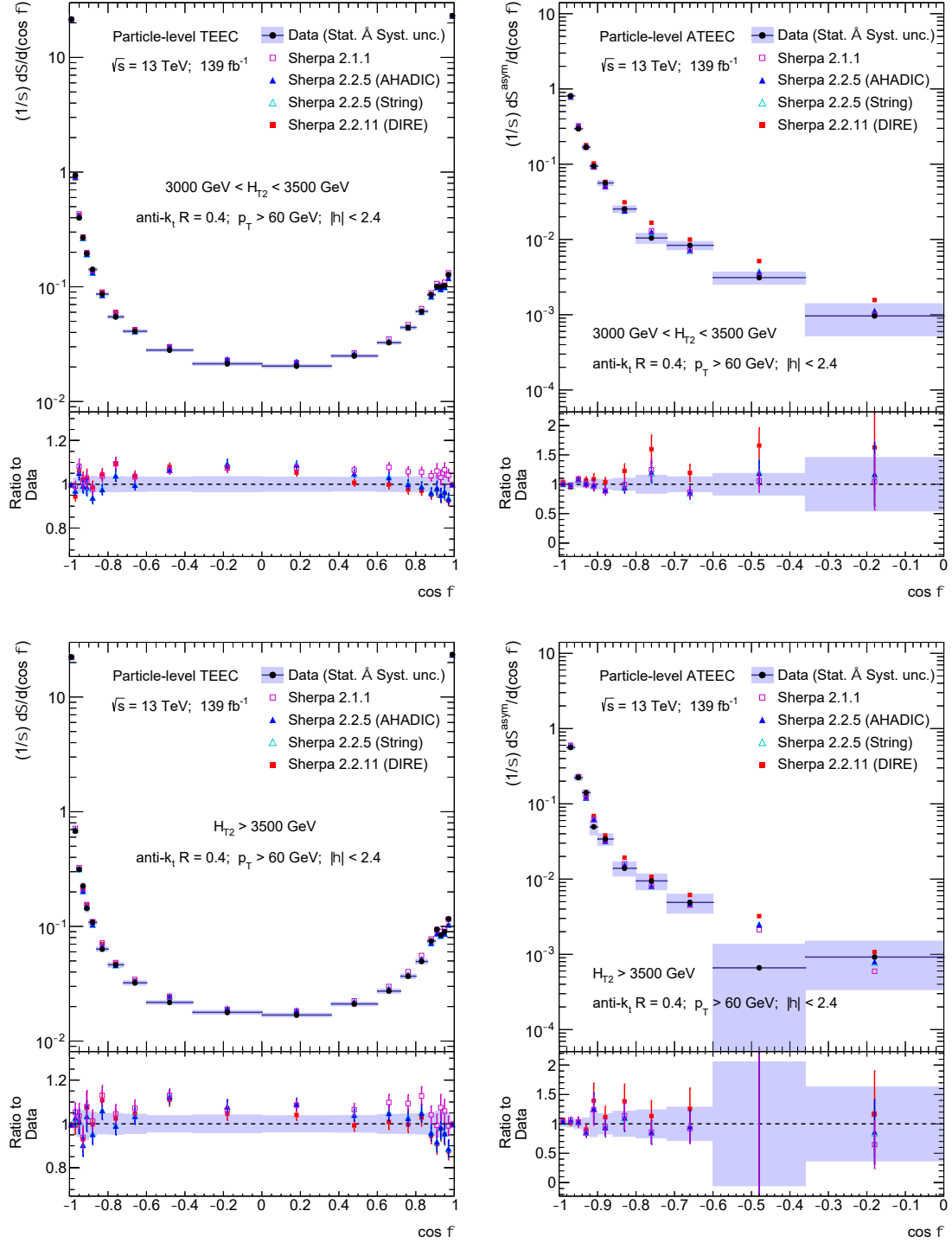


Figure A.10: Particle-level TEEC (left) and ATEEC (right) distributions in two exclusive H_{T2} bins with the total experimental uncertainty (blue area), along with particle-level MC predictions. The MC samples are simulated with SHERPA event generators and they differ in the parton shower, hadronization scheme, and matrix elements considered.

A.2 Fits using the binning in data

This section includes the results of Sections 6.8 and 6.9 for the correlations. However, the theory is binned the same way as the measurement in order to appreciate in detail the agreement in $\cos \phi$. The experimental results for the TEEC functions are compared to the pQCD predictions, once corrected for non-pQCD effects, in Figures A.11 to A.13. They show the ratio of the data to the theoretical predictions calculated using the PDF groups available at NNLO in pQCD with $\alpha_s(m_Z) = 0.1180$; taking into account all theoretical and experimental uncertainties. In addition, Figures A.14 to A.16 compare the experimental data to the pQCD predictions for each of the PDF groups available. In order to have an idea about the size of the so called K-factors, a comparison between the LO and NNLO predictions to the NLO calculations is also presented.

The value of the strong coupling is again determined from the comparison of unfolded experimental results with their theoretical predictions at NNLO in pQCD. The values of $\alpha_s(m_Z)$ extracted from a global fit to the TEEC function at NNLO as well as the individual fits in each H_{T2} bin and in the fully inclusive sample are summarized in Table A.1 using the same binning as experimental data. The theoretical predictions used for this extraction use MMHT 2014 as the nominal PDF set, which is the one providing a wider range of variations for $\alpha_s(m_Z)$. In addition, the extracted values using NNPDF 3.0 and CT14 as the PDF set are also presented in Tables A.2 and A.3, respectively.

The χ^2 values indicate that the agreement between the data and the theoretical predictions is good in each exclusive H_{T2} bin and in the fully inclusive sample. The critical value with a significance level of $\alpha = 0.05$ for the global fit is $\chi^2 = 391.4$. Thus, a slight tension arises in the global fit for the nominal PDF group. This tension comes from the drop at high energy scales of the fitted values of α_s in exclusive bins. However, this effect is not found when using the other PDF groups. Figures A.17 to A.19 compare the experimental results with fitted theoretical predictions, i.e. where the fitted values of $\alpha_s(m_Z)$ and the nuisance parameters are already constrained. The results are compatible with the ones obtained using a coarser binning. Thus, the extracted values are also in good agreement with the current world average, as well as with previous measurements both in ATLAS and in other experiments. The asymmetries are quite sensitive to statistical fluctuations, in particular, the region of the tail. Therefore, they are only studied with coarser intervals in order to extract reliable results for the strong coupling constant.

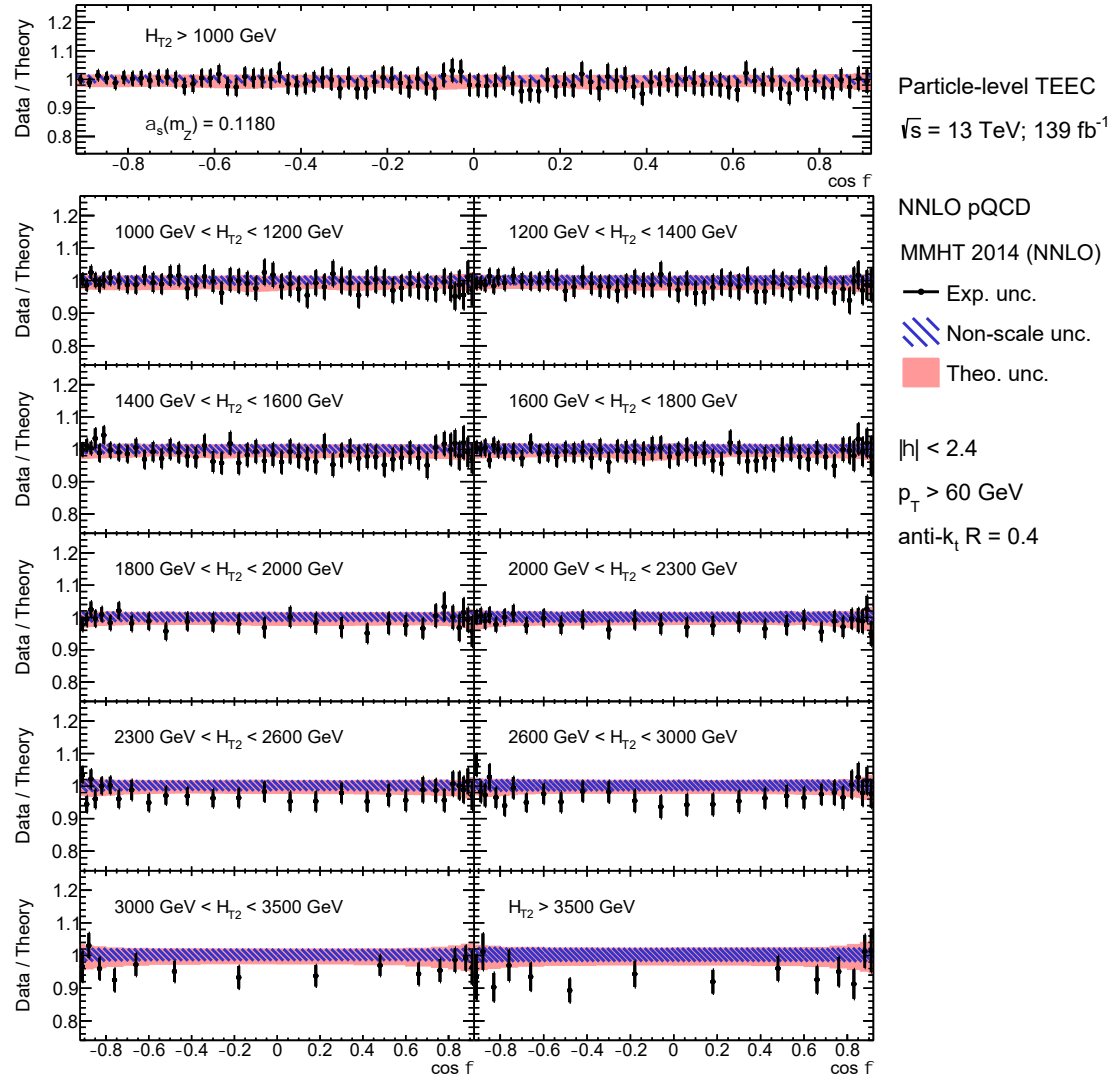


Figure A.11: Ratios of the unfolded data to the particle-level NNLO pQCD predictions for the TEEC function obtained using MMHT 2014 PDF group, in inclusive and exclusive H_{T2} bins. The strong coupling constant is set to $\alpha_s(m_Z) = 0.1180$. The non-scale uncertainty corresponds to the PDF parametrization uncertainty, the $\alpha_s(m_Z)$ parameter uncertainty and the non-pQCD uncertainty from the MC model added in quadrature. The theoretical uncertainty includes both non-scale and scale uncertainties. The experimental uncertainty includes the statistical uncertainty.

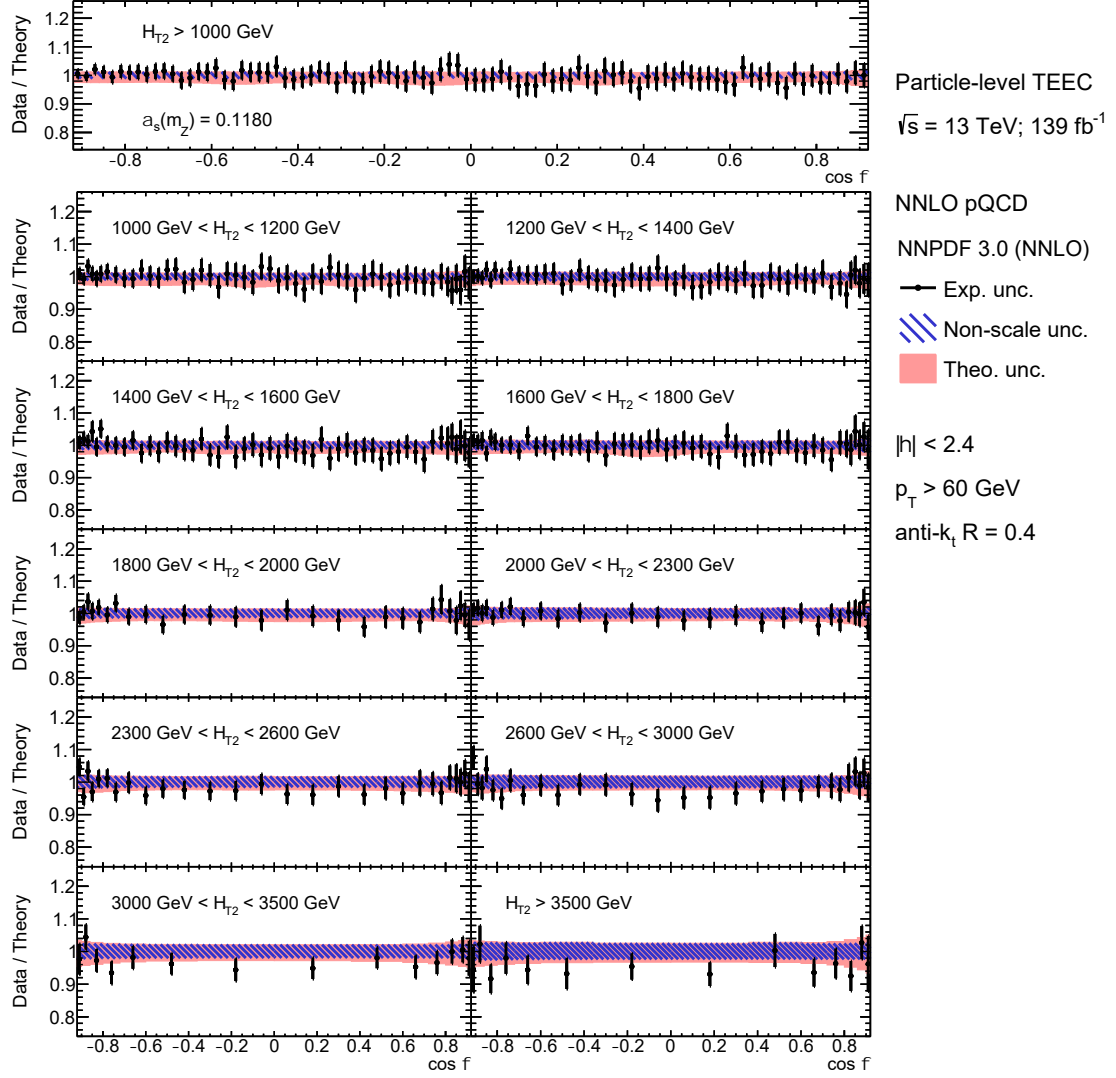


Figure A.12: Ratios of the unfolded data to the particle-level NNLO pQCD predictions for the TEEC function obtained using NNPDF 3.0 PDF group, in inclusive and exclusive H_{T2} bins. The strong coupling constant is set to $\alpha_s(m_Z) = 0.1180$. The non-scale uncertainty corresponds to the PDF parametrization uncertainty, the $\alpha_s(m_Z)$ parameter uncertainty and the non-pQCD uncertainty from the MC model added in quadrature. The theoretical uncertainty includes both non-scale and scale uncertainties. The experimental uncertainty includes the statistical uncertainty.

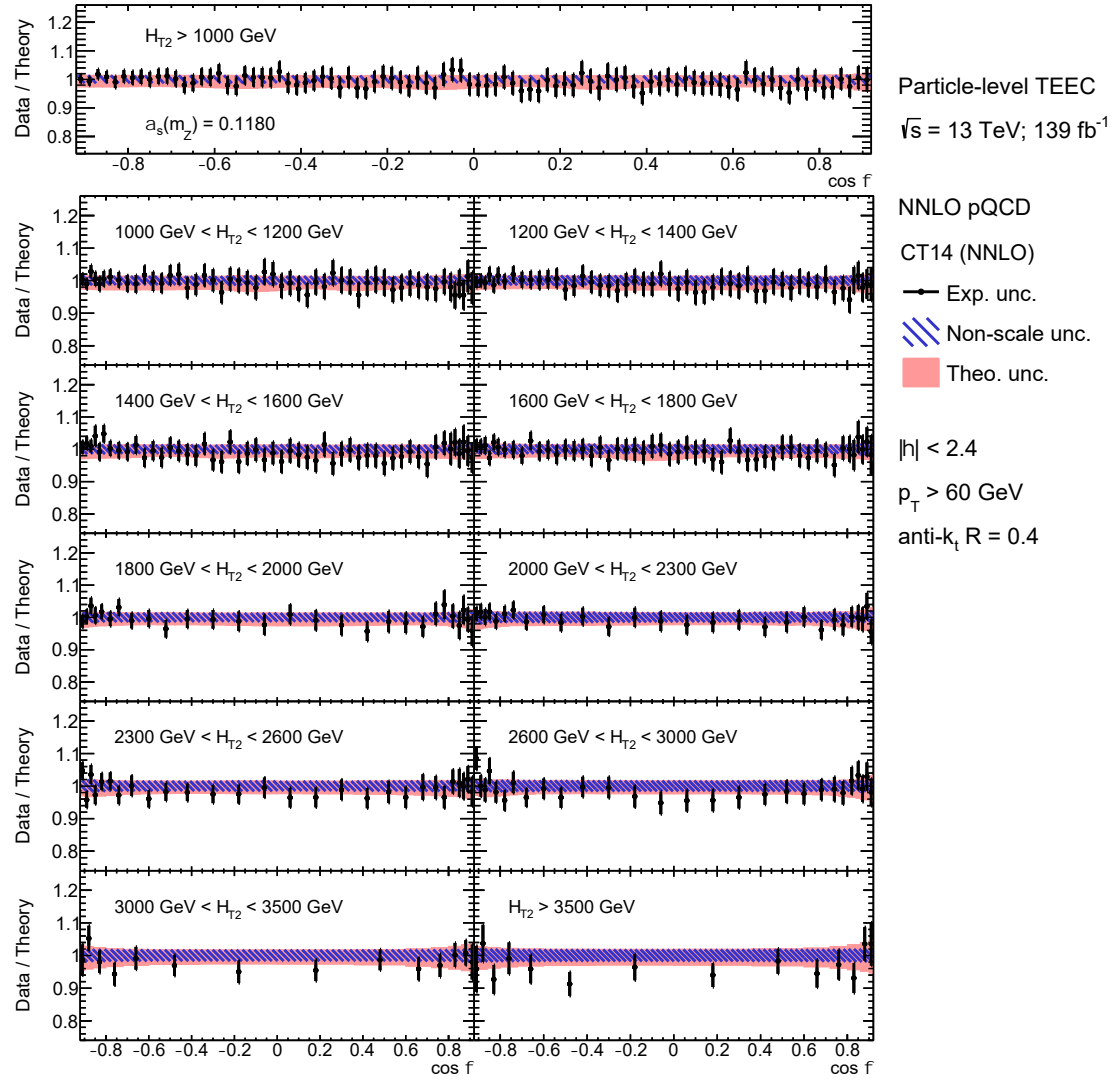


Figure A.13: Ratios of the unfolded data to the particle-level NNLO pQCD predictions for the TEEC function obtained using CT14 PDF group, in inclusive and exclusive H_{T2} bins. The strong coupling constant is set to $\alpha_s(m_Z) = 0.1180$. The non-scale uncertainty corresponds to the PDF parametrization uncertainty, the $\alpha_s(m_Z)$ parameter uncertainty and the non-pQCD uncertainty from the MC model added in quadrature. The theoretical uncertainty includes both non-scale and scale uncertainties. The experimental uncertainty includes the statistical uncertainty.

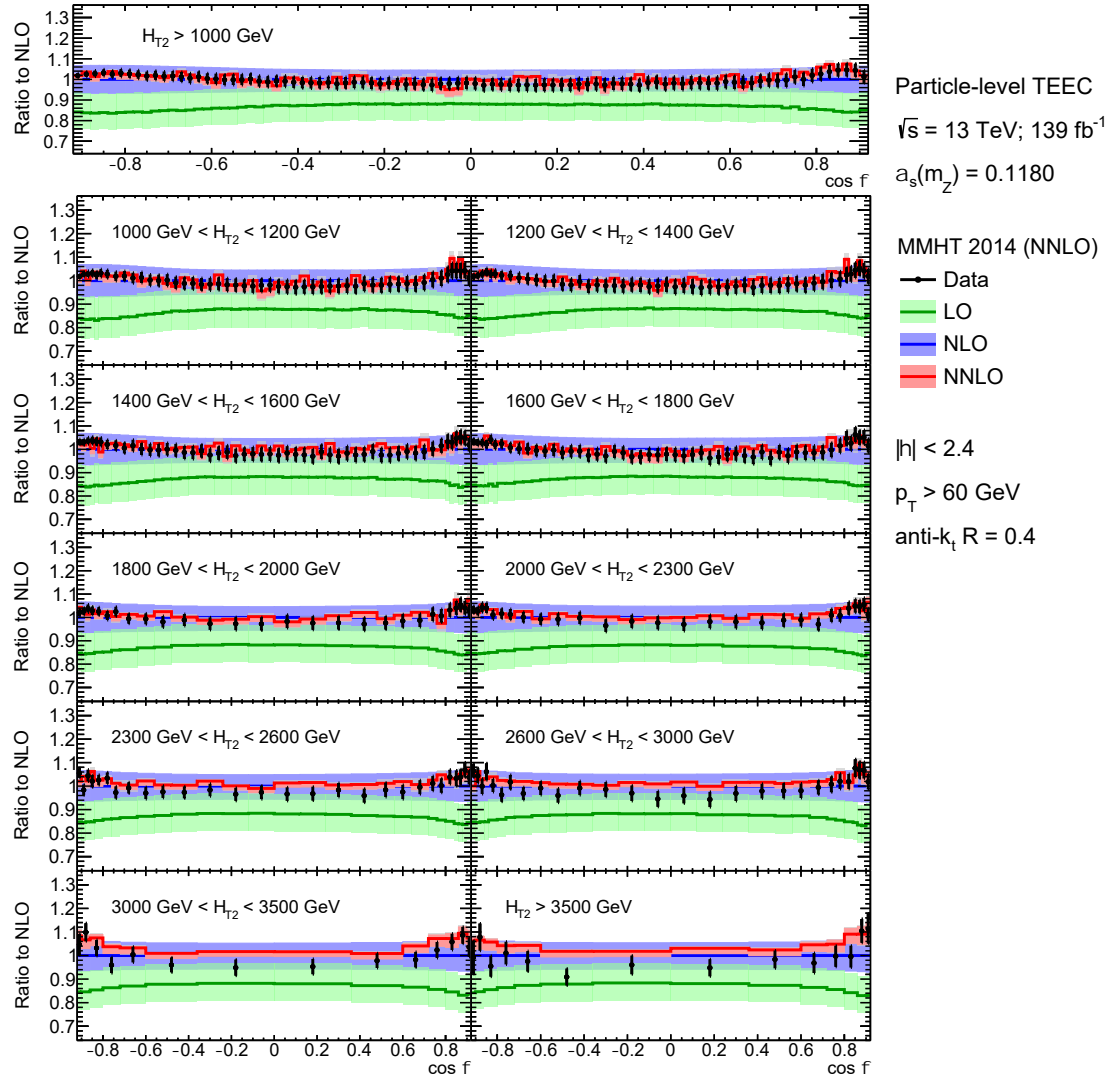


Figure A.14: Theoretical predictions using MMHT 2014 PDF group for the TEEC functions at LO (green) and NNLO (red) compared to the NLO calculations (blue), in inclusive and exclusive H_{T2} bins. The strong coupling constant is set to $\alpha_s(m_Z) = 0.1180$, the coloured areas show the scale uncertainties, and the shaded area (gray) shows the statistical uncertainties in the ratios between theoretical predictions. A comparison of unfolded data to pQCD predictions is also presented, where the error bars correspond to the experimental uncertainties.

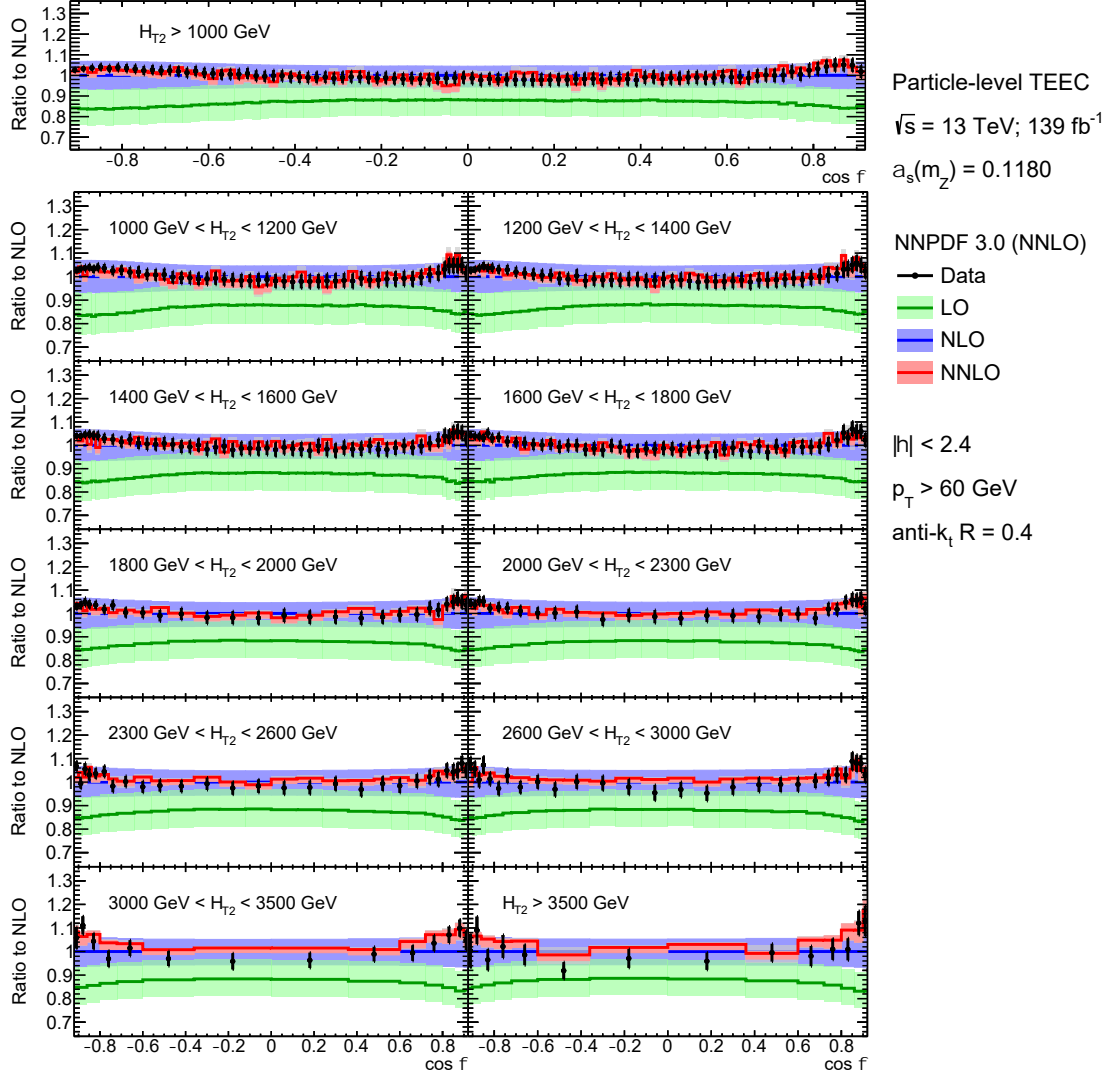


Figure A.15: Theoretical predictions using NNPDF 3.0 PDF group for the TEEC functions at LO (green) and NNLO (red) compared to the NLO calculations (blue), in inclusive and exclusive H_{T2} bins. The strong coupling constant is set to $\alpha_s(m_Z) = 0.1180$, the coloured areas show the scale uncertainties, and the shaded area (gray) shows the statistical uncertainties in the ratios between theoretical predictions. A comparison of unfolded data to pQCD predictions is also presented, where the error bars correspond to the experimental uncertainties.

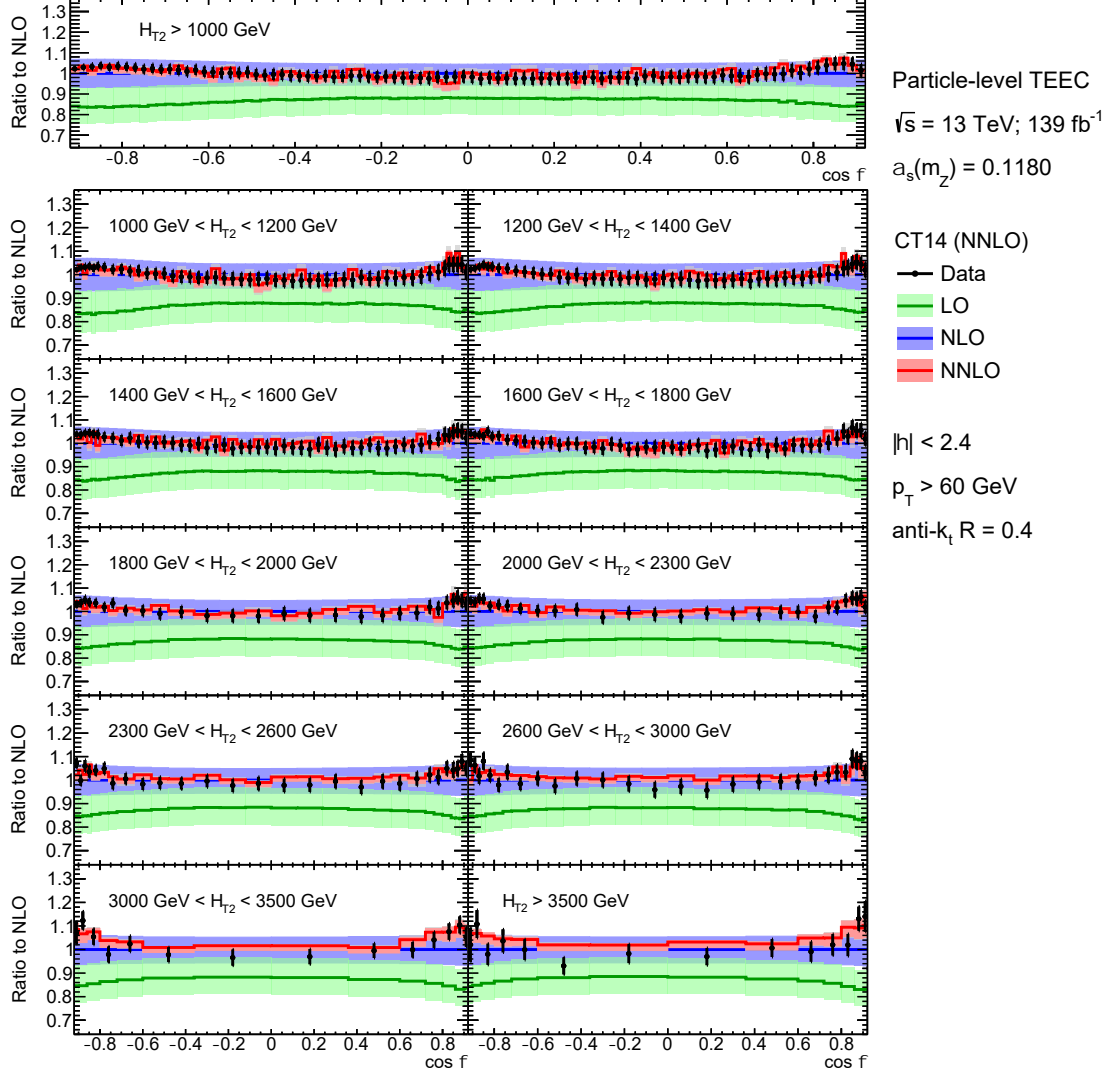


Figure A.16: Theoretical predictions using CT14 PDF group for the TEEC functions at LO (green) and NNLO (red) compared to the NLO calculations (blue), in inclusive and exclusive H_{T2} bins. The strong coupling constant is set to $\alpha_s(m_Z) = 0.1180$, the coloured areas show the scale uncertainties, and the shaded area (gray) shows the statistical uncertainties in the ratios between theoretical predictions. A comparison of unfolded data to pQCD predictions is also presented, where the error bars correspond to the experimental uncertainties.

$\langle Q \rangle$ [GeV]		$\alpha_s(m_Z)$	value (MMHT 2014)	$\chi^2/\text{N}_{\text{dof}}$
Global	0.1173 ± 0.0001 (stat.) ± 0.0006 (syst.)	$+0.0032$ (scale) -0.0011 (param.)	± 0.0002 (tune) ± 0.0005 (model)	$394.1 / 347$
Inclusive	0.1187 ± 0.0002 (stat.) ± 0.0007 (syst.)	$+0.0030$ (scale) -0.0002 (param.)	± 0.0002 (tune) ± 0.0008 (model)	$56.7 / 91$
1302	0.1184 ± 0.0003 (stat.) ± 0.0009 (syst.)	$+0.0031$ (scale) -0.0002 (param.)	± 0.0002 (tune) ± 0.0007 (model)	$33.0 / 51$
1518	0.1181 ± 0.0003 (stat.) ± 0.0009 (syst.)	$+0.0027$ (scale) -0.0005 (param.)	± 0.0003 (tune) ± 0.0008 (model)	$30.2 / 51$
1732	0.1189 ± 0.0003 (stat.) ± 0.0011 (syst.)	$+0.0030$ (scale) -0.0005 (param.)	± 0.0003 (tune) ± 0.0008 (model)	$49.4 / 51$
1944	0.1176 ± 0.0003 (stat.) ± 0.0011 (syst.)	$+0.0031$ (scale) -0.0005 (param.)	± 0.0005 (tune) ± 0.0009 (model)	$38.4 / 51$
2153	0.1175 ± 0.0004 (stat.) ± 0.0012 (syst.)	$+0.0029$ (scale) -0.0004 (param.)	± 0.0003 (tune) ± 0.0009 (model)	$32.9 / 27$
2396	0.1179 ± 0.0003 (stat.) ± 0.0012 (syst.)	$+0.0029$ (scale) -0.0005 (param.)	± 0.0012 (tune) ± 0.0012 (model)	$27.5 / 27$
2706	0.1164 ± 0.0004 (stat.) ± 0.0015 (syst.)	$+0.0030$ (scale) -0.0005 (param.)	± 0.0013 (tune) ± 0.0011 (model)	$35.1 / 27$
3042	0.1162 ± 0.0005 (stat.) ± 0.0017 (syst.)	$+0.0031$ (scale) -0.0005 (param.)	± 0.0002 (tune) ± 0.0015 (model)	$33.1 / 27$
3476	0.1141 ± 0.0007 (stat.) ± 0.0017 (syst.)	$+0.0033$ (scale) -0.0011 (param.)	± 0.0002 (tune) ± 0.0020 (model)	$15.1 / 13$
4189	0.1116 ± 0.0011 (stat.) ± 0.0018 (syst.)	$+0.0030$ (scale) -0.0009 (param.)	± 0.0002 (tune) ± 0.0020 (model)	$14.0 / 13$

Table A.1: Values of the strong coupling constant at the Z boson mass scale, $\alpha_s(m_Z)$, obtained from fits to the TEEC function at NNLO using the MMHT 2014 parton distribution functions. The values of the average interaction scale $\langle Q \rangle$ are shown in the first column, while the values of the χ^2 function at the minimum are shown in the third column. The label (stat.) includes the experimental and theoretical statistical uncertainties, whereas the label (syst.) indicates only the experimental systematic uncertainties added in quadrature. The uncertainty related to the MC model in the IB unfolding is displayed separately as (model) and the one referred to as (tune) is related to the non-pQCD corrections.

$\langle Q \rangle$ [GeV]		$\alpha_s(m_Z)$	value (NNPDF 3.0)	χ^2/N_{dof}
Global	0.1189 ± 0.0001 (stat.) ± 0.0006 (syst.)	$+0.00040$ (scale) -0.0010 (param.)	± 0.00020 (param.) ± 0.0003 (tune) ± 0.0007 (model)	$379.8 / 347$
Inclusive	0.1197 ± 0.0003 (stat.) ± 0.0008 (syst.)	$+0.00035$ (scale) -0.0003 (param.)	± 0.0014 (param.) ± 0.0002 (tune) ± 0.0009 (model)	$60.2 / 91$
1302	0.1194 ± 0.0004 (stat.) ± 0.0010 (syst.)	$+0.00036$ (scale) -0.0003 (param.)	± 0.0014 (param.) ± 0.0003 (tune) ± 0.0008 (model)	$34.4 / 51$
1518	0.1193 ± 0.0003 (stat.) ± 0.0010 (syst.)	$+0.00032$ (scale) -0.0005 (param.)	± 0.0015 (param.) ± 0.0004 (tune) ± 0.0008 (model)	$31.8 / 51$
1732	0.1204 ± 0.0004 (stat.) ± 0.0012 (syst.)	$+0.00035$ (scale) -0.0005 (param.)	± 0.0017 (param.) ± 0.0006 (tune) ± 0.0011 (model)	$50.7 / 51$
1944	0.1190 ± 0.0004 (stat.) ± 0.0012 (syst.)	$+0.00034$ (scale) -0.0005 (param.)	± 0.0018 (param.) ± 0.0006 (tune) ± 0.0010 (model)	$40.2 / 51$
2153	0.1189 ± 0.0004 (stat.) ± 0.0013 (syst.)	$+0.00036$ (scale) -0.0003 (param.)	± 0.0018 (param.) ± 0.0003 (tune) ± 0.0010 (model)	$33.8 / 27$
2396	0.1193 ± 0.0003 (stat.) ± 0.0014 (syst.)	$+0.00035$ (scale) -0.0005 (param.)	± 0.0020 (param.) ± 0.0011 (tune) ± 0.0014 (model)	$28.7 / 27$
2706	0.1175 ± 0.0004 (stat.) ± 0.0016 (syst.)	$+0.00033$ (scale) -0.0005 (param.)	± 0.0021 (param.) ± 0.0005 (tune) ± 0.0012 (model)	$35.1 / 27$
3042	0.1173 ± 0.0005 (stat.) ± 0.0018 (syst.)	$+0.00032$ (scale) -0.0004 (param.)	± 0.0022 (param.) ± 0.0003 (tune) ± 0.0016 (model)	$33.0 / 27$
3476	0.1151 ± 0.0007 (stat.) ± 0.0018 (syst.)	$+0.00035$ (scale) -0.0011 (param.)	± 0.0023 (param.) ± 0.0002 (tune) ± 0.0020 (model)	$15.4 / 13$
4189	0.1135 ± 0.0010 (stat.) ± 0.0014 (syst.)	$+0.0021$ (scale) -0.0008 (param.)	± 0.0019 (param.) ± 0.0015 (tune) ± 0.0015 (model)	$10.5 / 13$

Table A.2: Values of the strong coupling constant at the Z boson mass scale, $\alpha_s(m_Z)$, obtained from fits to the TEEC function at NNLO using the NNPDF 3.0 parton distribution functions. The values of the average interaction scale $\langle Q \rangle$ are shown in the first column, while the values of the χ^2 function at the minimum are shown in the third column. The label (stat.) includes the experimental and theoretical statistical uncertainties, whereas the label (syst.) indicates only the experimental systematic uncertainties added in quadrature. The uncertainty related to the MC model in the IB unfolding is displayed separately as (model) and the one referred to as (tune) is related to the non-pQCD corrections.

$\langle Q \rangle$ [GeV]		$\alpha_s(m_Z)$ value (CT14)	χ^2/N_{dof}
Global	0.1194 ± 0.0001 (stat.) ± 0.0006 (syst.)	$+0.0036$ (scale) -0.0010 (param.)	0.0006 (tune) ± 0.0002 (model)
Inclusive	0.1195 ± 0.0003 (stat.) ± 0.0008 (syst.)	$+0.0035$ (scale) -0.0003 (param.)	0.0010 (tune) ± 0.0002 (model)
1302	0.1191 ± 0.0004 (stat.) ± 0.0010 (syst.)	$+0.0036$ (scale) -0.0016 (param.)	0.0008 (tune) ± 0.0003 (model)
1518	0.1192 ± 0.0003 (stat.) ± 0.0011 (syst.)	$+0.0032$ (scale) -0.0006 (param.)	0.0004 (tune) ± 0.0004 (model)
1732	0.1204 ± 0.0003 (stat.) ± 0.0012 (syst.)	$+0.0034$ (scale) -0.0006 (param.)	0.0006 (tune) ± 0.0010 (model)
1944	0.1190 ± 0.0004 (stat.) ± 0.0013 (syst.)	$+0.0037$ (scale) -0.0018 (param.)	0.0006 (tune) ± 0.0012 (model)
2153	0.1192 ± 0.0004 (stat.) ± 0.0014 (syst.)	$+0.0034$ (scale) -0.0009 (param.)	0.0004 (tune) ± 0.0011 (model)
2396	0.1199 ± 0.0004 (stat.) ± 0.0014 (syst.)	$+0.0037$ (scale) -0.0007 (param.)	0.0019 (tune) ± 0.0015 (model)
2706	0.1185 ± 0.0005 (stat.) ± 0.0018 (syst.)	$+0.0035$ (scale) -0.0019 (param.)	0.0006 (tune) ± 0.0014 (model)
3042	0.1184 ± 0.0006 (stat.) ± 0.0019 (syst.)	$+0.0033$ (scale) -0.0008 (param.)	0.0020 (tune) ± 0.0019 (model)
3476	0.1161 ± 0.0009 (stat.) ± 0.0024 (syst.)	$+0.0041$ (scale) -0.0019 (param.)	0.0023 (tune) ± 0.0028 (model)
4189	0.1123 ± 0.0019 (stat.) ± 0.0029 (syst.)	$+0.0047$ (scale) -0.0025 (param.)	0.0042 (tune) ± 0.0042 (model)

Table A.3: Values of the strong coupling constant at the Z boson mass scale, $\alpha_s(m_Z)$, obtained from fits to the TEEC function at NNLO using the CT14 parton distribution functions. The values of the average interaction scale $\langle Q \rangle$ are shown in the first column, while the values of the χ^2 function at the minimum are shown in the third column. The label (stat.) includes the experimental and theoretical statistical uncertainties, whereas the label (syst.) indicates only the experimental systematic uncertainties added in quadrature. The uncertainty related to the MC model in the IB unfolding is displayed separately as (model) and the one referred to as (tune) is related to the non-pQCD corrections.

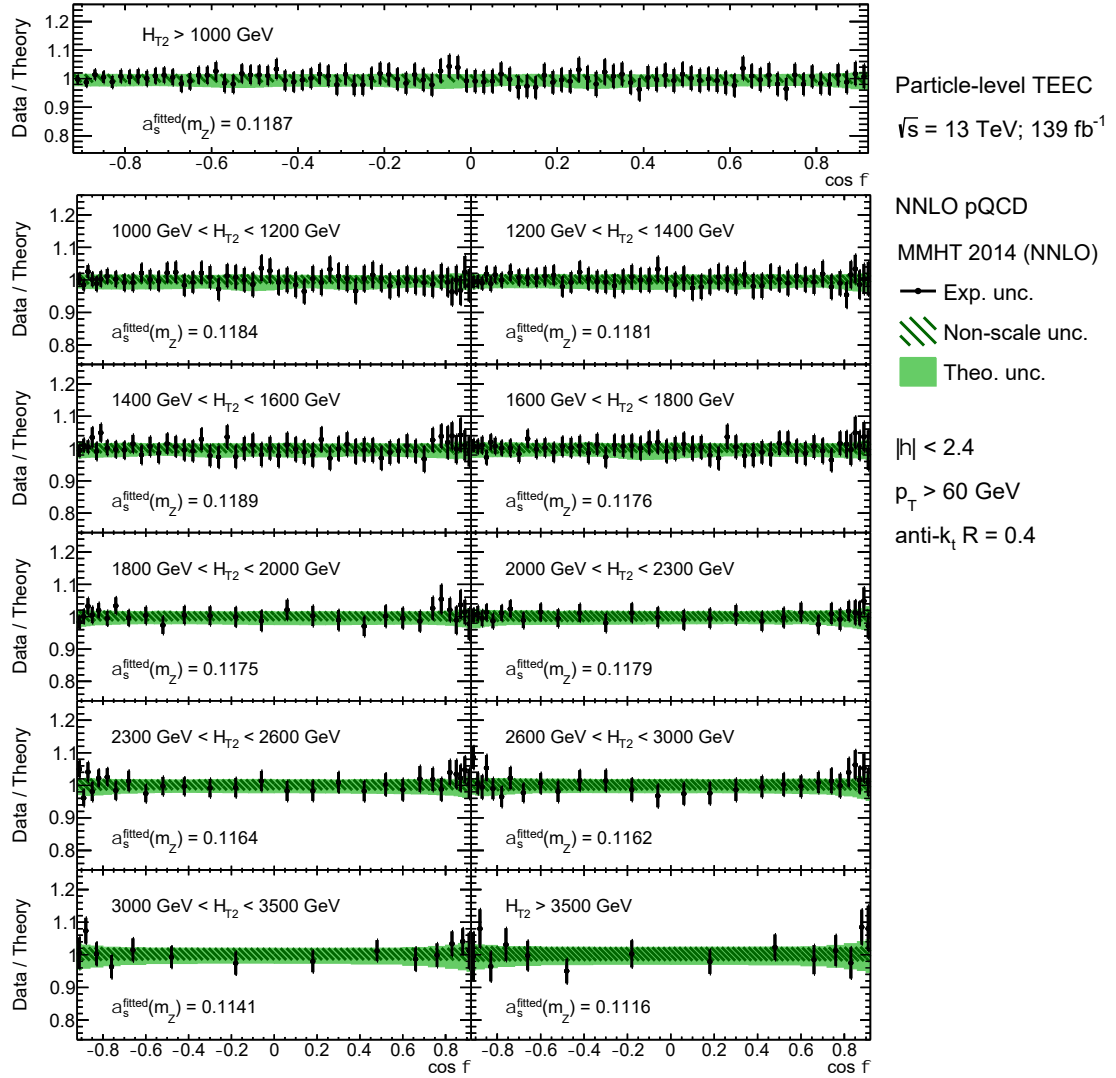


Figure A.17: Ratios of the data to the fitted theoretical predictions at NNLO for the TEEC measurements, obtained using MMHT 2014, in inclusive and exclusive H_{T2} bins. The green band shows the theoretical uncertainties, dominated by the scale variations, while the error bars show the experimental uncertainties, where correlations between the fit parameters have been taken into account. The label exp. also includes the theoretical statistical uncertainty.

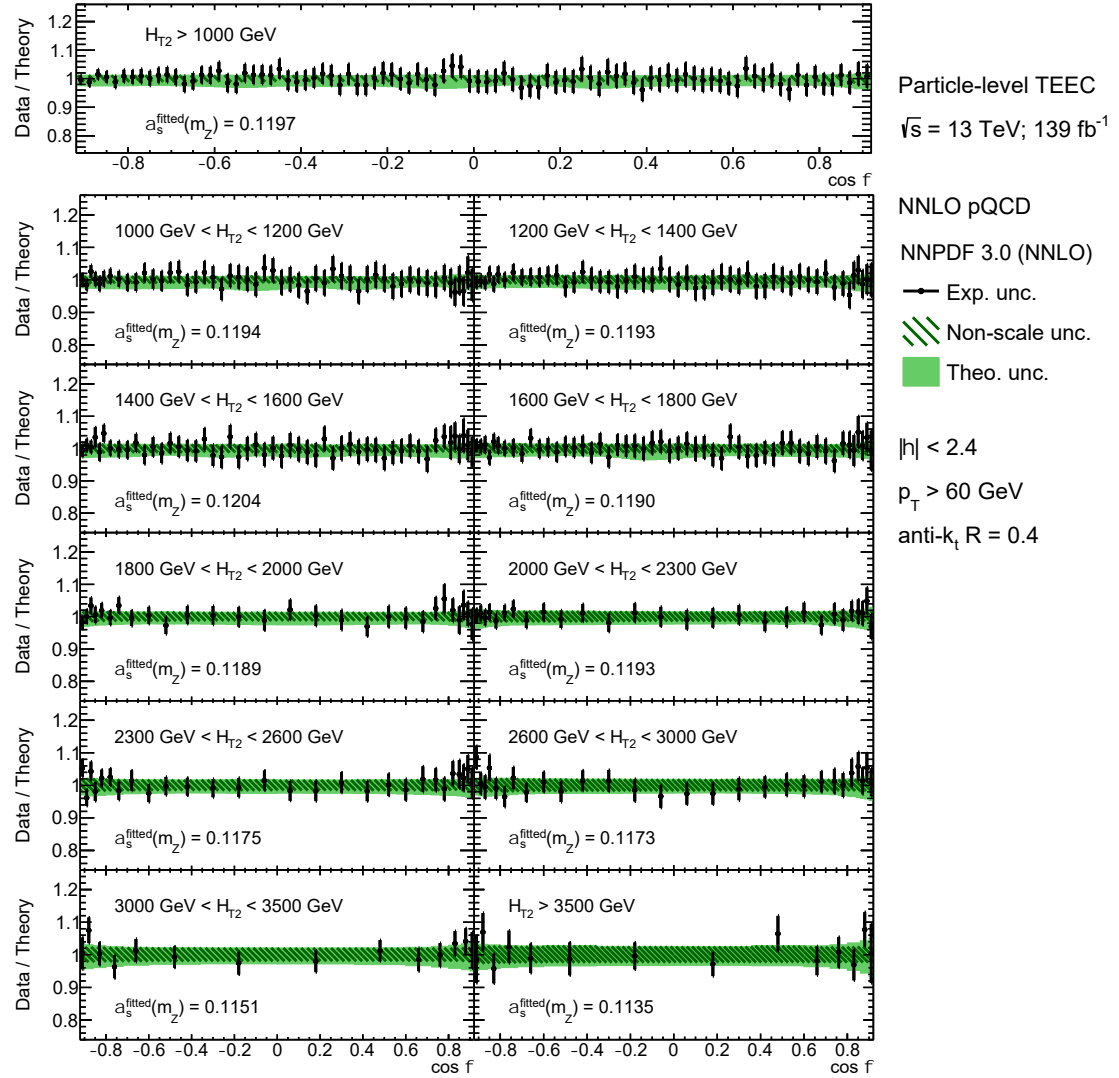


Figure A.18: Ratios of the data to the fitted theoretical predictions at NNLO for the TEEC measurements, obtained using NNPDF 3.0, in inclusive and exclusive H_{T2} bins. The green band shows the theoretical uncertainties, dominated by the scale variations, while the error bars show the experimental uncertainties, where correlations between the fit parameters have been taken into account. The label exp. also includes the theoretical statistical uncertainty.

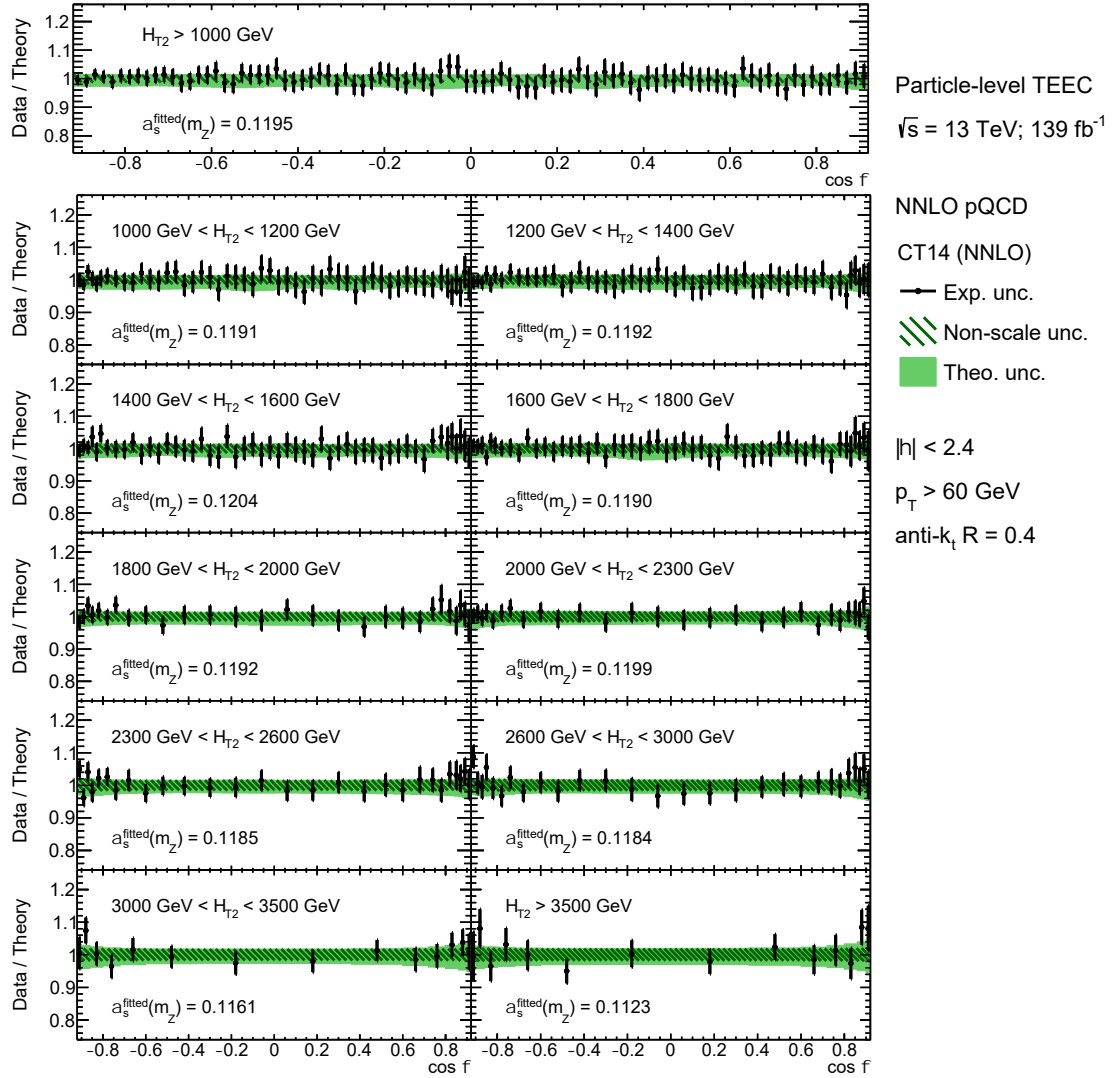


Figure A.19: Ratios of the data to the fitted theoretical predictions at NNLO for the TEEC measurements, obtained using CT14, in inclusive and exclusive H_{T2} bins. The green band shows the theoretical uncertainties, dominated by the scale variations, while the error bars show the experimental uncertainties, where correlations between the fit parameters have been taken into account. The label exp. also includes the theoretical statistical uncertainty.

Bibliography

- [1] ATLAS Collaboration. “Measurement of transverse energy–energy correlations in multi-jet events in pp collisions at $\sqrt{s} = 7\text{ TeV}$ using the ATLAS detector and determination of the strong coupling constant $\alpha_s(m_Z)$ ”. In: *Phys. Lett. B* 750 (2015), p. 427. DOI: 10.1016/j.physletb.2015.09.050. arXiv: 1508.01579 [hep-ex].
- [2] ATLAS Collaboration. “Determination of the strong coupling constant α_s from transverse energy-energy correlations in multijet events at $\sqrt{s} = 8\text{ TeV}$ using the ATLAS detector”. In: *Eur. Phys. J. C* 77 (2017), p. 872. DOI: 10.1140/epjc/s10052-017-5442-0. arXiv: 1707.02562 [hep-ex].
- [3] *Determination of the strong coupling constant and test of asymptotic freedom from transverse energy-energy correlations in multijet events at $\sqrt{s} = 13\text{ TeV}$ with the ATLAS detector*. Tech. rep. Geneva: CERN, 2020. URL: <https://cds.cern.ch/record/2725553>.
- [4] F.J. Dyson. “The Radiation Theories of Tomonaga, Schwinger, and Feynman”. In: *Phys. Rev.* 75 (3 1949), pp. 486–502. DOI: 10.1103/PhysRev.75.486. URL: <https://link.aps.org/doi/10.1103/PhysRev.75.486>.
- [5] J. Schwinger. “Quantum Electrodynamics. I. A Covariant Formulation”. In: *Phys. Rev.* 74 (10 1948), pp. 1439–1461. DOI: 10.1103/PhysRev.74.1439. URL: <https://link.aps.org/doi/10.1103/PhysRev.74.1439>.
- [6] R.P. Feynman. “Space-Time Approach to Quantum Electrodynamics”. In: *Phys. Rev.* 76 (6 1949), pp. 769–789. DOI: 10.1103/PhysRev.76.769. URL: <https://link.aps.org/doi/10.1103/PhysRev.76.769>.
- [7] C.N. Yang and R.L. Mills. “Conservation of Isotopic Spin and Isotopic Gauge Invariance”. In: *Phys. Rev.* 96 (1 1954), pp. 191–195. DOI: 10.1103/PhysRev.96.191. URL: <https://link.aps.org/doi/10.1103/PhysRev.96.191>.
- [8] D.J. Gross and F. Wilczek. “Ultraviolet Behavior of Non-Abelian Gauge Theories”. In: *Phys. Rev. Lett.* 30 (26 1973), pp. 1343–1346. DOI: 10.1103/PhysRevLett.30.1343. URL: <https://link.aps.org/doi/10.1103/PhysRevLett.30.1343>.
- [9] H.D. Politzer. “Reliable Perturbative Results for Strong Interactions?” In: *Phys. Rev. Lett.* 30 (26 1973), pp. 1346–1349. DOI: 10.1103/PhysRevLett.30.1346. URL: <https://link.aps.org/doi/10.1103/PhysRevLett.30.1346>.
- [10] S.A. Larin and J.A.M. Vermaasen. “The three-loop QCD β -function and anomalous dimensions”. In: *Physics Letters B* 303.3 (1993). ISSN: 0370-2693.

- DOI: [https://doi.org/10.1016/0370-2693\(93\)91441-0](https://doi.org/10.1016/0370-2693(93)91441-0). URL: <https://www.sciencedirect.com/science/article/pii/0370269393914410>.
- [11] R.L. Workman et al., Particle Data Group. “Review of Particle Physics”. In: *Progress of Theoretical and Experimental Physics* 2022.8 (2022). 083C01. ISSN: 2050-3911. DOI: 10.1093/ptep/ptac097.
- [12] T.D. Lee and M. Nauenberg. “Degenerate Systems and Mass Singularities”. In: *Phys. Rev.* 133 (6B 1964), B1549–B1562. DOI: 10.1103/PhysRev.133.B1549. URL: <https://link.aps.org/doi/10.1103/PhysRev.133.B1549>.
- [13] A. De Rujula. “QCD, from its inception to its stubbornly unsolved problems”. In: *International Journal of Modern Physics A* 34.32 (2019), p. 1930015. DOI: 10.1142/s0217751x19300151. URL: <https://doi.org/10.1142/2Fs0217751x19300151>.
- [14] M.E. Peskin and D.V. Schroeder. *An Introduction to quantum field theory*. Reading, USA: Addison-Wesley, 1995. ISBN: 978-0-201-50397-5.
- [15] G. Altarelli and G. Parisi. “Asymptotic freedom in parton language”. In: *Nuclear Physics B* 126.2 (1977), pp. 298–318. ISSN: 0550-3213. DOI: [https://doi.org/10.1016/0550-3213\(77\)90384-4](https://doi.org/10.1016/0550-3213(77)90384-4). URL: <https://www.sciencedirect.com/science/article/pii/0550321377903844>.
- [16] H.L. Lai et al. “Global QCD analysis of parton structure of the nucleon: CTEQ5 parton distributions”. In: *The European Physical Journal C* 12.3 (2000), pp. 375–392. ISSN: 1434-6052. DOI: 10.1007/s100529900196. URL: <http://dx.doi.org/10.1007/s100529900196>.
- [17] A.D. Martin et al. “Parton distributions: a new global analysis”. In: *The European Physical Journal C* 4.3 (1998), pp. 463–496. ISSN: 1434-6052. DOI: 10.1007/s100529800904. URL: <http://dx.doi.org/10.1007/s100529800904>.
- [18] R.P. Feynman. “Very High-Energy Collisions of Hadrons”. In: *Phys. Rev. Lett.* 23 (24 1969), pp. 1415–1417. DOI: 10.1103/PhysRevLett.23.1415. URL: <https://link.aps.org/doi/10.1103/PhysRevLett.23.1415>.
- [19] J.I. Friedman and H.W. Kendall. “Deep Inelastic Electron Scattering”. In: *Annual Review of Nuclear Science* 22.1 (1972), pp. 203–254. DOI: 10.1146/annurev.ns.22.120172.001223. URL: <https://doi.org/10.1146/annurev.ns.22.120172.001223>.
- [20] M. Gell-Mann. “THE EIGHTFOLD WAY: A THEORY OF STRONG INTERACTION SYMMETRY”. In: (1961). DOI: 10.2172/4008239. URL: <https://www.osti.gov/biblio/4008239>.
- [21] Y. Ne’eman. “Derivation of strong interactions from a gauge invariance”. In: *Nuclear Physics* 26.2 (1961), pp. 222–229. ISSN: 0029-5582. DOI: [https://doi.org/10.1016/0029-5582\(61\)90134-1](https://doi.org/10.1016/0029-5582(61)90134-1). URL: <https://www.sciencedirect.com/science/article/pii/0029558261901341>.
- [22] D. Amati and G. Veneziano. “Preconfinement as a Property of Perturbative QCD”. In: *Phys. Lett. B* 83 (1979), pp. 87–92. DOI: 10.1016/0370-2693(79)90896-7.
- [23] B. Andersson et al. “Parton fragmentation and string dynamics”. In: *Phys. Rep.* 97 (1983), p. 31. DOI: 10.1016/0370-1573(83)90080-7.
- [24] S. Brandt et al. “The principal axis of jets — an attempt to analyse high-energy collisions as two-body processes”. In: *Physics Letters* 12.1 (1964),

- pp. 57–61. ISSN: 0031-9163. DOI: [https://doi.org/10.1016/0031-9163\(64\)91176-X](https://doi.org/10.1016/0031-9163(64)91176-X). URL: <https://www.sciencedirect.com/science/article/pii/003191636491176X>.
- [25] E. Farhi. “Quantum Chromodynamics Test for Jets”. In: *Phys. Rev. Lett.* 39 (25 1977), pp. 1587–1588. DOI: 10.1103/PhysRevLett.39.1587. URL: <https://link.aps.org/doi/10.1103/PhysRevLett.39.1587>.
- [26] J.F. Donoghue, F.E. Low, and S.-Y. Pi. “Tensor analysis of hadronic jets in quantum chromodynamics”. In: *Phys. Rev. D* 20 (11 1979), pp. 2759–2762. DOI: 10.1103/PhysRevD.20.2759. URL: <https://link.aps.org/doi/10.1103/PhysRevD.20.2759>.
- [27] C.L. Basham et al. “Energy Correlations in Electron-Positron Annihilation: Testing Quantum Chromodynamics”. In: *Phys. Rev. Lett.* 41 (1978), p. 1585. DOI: 10.1103/PhysRevLett.41.1585.
- [28] C.L. Basham et al. “Energy correlations in electron-positron annihilation in quantum chromodynamics: Asymptotically free perturbation theory”. In: *Phys. Rev. D* 19 (1979), p. 2018. DOI: 10.1103/PhysRevD.19.2018.
- [29] A. Ali, E. Pietarinen, and W.J. Stirling. “Transverse energy-energy correlations: A test of perturbative QCD for the proton-antiproton collider”. In: *Phys. Lett. B* 141 (1984), p. 447. DOI: 10.1016/0370-2693(84)90283-1.
- [30] G. Sterman and S. Weinberg. “Jets from Quantum Chromodynamics”. In: *Phys. Rev. Lett.* 39 (23 1977), pp. 1436–1439. DOI: 10.1103/PhysRevLett.39.1436. URL: <https://link.aps.org/doi/10.1103/PhysRevLett.39.1436>.
- [31] J.E. Huth et al. “Toward a standardization of jet definitions”. In: *1990 DPF Summer Study on High-energy Physics: Research Directions for the Decade (Snowmass 90)*. 1990.
- [32] M. Cacciari, G.P. Salam, and G. Soyez. “The anti- k_t jet clustering algorithm”. In: *JHEP* 063 (2008), p. 0804. DOI: 10.1088/1126-6708/2008/04/063. arXiv: 0802.1189 [hep-ph].
- [33] J.M. Butterworth et al. “Jet Substructure as a New Higgs-Search Channel at the Large Hadron Collider”. In: *Phys. Rev. Lett.* 100 (24 2008), p. 242001. DOI: 10.1103/PhysRevLett.100.242001. URL: <https://link.aps.org/doi/10.1103/PhysRevLett.100.242001>.
- [34] A.J. Larkoski et al. “Soft drop”. In: *J. High Energ. Phys.* 146 (2014). DOI: 10.1007/JHEP05(2014)146. URL: [https://doi.org/10.1007/JHEP05\(2014\)146](https://doi.org/10.1007/JHEP05(2014)146).
- [35] B. Andersson et al. “Coherence effects in deep inelastic scattering”. In: *Z. Phys. C - Particles and Fields* 43 (1989), pp. 625–632. DOI: 10.1007/BF01550942. URL: <https://doi.org/10.1007/BF01550942>.
- [36] J. Thaler and K. Van Tilburg. “Identifying boosted objects with N-subjettiness”. In: *J. High Energ. Phys.* 15 (2011). DOI: 10.1007/JHEP03(2011)015. URL: [https://doi.org/10.1007/JHEP03\(2011\)015](https://doi.org/10.1007/JHEP03(2011)015).
- [37] A.J. Larkoski, G.P. Salam, and J. Thaler. “Energy correlation functions for jet substructure”. In: *J. High Energ. Phys.* 108 (2013). DOI: 10.1007/JHEP06(2013)108. URL: [https://doi.org/10.1007/JHEP06\(2013\)108](https://doi.org/10.1007/JHEP06(2013)108).

- [38] A.J. Larkoski, I. Moult, and D. Neill. “Power counting to better jet observables”. In: *J. High Energ. Phys.* 9 (2014). DOI: 10.1007/JHEP12(2014)009. URL: [https://doi.org/10.1007/JHEP12\(2014\)009](https://doi.org/10.1007/JHEP12(2014)009).
- [39] M. Cacciari and G.P. Salam. “Pileup subtraction using jet areas”. In: *Physics Letters B* 659.1 (2008), pp. 119–126. ISSN: 0370-2693. DOI: <https://doi.org/10.1016/j.physletb.2007.09.077>. URL: <https://www.sciencedirect.com/science/article/pii/S0370269307011094>.
- [40] ATLAS Collaboration. “Performance of pile-up mitigation techniques for jets in pp collisions at $\sqrt{s} = 8$ TeV using the ATLAS detector”. In: *Eur. Phys. J. C* 76 (2016), p. 581. DOI: 10.1140/epjc/s10052-016-4395-z. arXiv: 1510.03823 [hep-ex].
- [41] P. Berta et al. “Pileup and underlying event mitigation with iterative constituent subtraction”. In: *J. High Energ. Phys.* 175 (2019). DOI: 10.1007/JHEP08(2019)175. URL: [https://doi.org/10.1007/JHEP08\(2019\)175](https://doi.org/10.1007/JHEP08(2019)175).
- [42] L. Evans and P. Bryant. “LHC Machine”. In: *Journal of Instrumentation* 3.08 (2008), S08001–S08001. DOI: 10.1088/1748-0221/3/08/s08001. URL: <https://doi.org/10.1088/1748-0221/3/08/s08001>.
- [43] C. De Melis. “The CERN accelerator complex. Complexe des accélérateurs du CERN”. In: (2016). General Photo. URL: <https://cds.cern.ch/record/2119882>.
- [44] *ATLAS EXPERIMENT—Luminosity Public Results Run 2*. <https://twiki.cern.ch/twiki/bin/view/AtlasPublic/LuminosityPublicResultsRun2>. Accessed: 2021-08-30.
- [45] ATLAS Collaboration. “The ATLAS Experiment at the CERN Large Hadron Collider”. In: *JINST* 3 (2008). Also published by CERN Geneva in 2010, S08003. 437 p. DOI: 10.1088/1748-0221/3/08/S08003. URL: <https://cds.cern.ch/record/1129811>.
- [46] ATLAS Collaboration. *ATLAS Inner Detector: Technical Design Report, Volume 1*. ATLAS-TDR-4; CERN-LHCC-97-016. 1997. URL: <https://cds.cern.ch/record/331063>.
- [47] ATLAS Collaboration. *ATLAS Inner Detector: Technical Design Report, Volume 2*. ATLAS-TDR-5, CERN-LHCC-97-017. 1997. URL: <https://cds.cern.ch/record/331064>.
- [48] ATLAS Collaboration. *ATLAS Liquid Argon Calorimeter: Technical Design Report*. ATLAS-TDR-2; CERN-LHCC-96-041. 1996. URL: <https://cds.cern.ch/record/331061>.
- [49] ATLAS Collaboration. *ATLAS Tile Calorimeter: Technical Design Report*. ATLAS-TDR-3; CERN-LHCC-96-042. 1996. URL: <https://cds.cern.ch/record/331062>.
- [50] ATLAS Collaboration. *ATLAS Muon Spectrometer: Technical Design Report*. ATLAS-TDR-10; CERN-LHCC-97-022. CERN, 1997. URL: <https://cds.cern.ch/record/331068>.
- [51] ATLAS Collaboration. *ATLAS High-Level Trigger, Data Acquisition and Controls: Technical Design Report*. ATLAS-TDR-16; CERN-LHCC-2003-022. 2003. URL: <https://cds.cern.ch/record/616089>.

- [52] ATLAS Collaboration. *ATLAS TDAQ System Phase-I Upgrade: Technical Design Report*. ATLAS-TDR-023; CERN-LHCC-2013-018. 2013. URL: <https://cds.cern.ch/record/1602235>.
- [53] ATLAS Collaboration. “Operation of the ATLAS trigger system in Run 2”. In: *JINST* 15 (2020), P10004. DOI: 10.1088/1748-0221/15/10/P10004. arXiv: 2007.12539 [physics.ins-det].
- [54] I. Antcheva et al. “ROOT — A C++ framework for petabyte data storage, statistical analysis and visualization”. In: *Computer Physics Communications* 180.12 (2009), pp. 2499–2512. ISSN: 0010-4655. DOI: 10.1016/j.cpc.2009.08.005. URL: <http://dx.doi.org/10.1016/j.cpc.2009.08.005>.
- [55] A. Buckley et al. “Rivet user manual”. In: *Computer Physics Communications* 184.12 (2013), pp. 2803–2819. ISSN: 0010-4655. DOI: 10.1016/j.cpc.2013.05.021. URL: <http://dx.doi.org/10.1016/j.cpc.2013.05.021>.
- [56] C. Bierlich et al. “Robust Independent Validation of Experiment and Theory: Rivet version 3”. In: *SciPost Physics* 8.2 (2020). ISSN: 2542-4653. DOI: 10.21468/scipostphys.8.2.026. URL: <http://dx.doi.org/10.21468/SciPostPhys.8.2.026>.
- [57] A. Buckley et al. “LHAPDF6: parton density access in the LHC precision era”. In: *The European Physical Journal C* 75.3 (2015). ISSN: 1434-6052. DOI: 10.1140/epjc/s10052-015-3318-8. URL: <http://dx.doi.org/10.1140/epjc/s10052-015-3318-8>.
- [58] M. Cacciari, G.P. Salam, and G. Soyez. “FastJet user manual”. In: *The European Physical Journal C* 72.3 (2012). ISSN: 1434-6052. DOI: 10.1140/epjc/s10052-012-1896-2. URL: <http://dx.doi.org/10.1140/epjc/s10052-012-1896-2>.
- [59] ATLAS Collaboration. “Measurement of hadronic event shapes in high- p_T multijet final states at $\sqrt{s} = 13$ TeV with the ATLAS detector”. In: *JHEP* 01 (2021), p. 188. DOI: 10.1007/JHEP01(2021)188. arXiv: 2007.12600 [hep-ex].
- [60] S. Catani and M.H. Seymour. “A general algorithm for calculating jet cross sections in NLO QCD”. In: *Nuclear Physics B* 485.1-2 (1997), pp. 291–419. ISSN: 0550-3213. DOI: 10.1016/S0550-3213(96)00589-5. URL: [http://dx.doi.org/10.1016/S0550-3213\(96\)00589-5](http://dx.doi.org/10.1016/S0550-3213(96)00589-5).
- [61] Z. Nagy. “Three-jet cross sections in hadron-hadron collisions at NLO”. In: *Phys. Rev. Lett.* 88 (2002), p. 122003. DOI: 10.1103/PhysRevLett.88.122003. arXiv: [hep-ph/0110315](http://arxiv.org/abs/hep-ph/0110315).
- [62] Z. Nagy. “Next-to-leading order calculation of three-jet observables in hadron-hadron collisions”. In: *Phys. Rev. D* 68 (2003), p. 094002. DOI: 10.1103/PhysRevD.68.094002. arXiv: [hep-ph/0307268](http://arxiv.org/abs/hep-ph/0307268).
- [63] M. Czakon and D. Heymes. “Four-dimensional formulation of the sector-improved residue subtraction scheme”. In: *Nuclear Physics B* 890 (2015), pp. 152–227. ISSN: 0550-3213. DOI: 10.1016/j.nuclphysb.2014.11.006. URL: <http://dx.doi.org/10.1016/j.nuclphysb.2014.11.006>.
- [64] M. Czakon, A. Van Hameren, A. Mitov, and R. Poncelet. “Single-jet inclusive rates with exact color at $\mathcal{O}(\alpha_s^4)$ ”. In: *Journal of High Energy Physics* 2019.10

- (2019). ISSN: 1029-8479. DOI: 10.1007/jhep10(2019)262. URL: [http://dx.doi.org/10.1007/JHEP10\(2019\)262](http://dx.doi.org/10.1007/JHEP10(2019)262).
- [65] M. Czakon, A. Mitov, and R. Poncelet. “Next-to-Next-to-Leading Order Study of Three-Jet Production at the LHC”. In: *Phys. Rev. Lett.* 127 (2021), p. 152001. DOI: 10.1103/PhysRevLett.127.152001. arXiv: 2106.05331 [hep-ph].
- [66] F. Buccioni et al. “OpenLoops 2”. In: *The European Physical Journal C* 79.10 (2019). ISSN: 1434-6052. DOI: 10.1140/epjc/s10052-019-7306-2. URL: <http://dx.doi.org/10.1140/epjc/s10052-019-7306-2>.
- [67] S. Abreu et al. “Leading-color two-loop QCD corrections for three-photon production at hadron colliders”. In: *J. High Energ. Phys.* 78 (2021). DOI: 10.1007/JHEP01(2021)078. URL: [https://doi.org/10.1007/JHEP01\(2021\)078](https://doi.org/10.1007/JHEP01(2021)078).
- [68] D. Chicherin and V. Sotnikov. “Pentagon functions for scattering of five massless particles”. In: *Journal of High Energy Physics* 2020.12 (2020). ISSN: 1029-8479. DOI: 10.1007/jhep12(2020)167. URL: [http://dx.doi.org/10.1007/JHEP12\(2020\)167](http://dx.doi.org/10.1007/JHEP12(2020)167).
- [69] T. Sjöstrand, S. Mrenna, and P. Skands. “A Brief Introduction to PYTHIA 8.1”. In: *Comput. Phys. Commun.* 178 (2008), p. 852. DOI: 10.1016/j.cpc.2008.01.036. arXiv: 0710.3820 [hep-ph].
- [70] M. Bahr et al. “Herwig++ Physics and Manual”. In: *Eur. Phys. J. C* 58 (2008), p. 639. DOI: 10.1140/epjc/s10052-008-0798-9. arXiv: 0803.0883 [hep-ph].
- [71] J. Bellm et al. “Herwig 7.0/Herwig++ 3.0 release note”. In: *Eur. Phys. J. C* 76 (2016), p. 196. DOI: 10.1140/epjc/s10052-016-4018-8. arXiv: 1512.01178 [hep-ph].
- [72] T. Gleisberg et al. “Event generation with SHERPA 1.1”. In: *JHEP* 0902 (2008), p. 007. DOI: 10.1088/1126-6708/2009/02/007. arXiv: 0811.4622 [hep-ph].
- [73] ATLAS Collaboration. *ATLAS Pythia 8 tunes to 7 TeV data*. ATL-PHYS-PUB-2014-021. 2014. URL: <https://cds.cern.ch/record/1966419>.
- [74] S. Platzer and S. Gieseke. “Dipole Showers and Automated NLO Matching in Herwig++”. In: *Eur. Phys. J. C* 72 (2012), p. 2187. DOI: 10.1140/epjc/s10052-012-2187-7. arXiv: 1109.6256 [hep-ph].
- [75] R.D. Field and S. Wolfram. “A QCD Model for e^+e^- Annihilation”. In: *Nucl. Phys. B* 711 (1983), p. 65. DOI: 10.1016/0550-3213(83)90175-X.
- [76] S. Catani et al. “QCD Matrix Elements + Parton Showers”. In: *JHEP* 0111 (2001), p. 063. DOI: 10.1088/1126-6708/2001/11/063. arXiv: hep-ph/0109231.
- [77] R.D. Ball et al., NNPDF Collaboration. “Parton distributions with LHC data”. In: *Nucl. Phys. B* 867 (2013), p. 244. DOI: 10.1016/j.nuclphysb.2012.10.003. arXiv: 1207.1303 [hep-ph].
- [78] L.A. Harland-Lang et al. “Parton distributions in the LHC era: MMHT 2014 PDFs”. In: *Eur. Phys. J. C* 75 (2015), p. 204. DOI: 10.1140/epjc/s10052-015-3397-6. arXiv: 1412.3989 [hep-ph].

- [79] H.-L. Lai et al. “New parton distribution for collider physics”. In: *Phys. Rev. D* 82 (2010), p. 074024. DOI: 10.1103/PhysRevD.82.074024. arXiv: 1007.2241 [hep-ph].
- [80] S. Dulat et al. “New parton distribution functions from a global analysis of quantum chromodynamics”. In: *Phys. Rev. D* 93 (2016), p. 033006. DOI: 10.1103/PhysRevD.93.033006. arXiv: 1506.07443 [hep-ph].
- [81] ATLAS Collaboration. “ATLAS data quality operations and performance for 2015–2018 data-taking”. In: *JINST* 15 (2020), P04003. DOI: 10.1088/1748-0221/15/04/P04003. arXiv: 1911.04632 [physics.ins-det].
- [82] ATLAS Collaboration. “The ATLAS Simulation Infrastructure”. In: *Eur. Phys. J. C* 70 (2010), p. 823. DOI: 10.1140/epjc/s10052-010-1429-9. arXiv: 1005.4568 [physics.ins-det].
- [83] S. Agostinelli et al. “GEANT4 - a simulation toolkit”. In: *Nucl. Instrum. Meth. A* 506 (2003), p. 250. DOI: 10.1016/S0168-9002(03)01368-8.
- [84] R. Frühwirth. “Application of Kalman filtering to track and vertex fitting”. In: *Nuclear Instruments and Methods in Physics Research Section A: Accelerators, Spectrometers, Detectors and Associated Equipment* 262.2 (1987), pp. 444–450. ISSN: 0168-9002. DOI: [https://doi.org/10.1016/0168-9002\(87\)90887-4](https://doi.org/10.1016/0168-9002(87)90887-4). URL: <https://www.sciencedirect.com/science/article/pii/0168900287908874>.
- [85] ATLAS Collaboration. *Vertex Reconstruction Performance of the ATLAS Detector at $\sqrt{s} = 13$ TeV*. ATL-PHYS-PUB-2015-026. 2015. URL: <https://cds.cern.ch/record/2037717>.
- [86] ATLAS Collaboration. “Topological cell clustering in the ATLAS calorimeters and its performance in LHC Run 1”. In: *Eur. Phys. J. C* 77 (2017), p. 490. DOI: 10.1140/epjc/s10052-017-5004-5. arXiv: 1603.02934 [hep-ex].
- [87] ATLAS Collaboration. “Jet reconstruction and performance using particle flow with the ATLAS Detector”. In: *Eur. Phys. J. C* 77 (2017), p. 466. DOI: 10.1140/epjc/s10052-017-5031-2. arXiv: 1703.10485 [hep-ex].
- [88] ATLAS Collaboration. “Jet energy scale and resolution measured in proton–proton collisions at $\sqrt{s} = 13$ TeV with the ATLAS detector”. In: (2020). arXiv: 2007.02645 [hep-ex].
- [89] ATLAS Collaboration. *Determination of the jet energy scale and resolution at ATLAS using Z/ γ -jet events in data at $\sqrt{s} = 8$ TeV*. ATLAS-CONF-2015-057. 2015. URL: <https://cds.cern.ch/record/2059846>.
- [90] ATLAS Collaboration. *TeV-scale jet energy calibration using multijet events including close-by jet effects at the ATLAS experiment*. ATLAS-CONF-2013-003. 2013. URL: <https://cds.cern.ch/record/1504740>.
- [91] ATLAS Collaboration. *Tagging and suppression of pileup jets with the ATLAS detector*. ATLAS-CONF-2014-018. 2014. URL: <https://cds.cern.ch/record/1700870>.
- [92] R. Wigmans. *Calorimetry: energy measurement in particle physics*. Oxford University Press, 2017. URL: <https://cds.cern.ch/record/2280786>.
- [93] ATLAS Collaboration. *Selection of jets produced in 13 TeV proton–proton collisions with the ATLAS detector*. ATLAS-CONF-2015-029. 2015. URL: <https://cds.cern.ch/record/2037702>.

- [94] A. Ali and F. Barreiro. “An $\mathcal{O}(\alpha_s)^2$ calculation of energy-energy correlation in e^+e^- annihilation and comparison with experimental data”. In: *Phys. Lett. B* **118** (1982), p. 155. DOI: [10.1016/0370-2693\(82\)90621-9](https://doi.org/10.1016/0370-2693(82)90621-9).
- [95] A. Ali and F. Barreiro. “Energy-energy correlations in e^+e^- annihilation”. In: *Nucl. Phys. B* **236** (1984), p. 269. DOI: [10.1016/0550-3213\(84\)90536-4](https://doi.org/10.1016/0550-3213(84)90536-4).
- [96] D.G. Richards, W.J. Stirling, and S.D. Ellis. “Second order corrections to the energy-energy correlation function in quantum chromodynamics”. In: *Phys. Lett. B* **119** (1982), p. 193. DOI: [10.1016/0370-2693\(82\)90275-1](https://doi.org/10.1016/0370-2693(82)90275-1).
- [97] E.W. Nigel Glover and M.R. Sutton. “The Energy-energy correlation function revisited”. In: *Phys. Lett. B* **342** (1995), p. 375. DOI: [10.1016/0370-2693\(94\)01354-F](https://doi.org/10.1016/0370-2693(94)01354-F). arXiv: [hep-ph/9410234](https://arxiv.org/abs/hep-ph/9410234).
- [98] N.K. Falck and G. Kramer. “Theoretical studies of energy-energy correlation in e^+e^- annihilation”. In: *Z. Phys. C* **42** (1989), p. 459. DOI: [10.1007/BF01548452](https://doi.org/10.1007/BF01548452).
- [99] S.D. Ellis, D.G. Richards, and W.J. Stirling. “Fixed order perturbation theory and leading logarithms in energy-energy correlations”. In: *Phys. Lett. B* **136** (1984), p. 99. DOI: [10.1016/0370-2693\(84\)92064-1](https://doi.org/10.1016/0370-2693(84)92064-1).
- [100] C. Berger et al., PLUTO Collaboration. “Energy-energy correlations in e^+e^- annihilation into hadrons”. In: *Phys. Lett. B* **99**, 292 (1981). DOI: [10.1016/0370-2693\(81\)91128-X](https://doi.org/10.1016/0370-2693(81)91128-X).
- [101] M.Z. Akrawy et al., OPAL Collaboration. “A measurement of energy correlations and a determination of $\alpha_s(M_{Z^0}^2)$ in e^+e^- annihilations at $\sqrt{s} = 91$ GeV”. In: *Phys. Lett. B* **252**, 159 (1990). DOI: [10.1016/0370-2693\(90\)91098-V](https://doi.org/10.1016/0370-2693(90)91098-V).
- [102] D. Decamp et al., ALEPH Collaboration. “Measurement of α_s from the structure of particle clusters produced in hadronic Z decays”. In: *Phys. Lett. B* **257**, 479 (1991). DOI: [10.1016/0370-2693\(91\)91926-M](https://doi.org/10.1016/0370-2693(91)91926-M).
- [103] B. Adeva et al., L3 Collaboration. “Determination of α_s from energy-energy correlations measured on the Z^0 resonance”. In: *Phys. Lett. B* **257**, 469 (1991). DOI: [10.1016/0370-2693\(91\)91925-L](https://doi.org/10.1016/0370-2693(91)91925-L).
- [104] K. Abe et al., SLD Collaboration. “Measurement of $\alpha_s(M_Z^2)$ from hadronic event observables at the Z^0 resonance”. In: *Phys. Rev. D* **51**, 962 (1995). DOI: [10.1103/PhysRevD.51.962](https://doi.org/10.1103/PhysRevD.51.962).
- [105] D. Schlatter et al., MARKII Collaboration. “Measurement of Energy Correlations in $e^+e^- \rightarrow$ Hadrons”. In: *Phys. Rev. Lett.* **49**, 521 (1982). DOI: [10.1103/PhysRevLett.49.521](https://doi.org/10.1103/PhysRevLett.49.521).
- [106] B. Adeva et al., MARKJ Collaboration. “Model-Independent Second-Order Determination of the Strong-Coupling Constant α_s ”. In: *Phys. Rev. Lett.* **50**, 2051 (1983). DOI: [10.1103/PhysRevLett.50.2051](https://doi.org/10.1103/PhysRevLett.50.2051).
- [107] H.J. Behrend et al., CELLO Collaboration. “On the model dependence of the determination of the strong coupling constant in second order QCD from e^+e^- annihilation into hadrons”. In: *Phys. Lett. B* **138**, 311 (1984). DOI: [10.1016/0370-2693\(84\)91667-8](https://doi.org/10.1016/0370-2693(84)91667-8).
- [108] W. Bartel et al., JADE Collaboration. “Measurements of energy correlations in $e^+e^- \rightarrow$ hadrons”. In: *Z. Phys. C* **25**, 231 (1984). DOI: [10.1007/BF01547922](https://doi.org/10.1007/BF01547922).

- [109] E. Fernández et al., MAC Collaboration. “Measurement of energy-energy correlations in $e^+e^- \rightarrow$ hadrons at $\sqrt{s} = 29$ GeV”. In: *Phys. Rev. D* **31**, 2724 (1985). DOI: 10.1103/PhysRevD.31.2724.
- [110] W. Braunschweig et al., TASSO Collaboration. “A study of energy-energy correlations between 12 and 46.8 GeV c.m. energies”. In: *Z. Phys. C* **36**, 349 (1987). DOI: 10.1007/BF01573928.
- [111] I. Adachi et al., TOPAZ Collaboration. “Measurements of α_s in e^+e^- annihilation at $\sqrt{s} = 53.3$ GeV and 59.5 GeV”. In: *Phys. Lett. B* **227**, 495 (1989). DOI: 10.1016/0370-2693(89)90969-6.
- [112] P. Abreu et al., DELPHI Collaboration. “Energy-energy correlations in hadronic final states from Z^0 decays”. In: *Phys. Lett. B* **252**, 149 (1990). DOI: 10.1016/0370-2693(90)91097-U.
- [113] L.J. Dixon et al. “Analytical Computation of Energy-Energy Correlation at Next-to-Leading Order in QCD”. In: *Phys. Rev. Lett.* **120** (2018), p. 102001. DOI: 10.1103/PhysRevLett.120.102001. arXiv: 1801.03219 [hep-ph].
- [114] M.-x. Luo et al. “Analytic next-to-leading order calculation of energy-energy correlation in gluon-initiated Higgs decays”. In: *JHEP* **06** (2019), p. 037. DOI: 10.1007/JHEP06(2019)037. arXiv: 1903.07277 [hep-ph].
- [115] A.V. Belitsky et al. “Energy-energy correlations in $\mathcal{N} = 4$ SYM”. In: *Phys. Rev. Lett.* **112** (2014), p. 071601. DOI: 10.1103/PhysRevLett.112.071601. arXiv: 1311.6800 [hep-th].
- [116] J.M. Henn et al. “Energy-energy correlation in $\mathcal{N} = 4$ super Yang-Mills theory at next-to-next-to-leading order”. In: *Eur. Phys. D* **100** (2019), p. 036010. DOI: 10.1103/PhysRevD.100.036010. arXiv: 1903.05314 [hep-th].
- [117] D. De Florian and M. Grazzini. “The back-to-back region in e^+e^- energy-energy correlation”. In: *Nucl. Phys. B* **704** (2004), p. 387. DOI: 10.1016/j.nuclphysb.2004.10.051. arXiv: hep-ph/0407241.
- [118] I. Moult and H.X. Zhu. “Simplicity from recoil: the three-loop soft function and factorization for the energy-energy correlation”. In: *JHEP* **08** (2018), p. 160. DOI: 10.1007/JHEP08(2018)160. arXiv: 1801.02627 [hep-ph].
- [119] V. Del Duca et al. “Three-Jet Production in Electron-Positron Collisions at Next-to-Next-to-Leading Order Accuracy”. In: *Phys. Rev. Lett.* **117** (2016), p. 152004. DOI: 10.1103/PhysRevLett.117.152004. arXiv: 1603.08927 [hep-ph].
- [120] Z. Tulipánt, A. Kardos, and G. Somogyi. “Energy-energy correlation in electron-positron annihilation at NNLL + NNLO accuracy”. In: *Eur. Phys. J.C.* **77** (2017), p. 749. DOI: 10.1140/epjc/s10052-017-5320-9. arXiv: 1708.04093 [hep-ph].
- [121] A. Kardos et al. “Precise determination of $\alpha_s(m_Z)$ from a global fit of energy-energy correlation to NNLO+NNLL predictions”. In: *Eur. Phys. J.C.* **78** (2018), p. 498. DOI: 10.1140/epjc/s10052-018-5963-1. arXiv: 1804.09146 [hep-ph].
- [122] L.J. Dixon, I. Moult, and H.X. Zhu. “Collinear limit of the energy-energy correlator”. In: *Phys. Rev. D* **100** (2019), p. 014009. DOI: 10.1103/PhysRevD.100.014009. arXiv: 1905.01310 [hep-ph].

- [123] A. Ali et al. “Transverse Energy-Energy Correlations in Next-to-Leading Order in α_s at the LHC”. In: *Phys. Rev. D* 86 (2012), p. 114017. DOI: 10.1103/PhysRevD.86.114017. arXiv: 1205.1689 [hep-ph].
- [124] A. Gao et al. “Precision QCD Event Shapes at Hadron Colliders: The Transverse Energy-Energy Correlator in the Back-to-Back Limit”. In: *Phys. Rev. Lett.* 123 (2019), p. 062001. DOI: 10.1103/PhysRevLett.123.062001. arXiv: 1901.04497 [hep-ph].
- [125] G. Altarelli. “The development of Perturbative QCD”. In: *World Scientific* (1994). DOI: 10.1142/2300.
- [126] D.J. Gross and F. Wilczek. “Asymptotically Free Gauge Theories”. In: *Phys. Rev. D* 8 (1973), p. 3633. DOI: 10.1103/PhysRevD.8.3633.
- [127] D.E. Kaplan and M.D. Schwartz. “Constraining Light Colored Particles with Event Shapes”. In: *Phys. Rev. Lett.* 101 (2008), p. 022002. DOI: 10.1103/PhysRevLett.101.022002. arXiv: 0804.2477 [hep-ph].
- [128] D. Becciolini et al. “Constraining new coloured matter from ratio of 3- to 2-jets cross sections at the LHC”. In: *Phys. Rev. D* 91 (2015), p. 015010. DOI: 10.1103/PhysRevD.91.015010. arXiv: 1403.7411 [hep-ph].
- [129] J. Llorente and B. Nachman. “Limits on new coloured fermions using precision jet data from the LHC”. In: *Nucl. Phys. B* 936 (2018), p. 106. DOI: 10.1016/j.nuclphysb.2018.09.008. arXiv: 1807.00894 [hep-ph].
- [130] M. Rubin, G.P. Salam, and S. Sapeta. “Giant QCD K-factors beyond NLO”. In: *JHEP* 1009 (2010), p. 084. DOI: 10.1007/JHEP09(2010)084. arXiv: 1006.2144 [hep-ph].
- [131] ATLAS Collaboration. “Measurement of Dijet Azimuthal Decorrelations in pp Collisions at $\sqrt{s} = 7$ TeV”. In: *Phys. Rev. Lett.* 106 (2011), p. 172002. DOI: 10.1103/PhysRevLett.106.172002. arXiv: 1102.2696 [hep-ex].
- [132] ATLAS Collaboration. “Measurements of jet vetoes and azimuthal decorrelations in dijet events produced in pp collisions at $\sqrt{s} = 7$ TeV using the ATLAS detector”. In: *Eur. Phys. J. C* 74 (2014), p. 3117. DOI: 10.1140/epjc/s10052-014-3117-7. arXiv: 1407.5756 [hep-ex].
- [133] G. D’Agostini. “A multidimensional unfolding method based on Bayes’ theorem”. In: *Nucl. Instrum. Meth. A* 362 (1995), p. 487. DOI: 10.1016/0168-9002(95)00274-X.
- [134] T. Adye. “Ufolding algorithms and test using RooUnfold”. In: *Proceedings of the PHYSTAT 2011 Workshop, CERN Geneva, Switzerland, CERN-2011-006* (2011), p. 313. arXiv: 1105.1160 [[physics.data-an]]. URL: <http://cdsweb.cern.ch/record/1306523>.
- [135] ATLAS Collaboration. “Jet energy scale measurements and their systematic uncertainties in proton–proton collisions at $\sqrt{s} = 13$ TeV with the ATLAS detector”. In: *Phys. Rev. D* 96 (2017), p. 072002. DOI: 10.1103/PhysRevD.96.072002. arXiv: 1703.09665 [hep-ex].
- [136] R.D. Ball et al., NNPDF Collaboration. “Parton distributions with LHC data Run II”. In: *JHEP* 04 (2015), p. 040. DOI: 10.1007/JHEP04(2015)040. arXiv: 1410.8849 [hep-ph].

- [137] S. Dulat et al. “New CTEQ global analysis of quantum chromodynamics with high-precision data from the LHC”. In: *Phys. Rev. D* 103 (2021), p. 014013. DOI: 10.1103/PhysRevD.103.014013. arXiv: 1912.10053 [hep-ph].
- [138] J. Currie et al. “Infrared sensitivity of single jet inclusive production at hadron colliders”. In: *JHEP* 10 (2018), p. 155. DOI: 10.1007/JHEP10(2018)155. arXiv: 1807.03692 [hep-ph].
- [139] R. Corke and T. Sjöstrand. “Interleaved Parton Showers and Tuning Prospects”. In: *JHEP* 03 (2011), p. 032. DOI: 10.1007/JHEP03(2011)032.
- [140] S. Forte and Z. Kassabov. “Why α_s cannot be determined from hadronic processes without simultaneously determining the parton distributions”. In: *Eur. Phys. J. C* 80.182 (2020). DOI: 10.1140/epjc/s10052-020-7748-6. URL: <https://doi.org/10.1140/epjc/s10052-020-7748-6>.
- [141] ATLAS Collaboration. “Measurement of dijet azimuthal decorrelations in pp collisions at $\sqrt{s} = 8$ TeV with the ATLAS detector and determination of the strong coupling”. In: *Phys. Rev. D* 98 (2018), p. 092004. DOI: 10.1103/PhysRevD.98.092004. arXiv: 1805.04691 [hep-ex].
- [142] CMS Collaboration. “Measurement of the inclusive 3-jet production differential cross section in proton–proton collisions at 7 TeV and determination of the strong coupling constant in the TeV range”. In: *Eur. Phys. J. C* 75 (2015), p. 186. DOI: 10.1140/epjc/s10052-015-3376-y. arXiv: 1412.1633 [hep-ex].
- [143] CMS Collaboration. “Determination of the top-quark pole mass and strong coupling constant from the $t\bar{t}$ production cross section in pp collisions at $\sqrt{s} = 7$ TeV”. In: *Phys. Lett. B* 728 (2014), p. 496. DOI: 10.1016/j.physletb.2013.12.009. arXiv: 1307.1907 [hep-ex].
- [144] CMS Collaboration. “Measurement of the ratio of the inclusive 3-jet cross section to the inclusive 2-jet cross section in pp collisions at $\sqrt{s} = 7$ TeV and first determination of the strong coupling constant in the TeV range”. In: *Eur. Phys. J. C* 73 (2013), p. 2604. DOI: 10.1140/epjc/s10052-013-2604-6. arXiv: 1304.7498 [hep-ex].
- [145] CMS Collaboration. “Measurement and QCD analysis of double-differential inclusive jet cross sections in pp collisions at $\sqrt{s} = 8$ TeV and cross section ratios to 2.76 and 7 TeV”. In: *JHEP* 03 (2017), p. 156. DOI: 10.1007/JHEP03(2017)156. arXiv: 1609.05331 [hep-ex].
- [146] V.M. Abazov et al., D0 Collaboration. “Measurement of angular correlations of jets at $\sqrt{s} = 1.96$ TeV and determination of the strong coupling at high momentum transfers”. In: *Phys. Rev. B* 718 (2012), p. 56. DOI: 10.1016/j.physletb.2012.10.003. arXiv: 1207.4957 [hep-ex].
- [147] V.M. Abazov et al., D0 Collaboration. “Determination of the strong coupling constant from the inclusive jet cross section in $p\bar{p}$ collisions at $\sqrt{s} = 1.96$ TeV”. In: *Phys. Rev. D* 80 (2009), p. 111107. DOI: 10.1103/PhysRevD.80.111107. arXiv: 0911.2710 [hep-ex].
- [148] CMS Collaboration. “Measurement of $t\bar{t}$ normalised multi-differential cross sections in pp collisions at $\sqrt{s} = 13$ TeV, and simultaneous determination of the strong coupling strength, top quark pole mass, and parton distribution

Bibliography

- functions”. In: *Eur. Phys. J. C* 80 (2020), p. 658. DOI: 10.1140/epjc/s10052-020-7917-7. arXiv: 1904.05237 [hep-ex].
- [149] CMS Collaboration. “Determination of the strong coupling constant $\alpha_S(m_Z)$ from measurements of inclusive W^\pm and Z boson production cross sections in proton–proton collisions at $\sqrt{s} = 7$ and 8 TeV”. In: *JHEP* 06 (2020), p. 018. DOI: 10.1007/JHEP06(2020)018. arXiv: 1912.04387 [hep-ex].
- [150] CMS Collaboration. “Measurement of the $t\bar{t}$ production cross section, the top quark mass, and the strong coupling constant using dilepton events in pp collisions at $\sqrt{s} = 13$ TeV”. In: *Eur. Phys. J. C* 79 (2019), p. 368. DOI: 10.1140/epjc/s10052-019-6863-8. arXiv: 1812.10505 [hep-ex].
- [151] CMS Collaboration. “Measurement and QCD analysis of double-differential inclusive jet cross sections in proton-proton collisions at $\sqrt{s} = 13$ TeV”. In: *JHEP* 02 (2022), p. 142. DOI: 10.1007/JHEP02(2022)142. arXiv: 2111.10431 [hep-ex].

